frontiers | Research Topics

13th international congress on extremophiles: From extremophilic biomolecules and microorganisms to biotechnological and sustainable applications

Edited by
Isaac Cann and Melina Kerou

Coordinated by
Simone Antonio De Rose and Mohea Couturier

Published in
Frontiers in Microbiology

ISSN 1664-8714
ISBN 978-2-8325-4940-7
DOI 10.3389/978-2-8325-4940-7

About Frontiers

Frontiers is more than just an open access publisher of scholarly articles: it is a pioneering approach to the world of academia, radically improving the way scholarly research is managed. The grand vision of Frontiers is a world where all people have an equal opportunity to seek, share and generate knowledge. Frontiers provides immediate and permanent online open access to all its publications, but this alone is not enough to realize our grand goals.

Frontiers journal series

The Frontiers journal series is a multi-tier and interdisciplinary set of open-access, online journals, promising a paradigm shift from the current review, selection and dissemination processes in academic publishing. All Frontiers journals are driven by researchers for researchers; therefore, they constitute a service to the scholarly community. At the same time, the *Frontiers journal series* operates on a revolutionary invention, the tiered publishing system, initially addressing specific communities of scholars, and gradually climbing up to broader public understanding, thus serving the interests of the lay society, too.

Dedication to quality

Each Frontiers article is a landmark of the highest quality, thanks to genuinely collaborative interactions between authors and review editors, who include some of the world's best academicians. Research must be certified by peers before entering a stream of knowledge that may eventually reach the public - and shape society; therefore, Frontiers only applies the most rigorous and unbiased reviews. Frontiers revolutionizes research publishing by freely delivering the most outstanding research, evaluated with no bias from both the academic and social point of view. By applying the most advanced information technologies, Frontiers is catapulting scholarly publishing into a new generation.

What are Frontiers Research Topics?

Frontiers Research Topics are very popular trademarks of the *Frontiers journals series*: they are collections of at least ten articles, all centered on a particular subject. With their unique mix of varied contributions from Original Research to Review Articles, Frontiers Research Topics unify the most influential researchers, the latest key findings and historical advances in a hot research area.

Find out more on how to host your own Frontiers Research Topic or contribute to one as an author by contacting the Frontiers editorial office: frontiersin.org/about/contact

13th international congress on extremophiles: From extremophilic biomolecules and microorganisms to biotechnological and sustainable applications

Topic editors
Isaac Cann — University of Illinois at Urbana-Champaign, United States
Melina Kerou — University of Vienna, Austria

Topic coordinators
Simone Antonio De Rose — University of Exeter, United Kingdom
Mohea Couturier — UniLaSalle, France

Citation
Cann, I., Kerou, M., De Rose, S. A., Couturier, M., eds. (2024). *13th international congress on extremophiles: From extremophilic biomolecules and microorganisms to biotechnological and sustainable applications*. Lausanne: Frontiers Media SA.
doi: 10.3389/978-2-8325-4940-7

Table of contents

frontiers | Frontiers in Microbiology

TYPE Editorial
PUBLISHED 15 May 2024
DOI 10.3389/fmicb.2024.1414760

OPEN ACCESS

EDITED AND REVIEWED BY
Andreas Teske,
University of North Carolina at Chapel Hill, United States

*CORRESPONDENCE
Melina Kerou
melina.kerou@univie.ac.at

RECEIVED 09 April 2024
ACCEPTED 17 April 2024
PUBLISHED 15 May 2024

CITATION
Couturier M, De Rose SA, Cann I and Kerou M (2024) Editorial: 13th international congress on extremophiles: from extremophilic biomolecules and microorganisms to biotechnological and sustainable applications. *Front. Microbiol.* 15:1414760. doi: 10.3389/fmicb.2024.1414760

Editorial: 13th international congress on extremophiles: from extremophilic biomolecules and microorganisms to biotechnological and sustainable applications

Mohea Couturier[1], Simone Antonio De Rose[2], Isaac Cann[3] and Melina Kerou[4]*

[1]Département de la recherche et de l'innovation, Institut Polytechnique UniLaSalle, Beauvais, France, [2]The Henry Wellcome Building for Biocatalysis, Biosciences, College of Life and Environmental Sciences, University of Exeter, Exeter, United Kingdom, [3]Carl R. Woese Institute for Genomic Biology, University of Illinois Urbana–Champaign, Urbana, IL, United States, [4]Department of Functional and Evolutionary Ecology, Faculty of Life Sciences, University of Vienna, Vienna, Austria

KEYWORDS

extremophiles, biotechnology, origin of life, astrobiology, microbiology

Editorial on the Research Topic
13th international congress on extremophiles: from extremophilic biomolecules and microorganisms to biotechnological and sustainable applications

Extremophilic environments are routinely exposed to extreme environmental conditions, such as boiling/freezing temperatures, acidic/alkaline pH, high salinity, high pressure, or the presence of toxic substances, where conventional life forms might struggle to survive. These environments are often found in parts of the Earth with inclement conditions, such as deep-sea hydrothermal vents, acidic hot springs, polar ice caps, and hypersaline lakes. Extremophiles are organisms that thrive and adapt to these extreme conditions, demonstrating remarkable resilience and adaptation strategies. These extremophilic microorganisms, based on their living traits, provide insights into the conditions that may have prevailed on early Earth as the planet underwent dramatic environmental changes during its early history. Extremophiles therefore help us understand how life could have emerged and adapted to these extreme conditions. The search for extremophilic niches on Earth, and by extension the study of the associated microbial communities, serve as a model for potential habitats that astrobiology might explore in search for extraterrestrial life signatures. Extremophilic environments are also among the regions most affected by climate change, rendering their study essential in order to understand the impact of changing environmental parameters on microbial communities.

Extremophiles often produce unique biomolecules and enzymes adapted to extreme conditions, called extremolytes and extremozymes, respectively. Extremozymes, for example, can be used in various biocatalytic processes due to their stability under harsh conditions, leading to more efficient and sustainable industrial practices. Indeed, extremophilic enzymes may enhance the efficiency of biofuel production, wastewater treatment, synthesis of pharmaceuticals, and bioremediation efforts to environments contaminated with toxic substances.

Enzymes, antimicrobial peptides, and other bioactive compounds from extremophiles may serve as sources for the development of novel pharmaceuticals. Importantly, these molecules may have unique properties that make them effective in combating diseases.

This Research Topic was launched in collaboration with the 13th International Congress on Extremophiles[1], which took place on September 18–22 in Loutraki, Greece. This International Congress series, supported by the International Society for Extremophiles[2] aims to promote the latest advances and state-of-the-art research on basic and applied aspects of life in extreme environments. Within this topic, 10 articles have been published not only presenting microbial communities thriving in extremophilic environments but also the biomolecules sustaining such extremophilic lifestyle.

Learning about extremophilic traits starts by characterizing extremophilic environments. The goal is to unravel the role of distinct environmental drivers in such environments which can selectively determine the composition and activity of the resident microbial communities. This Research Topic includes studies presenting the community composition and investigating environmental drivers from radically diverse extremophilic environments such as sub-seafloor hydrothermal sediments of a volcanic field in the Mediterranean sea (Polymenakou et al.) and altitudinal transects of Antarctic valleys (Mashamaite et al.). Polymenakou et al. confirm that high temperature and availability of chemical energy in the form of electron donors and acceptors are major drivers of community structure and diversity, and uncover widespread adaptation strategies to heat stress such as the formation of endospores. Mashamaite et al., 2023 reveal the importance of altitude as a driver of prokaryotic and eukaryotic community structure in Antarctic ice-free soil habitats, resulting in clear distinction between trophic strategies at different altitudes. Among others, an important adaptation and survival strategy for such oligotrophic environments was found to be the capability for oxidation of trace-gases (trace-gas chemotrophy), with the respective taxa being identified as potential keystone taxa for soil communities at higher altitudes.

Taking the reverse approach and studying the distribution, genomic and physiological diversity and potential within a single lineage can also enable us to characterize extremophilic traits. This is the case of the study from Jiang et al., which investigated the distribution of the genus *Solirubrobacter*, showing the enrichment of the genus in arid deserts and high-altitude ecosystems that receive strong solar radiation, but also in the rhizosphere of various plants. Comparative genomic analyses subsequently revealed various molecular mechanisms for counteracting UV radiation, desiccation and osmotic stress, and offer intriguing hypotheses regarding their putatively beneficial role in plant health promotion.

Perhaps the most studied environmental driver for extreme ecosystems is temperature. The report by Lehmann et al. intriguingly challenges the basic assumptions of the study of thermophilic adaptations—that they evolved from a non-thermophilic background. Turning the tables, the study builds upon the widely accepted hypothesis that LUCA may have been a (moderate) thermophile, in which case mesophily would be considered the derived trait. To investigate the molecular evolutionary mechanisms of such a scenario, they subject a thermophilic bacterium with a proposed ancient metabolism (acetogenesis) to adaptive laboratory evolution by continuous cultivation at suboptimal low temperature and map the phenotypic changes that occur.

In addition to physiological investigations, "-omics" approaches can be very useful in extremophilic research in order to provide insights into the molecular mechanisms of adaptations, but their use is often plagued by technical difficulties due to the nature of the samples. Favreau et al. develop methods for -omics analyses of halite samples, and use proteomics to investigate the physiological changes during early acclimation of a model haloarchaeon to halite brine inclusions. Contrary to previous assumptions, the analyzed proteomes of *Halobacterium salinarum* reflect a slowdown in cellular activity and not a stress response during acclimation to the halite environment.

Biochemical characterization of extremophilic enzymes enable us to further deepen our understanding of the molecular mechanisms and trade-offs between stability and activity at extreme conditions, as well as offering candidates for industrial applications. In this Research Topic, the characterization of a novel intracellular subtilisin protease from the bacterium *Planococcus halocryophilus* Or1, metabolically active down to −25°C, is reported by Rasmussen et al., while De Rose et al. report the characterization of a novel cyclic 2,3-diphosphoglycerate synthetase involved in extremolyte production in the archaeon *Methanothermus fervidus*, reflecting the long-standing interest in understanding cellular responses to extreme temperatures. The challenges of overcoming radiation and desiccation stress are addressed by Rollo et al., in a study which aimed to unravel the role of endonuclease III-like enzymes in oxidative stress.

A deeper understanding of the molecular strategies involved in extremophilic adaptations is crucial to addressing societal issues such as toxic compounds contamination. The respective studies of the mechanisms involved in cesium and arsenic resistance offer impressive ways to develop bioremediation projects (Ishida et al. and Gouveia et al. respectively).

Conclusions

This collection of articles reveals the deep connections between basic and applied research in extremophiles and extremophilic environments. We maintain the notion that the understanding of extremophilic traits is crucial to developing future innovations. Extremophiles offer a rich source of novel biomolecules and enzymes with diverse applications in biotechnology, industrial processes, energy production, and healthcare. By tapping into the capabilities of extremophiles, researchers can contribute to the development of sustainable and innovative solutions that address global challenges and shed light on the process of origin of life on Earth. We anticipate that novel findings and studies, which will be presented during the 14th International Congress on Extremophiles[3] (September 22-26 2024, Loutraki, Greece), will open the road for future breakthroughs.

1 https://www.extremophiles2022.org/

2 https://extremophiles.org/

3 http://www.extremophiles2024.org/

Author contributions

MC: Conceptualization, Investigation, Writing – original draft, Writing – review & editing. SD: Conceptualization, Investigation, Writing – original draft, Writing – review & editing. IC: Writing – original draft, Writing – review & editing. MK: Conceptualization, Investigation, Writing – original draft, Writing – review & editing.

Funding

The author(s) declare that no financial support was received for the research, authorship, and/or publication of this article.

Acknowledgments

We thank the Organizing Committee and the Congress Chair of the 13th International Congress on Extremophiles, Professor Konstantinos Vorgias, for organization of this inspiring conference. Additionally, we thank the International Society for Extremophiles for their constant support toward young researchers entering this exciting field.

Conflict of interest

The authors declare that the research was conducted in the absence of any commercial or financial relationships that could be construed as a potential conflict of interest.

The author(s) declared that they were an editorial board member of Frontiers, at the time of submission. This had no impact on the peer review process and the final decision.

Publisher's note

frontiers | Frontiers in Microbiology

TYPE Original Research
PUBLISHED 26 January 2023
DOI 10.3389/fmicb.2022.1075274

OPEN ACCESS

EDITED BY
Melina Kerou,
University of Vienna,
Austria

REVIEWED BY
Cesar Perez-Fernandez,
Johns Hopkins University,
United States
Melanie R. Mormile,
Missouri University of Science and Technology, United States

*CORRESPONDENCE
Adrienne Kish
✉ adrienne.kish@mnhn.fr

SPECIALTY SECTION
This article was submitted to Extreme Microbiology, a section of the journal Frontiers in Microbiology

RECEIVED 20 October 2022
ACCEPTED 22 December 2022
PUBLISHED 26 January 2023

CITATION
Favreau C, Tribondeau A, Marugan M, Guyot F, Alpha-Bazin B, Marie A, Puppo R, Dufour T, Huguet A, Zirah S and Kish A (2023) Molecular acclimation of *Halobacterium salinarum* to halite brine inclusions.
Front. Microbiol. 13:1075274.
doi: 10.3389/fmicb.2022.1075274

Molecular acclimation of *Halobacterium salinarum* to halite brine inclusions

Charly Favreau[1], Alicia Tribondeau[2], Marie Marugan[1], François Guyot[3], Beatrice Alpha-Bazin[4], Arul Marie[1], Remy Puppo[1], Thierry Dufour[5], Arnaud Huguet[6], Séverine Zirah[1] and Adrienne Kish[1]*

[1]Unité Molécules de Communication et Adaptation des Microorganismes (MCAM), Muséum National d'Histoire Naturelle (MNHN), CNRS, Paris, France, [2]Unité Physiologie Moléculaire et Adaptation (PhyMA), MNHN, CNRS, Paris, France, [3]Institut de Minéralogie, de Physique des Matériaux et de Cosmochimie (IMPMC), MNHN, Sorbonne Université, CNRS, IRD, Paris, France, [4]Département Médicaments et Technologies pour la Santé (DMTS), Université Paris-Saclay, CEA, INRAE, SPI, Bagnols-sur-Cèze, France, [5]Laboratoire de Physique des Plasma (LPP), Sorbonne Université, CNRS, École Polytechnique, Université Paris-Sud, Observatoire de Paris, Paris, France, [6]Unité Milieux Environnementaux Transferts et Interactions dans les hydrosystèmes et les Sols (METIS), Sorbonne Université, CNRS, EPHE, PSL, Paris, France

Halophilic microorganisms have long been known to survive within the brine inclusions of salt crystals, as evidenced by the change in color for salt crystals containing pigmented halophiles. However, the molecular mechanisms allowing this survival has remained an open question for decades. While protocols for the surface sterilization of halite (NaCl) have enabled isolation of cells and DNA from within halite brine inclusions, "-omics" based approaches have faced two main technical challenges: (1) removal of all contaminating organic biomolecules (including proteins) from halite surfaces, and (2) performing selective biomolecule extractions directly from cells contained within halite brine inclusions with sufficient speed to avoid modifications in gene expression during extraction. In this study, we tested different methods to resolve these two technical challenges. Following this method development, we then applied the optimized methods to perform the first examination of the early acclimation of a model haloarchaeon (*Halobacterium salinarum* NRC-1) to halite brine inclusions. Examinations of the proteome of *Halobacterium* cells two months post-evaporation revealed a high degree of similarity with stationary phase liquid cultures, but with a sharp down-regulation of ribosomal proteins. While proteins for central metabolism were part of the shared proteome between liquid cultures and halite brine inclusions, proteins involved in cell mobility (archaellum, gas vesicles) were either absent or less abundant in halite samples. Proteins unique to cells within brine inclusions included transporters, suggesting modified interactions between cells and the surrounding brine inclusion microenvironment. The methods and hypotheses presented here enable future studies of the survival of halophiles in both culture model and natural halite systems.

KEYWORDS

***Halobacterium*, halophile, LC-MS, proteomics, halite (NaCl)**

1. Introduction

Extremely halophilic archaea are adapted to the highest possible salinity conditions, thriving in saturated brines. Microbial diversity in such environments is highly reduced and tends to be dominated by haloarchaea (Oren, 2006). Saturated brines are characterized by a low dissolved oxygen content at the surface despite their contact with air (Sherwood et al., 1991). The surface of saturated brines is often exposed to high temperatures and high levels of solar radiation (Oren, 2006; Merino et al., 2019), which can lead to evaporation. During evaporation events, the total contents of the brine, including salts, organics, some atmospheric gases, and any microorganisms present, are trapped within inclusions in the salt crystals. Viable halophilic bacteria and archaea have been isolated from halite (NaCl) of various ages, from months to years (Norton and Grant, 1988; Gramain et al., 2011; Huby et al., 2020), to geologically relevant timescales with the age of the primary halite given by the surrounding geological matrix. Some studies have even reported the observation or isolation of microorganisms from halite dated to several hundreds of millions of years (Vreeland et al., 2000; Schreder-Gomes et al., 2022). These observations have raised two important questions: (1) are these truly "ancient" cells? (2) what physiological changes are required for microbial cells to remain viable within halite brine inclusions?

The first question has been studied in greater detail, and while many questions still remain, these studies provided valuable insights into the potential for surface-contaminant microorganisms (Graur and Pupko, 2001; Maughan et al., 2002; Nickle et al., 2002). In response to these criticisms, appropriate surface sterilization and cleaning procedures for microbial cultivation and DNA isolation for micro-biodiversity studies from dissolved ancient halite (Gramain et al., 2011; Sankaranarayanan et al., 2011) were developed. These approaches enabled more accurate identification of only those microorganisms trapped within halite inclusions. Another opened question is whether the age determined from the geological context in which primary halite crystals were found can accurately be applied directly to the microorganisms in the brine inclusions (Hazen and Roedder, 2001). Dissolution and recrystallization of halite over geological time scales may contribute to the presence of more modern microorganisms (see discussion in Winters et al., 2015 and references therein). No known microbial survival mechanism to date can account for cell viability over millions of years. Some studies have examined the possibility that microbial cell-like biomorphs are preserved within brine inclusions (Nims et al., 2021).

An alternative approach is to experimentally confirm how microbial life is supported within brine inclusions over durations known to support viable microorganisms. Determining the cellular functions expressed by viable halophiles within halite brine inclusions requires the direct isolation of biomolecules such as proteins and nucleic acids for "-omics" analyses, including proteomics and transcriptomics. However, significant technical challenges are presented by the closed system of brine inclusions within halite. Accessing the contents of brine inclusions by rapid crystal dissolution leads to cell lysis by osmotic shock and biomolecule degradation, while the time required for gradual crystal dissolution preserving cellular integrity is also sufficient for alterations in the transcriptomes and proteomes of viable cells away from their state within the brine inclusions. In addition, the direct extraction of biomolecules from brine inclusions involves a large amount of NaCl, which is incompatible with direct mass spectrometry analysis due to the lack of sufficient desalination steps in standard protocols. Although current hypotheses concerning the modifications of halophile physiology during entrapment within halite brine inclusions include a change to anaerobic metabolism (Winters et al., 2015) along with potential for cell envelope modifications depending on conditions (Fendrihan et al., 2012; Kixmüller and Greie, 2012), these remain largely unverified at the molecular level due to these experimental challenges. New methods are needed to isolate proteins and other biomolecules directly from halite brine inclusions, without allowing the microorganisms to alter their gene expression during salt dissolution and processing. The development of a new analytical workflow compatible with "-omics" analyses is best conducted with a known model organism for which there is a large repertoire of physiological studies and multi-omics data for liquid cultures exposed to a range of conditions applicable to halite brine inclusions (different oxygen availabilities, salinities, nutrient availabilities, etc.). For these reasons, we choose the model haloarchaeon *Halobacterium salinarum*, the type strain of the *Halobacteriales* family (Gruber et al., 2004; Oren et al., 2009).

Halobacterium salinarum is an appropriate model as it is found both in contemporary NaCl-saturated aqueous environments such as Great Salt Lake (Post, 1977) and has been detected in halite and closely related to isolates from ancient salt deposit (Mormile et al., 2003) The red pigmentation of *H. salinarum* strain is directly correlated with transmembrane proteins (bacteriorhodopsin and halorhodopsin) and carotenoids (bacterioruberin) also used by cells as antioxidants (Eichler, 2019). The accumulation of high intracellular concentrations of potassium (K^+) and chloride (Cl^-) (Engel and Catchpole, 2005), needed to maintain osmotic homeostasis, induces both biochemical adaptations (in the form of a strongly acidic proteome) as well as technical challenges to desalt cellular extracts. *Halobacterium salinarum* survives in changing environments by using a complex variable energetic metabolism with a preference for aerobic respiration but is capable of switching to phototrophy *via* bacteriorhodopsin, arginine fermentation or anaerobic respiration using dimethyl sulfoxide (DMSO) and trimethylamine oxide (TMAO) if available (Hartmann et al., 1980; Müller and DasSarma, 2005; Falb et al., 2008; Gonzalez et al., 2009). This type of switch occurs under low oxygen conditions such as during increasing salinity linked to water evaporation. Moreover, according to Orellana et al. (2013), *H. salinarum* also seems to be able to use glycerol derived from microalgae of the genus *Dunaliella* as a source of carbon under certain specific conditions (in liquid co-culture condition with viable *Dunaliella* with high illumination over a set diurnal cycle

and nitrate-limiting conditions). Established multi-omics protocols for liquid cultures of *H. salinarum* have permitted analyses of the cellular responses to a broad range of environmental conditions, including variations in NaCl (Leuko et al., 2009), pH (Moran-Reyna and Coker, 2014), oxygen (Schmid et al., 2007), and temperature (Coker et al., 2007), all relevant to halite brine inclusions. This existing knowledge base far exceeds that developed to date for halophiles isolated directly from ancient halite.

Here we present an efficient new analytical method for the study of microorganisms within halite, validated using *H. salinarum* entrapped in laboratory-grown halite to probe the question of what physiological changes are required for microbial cells to remain viable within halite brine inclusions, focusing on the initial phase of halite entrapment. The developed workflow includes removal of not only surface-attached cells and nucleic acids but also proteins, with subsequent extraction and desalting of proteins directly from brine inclusions compatible with mass spectrometry analyses. Applying these methods, we determined the acclimation of *H. salinarum* cells to inclusions at molecular level within laboratory-grown halite by analyzing the differences in the expressed proteome prior to evaporation and 2 months after culture evaporation. Analyses focused on the characterization of cellular activity compared to stationary cells not trapped within halite, as well as the interactions of cells with halite brine inclusion environment.

2. Materials and methods

All reagents used were analytical grade and suitable for molecular biology.

2.1. Strain and culture conditions

Halobacterium salinarum strain NRC-1 (JCM 11081) was grown under oxic conditions in autoclaved complex medium (CM: 4.28 M NaCl, 81 mM $MgSO_4.7H_2O$, 27 mM KCl, 10 mM trisodium-citrate.$2H_2O$, 1% (w/v) peptone Oxoïd® LP0034, pH adjusted to 7.4) following Oesterhelt and Stoeckenius (1974) at 37°C, 180 rpm in glassware washed and then rinsed multiple times in MilliQ® water with vigorous shaking to remove all traces of detergents that can inhibit the growth of haloarchaea. Growth was monitored by spectrophotometry at 600 nm (OD_{600}). Cultures for crystallizations and protein extractions were grown to stationary phase (OD_{600} = 1.0–1.6) avoiding decline phase to approximate the physiological condition of haloarchaea under natural conditions during evaporation.

2.2. Laboratory-grown halite

2.2.1. Internally inoculated halite

Modeling entombment of haloarchaea within halite was already done in laboratory by Norton and Grant (1988), Gramain et al. (2011), and Kixmüller and Greie (2012). In this study, laboratory-grown halite crystals were produced following a modified version of protocols of Fendrihan et al. (2012), by adding nutrients to their Tris-buffered NaCl solution (TN buffer; 100 mM Tris–HCl pH 7.4, 4.28 M NaCl) to simulate organic matter and nutrients in the natural environment just prior to halite precipitation (Winters et al., 2015). Briefly, *H. salinarum* cells in stationary growth phase were harvested by centrifugation at 7,500*g*, 10 min, 20°C and the growth medium removed by washing with sterile TN buffer. Cells were then resuspended in sterile TNPA buffer (TN buffer with 1% (w/v) Oxoïd® peptone LP0034 and 0.5% (w/v) L-Arg HCl, adjusted pH 7.4) with a ratio of 10 mL TNPA buffer per 500 mg of cells (wet weight, equal to 9.6×10^{11} cells). Then 20 mL TNPA crystallization buffer containing 3.2×10^{11} cells was evaporated in each sterile 90/14.3 mm Petri dish in a 37°C with a 12 h:12 h light: dark photoperiod (66.75 µmol photons. $m^{-2}.s^{-2}$, verified by a Li-250A, Li-Cor Inc., Germany) to model natural brine-surfaces. Complete evaporation and drying of precipitated halite were obtained after ~22 days, followed by a further 60 days (2 months) of incubation to study the early phase of *H. salinarum* entombment within halite brine inclusions.

2.2.2. Externally inoculated halite

To produce halite with *H. salinarum* cells localized exclusively at the halite surface, 20 mL of sterile TN buffer was first evaporated as described above until complete drying (~22 days). The resultant crystals were then collected aseptically using sterilized forceps and the surfaces of each crystal inoculated with 9×10^9 *H. salinarum* cells in stationary phase, applied as a highly concentrated cell solution after centrifugation (7,500*g*, 10 min, room temperature, RT°C). Crystals were inoculated on the largest faces (designated here as "top" and "bottom") by first inoculating the "top" face with 4.5×10^9 cells drop-by-drop and spreading out using a sterile inoculating loop. Halite were then dried overnight at 37°C, followed by the "bottom" face the next day with the same protocol.

2.3. Scanning electron microscopy

Observations and analyses of halite crystals were performed by first attaching the crystals directly to aluminum supports with carbon tape followed by carbon thin coating. Observations were performed using a Zeiss Ultra 55 field emission gun scanning electron microscope (SEM-FEG) equipped with a Brucker Energy dispersive X-ray spectroscopy (EDX) QUANTAX detector. Secondary and backscattered electron images and EDX analyses and maps were obtained at 10 kV and a working distance of 7.5 mm.

2.4. Post-evaporation cellular viability tests

To assess cell viability after halite inclusion, salt crystals were weighted to determine the appropriated NaCl concentration

required for the complex medium to obtain a final concentration of 4.28 M after halite dissolution as previously described by Gramain et al. (2011). Halite and complex medium were then incubated at 37°C, 180 rpm. After crystal dissolution, culture OD_{600} was measured by spectrophotometry. Pigmented (red) cultures reaching a normal stationary phase culture ($OD_{600} > 1.0$) were classified as viable and cultures showing no increase in OD_{600} after 1 month ($OD_{600} < 0.1$) were classified as non-viable.

2.5. Halite surface cleaning (removal of cells and proteins)

2.5.1. Cold atmospheric plasma treatment

Cold atmospheric plasmas (i.e., weakly ionized gases) were generated were generated using either a dielectric barrier device (DBD) or an atmospheric pressure plasma jet (APPJ). They were polarized to the high voltage using two types of electrical power supply: (1) an alternative current (AC) generator composed of a function generator (ELC, GF467AF) and a power amplifier (Crest Audio, CC5500) as well as (2) a pulse generator (RLC electronic Company, NanoGen1 model) coupled with a high voltage power supply (Spellman company, SLM 10 kV 1,200 W model). DBD and APPJ were supplied with different a carrier gas (helium or argon) with/without oxygen. Hence several plasma conditions were performed to produce active species (radicals, reactive oxygen species but also electrons and photons). The Table 1 details the experimental plasma conditions that were investigated as well as the resulting proteolysis to assess the efficiency of protein removal.

2.5.2. Chemical treatments

Previous studies applied surface cleaning protocols developed for removal of cells and nucleic acids, as detailed in Supplementary Table 1-1. To adapt these protocols for the removal of surface-bound proteins, we modified the protocol of Sankaranarayanan et al. (2011) using shorter time for baths to avoid dissolution of smaller laboratory-grown crystals. Briefly, crystals were incubated in successive 5 min baths: 4.00%–4.99% NaOCl (Honeywell Research Chemicals; avoiding commercial bleach solutions that induced rapid and near-complete crystal dissolution) in saturated NaCl and 10 M NaOH in saturated NaCl supplied or not with 10 N HCl followed by 100 mM Na_2CO_3 in saturated NaCl. A sterile saturated NaCl was used to wash off each treatment solution between each successive bath, testing both passive wash baths and active-spray washes using a hemolytic pump.

2.6. Protein extraction and preliminary desalting

We optimized a protocol for protein extraction directly from halite crystals using TRIzol Reagent™ (Ambion, Life Technologies). TRIzol allows for the sequential separation of RNA and DNA prior to protein extraction (see Supplementary Figure 2-1). The protocol described below was based on both the manufacturer's protocol and that of Kirkland et al. (2006) used for protein extractions from liquid cultures of *Haloferax volcanii*. All steps described were performed with autoclaved glassware to avoid any organics contamination from plastics (bench top protocol see Supplementary Information Section 2). All solvents used for protein extractions were HPLC-grade and suitable for mass spectrometry analysis. Crystals were fully immersed in 5 mL of TRIzol reagent in 30 mL glass centrifuge tube and crushed using autoclaved glass stir-rod. After 20 min incubation at 60°C, total RNA was extracted from the resulting cell lysate by adding 1 mL of 100% chloroform, incubating for 5 min at room temperature followed by phase separation by centrifugation (10,000*g*, 20 min, 4°C). The chloroform-containing aqueous phase was removed with autoclaved glass Pasteur pipet and 1.5 mL of 100% ethanol was added to precipitate DNA. After 3 min at room temperature, supernatant was collected by centrifugation (2,000*g*, 10 min, 4°C). Proteins were precipitated with 7.5 mL of 100% isopropanol and collected by centrifugation (10,000*g*, 20 min, 4°C). The resulting protein pellet was washed twice to remove phenol traces using 5 mL of 0.3 M guanidine-HCl in 95% ethanol to denature the proteins, followed by a third wash step with 5 mL of 100% ethanol to remove any residual guanidine-HCl. Each wash step was performed by incubating the protein pellet in the solution for 20 min at room temperature followed by centrifugation (10,000*g*, 20 min, 4°C). Protein desalting was accomplished by two successive protein precipitations with 2 mL of 100% glacial acetone (−20°C) and centrifugation (10,000*g*, 20 min, 4°C). After acetone removal, the pellet was completely dried under laminar flow. Proteins were then solubilized in 1 M $NaHCO_3$ with 0.1% SDS at room temperature for 2 days and quantified with a bicinchoninic acid (BCA) proteins assay (Pierce) using either bovine serum albumin (BSA) standards concentration from manufacturer's instruction for quantitative mass spectrometry or adapted BSA standard concentrations for low protein concentrations (see Supplementary Information Section 3) for evaluating removal of halite surface-bound proteins. Proteolysis rate was determined by proteins quantity comparison with and without treatments.

Total proteins were extracted from *H. salinarum* cultures in stationary growth stage using a similar procedure. For this, 2.0×10^{10} cells from liquid cultures were pelleted by centrifugation (7,500*g*, 10 min, 20°C) and the cell pellets directly resuspended in 5 mL TRIzol prior to following all steps described above for halite samples. After solubilization of the protein pellet, solubilization with 1 M $NaHCO_3$ with 0.1% SDS at room temperature, protein quantification was performed using the BCA assay (Pierce) protein assays as per the manufacturer's instructions.

2.7. iTRAQ® isobaric labeling and mass spectrometry

Aliquots of 100 µg of proteins for each sample condition and replicate were reduced using 2 mM of tris-(2-carboxyethyl) phosphine (TCEP) at 37°C for 1 h, and alkylated with 5 mM of

TABLE 1 Experimental parameters of cold plasma sources used to remove surface-bound proteins.

Plasma source	Excitation mode	Electrical parameters			Gas and flow rate	Proteolysis
		Ampl.	Freq.	Duty cycle		
DBD	Alternative Current	7 kV	500 Hz	–	He (1 slm)	0.00%
					He-O_2 (1 slm–150 sccm)	0.00%
					He-O_2 (1 slm–3 sccm)	0.00%
					Ar (1 slm)	0.00%
APPJ	Alternative Current	7 kV	700 Hz	–	He (6 slm)	0.00%
	Pulse	7 kV	700 Hz	1%	He (6 slm)	29.30%
					He-O_2 (6 slm–100 sccm)	39.10%

Proteolysis was measured as a percentage of total proteins removed (as determined by modified BCA assay) compared to untreated halite. DBD means dielectric barrier device; APPJ for atmospheric pressure plasma jet. The abbreviations "slm" and "sccm" are used for standard liters per minute and sccm standard centimeters cube per minute, respectively.

iodoacetamide 30 min in the dark at RT°C prior to digestion with 5 µg of trypsin Gold (Promega) for 15 h at 37°C. After digestion, additional desalting of peptides was done directly by solid phase extraction (SPE) using C18 cartridges (Sep-Pak C18 Plus Short 400 mg Sorbent, Waters). The resulting peptides were dried by speed-vac and resuspended in tetraethylammonium bromide (TEAB) 0.5 M prior to labeling. iTRAQ® labeling was performed according manufacturer's instructions (Applied Biosystems). Briefly, each of the iTRAQ® isobaric labeling reagents were reconstituted with isopropanol and then added to the 50 µg of protein digest (113, 114, 115, and 116 iTRAQ® isobaric labels for proteins from liquid controls and 117, 118, 119, and 121 for halite brine inclusions protein extractions). After 2 h at room temperature, samples were desalted again with C18 SPE. The labeled peptides eluted were then dried by speed-vac and resuspended in 2% acetonitrile, 98% H_2O with 0.1% formic acid (see Supplementary Information Section 4 for additional details).

Labeled peptide samples were analyzed by mass spectrometry as previously described (Pinel-Cabello et al., 2021) on a Q Exactive HF tandem mass spectrometer (Thermo Scientific) coupled to an UltiMate 3000 Nano LC System. Peptides were desalted online on an AcclaimPepmap100 C18 precolumn (5 µm, 100 Å, 300 µm i.d. × 5 mm) and further resolved on a nanoscale AcclaimPepmap100 C18 column (3 µm, 100 Å, 75 µm i.d. × 500 mm) at a flow rate of 200 nl.min^{-1} using a 120-min gradient of 4%–32% acetonitrile. A Top 20 strategy was applied in data dependent acquisition mode. Full scan mass spectra were acquired from 350 to 1800 *m/z* at a resolution of 60,000 with an automatic gain control (AGC) target set at 3×10^6 ions. MS/MS fragmentation was initiated when the ACG target reached 10^5 ions with an intensity threshold of 9×10^4. Only precursor ions with potential charge states of 2^+ and 3^+ were selected for fragmentation applying a dynamic exclusion time of 10 s.

2.8. Mass spectrometry data analyses

2.8.1. Protein identification

Protein identifications were performed using PEAKS® X-Pro software (64 bits version, 2020, BioInformatics solutions). It allows database search assisted *de novo* sequencing against the protein coding sequences from *H. salinarum* NRC-1 (8,533 entries from NCBI, download date 2021/08/03). Spectral peptides matching was carried out with the following parameters: (1) mass tolerance of 10 ppm on the parent ion, (2) mass tolerance of 0.005 Da for fragment ions from MS/MS, (3) carbamidomethylated Cys (+57.0215) and iTRAQ® isobaric tag Lys and N-terminal (+304.2054) as fixed modifications; and (4) oxidized Met (+15.9949), deamidated Asn and Gln (+0.9840) and iTRAQ® isobaric tag Tyr (+304.2054) as variable modification. The false discovery rate (FDR) was estimated with decoy-fusion option included in the software. Proteins were then filtered with FDR < 1% (corresponding to a −10logP score above 25) for peptide-spectrum matches (PSMs) and a valid protein identification required minimum 2 unique peptides with a −10logP score above the peptide filtering threshold that can be mapped to only one protein group.

2.8.2. Protein iTRAQ® quantitation

The eight labeled samples (four replicates each of proteins from liquid stationary cultures and from halite brine inclusions) were mixed in equimolar ratios and injected in nanoLC-MS/MS in triplicate to reduce instrument variability as previously described. Quantitation was performed using PEAKS Q (quantitation program) iTRAQ 8-plex type with 10 ppm mass tolerance and only peptides with a score above FDR threshold 1% are used to quantify the identified proteins. Resulted quantitation was filtered accepting only proteins groups with fold change ≥2, at least two unique peptides and FDR adjusted ≤1% for both proteins identification and fold change significance using ANOVA significance method. Mass spectrometry proteomics data have been deposited to the ProteomeXchange Consortium *via* the PRIDE partner repository with the dataset identifier PXD037167 (project DOI: 10.6019/PXD037167).

2.8.3. Sample comparisons and functional annotation

Potential biases during analysis were avoided by filtering protein identifications produced using the PEAKS software to

group proteins having multiple annotations in the NCBI database. To do so, we developed custom BASH and PYTHON scripts to merge all descriptions for one proteins identifier (favoring in order AAG-type, DAC-type, WP-type and then Q9H-type identifier). Venn diagrams were computed with VennDiagram and ggplot2 packages in R script. Functional proteins annotation was done with Kyoto Encyclopaedia of Genes and Genomes (KEGG, Kanehisa and Goto, 2000) using blastKOALA tool (Kanehisa et al., 2016; https://www.kegg.jp/blastkoala/), assigning KEGG Orthology identifier (also called K numbers) to identified proteins (see Supplementary Table 6-2). K number were then used for mapping identified proteins onto pre-existing metabolic pathways using KEGG Mapper search tools (https://www.kegg.jp/kegg/mapper/search.html; see Supplementary Table 6-3).

3. Results

3.1. Characterization of laboratory-grown halite containing *Halobacterium salinarum*

In order to study the physiology of *H. salinarum* cells after entombment within brine inclusions, we first needed to characterize the laboratory-grown halite, including resultant crystal size, cell localization, and surface-bound biomolecules. This enabled the establishment of selection criteria for downstream proteomics analyses and the development of protocols to exclude any "contaminant" proteins from the surface of the crystal.

3.1.1. Variability of *Halobacterium salinarum* cells from inoculated laboratory-grown halite

Laboratory-grown halite crystals produced from TNPA solutions containing *H. salinarum* cells using a slow evaporative process exhibited heterogeneous crystallization with respect to crystal size and coloration. As shown in Figure 1, even replicates produced under the same conditions produced different quantities of crystals of varying lengths and widths, but with relatively uniform thicknesses (±1 mm) of hopper and fishtail crystals. Color variations observed for halite in this study were likely the result of heterogeneities in the number of brine inclusions containing pigmented *Halobacterium* cells. The red color indicative of *H. salinarum* cells tended to concentrate in the center of hopper crystals where inclusions were most abundant (Roedder, 1984). Individual crystals of similar size and coloration were collected aseptically for further study, selecting only halite without visible defects signaling potential rupture of near-surface brine inclusions.

3.1.2. Contaminating surface-bound cells and proteins

To evaluate the potential for 'contaminating' microbial cells or residual biomolecules at the crystal surface, the elemental composition of halite with and without *H. salinarum* cells (Figures 2A, B, G, H, K, L) were determined by SEM-EDX. Elemental analyses of control halite derived from evaporation of the TNPA solution only exhibited the expected sodium chloride crystal surface, along with dense, irregular C agglomerates (Figures 2C–F) derived from the presence of organics (peptone, L-Arg) in the TNPA solution. The addition of *H. salinarum* cells to the TNPA solution prior to evaporation produced similar structures to control crystals, with no intact cells of *H. salinarum* visible on halite surfaces (Figures 2I, J). However, EDX analyses revealed differences in the distribution of carbon compared to control samples, as well as the presence of microscopic KCl crystals at the halite surface (Figures 2I, B) that were not found on control TNPA-derived crystals without *H. salinarum* cells. These differences were due to lysis of surface adhered *H. salinarum* cells releasing high concentration of cytosolic K^+ and Cl^- accumulated as part of the "salt-in" osmoadaptation strategy (Engel and Catchpole,

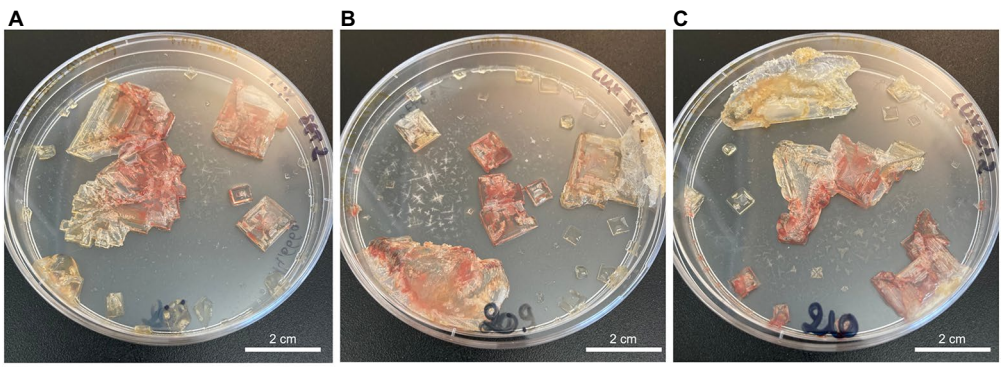

FIGURE 1
TNPA laboratory-grown halite crystals internally inoculated with *Halobacterium salinarum* cells observed after two months of incubation at 37°C for crystallization replicates 1–3 (**A–C**, respectively).

2005). In order to assess both the potential for surface bound contaminants, including viable cells as well as proteins, externally inoculated halite were produced (Figure 2K). After these externally inoculated halite crystals were dissolved in growth medium and incubated at 37 °C, 180 rpm to assess viability. Such cultures reached a normal stationary phase culture (OD_{600} > 1.0), demonstrating that at least a sub-population of halite surface-attached cells were viable. Additionally, SEM-EDX analysis of externally inoculated crystals revealed a similar elemental composition and distribution to that of internally inoculated halite (bearing cells both within brine inclusions as well as on the halite surface) after two months post-evaporation (Figures 2M, N). Taken together, these results confirm the presence of both viable cells and cellular debris on the surface of halite after two months of desiccation, validating the need for halite surface cleaning procedure to remove any residual proteins.

3.2. Development of total protein isolation methods for halite

For proteomics approaches, a new methodology was developed. This method was based on the protocol of Kirkland et al. (2006) using TRIzol reagent. Briefly, protocol was modified to optimize desalting steps (due to direct halite extraction with high NaCl content), protein pellet dissolution and protein digestion (see Supplementary Information Section 4 for details on the parameters tested during protocol development and optimization). To ensure that only proteins contained within fluid inclusions are extracted using this protocol, it was also necessary to develop methods to remove contaminating proteins from halite crystal surfaces.

3.3. Development of proteolysis protocols for removal of halite surface-bound contaminants

Previous halite cleaning procedures from Gramain et al. (2011) and Sankaranarayanan et al. (2011) (see Supplementary Table 1-1) were developed to deactivate surface-contaminating microorganisms and remove surface-contaminating DNA. However, these methods were not designed for the removal of other types of biomolecule contaminants, such as proteins. A new, modified surface cleaning procedure was therefore needed to remove surface protein contamination to enable extraction of proteins only from within halite brine

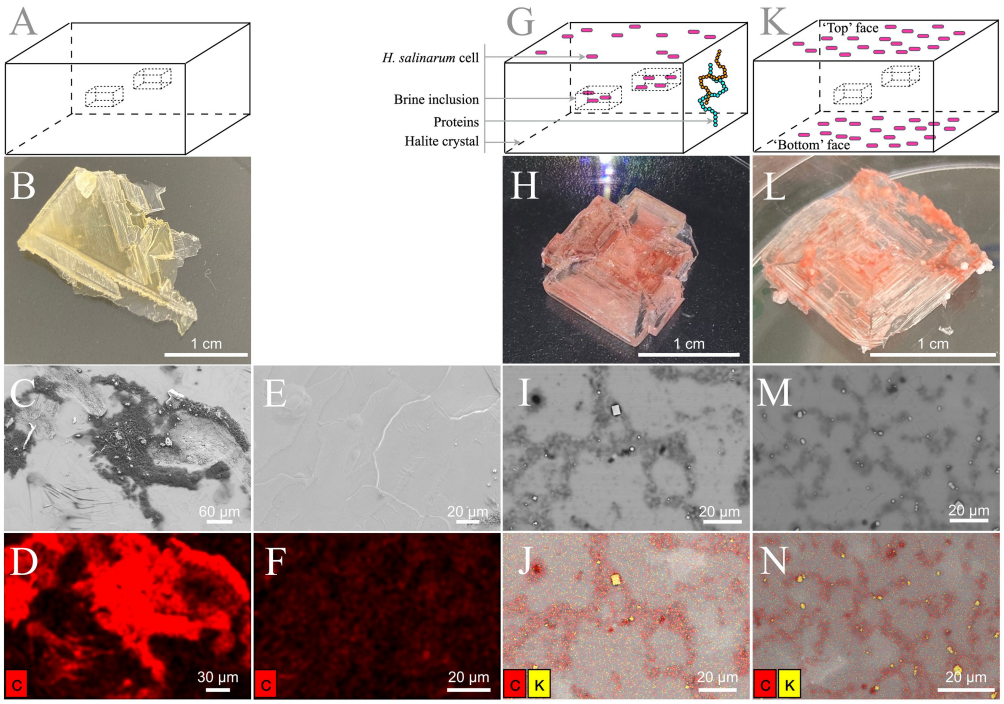

FIGURE 2
Laboratory-grown halite surface observation. (**A–F**) TNPA crystals without cells. (**G–J**) Internally inoculated TNPA crystals with *Halobacterium salinarum* cells incubated 2months at 37°C. (**K–N**) Externally inoculated TNPA crystals with *Halobacterium salinarum* cells after ~1week incubated at 37°C. (**A, G, K**) Schematic representation of halite crystals without cells, internally inoculated and externally inoculated, respectively. (**B, H, L**) Visual observation of crystals without cells, internally inoculated and externally inoculated, respectively. (**C, E**) Secondary electron images. (**I, M**) Backscattered images. (**D, F, J, N**) Elemental composition analysis by EDX spectroscopy correlated, respectively, to the SEM images in panels **C, E, I, M**. Carbon and potassium appear in red and yellow, respectively.

inclusions while avoiding crystal dissolution during the cleaning process. To meet these requirements, both cold plasma treatments and chemical protocols were tested using externally inoculated halite.

Cold plasma exposure is routinely used in astrobiology to sterilize spacecraft surfaces of microbial contaminants prior to launch. For this reason, a cold plasma approach was investigated here for the decontamination of halite surface. Two plasma sources – a DBD and an APPJ – were tested as an alternative to conventional liquid solvents. The expected benefit was to minimize halite dissolution-recrystallization events, hence ensuring the survival of the microorganisms within the halite. However, owing to their insulating properties and irregular topography, halite crystals attenuate plasma electric field and/or bend its field lines. As a result, and whatever the implemented plasma treatment (Ar, He, He mixed with O_2), the externally inoculated halite crystals still retained the pink coloration which is indicative of the protein and lipid pigments of *H. salinarum* cells (data not shown). As shown in Table 1, the most efficient plasma treatment drove to partial cell lysis (as determined by culture-based viability tests following growth by OD_{600}) and to a proteolysis of only 39.1% based on extraction and quantification of remaining proteins from halite surfaces using a modified BCA assay for low protein quantities; a value that remains insufficient for the application.

As an alternative, chemical treatments were tested, using protocols modified from the microorganism deactivation and DNA removal treatments of Sankaranarayanan et al. (2011) to extend to proteolysis. First, reduction of the exposure times in each chemical bath from previously published protocols were tested to avoid crystal dissolution, while maintaining the use of NaCl-saturated chemical solutions to avoid crystal dissolution. Subsequent, 5-min sequential NaOCl and NaOH treatments, either with or without additional HCl treatments, resulted in insufficient halite surface proteolysis (Supplementary Figure 5-1a). This was likely due to the rough structure of hopper crystals, which could allow proteins to remain attached during passive chemical baths. After chemical treatments partially degraded the contaminating biomolecules and reduced their attachment to the halite surface, an active-spray method was used for wash steps to increase the efficiency of biomolecule removal and prevent re-association with halite surfaces, compared to the use of passive wash baths (Supplementary Figure 5-1b). This active-spray method also allowed for both deactivation of halite surface-bound microorganisms (as indicated by a lack of culture growth in post-treatment viability tests) and better protein lysis compared to passive chemical bath washes. Using the protein extraction method described above, the efficacy of active-spray method for removal of surface-bound proteins was tested comparing NaOCl-NaOH and NaOCl-NaOH-HCl protocols. A shown in Figure 3A, addition of an acid wash results in a proteolysis efficiency of 93.0 ± 4.3%, compared to from of 83.7 ± 15.9% without the HCl treatment step (residual proteins 51.6 ± 31.6 μg and 120.5 ± 117.6 μg, respectively, $n = 3$). These results suggest that NaOCl-NaOH-HCl active-spray washes protocol (Figure 3B) present optimal and more consistent surface proteolysis, particularly for the small laboratory-grown halite crystals used in this study.

To ensure that this active-spray chemical treatment did not affect *H. salinarum* cells within the halite brine inclusions, growth was monitored for crystals containing cells trapped in brine inclusions after surface chemical cleaning with active-spray NaOCl-NaOH-HCl treatment. Viable cultures were obtained from dissolution of the crystals in CM growth medium, thereby validating the active-spray chemical surface protein removal protocol for use in studying biomolecules within halite brine inclusions.

These new methods for removal of surface-bound proteins followed by extraction of total proteins from halite brine inclusions using a modified TRIzol-based method with desalting were then applied to answer the question of how *H. salinarum* acclimates to halite brine inclusions over the initial phase post-evaporation using proteomics.

3.4. Proteomic shifts in *Halobacterium salinarum* induced by acclimation to halite brine inclusions

Total proteins were extracted from the brine inclusions of halite after two months of complete dryness, with surface-bound proteins removed using the new protocol detailed above. These brine inclusions extracts were compared to total proteins extracted from *H. salinarum* cultures in stationary growth phase, representing conditions prior to halite formation. The proteins unique to each condition, as well as the common proteome between liquid cultures and from halite interiors were analyzed to determine how *H. salinarum* acclimates to halite brine inclusions.

Using the mass spectrometry data of four replicates from each condition, 1,249 total proteins were identified from stationary phase liquid cultures and 1,052 from halite brine inclusions, representing 1,342 unique proteins. Comparisons of the four replicate samples per condition revealed a core proteome composed of 839 proteins common to all sample replicates for liquid cultures and 715 proteins for halite brine inclusions extracts (Figures 4A, B). Of these, 655 proteins were expressed by cells both in liquid cultures and within halite brine inclusions (hereafter referred to as "shared proteins"); while 60 were specific to halite brine inclusions samples and another 184 were only identified from liquid cultures (Figure 4C; Supplementary Table 6-1). KEGG blastKOALA searches provided matches for roughly 75% of these shared proteins (488 of 655 shared proteins), as well as 62% of proteins unique to halite brine inclusions samples (37 of 60 proteins) and 52% of proteins unique to liquid cultures (95 of 184 proteins; see Supplementary Table 6-2), allowing for functional pathway reconstruction (see Supplementary Table 6-3).

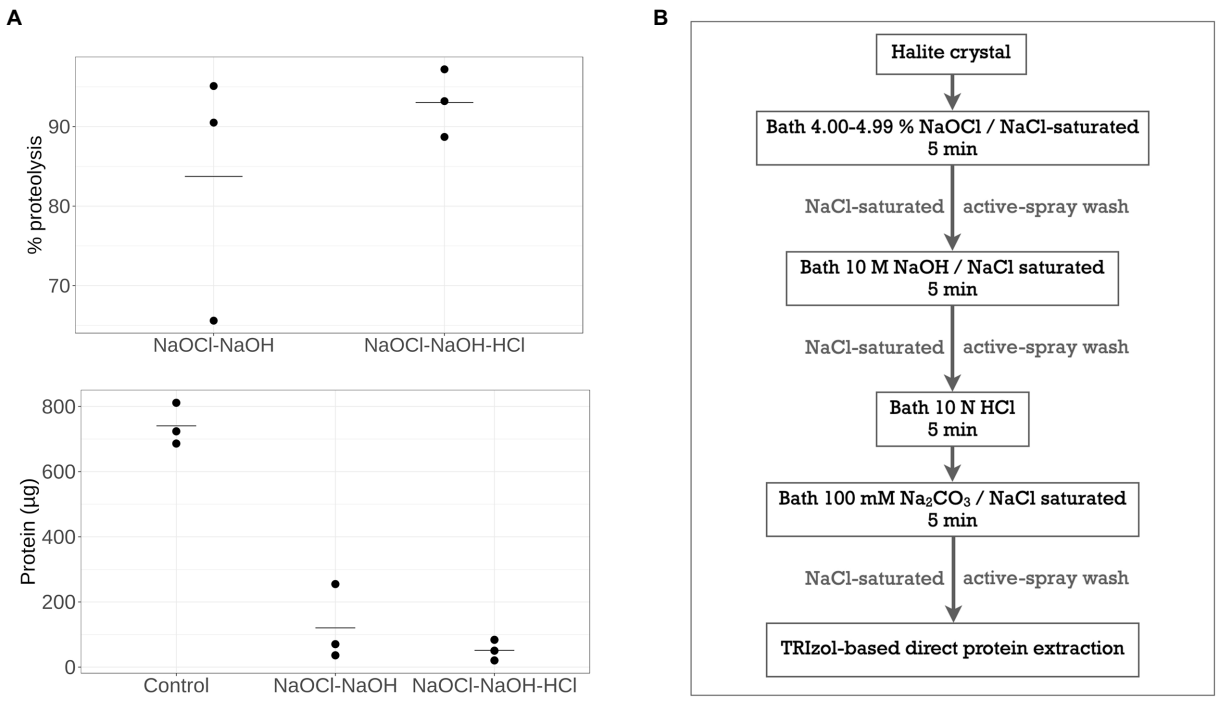

FIGURE 3
Surface-bounded protein removal by chemical treatments with active-spray washes. **(A)** Percentage of proteins removed after NaOCl-NaOH treatment with or without an additional HCl treatment step, and subsequent residual protein quantity. **(B)** Overview of optimal NaOCl-NaOH-HCl chemical treatment with active-spray washes.

As a qualitative approach is insufficient to determine the regulation of proteins leading to their differential expression for *H. salinarum* cells within halite brine inclusions, a semi-quantitative mass spectrometry analysis was also performed. Results from all three injections were pooled to reduce instrument variability (Figure 5). Subsequently 68 proteins from halite brine inclusions were identified with statistically significant changes in expression levels compared to liquid cultures (fold change ≥2; see Supplementary Table 6-4 and Supplementary Figure 6-1). KEGG blastKOALA searches provided functional pathway results for 80% of down-regulated proteins (35 of 44 proteins) and 71% of up-regulated proteins (17 of 24 proteins; see Supplementary Table 6-2).

A summary of the proteomics results is shown in Figure 6 (and Supplementary Table 6-5), showing shared proteins between cells from the stationary growth phase cultures and brine extracts as well proteins differentially expressed (up- or down-regulated) in halite-derived samples. Investigations of the cell activity targeted proteins involved in central metabolism, energy production, cell division, replication, transcription and translation pathways. The cell interactions with the closed halite brine inclusions microenvironment were examined *via* cell envelope proteins (surface layer cell wall proteins and transporters) as well as proteins involved in the motility processes (chemotaxis, gas vesicle and archaellum).

3.4.1. Retention of proteins for central metabolism

Proteins involved in central metabolism, including key enzymes involved in glycolysis/gluconeogenesis and the TCA cycle, formed part of the shared proteome between halite brine inclusions extracts and stationary phase liquid cultures (Figure 6; Supplementary Table 6-5). Additionally, proteins involved in arginine fermentation and aerobic respiration were shared between halite brine inclusions and stationary growth phase liquid cultures. Quantitative analyses showed that the majority of proteins involved in pyruvate metabolism maintained consistent expression levels after two months of halite inclusion with the exception of up-regulation of proteins involved in acetyl-CoA production. Surprisingly, transporters and enzymes involved in ADI pathway were expressed by both cells in stationary phase liquid cultures and brine inclusions extracts, including the arginine deiminase, ornithine-carbamoyl transferase, carbamate kinase, arginosuccinase, arginosuccinate synthetase, arginine-ornithine antiporter and an IclR family transcriptional regulator. Only arginine deaminase was found significantly up-regulated for cells from halite brine inclusions. Proteins for key components of the electron transport chain, including NADH dehydrogenase/oxidoreductase subunits B, C, D, and I, NAD(P)/FAD-dependent oxidoreductase, succinate dehydrogenases and ATP synthase subunits A, B, C, D, E, H,

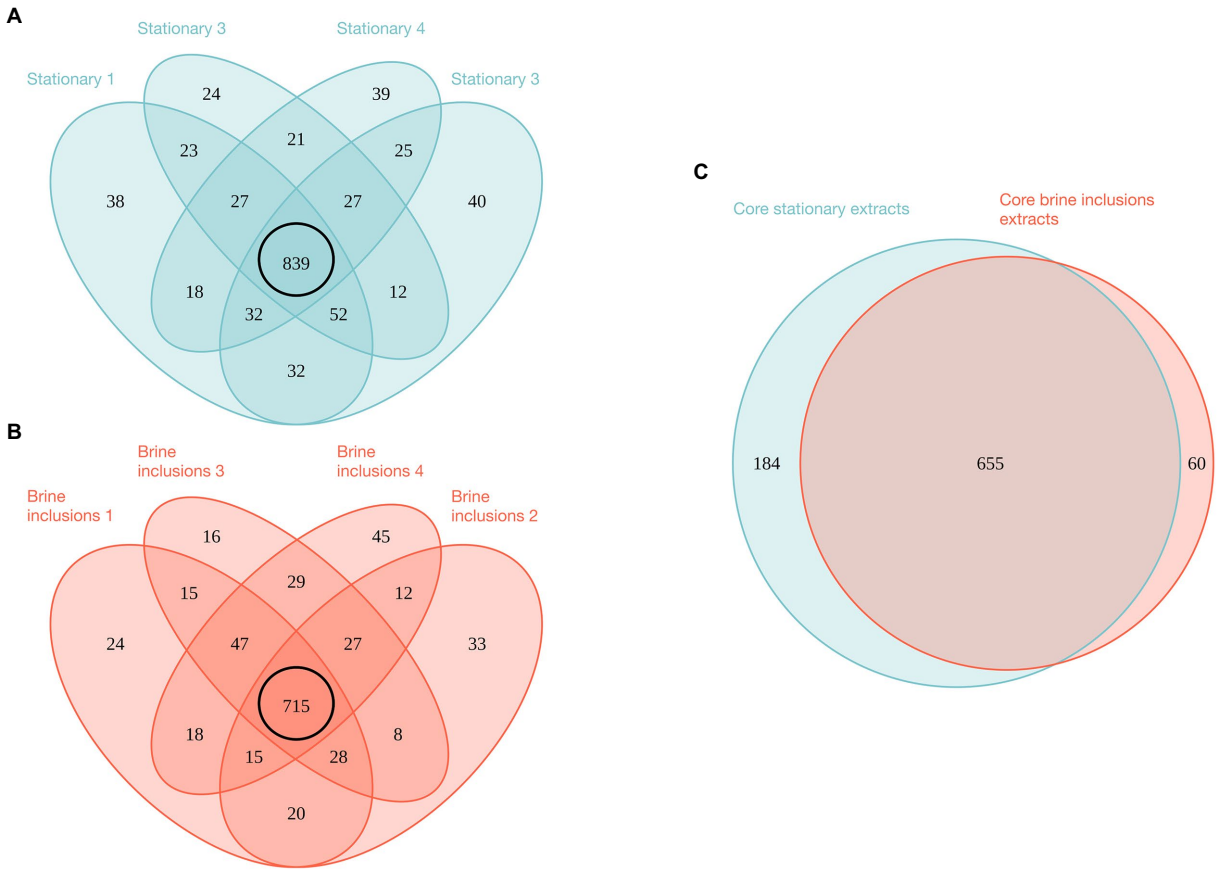

FIGURE 4
Venn diagrams of proteins identified by mass spectrometry for brine inclusions and liquid stationary culture samples. **(A)** Comparison of biological replicates for liquid stationary culture extracts. **(B)** Comparison of biological replicates for brine inclusions extracts. Black circles in **(A,B)** represent "core" proteins shared by the four replicates in both cases. **(C)** Comparison of core proteins between brine inclusion extracts and liquid stationary culture cells.

and I were not found to be differentially regulated between cells from free-living (liquid cultures) or trapped within halite brine inclusions (with the exception of with F subunit lacked in one brine inclusions extract).

3.4.2. Similar expression of DNA repair, replication, and cell division proteins

Eight proteins involved in chromosome partitioning were common to halite brine inclusions extracts and stationary growth phase cultures, along with 11 other proteins involved in DNA replication including matches for DNA primase, polymerase, gyrase, topoisomerase and replication factors. Only four DNA replication proteins were found to be specific to stationary growth phase proteomes. DNA repair processes were represented both within halite brine inclusions and liquid cultures by the DNA photolyase, Rad50, the UvrD repair helicase, UvrA excinuclease, RadA recombinase, Rad25 DNA repair helicase, Fen1 repair endonuclease and the Hel208 helicase are found shared between liquids and brine extracts. Other DNA repair proteins were specific to either halite or liquid samples. Stationary growth phase cultures contained additional repair proteins including the RmeR site-specific deoxyribonuclease, endonuclease IV, RecJ single-strand exonuclease, MutL mismatch repair protein, DNA gyrase and N-glycosylase, whereas the UvrB, MutS and endonuclease III proteins were exclusive to halite brine inclusions proteomes.

3.4.3. Shared transcriptional but reduced translational proteomes

Investigations of DNA transcription identified a shared proteome between liquid cultures and brine inclusions including proteins for transcriptional initiation factors (TFIIE and TFIID) and transcriptional machinery (RNA polymerase subunits RpoA2, RpoB1, RpoB2, RpoD, and RpoE1). Proteins involved in transfer RNA biogenesis such as tRNA ligases for 18 different amino acids along with two ribonucleases completed the shared transcriptional proteome of liquid cultures cells and halite extracts. Only tRNA ligases specific for tryptophan and threonine, four unique transcriptional proteins (RpoF, RpoH, RpoN, and RusA termination protein) and one unique transcription initiation

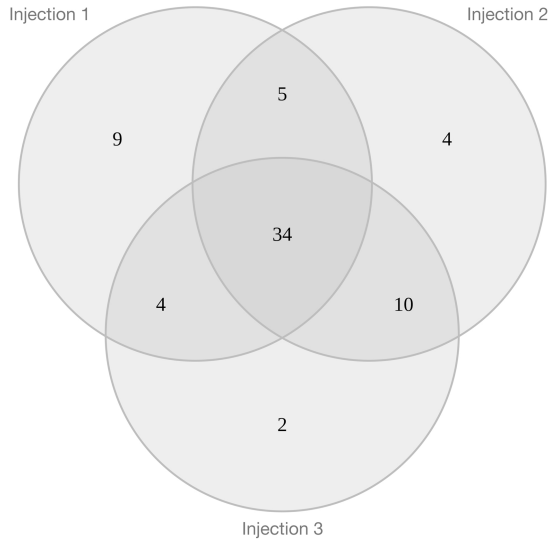

FIGURE 5
Venn diagram of the 68 proteins quantified by iTRAQ® with triple injection which exhibit significative differential expression in brine extracts compared to liquid stationary culture cells.

factor (TFIIB) were only found only in stationary growth phase cell extracts.

Translational activities were severely restricted for cell within halite brine inclusions, as evidenced by the down-regulation of 27 of the 42 ribosomal proteins shared by cells from both conditions tested. Only one ribosomal protein was up-regulated. The shared proteome between cells in halite brine inclusions and those in liquid culture included an additional 10 proteins involved in ribosome biogenesis, and 10 translation initiation factors for which none showed any significant up- or down-regulation. We attempted to corroborate the low ribosomal abundances by isolating RNA using the same TRIzol-based method (see Supplementary Figure 2-1). However, the RNA obtained from halite samples was of too low quality and quantity compared to that from liquid cultures (see Supplementary Table 8-1) for quantitative and transcriptional analyses. This was likely due to a combination of low RNA abundance in the halite fluid inclusions (based on ribosomal protein abundances) and some RNA degradation during extraction due to inefficient desalting using TRIzol alone (see Supplementary Information Section 8 for further details). Chaperones proteins showed a high degree of conservation between conditions, with thioredoxin, chaperone DnaJ, DnaK along with the GrPE stimulator, Hsp20, thermosome subunit and prefoldin all shared by both liquid and halite extracts. Only prefoldin beta subunit was down-regulated for cells from halite brine inclusions.

3.4.4. S-layer maintained with minor cell envelope proteome changes in brine inclusions

S-layer proteins were identified in all liquid culture and halite samples without significant up- or down-regulation. Of the 20 membrane transporters shared between the proteomes of liquid cultures and cells inside halite brine inclusions, four were found to be up-regulated in halite brine inclusions extract, including the UgpB glycerol-3-phosphate-binding protein precursor. Moreover, six proteins were found to be unique to the halite brine inclusions proteome, with up-regulations of the phosphate, iron, peptide/nickel, and glycerol-3-phosphate transporters.

3.4.5. Modified sensory detection and motility

A high degree of variability was noted in the expression of these proteins between halite brine inclusions extracts and stationary growth phase cultures. Some proteins were common to both proteomes without any differences in protein quantities, including for the gas vesicle protein (Gvp) subunits F, C, N of cluster A, while GvpA was found only in two of the four liquid cultures and two of four halite samples. GvpD and I subunits of A cluster and F of B cluster were found punctually in liquid samples. However, the GvpO cluster A and B were significantly down-regulation in halite brine inclusions extracts.

The bacterio-opsin activator-like protein (Bat HTH-10 family transcription regulator; AAG 18778.1), along the 11 Htr signal transducers (including Htr-I and Htr-II that accompany the two sensory rhodopsins) were common to all conditions and replicates. In contrast, the bacterio-opsin activator (Bat; AAG19769.1) was only found in two of the four halite brine inclusions replicate samples. While this protein is hypothesized to be a DNA-binding transcriptional regulator in the photosensory network, its role remains unconfirmed. For the archaellum proteins, only archaellin B1 was down-regulated in halite samples whereas archaellin A1 and prearchaellin peptidase were identified punctually in liquid culture samples. Archaellin B2, A2 and flagellin related H protein were found in all liquid culture replicates but only in one halite replicate. An examination of chemotaxis proteins showed that the 18 identified proteins including CheR, CheA, CheW, CheC, CheB, and the methyl-accepting chemotaxis (MCP)-family proteins Htr transducers, were shared between halite brine inclusions extract and stationary growth phase liquid cultures.

4. Discussion

The initial objective of this study was to determine the molecular acclimation of haloarchaea to entrapment within halite brine inclusions using a proteomics approach. To this aim, we first needed to (1) better characterize the process of laboratory-based evaporation for halite entrapment of haloarchaea and its effects on both the resulting halite and the microbial cells, (2) develop efficient methods for the removal of halite surface-bound cells and biomolecules in order to isolate only proteins contained within the brine inclusions, (3) develop effective methods for protein extraction directly from halite brine inclusions in a shorter time period to avoid alterations in protein expression that can occur during gradual salt dissolution, and finally (4) combine these

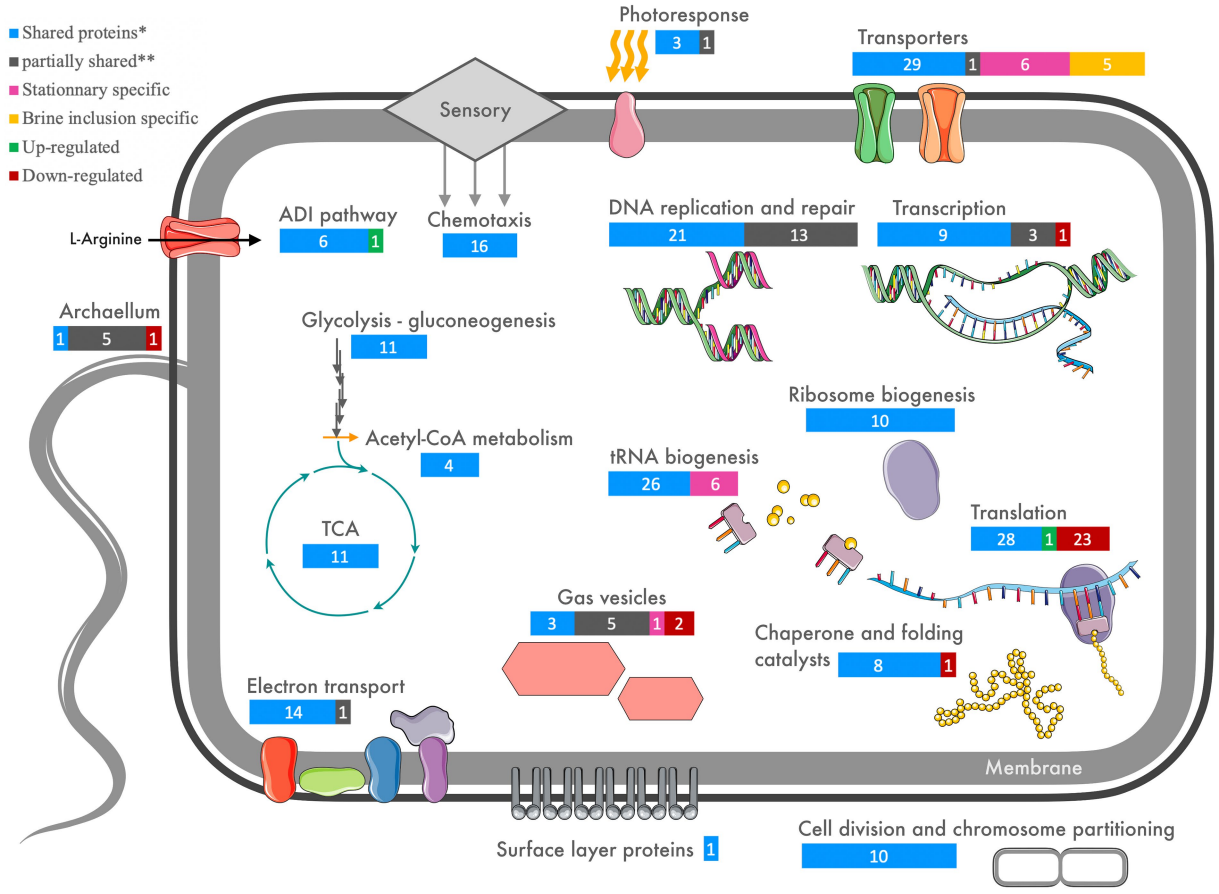

FIGURE 6
Schematic overview of targets cellular functions involved in early acclimation of *Halobacterium salinarum* through halite brine inclusions (for extended matched proteins, see Supplementary Table 6-5). Shared (*) indicates proteins found in all four brine inclusion extracts and all four liquid stationary culture extracts. Partially shared (**) indicates proteins found in both brine inclusions and stationary phase liquid cultures, but not for all replicate samples for each condition.

approaches to analyze total proteins from *H. salinarum* extracted from halite brine inclusions and compare these to control samples from stationary phase liquid cultures in order to propose a model of acclimation within halite. A slow evaporative process was chosen to generate the internally inoculated halite to model natural processes that occur over time scales sufficient for cellular acclimation to the environmental changes, rather than a rapid "shock" evaporative process.

4.1. Biotic/abiotic interactions influencing halite formation and *Halobacterium salinarum* viability

Similar to previous studies of survival of halophiles within halite brine inclusions, a NaCl-based buffered evaporation solution was used in this study (Norton and Grant, 1988; Fendrihan et al., 2012; Kixmüller and Greie, 2012). However, here we chose to add nutrient sources (1% peptone, 0.5% L-Arg HCl) to simulate organics present in the natural environment. This enabled us to study the role of metabolism in the survival and acclimation processes of *H. salinarum* cells to the early phases of entrapment within halite brine inclusions. The presence of microbial biomass and additional organics can affect halite precipitation processes and also explain the observed crystallization heterogeneity observed. For example, Norton and Grant (1988) previously demonstrated a positive correlation between the initial microbial cell density in liquid culture and the quantity of halite brine inclusions formed during evaporation.

The presence of nutrients seemed to diminish rather than increase the duration of survival. While Gramain et al. (2011) observed growth of *H. salinarum* NRC-1 after 27 months post-entombed in halite, there were some notable differences in the experimental parameters used. Gramain et al. (2011) used evaporation buffers with different compositions of nutrients to the evaporation buffer (either without nutrients or with addition of 0.01% Difco yeast extract and 0.0075% Merck casein hydrolysate diluted from the standard concentrations in modified Payne's medium of 1% and 0.75%, respectively (Payne et al., 1960)), incubated the resulting salt crystals in the dark at room temperature

rather than with a 12 h:12 h diurnal cycle at 37°C as used here, and did not appear to employ halite surface sterilization or cleaning protocols prior to these survival tests. In contrast, our viability tests of *H. salinarum* cells from internally inoculated crystals incubated at 37°C over 80 days prior to subjected to surface organics cleaning treatments, dissolution and culturing showed no growth. The lower duration of survival observed for *H. salinarum* cells inside halite in our study may be the result of increased metabolic activity due to the higher concentration of nutrients in TNPA solution compared to the 100-time diluted modified Payne's medium used in Gramain et al. (2011). *H. salinarum* is capable of regulating changes in metabolic pathways in response to changes in carbon source availability (Schmid et al., 2009). This could result in an inhibitory effect due to the accumulation of metabolic waste products (Nyström, 2004) within the closed microenvironment of halite brine inclusions. The products of arginine fermentation include ornithine, CO_2 and NH_4^+. While the addition of peptone in this present study provided sufficient trace elements (Mg^{2+}, K^+, etc.) for nominal cell functions and S-layer stability at the moment of halite formation, these nutrients may be depleted over time within the closed environment of brine inclusions (Kixmüller and Greie, 2012), concurrent with the buildup of waste products. In contrast, Winters et al. (2015) showed that starvation of *H. salinarum* leads to smaller cell size, and hypothesized that this condition could contribute to extended survival within halite brine inclusions. This is somewhat counter-intuitive as natural evaporite environments contain the lysed remains of dead cells and other sources of organics.

On the other hand, in the absence of surface sterilization of halite used in the viability studies in Gramain et al. (2011), some of the surviving cells observed in the study may have been the result of surface-adhered cells rather than cells within the halite brine inclusions. These results also suggest a possible survival advantage for cells on halite surfaces rather than those within the brine inclusions over the early stages of evaporation and acclimation, a hypothesis supported by the findings of Gramain et al. (2011) showing no difference in growth for *H. salinarum* cells evaporated in salt buffer without nutrients and those containing the diluted Payne's medium nutrients. This epilithic lifestyle is likely supported in part by the organics, K, and Cl observed in this study by SEM–EDX analyses to accumulate on the halite surface, derived from the lysis of *H. salinarum* cells. It is important to note that the vacuum conditions for SEM observations may have resulted in rupture of unfixed *H. salinarum* cells, which may have otherwise remained intact under normal atmospheric conditions.

Altogether, these results of surface contamination confirm that the isolation of proteins exclusively from halite brine requires the removal of halite surface-bound cells and biomolecules.

4.2. Removal of halite surface-bound microorganisms and biomolecules

The small sizes of laboratory-grown halite proscribe the use of treatment processes that could result in salt dissolution. Cold atmospheric plasmas were therefore tested in an effort to avoid the use of liquid cleaners based on their effectiveness for the sterilization of spacecraft surfaces for planetary protection (Shimizu et al., 2014) and agricultural applications (Judée et al., 2018). Unfortunately, none of the plasma conditions tested in this study (gas mixtures, power delivery modalities) enabled a complete removal of proteins from the rough textured halite surfaces. However, the results remain encouraging insofar as cold plasma has demonstrated some effects on proteolysis that must now be amplified. Further experiments will be required to innovate an *ad hoc* plasma process delivering active species at higher densities while treating the whole surface of halite regardless their roughness surface, dimensions or dielectric permittivity.

The deactivation of microorganisms and removal of nucleic acids from halite surfaces were been therefore instead performed by adapting chemical wash methods first developed by Rosenzweig et al. (2000) and then optimized by Gramain et al. (2011) and Sankaranarayanan et al. (2011). By reducing the exposure times in sequential NaOCl, NaOH, and HCl treatments, and replacing passive chemical baths with an active spray process, we were able to achieve sufficient proteolysis of surface-bound proteins for downstream isolation of proteins exclusively from within halite brine inclusions, while avoiding halite dissolution during treatment. Compared to total proteins extracted from surface sterilized internally inoculated crystals (±1 mg order), residual surface bound proteins (51.6 µg) were marginal. However, observations of residual pigmentation after removal of halite surface-bound proteins suggests the presence of non-protein pigments such as carotenoids. Further refinements are therefore needed before future studies can isolate lipids exclusively from within halite brine inclusions.

4.3. Benefits and limitations of the TRIzol-based method for direct extraction of biomolecules from halite brine inclusions

TRIzol reagent has the distinct benefit of sequential separation of RNA, DNA, and proteins. TRIzol-based protein extraction methods have previously been used and validated to study proteins from liquid cultures of haloarchaea (Kirkland et al., 2006; Bidle et al., 2008). In this study, we developed and employed a modified procedure that allowed for direct protein extraction from salt crystals, with subsequent desalinations steps compatible with semi-quantitative mass spectrometry analyses from these high salt extracts. Most importantly, our approach avoids induced bias in proteome due to alterations in protein expression over the extended times needed for a slow crystal dissolution prior to protein extraction using other methods.

Although peripheral membrane proteins were identified using this approach, transmembrane peptides were absent in the mass spectrometry dataset. We hypothesize that this was due to retention of transmembrane protein domains with the lipid membrane fraction

during TRIzol extraction in residual phenol phase after protein precipitation with isopropanol (see Supplementary Figure 2-1). Importantly, some transmembrane proteins could be identified by peptides outside the membrane-spanning domains, e.g., the ArcD arginine-ornithine antiporter protein, for which seven cytosolic- and extracellular-facing peptides were identified (see Supplementary Figure 7-1). However, not all transmembrane proteins were identified as evidenced by the lack of identified peptides for bacteriorhodopsin in any samples (stationary phase liquid cultures and brine inclusions). One plausible explanation of this phenomenon is the desalting effect of isopropanol (as suggested by Kirkland et al. (2006)) that can result in increased protein instability, leading to loss of conformation and subsequent peptide fragmentation for peptides outside the transmembrane regions. While these results indicate that further membrane disruption steps may be needed for complete extraction of all transmembrane proteins, similar to the protocol used by Podechard et al. (2018) to isolate membrane lipids using TRIzol, the potential bias introduced by our methodology is limited, as evidenced by the identified peptides on either side of the lipid membrane.

Moreover, while TRIzol-based methods have been used for RNA extraction from liquid cultures of *H. salinarum* (De Lomana et al., 2020), it was shown here to be produce RNA from halite fluid inclusions of insufficient quality for RNA-Seq. Indeed, it would appear that further desalting steps would be needed and optimized for extraction of high-quality RNA (see Supplementary Information Section 8 for further details).

4.4. Postulate of cellular origin of total brine extracted proteome

The proteins extracted using the protocol presented here represent the total protein complement of the halite brine inclusions. These proteins may be components of viable or non-viable cells, or even proteins released by cells into the extracellular environment of the brine inclusions. Many questions remain about the potential for salts to preserve proteins over time as molecular biosignatures, particularly within the protected evaporite brine inclusions microenvironment. Considering that viability tests performed on the internally inoculated halite crystals demonstrate cell viability after two months of *H. salinarum* entrapment, we postulate here a cellular origin for the extracted proteins.

4.5. Acclimation of *Halobacterium salinarum* to halite brine inclusions

We applied the slow laboratory evaporation method to *H. salinarum* cultures in TNPA buffer followed by removal of halite surface-bound cells and organics (particularly proteins) and selective extraction of proteins from within halite brine inclusions described in the preceding sections. This allowed us to study the early (two months) acclimation of the haloarchaeal cells to halite brine inclusions using a proteomics approach. Stationary growth phase cultures were used as a control to approximate the cell physiology prior to a slow evaporative process. Our analyses were focused on two main themes: (1) cell activity, and (2) interactions between cells and local microenvironment within the brine inclusion. Halite brine inclusions are enclosed microenvironments. While questions remain about possible alterations of brine inclusion composition over geological time scales, during the initial phase after crystal formation the composition is based on the initial hypersaline environment. Conditions of near-saturating salt concentrations lead to low dissolved oxygen available to cells. Cells are therefore hypothesized to be in a physiological state similar to stationary growth phase, with low cell division and altered metabolic activity. Here we examined proteome alterations in response to acclimation to this unique microenvironment.

4.5.1. Cell activity within halite brine inclusions

The metabolism of *Halobacterium* cells trapped within brine inclusions is hypothesized to shift from aerobic metabolism by respiratory chain to anaerobic fermentation through arginine deiminase pathway (ADI) or ATP generation *via* photoheteroorganotrophy. Halite incubations were performed in this study with a 12 h:12 h light:dark photoperiod, allowing for both phototrophy *via* bacteriorhodopsin and arginine fermentation under oxygen-limited conditions (Hartmann et al., 1980), as are presumed to exist inside closed brine inclusions. These two ATP-generating pathways are antagonistic for liquid cultures of *H. salinarum*, but can theoretically alternate over the diurnal cycle used here to simulate surface conditions two months after halite precipitation. However, exposure to light also depends on the location of the brine inclusion within the halite crystal, with inclusions near the crystal surface receiving higher total irradiance than inclusions near the crystal center. While the extraction protocol used enabled identification of phototrophy-related proteins such as bacteriorhodopsin activators, it did not allow for extraction of many membrane proteins including bacteriorhodopsin itself. Thus, it is not possible to determine if phototrophy-related proteins were differentially expressed in liquid and halite samples. Under anaerobic conditions, Hartmann et al. (1980) showed that while retinal biosynthesis was inhibited by the absence of oxygen, even low levels of bacteriorhodopsin could produce appreciable levels of ATP. A basal expression of proteins for different ATP generating pathways could enable the survival of *H. salinarum* in the early stages of halite entombment. Additionally, the potential exists for biomolecule recycling within brine inclusions, similar to that demonstrated by prokaryotes in deep subsurface (Thomas et al., 2019) or other resource-limited environments to limit energy consumption linked to biosynthesis. The reduced viability of *H. salinarum* in brine inclusions in the presence of organics including arginine compared to starvation conditions seems to favor fermentative metabolism leading to the accumulation of metabolic waste products. Confirmation of the precise metabolic pathways used by *H. salinarum* within halite brine inclusions will require further analyses, overcoming the challenges of accessing the closed halite system.

Acclimation to the halite brine inclusions microenvironment could presumably involve reduced or silenced cell division, DNA replication and repair pathways. However, the majority of proteins detected implicated in genome maintenance were not differentially expressed between halite brine inclusions and stationary growth phase cultures. This suggests that either such proteins are constitutively expressed, or that DNA replication and cell division occur in a similar fashion for both stationary growth phase cells and those within halite brine inclusions. While early acclimation to the halite brine inclusions microenvironment resulted in nuanced differences in the proteome of *H. salinarum* cells regarding cell division, replication, DNA repair and transcriptional processes, stark differences were observed for proteins involved in translation activities. Among the shared proteome showing no differential expression between conditions were proteins involved in DNA replication, reparation and transcriptional pathways. This suggests similar levels of genome maintenance between late growth stage cultures and brine entombment. However, translational proteins were not detected in brine extracts, potentially indicating decreased *de novo* protein synthesis compared to stationary cells. These seemingly contradictory results can be explained by transcriptional activity directed not to mRNA synthesis but to regulatory RNA. However, this hypothesis is not fully satisfactory as tRNA synthesis and ribosomal biogenesis protein quantities remain similar for both conditions.

Taken together, these data suggest a model for cellular activity during early acclimation to halite brine inclusion highly similar to that of stationary growth phase cells in liquid culture. Active metabolism appears to continue, with data suggesting anaerobic fermentation. However, it is important to note that the extraction method used had limited success in isolating membrane proteins such as bacteriorhodopsin and sensory rhodopsins. Therefore, their absence in this data set cannot be taken as confirmation of absence in the cell, and as such diurnal cycling between anaerobic metabolisms (arginine fermentation in the dark and photoheteroorganotrophy in the light) cannot be ruled out. It is important to note as well that proteomic analyses considered all brine inclusions of a given crystal in a bulk analysis that did not distinguish between brine inclusions near the crystal surface receiving higher irradiance from those deeper within the crystal. Cells maintain at least the capacity for central metabolism, DNA repair, replication, and even cell division comparable to stationary growth phase cells. Acclimation to the closed brine inclusions microenvironment appears to severely limit translational activity. However, expressed proteins are preserved indicating low levels of protein turnover. This raises the question of how cells are able to interface with the surrounding microenvironment within the inclusions.

4.5.2. Interactions between cells and the brine inclusions microenvironment

The potential interactions between *H. salinarum* cells and the local microenvironment within halite brine inclusions focusing on cell surface and mobility processes involved in responses to external stimuli. Previous investigations on the survival of *Halobacterium* cells trapped within salt crystals have proposed potential for cell envelope modifications with surface proteinaceous layer (S-layer) shed (Fendrihan et al., 2012). However, this result seems to be the due to a lack of trace elements in the TN buffer (4.28 M NaCl, Tris–HCl pH 7.4) used in the 2012 study, as argued by Kixmüller and Greie (2012). The peptone added to the TNPA crystallization buffer used here provided sufficient trace elements (including Mg, Ca, K) for S-layer maintenance and cell envelope function. S-layer shedding within halite brine inclusions was previously thought to improve exchanges between cells and the local microenvironment. However, in this study S-layer proteins were identified in all liquid culture and halite samples without significant up- or down-regulation. This either indicates the S-layer is maintained by *H. salinarum* cells, or that the S-layer proteins were preserved within the brine inclusion. The fact that S-layer proteins quantities remained comparable to stationary phase cultures with intact S-layers suggests that the S-layer proteins remain associated with *H. salinarum* cells within brine inclusions.

The increased expression of membrane transporters suggests that transport capacity is not only maintained but enhanced in cells during acclimation to halite brine inclusions, likely to maximize extraction of essential molecules and trace elements from the local microenvironment. This may represent a form of biomolecule recycling similar to that demonstrated by procaryotes in deep subsurface (Thomas et al., 2019) or other resource-limited environments to limit energy consumption linked to biosynthesis. The up-regulation of the glycerol-3-phosphate-binding protein precursor may suggest a role for membrane lipid modification within brine inclusions.

Cell motility could logically be assumed to be of lesser importance for *H. salinarum* cells inside the restricted microenvironment of a brine inclusion. The small volume of such inclusions limits the heterogeneity of available oxygen and nutrients, as well as constraining the ability of cells to move away from potentially damaging elements. However, the detection of the Htr signal transducers of the sensory rhodopsin I and II as part of the common proteome of all conditions tested indicates that despite being constrained to brine inclusions, the phototaxis remains functional both prior to and after evaporation of *H. salinarum* cultures.

In contrast, down-regulations of the GvpO cluster A and B were observed for halite brine inclusions extracts. A similar down-regulation of *gvpO* mRNA was observed in response to UV irradiation (Baliga et al., 2004), and GvpO protein expression levels after exposure to ionizing radiation (Webb et al., 2013). Lack of the GvpO gas vesicle expression regulator is thought to inhibit gas vesicle formation, and growth by anoxic arginine fermentation is also known to reduce the number of gas vesicles in *H. salinarum* NRC-1 (Hechler and Pfeifer, 2009). Therefore, the lack of gas vesicle production could be linked to anaerobic metabolism. Gas vesicle down-regulation suggests a lack of needed capacity for vertical movement in a water column in response to oxygen levels,

consistent with the restricted confines of a microscopic halite brine inclusions. This correlates with previous published transcriptomics and proteomics studies on *H. salinarum* cell showing the impact of salinity and dissolved oxygen concentrations on motility (Schmid et al., 2007; Leuko et al., 2009).

If the sensory pathways leading to cell motility remain intact, the proteins required for motility itself are absent. Our data show a general down-regulation of archaellin proteins involved in motility for cells in brine inclusions compared to stationary phase liquid cultures. So, while chemo- and photo-taxis proteins (including Che-family proteins and Htr signal transducers) are maintained in brine inclusions, the accompanying archaellum motility is not. Reduced motility may be induced in halite brine inclusions to preserve energy. The expression of multiple transducer proteins is often correlated with changing environmental conditions, and in this case may be the remanent proteins from the acclimation of *H. salinarum* to halite brine inclusions.

5. Conclusion

This is the first study that demonstrate the possibility to isolate proteins directly and efficiently from halite brine inclusions while simultaneously excluding surface-bound contaminating proteins and avoiding changes in cell protein expression during salt dissolution. Also, this work provides the first insights into the molecular mechanisms involved in the early acclamation of *H. salinarum* within brine inclusions. Based on our findings, the cells of *H. salinarum* appear to be in a low activity "maintenance" or "semi-dormant" state, similar to other bacteria and archaea in low-energy environments such as the deep biosphere (reviewed in Lever et al. (2015)). Whether or not *H. salinarum* cells inside brine inclusions are true "persister" cells (Megaw and Gilmore, 2017) will require future study. Further investigation is also needed to explore the hypothesis of biomolecules recycling similar to that observed in deep sediments (Thomas et al., 2019). Despite the reasonable assumption brine inclusions represent stress conditions for *Halobacterium* cells, no increased expression of stress-response proteins such as chaperones was observed. The acclimation to the halite environment may therefore be less a stress response than a reduction in cell activity.

Shifts in the proteome of *H. salinarum* NRC-1 have been studied using liquid cultures under conditions similar to those thought to exist inside halite brine inclusions: reduced oxygen content (Schmid et al., 2007), increased salinity (Leuko et al., 2009), and transitions from aerobic to anaerobic growth (Tebbe et al., 2009). While the down-regulation of certain ribosomal proteins and archaellum precursors was also observed following salinity stress (Leuko et al., 2009) not all protein expression shifts conformed to this pattern. The same was observed for the transition from aerobic to anaerobic growth, with increased expression of the arginine deaminase as observed by Tebbe et al. (2009) but other protein expression differences due to the use of culturing conditions that were not identical to those in previous studies. Thus, while proteomics analyses from liquid cultures can provide hints to aid in the interpretation of the data presented here, they cannot fully explain the observed patterns of protein expression within halite brine inclusions.

The unique environment of halite brine inclusions limits exchange of nutrients between cells and their surrounding environment. It also allows for the buildup of metabolic waste products which appear to limit the duration of cell viability within the brine inclusions. Further functional investigations are clearly needed to confirm the hypotheses generated by proteomics data in this study, particularly in regards to cell activity. While this study does not resolve the question of how long microorganisms are able to retain viability within halite brine inclusions, it offers clear insights into the process of early microbial acclimation to evaporation of hypersaline environments in halophilic archaea. The methodologies presented here will also enable future study of the biomolecules of microorganisms in halite inclusions in natural settings, particularly small-sized halite crystals.

Data availability statement

The datasets presented in this study can be found in online repositories. The names of the repository/repositories and accession number(s) can be found in the article/Supplementary material.

Author contributions

Study was designed by AK in collaboration with CF, with the participation of AH and SZ in experimental design and supervision. Experiments were conducted by CF with the help of MM for crystals forming. AM and RP for mass spectrometry and improvements of extraction methods. BA-B for nanoLC-MS/MS data acquisition. FG for MEB-EDX analyses. AT for RNA extraction and TD for plasma treatments. Proteomics data treatments were conducted by AT and CF. Manuscript was written by CF. All authors contributed to the article and approved the submitted version.

Funding

This work was supported by the X-life program of CNRS-MITI, the ATM program of the Muséum National d'Histoire Naturelle, the French National Research Agency ANR-PRCI "ExocubeHALO" project (ANR-21-CE49-0017-01_ACT), and the Sorbonne Université (graduate stipend CF).

Acknowledgments

UHPLC MS/MS data were acquired at the Plateau Technique de Spectrométrie de Masse Bio-organique, UMR 7245 Molécules de Communication et d'Adaptation des Microorganismes, Muséum national d'Histoire naturelle, Paris, France. The nanoLC-MS/MS data were acquired at ProGenoMix MS-platform, IBiSA labeled, at CEA/SPI/Li2D. Thanks to Imène Esteve of the

FIB and SEM facility of IMPMC which was supported by Région Ile de France Grant SESAME 2006 NOI-07-593/R, Institut National des Sciences de l'Univers (INSU)–CNRS, Institut de Physique–CNRS, Sorbonne Université, and the French National Research Agency (ANR) grant ANR-07-BLAN-0124-01. Parts of figures used images from Servier Medical Art. Servier Medical Art by Servier is licensed under a Creative Commons Attribution 3.0 Unported License (https://creativecommons.org/licenses/by/3.0/).

Conflict of interest

The authors declare that the research was conducted in the absence of any commercial or financial relationships that could be construed as a potential conflict of interest.

Publisher's note

Supplementary material

The Supplementary material for this article can be found online at: https://www.frontiersin.org/articles/10.3389/fmicb.2022.1075274/full#supplementary-material

References

Baliga, N. S., Bjork, S. J., Bonneau, R., Pan, M., Iloanusi, C., Kottemann, M. C. H., et al. (2004). Systems level insights into the stress response to UV radiation in the halophilic archaeon *Halobacterium NRC-1*. *Genome Res.* 14, 1025–1035. doi: 10.1101/gr.1993504

Bidle, K. A., Kirkland, P. A., Nannen, J. L., and Maupin-Furlow, J. A. (2008). Proteomic analysis of *Haloferax volcanii* reveals salinity-mediated regulation of the stress response protein PspA. *Microbiology* 154, 1436–1443. doi: 10.1099/mic.0.2007/015586-0

Coker, J. A., Das Sarma, P., Kumar, J., Müller, J. A., and Das Sarma, S. (2007). Transcriptional profiling of the model archaeon *Halobacterium* sp. NRC-1: responses to changes in salinity and temperature. *Saline Syst.* 3:6. doi: 10.1186/1746-1448-3-6

De Lomana, A. L. G., Kusebauch, U., Raman, A. V., Pan, M., Turkarslan, S., Lorenzetti, A. P. R., et al. (2020). Selective translation of low abundance and upregulated transcripts in *Halobacterium salinarum*. *mSystems* 5, e00329–e00320. doi: 10.1128/msystems.00329-20

Eichler, J. (2019). Halobacterium salinarum. *Trends Microbiol.* 27, 651–652. doi: 10.1016/j.tim.2019.02.005

Engel, M. B., and Catchpole, H. R. (2005). A microprobe analysis of inorganic elements in *Halobacterium salinarum*. *Cell Biol. Int.* 29, 616–622. doi: 10.1016/j.cellbi.2005.03.024

Falb, M., Müller, K., Königsmaier, L., Oberwinkler, T., Horn, P., von Gronau, S., et al. (2008). Metabolism of halophilic archaea. *Extremophiles* 12, 177–196. doi: 10.1007/s00792-008-0138-x

Fendrihan, S., Dornmayr-Pfaffenhuemer, M., Gerbl, F. W., Holzinger, A., Grösbacher, M., Briza, P., et al. (2012). Spherical particles of halophilic archaea correlate with exposure to low water activity – implications for microbial survival in fluid inclusions of ancient halite. *Geobiology* 10, 424–433. doi: 10.1111/j.1472-4669.2012.00337.x

Gonzalez, O., Gronau, S., Pfeiffer, F., Mendoza, E., Zimmer, R., and Oesterhelt, D. (2009). Systems analysis of bioenergetics and growth of the extreme halophile *Halobacterium salinarum*. *PLoS Comput. Biol.* 5:e1000332. doi: 10.1371/journal.pcbi.1000332

Gramain, A., Díaz, G. C., Demergasso, C., Lowenstein, T. K., and McGenity, T. J. (2011). Archaeal diversity along a subterranean salt core from the Salar Grande (Chile). *Environ. Microbiol.* 13, 2105–2121. doi: 10.1111/j.1462-2920.2011.02435.x

Graur, D., and Pupko, T. (2001). The Permian bacterium that Isn't. *Mol. Biol. Evol.* 18, 1143–1146. doi: 10.1093/oxfordjournals.molbev.a003887

Gruber, C., Legat, A., Pfaffenhuemer, M., Radax, C., Weidler, G., Busse, H.-J., et al. (2004). *Halobacterium noricense* sp. nov., an archaeal isolate from a bore core of an alpine Permian salt deposit, classification of *Halobacterium* sp. NRC-1 as a strain of *H. salinarum* and emended description of *H. salinarum*. *Extremophiles* 8, 431–439. doi: 10.1007/s00792-004-0403-6

Hartmann, R., Sickinger, H. D., and Oesterhelt, D. (1980). Anaerobic growth of halobacteria. *Proc. Natl. Acad. Sci. U. S. A.* 77, 3821–3825. doi: 10.1073/pnas.77.7.3821

Hazen, R. M., and Roedder, E. (2001). How old are bacteria from the Permian age? *Nature* 411, 155–156. doi: 10.1038/35075663

Hechler, T., and Pfeifer, F. (2009). Anaerobiosis inhibits gas vesicle formation in halophilic archaea. *Mol. Microbiol.* 71, 132–145. doi: 10.1111/j.1365-2958.2008.06517.x

Huby, T. J. C., Clark, D. R., McKew, B. A., and McGenity, T. J. (2020). Extremely halophilic archaeal communities are resilient to short-term entombment in halite. *Environ. Microbiol.* 23, 3370–3383. doi: 10.1111/1462-2920.14913

Judée, F., Simon, S., Bailly, C., and Dufour, T. (2018). Plasma-activation of tap water using DBD for agronomy applications: identification and quantification of long lifetime chemical species and production/consumption mechanisms. *Water Res.* 133, 47–59. doi: 10.1016/j.watres.2017.12.035

Kanehisa, M., and Goto, S. (2000). KEGG: Kyoto encyclopedia of genes and genomes. *Nucleic Acids Res.* 28, 27–30. doi: 10.1093/nar/28.1.27

Kanehisa, M., Sato, Y., and Morishima, K. (2016). BlastKOALA and GhostKOALA: KEGG tools for functional characterization of genome and metagenome sequences. *J. Mol. Biol.* 428, 726–731. doi: 10.1016/j.jmb.2015.11.006

Kirkland, P. A., Busby, J., Stevens, S., and Maupin-Furlow, J. A. (2006). Trizol-based method for sample preparation and isoelectric focusing of halophilic proteins. *Anal. Biochem.* 351, 254–259. doi: 10.1016/j.ab.2006.01.017

Kixmüller, D., and Greie, J. (2012). An ATP-driven potassium pump promotes long-term survival of *Halobacterium salinarum* within salt crystals. *Env. Microbiol. Rep.* 4, 234–241. doi: 10.1111/j.1758-2229.2012.00326.x

Leuko, S., Raftery, M. J., Burns, B. P., Walter, M. R., and Neilan, B. A. (2009). Global protein-level responses of *Halobacterium salinarum* NRC-1 to prolonged changes in external sodium chloride concentrations. *J. Proteome Res.* 8, 2218–2225. doi: 10.1021/pr800663c

Lever, M. A., Rogers, K. L., Lloyd, K. G., Overmann, J., Schink, B., Thauer, R. K., et al. (2015). Life under extreme energy limitation: a synthesis of laboratory- and field-based investigations. *FEMS Microbiol. Rev.* 39, 688–728. doi: 10.1093/femsre/fuv020

Maughan, H., Birky, W., Nicholson, W., Rosenzweig, W., and Vreeland, R. (2002). The paradox of the "ancient" bacterium rich contains "modern" protein-coding genes. *Mol. Biol. Evol.* 19, 1637–1639. doi: 10.1093/oxfordjournals.molbev.a004227

Megaw, J., and Gilmore, B. F. (2017). Archaeal Persisters: Persister cell formation as a stress response in *Haloferax volcanii*. *Front. Microbiol.* 8:1589. doi: 10.3389/fmicb.2017.01589

Merino, N., Aronson, H. S., Bojanova, D. P., Feyhl-Buska, J., Wong, M. L., Zhang, S., et al. (2019). Living at the extremes: extremophiles and the limits of life in a planetary context. *Front. Microbiol.* 10:780. doi: 10.3389/fmicb.2019.00780

Moran-Reyna, A., and Coker, J. A. (2014). The effects of extremes of pH on the growth and transcriptomic profiles of three haloarchaea. *F1000Research* 3:168. doi: 10.12688/f1000research.4789.2

Mormile, M. R., Biesen, M. A., Gutierrez, M. C., Ventosa, A., Pavlovich, J. B., Onstott, T. C., et al. (2003). Isolation of *Halobacterium salinarum* retrieved directly from halite brine inclusions. *Environ. Microbiol.* 5, 1094–1102. doi: 10.1046/j.1462-2920.2003.00509.x

Müller, J. A., and DasSarma, S. (2005). Genomic analysis of anaerobic respiration in the archaeon *Halobacterium* sp. strain NRC-1: dimethyl sulfoxide and

trimethylamine N-oxide as terminal electron acceptors. *J. Bacteriol. Res.* 187, 1659–1667. doi: 10.1128/jb.187.5.1659-1667.2005

Nickle, D. C., Learn, G. H., Rain, M. W., Mullins, J. I., and Mittler, J. E. (2002). Curiously modern DNA for a "250 million-year-old" bacterium. *J. Mol. Evol.* 54, 134–137. doi: 10.1007/s00239-001-0025-x

Nims, C., Lafond, J., Alleon, J., Templeton, A. S., and Cosmidis, J. (2021). Organic biomorphs may be better preserved than microorganisms in early earth sediments. *Geology* 49, 629–634. doi: 10.1130/g48152.1

Norton, C. F., and Grant, W. D. (1988). Survival of Halobacteria within fluid inclusions in salt crystals. *J. Gen. Microbiol.* 134, 1365–1373. doi: 10.1099/00221287-134-5-1365

Nyström, T. (2004). Stationary-phase physiology. *Annu. Rev. Microbiol.* 58, 161–181. doi: 10.1146/annurev.micro.58.030603.123818

Oesterhelt, D., and Stoeckenius, W. (1974). Methods in enzymology. *Methods Enzymol* 31, 667–678. doi: 10.1016/0076-6879(74)31072-5

Orellana, M. V., Pang, W. L., Durand, P. M., Whitehead, K., and Baliga, N. S. (2013). A role for programmed cell death in the microbial loop. *PloS One* 8:e62595. doi: 10.1371/journal.pone.0062595

Oren, A. (2006). Life at high salt concentrations. *Prokaryotes* 3, 263–282. doi: 10.1007/0-387-30742-7-9

Oren, A., Arahal, D. R., and Ventosa, A. (2009). Emended descriptions of genera of the family *Halobacteriaceae*. *Int. J. Syst. Evol. Microbiol.* 59, 637–642. doi: 10.1099/ijs.0.008904-0

Payne, J. I., Sehgal, S. N., and Gibbons, N. E. (1960). Immersion refractometry of some halophilic bacteria. *Can. J. Microbiol.* 6, 9–15. doi: 10.1139/m60-002

Pinel-Cabello, M., Chapon, V., Ruiz-Fresneda, M. A., Alpha-Bazin, B., Berthomieu, C., Armengaud, J., et al. (2021). Delineation of cellular stages and identification of key proteins for reduction and biotransformation of se(IV) by Stenotrophomonas bentonitica BII-R7. *J. Hazard. Mater.* 418:126150. doi: 10.1016/j.jhazmat.2021.126150

Podechard, N., Ducheix, S., Polizzi, A., Lasserre, F., Montagner, A., Legagneux, V., et al. (2018). Dual extraction of mRNA and lipids from a single biological sample. *Sci. Rep.* 8:7019. doi: 10.1038/s41598-018-25332-9

Post, F. J. (1977). The microbial ecology of the great salt Lake. *Microb. Ecol.* 3, 143–165. doi: 10.1007/bf02010403

Roedder, E. (1984). The fluids in salt. *Am. Mineral.* 69, 413–439.

Rosenzweig, W. D., Peterson, J., Woish, J., and Vreeland, R. H. (2000). Development of a protocol to retrieve microorganisms from ancient salt crystals. *Geomicrobiol J.* 17, 185–192. doi: 10.1080/01490450050121152

Sankaranarayanan, K., Timofeeff, M. N., Spathis, R., Lowenstein, T. K., and Lum, J. K. (2011). Ancient microbes from halite fluid inclusions: optimized surface sterilization and DNA extraction. *PLoS One* 6:e20683. doi: 10.1371/journal.pone.0020683

Schmid, A. K., Reiss, D. J., Kaur, A., Pan, M., King, N., Van, P. T., et al. (2007). The anatomy of microbial cell state transitions in response to oxygen. *Genome Res.* 17, 1399–1413. doi: 10.1101/gr.6728007

Schmid, A. K., Reiss, D. J., Pan, M., Koide, T., and Baliga, N. S. (2009). A single transcription factor regulates evolutionarily diverse but functionally linked metabolic pathways in response to nutrient availability. *Mol. Syst. Biol.* 5:282. doi: 10.1038/msb.2009.40

Schreder-Gomes, S. I., Benison, K. C., and Bernau, J. A. (2022). 830-million-year-old microorganisms in primary fluid inclusions in halite. *Geology* 50, 918–922. doi: 10.1130/g49957.1

Sherwood, J. E., Stagnitti, F., Kokkinn, M. J., and Williams, W. D. (1991). Dissolved oxygen concentrations in hypersaline waters. *Limnol. Oceanogr.* 36, 235–250. doi: 10.4319/lo.1991.36.2.0235

Shimizu, S., Barczyk, S., Rettberg, P., Shimizu, T., Klaempfl, T., Zimmermann, J. L., et al. (2014). Cold atmospheric plasma – a new technology for spacecraft component decontamination. *Planet. Space Sci.* 90, 60–71. doi: 10.1016/j.pss.2013.10.008

Tebbe, A., Schmidt, A., Konstantinidis, K., Falb, M., Bisle, B., Klein, C., et al. (2009). Life-style changes of a halophilic archaeon analyzed by quantitative proteomics. *Proteomics* 9, 3843–3855. doi: 10.1002/pmic.200800944

Thomas, C., Grossi, V., Antheaume, I., and Ariztegui, D. (2019). Recycling of archaeal biomass as a new strategy for extreme life in Dead Sea deep sediments. *Geology* 47, 479–482. doi: 10.1130/g45801.1

Vreeland, R. H., Rosenzweig, W. D., and Powers, D. W. (2000). Isolation of a 250 million-year-old halotolerant bacterium from a primary salt crystal. *Nature* 407, 897–900. doi: 10.1038/35038060

Webb, K. M., Yu, J., Robinson, C. K., Noboru, T., Lee, Y. C., and DiRuggiero, J. (2013). Effects of intracellular Mn on the radiation resistance of the halophilic archaeon *Halobacterium salinarum*. *Extremophiles* 17, 485–497. doi: 10.1007/s00792-013-0533-9

Winters, Y. D., Lowenstein, T. K., and Timofeeff, M. N. (2015). Starvation-survival in Haloarchaea. *Life* 5, 1587–1609. doi: 10.3390/life5041587

frontiers | Frontiers in Microbiology

TYPE Original Research
PUBLISHED 23 February 2023
DOI 10.3389/fmicb.2023.1121857

OPEN ACCESS

EDITED BY
Abhishek Walia,
Chaudhary Sarwan Kumar Himachal Pradesh Krishi Vishvavidyalaya, India

REVIEWED BY
Yuichi Koga,
Okayama University of Science, Japan
Elizaveta Bonch-Osmolovskyaya,
Winogradsky Institute of Microbiology (RAS), Russia

*CORRESPONDENCE
Mariane Schmidt Thøgersen
✉ mst@envs.au.dk

SPECIALTY SECTION
This article was submitted to Microbiotechnology, a section of the journal Frontiers in Microbiology

RECEIVED 12 December 2022
ACCEPTED 03 February 2023
PUBLISHED 23 February 2023

CITATION
Rasmussen CB, Scavenius C, Thøgersen IB, Harwood SL, Larsen Ø, Bjerga GEK, Stougaard P, Enghild JJ and Thøgersen MS (2023) Characterization of a novel cold-adapted intracellular serine protease from the extremophile *Planococcus halocryophilus* Or1. *Front. Microbiol.* 14:1121857. doi: 10.3389/fmicb.2023.1121857

Characterization of a novel cold-adapted intracellular serine protease from the extremophile *Planococcus halocryophilus* Or1

Casper Bøjer Rasmussen[1], Carsten Scavenius[2], Ida B. Thøgersen[1], Seandean Lykke Harwood[1], Øivind Larsen[3], Gro Elin Kjaereng Bjerga[3], Peter Stougaard[4], Jan J. Enghild[1] and Mariane Schmidt Thøgersen[4]*

[1]Department of Molecular Biology and Genetics, Aarhus University, Aarhus, Denmark, [2]Danish Technological Institute, Aarhus, Denmark, [3]NORCE Climate and Environment, NORCE Norwegian Research Centre AS, Bergen, Norway, [4]Department of Environmental Science, Aarhus University, Roskilde, Denmark

The enzymes of microorganisms that live in cold environments must be able to function at ambient temperatures. Cold-adapted enzymes generally have less ordered structures that convey a higher catalytic rate, but at the cost of lower thermodynamic stability. In this study, we characterized P355, a novel intracellular subtilisin protease (ISP) derived from the genome of *Planococcus halocryophilus* Or1, which is a bacterium metabolically active down to −25°C. P355's stability and activity at varying pH values, temperatures, and salt concentrations, as well as its temperature-dependent kinetics, were determined and compared to an uncharacterized thermophilic ISP (T0099) from *Parageobacillus thermoglucosidasius*, a previously characterized ISP (T0034) from *Planococcus* sp. AW02J18, and Subtilisin Carlsberg (SC). The results showed that P355 was the most heat-labile of these enzymes, closely followed by T0034. P355 and T0034 exhibited catalytic constants (k_{cat}) that were much higher than those of T0099 and SC. Thus, both P355 and T0034 demonstrate the characteristics of the stability-activity trade-off that has been widely observed in cold-adapted proteases.

KEYWORDS

characterization, cold adaptation, protein chemistry, intracellular subtilisin protease, maturation, calcium, *Planococcus*

Introduction

Microorganisms that thrive at sub-zero temperatures are called psychrophilic or cold-adapted organisms and have been isolated from the high Arctic and Antarctic permafrost (Wilhelm et al., 2012; Goordial and Whyte, 2014; Goordial et al., 2017; Bhatia et al., 2021). One example is *Planococcus halocryophilus* Or1, which grows at −15°C and remains metabolically active at −25°C in water containing 18% (3.08 M) NaCl (Mykytczuk et al., 2012, 2013). These are the lowest temperatures reported for any microbial activity, although optimal temperature for its growth is 25°C and it remains viable at up to 37°C. Therefore, *P. halocryophilus* must be able to express enzymes that can carry out essential metabolic and cellular processes at these sub-zero temperatures. Generally, the enzymes of psychrophilic microorganisms, or cold-adapted enzymes, are thought to be adapted to lower temperatures

by increasing their catalytic activity, i.e., the catalytic rate constant (k_{cat}), which usually also results in a higher Michaelis-Menten constant (K_m). This is in turn reflected in an increased structural flexibility at the cost of thermodynamic stability (Santiago et al., 2016; Furhan, 2020). This flexibility-stability trade-off is apparent in the enzyme structure of cold-adapted enzymes as (1) larger loop regions, (2) bulkier residues around the active site, (3) a less dense hydrophobic core, and (4) fewer stabilizing salt bridges, among others (Santiago et al., 2016).

Cold-adapted proteins such as proteases are interesting not only from a basic research point of view, but also in the context of applied enzymatic processes (Davail et al., 1994; Lylloff et al., 2016; Pereira et al., 2017; Park et al., 2018). Cold-adapted enzymes have properties that are advantageous in industrial contexts by reducing energy consumption, chemical side-products, and bacterial contaminations. Furthermore, thermal inactivation, as an attractive procedure to denature the enzyme, is easier for cold-adapted enzymes due to their intrinsic thermal lability (Bruno et al., 2019). A number of subtilisins see industrial use, especially in detergents since they are active at alkaline pH (up to pH 12) (Fujinami and Fujisawa, 2010), where proteins become more soluble (Zhang et al., 2015) and show specificity toward aromatic and hydrophobic residues (Groen et al., 1992; Furhan, 2020). All currently available commercial subtilisins are isolated from bacteria within the genus *Bacillus*, ranging from the mesophilic Subtilisin Carlsberg (SC) (e.g., Alcalase^{TM}) (Linderstrøm-Lang and Ottesen, 1947; Fasim et al., 2021) to a few cold-adapted subtilisins (Sarmiento et al., 2015). Cold-adapted proteases can be engineered from mesophilic proteases (Wintrode et al., 2000; Tindbaek et al., 2004), where thermal stability may be significantly affected by a single point mutation (Narinx et al., 1997). The demand for cold-adapted enzymes is anticipated to increase (Furhan, 2020); thus, there is a continued need to study naturally occurring cold-adapted enzymes both to understand the mechanisms of cold-adaption and to identify new useful enzymes.

Subtilisins are found both as extracellular subtilisin proteases (ESPs) and intracellular subtilisin proteases (ISPs). ESPs contain a signal peptide that directs their secretion from the cell, as well as a pro-peptide that inhibits activity in their zymogen state and functions as a chaperone during their folding (Zhu et al., 1989; Ohta et al., 1991). The pro-peptide is autoproteolytically removed to produce the active ESP (Ikemura et al., 1987; Ikemura and Inouye, 1988). ISPs do not contain signal peptides but are also synthesized as zymogens. They contain a short (16–25 residues) N-terminal pro-peptide with a LIPY/F motif that is removed during activation in a calcium-dependent manner (Gamble et al., 2011). Calcium additionally stabilizes subtilisins, preventing their auto-proteolysis (Braxton and Wells, 1992) and thermal inactivation (Voordouw et al., 1976; Veltman et al., 1998). ISPs constitute most of the intracellular degradome in *Bacillus subtilis* (Orrego et al., 1973; Burnett et al., 1986) and share 40–50% amino acid sequence identity with ESPs (Vévodová et al., 2010). Gamble et al. (2011) proposed a maturation model of the ISP from *Bacillus clausii* where a small fraction of pro-ISP adopts an "open" conformation where the pro-peptide is transiently dislocated from the active site. They proposed that calcium may facilitate this conformation by binding at the S1 site, thus replacing water as the ligand to Glu20 with sodium, stabilizing the "open" conformation, which can then process zymogenic ISP to active ISP in an intermolecular manner.

This study aimed to characterize new cold-active proteases to learn more about cold-adaptation in enzymes to harness their potential for industrial applications. The novel ISP gene encoding P355 was mined from the genome of the cold-active permafrost bacterium *P. halocryophilus* Or1 (Mykytczuk et al., 2012, 2013) and was expressed in *Escherichia coli* as a C-terminally His-tagged enzyme. We performed a thorough characterization of P355 and compared this with another uncharacterized, putatively thermophilic ISP (T0099), as well as two previously characterized serine proteases: the putative mesophilic ISP (T0034) from *Planococcus* sp. AW02J18 (Bjerga et al., 2018) and the mesophilic ESP Subtilisin Carlsberg, as an industrial reference protease.

Materials and methods

Materials

All chemicals were purchased from Merck KGaA (Darmstadt, Germany) with purity >98% unless otherwise noted. A commercial formulation of the ESP Subtilisin Carlsberg (SC) from *Bacillus licheniformis*, type VIII, (Merck, cat. no. P5380) was included in activity assays.

Identification of an intracellular subtilisin protease

The DNA sequence encoding a subtilisin-like intracellular protease was identified by sequence-based mining of the cryophilic permafrost bacterium *P. halocryophilus* Or1 (GenBank acc. no. ANBV00000000) (Mykytczuk et al., 2012). Isolation and sequencing of genomic DNA followed by assembly of the genome were carried out in a different study (Mykytczuk et al., 2013). Annotation was carried out using the Rapid Annotation Technology (RAST) (Aziz et al., 2008; Brettin et al., 2015) and potential subtilisin-coding ORFs were identified in Geneious (ver. 2020.0.4). Subtilisin candidates were analyzed for subtilisin domains and leader sequences using InterProScan (Jones et al., 2014) and SignalP 6.0 (Nielsen et al., 1997; Teufel et al., 2022), respectively. Three potential subtilisin genes were identified, but only one was active in pre-liminary protease assays, and became the target for this study: The codon-optimized DNA sequence of the identified active candidate, ISP P355, has been deposited in GenBank with accession no. OP748402. For comparative studies, we used the previously reported ISP from *Planococcus* sp. AW02J18 (Bjerga et al., 2018) (T0034, Genbank accession no. MG786190) and an uncharacterized ISP from *Parageobacillus thermoglucosidasius* (T0099; Genbank accession no. WP_003251350), which is known to be a thermophilic Gram-positive bacterium (Aliyu et al., 2016). Similarities of protein sequences were analyzed in Geneious Prime (v. 2022.2.2). Distances were calculated by pairwise alignment using Clustal Omega 1.2.2.

Abbreviations: AAPF, N-Succinyl-Ala-Ala-Pro-Phe p-nitroanilide; DMSO, dimethylsulfoxide; ESP, extracellular subtilisin protease; Gnd, guanidium chloride; ISP, extracellular subtilisin protease; PVDF, polyvinylidene difluoride; raBSA, reduced and alkylated BSA; SC, Subtilisin Carlsberg; RT, room temperature.

Sub-cloning of the ISP gene to expression vectors

For recombinant cloning and enzyme expression, we used a previously developed screening procedure for subtilisin-like proteases (Bjerga et al., 2016). The P355 and T0099 ISP protein sequences were used as templates for gene synthesis (GenScript), and the gene was codon optimized for expression in *E. coli*. The *isp* gene was synthesized with flanking *Sap*I restriction sites and produced in a *Sap*I-free pUC57 vector (kanamycin resistant). The *isp* gene was sub-cloned from the delivery vector to the p12 FX-cloning vector (ampicillin resistant) used in Bjerga et al. (2016) to allow a fusion of a C-terminal hexahistidine tag for downstream purification. T0034 was prepared in the exact same manner, as outlined in Bjerga et al. (2018). The constructs were transformed into chemically competent *E. coli* MC1061 for expression.

Expression and protein purification

Intracellular subtilisin proteases with C-terminal His-tags were expressed from *E. coli*. Cells were cultured on lysogeny broth (LB) agar plates containing 100 μg/mL ampicillin overnight at 37°C. A single colony was inoculated in 10 mL LB with 100 μg/mL ampicillin and incubated overnight at 37°C, 200 rpm. Five mL overnight culture was transferred to 100 mL LB with 100 μg/mL ampicillin and incubated for approx. 5 h at 37°C with 200 rpm until an OD_{600} of 0.5–0.7 before 1 mL sterile 10% L-arabinose was added for induction. The incubation temperature was then adjusted to 20°C, and cultures were incubated overnight at 200 rpm. Cells were harvested by centrifuged at 1000 × *g* for 10 min and resuspended in 40 mL buffer A1 (500 mM NaCl, 30 mM imidazole, 20 mM sodium phosphate, pH 7.4). Cells were lysed by sonication (Qsonica) using a 12 mm probe in ice water using a cycle of 1-s sonication and 1-s pause for 6 min in total at 13% amplitude. The lysate was centrifuged at 22,000 × *g* at 4°C to remove cell debris. The following steps were performed at room temperature (RT), but the protein was kept on ice whenever possible. A 5 mL HisTrap high performance (HP) column (GE Healthcare) was equilibrated in buffer A1 using an ÄKTA purifier system (GE Healthcare) before lysate was loaded. The column was then washed with 5 column volumes of buffer A1 followed by 5 column volumes of 10% B1 where 100% B1 is 500 mM imidazole, 20 mM sodium phosphate, pH 7.4. Finally, the protein was eluted using 100% B1. Additional impurities were removed by applying eluate from the HisTrap HP column to a 5 mL HiTrap Q high performance (GE Healthcare) pre-equilibrated in buffer A2 (10 mM Tris, pH 8). The column was washed with 5 column volumes of buffer A2 before a linear gradient from 0 to 1 M NaCl was applied. A flow of 5 mL/min was used throughout the FPLC-steps and collected into 1 mL fractions. Purity (**Supplementary Figure 1**) was assessed by SDS-PAGE (see Section "SDS-PAGE"), and fractions were tested for protease activity (see Section "Protease activity assays"). The yield was typically 5–20 mg protein pr. L medium. SC was dissolved in MQ (2 or 3.74 μg/μL) with no further purification. Protein concentrations were determined by absorbance at 280 nm (path length = 1 cm) and using the extension coefficients calculated by ProtParam (Gasteiger et al., 2005) and stored at −20°C.

SDS-PAGE

Proteins for SDS-PAGE were denatured by heating to 95°C for 5 min in sample buffer (1% SDS, 5–15 mM DTT, bromphenol blue) and separated using the glycine/2-amino-2-methyl-1,3-propanediol/HCl (ammediol) system in 5–15 or 10–15% acrylamide gradient gels (Bury, 1981) casted in-house (10 × 10 × 0.15 cm). The gels were stained with Coomassie Brilliant Blue.

Protease maturation

Proteases P355, T0034, T0099, and SC (1.9, 2, 2, and 2.5 μM, respectively) were incubated in maturation buffer (25 mM $CaCl_2$, 0.1% (w/w) Triton X-100 (1.7 mM), 100 mM NaCl, and 100 mM glycine, pH 9.5). The proteases were incubated for 10, 30, 60, 90, 120, and 180 min at RT before SDS-PAGE and activity measurement. For SDS-PAGE, 20 μL of each protease solution, each containing approximately 1 μg of the enzyme, was mixed with 12 μL sample buffer (see Section "SDS-PAGE") and denatured at 95°C for 5 min. Additionally, 10 μL was tested for activity where the final protease concentration of P355, T0034, T0099, and SC were 1.63, 1.75, 2.06, and 0.94 nM, respectively (see Section "Protease activity assay").

N-terminal sequencing

Samples destined for Edman degradation were separated by SDS-PAGE as described above, except that the samples were denatured at 80°C for 5 min. The unstained gel was equilibrated in blotting buffer (20% ethanol (v/v) and 0.1 M CAPS pH 11) and electrotransferred to polyvinylidene difluoride (PVDF) membranes (Matsudaira, 1987). The PVDF membranes were stained with Coomassie Brilliant Blue in 50% (v/v) methanol and destained with 50% (v/v) methanol. Protein bands were excised with a clean scalpel and applied to trifluoroacetic acid-treated glass fiber membranes. SC was not electroblotted. Instead, Edman degradation was done directly on a SC stock (2 μg/μL in MQ). The automated Edman degradation was performed in a PPSQ-31B protein sequencer (Shimadzu Biotech) with in-line phenylthiohydantoin analysis using an LC-20AT HPLC system and recorded by the Shimadzu PPSQ-31B software. The sequence was determined through manual inspection of the UV 269 nm chromatograms.

Protease activity assays

Preparation for activity assays and reaction conditions

Matured protease stocks were prepared by incubating for 2 h at RT in maturation buffer (25 mM $CaCl_2$, 0.1% (w/w) Triton X-100, 100 mM NaCl, and 100 mM glycine, pH 9.5) as described in "Protease maturation" to mature the proteases before activity assays except for the "Calcium titration" experiment. Matured proteases were kept on ice before experiments. Protease activity was measured in a FLOUstar Omega plate reader (Thermo-Fischer^{TM})

in half-area plates (Corning®) at 410 nm and at RT using 0.2 mM N-Succinyl-Ala-Ala-Pro-Phe p-nitroanilide (AAPF) as substrate. A 100 mM AAPF stock was made in 100% dimethylsulfoxide (DMSO). The final reaction volume was 100 μL containing 0.2% DMSO and 0.2 mM AAPF.

All protease activity assays contained reaction buffer (25 mM $CaCl_2$, 100 mM glycine, pH 9.5, 0.1% (w/w) Triton X-100, and 100 mM NaCl) unless otherwise stated and carried out at RT. The final protease concentration was approximately 1–4 nM in every activity assay described below unless otherwise stated. This amount of protease produced linear curves with $r^2 \geq 0.99$ based on linear regression of the initial reaction (0–4 min). Every incubation was carried out at RT unless otherwise stated and activity measurement was done in at least technical triplicates.

Calcium titration

Matured protease incubated in reaction buffer containing 0–62.5 mM $CaCl_2$ for 30 min before AAPF was added. pH was adjusted to pH 9.5 except for T0099, which was incubated at pH 7.5.

Inhibition

Inhibition of activity was assessed by testing the effect of EDTA and Pefabloc® on protease activity. For the EDTA assay, 2 μL protease was added to the reaction buffer with no added $CaCl_2$ (protease solution contributed with 63 μM $CaCl_2$ from the maturation step) and 0–1 mM EDTA and incubated for 60 min. For the Pefabloc® assay, 5 μL matured protease was added to the reaction buffer with calcium in 0–5 mM Pefabloc®. Tris at pH 7.5 was used in the reaction buffer to reduce the auto-hydrolysis of Pefabloc®. The protease was incubated with Pefabloc for 2.5 h RT.

pH optimum

Matured protease was added to a reaction buffer containing the following buffers to determine the pH optimum: glycine at pH 2.5–3.5; sodium acetate at pH 4–5.5; MES at pH 5.5–6.5; HEPES at 7–7.5; Tris at pH 7.5–8.5; and glycine at pH 9–10.5. Buffer concentrations were 0.1 M.

Temperature optimum

Half-area plates containing reaction buffer were adjusted to 25 or 45°C on an Eppendorf ThermoMixer C. Water filled the gaps between the wells to stabilize the temperature resulting in low standard deviations along with $r^2 > 0.99$. CAPS at pH 9.7 was used as a buffer instead of glycine as growth occurred in prolonged storage of glycine buffer (0.4 M glycine). The effect of temperature on pK_a of CAPS was compensated by using $d(pK_a)/dT = -0.009$. AAPF stock (100 mM) was diluted with temperature-adjusted water and incubated for 10 min. at either 25 or 45°C in the plate. Finally, 5 μL matured protease was added, and activity was measured immediately.

pH stability

Five μL matured protease was incubated in 95 μL incubation solution [0.1% Triton X-100, 100 mM NaCl, and 100 mM buffer (glycine for pH 2.5 and 3.5, sodium acetate for pH 4.5 and 5.5, MES for pH 6.5, Tris for pH 7.5 and 8.5, and glycine for pH 9.5 and 10.5)]. Five μL of the incubation solution was aspirated after 10, 30, 60, 120, and 180 min, and activity was measured in reaction buffer with a final volume of 100 μL. The pH was adjusted to pH 9.5 by the reaction buffer for all measurements. Calcium was omitted in the incubations and reaction steps due to precipitation, except for the carry-over calcium from the stock solutions.

Temperature stability

Matured proteases were incubated in maturation buffer at different temperatures, and samples were aspirated at different time intervals: 0°C (ice-water) for 24, 48, and 120 h; 25°C for 24, 48, and 120; 45°C for 10, 20, 30 min, 1–4, 24, and 48 h; and 65°C for 10, 20, 30 min, 1–4, 24, and 48 h The remaining activity was measured as described above and normalized to the corresponding matured protease, which had incubated for 0 h at the given temperatures.

Salt titration

Five μL matured protease was added to a reaction buffer containing titrated NaCl (1–1000 mM), KCl (1–1000 mM), urea (4–4000 mM), or guanidine hydrochloride (Gnd) (4–4000 mM) and incubated for 30 min before the activity was measured. The activity was normalized to the lowest salt concentration: 0.98 mM for NaCl and KCl and 3.91 mM for urea and Gnd.

Michaelis-Menten kinetics

Michaelis-Menten kinetics were determined by measuring the activity at different substrate concentrations ranging from 0.03 to 4 mM (using a 400 mM AAPF stock) in reaction buffer at 25 and 45°C. Protease concentrations were 0.94, 10.02, 4.06, and 2.37 nM for P355, T0034, T0099, and SC, respectively. The concentration of T0034 was lowered to 1.02 nM at 45°C. Initial rate was determined by linear regression ($r^2 > 0.99$). Absorbance was converted to mM by the slope of the linear standard curve ($r^2 > 0.99$), where the substrate had been hydrolyzed completely. Enzymatic activity was defined as the turnover rate of millimolar substrate pr. hour (mmol/h). The kinetics constants were derived with R (v. 4.0.5) using the add-on package *drc* (Ritz et al., 2016) by non-linear fit (least squares estimation) with a confidence interval of 0.99.

Casein digest

Proteolysis of resorufin-labeled casein was assessed by incubating 3 nM matured P355, T0034, and SC, and 60 nM matured T0099 with 0.5 μg/μL resorufin-labeled casein in 100 mM or 1000 mM NaCl. A reaction was quenched every 2.5 min with 2% (v/v) TCA and incubated for 10 min at 37°C, precipitating undigested casein. The solution was filtered using a MultiScreen Solvinert Filter plate (Millipore) by centrifugation at 500 × *g* for 5 min. and filtrate was collected in a Corning® 96 well plate. The filtrate was adjusted to pH 8.8 using 3.9 M Tris, and absorbance was measured at 574 nm. The reaction rate was linear within the first 10 min ($r^2 > 0.99$). Proteolytic activity against casein was defined as $A \times h^{-1} \times nM^{-1}$ (the slope divided with the protease concentration).

raBSA digest in ice-water

The BSA was dissolved in 8 M urea (0.27 mM), and the disulfide bridges were reduced using 10 mM DTT for 60 min at RT. Iodoacetamide (30 mM) was added, and the sample was incubated for 60 min at RT in the dark before 35 mM DTT was added to quench the reaction. The reduced and alkylated BSA (raBSA) was

dialyzed into 10 mM Tris pH 8 so that [urea] <10 mM and stored at −20°C. Titrated matured protease (0.4–100 nM) incubated with 3.75 μg raBSA (1.88 μM) in reaction buffer containing 100 or 1000 mM NaCl for 2 h in ice-water. Controls were raBSA without protease and protease (highest concentration) without raBSA. The pH shift in the reaction buffer due to the lower temperature was considered by using d(pKa)/dT = −0.025. The reaction was terminated by adding SDS-PAGE sample buffer, DTT (see Section "SDS-PAGE") along with 42 mM EDTA and heating to 95°C for 10 min. Digestion patterns were examined with SDS-PAGE, and the density of the raBSA band was measured using Gel Doc^{TM} EZ imager (Biorad) software.

Cleavage sites in BSA and micro purification for mass spectrometry

A total of 3.8 μg raBSA (BSA digest in ice water) was loaded onto an SDS-PAGE to separate intact raBSA from impurities and nicked raBSA. The raBSA band was cut out and washed twice with 500 μL H_2O followed by two times incubation of 15 min with 50 μL 50% acetonitrile. Then, 50 μL of 100% acetonitrile was added and incubated for 15 min before the reaction buffer was added to a 1:1 ratio. The liquid was removed after 15 min and lyophilized until the gel plug was dry. Matured protease (600 nM) was added to the dried plugs and incubated for 10 min. Thirty μL reaction buffer was added and incubated for 1.5 h. Triton X-100 was excluded as detergents are not compatible with MS. All incubation was performed at RT except protease digestions, which were allowed to proceed at 37°C. The reaction was quenched with 7.1% formic acid. The resulting peptides from protease digestion were micro-purified using C18 column material (Empore^{TM}) in P10 pipette tips (Sarstedt). The column material was activated with solvent B (99.9% acetonitrile and 0.1% formic acid) and then equilibrated with solvent A (0.1% formic acid). Peptides were then loaded and washed in solvent A before being eluted with 70% solvent B and dried for MS. The experiment was carried out in triplicates.

LC-MS/MS and data processing

Nano LC-MS/MS was carried out on an Orbitrap Eclipse Tribrid mass spectrometer connected online to an EASY nanoLC 1200 (both instruments were from Thermo Fisher Scientific). Samples were dissolved in solvent A, desalted on a ReproSil-Pur C18-AQ trap column (2 cm × 100-μm inner diameter packed in-house with 3 μm resin (Dr. Marisch GmbH, Ammerbuch-Entringen, Germany). The raBSA-peptides from the protease digestion were eluted and separated on a 15-cm analytical column (75 μm inner diameter) packed in-house with ReproSil-Pur C18-AQ 3 μm resin (Dr. Marisch GmbH, Ammerbuch-Entringen, Germany). A flow rate of 250 nL/min was used to elute the peptides with a 50-min gradient from 5 to 35% solvent B.

The generated raw files were converted to Mascot generic format. Data was searched in Mascot (version 2.5.0) against the SwissProt Data base (565,928 sequences composed of 204,173,280 residues). The entire SwissProt database was used as a decoy database (random sequence). The following search parameters were (1) 'none' as the protease, (2) minimum 6 residues in a peptide, (3) precursor mass deviation of maximum 10 ppm, (4) fragment mass deviation of maximum 0.02 Da, (5) dynamic modification with oxidation on Met, and (6) fixed modification with alkylation (carbamidomethyl) on Cys. The false discovery rate was set to 1% before data was exported to MS Data Miner (Dyrlund et al., 2012). Peptides having a score lower than the significant score provided by the Mascot search were discarded.

R programming and statistics

Data analysis and figures were made in R (version 4.0.5) (R Core Team, 2021) coupled with RStudio Team (2020). The following packages were employed for general data analysis: *tidyverse* (Wickham et al., 2019), *tagger* (Campitelli, 2022), *lemon* (McKinnon Edwards, 2020), *readxl* (Wickham and Bryan, 2019), and *ggExtra* (Attali and Baker, 2019). Additional packages used for a specific experiment are cited in the given method description. All error bars show the standard deviation (SD) of triplicates or more.

Results

Sequence alignment of ESP and ISP

The well-known, mesophilic ESP Subtilisin Carlsberg (SC) from *Bacillus licheniformis* (Linderstrøm-Lang and Ottesen, 1947) was compared to two uncharacterized ISP proteases, the putative cold-adapted P355 and the putative thermophilic T0099 from *Parageobacillus thermoglucosidasius*, and to a previously characterized ISP protease, T0034 from *Planococcus* sp. AW02J18. The latter origin from a marine bacterium isolated from coastal waters near Lofoten in Norway (Bjerga et al., 2018). P355 is presumed to be cold-adapted as it is from the genome sequence of the extremophile *P. halocryophilus* Or1 identified in Arctic permafrost (Mykytczuk et al., 2013). T0099 is presumed to be thermophilic as it originates from the genome of *Parageobacillus thermoglucosidasius*, known to thrive at temperatures up to 68°C (Aliyu et al., 2016). To the authors' knowledge, no thermophilic ISP has been described.

Pairwise alignment of full ISP protein sequences, including pre-sequences, revealed that the closest related protein sequences to T0099 were an ISP from *Paenibacillus polymyxa* (acc. no. P29139) (64% amino acid similarity) (Takekawa et al., 1991) as well as the major ISP from *B. subtilis* subsp. *subtilis* str. 168 (acc. no. P11018) (64% amino acid similarity) (Koide et al., 1986). P355 shared 72% amino acid sequence identity to the characterized ISP from *Planococcus* sp. AW02J18, henceforth referred to as T0034 (Bjerga et al., 2018), which is included in this study for comparison. As expected, analysis using SignalP showed that neither of the ISP sequences were predicted to have an N-terminal signal peptide for extracellular export. Similar to T0034 (Bjerga et al., 2018), the novel ISPs T0099 and P355 contained a short pro-peptide with a conserved LIPY/F-sequence at the N-terminus (T0099: LIPF, P355: LIPY) (**Supplementary Figure 2**; Vévodová et al., 2010; Gamble et al., 2011; Bjerga et al., 2018). The catalytic domains of ESPs and ISPs are homologous, with all three residues involved

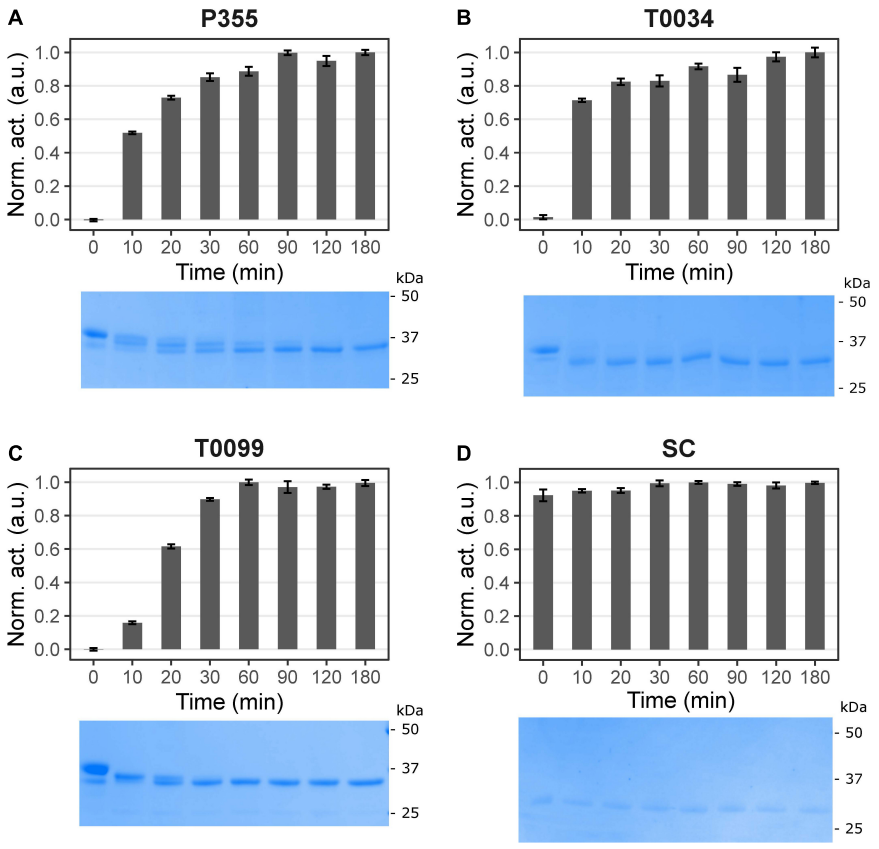

FIGURE 1
Time course maturation of the proteases. Maturation was started by incubating in 100 mM NaCl, 25 mM $CaCl_2$, 100 mM glycine pH 9.5, and 0.1% Triton X-100. The maturation process was monitored with activity assay using 0.2 mM N-Succinyl-Ala-Ala-Pro-Phe p-nitroanilide (AAPF) and SDS-PAGE at different time intervals in minutes: after 0, 10, 20, 30, 60, 120, and 180 min incubation. The sample at 0 min had not received $CaCl_2$. The activity was normalized to the highest activity measured for the given proteases and plotted against the conditions. No activity and proteolytic processing occurred for panel **(A)** P355, **(B)** T0034, and **(C)** T0099 without calcium. Calcium induced activity and proteolytic processing, i.e., maturation. Maturation was complete after 90, 120, and 60 min for P355, T0034, and T0099, respectively, judged by the activity plateau and no further band migration. Subtilisin Carlsberg (SC) **(D)** was unaffected throughout the incubation. Error bars show standard deviation (n = 3). Note that the figures are cropped. See **Supplementary Figure 4** for uncropped images.

in the catalytic tried being conserved, and both members are part of the Subtilisin Peptidase S8 family as classified by Pfam. The major difference between ISPs and ESPs lies in the absence of signal sequences in the ISPs and the presence of a shorter pro-sequence for the regulation of catalytic activity (Gamble et al., 2011).

Calcium induces the activation of P355, T0034, and T0099

Subtilisins are zymogens, i.e., they become proteolytically active through a maturation process where the pro-peptide at the N-terminal is removed (Neurath and Walsh, 1976). This process can be calcium-dependent (Gamble et al., 2011; Bjerga et al., 2018) as well as pH-dependent (Bjerga et al., 2018), and can be a relatively slow process (Gamble et al., 2011). For this study, the three ISPs, P355, T0034, and T0099, were recombinantly expressed in *E. coli* with their pro-peptide sequences intact. Histidine tags fused to the C-terminal allowed downstream purification by nickel affinity and anion exchange chromatography in the absence of calcium to avoid maturation (Bjerga et al., 2018). A commercial formulation of ESP, SC, was purchased, and used as a reference in the experiments. To investigate the activation of the ISPs, we determined their proteolytic activity toward a colorimetric peptide [N-Succinyl-Ala-Ala-Pro-Phe p-nitroanilide (AAPF)] as a model substrate after incubation with a titration series of calcium. The proteolytic activity of the three recombinant ISPs showed dependence on $CaCl_2$ ranging from 0.2 to 62.5 mM $CaCl_2$ (**Supplementary Figure 3**) with no activity observed at 0 mM $CaCl_2$. The ESP was independent of $CaCl_2$, i.e., activity was observed at 0 mM $CaCl_2$ with a slight decrease in activity in the same $CaCl_2$ concentration range. Next, we investigated the maturation of the ISPs over time after initiation using 25 mM $CaCl_2$, as assessed by AAPF activity and SDS-PAGE (**Figure 1**). All three ISPs in their zymogenic form were inactive and unprocessed before 25 mM $CaCl_2$ was added (**Figures 1A–C**). No processing or activity was observed even after 180 min incubation without calcium (**Supplementary Figures 4E, F**). In the presence of 25 mM $CaCl_2$, the activity of the ISPs increased over time, concurrent with a corresponding change in the migration of bands visualized by SDS-PAGE from the full-length zymogen to the truncated active protease. N-terminal protein sequencing of zymogens, prepared in the absence of calcium treatment, showed

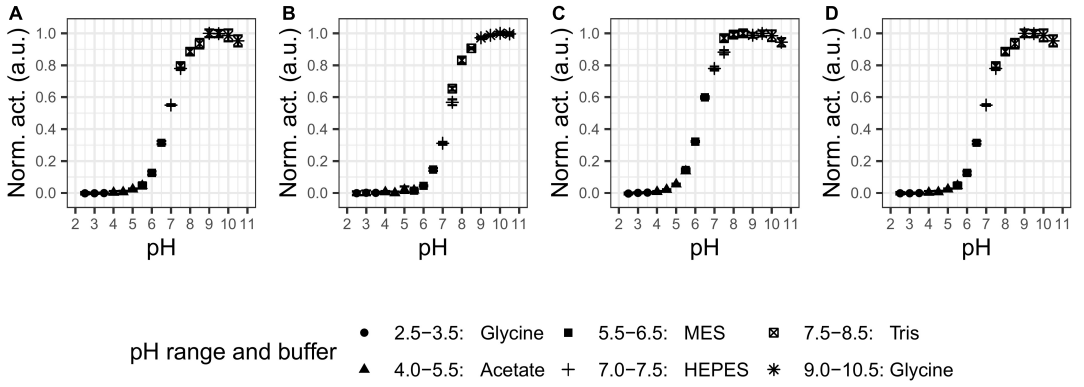

FIGURE 2
pH optima. Activity was assessed with 0.2 mM N-Succinyl-Ala-Ala-Pro-Phe p-nitroanilide (AAPF) for matured proteases under different pH values. The legend shows the buffers used in the different pH ranges. Every protease showed activity the alkaline range with optimal pH at **(A)** 9–9.5 for P355; **(B)** 10 for T0034; **(C)** 8–9.5 for T0099; and **(D)** 9–9.5 for Subtilisin Carlsberg (SC). Activity was normalized to the highest activity for the given protease. Error bars show standard deviation (n = 3). Note that some error bars are within the marker.

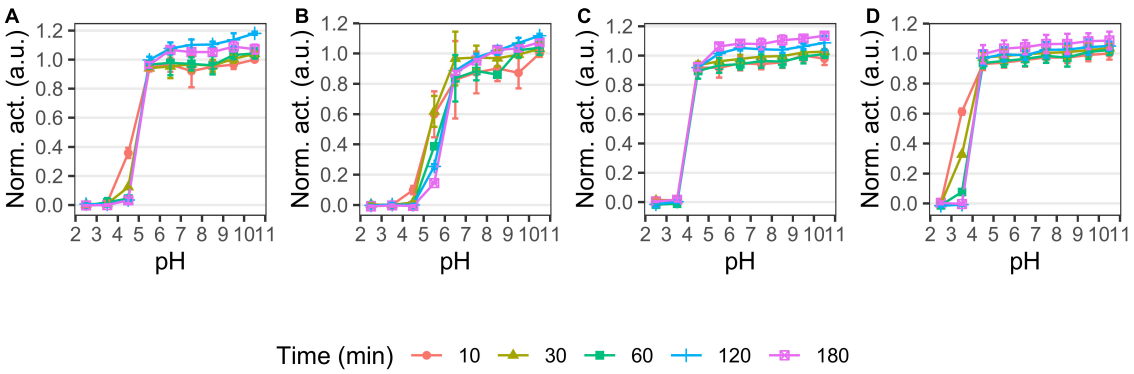

FIGURE 3
pH stability of P355 **(A)**, T0034 **(B)**, T0099 **(C)**, and Subtilisin Carlsberg (SC) **(D)**. Matured proteases were incubated in different pH values and activity was measured after 10, 30, 60, 120, and 180 min at pH 9.5 with 0.2 mM N-Succinyl-Ala-Ala-Pro-Phe p-nitroanilide (AAPF) at room temperature (RT). Activity was normalized to the highest activity for the given protease at 10 min. The protease activity did not decline over time in the alkaline range, but activity in the acidic range decreased in the following order: SC > T0099 > P355 > T0034. Error bars show standard deviation (n = 3).

that zymogens lacked the first amino acid (Met). Active P355, T0034, and T0099, i.e., 2 h incubation with 25 mM $CaCl_2$ at pH 9.5, lacked an additional 9, 15, and 16 N-terminal residues, respectively (**Supplementary Figure 2**), demonstrating that the pro-peptide and its LIPY/F motif were removed in all three active ISPs. Additional intermediate bands were visible for P355 (**Figure 1A**) and T0099 (**Figure 1C**) in SDS-PAGE analysis of the maturation process, indicating that their activation may occur in distinct steps. The activity reached a maximum and the conversion to the active protease was complete after 120, 120, and 60 min. for P355, T0034, and T0099, respectively. SC showed no change in activity or processing with or without calcium incubation (**Figure 1D** and **Supplementary Figures 4E, F**) thus verifying that its pro-peptide was fully removed during commercial production and formulation. Based on these data, we defined the conditions that produce matured and active proteases and henceforth, the three ISPs are referred to simply as proteases. Based on these data, ISPs were routinely activated for 2 h in the presence of calcium prior to their use in subsequent assays. The relative number of active sites between the subtilisins were estimated by α-2-macroglobulin titration (**Supplementary Figures 5–9**). By a rough estimation, P355, T0034, and SC contained relatively the same number of active sites, while T0099 contained approximately half as many (**Supplementary Figure 8**) indicating less correctly folded protein. The metal chelator EDTA inhibited the three ISPs, but SC was largely unaffected (**Supplementary Figure 10A**). The commercial serine protease specific inhibitor Pefabloc® blocked activity from all proteases (**Supplementary Figure 10B**).

Effect of pH and temperature on activity and stability

We examined the pH and temperature profiles, in part to determine the optimal experimental conditions, but also to establish temperature optima and stability, which is typically lower for cold-adapted enzymes compared to meso- and thermophilic enzymes (Furhan, 2020). All proteases showed activity in a broad alkaline range (**Figure 2**) with optima at pH 9–9.5 for P355, pH 10 for T0034, pH 8–9.5 for T0099, and pH 9–9.5 for SC. The

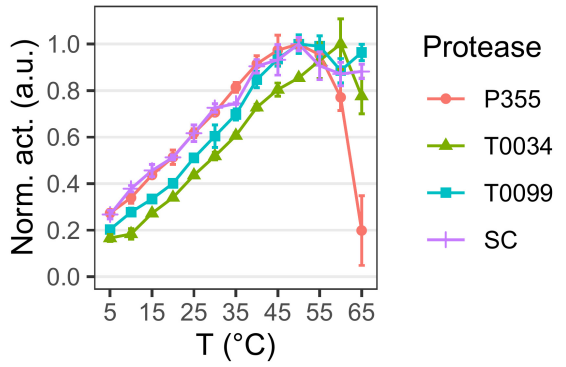

FIGURE 4
Temperature optima. Matured protease activity was measured under different temperatures using 0.2 mM N-Succinyl-Ala-Ala-Pro-Phe p-nitroanilide (AAPF). Activity was measured at pH 9.7 using 0.1 M CAPS. Changes in pK_a with temperature were compensated with d(pKa)/dT = −0.009 in buffer preparation. Activity was normalized to the highest activity for the given protease. Matured P355, T0034, and Subtilisin Carlsberg (SC) have a temperature optimum at 50°C, while matured T0034 has a temperature optimum at 60°C. Matured P355 showed less activity at the highest temperatures compared to the others. Error bars show standard deviation (n = 3).

proteases were stable at alkaline pH and restored full activity after 3 h (Figure 3). There was a tendency for activities to slightly increase after 1 h incubation in alkaline conditions. The stability declined toward the acidic range for all enzymes, where no activity remained after 3 h pre-incubations at pH ≤ 3.5 for any of the proteases (Figures 2, 3). The stabilities ranked in the following order from most to least stable based on the remaining activity at pH 3.5–5.5: SC > T0099 > P355 > T0034.

The temperature optimum (Figure 4) of the proteases was determined to be 50°C for P355, T0099, and SC, and 60°C for T0034. The proteases were active at 65°C, but P355 activity dropped to 20% of its maximum activity. P355 and SC showed roughly 50% higher activity at 5°C than T0034 and T0099. Thermal stability was determined by measuring the remaining activity after incubation at different temperatures. Every protease retained 100% activity at 0°C for the duration of the experiment (120 h). While T0099 and SC also remained 100% active after 120 h at 25°C, P355 and T0034 had lost 30–40% of their activity (Figure 5). P355 and T0034 lost all activity after 48 h at 45°C, where T0099 and SC still retained approximately 70 and 50% activity, respectively. At 65°C, P355 and T0034 lost their activities after 30 and 60 min, respectively, while T0099 and SC restored 11% and 3% activity after 48 h, respectively.

Overall, the pH profiles indicate active and stable proteases in the alkaline range. P355 and T0034 have lower thermal stability than T0099 and SC, consistent with the expectations for cold-adapted proteases. However, the temperature optima were similar, although P355 was relatively less active at 65°C.

Salt titrations and casein digest

Chemical stability was also investigated, as cold-adapted proteases are usually more susceptible to chemical denaturation by guanidium chloride (Gnd) and urea than their meso- and thermophilic counterparts (D'Amico et al., 2003). Overall, increasing concentrations of urea (Figure 6A) and Gnd (Figure 6B) reduced the activity of all proteases. P355 and T0034 lost more activity at lower urea concentrations relative to SC and T0099, where T0099 retained most activity. Titration with Gnd showed a different pattern: while the curves of P355 and T0034 are to the left of T0099 and SC in the urea titration (Figure 6A), the activity profiles cross each other with increasing Gnd (Figure 6B). At 0.5 M Gnd P355 and T0034 show the least activity followed by T0099 and SC. These data are in line with prior data (D'Amico et al., 2003), which indicated that cold-adapted proteases are more prone to chemical denaturation.

Microorganisms that thrive in subzero degrees are usually also halophilic or halotolerant as salt lowers the freezing point of water (Mykytczuk et al., 2013). Thus, the effect of ionic strength on the catalytic activity using NaCl or KCl was investigated. Increasing concentrations of NaCl and KCl enhanced the activity of P355 and T0034 toward the AAPF peptide substrate. 1M NaCl increased their activities approximately 4-fold (Figure 6C), whereas 1M KCl increased P355′s and T0034′s activity by approximately 2-fold (Figure 6D). We investigated whether the enhancement of activity with increasing NaCl also occurred for other types of substrates, e.g., larger substrates, as these are also potential substrates. For this purpose, we used resorufin labeled casein (20 kDa). When casein is used as a substrate instead of the AAPF peptide, activity decreased for all proteases when NaCl concentration increased from 100 to 1000 mM (Figure 7A). Thus, it seems that the effect of NaCl is substrate-dependent. Normalizing the activity to the protein concentration shows that P355 and T0034 hydrolyzed casein most efficiently followed by SC and finally T0099 (Figure 7B).

P355 and T0034 have higher catalytic constants compared to T0099 and SC

Cold-adapted enzymes typically have a higher catalytic constant (k_{cat}) than their meso- and thermophilic homologs to compensate for the general decrease in activity at low temperatures (Feller et al., 1992). This was examined by performing Michaelis-Menten kinetics at 25 and 45°C. Judging from the fitted curves (Supplementary Figure 11) and the residuals of the fitted curves to the experimental data points (Supplementary Figure 12) and the low deviations of the fitting parameters (Supplementary Table 1), the proteases mostly follow Michaelis-Menten kinetics. However, T0099 deviates from Michaelis-Menten kinetics at high substrate concentrations (3 and 4 mM), which is also reflected in the residual plot (Supplementary Figures 12E, F). P355 and T0034 have higher k_{cat} values than T0099 and SC at 25° and 45°C (Table 1); these results, based on AAPF hydrolysis, are consistent with the results from the casein digestion assay (Figure 7) where P355 and T0034 demonstrated a higher activity. T0034 had the highest K_m at 25° and 45°C, closely followed by P355, whereas K_m of SC and T0099 are lower. K_m increased between 0.02 and 0.06 mM with higher temperatures for every protease, except for T0034, which decreased from 1.83 to 1.26 mM. SC displayed the highest catalytic efficiency (k_{cat}/K_m) at 25°C of all proteases, while P355 and T0034 displayed the highest at 45°C. The catalytic efficiency increased approximately 1.5 to 2.5-fold for every protease from 25 to 45°C, except for T0034, which quadrupled from 2.09×10^5 to 8.55×10^5

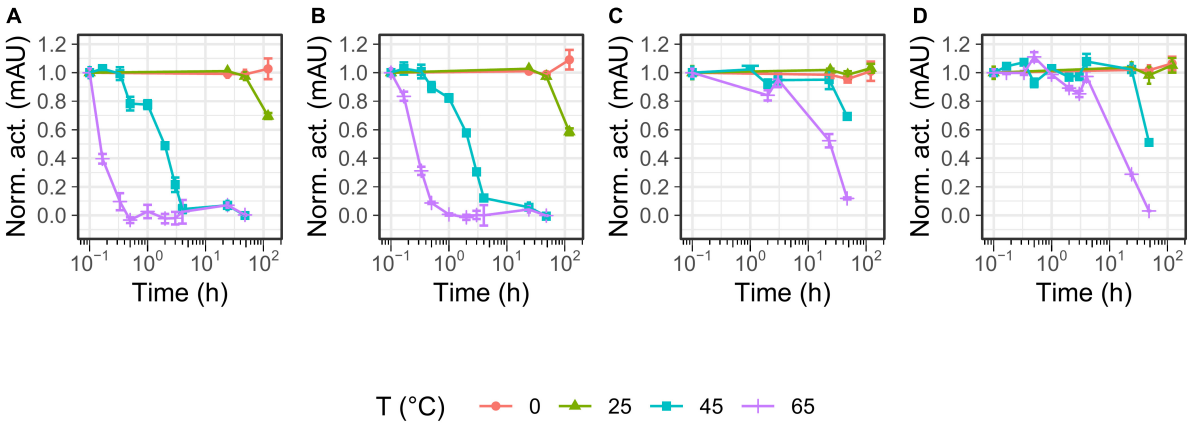

FIGURE 5
Temperature stability of P355 **(A)**, T0034 **(B)**, T0099 **(C)**, and Subtilisin Carlsberg (SC) **(D)**. The matured protease incubated in maturation buffer [25 mM CaCl2, 0.1% (w/w) Triton X-100, 100 mM NaCl, and 100 mM glycine pH 9.5] at 0 (ice-water), 25, 45, and 65°C ranging between 10 min and 120 hr. Remaining activity was assessed with 0.2 mM N-Succinyl-Ala-Ala-Pro-Phe p-nitroanilide (AAPF) and normalized to 0 h. Note that 10^{-1} h is defined here as 0 h and was only exposed to room temperature (RT). Every protease was stable for 120 h at 0°C. P355 lost all activity after 30 min at 65°C, while T0034 lost all activity after 1 h. T0099 was the most stable with approximately 10% remaining after 48 h incubation at 65°C. Activity was almost gone after 48 h for SC. Error bars show standard deviation (n = 3).

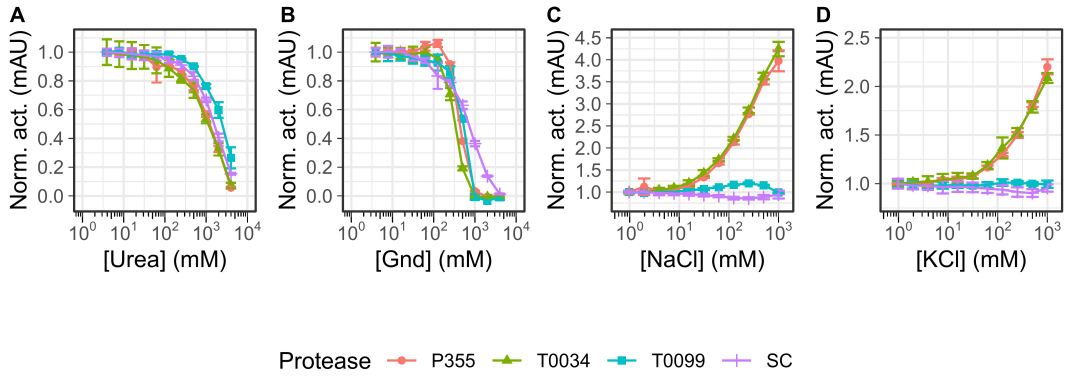

FIGURE 6
Salt titrations. Matured protease was titrated with 1–1000 mM NaCl or KCl or 4–4000 mM urea or guanidium chloride (Gnd) and incubated for 30 min at room temperature (RT) before activity was measured with 0.2 mM N-Succinyl-Ala-Ala-Pro-Phe p-nitroanilide (AAPF). **(A)** Urea titration lowers protease activity with T0099 being the most resilient. **(B)** Gnd decreases protease activity where Subtilisin Carlsberg (SC) was the most resilient. One M Gnd effectively inhibited protease activity for P355, T0034, and T0099, while 4 M Gnd was needed to abolish SC activity. **(C)** NaCl enhanced P355 and T0034 activity with increasing salt concentration, while T0099 and SC were largely unaffected in comparison. **(D)** KCl also enhanced activity of P355 and T0034 and as with NaCl, T0099 and SC were largely unaffected. Data were normalized to the lowest salt concentration in question. Error bars show standard deviation (n = 3).

M^{-1} s^{-1}. The kinetic data (Table 1) indicate that P355 and T0034 are cold-adapted ISPs due to higher k_{cat} and K_m values at both temperatures tested relative to the reference enzymes T0099 and SC. However, T0099 and SC showed similar catalytic efficiency to P355 and T0034 owing to their low K_m values.

Reduced and alkylated BSA is readily digested by P355 and T0034 at around 0°C

A critical trait in cold-adaptation is higher catalytic activity at low temperatures compared to meso- and thermophilic conditions (Åqvist et al., 2017). We tested the proteolysis at low temperature by incubating an equal molar titration series of P355, T0034, T0099, or SC with a fixed amount of reduced and alkylated BSA (raBSA) at 0°C (ice water). Digestion of the raBSA substrate was tested at low (0.1 M) or high (1 M) concentration of NaCl salt to examine whether the same effect was observed for raBSA as with casein. The digestion of raBSA were in line with the kinetic data (Table 1) and casein digestion (Figure 7B); P355 and T0034 degraded raBSA quicker than T0099 and SC. It was observed that 1 M NaCl inhibited proteolytic activity for every protease, except for T0099, where activity was largely unaffected by NaCl at all protease concentrations (Figure 8) in line with the casein digest (Figure 7). P355 (Figure 8, panels A1–3) and T0034 (Figure 8, panels B1–3) followed the same pattern: at the highest substrate:protease ratios, the semi-quantitative band intensities of intact raBSA was reduced by >75% in 0.1 M NaCl. Increasing the NaCl concentration to 1 M resulted in less efficient hydrolysis by

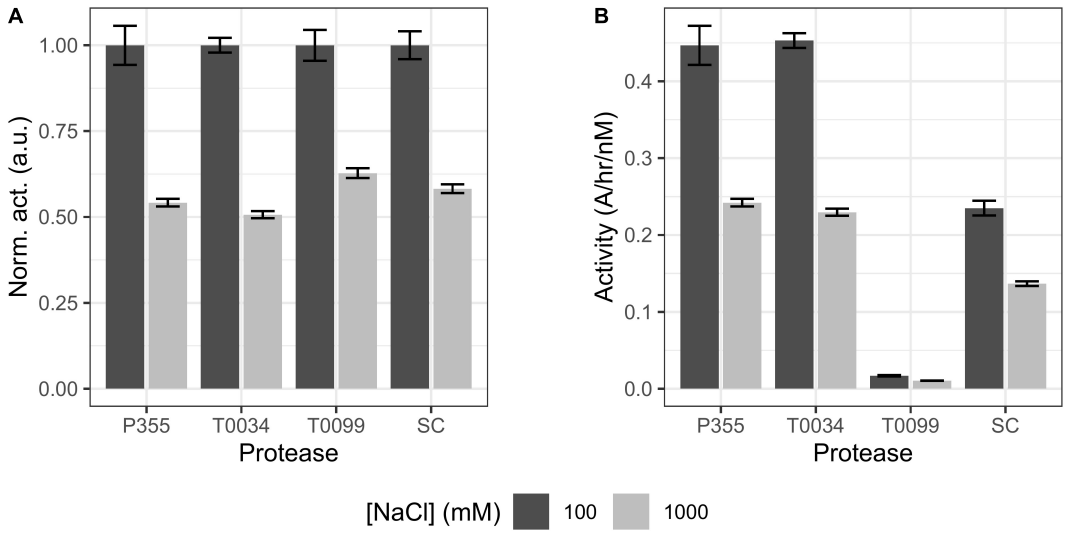

FIGURE 7
Bar plot of casein digest. The ability of matured proteases to digest casein in the presence of 100 or 1000 mM NaCl was examined. P355, T0034, and Subtilisin Carlsberg (SC) concentrations were 3 nM, while T0099 concentration was 60 nM as no activity was observed at 3 nM (data not shown). **(A)** Activity was normalized to the maximum activity of the respective protease. Increasing [NaCl] from 0.1 to 1 M reduced the hydrolysis of casein of every protease by 40–50%. **(B)** The same data set, but with activity normalized to matured protease concentration (nM). P355 and T0034 showed equal activity, while T0099 was poor in comparison. SC showed intermediate efficiency. Error bars show standard deviation (n = 3). Every regression had $r^2 > 0.99$. Casein did not precipitate in 1 M NaCl (data not shown).

P355, T0034 and SC, i.e., cleaving about 40–50% raBSA. T0099 was the least efficient enzyme in this assay, showing a reduced band intensity by around 20% at the same substrate:protease ratios at both NaCl conditions (Figure 8, panels C1–3). SC showed intermediate digestion capabilities: at the highest substrate:protease rations conditions, SC reduced the intact raBSA band intensity with approximately 50% in 0.1 M NaCl, with a slight inhibition by higher NaCl concentration (Figure 8, panels D1–3). These results align with the casein digestion assay (Figure 7B). The position of the degradation bands from raBSA were not identical between the proteases, indicating different specificities. We employed mass spectrometry (MS) to investigate digestion products to examine whether there were differences in hydrolysates of raBSA depending on the amino acid at position P1. MS/MS analysis of peptide products revealed that the proteases cleaved at the same residues, which included hydrophobic, basic, and acidic residues (see Section "Data availability statement"). Additionally, NaCl also changed the degradation pattern slightly. For instance, at the 25 kDa marker in Figure 8, panels A1–2, a few bands disappear, which indicate changes in substrate specificity. However, this was not investigated further.

TABLE 1 Derived kinetic constants.

Protease	T (°C)	K_m (mM)	k_{cat} (s^{-1})	k_{cat}/K_m (M^{-1} s^{-1})
P355	25	1.12 ± 0.02	386 ± 3	3.45×10^5
	45	1.17 ± 0.02	996 ± 9	8.52×10^5
T0034	25	1.83 ± 0.05	382 ± 5	2.09×10^5
	45	1.26 ± 0.03	1077 ± 11	8.55×10^5
T0099	25	0.10 ± 0.01	35 ± 1	3.49×10^5
	45	0.12 ± 0.01	69 ± 1	5.73×10^5
SC	25	0.38 ± 0.01	208 ± 1	5.48×10^5
	45	0.44 ± 0.01	348 ± 2	7.91×10^5

Deviations show the confidence interval (0.99), n = 3.

Discussion

P355, T0034, and T0099 depend on calcium for maturation and activity

The goal of this paper was to identify, produce, and characterize a novel protease from the cold-adapted and halo-tolerant bacterium *P. halocryophilus* Or1, which can grow down to −15°C (Mykytczuk et al., 2013). We identified a gene encoding a putative intracellular subtilisin protease (ISP) denoted P355 in the genome sequence, which we expected to harbor cold-adapted traits. We successfully cloned and produced the recombinant P355 protease in *E. coli* and characterized the enzyme. In addition, we compared it to homologous ISPs and an ESP identified from literature or databases: The putative mesophilic T0034 from *Planococcus* sp. AW02J18 (Bjerga et al., 2018), the presumably thermostable T0099 from *Parageobacillus thermoglucosidasius* and the ESP industry reference Subtilisin Carlsberg (SC). The results are summarized in Table 2.

The ISPs, P355, T0034, and T0099, showed a dependency on calcium for activation (Figure 1 and Supplementary Figure 3), and up to 2 h were required for complete processing in order to gain full activation (Figure 1). N-terminal sequencing confirmed the removal of the pro-peptide and its LIPY/F motif in every ISP. We also observed maturation intermediates for P355 and T0099, indicating that activation may be a multi-step process.

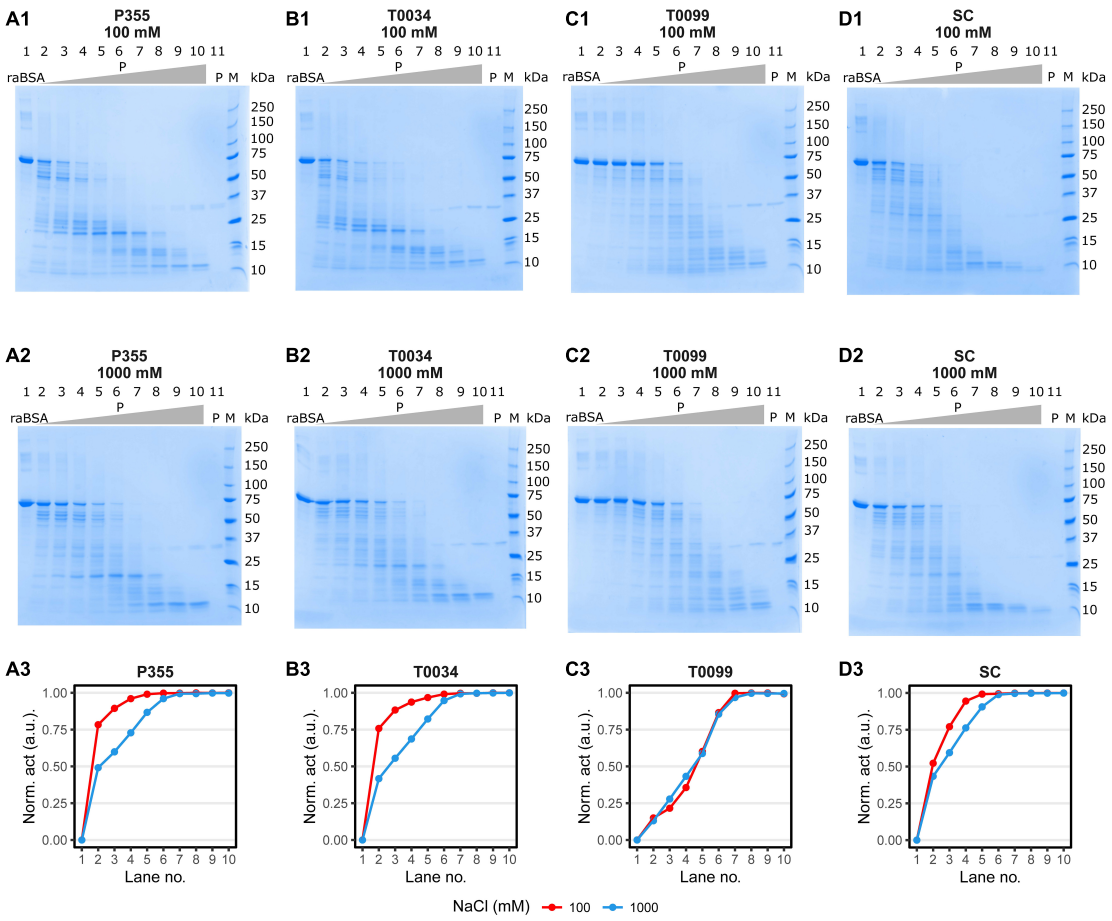

FIGURE 8
raBSA digest in ice-water (0°C). 3.75 μg (1.88 μM) raBSA (approximately apparent 70 MW) was digested by an increasing concentration of matured protease for 2 h in ice-water in the presence of 100 or 1000 M NaCl before being heated to 95°C for 10 min. The protease concentration in each lane was as follows: (1) 0nM, (2) 0.4 nM, (3) 0.8 nM, (4) 1.6 nM, (5) 3.1 nM, (6) 6.3 nM, (7) 12.5 nM, (8) 25 nM, (9) 50 nM, (10) 100 nM, and (11) 100 nM. Lane 11 contained no raBSA. The digestion patterns of P355, T0034, T0099, and Subtilisin Carlsberg (SC) and the corresponding degree of raBSA digestion are shown in panels **(A1–3,B1–3,C1–3,D1–3)**, respectively. The normalized activity values were obtained by normalizing the intact raBSA bands (lane 2 through 10) to the intact raBSA band control (lane 1) and subsequently subtracted from 1. Hence, the activity values correspond to a relative reduction in band intensity. P355 and T0034 were most efficient in digestion raBSA: They lowered the intensity of the BSA band of approx. 75% at 0.4 nM enzyme, while T0099 and SC had lowered the intensity with approx. 20 and 50%, respectively. The increase to 1000 mM NaCl decreased the ability of all proteases, most prominent for P355 and T0034, although P355 was slightly more efficient in digestion raBSA compared to T0034 at 1000 mM. SC was slightly inhibited by 1000 mM NaCl, while T0099 was largely unaffected. raBSA, reduced and alkylated BSA; P, protease.

No intermediates were observed for T0034, in contrast to what has been previously reported (Bjerga et al., 2018). However, maturation is calcium- and pH-dependent (Bjerga et al., 2018) and experimental variation in assay conditions may explain the deviation to the previous report. In this study, the combination of a higher calcium concentration and higher pH compared to the previous study on T0034 (Bjerga et al., 2018) likely caused a swifter maturation and lack of observable intermediates. Inhibition of the ISPs by EDTA (**Supplementary Figure 10A**) shows that not only is calcium necessary for ISP activation, but it is also needed to sustain activity in the ISPs in this study. In contrast, the ESP SC was largely unaffected by the presence of EDTA.

Gamble et al. (2011) reported a lag phase during the maturation of an ISP from *Bacillus clausii* NN010181 before an exponential increase in active ISP followed by a plateau. This is due to a positive feedback mechanism where protease removes the N-terminal propeptide and activates the unprocessed protease (Gamble et al., 2011). Lag phases were not observed in this study, possibly due to a more rapid maturation at higher pH values and calcium concentrations.

The matured proteases are active and stable in alkaline pH

Alkaline activity is expected for serine proteases, as the His and Asp residues of the catalytic triad must be in their deprotonated form to deprotonate Ser (Hofer et al., 2020). Every protease in this study showed activity and stability in the alkaline range.

T0034 has been characterized previously by Bjerga et al. (2018), and we chose to include this close homolog in comparative studies of P355 due to their relatively high sequence homology. This and the past study of T0034 report some differences in pH profiles. We both find maximum activity at a plateau around

TABLE 2 Collected and summarized results obtained in this study.

		P355	T0034	T0099	SC	Figure/Table
Subtilisin type		ISP	ISP	ISP	ESP	Supplementary Figure 2
Maturation dependent on calcium		Yes	Yes	Yes	Not examined	Figure 1
Maturation time course (min)		90	120	60	Not examined	Figure 1
Activity dependent on calcium		Yes	Yes	Yes	No	Supplementary Figure S3
Inhibition by EDTA		Yes	Yes	Yes	No	Supplementary Figure 10A
Inhibition by Pefabloc®		Yes	Yes	Yes	Yes	Supplementary Figure 10B
pH activity		Alkaline	Alkaline	Alkaline	Alkaline	Figure 2
pH stability range		5.5–10.5	6.5–10.5	4.5–10.5	4.5–10.5	Figure 3
Temperature optimum (°C)		50	60	50	50	Figure 4
Temperature stability		Lowest	Low	Highest	High	Figure 5
k_{cat} (s^{-1})	45°C	386 ± 3	382 ± 5	35 ± 1	208 ± 1	Table 1
	25°C	996 ± 9	1077 ± 11	69 ± 1	348 ± 2	
Relative casein/raBSA digest efficiency		High	High	Low	Intermediate	Figures 7B, 8
Activity affected by increasing [NaCl]	AAPF	Increased	Increased	Small effect	Small effect	Figure 6C
	Casein/raBSA	Decreased	Decreased	Decreased	Decreased	Figures 7A, 8
Cleavage sites observed		Hydrophobic, acidic, and basic	Hydrophobic, acidic, and basic	Hydrophobic, acidic, and basic	Hydrophobic, acidic, and basic	See section "Data availability statement"

pH 9–11, but we also found that T0034 maintain activity at both pH 6.5 and 7.0 (**Figure 2B**), whereas Bjerga et al. found little to no activity at pH 7 and lower. We could reproduce the results from Bjerga et al. when calcium was added immediately prior to performing the assays (data not shown), allowing a pH-dependent progression of maturation taking place during the assay. Experimental data included in this study are from assays where the enzymes were pre-incubated 2 h with calcium to ensure a complete maturation. We therefore propose that these differences can be explained by experimental variations. For activity assessment, we thus recommend that complete maturation should be achieved prior to assaying.

NaCl affects the activity depending on substrate size

Increasing NaCl and KCl concentrations enhanced P355 and T0034 activity when the peptide AAPF was used as a substrate, while T0099 and SC were largely unresponsive in comparison (**Figures 6C, D**). However, increasing concentration of NaCl decreased activity for all proteases when the larger substrates casein and raBSA were used (**Figures 7B**, **8**, panels A3, B3, and D3), apart from T0099 activity against raBSA, which was not affected by NaCl (**Figure 8, panel C3**). NaCl can favor a particular structural conformation and indirectly influence catalytic activity (Ortega et al., 2011). NaCl and KCl could favor a more rigid structural conformation for P355 and T0034 where a small substrate, e.g., the AAPF peptide, can easily enter the catalytic cleft. The same putative rigid structure could at the same time make it more difficult for a larger substrate to fit into the catalytic cleft. Mykytczuk et al. (2013) report a high copy number of osmolyte transporters in *P. halocryophilus* Or1 could indicate a high intracellular ionic strength. Whether this is also the case for *Planococcus* sp. AW02J18 is uncertain as the genome sequence is unknown.

P355 has cold-adaptive traits

We conducted an array of experiments to determine whether P355 is, in fact, a cold-adapted protease, including temperature optimum and stability, salt stability, Michaelis-Menten kinetics at two temperatures, and digestion of a large substrate at 0°C.

Thermal stability and temperature optimum are usually reduced for cold-adapted enzymes compared to their meso- and thermophilic counterparts (Siddiqui and Cavicchioli, 2006; Gerday, 2014). The proteases in this study showed increasing stability against thermal inactivation in the following order: P355, T0034, SC, and T0099 (**Figure 5**). This showed that P355 is the most heat-labile protease in this study. Ice water (0°C) preserved the activity of the proteases after 120 h of incubation. Strongin et al. (1978) reported an ISP from *B. subtilis*, which retained all its activity after 2 months at 4°C. One should keep in mind that *in vivo* and *in vitro* experiments can differ; molecular crowding, molecular interactions, chaperones, and translation rates can influence protein stability (McGuffee and Elcock, 2010; Gershenson and Gierasch, 2011). Simply adding BSA has shown to enhance protease stability (Narinx et al., 1997).

The temperature optimum of P355 is equal to that of the putative thermophile T0099 (50°C), in contrast to what might be expected from a cold-adapted protease. However, it is not unheard of that some cold-active enzymes display a relatively high-temperature optimum (Siddiqui and Cavicchioli, 2006).

The temperature optimum of T0034 determined in this study (60°C) is higher than previously determined by Bjerga et al. (45°C) (Bjerga et al., 2018). This is most likely due to the difference in experimental approaches with and without a calcium-maturation step before assaying as described for the pH optimum experiments. The explanation for the higher temperature optimum of T0034 in this study is likely due to an improved thermal stability in the presence of calcium (Voordouw et al., 1976; Veltman et al., 1998; Bjerga et al., 2018). P355 showed much less activity at 65°C than the others due to its instability at 65°C (**Figure 5**).

Chemical denaturation is usually correlated with thermal lability (D'Amico et al., 2003). This trend is observed for urea (**Figure 6A**), where increasing concentrations inactivate the ISPs and the ESP, and where P355 and T0034 are somewhat more sensitive to urea than the two other enzymes. Denaturation with Gnd (**Figure 6B**) exhibits a more complex pattern with overlapping graphs: at lower range concentrations P355 activity is slightly enhanced, peaking at 125 mM Gnd, but a Student's *t*-test indicated no significant difference ($p < 0.05$) between the lowest Gnd concentration (3.9 mM) and 125 mM Gnd. Overall, SC is the most stable protease in Gnd, while ISPs, and in particular T0034, are less stable.

Other indications of cold adaption in P355 are its relatively high catalytic constant (k_{cat}) and K_m compared to SC and T0099 (**Table 1**). The general increase in k_{cat} from 25 to 45°C likely accounts for the increase in K_m. However, K_m for T0034 decreased, which explains why the catalytic efficiency increased more for T0034 compared to the other proteases. The order of thermal and chemical (urea) stability correlates with k_{cat}, i.e., P355 has traded stability for higher activity (Santiago et al., 2016). A higher k_{cat} is explained by a lower energy of activation due to fewer intramolecular bonds–accompanied by a higher entropy of activation–that needs to be broken during a chemical reaction (Feller and Gerday, 2003; Siddiqui and Cavicchioli, 2006). SC showed intermediate values in line with previously reported parameters (Evans et al., 2000). k_{cat} for cold-adapted proteases decreases at a lower rate compared to thermophilic counterparts with decreasing temperature (Åqvist et al., 2017). However, this was not the case for neither P355 nor T0034; their k_{cat} decreased relatively fast from 45 down to 25°C compared to T0099 and SC. Even so, k_{cat} for P355 and T0034 were still higher than T0099 and SC at both temperatures in line with the casein (**Figure 7B**) and raBSA digest assays (**Figure 8**). The digestion of raBSA demonstrates that P355 and T0034 have relatively high activity at 0°C compared to T0099 and SC. The tendencies discussed above regarding the kinetic assay and the casein and raBSA digestion assays still hold true when taking the relatively lower number of active sites of T0099 into account, which was roughly half compared to P355, T0034, and SC (**Supplementary Figures 6–9**). k_{cat} of T0099 and digestion of casein and raBSA would approximately double but T0099 would still exhibit the lowest activity of all 4 proteases. The degradation patterns of raBSA differed, which likely reflects differences in substrate specificities between the proteases. MS/MS analysis of digested raBSA indicated a broad substrate specificity of the proteases used in this study; all proteases were able to cleave at hydrophobic, basic, and acidic residues at the P1 location. This has previously been shown for SC (Evans et al., 2000). They were also capable of cleaving at modified Cys residues (alkylated through reaction with iodoacetamide for MS analysis). An ISP able to cleave after Lys and hydrophobic residues has been reported previously (Gamble et al., 2012).

In summary, we produced and characterized a novel cold-adapted ISP (P355) from the *P. halocryophilus* Or1 genome. The putative mesophilic T0034 turned out to be a cold-adapted ISP like P355 and both showed activity-stability trade-off compared to T0099 and SC. All proteases in this study were active and stable at alkaline pH. P355 showed the highest thermal and chemical lability followed closely by T0034. Titration with NaCl and KCl enhanced P355 and T0034 activity considerably when using AAPF as a substrate, while NaCl decreased activity when using casein or raBSA as substrate, suggesting that substrate binding is affected by the ionic strength of the buffer. The k_{cat} values correlated well with the degree of casein and raBSA digestion; both P355 and T0034 exhibited higher k_{cat} values compared to T0099 and SC, which likely accounts for the higher digestion efficiency of casein (RT) and raBSA digestion (0°C) in line with the activity-stability trade-off characteristic in cold adaptation. Altogether, we conclude that P355 along with T0034 are cold-adapted proteases.

Data availability statement

The datasets presented in this study can be found in online repositories. The names of the repository/repositories and accession number(s) can be found in the article/**Supplementary material**.

Author contributions

CR and JE: conceptualization. CR and SH: methodology. CR: software, formal analysis, data curation, writing—original draft, and visualization. CR and IT: investigation. JE, ØL, and GB: resources. CR, MT, SH, ØL, GB, PS, and CS: writing—review and editing. JE and MT: supervision and project administration. JE and CS: funding acquisition. All authors contributed to the article and approved the submitted version.

Funding

This study was supported by the Danish Council for Independent Research (DFF-8022-00385B) and the Novo Nordisk Foundation (BIO-MS) (NNF18OC0032724). GB and ØL acknowledge financial support from the Norwegian Research Council (grant ID: 221568), and basic funding from NORCE Norwegian Research Centre.

Acknowledgments

We thank Professor Lyle Whyte for giving us access to the genome sequence of *Planococcus halocryophilus* Or1.

Conflict of interest

The authors declare that the research was conducted in the absence of any commercial or financial relationships that could be construed as a potential conflict of interest.

Publisher's note

All claims expressed in this article are solely those of the authors and do not necessarily represent those of their affiliated organizations, or those of the publisher, the editors and the reviewers. Any product that may be evaluated in this article, or claim that may be made by its manufacturer, is not guaranteed or endorsed by the publisher.

Supplementary material

The Supplementary Material for this article can be found online at: https://www.frontiersin.org/articles/10.3389/fmicb.2023.1121857/full#supplementary-material

References

Aliyu, H., Lebre, P., Blom, J., Cowan, D., and De Maayer, P. (2016). Phylogenomic re-assessment of the thermophilic genus *Geobacillus*. *Syst. Appl. Microbiol.* 39, 527–533. doi: 10.1016/j.syapm.2016.09.004

Åqvist, J., Isaksen, G. V., and Brandsdal, B. O. (2017). Computation of enzyme cold adaptation. *Nat. Rev. Chem.* 1:0051. doi: 10.1038/s41570-017-0051

Attali, D., and Baker, C. (2019). ggExtra: Add Marginal Histograms to 'ggplot2', and More 'ggplot2' Enhancements.

Aziz, R. K., Bartels, D., Best, A. A., DeJongh, M., Disz, T., Edwards, R. A., et al. (2008). The RAST server: Rapid annotations using subsystems technology. *BMC Genomics* 9:75. doi: 10.1186/1471-2164-9-75

Bhatia, R. K., Ullah, S., Hoque, M. Z., Ahmad, I., Yang, Y.-H., Bhatt, A. K., et al. (2021). Psychrophiles: A source of cold-adapted enzymes for energy efficient biotechnological industrial processes. *J. Environ. Chem. Eng.* 9:104607. doi: 10.1016/j.jece.2020.104607

Bjerga, G. E. K., Larsen, Ø, Arsın, H., Williamson, A., García-Moyano, A., Leiros, I., et al. (2018). Mutational analysis of the pro-peptide of a marine intracellular subtilisin protease supports its role in inhibition. *Proteins* 86, 965–977. doi: 10.1002/prot.25528

Bjerga, G., Arsin, H., Larsen, O., Puntervoll, P., and Kleivdal, H. (2016). A rapid solubility-optimized screening procedure for recombinant subtilisins in *E. coli*. *J. Biotechnol.* 222, 38–46. doi: 10.1016/j.jbiotec.2016.02.009

Braxton, S., and Wells, J. A. (1992). Incorporation of a stabilizing calcium-binding loop into subtilisin BPN'. *Biochemistry* 31, 7796–7801. doi: 10.1021/bi00149a008

Brettin, T., Davis, J. J., Disz, T., Edwards, R. A., Gerdes, S., Olsen, G. J., et al. (2015). RASTtk: A modular and extensible implementation of the RAST algorithm for building custom annotation pipelines and annotating batches of genomes. *Sci. Rep.* 5:8365. doi: 10.1038/srep08365

Bruno, S., Coppola, D., di Prisco, G., Giordano, D., and Verde, C. (2019). Enzymes from marine polar regions and their biotechnological applications. *Mar. Drugs* 17:544.

Burnett, T. J., Shankweiler, G. W., and Hageman, J. H. (1986). Activation of intracellular serine proteinase in *Bacillus subtilis* cells during sporulation. *J. Bacteriol.* 165, 139–145. doi: 10.1128/jb.165.1.139-145.1986

Bury, A. F. (1981). Analysis of protein and peptide mixtures: Evaluation of three sodium dodecyl sulphate-polyacrylamide gel electrophoresis buffer systems. *J. Chromatogr. A* 213, 491–500. doi: 10.1016/S0021-9673(00)80500-2

Campitelli, E. (2022). *tagger: Adds tags to 'ggpot2' facets*.

D'Amico, S., Marx, J.-C., Gerday, C., and Feller, G. (2003). Activity-stability relationships in extremophilic enzymes. *J. Biol. Chem.* 278, 7891–7896. doi: 10.1074/jbc.M212508200

Davail, S., Feller, G., Narinx, E., and Gerday, C. (1994). Cold adaptation of proteins. Purification, characterization, and sequence of the heat-labile subtilisin from the antarctic psychrophile Bacillus TA41. *J. Biol. Chem.* 269, 17448–17453.

Dyrlund, T. F., Poulsen, E. T., Scavenius, C., Sanggaard, K. W., and Enghild, J. J. (2012). MS data miner: A web-based software tool to analyze, compare, and share mass spectrometry protein identifications. *Proteomics* 12, 2792–2796. doi: 10.1002/pmic.201200109

Evans, K. L., Crowder, J., and Miller, E. S. (2000). Subtilisins of *Bacillus* spp. hydrolyze keratin and allow growth on feathers. *Can. J. Microbiol.* 46, 1004–1011. doi: 10.1139/w00-085

Fasim, A., More, V. S., and More, S. S. (2021). Large-scale production of enzymes for biotechnology uses. *Curr. Opin. Biotechnol.* 69, 68–76. doi: 10.1016/j.copbio.2020.12.002

Feller, G., and Gerday, C. (2003). Psychrophilic enzymes: Hot topics in cold adaptation. *Nat. Rev. Microbiol.* 1, 200–208. doi: 10.1038/nrmicro773

Feller, G., Lonhienne, T., Deroanne, C., Libioulle, C., Van Beeumen, J., and Gerday, C. (1992). Purification, characterization, and nucleotide sequence of the thermolabile alpha-amylase from the antarctic psychrotroph *Alteromonas haloplanctis* A23. *J. Biol. Chem.* 267, 5217–5221. doi: 10.1016/S0021-9258(18)42754-8

Fujinami, S., and Fujisawa, M. (2010). Industrial applications of alkaliphiles and their enzymes – past, present and future. *Environ. Technol.* 31, 845–856. doi: 10.1080/09593331003762807

Furhan, J. (2020). Adaptation, production, and biotechnological potential of cold-adapted proteases from psychrophiles and psychrotrophs: Recent overview. *J. Genet. Eng. Biotechnol.* 18:36. doi: 10.1186/s43141-020-00053-7

Gamble, M., Künze, G., Brancale, A., Wilson, K. S., and Jones, D. D. (2012). The role of substrate specificity and metal binding in defining the activity and structure of an intracellular subtilisin. *FEBS Open Bio* 2, 209–215. doi: 10.1016/j.fob.2012.07.001

Gamble, M., Künze, G., Dodson, E. J., Wilson, K. S., and Jones, D. D. (2011). Regulation of an intracellular subtilisin protease activity by a short propeptide sequence through an original combined dual mechanism. *Proc. Natl. Acad. Sci. U.S.A.* 108, 3536–3541. doi: 10.1073/pnas.1014229108

Gasteiger, E., Hoogland, C., Gattiker, A., Duvaud, S. e., Wilkins, M. R., Appel, R. D., et al. (2005). "Protein identification and analysis tools on the ExPASy server," in *The proteomics protocols handbook*, ed. J. M. Walker (Totowa, NJ: Humana Press), 571–607.

Gerday, C. (2014). "Fundamentals of cold-active enzymes," in *Cold-adapted Yeasts: Biodiversity, adaptation strategies and biotechnological significance*, eds P. Buzzini and R. Margesin (Berlin: Springer Berlin Heidelberg), 325–350.

Gershenson, A., and Gierasch, L. M. (2011). Protein folding in the cell: Challenges and progress. *Curr. Opin. Struct. Biol.* 21, 32–41. doi: 10.1016/j.sbi.2010.11.001

Goordial, J., and Whyte, L. (2014). "Microbial life in antarctic permafrost environments," in *Antarctic terrestrial microbiology: Physical and biological properties of antarctic soils*, ed. D. A. Cowan (Berlin: Springer Berlin Heidelberg), 217–232.

Goordial, J., Davila, A., Greer, C. W., Cannam, R., DiRuggiero, J., McKay, C. P., et al. (2017). Comparative activity and functional ecology of permafrost soils and lithic niches in a hyper-arid polar desert. *Environ. Microbiol.* 19, 443–458. doi: 10.1111/1462-2920.13353

Groen, H., Meldal, M., and Breddam, K. (1992). Extensive comparison of the substrate preferences of two subtilisins as determined with peptide substrates which are based on the principle of intramolecular quenching. *Biochemistry* 31, 6011–6018. doi: 10.1021/bi00141a008

Hofer, F., Kraml, J., Kahler, U., Kamenik, A. S., and Liedl, K. R. (2020). Catalytic site pKa values of aspartic, cysteine, and serine proteases: Constant pH MD simulations. *J. Chem. Inform. Model.* 60, 3030–3042. doi: 10.1021/acs.jcim.0c00190

Ikemura, H., and Inouye, M. (1988). In vitro processing of pro-subtilisin produced in *Escherichia coli*. *J. Biol. Chem.* 263, 12959–12963. doi: 10.1016/S0021-9258(18)37656-7

Ikemura, H., Takagi, H., and Inouye, M. (1987). Requirement of pro-sequence for the production of active subtilisin E in *Escherichia coli*. *J. Biol. Chem.* 262, 7859–7864.

Jones, P., Binns, D., Chang, H.-Y., Fraser, M., Li, W., McAnulla, C., et al. (2014). InterProScan 5: genome-scale protein function classification. *Bioinformatics* 30, 1236–1240. doi: 10.1093/bioinformatics/btu031

Koide, Y., Nakamura, A., Uozumi, T., and Beppu, T. (1986). Cloning and sequencing of the major intracellular serine protease gene of *Bacillus subtilis*. *J. Bacteriol.* 167, 110–116. doi: 10.1128/jb.167.1.110-116.1986

Linderstrøm-Lang, K., and Ottesen, M. (1947). A new protein from ovalbumin. *Nature* 159, 807–808. doi: 10.1038/159807a0

Lylloff, J. E., Hansen, L. B. S., Jepsen, M., Sanggaard, K. W., Vester, J. K., Enghild, J. J., et al. (2016). Genomic and exoproteomic analyses of cold- and alkaline-adapted bacteria reveal an abundance of secreted subtilisin-like proteases. *Microbial Biotechnol.* 9, 245–256. doi: 10.1111/1751-7915.12343

Matsudaira, P. (1987). Sequence from picomole quantities of proteins electroblotted onto polyvinylidene difluoride membranes. *J. Biol. Chem.* 262, 10035–10038.

McGuffee, S. R., and Elcock, A. H. (2010). Diffusion, crowding & protein stability in a dynamic molecular model of the bacterial cytoplasm. *PLoS Comput. Biol.* 6:e1000694. doi: 10.1371/journal.pcbi.1000694

McKinnon Edwards, S. (2020). *lemon: Freshing Up your 'ggplot2' Plots*.

Mykytczuk, N. C. S., Foote, S. J., Omelon, C. R., Southam, G., Greer, C. W., and Whyte, L. G. (2013). Bacterial growth at −15°C; molecular insights from the permafrost bacterium *Planococcus halocryophilus* Or1. *ISME J.* 7, 1211–1226. doi: 10.1038/ismej.2013.8

Mykytczuk, N. C. S., Wilhelm, R. C., and Whyte, L. G. (2012). *Planococcus halocryophilus* sp. nov., an extreme sub-zero species from high Arctic permafrost. *Int. J. Syst. Evol. Microbiol.* 62(Pt 8), 1937–1944. doi: 10.1099/ijs.0.035782-0

Narinx, E., Baise, E., and Gerday, C. (1997). Subtilisin from psychrophilic Antarctic bacteria: Characterization and site-directed mutagenesis of residues possibly involved in the adaptation to cold. *Protein Eng. Design Select.* 10, 1271–1279. doi: 10.1093/protein/10.11.1271

Neurath, H., and Walsh, K. A. (1976). Role of proteolytic enzymes in biological regulation (a review). *Proc. Natl. Acad. Sci. U.S.A.* 73, 3825–3832. doi: 10.1073/pnas.73.11.3825

Nielsen, H., Engelbrecht, J., Brunak, S., and von Heijne, G. (1997). Identification of prokaryotic and eukaryotic signal peptides and prediction of their cleavage sites. *Protein Eng.* 10, 1–6. doi: 10.1093/protein/10.1.1

Ohta, Y., Hojo, H., Aimoto, S., Kobayashi, T., Zhu, X., Jordan, F., et al. (1991). Pro-peptide as an intermolecular chaperone: Renaturation of denatured subtilisin E with a synthetic pro-peptide. *Mol. Microbiol.* 5, 1507–1510. doi: 10.1111/j.1365-2958.1991.tb00797.x

Orrego, C., Kerjan, P., Manca de Nadra, M. C., and Szulmajster, J. (1973). Ribonucleic acid polymerase in a thermosensitive sporulation mutant (ts-4) of *Bacillus subtilis*. *J. Bacteriol.* 116, 636–647. doi: 10.1128/jb.116.2.636-647.1973

Ortega, G., Laín, A., Tadeo, X., López-Méndez, B., Castaño, D., and Millet, O. (2011). Halophilic enzyme activation induced by salts. *Sci. Rep.* 1:6. doi: 10.1038/srep00006

Park, H. J., Lee, C. W., Kim, D., Do, H., Han, S. J., Kim, J. E., et al. (2018). Crystal structure of a cold-active protease (Pro21717) from the psychrophilic bacterium, *Pseudoalteromonas arctica* PAMC 21717, at 1.4 Å resolution: Structural adaptations to cold and functional analysis of a laundry detergent enzyme. *PLoS One* 13:e0191740. doi: 10.1371/journal.pone.0191740

Pereira, J. Q., Ambrosini, A., Passaglia, L. M. P., and Brandelli, A. (2017). A new cold-adapted serine peptidase from Antarctic *Lysobacter* sp. A03: Insights about enzyme activity at low temperatures. *Int. J. Biol. Macromol.* 103, 854–862. doi: 10.1016/j.ijbiomac.2017.05.142

R Core Team (2021). *R: A language and environment for statistical computing*. Vienna: R Foundation for Statistical Computing.

Ritz, C., Baty, F., Streibig, J. C., and Gerhard, D. (2016). Dose-Response Analysis Using R. *PLoS One* 10:e0146021. doi: 10.1371/journal.pone.0146021

RStudio Team (2020). *RStudio: Integrated development for R*. Boston, MA: RStudio, PBC.

Santiago, M., Ramírez-Sarmiento, C. A., Zamora, R. A., and Parra, L. P. (2016). Discovery, molecular mechanisms, and industrial applications of cold-active enzymes. *Front. Microbiol.* 7:1408. doi: 10.3389/fmicb.2016.01408

Sarmiento, F., Peralta, R., and Blamey, J. M. (2015). Cold and hot extremozymes: Industrial relevance and current trends. *Front. Bioeng. Biotechnol.* 3:148. doi: 10.3389/fbioe.2015.00148

Siddiqui, K. S., and Cavicchioli, R. (2006). Cold-adapted enzymes. *Annu. Rev. Biochem.* 75, 403–433. doi: 10.1146/annurev.biochem.75.103004.142723

Strongin, A. Y., Izotova, L. S., Abramov, Z. T., Gorodetsky, D. I., Ermakova, L. M., Baratova, L. A., et al. (1978). Intracellular serine protease of *Bacillus subtilis*: sequence homology with extracellular subtilisins. *J. Bacteriol.* 133, 1401–1411. doi: 10.1128/jb.133.3.1401-1411.1978

Takekawa, S., Uozumi, N., Tsukagoshi, N., and Udaka, S. (1991). Proteases involved in generation of beta- and alpha-amylases from a large amylase precursor in *Bacillus polymyxa*. *J. Bacteriol.* 173, 6820–6825. doi: 10.1128/jb.173.21.6820-6825.1991

Teufel, F., Almagro Armenteros, J. J., Johansen, A. R., Gíslason, M. H., Pihl, S. I., Tsirigos, K. D., et al. (2022). SignalP 6.0 predicts all five types of signal peptides using protein language models. *Nat. Biotechnol.* 40, 1023–1025. doi: 10.1038/s41587-021-01156-3

Tindbaek, N., Svendsen, A., Oestergaard, P. R., and Draborg, H. (2004). Engineering a substrate-specific cold-adapted subtilisin. *Protein Eng. Design Select.* 17, 149–156. doi: 10.1093/protein/gzh019

Veltman, O. R., Vriend, G., Berendsen, H. J. C., Van den Burg, B., Venema, G., and Eijsink, V. G. H. (1998). A single calcium binding site is crucial for the calcium-dependent thermal stability of thermolysin-like proteases. *Biochemistry* 37, 5312–5319. doi: 10.1021/bi9725879

Vévodová, J., Gamble, M., Künze, G., Ariza, A., Dodson, E., Jones, D. D., et al. (2010). Crystal structure of an Intracellular subtilisin reveals novel structural features unique to this subtilisin family. *Structure* 18, 744–755. doi: 10.1016/j.str.2010.03.008

Voordouw, G., Milo, C., and Roche, R. S. (1976). Role of bound calcium ions in thermostable, proteolytic enzymes. Separation of intrinsic and calcium ion contributions to the kinetic thermal stability. *Biochemistry* 15, 3716–3724. doi: 10.1021/bi00662a012

Wickham, H., and Bryan, J. (2019). *readxl: Read Excel Files*.

Wickham, H., Averick, M., Bryan, J., Chang, W., and D'Agostino McGowan, L. (2019). Welcome to the {tidyverse}. *J. Open Sour. Softw.* 4:1686. doi: 10.21105/joss.01686

Wilhelm, R. C., Radtke, K. J., Mykytczuk, N. C. S., Greer, C. W., and Whyte, L. G. (2012). Life at the wedge: The activity and diversity of arctic ice wedge microbial communities. *Astrobiology* 12, 347–360. doi: 10.1089/ast.2011.0730

Wintrode, P. L., Miyazaki, K., and Arnold, F. H. (2000). Cold adaptation of a mesophilic subtilisin-like protease by laboratory evolution. *J. Biol. Chem.* 275, 31635–31640. doi: 10.1074/jbc.M004503200

Zhang, C., Sanders, J. P., Xiao, T. T., and Bruins, M. E. (2015). how does alkali aid protein extraction in green tea leaf residue: A basis for integrated biorefinery of leaves. *PLoS One* 10:e0133046. doi: 10.1371/journal.pone.0133046

Zhu, X., Ohta, Y., Jordan, F., and Inouye, M. (1989). Pro-sequence of subtilisin can guide the refolding of denatured subtilisin in an intermolecular process. *Nature* 339, 483–484. doi: 10.1038/339483a0

frontiers | Frontiers in Microbiology

TYPE Original Research
PUBLISHED 21 June 2023
DOI 10.3389/fmicb.2023.1201121

OPEN ACCESS

EDITED BY
Philippe M. Oger,
Adaptation et Pathogenie (MAP), France

REVIEWED BY
Christoph Engl,
Queen Mary University of London,
United Kingdom
Somnath Chakravorty,
Bharat Serums and Vaccines, India

*CORRESPONDENCE
Masahiro Ito
✉ masahiro.ito@toyo.jp

RECEIVED 06 April 2023
ACCEPTED 06 June 2023
PUBLISHED 21 June 2023

CITATION
Ishida Y, Zhang C, Satoh K and Ito M (2023) Physiological importance and role of Mg^{2+} in improving bacterial resistance to cesium. *Front. Microbiol.* 14:1201121. doi: 10.3389/fmicb.2023.1201121

Physiological importance and role of Mg^{2+} in improving bacterial resistance to cesium

Yoshiki Ishida[1], Chongkai Zhang[2], Katsuya Satoh[3] and Masahiro Ito[1,2,4,5]*

[1]Graduate School of Life Sciences, Toyo University, Oura-gun, Gunma, Japan, [2]Faculty of Life Sciences, Toyo University, Oura-gun, Gunma, Japan, [3]Department of Quantum-Applied Biosciences, Takasaki Institute for Advanced Quantum Science, Foundational Quantum Technology Research Directorate, National Institutes for Quantum and Radiological Science and Technology, Takasaki, Gunma, Japan, [4]Bio-Resilience Research Project (BRRP), Toyo University, Oura-gun, Gunma, Japan, [5]Bio Nano Electronics Research Centre, Toyo University, Kawagoe, Saitama, Japan

Cesium (Cs) is an alkali metal with radioactive isotopes such as ^{137}Cs and ^{134}Cs. ^{137}Cs, a product of uranium fission, has garnered attention as a radioactive contaminant. Radioactive contamination remediation using microorganisms has been the focus of numerous studies. We investigated the mechanism underlying Cs^+ resistance in *Microbacterium* sp. TS-1 and other representative microorganisms, including *Bacillus subtilis*. The addition of Mg^{2+} effectively improved the Cs^+ resistance of these microorganisms. When exposed to high concentrations of Cs^+, the ribosomes of Cs^+-sensitive mutants of TS-1 collapsed. Growth inhibition of *B. subtilis* in a high-concentration Cs^+ environment was because of a drastic decrease in the intracellular potassium ion concentration and not the destabilization of the ribosomal complex. This is the first study demonstrating that the toxic effect of Cs^+ on bacterial cells differs based on the presence of a Cs^+ efflux mechanism. These results will aid in utilizing high-concentration Cs^+-resistant microorganisms for radioactive contamination remediation in the future.

KEYWORDS

cesium-resistant microorganism, magnesium, *Microbacterium*, *Bacillus subtilis*, ribosome

1. Introduction

After the Fukushima nuclear power plant accident in 2011, a large amount of radioactive cesium (Cs), ^{134}Cs and ^{137}Cs, was released into the environment, resulting in serious impacts on human health and the environment (Hirose, 2016; Nakamura et al., 2022; Wu et al., 2022). Since then, studies on contamination of the soil with radioactive Cs ions (Cs^+), decontamination and bioremediation efforts, and the quest to identify Cs^+-tolerant microorganisms have been prominent. Imparting radio resistance to Cs^+-resistant microorganisms would lead to the creation of highly functional radiation-tolerant bacteria, which could efficiently recover radioactive Cs from radioactive Cs-contaminated environments. Therefore, creating highly functional microorganisms to be used for bioremediation in environments contaminated with radioactive Cs is desirable.

Cs, an alkali metal, generally exists as a monovalent cation in solutions. Radioactive isotopes of Cs are water-soluble and can be taken up by the ion uptake system of living organisms. The isotopes ^{134}Cs and ^{137}Cs have long half-lives (^{134}Cs, 2.0652 years; ^{137}Cs, 30.1 years), are discharged into the external environment during nuclear power generation and emit γ- and β-rays when

they decay (Hampton et al., 2004; Sanial et al., 2017). In addition, as Cs^+ possess physicochemical properties similar to those of potassium ions (K^+), Cs^+ is transported into the cells through the K^+ transport system (Perkins and Gadd, 1995). Since *Escherichia coli* does not have a Cs^+ efflux system, Cs^+ accumulates inside its cell. K^+ is excreted from the cell by the K^+ efflux system instead of Cs^+. As a result, intracellular K^+ concentration is significantly reduced (Jung et al., 2001). In addition, K^+ contributes to the stabilization of ribosomes, and its deficiency results in growth inhibition (Avery, 1995; Hampton et al., 2004).

Microbacterium sp. TS-1 (TS-1), an alkaliphilic bacterium, was isolated from a jumping spider (*Salticidae*) in our laboratory (Fujinami et al., 2013). It is a gram-positive aerobic bacterium with an optimum pH range of 8.0–9.0. In addition, it is a high-concentration Cs^+-resistant bacterium that can grow in media containing 1,200 mM CsCl (Koretsune et al., 2022). Two significant mechanisms of Cs^+ resistance in TS-1 have been reported (Koretsune et al., 2022; Ishida et al., 2023). The first mechanism works through the Cs^+/H^+ antiporter CshA, which excretes Cs^+ from the cell and maintains a low intracellular Cs^+ concentration. The Cs^+-sensitive mutant strain Mut4 is a CshA defective mutant isolated previously (Koretsune et al., 2022). The second mechanism involves maintaining Cs^+ resistance through the uptake of magnesium ions (Mg^{2+}) into cells via the magnesium transporter MgtE, even when the Cs^+ concentration increases (Ishida et al., 2023). A mutation in the *mgtE* gene of TS-1 (mutant strain Mut5) leads to Cs^+-sensitivity because of the deficiency of intracellular Mg^{2+} (Ishida et al., 2023), suggesting that Mg^{2+} plays an essential role in Cs^+ resistance in TS-1. Magnesium is a group 2 element and an essential trace element for organisms (Fiorentini et al., 2021). It plays various roles, such as maintaining the structure of ribosomes and enzymatic activity (Akanuma et al., 2014; Pontes et al., 2016). If the Mg^{2+} transporter MgtE contributes toward improving Cs^+ resistance in TS-1, it would be interesting to investigate whether Mg^{2+} uptake into cells also leads to the enhancement of Cs^+ tolerance in other microorganisms. These strains have multiple Mg^{2+} transporters but no Cs^+/H^+ antiporter CshA homologous proteins.

Therefore, to verify whether Mg^{2+} plays an essential role in Cs^+ resistance in microorganisms, we used the gram-positive bacteria *Bacillus subtilis* BR151MA (wild-type), *Staphylococcus aureus* IAM12544, gram-negative *E. coli* W3110, and *Pseudomonas aeruginosa* NBRC13275 as representative microorganisms. In addition, the eukaryote *Saccharomyces cerevisiae* JCM1499 was used for Cs^+-resistant growth testing with $MgCl_2$ added to the medium.

Functional analysis of TS-1 showed that in an environment with a Cs^+ concentration of ≤200 mM, Cs^+ resistance was maintained by increasing the Mg^{2+} concentration in cells. Conversely, in a high Cs^+ outer environment of >200 mM, Cs^+ resistance was maintained with a low Cs^+ concentration in cells through CshA. However, the exact mechanism by which the increase in cell Mg^{2+} concentration affects Cs^+ resistance of TS-1 and the underlying physiological functions of CshA maintaining intracellular Cs^+ concentration remain unknown.

Mg^{2+} stabilizes ribosomal complexes (Hsiao et al., 2009; Nierhaus, 2014; Akanuma et al., 2018). In *B. subtilis*, intracellular Mg^{2+} is stored in ribosomes and contributes to the stabilization of complex ribosomal formation (Akanuma et al., 2014, 2018). The intracellular accumulation of Cs^+ in *E. coli* reduces intracellular K^+ concentrations and inhibits growth (Bossemeyer et al., 1989; Avery, 1995). Based on these findings, in this study, we considered the intracellular actions of the Cs^+ resistance mechanism in TS-1 and hypothesized that in an environment with a Cs^+ concentration < 200 mM, ribosomes are destabilized when Cs^+ is taken up into the cells. As Mg^{2+} stabilizes the ribosomal complex, Cs^+ resistance is acquired by enhancing the Mg^{2+} uptake by MgtE. In a Cs^+ environment >200 mM, Cs^+ resistance is achieved by excreting intracellular Cs^+ through CshA to prevent intracellular accumulation of Cs^+ and decrease intracellular K^+ concentration.

Therefore, we analyzed the ribosomal complex to verify the hypothesis regarding the acquisition of Cs^+ resistance by incorporating Mg^{2+} into TS-1. To investigate the role of Mg^{2+} in Cs^+ resistance, we attempted to measure changes in Cs^+, K^+, and Mg^{2+} concentrations in the cells. Through these experiments, we attempted to elucidate the effects of Cs^+ concentration on TS-1 and also on *B. subtilis*, in which the relationship between ribosomes and Mg^{2+} has been well studied (Akanuma et al., 2014; Nierhaus, 2014; Akanuma et al., 2018; Lee et al., 2019; Akanuma, 2021).

2. Materials and methods

2.1. Bacterial strains, growth media, and conditions for culture

The bacterial strains used in this study are listed in Table 1. *B. subtilis* BR151MA (Henkin et al., 1991), *S. aureus* JCM20624, *E. coli* W3110, *P. aeruginosa* IFO13275, and *S. cerevisiae* JCM1499 were used to assess improvements in Cs^+ resistance. Luria-Bertani (LB), Miller medium (2 mL; BD Difco™; BD Biosciences, Franklin Lakes, NJ, United States) (pH 7.5 for *B. subtilis*, pH 7.0 for others) was dispensed into a 14-mL culture tube, inoculated with each single colony, and cultured with shaking at 37°C and 200 rpm for 8 h. This culture solution was used as the pre-culture. A bioshaker BR-43FM (TAITEC Co., Ltd., Koshigaya, Japan) was used for shaking the culture, and the same equipment was used unless otherwise specified.

Various concentrations of $MgCl_2$ (25–200 mM final concentration) were added to 2 mL of LB medium supplemented with different concentrations of CsCl (100–600 mM final concentration). Ten microliters of the pre-culture solution were inoculated and cultured with shaking at 37°C and 200 rpm, and the OD_{600} was measured after 16 h. Turbidity was measured using a UV-1800 ultraviolet–visible spectrophotometer (Shimadzu Co., Ltd., Kyoto, Japan). For *S. cerevisiae*, 2 mL of yeast malt (YM) broth (BD Difco™; BD Biosciences) was dispensed into a 14-mL capacity culture tube, inoculated using a single colony, and cultured with shaking at 25°C and 200 rpm for 24 h. This was used as the pre-culture. Similar to eubacteria, CsCl and $MgCl_2$ were added to the YM broth; approximately 10 µL of the pre-culture was inoculated and cultured with shaking at 25°C and 200 rpm for 24 h, and turbidity was measured at OD_{600}.

Alkaliphilic *Microbacterium* sp. TS-1 was grown at 30°C in neutral complex (NC medium) and Tris media (Imazawa et al., 2016). Tris medium consisted of 3.63 g L^{-1} Tris base, 1.47 g L^{-1} citric acid monohydrate, 0.5 g L^{-1} yeast extract, 9 g L^{-1} glucose, and 1% (w/v) trace elements (Cohen-Bazire et al., 1957). Deionized (DI) water was used as the solvent. The pH was adjusted to 8 and 9 using 1 M *N*-methyl-*D*-glucamine. The pH was adjusted to 7 using 5 N sulfuric

TABLE 1 Bacterial strains and plasmids used in the present study.

Strain	Genotype	References
Microbacterium sp. TS-1	Wild-type	Fujinami et al. (2013)
Mut4	Cs^+-sensitive mutant from TS-1, MTS1_00475 (CshA: W253*)	Koretsune et al. (2022)
Mut5	Cs^+-sensitive mutant from TS-1, MTS1_03028 (MgtE: T396I)	Ishida et al. (2023)
Mut4R	Cs^+-resistant revertant from Mut4, MTS1_00475 (W253* → *253R) (Intragenic suppression)	Koretsune et al. (2022)
Mut5R	Cs^+-resistant revertant from Mut5, MTS1_03028 (T396I → I396T) (true reversion)	Ishida et al. (2023)
Escherichia coli W3110	F^- *IN(rrnD-rrnE1) rph-1*	*E. coli* genetic stock center
Bacillus subtilis BR151MA	*lys3, trpC2* (wild-type)	Grundy et al. (1994)
Staphylococcus aureus IAM12544	Wild-type	Biological Resource Center, NITE (NBRC), Japan
Pseudomonas aeruginosa NBRC13275	Wild-type	Biological Resource Center, NITE (NBRC), Japan
Saccharomyces cerevisiae JCM1499	Wild-type	RIKEN Bioresource Research Center, Japan

acid (H_2SO_4). Tris medium was used for the monovalent cation resistance test to avoid underestimation of cation influx. The NC medium consisted of 15.5 g L^{-1} K_2HPO_4, 4.5 g L^{-1} KH_2PO_4, 0.05 g L^{-1} $MgSO_4 \bullet 7H_2O$, 0.34 g L^{-1} citric acid, 5 g L^{-1} peptone, 2 g L^{-1} yeast extract, 5 g L^{-1} glucose, and 11.7 g L^{-1} NaCl. Deionized water was used as a solvent. The final pH was adjusted to the desired value using KOH or H_2SO_4 (Fujinami et al., 2011).

2.2. Measurement of intracellular Cs^+, K^+, and Mg^{2+} concentration

Intracellular Cs^+, K^+, and Mg^{2+} concentrations were measured in TS-1 wild-type, Cs^+-sensitive mutants (Mut4 and Mut5), and *B. subtilis*. As TS-1 Cs^+-sensitive mutants and *B. subtilis* did not grow under high Cs^+ concentration conditions, CsCl was added after culturing. Intracellular ion concentrations were measured 1 h after the addition of CsCl.

Strain TS-1 was inoculated from a single colony by dispensing 2 mL of neutral complex medium (pH 8.0) into a 14-mL culture tube and cultured at 30°C and 200 rpm for 18 h. The culture solution (100 µL) was inoculated into a medieval composite agar medium and pre-incubated at 37°C for 18 h. The cultured neutral complex agar medium was inoculated into 200 mL of 30 mM Tris medium (pH 8.0) such that the turbidity at OD_{600} was 0.1 and cultured at 37°C and 150 rpm. When the turbidity at OD_{600} reached 0.4, 20-mL portions were dispensed, various concentrations of CsCl (0, 100, 200, 300, and 400 mM) were added, and the cells were further cultured for 1 h. The culture solution was centrifuged at 9,100 × *g* at 20°C for 3 min to collect the cells. Unless otherwise specified, the TOMY Seiko MX-305 centrifuge (TOMY SEIKO Co., Ltd., Tokyo, Japan) was used. The supernatant was removed, and the cell pellet was suspended in 5 mL of 300 mM sucrose solution. The suspension was centrifuged at 9,000 × *g* for 3 min at 20°C, and the cell pellet was resuspended in 5 mL of 300 mM sucrose solution. The protein concentration was determined via the Lowry method using a 100-µL aliquot of the suspension. One milligram of protein was used in a volume of 3 µL of bacterial cells. The suspension was then centrifuged at 9,000 × *g* for 3 min at 20°C. The cell pellet was suspended in 5 mL of 5% trichloroacetic acid (TCA) and incubated at 100°C for 10 min. After that, the mixture was centrifuged at 4°C and 9,000 × *g* for 5 min, and the supernatant was used for intracellular ion concentration measurement. The Cs^+ concentration was measured by taking 1 mL of the intracellular ion concentration measurement sample using an atomic absorption photometer (iCE3400; Thermo Fisher Scientific, Waltham, MA, United States). A 1-mL aliquot was taken from the measurement sample, and the K^+ concentration was measured using an ANA-135 flame photometer (Tokyo Koden Co., Ltd., Tokyo, Japan). Mg^{2+} concentration was measured using a metalloassay magnesium assay LS kit (Metallogenics Co., Ltd., Chiba, Japan) according to the manufacturer's instructions. First, 4.5 µL of 5 M NaOH was added to 100 µL of the measurement sample to adjust the pH from 2 to 7.

Subsequently, 3 µL of the pH-adjusted measurement sample was added to 250 mL of the coloring solution, vortexed, and allowed to stand at 20°C for 5 min. Absorbance at OD_{660} was then measured. The Mg^{2+} concentration of the samples was calculated from the obtained value using the following formula:

$$\text{Sample } Mg^{2+}\text{concentration (mM)} = \frac{(\text{Sample absorbance - blank absorbance}) \times 2}{\text{Standard solution absorbance - blank absorbance}}$$

2.3. Data analysis

Statistical analysis was performed with BellCurve for Excel (Social Survey Research Information Co., Ltd., Tokyo, Japan). Tukey test data for *post hoc* analysis of the results in Figures 1, 2 are presented in Supplementary Tables S1, S2, respectively. In Figures 1A–C, multiple comparison analysis was performed between strains after confirming a significant difference by two-way analysis of variance.

2.4. Ribosome preparation

Ribosome preparation and fractionation were based on a previously reported method (Takada et al., 2021). Wild-type strain TS-1 and its Cs^+-sensitive mutants Mut4 and Mut5 were streaked on

10.3389/fmicb.2023.1201121

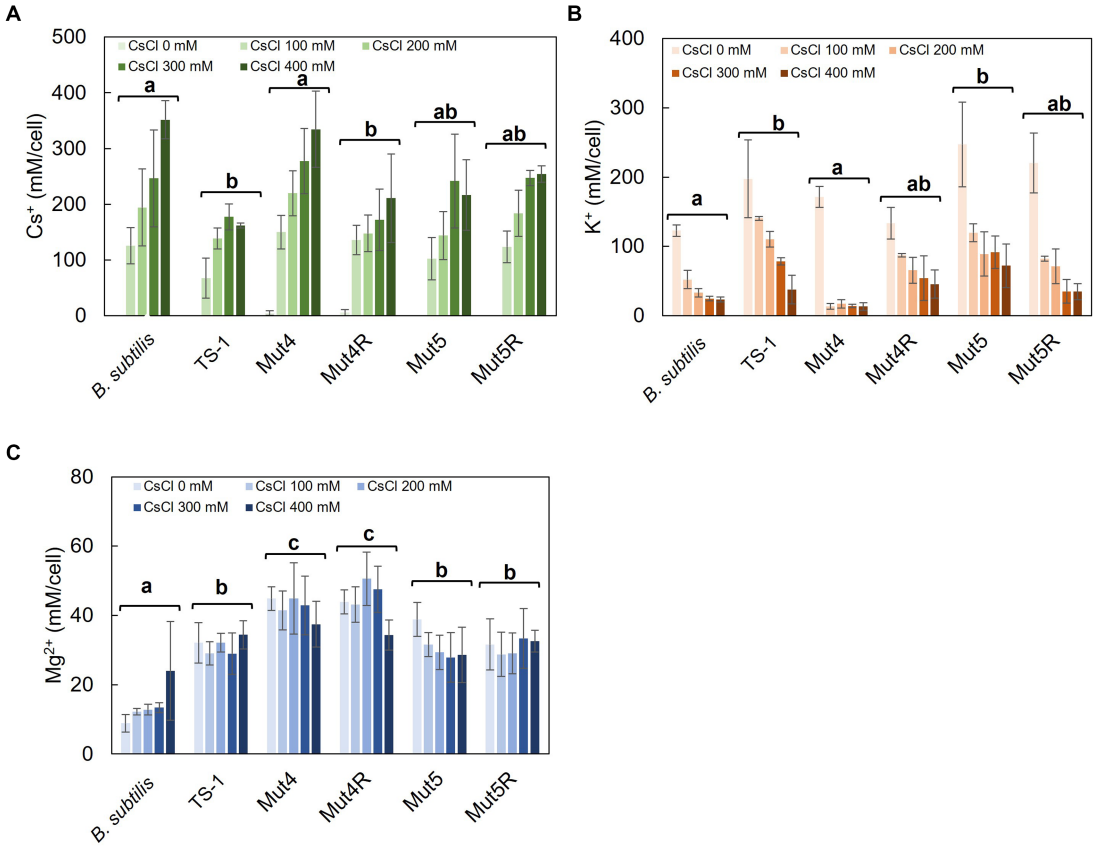

FIGURE 1
Intracellular Cs^+, K^+, and Mg^{2+} concentrations after CsCl treatment in strain TS-1, its mutants, and *B. subtilis*. Strain TS-1 and its derivative mutants were cultured in Tris medium (pH 8.0) and *B. subtilis* in LB medium (pH 7.5) until turbidity reached 0.4. Subsequently, the cells were treated with CsCl for 1h, collected, and treated with 5% TCA, and the intracellular Cs^+ concentration **(A)**, intracellular K^+ concentration **(B)**, and intracellular Mg^{2+} concentration **(C)** were measured. The vertical axis indicates the intracellular concentration (mM/cell), and the series shows the results when each strain was treated with CsCl (0, 100, 200, 300, and 400mM). Error bars indicate the standard deviation of at least three independent experiments. Different lowercase letters indicate significant differences. In panels **A–C**, multiple comparison analysis was performed between strains after confirming a significant difference by two-way analysis of variance. Different superscript letters (a, b, c) denote significant differences from each other in all combinations.

a pH 8.5 neutral composite agar medium and used as pre-culture (37°C, 18 h). Using an inoculation loop, cells grown on the plate were collected and inoculated (37°C, 200 rpm) in 1,000 mL of Tris medium (pH 8.0). This was used as the culture medium. Cultivation was started at an initial turbidity (OD_{600} = 0.1), and after 4 h of culture initiation, 25 and 50 mL of 8 M CsCl were added. To collect the bacteria, centrifugation (5,000 × *g*, 4°C, 10 min) was performed using an NA-600C rotor (TOMY SEIKO Co. Ltd.) The cells were resuspended in 10 mL Buffer I and subjected to a French press operation twice at 8,000 psi to disrupt the cells. Buffer I (pH 7.6) consisted of 2.42 g L^{-1} tris base, 2.15 g L^{-1} magnesium acetate tetrahydrate, 7.7 g L^{-1} ammonium acetate, 0.015 g L^{-1} ammonium acetate, and 8 mL of 0.1 M phenylmethylsulfonyl fluoride (PMSF). The pH was adjusted to 7.6 with 6 N HCl. Undisrupted cells were removed via centrifugation (12,000 × *g*, 4°C, 15 min), and crude cell debris containing ribosomes in the supernatant was collected. The absorbance of the cell debris at 260 nm was measured using a spectrophotometer and stored at 4°C until ultracentrifugation. Cell lysates were subjected to ultracentrifugation within 3 days of preparation. The same experiment was performed twice to confirm reproducibility.

For *B. subtilis*, 2 mL of LB medium (pH 7.5) was dispensed into a 14-mL culture tube, inoculated using a single colony, and cultured at 37°C and 200 rpm for 8 h. The culture solution (100 μL) was inoculated onto LB agar medium (pH 7.5) and pre-cultured at 37°C for 16 h. The cultured LB agar medium was inoculated into 1 L of LB medium (pH 7.5) such that the turbidity at OD_{600} was 0.03 and cultured at 37°C and 150 rpm. After 2.5 h of culture initiation, CsCl (0, 200, and 400 mM) and 50 mM $MgCl_2$ were added, and the mixture was further cultured for 1 h. A crude cell extract was obtained from the culture solution in the same manner as described for strain TS-1.

2.5. Ribosome analysis

For strain TS-1 and its Cs^+-sensitive mutants Mut4 and Mut5, an Ultra-Clear™ centrifuge tube (14 mL; Beckman Coulter, Brea, CA, United States) was used for sucrose density gradient ultracentrifugation with 4 mL of 10% sucrose in Buffer I. Thereafter, 4 mL of 35% sucrose in Buffer I was added to the bottom of the tube using a syringe. The upper lid of the tube was covered with parafilm, and the tube was allowed to stand tilted to form a sucrose density gradient at 20°C for

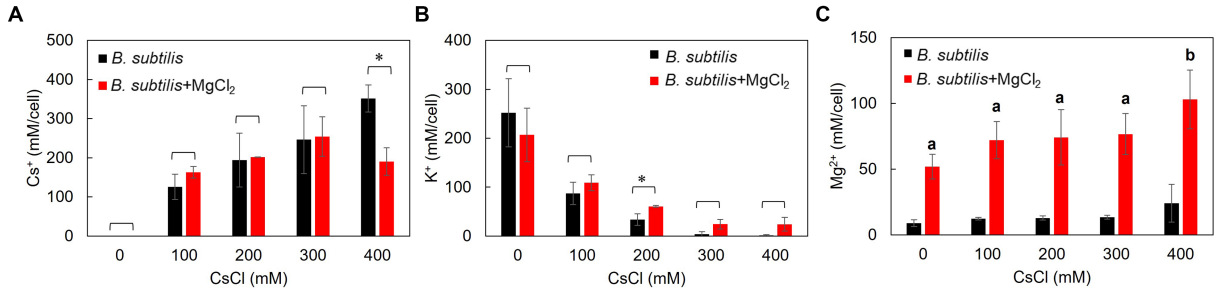

FIGURE 2
Intracellular Cs^+, K^+, and Mg^{2+} concentrations of *B. subtilis* with the addition of CsCl and $MgCl_2$. After culturing in LB medium (pH 7.5) to a turbidity of 0.4, the cells were treated with CsCl and $MgCl_2$ for 1h, collected, and suspended in 5% TCA, and the Cs^+ **(A)**, K^+ **(B)**, and Mg^{2+} **(C)** concentrations were measured. The vertical axis indicates the intracellular Cs^+ concentration (mM/cell), and the series shows the results when each strain was treated with CsCl (0, 100, 200, 300, and 400mM). Error bars indicate the standard deviation of three independent experiments. Asterisk (*) indicates $p<0.05$, indicating a significant difference. Different superscript letters (a, b) denote significant differences from each other in all combinations.

2 h, after which the tube was left at 4°C for 1 h. Crude ribosomal cell extract prepared as described above was layered on top of the sucrose density gradient. An OptimaTML-80XP Ultracentrifuge (Beckman Coulter) was used for ultracentrifugation (222,000 × *g*, 4°C, 3 h) using an SW40Ti rotor (6 × 14 mL; Beckman Coulter). Fractions of 200 μL each were taken from the upper layer of the tube (45 fractions), and the A_{260} of each fraction was measured using a Thermo Nano Drop200C (Thermo Fisher Scientific K.K., Tokyo, Japan). The sucrose concentration was measured using an Atago handheld refractometer (MASTER-PM, ATAGO Co., Ltd., Tokyo, Japan). After the measurements, a separation profile diagram was constructed.

For *B. subtilis*, 4.5 mL of 10% sucrose in Buffer I was poured into a 14-mL Ultra-Clear™ centrifuge tube, after which the 4.5 mL of 35% sucrose in Buffer I was added to the bottom of the tube using a syringe. Subsequent experiments were performed as described above for the TS-1 to create a ribosome profile.

3. Results

3.1. Effect of treatment with or without Mg^{2+} addition on the growth of the representative Cs^+-resistant microorganisms

Using *B. subtilis*, *S. aureus*, *E. coli*, *P. aeruginosa*, and *S. cerevisiae* as representative microorganisms, the effect of Mg^{2+} addition on Cs^+ resistance was investigated. Cs^+ resistance improved upon the addition of Mg^{2+} to the culture media for all microorganisms, although there was a difference in the degree of Cs^+ resistance observed between them. *B. subtilis* showed only a slight increase in Cs^+ tolerance with the addition of Mg^{2+} when the pH of LB medium was 7.0 (data not shown). Therefore, the experiment was performed at pH 7.5, where a more pronounced effect was observed. In *B. subtilis*, Cs^+ resistance improved to 300 mM (Figure 3A) when 50 mM $MgCl_2$ was added to the medium compared with 100 mM without Mg^{2+}. Regarding the Cs^+ resistance of *S. aureus*, growth inhibition was observed at 300 mM CsCl without Mg^{2+}. However, growth was observed even with 600 mM CsCl when 100 mM $MgCl_2$ was added (Figure 3B). *E. coli* cultures were resistant to 400 mM CsCl when 50 mM $MgCl_2$ was added compared with 300 mM without Mg^{2+} (Figure 3C). *P. aeruginosa* grew in the presence of 200 mM CsCl when 125 mM $MgCl_2$ was added, compared with only 100 mM CsCl without Mg^{2+} (Figure 3D). *S. cerevisiae* grew in the presence of 200 mM CsCl when 150 mM $MgCl_2$ was added, compared to its growth in the absence of Mg^{2+} (Figure 3E).

3.2. Comparison of changes in intracellular Cs^+, K^+, and Mg^{2+} concentrations in strain TS-1, its Cs^+-sensitive mutants, its revertants, and *B. subtilis* with and without CsCl treatment

Intracellular Cs^+ concentrations were measured in TS-1 wild-type, Cs^+-sensitive mutants (Mut4 and Mut5), revertants (Mut4R and Mut5R), and *B. subtilis* with and without CsCl treatment (Figure 1A). In *B. subtilis*, intracellular Cs^+ concentration increased with increasing CsCl concentration. Conversely, the intracellular Cs^+ concentration was maintained at <200 mM in the TS-1 wild-type. In Mut4, the intracellular Cs^+ concentration increased with increasing CsCl concentration, similar to the trend seen in *B. subtilis*. Mut4R had a lower Cs^+ concentration than that of Mut4, and this was comparable to the wild-type. Strains Mut5 and Mut5R exhibited intracellular Cs^+ concentrations intermediate to those of TS-1 wild-type and *B. subtilis*.

Intracellular K^+ concentrations were measured in TS-1 wild-type, Cs^+-sensitive mutants, revertants, and *B. subtilis* with and without Cs^+ treatment (Figure 1B). The addition of CsCl to *B. subtilis* significantly decreased intracellular K^+ concentration. The TS-1 wild-type showed a more gradual decrease in intracellular K^+ concentration than that of *B. subtilis* following CsCl addition, showing a significant difference ($p < 0.05$). Similar to *B. subtilis*, Mut4 showed a drastic reduction in the intracellular K^+ concentration when CsCl was added. Mut4R, Mut5, and Mut5R exhibited approximately similar behaviors as the wild-type strain.

Intracellular Mg^{2+} concentrations were measured in TS-1 wild-type, Cs^+-sensitive mutants, revertants, and *B. subtilis* with and without Cs^+ treatment (Figure 1C). There was no significant difference in intracellular Mg^{2+} concentrations between TS-1 wild-type, Mut5,

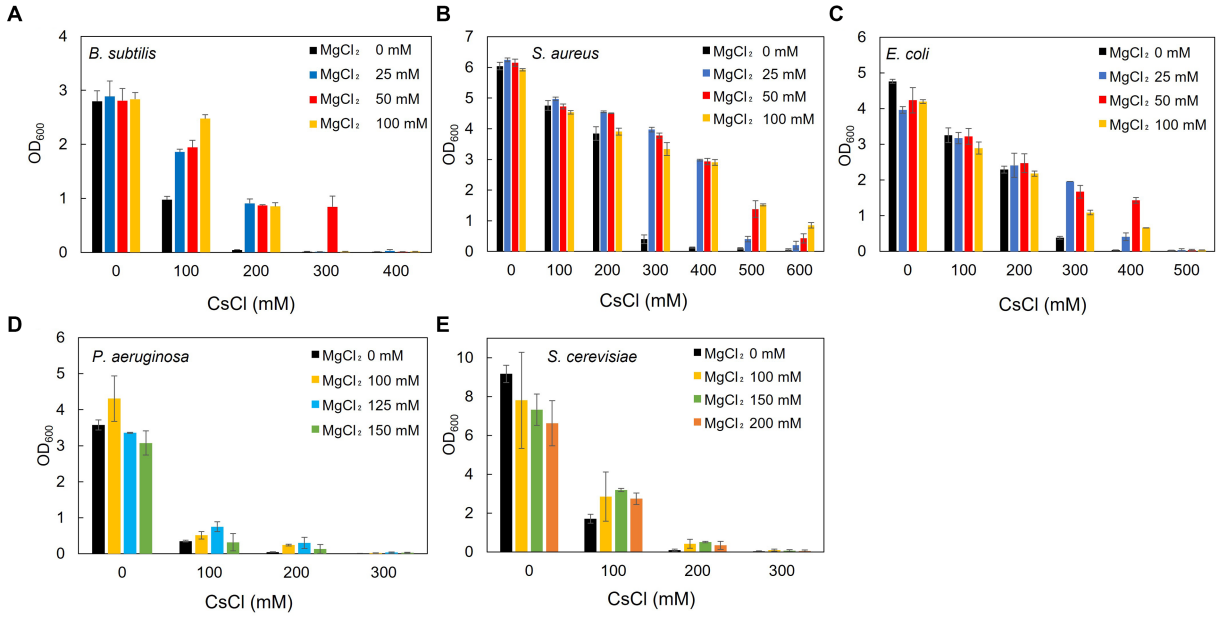

FIGURE 3
Effect of Mg^{2+} addition on the growth of the representative Cs^+-resistant microorganisms. *B. subtilis* BR151MA **(A)**, *S. aureus* IAM12544 **(B)**, *E. coli* W3110 **(C)**, and *P. aeruginosa* IFO13275 **(D)** were cultured in LB medium for 16h, and turbidity at OD_{600} was measured. *B. subtilis* was cultured in an LB medium at pH 7.5 and the others at pH 7.0. *S. cerevisiae* JCM1499 **(E)** was cultured in YM broth for 24h, and turbidity at OD_{600} was measured. The vertical axis indicates turbidity, and the horizontal axis indicates the CsCl concentration of the medium. Error bars indicate the standard deviation of three independent experiments.

and Mut5R. In contrast, Mut4 and Mut4R showed high intracellular Mg^{2+} concentrations.

Tukey test raw data for *post hoc* analysis of the results in Figure 1 are presented in Supplementary Table S1.

3.3. Comparison of Cs^+ resistance in *B. subtilis* with Mg^{2+} addition and changes in intracellular Cs^+, K^+, and Mg^{2+} concentrations

Intracellular Cs^+ concentrations in *B. subtilis*, representing common microorganisms, were measured with and without CsCl and $MgCl_2$ treatments (Figure 2A). At CsCl concentrations of 0–300 mM, adding 50 mM $MgCl_2$ did not change the intracellular Cs^+ concentration, but at 400 mM CsCl, intracellular Cs^+ concentration decreased by approximately 50%.

Similarly, the intracellular K^+ concentration in *B. subtilis* was also measured (Figure 2B). There was no significant difference in the intracellular K^+ concentrations with the addition of 50 mM $MgCl_2$ at CsCl concentrations of 0, 100, 300, and 400 mM. However, intracellular K^+ concentrations significantly increased at a CsCl concentration of 200 mM.

Likewise, intracellular Mg^{2+} concentrations were also measured in *B. subtilis* (Figure 2C). Without CsCl treatment, adding 50 mM $MgCl_2$ increased the intracellular Mg^{2+} concentration by approximately 40 mM. As the amount of CsCl increased, the intracellular Mg^{2+} concentration increased slightly, and a significant difference ($p < 0.05$) was observed at a CsCl concentration of 400 mM.

Tukey test raw data for *post hoc* analysis of the results in Figure 2 are presented in Supplementary Table S2.

3.4. Effects of CsCl treatment on the growth of TS-1 and *B. subtilis*

TS-1 wild-type, Mut4, and Mut5 were cultured, treated with CsCl after 4 h of culturing, and harvested after 1 h to prepare ribosomes. The doubling times of TS-1 wild-type, Mut4, and Mut5 up to 4 h of culture were approximately 2.6, 2.5, and 2.5 h, respectively. The growth of the TS-1 wild-type continued regardless of the presence or absence of CsCl treatment (Figure 4A). In contrast, growth inhibition of both Mut4 and Mut5 was observed after the addition of CsCl (Figures 4B,C). Next, *B. subtilis* was cultured, CsCl treatment was performed after 2.5 h of culture, and the cells were harvested after 1 h to prepare ribosomes. The doubling time of *B. subtilis* up to 2.5 h before culture was approximately 37 min, and growth inhibition was observed after the addition of CsCl (Figure 4D).

3.5. Effects of CsCl treatment in TS-1 on ribosomal complexes

To investigate the effect of Cs^+ treatment on ribosome complex formation in the TS-1 wild-type and its mutants, crude cell extracts were prepared from cultured cells, and the ribosome complexes were separated using sucrose density gradient ultracentrifugation (Figure 5A). In the TS-1 wild-type, no effect was observed on the formation of ribosomal complexes, regardless of the presence or

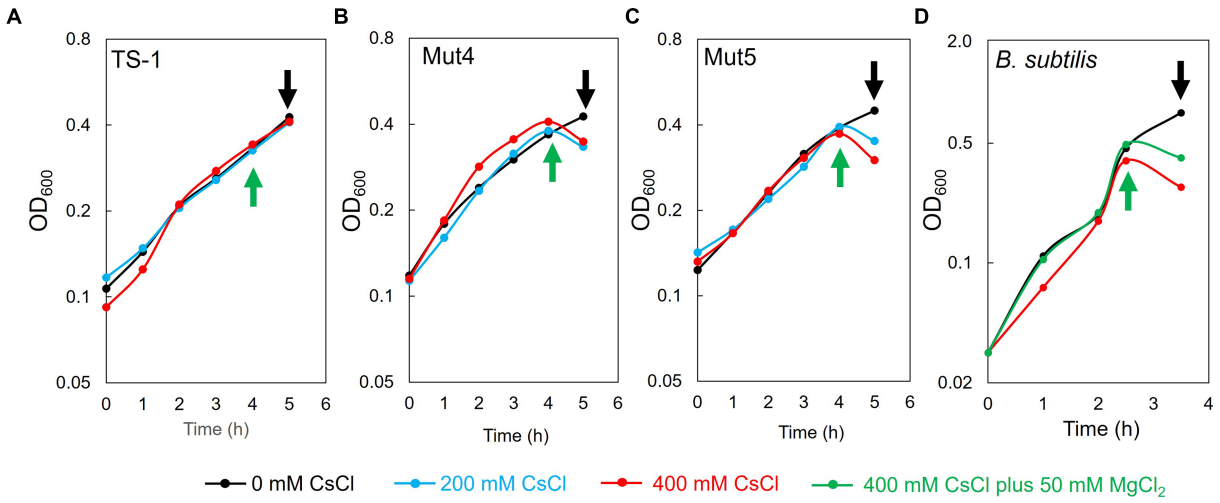

FIGURE 4
Effects of CsCl treatment on the growth of TS-1 and *B. subtilis*. The horizontal axis indicates culture time (h), and the vertical axis indicates turbidity (OD_{600}). For TS-1 **(A)**, Mut4 **(B)**, Mut5 **(C)**, and *B. subtilis* **(D)**, CsCl was added at the time points indicated by the green upward arrow and collected at the time points indicated by the black downward arrow.

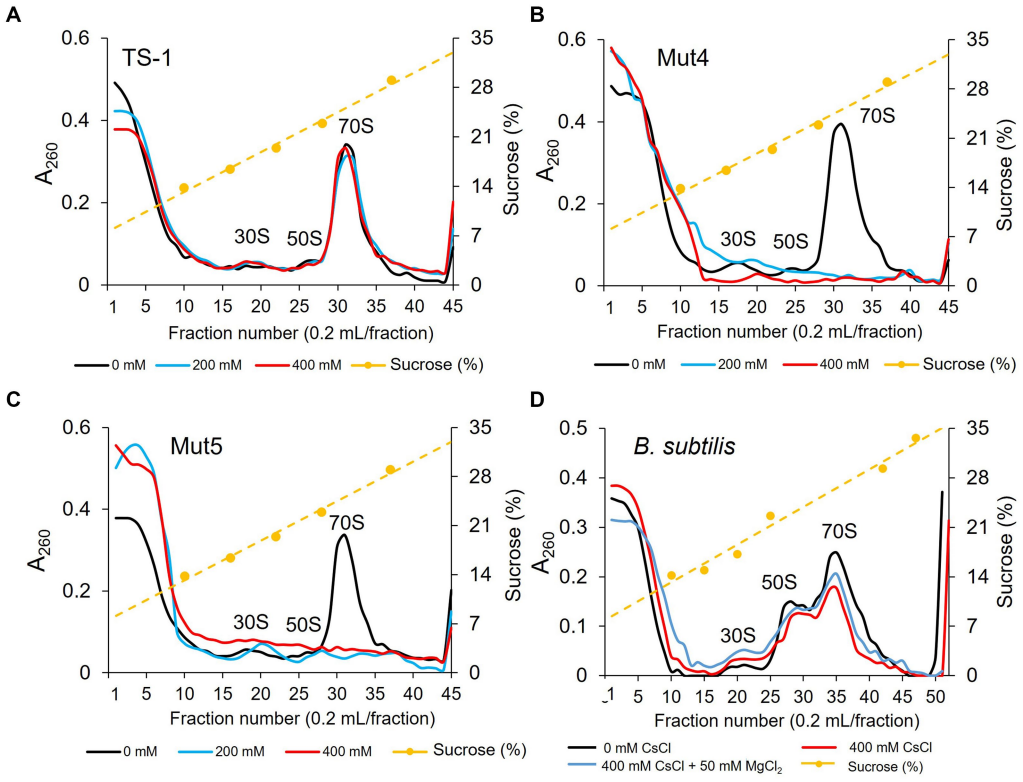

FIGURE 5
Ribosomal complex profiles with and without CsCl treatment in strain TS-1, its mutants, and *B. subtilis*. The effects of CsCl treatment on complex ribosome formation in strain TS-1 **(A)**, its mutant strains Mut4 **(B)** and Mut5 **(C)**, and *B. subtilis* **(D)** were investigated. Each crude cell extract was obtained and analyzed for ribosomal complexes using sucrose density gradient ultracentrifugation. The first vertical axis indicates the absorbance at A_{260}, the second vertical axis shows the sucrose concentration, and the horizontal axis indicates the fraction number. Two independent experiments were performed to confirm reproducibility.

absence of CsCl treatment. Next, the ribosome complexes were analyzed for the Cs^+-sensitive mutants, Mut4 and Mut5, in the same manner as the wild-type (Figures 5B,C). Both mutants were treated with CsCl at 200 and 400 mM, upon which the 70S ribosomes collapsed, and a finer peak than that of 30S ribosomes was observed.

3.6. Effects of CsCl and $MgCl_2$ treatment in *B. subtilis* on ribosomal complexes

The effect of CsCl treatment on ribosome complex formation was investigated in *B. subtilis*. We also investigated whether ribosome complex formation was affected by the addition of $MgCl_2$. Ribosome complexes were analyzed using sucrose density gradient ultracentrifugation in the same manner as that described for the TS-1 strain (Figure 5D). Even when *B. subtilis* was treated with CsCl, 70S ribosomes tended to decrease slightly; however, ribosomes were not significantly affected. In addition, no effect on the ribosome complex was observed when $MgCl_2$ was added to the culture medium.

4. Discussion

4.1. Effect of treatment with and without Mg^{2+} addition on the growth of representative microorganisms showing Cs^+ resistance

Examining the effect of Mg^{2+} addition on Cs^+ resistance in *B. subtilis*, *P. aeruginosa*, *E. coli*, *S. aureus*, and *S. cerevisiae* as representative microorganisms showed that Cs^+ resistance was improved by adding Mg^{2+} to the medium for all the five strains tested in this study. Furthermore, it was effective not only for TS-1 but also for microorganisms in general.

Mg^{2+} plays various essential roles in many organisms, including maintaining ribosome structure, genome stabilization, and enzyme activation (Akanuma et al., 2018). It has been reported that increasing the intracellular Mg^{2+} concentration stabilizes ribosomes in *B. subtilis*, in which the structure of the ribosome is destabilized due to the deletion of a part of the ribosomal protein (Akanuma et al., 2018). Therefore, we hypothesized that Mg^{2+} enhanced Cs^+ tolerance. Cs^+ uptake by cells affected ribosome complex formation. As Mg^{2+} stabilized the structure of ribosomes, the upper limit of Cs^+ concentrations tolerated by the strain was considered to be improved.

Differences were found in the improvement in Cs^+ tolerance and the amount of Mg^{2+} required for the outcome obtained by adding Mg^{2+} to each microbial species culture. It was speculated that the increase in intracellular Mg^{2+} could counteract the drastic decrease in intracellular K^+ concentration to some extent or that the stability of ribosomes might differ among microorganisms or both.

4.2. Comparison of changes in intracellular Cs^+, K^+, and Mg^{2+} concentrations in strain TS-1, its Cs^+-sensitive mutants, its revertants, and *B. subtilis* with and without CsCl treatment

Changes in intracellular Cs^+, K^+, and Mg^{2+} concentrations in strains TS-1 and *B. subtilis* with and without CsCl treatment were measured.

In *B. subtilis*, intracellular Cs^+ concentration increased with increasing CsCl concentration in the medium, and the K^+ concentration decreased sharply. From the Cs^+-tolerant growth test results, the intracellular K^+ concentration decreased to approximately 13% of that in the absence of Cs^+ at 200 mM CsCl, at which *B. subtilis* could not grow. It was speculated that the extreme decrease in intracellular K^+ concentration in *B. subtilis* impeded the maintenance of vital functions. This was consistent with results reported for *E. coli* (Avery, 1995). *B. subtilis* and *E. coli* do not harbor a Cs^+ efflux mechanism. Thus, it was inferred that a decrease in intracellular K^+ concentration was the leading cause of growth inhibition in these bacteria. CsCl treatment slightly increased intracellular Mg^{2+} but did not make a significant difference. Contrastingly, in strain TS-1, the intracellular Cs^+ concentration remained lower than that in *B. subtilis* even when the CsCl concentration increased, and the concentration was maintained at approximately <200 mM. Intracellular K^+ concentration was moderately decreased in TS-1 following Cs^+ treatment compared to that in *B. subtilis*, and intracellular K^+ concentration was high compared to that in *B. subtilis*. This may be because TS-1 harbors a Cs^+ efflux system, CshA (Koretsune et al., 2022). The apparent K_m value of CshA at pH 8.0 was approximately 250 mM, indicating that TS-1 prevented the intracellular Cs^+ concentration from increasing and K^+ deficiency.

Analysis of the changes in intracellular Cs^+, K^+, and Mg^{2+} concentrations with and without Cs^+ treatment in the TS-1 Cs^+-sensitive mutants and its revertants revealed that CsCl treatment of Mut4 resulted in an influx of Cs^+ into cells, and the K^+ concentration was significantly reduced. This was similar to the results obtained for *B. subtilis*, which does not possess a Cs^+ efflux system. This suggested that Cs^+ excretion by CshA was essential for Cs^+ resistance in TS-1 cells. In addition, the intracellular Mg^{2+} concentration in Mut4 was maintained at higher levels than those in the wild-type strain. This suggested that Mg^{2+} was incorporated into cells to resist the toxicity caused by the influx of a large amount of Cs^+ into the cells. Since CshA in the Cs^+ efflux system is active in Mut5, which is a MgtE mutant, Cs^+ and K^+ concentrations were similar to those of the wild-type even after Cs^+ treatment. No significant difference was observed in the intracellular Mg^{2+} concentration. This suggested the possibility that another Mg^{2+} transporter performed the uptake of Mg^{2+} into the cell and functioned when Cs^+ entered the cells of Mut5.

Mg^{2+} has been shown to improve Cs^+ resistance in several microorganisms. We investigated changes in intracellular Cs^+, K^+, and Mg^{2+} concentrations when $MgCl_2$ was added simultaneously with CsCl in *B. subtilis*. The addition of 50 mM of $MgCl_2$ decreased the intracellular Cs^+ concentration at a CsCl concentration of 400 mM. The *E. coli* Cs^+ uptake system, Kup, becomes less active when the cell is filled with K^+ (Dosch et al., 1991). Although the details of the Cs^+ uptake system of *B. subtilis* have not been elucidated, the K^+ uptake system is expected to take up Cs^+. A significant increase in the intracellular K^+ concentration was observed when Mg^{2+} was added at a CsCl concentration of 200 mM ($p = 0.03$). Although there was no significant difference in this experiment, the intracellular K^+ concentration increased at CsCl concentrations of 300 and 400 mM at a level close to the CsCl concentration of 200 mM (300 mM: $p = 0.06$, 400 mM: $p = 0.08$). This was presumed to be because the addition of high concentrations of CsCl and $MgCl_2$ enhanced the uptake of K^+ to adapt to the high osmotic pressure environment.

4.3. Effects of CsCl treatment of TS-1, its Cs^+-sensitive mutants, and *B. subtilis* on ribosomal complexes

To elucidate the mechanism of Cs^+ resistance through Mg^{2+} uptake in TS-1, we investigated whether the presence or absence of

CsCl treatment in TS-1, its Cs^+-sensitive mutants, and *B. subtilis* affected the formation of ribosomal complexes. In addition, we investigated whether the ribosomal complex was affected when Mg^{2+} was added to *B. subtilis* cultures to improve Cs^+ tolerance. We observed that Cs^+ treatment did not affect the ribosomal complex in the TS-1 wild-type. However, in the Cs^+-sensitive strains Mut4 and Mut5, the 70S ribosomes collapsed following CsCl treatment. However, CsCl treatment did not affect the ribosomal complex of *B. subtilis*.

Mut4 is a CshA mutant, and a large amount of Cs^+ accumulated in the cells based on the measurement results of intracellular Cs^+ concentration. Therefore, it is suggested that high concentrations of intracellular Cs^+ destabilize ribosomes. Strain Mut5 is an MgtE mutant, and although it has no issue with Mg^{2+} uptake, it is presumed that Mg^{2+} uptake cannot be enhanced when Mg^{2+} is required. Therefore, it was speculated that ribosomes destabilized by Cs^+ could be stabilized owing to the lack of Mg^{2+}. High concentrations of K^+ inhibit ribosome complex formation by competing with Mg^{2+} (Nierhaus, 2014; Senbayram et al., 2015). Because Cs^+ has physicochemical properties similar to those of K^+, it was speculated that Cs^+ destabilized ribosomes by competing with Mg^{2+}.

TS-1 wild-type suppressed intracellular Cs^+ to ≤200 mM in a high-concentration Cs^+ environment by excreting intracellular Cs^+ using CshA. In a Cs^+ environment of ≤200 mM, MgtE is considered to enhance Mg^{2+} uptake and stabilize the ribosomal complex, thereby adapting to the Cs^+ environment.

Bacillus subtilis did not exhibit Cs^+ resistance, and when treated with CsCl, Cs^+ accumulated in the cells, similar to Mut4. Thus, the ribosome complex is expected to be similarly destroyed by CsCl treatment. However, CsCl treatment did not have a significant effect on ribosomal complexes. The impact of improving Cs^+ tolerance by adding Mg^{2+} differed depending on the microbial species. Hence, the stability of ribosomes to Cs^+ was expected to vary depending on the microbial species. Certain ribosomal proteins function to replace Mg^{2+} for ribosomal stabilization (Hsiao et al., 2009; Akanuma et al., 2014). Although Cs^+ competes with Mg^{2+} to destabilize ribosomes, it does not affect ribosome stabilization by ribosomal proteins, suggesting that *B. subtilis* ribosomes are not affected by Cs^+. However, it has been suggested that the influx of Cs^+ into the cells of *B. subtilis* leads to an extreme decrease in K^+ and that a shortage of K^+ interferes with life support.

5. Conclusion

In the present study, it was found that Cs^+ treatment of *B. subtilis* increased the intracellular Cs^+ concentration, similar to the trend observed in Mut4; therefore, it was presumed that the ribosomal complex would also be disrupted, but no significant effect was observed. This suggests that the degree of cell dependence on Mg^{2+} in the context of the strength of the ribosomal complex differs depending on the microbial species.

In TS-1, when the intracellular Cs^+ concentration is ≤200 mM, the Cs^+ that flows into the cell competes with Mg^{2+} and destabilizes the ribosome. Therefore, we inferred that the stability of the ribosomal complex was enhanced by maintaining a high intracellular Mg^{2+} concentration.

Prospects for these results include the application of the Cs^+/H^+ antiporter CshA in bioremediation using Mg^{2+} as an additive. Because CshA is a low-affinity antiporter (apparent K_m value of 250 mM for Cs^+), it is not suitable for recovering low concentrations of Cs^+. Therefore, its affinity should be further improved. We plan to elevate the affinity of CshA for Cs^+ by molecular evolution engineering, such as error-prone PCR. In addition, when using microorganisms that accumulate Cs^+ but have low Cs^+ resistance for bioremediation, using Mg^{2+} as an additive is expected to enhance the Cs^+ resistance of microorganisms and increase the efficiency of their recovery.

Data availability statement

The original contributions presented in the study are included in the article/Supplementary material, further inquiries can be directed to the corresponding author.

Author contributions

MI designed the research and wrote the manuscript. YI, CZ, KS, and MI conducted the research. YI, CZ, and MI analyzed the data. All authors contributed to the article and approved the submitted version.

Funding

This work was supported by a grant for the Toyo University Top Priority Research Promotion Program and the Toyo University intellectual property practical application promotion program.

Acknowledgments

We would like to thank Editage (www.editage.com) for the English language editing of the manuscript.

Conflict of interest

The authors declare that the research was conducted in the absence of any commercial or financial relationships that could be construed as a potential conflict of interest.

Publisher's note

Supplementary material

The Supplementary material for this article can be found online at: https://www.frontiersin.org/articles/10.3389/fmicb.2023.1201121/full#supplementary-material

References

Akanuma, G. (2021). Diverse relationships between metal ions and the ribosome. *Biosci. Biotechnol. Biochem.* 85, 1582–1593. doi: 10.1093/bbb/zbab070

Akanuma, G., Kobayashi, A., Suzuki, S., Kawamura, F., Shiwa, Y., Watanabe, S., et al. (2014). Defect in the formation of 70S ribosomes caused by lack of ribosomal protein L34 can be suppressed by magnesium. *J. Bacteriol.* 196, 3820–3830. doi: 10.1128/JB.01896-14

Akanuma, G., Yamazaki, K., Yagishi, Y., Iizuka, Y., Ishizuka, M., Kawamura, F., et al. (2018). Magnesium suppresses defects in the formation of 70S ribosomes as well as in sporulation caused by lack of several individual ribosomal proteins. *J. Bacteriol.* 200:e00212-18. doi: 10.1128/JB.00212-18

Avery, S. V. (1995). Caesium accumulation by microorganisms: uptake mechanisms, cation competition, compartmentalization and toxicity. *J. Ind. Microbiol.* 14, 76–84. doi: 10.1007/BF01569888

Bossemeyer, D., Schlosser, A., and Bakker, E. P. (1989). Specific cesium transport via the *Escherichia coli* Kup (TrkD) K^+ uptake system. *J. Bacteriol.* 171, 2219–2221. doi: 10.1128/jb.171.4.2219-2221.1989

Cohen-Bazire, G., Sistrom, W. R., and Stanier, R. Y. (1957). Kinetic studies of pigment synthesis by non-sulfur purple bacteria. *J. Cell. Comp. Physiol.* 49, 25–68. doi: 10.1002/jcp.1030490104

Dosch, D. C., Helmer, G. L., Sutton, S. H., Salvacion, F. F., and Epstein, W. (1991). Genetic analysis of potassium transport loci in *Escherichia coli*: evidence for three constitutive systems mediating uptake potassium. *J. Bacteriol.* 173, 687–696. doi: 10.1128/jb.173.2.687-696.1991

Fiorentini, D., Cappadone, C., Farruggia, G., and Prata, C. (2021). Magnesium: biochemistry, nutrition, detection, and social impact of diseases linked to its deficiency. *Nutrients* 13:1136. doi: 10.3390/nu13041136

Fujinami, S., Sato, T., and Ito, M. (2011). The relationship between a coiled morphology and Mbl in alkaliphilic *Bacillus halodurans* C-125 at neutral pH values. *Extremophiles* 15, 587–596. doi: 10.1007/s00792-011-0389-9

Fujinami, S., Takeda, K., Onodera, T., Satoh, K., Sano, M., Narumi, I., et al. (2013). Draft genome sequence of sodium-independent alkaliphilic *Microbacterium* sp. strain TS-1. *Genome Announc.* 1:e01043-13. doi: 10.1128/genomeA.01043-13

Grundy, F. J., Turinsky, A. J., and Henkin, T. M. (1994). Catabolite regulation of *Bacillus subtilis* acetate and acetoin utilization genes by CcpA. *J. Bacteriol.* 176, 4527–4533. doi: 10.1128/jb.176.15.4527-4533.1994

Hampton, C. R., Bowen, H. C., Broadley, M. R., Hammond, J. P., Mead, A., Payne, K. A., et al. (2004). Cesium toxicity in *Arabidopsis*. *Plant Physiol.* 136, 3824–3837. doi: 10.1104/pp.104.046672

Henkin, T. M., Grundy, F. J., Nicholson, W. L., and Chambliss, G. H. (1991). Catabolite repression of alpha-amylase gene expression in *Bacillus subtilis* involves a trans-acting gene product homologous to the *Escherichia coli lacI* and *galR* repressors. *Mol. Microbiol.* 5, 575–584. doi: 10.1111/j.1365-2958.1991.tb00728.x

Hirose, K. (2016). Fukushima Daiichi nuclear plant accident: atmospheric and oceanic impacts over the five years. *J. Environ. Radioact.* 157, 113–130. doi: 10.1016/j.jenvrad.2016.01.011

Hsiao, C., Mohan, S., Kalahar, B. K., and Williams, L. D. (2009). Peeling the onion: ribosomes are ancient molecular fossils. *Mol. Biol. Evol.* 26, 2415–2425. doi: 10.1093/molbev/msp163

Imazawa, R., Takahashi, Y., Aoki, W., Sano, M., and Ito, M. (2016). A novel type bacterial flagellar motor that can use divalent cations as a coupling ion. *Sci. Rep.* 6:19773. doi: 10.1038/srep19773

Ishida, Y., Koretsune, T., Ishiuchi, E., Teshima, M., and Ito, M. (2023). A magnesium transporter is involved in the cesium ion resistance of the high-concentration cesium ion-resistant bacterium *Microbacterium* sp. TS-1. *Front. Microbiol.* 14:1136514. doi: 10.3389/fmicb.2023.1136514

Jung, K., Krabusch, M., and Altendorf, K. (2001). Cs^+ induces the kdp operon of *Escherichia coli* by lowering the intracellular K^+ concentration. *J. Bacteriol.* 183, 3800–3803. doi: 10.1128/JB.183.12.3800-3803.2001

Koretsune, T., Ishida, Y., Kaneda, Y., Ishiuchi, E., Teshima, M., Marubashi, N., et al. (2022). Novel cesium resistance mechanism of alkaliphilic bacterium isolated from jumping spider ground extract. *Front. Microbiol.* 13:841821. doi: 10.3389/fmicb.2022.841821

Lee, D. D., Galera-Laporta, L., Bialecka-Fornal, M., Moon, E. C., Shen, Z., Briggs, S. P., et al. (2019). Magnesium flux modulates ribosomes to increase bacterial survival. *Cells* 177, 352–360.e13. doi: 10.1016/j.cell.2019.01.042

Nakamura, K., Chiba, S., Kiuchi, T., Nabeshi, H., Tsutsumi, T., Akiyama, H., et al. (2022). Comprehensive analysis of a decade of cumulative radiocesium testing data for foodstuffs throughout Japan after the 2011 Fukushima Daiichi nuclear power plant accident. *PLoS One* 17:e0274070. doi: 10.1371/journal.pone.0274070

Nierhaus, K. H. (2014). Mg^{2+}, K^+, and the ribosome. *J. Bacteriol.* 196, 3817–3819. doi: 10.1128/JB.02297-14

Perkins, J., and Gadd, G. M. (1995). The influence of pH and external K^+ concentration on caesium toxicity and accumulation in *Escherichia coli* and *Bacillus subtilis*. *J. Ind. Microbiol.* 14, 218–225. doi: 10.1007/BF01569931

Pontes, M. H., Yeom, J., and Groisman, E. A. (2016). Reducing ribosome biosynthesis promotes translation during low mg(2+) stress. *Mol. Cell* 64, 480–492. doi: 10.1016/j.molcel.2016.05.008

Sanial, V., Buesseler, K. O., Charette, M. A., and Nagao, S. (2017). Unexpected source of Fukushima-derived radiocesium to the coastal ocean of Japan. *Proc. Natl. Acad. Sci. U. S. A.* 114, 11092–11096. doi: 10.1073/pnas.1708659114

Senbayram, M., Gransee, A., Wahle, V., and Thiel, H. (2015). Role of magnesium fertilisers in agriculture: plant-soil continuum. *Crop Pasture Sci.* 66, 1219–1229. doi: 10.1071/cp15104

Takada, H., Roghanian, M., Caballero-Montes, J., Van Nerom, K., Jimmy, S., Kudrin, P., et al. (2021). Ribosome association primes the stringent factor Rel for tRNA-dependent locking in the A-site and activation of (p)ppGpp synthesis. *Nucleic Acids Res.* 49, 444–457. doi: 10.1093/nar/gkaa1187

Wu, J., Zheng, X., Chen, J., Yang, G., Zheng, J., and Aono, T. (2022). Distributions and impacts of plutonium in the environment originating from the Fukushima Daiichi nuclear power plant accident: an overview of a decade of studies. *J. Environ. Radioact.* 248:106884. doi: 10.1016/j.jenvrad.2022.106884

frontiers | Frontiers in Microbiology

TYPE Original Research
PUBLISHED 29 June 2023
DOI 10.3389/fmicb.2023.1188544

OPEN ACCESS

EDITED BY
Melina Kerou,
University of Vienna, Austria

REVIEWED BY
Angelina Cordone,
University of Naples Federico II, Italy
Katrina I. Twing,
Weber State University, United States

*CORRESPONDENCE
Paraskevi N. Polymenakou
✉ polymen@hcmr.gr

RECEIVED 17 March 2023
ACCEPTED 12 June 2023
PUBLISHED 29 June 2023

CITATION
Polymenakou PN, Nomikou P, Hannington M, Petersen S, Kilias SP, Anastasiou TI, Papadimitriou V, Zaka E, Kristoffersen JB, Lampridou D, Wind S, Heinath V, Lange S and Magoulas A (2023) Taxonomic diversity of microbial communities in sub-seafloor hydrothermal sediments of the active Santorini-Kolumbo volcanic field. *Front. Microbiol.* 14:1188544. doi: 10.3389/fmicb.2023.1188544

Taxonomic diversity of microbial communities in sub-seafloor hydrothermal sediments of the active Santorini-Kolumbo volcanic field

Paraskevi N. Polymenakou[1]*, Paraskevi Nomikou[2], Mark Hannington[3], Sven Petersen[3], Stephanos P. Kilias[2], Thekla I. Anastasiou[1], Vasiliki Papadimitriou[1], Eleutheria Zaka[1,4], Jon Bent Kristoffersen[1], Danai Lampridou[2], Sandra Wind[5], Verena Heinath[6], Sabine Lange[3] and Antonios Magoulas[1]

[1]Hellenic Centre for Marine Research, Institute of Marine Biology, Biotechnology, and Aquaculture, Heraklion, Greece, [2]Faculty of Geology and Geoenvironment, National and Kapodistrian University of Athens, Athens, Greece, [3]GEOMAR Helmholtz Centre for Ocean Research Kiel, Kiel, Germany, [4]Department of Biology, University of Crete, Heraklion, Greece, [5]Department of Earth and Environmental Sciences, University of Ottawa, Ottawa, ON, Canada, [6]Institute of Geosciences, University of Kiel (CAU), Kiel, Germany

Introduction: Active hydrothermal vents of volcanic origin provide a remarkable manifestation of life on Earth under extreme conditions, which may have consequences for our understanding of habitability on other terrestrial bodies as well.

Methods: Here, we performed for the first time Illumina sequencing of bacterial and archaeal communities on sub-seafloor samples collected from the Santorini-Kolumbo volcanic field. A total of 19 (3-m long) gravity corers were collected and processed for microbial community analysis.

Results: From a total of 6,46,671 produced V4 sequences for all samples, a total of 10,496 different Operational Taxonomic Units (OTUs) were identified that were assigned to 40 bacterial and 9 archaeal phyla and 14 candidate divisions. On average, the most abundant phyla in all samples were Chloroflexi (Chloroflexota) (24.62%), followed by Proteobacteria (Pseudomonadota) (11.29%), Firmicutes (Bacillota) (10.73%), Crenarchaeota (Thermoproteota) (8.55%), and Acidobacteria (Acidobacteriota) (8.07%). At the genus level, a total of 286 known genera and candidate genera were mostly dominated by members of *Bacillus, Thermoflexus, Desulfatiglans, Pseudoalteromonas*, and *Pseudomonas*.

Discussion: In most of the stations, the Chao1 values at the deeper layers were comparable to the surface sediment samples denoting the high diversity in the subsurface of these ecosystems. Heatmap analysis based on the 100 most abundant OTUs, grouped the sampling stations according to their geographical

location, placing together the two hottest stations (up to 99°C). This result indicates that this specific area within the active Kolumbo crater create a distinct niche, where microorganisms with adaptation strategies to withstand heat stresses can thrive, such as the endospore-forming Firmicutes.

KEYWORDS

submarine volcano, Santorini (Greece), microbial community composition and diversity, diversity, hydrothermal vent field, Kolumbo volcano

1. Introduction

Beneath the sediment surface lies a world of microscopic life inhabited by a great diversity of bacteria and archaea, most of them largely unknown (Jørgensen and Marshall, 2016). Today, it has been estimated that the sub-seafloor microorganisms account for about 2.9×10^{29} cells, which is equivalent to half of the microbial cells worldwide in the oceans (Kallmeyer et al., 2012). These extreme sub-seafloor organisms were the first representatives of life on Earth and they are responsible for the genesis of geological structures during the evolution and creation of all currently known ecosystems (Pikuta et al., 2007). So far, most of sub-seafloor studies of microbial life have been mainly performed in environments with *in situ* temperatures < 30°C and thus our knowledge about the habitability of higher temperature environments, such as the hydrothermal vent systems, is still limited (LaRowe et al., 2017). Only recently, Heuer et al. (2020) demonstrated for the first time, the dependence of microbial abundance and activity to critical temperatures around 40 to 50°C and 70°C and showed that life in the deep subseafloor is not constrained by an upper temperature limit below 120°C (Heuer et al., 2020). The geochemical conditions in such systems are favorable for microbial metabolism and they can support colonization of non-photosynthetic, lithotrophic communities (Orcutt et al., 2011; Ivarsson et al., 2013). Microbes isolated from hydrothermal vent environments can live at temperatures up to ?122°C (Takai et al., 2008). These hyperthermophiles are fueled by high fluxes of oxidants and reductants (Heuer et al., 2020). Interestingly, hot hydrothermal vents in some places are dominated by archaea (e.g., Lost City Hydrothermal Field of Mid-Atlantic Ridge, a deep-sea hydrothermal field in the Central Indian Ridge; Takai et al., 2004; Brazelton et al., 2010; Lagostina et al., 2021) whereas in other places by bacteria (Takai et al., 2006; Lagostina et al., 2021). A possible explanation for these differences is that archaea can live in low-energy environments whereas bacteria can cope better in energy-rich or unstable environments (Valentine, 2007; Lagostina et al., 2021).

The Hellenic Volcanic Arc (HVA) located in the Aegean Sea contains unique hydrothermal vents where its development is a response to the subduction of the African plate beneath the active margin of the European plate (Le Pichon and Angelier, 1979; Nomikou et al., 2012). HVA consists of five islands i.e., Methana, Milos, Santorini, Nisiros, and Kos. Among these, the Santorini volcano is world famous because of its recent explosive eruption (~3,600 years ago) which was one of the largest known volcanic events in historical time. The Santorini volcanic field consists of more than 20 submarine cones with the largest one, the Kolumbo volcano, being located 505 m below sea level. High (up to 220°C) and low (up to 70°C) temperature polymetallic chimneys and vents covers the seafloor at the norther part of the Kolumbo crater. The exterior of the chimneys and large areas of the seabed around Kolumbo were covered with reddish/orange microbial mats and streams of white/gray mats. Major elements in the area include Fe, S, Pb, Na, As, Sb, Mn and Sr with average concentrations of 111,333 ppm Fe, 23,850 ppm S, 6,043 ppm Pb, 4,182 ppm Na, 2,656 ppm As, 2,616 ppm Sb, 2,075 ppm Mn and 1,828 ppm Sr (Christakis et al., 2018). The discharge of gaseous CO_2 (> 99%) of active vent chimneys of Kolumbo (Rizzo et al., 2016) causes an increase of water density that leads to the accumulation of acidic seawater (as low as pH 5.0) near the crater floor (Carey et al., 2013).

Previous bio-geochemical (Kilias et al., 2013; Christakis et al., 2018) and metagenomic investigation (Oulas et al., 2016) conducted on microbial mat samples covering the seafloor of the Santorini-Kolumbo volcanic system and the surfaces of Kolumbo chimneys, revealed that both Kolumbo crater and Santorini caldera harbor highly complex bacterial and archaeal communities mostly dominated by chemolithoautotrophs, methanotrophs, as well as heterotrophs that perform anaerobic degradation of aromatic hydrocarbons. Kilias et al. (2013) demonstrated that iron microbial-mat in Kolumbo volcano is dominated by ferrihydrite-type phases and microbial sequences akin to "*Nitrosopumilus maritimus*," a mesophilic Thaumarchaeota strain capable of chemoautotrophic growth on hydrothermal ammonia and CO_2. This result was further confirmed by Christakis et al. (2018), for microbial communities inhabiting the surfaces of the inactive polymetallic chimneys of Kolumbo volcano. In this study, the active chimney communities were found to be dominated by operational taxonomic units (OTUs) related to thermophilic members of Epsilonproteobacteria, Aquificae, and Deltaproteobacteria whereas the inactive chimney communities were dominated by an OTU closely related to the archaeon *Nitrosopumilus* sp., and by members of Gammaproteobacteria, Deltaproteobacteria, Planctomycetes, and Bacteroidetes. These lineages are closely related to phylotypes typically involved in iron, sulfur, nitrogen, hydrogen and methane cycling.

Although we have demonstrated the enormous structural and functional diversity of seafloor microbial communities in Santorini-Kolumbo volcanic complex, we still do not know anything on the status of its sub-seafloor ecosystems. Of all the potentially habitable environments on Earth, the submarine volcanoes with active hydrothermal vents are among the most intriguing, extreme, and challenging environments to investigate

10.3389/fmicb.2023.1188544

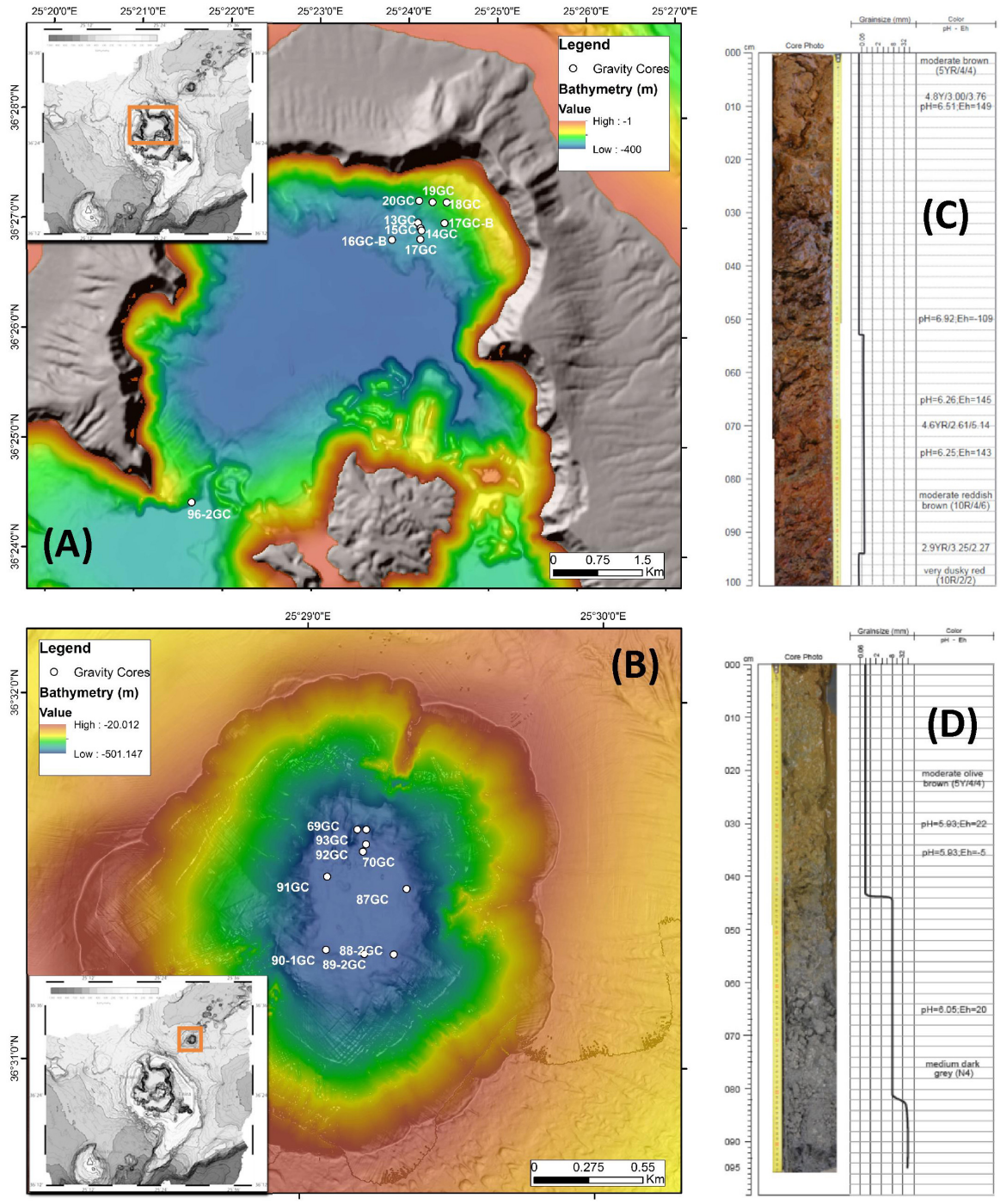

FIGURE 1
Detailed bathymetry maps showing the locations of gravity coring stations during POS510 expedition in **(A)** Santorini caldera and **(B)** Kolumbo volcano. Top 100 cm of two representative gravity corers of **(C)** Santorini caldera: 20GC and **(D)** Kolumbo volcano: 92GC. Values of pH and Eh of the different layers are also shown.

the origins and importance of sub-seafloor communities, the development and maintenance of life and to uncover its valuable genetic resources. The active Santorini-Kolumbo volcanic complex serves as the best candidate to face these quite exciting and cutting-edge research challenges. In the present study, for the first time, microbiological data from sub-seafloor hydrothermal sediments from this unique submarine volcanic-arc setting are presented.

2. Results

2.1. Lithology and physicochemical characteristics

Stations with numbers from 13GC to 20GC were located at the norther part of Santorini caldera whereas stations numbering

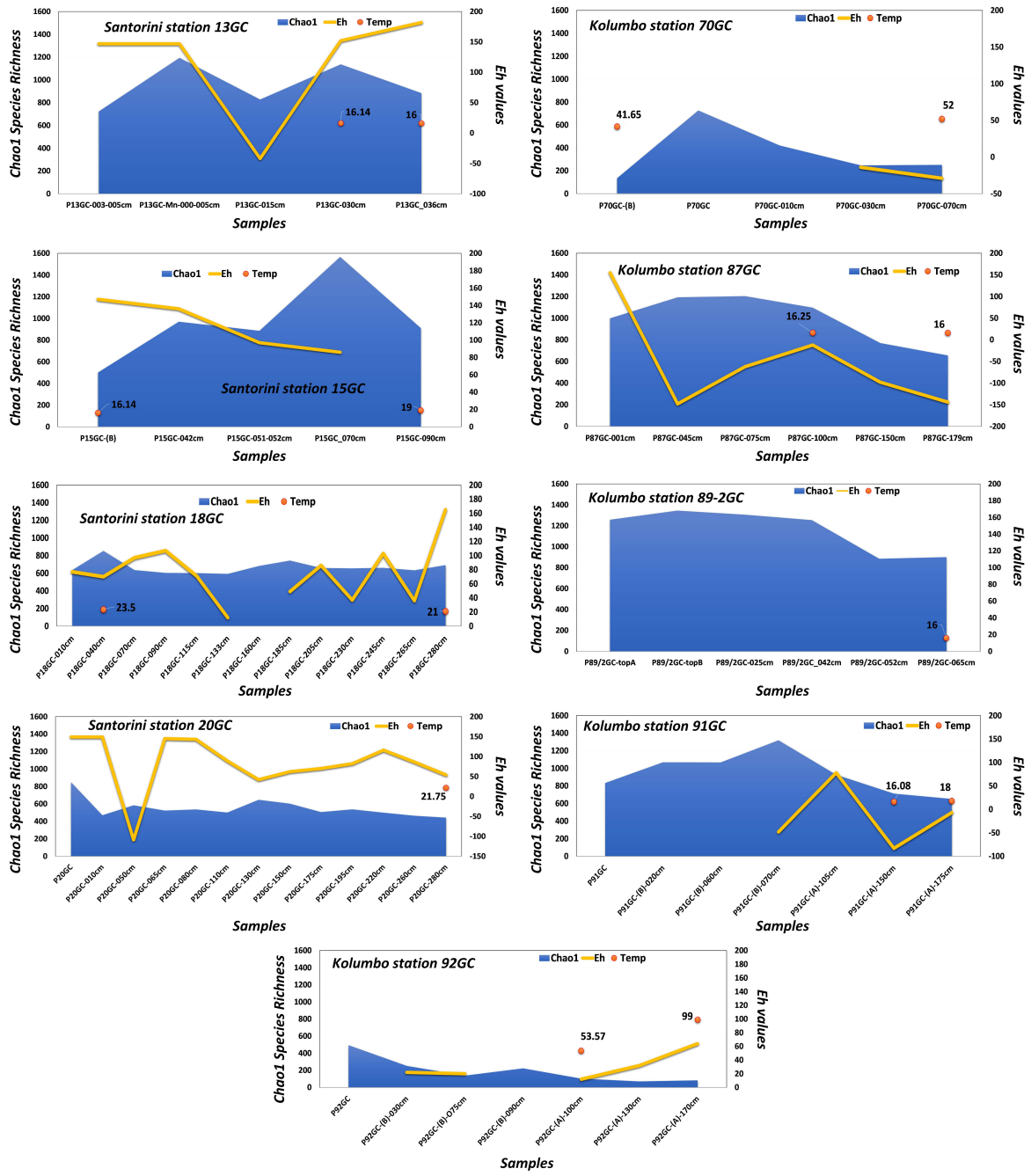

FIGURE 2
Variation of Chao1, Eh and temperature values of the nine sliced cores.

from 69GC to 93GC were located inside Kolumbo volcano. Station 96-2GC was located at the southern part of Santorini caldera (Figure 1 and Supplementary Table 1). Core sediments were primarily Fe-oxide rich mud silt and/or Fe-oxide rich reddish-brown silt with Mn or Fe-Mn crusts. Of particular note, several olive brown or olive gray clay zones were observed at the deeper sediment layers in some cores (Supplementary Table 1). Maximum probe temperatures ranged from 15.82°C at station 89-2GC to 53.57°C at station 92GC, both located inside the Kolumbo volcano (Figure 2 and Supplementary Table 2). Probe temperatures inside the Santorini caldera varied between 15.88°C at the southern part of the caldera to 23.5°C at the north. Temperature at the bottom of each corer ranged from 15°C at station 69GC to 99°C at station 92GC, both located inside the crater of Kolumbo volcano. Bottom temperature at Santorini caldera stations varied between 15 and 21°C (Figure 2 and Supplementary Table 2). The minimum pH value was recorded inside the Santorini caldera at the bottom gravity corer of station 20GC (i.e., 5.83), whereas the maximum value was recorded inside the Kolumbo volcano at station 13GC and the sediment layer of 30 cm (i.e., 7.69). Values of redox potential varied from −148 to 182 mV with minimum values close to anaerobic

10.3389/fmicb.2023.1188544

TABLE 1 Values of OTUs and biodiversity indices (alpha diversity) including Chao1, Shannon–Weaver diversity index (H) and evenness (E_H) and Simpson Diversity index (D, 1-D, 1/D) for 16S amplicon data.

Samples	Obs. OTUs	Alpha diversity					
		Chao1	Shannon–Weaver (H)	Evenness (E_H)	Simpson (D)	1-D	1/D
P13GC-003-005cm	580	723	2.76	0.43	0.35	0.65	2.85
P13GC-Mn-000-005cm	981	1,194	5.30	0.77	0.02	0.98	51.44
P13GC-015cm	701	828	5.73	0.88	0.01	0.99	160.46
P13GC-030cm	975	1,137	5.63	0.82	0.01	0.99	95.80
P13GC_036cm	775	884	5.42	0.81	0.01	0.99	85.95
P14GC	536	647	4.44	0.71	0.05	0.95	18.56
P15GC-(B)	404	502	4.78	0.80	0.03	0.97	35.12
P15GC-042cm	783	969	4.93	0.74	0.04	0.96	26.11
P15GC-051-052cm	745	885	4.97	0.75	0.03	0.97	33.28
P15GC_070cm	1,395	1,567	5.68	0.78	0.02	0.98	66.32
P15GC-090cm	794	910	5.05	0.76	0.03	0.97	36.04
P15GC-cc	1,013	1,158	6.01	0.87	0.01	0.99	125.32
P16GC-B	915	1,037	5.60	0.82	0.01	0.99	68.12
P17GC	1,151	1,307	5.81	0.82	0.01	0.99	123.35
P17GC-B-010cm	1,090	1,213	5.92	0.85	0.01	0.99	142.65
P18GC-010cm	509	637	4.41	0.71	0.03	0.97	29.24
P18GC-040cm	704	853	4.41	0.67	0.04	0.96	27.26
P18GC-070cm	498	635	4.45	0.72	0.03	0.97	29.90
P18GC-090cm	423	604	4.65	0.77	0.02	0.98	40.65
P18GC-115cm	494	601	4.51	0.73	0.03	0.97	37.31
P18GC-133cm	503	593	4.58	0.74	0.03	0.97	34.94
P18GC-160cm	507	682	4.42	0.71	0.04	0.96	24.71
P18GC-185cm	625	744	4.59	0.71	0.03	0.97	35.90
P18GC-205cm	571	659	4.47	0.70	0.04	0.96	28.31
P18GC-230cm	570	655	4.34	0.68	0.04	0.96	24.92
P18GC-245cm	538	661	4.25	0.68	0.05	0.95	20.67
P18GC-265cm	529	633	4.27	0.68	0.04	0.96	23.65
P18GC-280cm	627	692	4.55	0.71	0.03	0.97	37.22
P19GC	597	708	4.70	0.74	0.04	0.96	26.00
P20GC	742	848	4.37	0.66	0.05	0.95	18.88
P20GC-010cm	375	470	4.02	0.68	0.04	0.96	22.74
P20GC-050cm	452	584	4.29	0.70	0.04	0.96	27.74
P20GC-065cm	447	523	4.40	0.72	0.03	0.97	34.43
P20GC-080cm	422	536	4.23	0.70	0.04	0.96	24.57
P20GC-110cm	444	501	4.43	0.73	0.04	0.96	26.99
P20GC-130cm	555	647	4.18	0.66	0.07	0.93	14.63
P20GC-150cm	512	602	4.10	0.66	0.07	0.93	14.18
P20GC-175cm	417	506	4.36	0.72	0.03	0.97	30.23
P20GC-195cm	451	537	4.26	0.70	0.04	0.96	22.41
P20GC-220cm	428	499	4.15	0.68	0.06	0.94	18.06

(Continued)

10.3389/fmicb.2023.1188544

TABLE 1 (Continued)

Samples	Obs. OTUs	Alpha diversity					
		Chao1	Shannon–Weaver (H)	Evenness (E_H)	Simpson (D)	1-D	1/D
P20GC-260cm	402	464	3.99	0.67	0.06	0.94	15.41
P20GC-280cm	391	442	4.40	0.74	0.03	0.97	35.59
P96/2GC-009cm	901	996	5.91	0.87	0.01	0.99	111.36
P69GC-008cm	950	964	5.98	0.87	0.01	0.99	174.36
P70GC-(B)	108	135	1.91	0.41	0.29	0.71	3.46
P70GC	683	727	3.92	0.60	0.08	0.92	12.76
P70GC-010cm	406	421	3.45	0.57	0.11	0.89	8.94
P70GC-030cm	194	247	2.88	0.55	0.18	0.82	5.59
P70GC-070cm	155	251	2.41	0.48	0.23	0.77	4.33
P87GC-001cm	878	999	5.92	0.87	0.01	0.99	128.82
P87GC-045cm	974	1,193	5.78	0.84	0.01	0.99	97.49
P87GC-075cm	970	1,204	5.94	0.86	0.01	0.99	161.79
P87GC-100cm	916	1,097	5.78	0.85	0.01	0.99	122.18
P87GC-150cm	644	770	4.98	0.77	0.02	0.98	44.72
P87GC-179cm	554	655	4.79	0.76	0.03	0.97	36.71
P88/2GC-top	1,131	1,374	6.18	0.88	0.00	1.00	202.13
P89/2GC-topA	1,042	1,258	6.14	0.88	0.00	1.00	204.48
P89/2GC-topB	1,111	1,345	6.07	0.87	0.01	0.99	173.94
P89/2GC-025cm	1,105	1,306	6.10	0.87	0.01	0.99	199.54
P89/2GC_042cm	1,033	1,254	5.80	0.84	0.01	0.99	121.75
P89/2GC-052cm	740	885	3.00	0.45	0.01	0.99	126.92
P89/2GC-065cm	738	901	5.36	0.81	0.01	0.99	76.83
P90-1GC	1,147	1,382	5.98	0.85	0.01	0.99	162.64
P91GC	731	833	5.30	0.80	0.02	0.98	41.22
P91GC-(B)-020cm	825	1,069	5.57	0.83	0.01	0.99	78.33
P91GC-(B)-060cm	1,026	1,068	5.28	0.76	0.02	0.98	54.76
P91GC-(B)-070cm	1,148	1,319	5.22	0.74	0.02	0.98	63.08
P91GC-(A)-105cm	831	927	4.91	0.73	0.03	0.97	39.85
P91GC-(A)-150cm	592	712	4.74	0.74	0.02	0.98	43.02
P91GC-(A)-175cm	592	652	4.45	0.70	0.03	0.97	32.26
P92GC	473	494	4.34	0.71	0.03	0.97	28.73
P92GC-(B)-030cm	234	252	3.42	0.63	0.08	0.92	13.11
P92GC-(B)-075cm	135	138	3.33	0.68	0.09	0.91	11.69
P92GC-(B)-090cm	219	223	3.95	0.73	0.04	0.96	23.93
P92GC-(A)-100cm	70	103	1.95	0.46	0.27	0.73	3.65
P92GC-(A)-130cm	53	70	1.85	0.47	0.28	0.72	3.59
P92GC-(A)-170cm	64	83	1.72	0.41	0.32	0.68	3.16
P93/2GC-008cm	915	1,064	5.79	0.85	0.01	0.99	112.86
Min	53	70	1.72	0.41	0.00	0.65	2.85
Max	1,395	1,567	6.18	0.88	0.35	1.00	204.48
Santorini	6,314	6,343	5.58	0.64	0.02	0.98	52.33
Kolumbo	6,920	6,938	6.06	0.69	0.01	0.99	68.66
Total	10,496	10,496	6.14	0.66	0.01	0.99	86.73

conditions being recorded inside the Kolumbo volcano (Figure 2 and Supplementary Table 1).

2.2. Sequencing data analysis

For studying the microbial diversity within each sample, we used direct counts of the number of operational taxonomic units (OTUs) at 97% similarity level, and various metrics that take into account the abundance of the more rare taxa (Chao1), the abundance and distribution of the taxa [Shannon–Weaver diversity index (H) and evenness (E_H)] and the richness and evenness of the taxa (Simpson D, 1-D, and 1/D indices) (Figure 2 and Table 1). Although, the amplicon sequencing variants (ASVs) have been proposed as an alternative to OTUs for microbial communities analysis, in order our results to be comparable to previous studies at the same investigated area, we decided to follow the classical OTU approach. In addition, according to Schloss (2021), ASVs may artificially split bacterial genomes into separate clusters. Thus, the use of ASVs may lead to conflicting inferences about the ecology of different ASVs derived from the same genome. In the present study, OTUs were defined at 97% sequence similarity, although this threshold may cluster different bacterial species into the same OTU. Results of sequencing analysis allowed the identification of thousands of OTUs for each sample. After processing, a total of 660,252 high quality sequences remained across all 78 samples. Following the recommendations of Salter et al. (2014) and Sheik et al. (2018), we further removed a total of 13,579 sequences assigned to previously identified genera as contaminants from the DNA extraction reagents. A total of 35 genera were removed (Supplementary Table 3), whereas the sequences of the genera *Pseudomonas* and *Bacillus* were kept to our database since our recent investigations have showed them to be among the key players of the Kolumbo volcano (Mandalakis et al., 2019; Bravakos et al., 2021). In addition, we have recently isolated a series of *Bacillus* strains from sample P92GC capable to grow at high temperatures of up to 99°C (unpublished data). The number of retained sequences per sample varied from 2,365 to 18,651. A total of 10,496 OTUs were generated after clustering of the remaining 646,671 sequences at 97% similarity level. The number of OTUs per sample was ranging from 53 to 1,395 (Table 1). Slightly higher OTUs were recorded at Kolumbo stations and at all depths compared to Santorini samples (6,920 and 6,314, respectively; Table 1). Maximum OTU values were calculated at samples P15GC-070cm (1,395; Table 1) and P17GC (1,151; Table 1) of Santorini caldera and at samples P91GC-(B)-070cm (1,148; Table 1) and P90-1GC (1,147; Table 1) of Kolumbo volcano. Interestingly, the minimum values of OTUs were recorded at the deeper sediment layers of station 92GC and more specifically at 100, 130 and 170 cm sediment layers (70, 53, 64, respectively; Table 1) and at the deeper sediment layers of station 70GC (194 and 155 at sediment layers of 30 and 70 cm, respectively). Station 92GC and its adjacent station 70GC were characterized by the higher recorded bottom temperatures of 99 and 54°C, respectively, compared to the rest sampling locations (15–21°C). Chao1, Shannon–Weaver (H) and Simpson Reciprocal (1/D) indices revealed comparable species diversity between Santorini (Chao1 = 6,343; H = 5.58; 1/D = 52.33; Table 1) and Kolumbo samples (Chao1 = 6,938; H = 6.06; 1/D = 68.66; Table 1). Regarding the Santorini samples, all calculated indices varied from 442 to 1,567 (Chao1), from 2.76 to 6.01 (H) and from 2.85 to 160.46 (1/D) whereas in Kolumbo samples the corresponding values range were 70–1, 1,382 (Chao1), 1.72–5.94 (H) and 3.16–204.48 (1/D). Chao1 reached its maximum value at sample P15GC_070cm of Santorini caldera and at sample P90-1GC, whereas the minimum Chao1 values were calculated at the deeper layers of station 92GC sample [P92GC-(A)-130cm: 70; P92GC-(A)-170cm: 83; Table 1]. Maximum values of the rest diversity indices were recorded at sample P15GC-cc of Santorini seafloor (H = 6.01; 1/D = 125.32; Table 1) and at sample P87GC_075cm of Kolumbo seafloor (H = 5.94; 1/D = 161.79; Table 1). Minimum values were calculated at the surface layer of Kolumbo sample P70GC-(B) (H = 1.91; 1/D = 3.46; Table 1) and at the deeper layer of station 92GC, similarly to the Chao1 values [sample P92GC-(A)-170cm: H = 1.72; 1/D = 3.16; Table 1]. Both Kolumbo stations 70GC and 92GC displayed the minimum values of Chao1 whereas in Santorini caldera, the lowest Chao1 values were calculated at stations 18GC and 20GC compared to the rest ones (Figure 2).

2.3. Taxonomic composition analysis

The identified OTUs were phylogenetically assigned to 40 bacterial and 9 archaeal phyla, 14 candidate divisions and 283 bacterial and archaeal families (Figure 3 and Supplementary Table 3). Since the renaming of phyla by Oren and Garrity (2021) remains controversial among microbiologists, we use here the earlier names of phyla and in parenthesis the proposed names voted by the International Committee on Systematics of Prokaryotes which include the ending -ota. On average, the most abundant phyla in all samples were Chloroflexi (Chloroflexota) (24.62%), followed by Proteobacteria (Pseudomonadota) (11.29%), Firmicutes (Bacillota) (10.73%), Crenarchaeota (Thermoproteota) (8.55%) and Acidobacteria (Acidobacteriota) (8.07%) (Figure 3; % of total sequences). Other phyla with intermediate abundances included Planctomycetes (Planctomycetota) (4.26%), Aerophobetes (3.86%), Acetothermia (2.85%), Patescibacteria (2.69%), Nanoarchaeota (2.31%), Euryarchaeota (1.94%), Elusimicrobia (Elusimicrobiota) (1.57%), Omnitrophicaeota (1.48%), Bacteroidetes (Bacteroidota) (1.32%) etc (Figure 3 and Supplementary Table 3). Some rare phyla such as Aerophobetes, Acetothermia and Nanoarchaeota were found to be more prominent in specific samples (up to 20.20% of total sample sequences). More specifically, both Aerophobetes and Acetothermia were abundant in the sample P92GC-(B)-030cm of the hottest station 92GC of Kolumbo volcano (15.94 and 20.20%, respectively), whereas Nanoarchaeota was abundant in a single sample of Santorini caldera (i.e., P16GC-B; 14.57%). At all samples, the dominance of Proteobacteria (Pseudomonadota) was driven by the classes of Delta- (8.69%), Gamma- (5.22%), and Alphaproteobacteria (1.77%), whereas Zetaproteobacteria (0.03%), Magnetococcia (< 0.01%) and the newly characterized phylum of Epsilonbacteraeota (< 0.01%), previously known as Epsilonproteobacteria class (Waite et al., 2017), were recorded in very low abundances. The dominance of Firmicutes

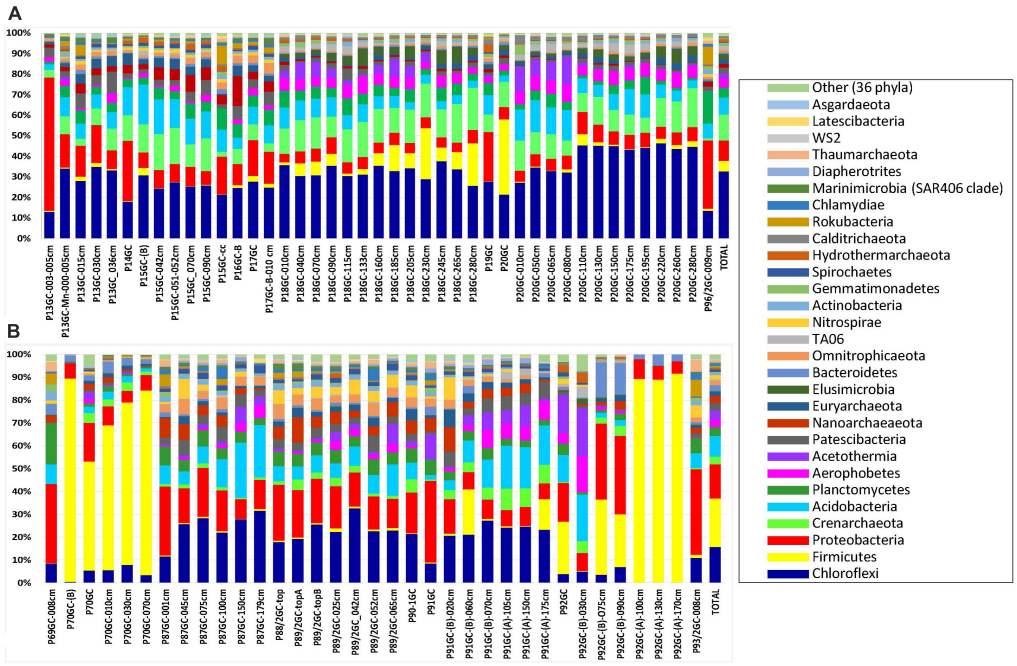

FIGURE 3
The relative abundance of major phyla in the microbial community structure on **(A)** Santorini and **(B)** Kolumbo samples.

(Bacillota) was driven by the classes of Bacilli (13.43%), Clostridia (1.37%), and Negativicutes (0.13%), whereas within Chloroflexi (Chloroflexota), the dominant classes were Anaerolineae (17.86%) and Dehalococcoidia (15.03%). Additionally, among the most abundant classes were Bathyarchaeia (11.85%), formerly known as the Miscellaneous Crenarchaeotal group (Zhou et al., 2018), of the phylum Crenarchaeota (Ca. Bathyarchaeota phylum), Aminicenantia (10.36%) of the phylum Acidobacteria, Acetothermia (3.97%) of the phylum Acetothermia, Phycisphaerae (3.25%) of the phylum Planctomycetes (Planctomycetota), Woesearchaeia (2.60%) of the phylum Nanoarchaeota and Thermoplasmata (2.55%) of the phylum Euryarchaeota.

In Santorini caldera the prevailing phyla were Proteobacteria (Pseudomonadota) in samples P13GC-003-005cm (64.84%) and P14GC (29.42%), Firmicutes (Bacillota) in sample P20GC (36.60%) and Chloroflexi (Chloroflexota) in the rest samples (12.−44.88%). In Kolumbo volcano, predominant phyla included Firmicutes (Bacillota) (20.11%), Proteobacteria (Pseudomonadota) (14.21%), Chloroflexi (Chloroflexota) (14.76%) and Acidobacteria (8.49%). In both Santorini caldera and Kolumbo volcano, the dominance of Firmicutes (Bacillota) was driven by the family of Bacillaceae (3.28 and 12.82% of total Santorini and Kolumbo sequences, respectively) whereas the prevailing families within Chloroflexi (Chloroflexota) were Thermoflexaceae (2.92% in Santorini and 1.20% in Kolumbo sequences) and Anaerolineaceae (1.62% in Santorini and 5.29% in Kolumbo sequences). The dominance of Gammaproteobacteria was driven by the family of Pseudoalteromonadaceae in Santorini (2.17% of total Santorini sequences). However, in Kolumbo samples, the Pseudoalteromonadaceae members were almost absent accounting for less than 0.03% of total Kolumbo sequences. In both areas, Deltaproteobacteria were dominated by members of Desulfarculaceae (1.70% in Santorini and 2.50% in Kolumbo sequences) and Desulfobacteraceae (0.36% in Santorini and 1.85% in Kolumbo sequences). Other abundant families in Santorini were Pirellulaceae (0.80%) of the phylum Planctomycetes, Calditrichaceae (0.75) of the phylum Calditrichaeota, Methylomirabilaceae (0.53%) of the phylum Rokubacteria and Pseudomonadaceae (0.33%) of the phylum Proteobacteria and in Kolumbo, Clostridiaceae 1 (1.84%) of the phylum Clostridia, Weeksellaceae (1.73%) of the phylum Bacteroidetes, and Planococcaceae (1.19%) of the phylum Firmicutes.

At the genus level, a total of 286 known genera and candidate genera (176 in Santorini and 223 in Kolumbo) were mostly dominated by members of *Bacillus* (3.28% in Santorini and 12.81% in Kolumbo sequences; Figure 4A), *Thermoflexus* (2.92% in Santorini and 1.20% in Kolumbo sequences; Figure 4A), *Desulfatiglans* (1.62% in Santorini and 2.45% in Kolumbo sequences; Figure 4A), *Pseudoalteromonas* (2.17% in Santorini and 0.03% in Kolumbo sequences; Figure 4A) and *Pseudomonas* (0.33% in Santorini and 1.71% in Kolumbo sequences; Figure 4A). In Santorini samples, the relative abundance of the dominant genera varied among the different sediment layers. It is interesting to note that at station 18GC, the relative abundance of *Bacillus* related sequences showed an increased trend toward the deeper sediment layers whereas the opposite trend was observed for *Thermoflexus* sequences (Figure 4B). In three samples i.e., P13GC-003-005cm, P14GC, and P19GC, the dominance of *Pseudoalteromonas* was prominent accounting for 94.29, 56.99 and 53.62% of the total sample sequences, respectively. In Kolumbo samples, we observed large differences in the distribution of the dominant genera among stations and sediment layers. In stations 87GC, 88GC, and 89/2GC, members of the genus *Desulfatiglans* (Figure 4C) were

10.3389/fmicb.2023.1188544

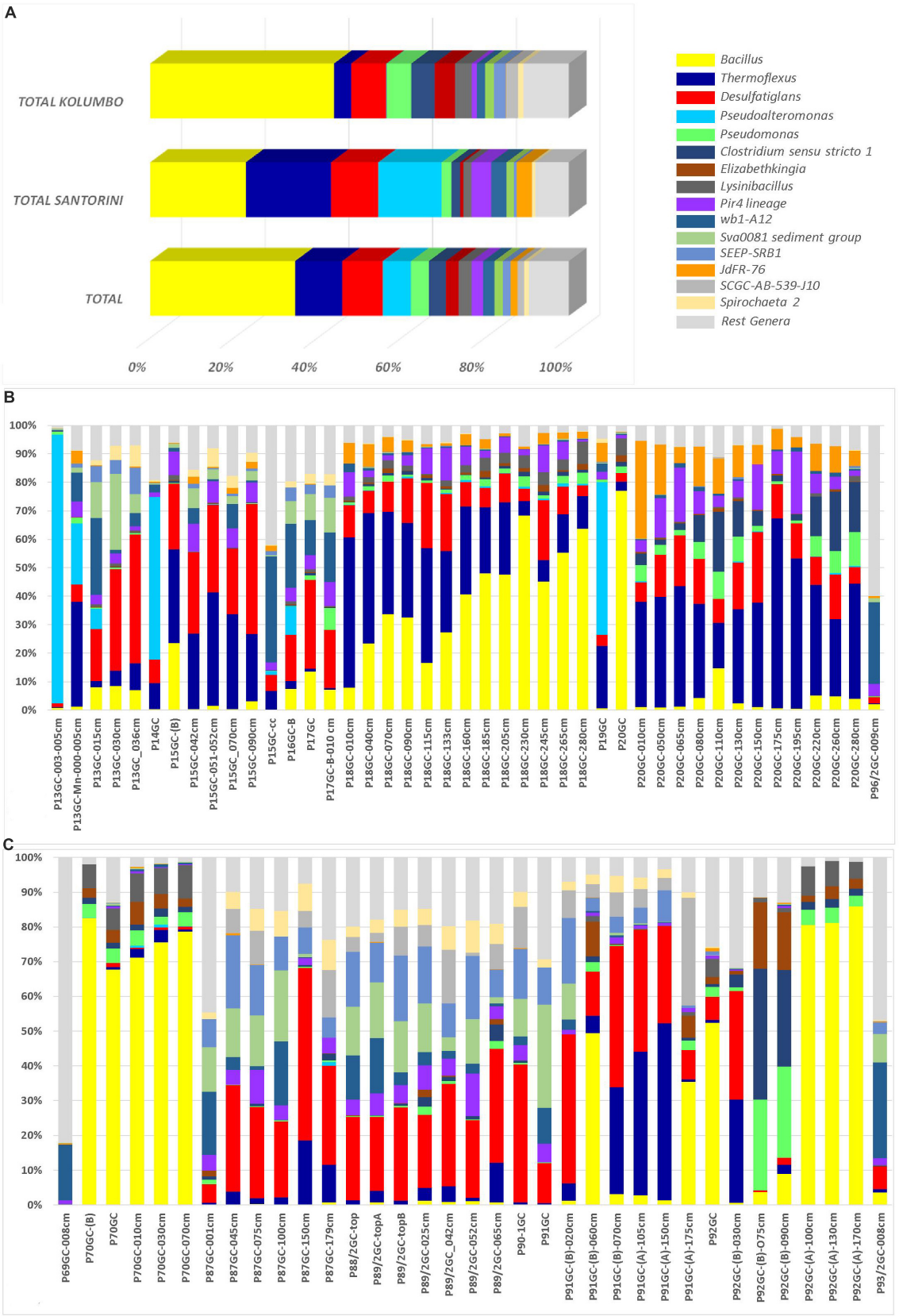

FIGURE 4
The relative abundances of the 15 major genera and candidate genera in microbial community structure **(A)** on total Kolumbo and Santorini samples and on the different sediment layers of **(B)** the Santorini and **(C)** the Kolumbo samples. Crenarchaeota (Ca. Bathyarchaeota) members were not included.

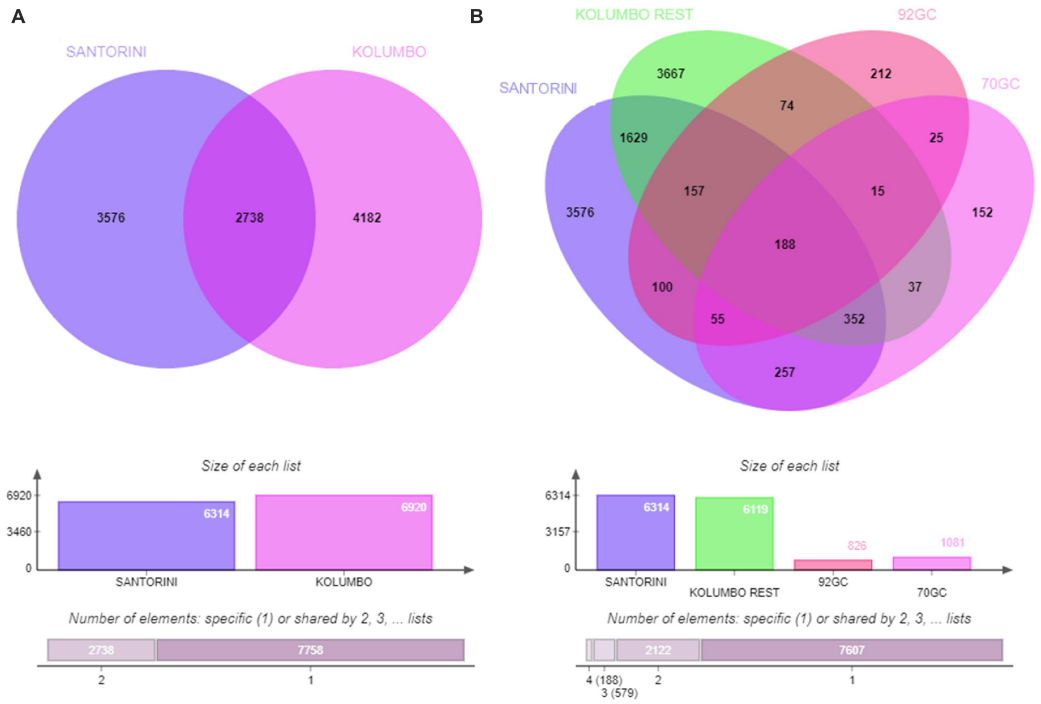

FIGURE 5
Venn diagrams showing the number of shared and unique OTUs **(A)** between Santorini and Kolumbo samples and **(B)** among Santorini samples, the hottest stations 92GC and 70GC of the Kolumbo volcano and the rest Kolumbo samples.

abundant whereas *Thermoflexus* appeared to dominate the sub-seafloor samples P91GC-(B)-070cm, P91GC-(A)-105cm, P91GC-(A)-150cm, P92GC-(B)-030cm, and P87GC-150cm. Members of *Pseudomonas* were found abundant in the sub-seafloor samples P92GC-(B)-075cm and P92GC-(B)-090cm, whereas *Bacillus* genus was dominant in all sediment layers of station 70GC, in the sediment layers of 60 and 175 cm of station 91GC, and in the surface and the deeper layers of station 92GC (i.e., 100 cm, 130 cm, 170 cm). Stations 69GC and 93GC showed a different genera distribution compared to the rest samples mostly dominated by members of *Woeseia* and the taxon at genus level *wb1-A12*.

2.4. Dominant OTUs

According to the Venn analysis, Santorini samples and Kolumbo samples harbor 3,576 and 4,182 unique OTUs, respectively, while sharing 2,738 OTUs (Figure 5). The hottest stations 92GC and 70GC share 500 and 852 OTUs with the Santorini samples, respectively. When comparing the hottest stations with the rest Kolumbo and Santorini samples a core of 188 OTUs was identified (Supplementary Table 4). These included the most abundant OTU which was closely related to an unidentified bacterium of the Anaerolineae class (6.64% of all sequences), and two highly abundant OTUs which were closely related to an unidentified bacterium of Aminicenantales (2.35% of all sequences), and to an unidentified archaeon of Bathyarchaeia (2.50% of all sequences). In order to detect differences among the samples, we performed heatmap analysis using the 100 most dominant OTUs. This specific analysis produced four distinct clusters according to their geographic location (Figure 6 and Supplementary Tables 5, 6). Clusters S1 and S2 consist of Santorini stations whereas clusters K1 and K2 included all Kolumbo stations. Samples from the adjacent stations 70GC and 92GC within the active area of Kolumbo volcano were grouped together in K2 cluster, whereas samples from stations located at the northern part of Santorini caldera i.e., the 18GC, 19GC and 20GC formed a well-separated cluster (S2) from the rest Santorini samples (S1 cluster). The single sample P69GC-008 located at the southern part of Santorini caldera and the sample P96/2GC-009 of Kolumbo did not group with the rest samples.

3. Discussion

Microbial communities obtained from the hottest station 92GC are living at the thermophilic range (> 45°C) 1 meter below the seafloor and at the hyperthermophilic range (> 75°C) at the deepest layer. Close to the seafloor, microorganisms were found to be highly diverse represented by 38 bacterial and 6 archaeal phyla including Firmicutes, Chloroflexi, Bacteroidetes, Proteobacteria, Crenarchaeota (Ca. Bathyarchaeota) etc. At the deeper layer (i.e., 170 cm), microbial communities were composed of only Firmicutes, Proteobacteria and Acetothermia. Heatmap analysis grouped the sampling stations according to their geographical location and the hottest station 92GC was placed together with the adjacent thermophilic station 70GC (Figures 1, 5). It seems that this specific area within Kolumbo volcano create a distinct niche where well adapted microorganisms can thrive. In a previous comparative analysis of microbial diversity across temperature gradients, Podar

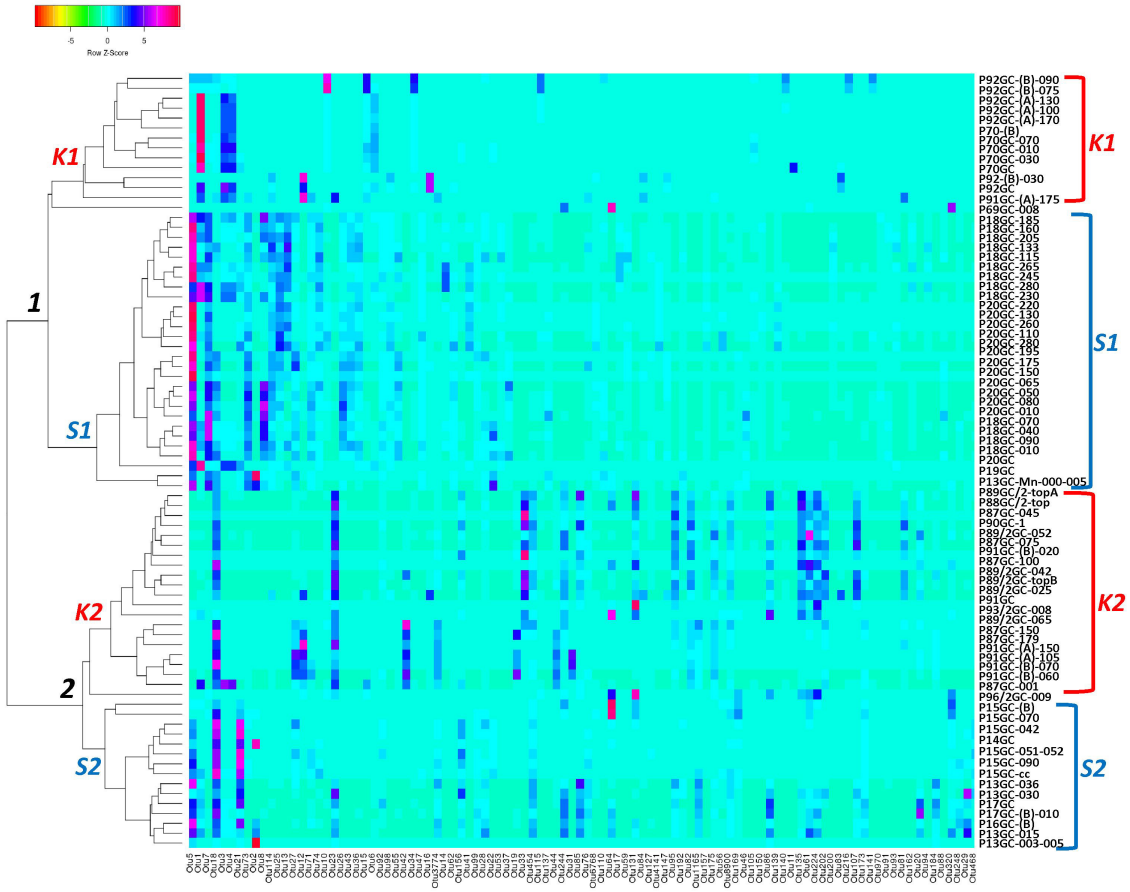

FIGURE 6
Occurrence of the major 100 OTUs clusters at 3% cutoff level (**Supplementary Table 6**). Cluster analysis was based on Spearman rank correlation. Color intensity signifies abundance ranging from orange (low abundance), to light blue (medium abundance) and to red (high abundance). Four clusters were formed: *K1* and *K2* (Kolumbo crater samples), *S1* and *S2* (Santorini caldera samples).

et al. (2020) have noticed that in the 67–80°C temperature range there are major shifts in the microbial communities where photosynthetic groups such as Chloroflexi, being replaced by various extreme thermophilic taxa such as Thermi, Aquificae and Crenarchaeota (Podar et al., 2020). In the case of Kolumbo station 92GC, microbial communities were dominated by members of the endospore-forming Firmicutes, Proteobacteria and Bacteroidetes compared to the rest low temperature stations where Chloroflexi was the prevailing phylum. The dominance of Firmicutes fits the Petro et al. (2017) hypothesis that microbial communities in subseafloor environments are driven by selection mechanisms which leave a subset of microbes from the surface to harbor favorable traits (Wörmer et al., 2019). Such traits include the formation of dormant, spore-like cells which permits microbes to face extreme environmental conditions such as intense heat and desiccation (Wörmer et al., 2019). Indeed, with a temperature at the deeper layers close to boiling point, station 92GC contains one of the most challenging environmental conditions and this is reflected on a unique microbial assembly. The dominance of spore forming cells in high temperature sediments is also confirmed by the Heuer et al. (2020) study in a subduction zone off the coast of Japan. Heuer et al. (2020) demonstrated that at temperatures above 45°C, bacterial endospores become more than 6,000 times more abundant than vegetative cells, whereas at temperatures > 100°C, acetate-degrading hyperthermophiles prevail.

Values of Chao1 and Shannon indices confirmed the high diversity of these ecosystems. Diversity values were in the same range between Santorini caldera and Kolumbo volcano sediment samples (Chao1: 70–1,567; **Figure 2** and **Table 1**). Chao1 values were lower compared to previous estimates for microbial mat samples obtained from the polymetallic chimneys of Kolumbo volcano (Chao1: 1,309–6,973; Christakis et al., 2018), and to deep-sea hydrothermal vents of the Southwest Indian Ridge (Chao 1: 1,000–4,000; Ding et al., 2017) and higher compared to Chao1 values from other geothermal sites (i.e., Tengchong Geothermal Field, China; Chao1: 3–21; Li et al., 2015). Interestingly, the minimum Chao1 and Shannon values were calculated at the deeper layers of the hottest stations 70GC and 92GC. These results confirm previous studies in other geothermal field sites such as the Tengchong Geothermal Field in China (Li et al., 2015) and Yellowstone hot springs (Podar et al., 2020) which demonstrated that microbial communities at high temperature seem to be substantially simpler than those at the lower temperature sites.

Regarding the diversity variations with depth, in most of the stations, the Chao1 values in the deeper layers were comparable to the surface sediment samples (**Figure 2** and **Table 1**). A recent study

on global taxonomic diversity of marine sedimentary communities by Hoshino et al. (2020), showed that bacterial and archaeal richness both generally decrease with increasing depth in anoxic sediment. However, such observation was not the case for the Santorini and Kolumbo sub-seafloor microbiome even for the close to anoxic condition samples. Generally, microbial diversity decrease with depth can be ascribed to the ongoing starvation that microbes face in an ecosystem gradually depleted of available energy sources (Wörmer et al., 2019). A possible explanation for the observed diversity values at the deeper sediment layers of the present study, is that the sub-seafloor microbial life may not suffer by food limitation. Previous studies have shown that both Santorini and Kolumbo environments are characterized by a unique availability of chemical energy provided by high concentrations of several compounds such as ferrous iron (Kilias et al., 2013; Christakis et al., 2018). This is probably the main driving force in maintaining the high diversity at the subsurface of these ecosystems. This is in accordance with previous estimates by Jørgensen and Marshall (2016) who have shown that the level of diversity in sub-seafloor sediments is approximately as high as in the surface ocean.

In addition to high phylogenetic diversity, the investigated area was found to host metabolically diverse microbes. Indeed, a core of genera was found for all sediment samples and the most abundant ones included *Bacillus*, *Thermoflexus*, and *Desulfatiglans*. We further examined the ecological roles of these genera and we found that metabolically diverse bacteria are inhabiting the seafloor and sub-seafloor sediments of both Santorini caldera and Kolumbo volcano. The most abundant *Bacillus* genus is known for its ability to survive in harsh environmental conditions and its metabolic versatility, whereas the second and third most abundant *Thermoflexus* and *Desulfatiglans* genera, also known for their difficulty to be isolated in lab conditions, are associated with chemoorganotrophy, protein degradation (Thomas et al., 2021), dissimilatory sulfate reduction and aromatic hydrocarbon degradation (Jochum et al., 2018). Indeed, microorganisms of the genus *Desulfatiglans* are dissimilatory sulfate reducers that can degrade aromatic hydrocarbons in marine sediments. Little is known regarding the ecophysiology of these microbes. However, their ability to grow by utilizing aromatic organic compounds may explain their occurrence in high abundances in marine subsurface sediments (Jochum et al., 2018).

In our investigation, we examined for the first time, microbial communities inhabiting the sub-seafloor of Santorini-Kolumbo volcanic system. We uncovered the presence of diverse microbiota in this system with unique adaptation strategies including resistant forms to withstand heat stresses (e.g., endospores). It is interesting to note that in our previous investigations (Mandalakis et al., 2019; Bravakos et al., 2021) we suggested that the high concentration of reductants in Kolumbo volcano (e.g., metal enrichment) may have provided selective pressure in microorganisms to maintain resistance mechanisms including those for antibiotic resistance. Given the high and unique diversity of the sub-seafloor, we are expecting that such mechanisms can be activated in the deeper sediment layers of this volcanic system. The exploration of the deep sub-seafloor through the International Ocean Discovery Program (Expedition 398 at the Hellenic Arc Volcanic Field), will allow us to learn more about the size and the factors that shape and limit life in the deep sub-seafloor of active volcanic systems, and to reveal novel factors about the evolution of life on Earth.

4. Materials and methods

4.1. Samples collection and physicochemical analysis

Gravity corers were collected during R/V POSEIDON cruise P510 that took place in March 2017. A short (3-m long) gravity corer was used to recover sediments samples. Cores were collected along the Kolumbo line in the area of hydrothermal venting in the Kolumbo crater, and throughout the North basin of the Santorini caldera. A total of 19 corers were collected and processed for microbial community analysis. Upon recovery, the first operation was removal of the core catcher and measurement of several parameters with a portable multi-parameter probe (Lange SenSion) in the sediment (i.e., pH, Eh) and at the bottom of each corer (i.e., pH, Eh and temperature). The core sections were split longitudinally using a hand-held, power disk-saw (Fein-Multimaster), opened in two halves and subsampled for microbiology. From 10 corers only the surface layer was aseptically collected, whereas 9 corers were sliced down to different layers. Immediately after corers slicing, samples for microbiology were stored at −20°C until further analysis in the laboratory. Probe temperature measurements were made with a standard multipenetration approach using a specially redesigned heat flow probe (Modell FIELAX GmbH, Bremerhaven) consisting of a 2-m stainless steel lance attached to a modified gravity corer. Each station consisted of multiple penetrations of 15 min each for temperature measurements (Hannington et al., 2018).

4.2. DNA extraction, amplification and sequencing

About 1 g of material from each sample was used to extract genomic DNA from microbial communities by using the MoBio UltraClean Soil DNA isolation kit (MoBio Laboratories, Carlsbad, CA, USA) with a slightly modified protocol by the manufacturer. More specifically, the bead-beating step was replaced by a tissue lyser for at least 30 min (frequency at 30 l/s; TissueLyser II, Qiagen, Germany). Concentrations of the extracted DNA were quantified using the NanoDrop ND-1000 UV-Vis spectrophotometer (NanoDrop Technologies, USA). Then, the hypervariable V4 region of the 16S rRNA gene was amplified using the universal primers 515f (5′- GTG CCA GCMGCC GCG GTA A-3′) and 806r (5′-GGA CTA CHV GGG TWT CTA AT-3′; 25) in a PCR reaction with the KAPA HiFi HotStart DNA polymerase (1 U μl-1) (KAPA Biosystems, USA) under the following conditions: initial denaturation at 95°C for 2 min, followed by 32 cycles of 98°C for 20 s (denaturation), primer annealing at 61°C for 10 s and extension at 72°C for 15 sec, with a final extension at 72°C for 5 min. An amount of 5 μl of the PCR products was used to check amplification and intensity of the bands on a 1.5% agarose gel whereas the remaining products were purified with AMPure XP magnetic beads (Perkin-Elmer, UK). PCR products were

quantified using Quant-iT PicoGreen dsDNA Assay and a TECAN Infinite F2000 Pro. The PCR negative control samples were also sequenced, in order to assess possible contamination during the library preparation. An equimolar pool of all samples was prepared and the final quantification was performed by qPCR (KAPA Library Quantification Kit—Illumina/Universal). The sequencing was performed at the premises of the Institute of Marine Biology, Biotechnology and Aquaculture (IMBBC) of HCMR in Heraklion of Crete using one run on an Illumina MiSeq with v3 chemistry for 2 × 280 cycles.

4.3. Data analysis

Analysis of the 16S rRNA MiSeq sequencing data was performed using the pipeline PEMA developed by IMBBC (Zafeiropoulos et al., 2020). In total, PEMA pipeline comprises 4 steps. The first one is the quality control and pre-processing of the Illumina sequencing reads using tools for the case of 16S rRNA genes such as FastQC (Andrews, 2019), Trimmomatic (Bolger et al., 2014), BayesHammer (Nikolenko et al., 2013), PANDAseq (Masella et al., 2012) and VSEARCH package (Rognes et al., 2016). The second step is the clustering of reads to operational taxonomic units (OTUs) using VSEARCH (Rognes et al., 2016). Singletons i.e., sequences with only 1 read, occurring after the (M)OTU clustering were removed from further analysis. In the third step, for the case of the 16S rRNA genes, the LCAClassifier algorithm of the CREST set of resources and tools (Lanzén et al., 2012) is used together with the Silva (Quast et al., 2013) database to assign taxonomy to the generated OTUs. In the fourth step, the PEMA's major output is an OTU table with the assigned taxonomies and the abundances of each taxon of every sample. OTUs were defined at the species level at 97% sequence similarity. Alpha diversity which is the analysis of species diversity in a single sample, including Chao1, Shannon–Weaver and the Simpson indices was also calculated. Venn diagrams were employed to identify the shared microbial communities among the samples using the EVenn online tool (Chen et al., 2021). Cluster analysis dendrogram and heatmap were created using the freely available web server heatmapper (heatmapper.ca; Babicki et al., 2016). Cluster analysis was based on Spearman rank correlation using the first 100 most abundant OTUs which accounted for 59, 72% of the total sequences. The produced raw tag data are available through NCBI's Sequence Read Archive under BioProject ID PRJNA898256.

Data availability statement

The datasets presented in this study can be found in online repositories. The names of the repository/repositories and accession number(s) can be found below: https://www.ncbi.nlm.nih.gov/genbank/, PRJNA898256.

Author contributions

PP, PN, MH, SP, SK, and AM contributed to the study design. TA, VP, EZ, and JK performed sample preparation and Illumina analysis. DL constructed the detailed bathymetry maps. PN, SW, VH, and SL collected the gravity corer samples and performed the temp/pH/Eh measurements on board the research vessel Poseidon. All authors contributed to data interpretation, article preparation, and approved the submitted version.

Funding

This study was supported by the project "SANTORini's seafloor volcanic observatorY" (SANTORY) [Hellenic Foundation for Research and Innovation (HFRI) Grant Number 185], by the project THIRA (funded by Municipality of Thira), by the project "New catalytic enzymes and enzymatic processes from the marine microbiome for refining marine seaweed biomass" (MARIKAT) (European Union's Horizon 2020 research and innovation programme under Grant Agreement 817992), by the project "Centre for the study and sustainable exploitation of Marine Biological Resources (CMBR)" (MIS 5002670), and the project "Managing and Analyzing Life Sciences Data (ELIXIR-GR)" (MIS 5002780). This research was supported in part through computational resources provided by the IMBBC (Institute of Marine Biology, Biotechnology and Aquaculture) of the HCMR. Funding for establishing the IMBBC HPC has been received by the MARBIGEN (EU Regpot) project, LifeWatchGreece RI and the CMBR (Centre for the study and sustainable exploitation of Marine Biological Resources) RI. Sampling was performed within the framework of the POSEIDON POS510 Expedition of GEOMAR-Helmholtz Centre for Ocean Research Kiel that took place from 06.03.2017-29.03.2017 in the Mediterranean Sea—Aegean Sea with the RV Poseidon.

Conflict of interest

The authors declare that the research was conducted in the absence of any commercial or financial relationships that could be construed as a potential conflict of interest.

Publisher's note

Supplementary material

The Supplementary Material for this article can be found online at: https://www.frontiersin.org/articles/10.3389/fmicb.2023.1188544/full#supplementary-material

References

Andrews, S. (2019). *FastQC*. Available online at: http://www.bioinformatics.babraham.ac.uk/projects/fastqc/ (accessed July 8, 2019).

Babicki, S., Arndt, D., Marcu, A., Liang, Y., Grant, J. R., Maciejewski, A., et al. (2016). Heatmapper: Web-enabled heat mapping for all. *Nucleic Acids Res.* 44, W147–W153.

Bolger, A. M., Lohse, M., and Usadel, B. (2014). Trimmomatic: A flexible trimmer for illumina sequence data. *Bioinformatics* 30, 2114–2120.

Bravakos, P., Mandalakis, M., Nomikou, P., Anastasiou, T. I., Kristoffersen, J. B., Stavroulaki, M., et al. (2021). Genomic adaptation of *Pseudomonas* strains to acidity and antibiotics in hydrothermal vents at Kolumbo submarine volcano, Greece. *Sci. Rep.* 11:1336. doi: 10.1038/s41598-020-79359-y

Brazelton, W. J., Ludwig, K. A., Sogin, M. L., Andreishcheva, E. N., Kelley, D. S., Shen, C.-C., et al. (2010). Archaea with surprising microdiversity show shifts in dominance over 1,000-year time scales in hydrothermal chimneys. *Proc. Natl. Acad. Sci. U. S. A.* 107, 1612–1617. doi: 10.1073/pnas.0905369107

Carey, S., Nomikou, P., Croff Bell, K., Lilley, M., Lupton, J., Roman, C., et al. (2013). CO_2 degassing from hydrothermal vents at Kolumbo submarine volcano, Greece, and the accumulation of acidic crater water. *Geology* 41, 1035–1038.

Chen, T., Zhang, H., Liu, Y., Liu, Y.-X., and Huang, L. (2021). EVenn: Easy to create repeatable and editable Venn diagrams and Venn networks online. *J. Genet. Genomics* 48, 863–866. doi: 10.1016/j.jgg.2021.07.007

Ding, J., Zhang, Y., Wang, H., Jian, H., Leng, H., and Xiao, X. (2017). Microbial community structure of deep-sea hydrothermal vents on the Ultraslow Spreading Southwest Indian Ridge. *Front. Microbiol.* 8:1012.

Christakis, C. A., Polymenakou, P. N., Mandalakis, M., Nomikou, P., Kristoffersen, J. B., Lampridou, D., et al. (2018). Microbial community differentiation between active and inactive sulfide chimneys of the Kolumbo submarine volcano, Hellenic Volcanic Arc. *Extremophiles* 22, 13–27.

Hannington, M. D., Petersen, S., Nomikou, P., Wind, S., Heinath, V., Large, S., et al. (2018). RV POSEIDON Faghrtbericht/Cruise Report POS510. ANYDROS: Rifting and hydrothermal activity in the Cyclades back-arc basin. *GEOMAR Helmhotz-Zentrum Ozeanforschung Kiel* 43, 2193–8113. doi: 10.3289/GEOMAR_REP_NS_43_2018

Heuer, V. B., Inagaki, F., Morono, Y., Kubo, Y., Spivack, A. J., Viehweger, B., et al. (2020). Temperature limits to deep subseafloor life in the Nankai Trough subduction zone. *Science* 370, 1230–1234.

Hoshino, T., Doi, H., Uramoto, G.-I., Wörmer, L., Adhikari, R. R., Xiao, N., et al. (2020). Global diversity of microbial communities in marine sediments. *Proc. Natl Acad. Sci. U. S. A.* 117, 27587–27597.

Ivarsson, M., Broman, C., Sturkell, E., Ormö, J., Siljeström, S., van Zuilen, M., et al. (2013). Fungal colonization of an Ordovician impact-induced hydrothermal system. *Sci. Rep.* 3:3487. doi: 10.1038/srep03487

Jochum, L. M., Schreiber, L., Marshall, I. P. G., Jørgensen, B. B., Schramm, A., and Kjedsen, K. U. (2018). Single-cell genomics reveals a diverse metabolic potential of uncultivated Desulfatiglans-related Deltaproteobacteria widely distributed in marine sediment. *Front. Microbiol.* 9:2038. doi: 10.3389/fmicb.2018.02038

Jørgensen, B. B., and Marshall, I. P. G. (2016). Slow microbial life in the seabed. *Annu. Rev. Mar. Sci.* 8, 5.1–5.22.

Kallmeyer, J., Pockalny, R., Adhikari, R. R., Smith, D. C., and D'hondt, S. (2012). Global distribution of microbial abundance and biomass in subseafloor sediment. *Proc. Natl. Acad. Sci. U. S. A.* 109, 16213–16216.

Kilias, S. P., Nomikou, P., Papanikolaou, D., Polymenakou, P. N., Godelitsas, A., Argyraki, A., et al. (2013). New insights into hydrothermal vent processes in the unique shallow-submarine arc-volcano Kolumbo (Santorini). Greece. *Sci. Rep.* 3:2421. doi: 10.1038/srep02421

Lagostina, L., Frandsen, S., MacGregor, B. J., Glombitza, C., Deng, L., Fiskal, A., et al. (2021). Interactions between temperature and energy supply drive microbial communities in hydrothermal sediment. *Commun. Biol.* 4, 1–14. doi: 10.1038/s42003-021-02507-1

Lanzén, A., Jørgensen, S. L., Huson, D. H., Gorfer, M., Grindhaug, S. H., Jonassen, I., et al. (2012). CREST–Classification resources for environmental sequence tags. *PLoS One* 7:e49334. doi: 10.1371/journal.pone.0049334

LaRowe, D. E., Burwicz, E., Arndt, S., Dale, A. W., and Amend, J. P. (2017). The temperature and volume of global marine sediments. *Geology* 45, 275–278.

Le Pichon, X., and Angelier, J. (1979). The Hellenic Arc and Trench system: A key to the neotectonic evolution of the Eastern Mediterranean area. *Tectonophysics* 60, 1–42.

Li, H., Yang, Q., Li, J., Gao, H., Li, P., and Zhou, H. (2015). The impact of temperature on microbial diversity and AOA activity in the Tengchong Geothermal Field, China. *Sci. Rep.* 5:17056. doi: 10.1038/srep17056

Mandalakis, M., Gavriilidou, A., Polymenakou, P. N., Christakis, C. A., Nomikou, P., Medvecki, et al. (2019). Microbial strains isolated from CO_2-venting Kolumbo submarine volcano show enhanced co-tolerance to acidity and antibiotics. *Mar. Environ. Res.* 144, 102–110. doi: 10.1016/j.marenvres.2019.01.002

Masella, A. P., Bartram, A. K., Truszkowski, J. M., Brown, D. G., and Neufeld, J. D. (2012). PANDAseq: paired-end assembler for illumine sequences. *BMC Bioinform.* 13:31. doi: 10.1186/1471-2105-13-31

Nikolenko, S. I., Korobeynikov, A. I., and Alekseyev, M. A. (2013). BayesHammer: Bayesian clustering for error correction in single-cell sequencing. *BMC Genom.* 14:S7. doi: 10.1186/1471-2164-14-S1-S7

Nomikou, P., Carey, S., Papanikolaou, D., Croff Bell, K., Sakellariou, D., Alexandri, S., et al. (2012). Submarine volcanoes of the Kolumbo volcanic zone NE of Santorini caldera, Greece. *Glob. Planet. Change* 90, 135–151.

Orcutt, B., Sylvan, J. B., Knab, N. J., and Edwards, K. J. (2011). Microbial ecology of the dark ocean above, at, and below the seafloor. *Microbiol. Mol. Biol. Rev.* 75, 361–422. doi: 10.1128/MMBR.00039-10

Oren, A., and Garrity, G. M. (2021). Valid publication of the names of forty-two phyla of prokaryotes. *Int. J. Syst. Evol. Microbiol.* 71:005056. doi: 10.1099/ijsem.0.005056

Oulas, A., Polymenakou, P. N., Seshadri, R., Tripp, H. J., Mandalakis, M., Paez-Espino, A. D., et al. (2016). Metagenomic investigation of the geologically unique Hellenic Volcanic Arc reveals a distinctive ecosystem with unexpected physiology. *Environ. Microbiol.* 18, 1122–1136. doi: 10.1111/1462-2920.13095

Petro, C., Starnawski, P., Schramm, A., and Kjeldsen, K. U. (2017). Microbial community assembly in marine sediments. *Aquat. Microb. Ecol.* 79, 177–195.

Pikuta, E. V., Hoover, R. B., and Tang, J. (2007). Microbial extremophiles at the limits of life. *Crit. Rev. Microbiol.* 33, 183–209.

Podar, P. T., Yang, Z., Björnsodóttir, S. H., and Podar, M. (2020). Comparative analysis of microbial diversity across temperature gradients in hot springs from Yellowstone and Iceland. *Front. Microbiol.* 11:1625. doi: 10.3389/fmicb.2020.01625

Quast, C., Pruesse, E., Yilmaz, P., Gerken, J., Schweer, T., Yarza, P., et al. (2013). The SILVA ribosomal RNA gene database project: improved data processing and webbased tools. *Nucleic Acids Res.* 41, D590–D596. doi: 10.1093/nar/gks1219

Rizzo, A. L., Caracausi, A., Chavagnac, V., Nomikou, P., Polymenakou, P. N., Mandalakis, M., et al. (2016). Kolumbo submarine volcano (Greece): an active window into the Aegean subduction system. *Sci. Rep.* 6:28013. doi: 10.1038/srep28013

Rognes, T., Flouri, T., Nichols, B., Quince, C., and Mahé, F. (2016). VSEARCH: a versatile open source tool for metagenomics. *PeerJ* 4:e2584. doi: 10.7717/peerj.2584

Salter, S. J., Cox, M. J., Turek, E. M., Calus, S. T., Cookson, W. O., Moffatt, M. F., et al. (2014). Reagent and laboratory contamination can critically impact sequence-based microbiome analyses. *BMC Biol.* 12:87. doi: 10.1186/s12915-014-0087-z

Schloss, R. D. (2021). Amplicon sequence variants artificially split bacterial genomes into separate clusters. *mSphere* 6:e00191-21. doi: 10.1128/mSphere.00191-21

Sheik, C. S., Reese, B. K., Twing, K. I., Sylvan, J. B., Grim, S. L., Schrenk, M. O., et al. (2018). Identification and removal of contaminant sequences from ribosomal gene databases: lessons from the Census of Deep Life. *Front. Microbiol.* 9:840. doi: 10.3389/fmicb.2018.00840

Takai, K., Gamo, T., Tsunogai, U., Nakayama, N., Hirayama, H., Nealson, K. H., et al. (2004). Geochemical and microbiological evidence for a hydrogen-based, hyperthermophilic subsurface lithoautotrophic microbial ecosystem (HyperSLiME) beneath an active deep-sea hydrothermal field. *Extremophiles* 8, 269–282. doi: 10.1007/s00792-004-0386-3

Takai, K., Nakagawa, S., Reysenbach, A. L., and Hoek, J. (2006). Microbial ecology of midocean ridges and back-arc basins. *Geophys. Monogr. Ser.* 166, 185–213.

Takai, K., Nakamura, K., Toki, T., Tsunogai, U., Miyazaki, M., Miyazaki, J., et al. (2008). Cell proliferation at 122°C and isotopically heavy CH_4 production by a hyperthermophilic methanogen under high-pressure cultivation. *Proc. Natl Acad. Sci. U. S. A.* 105, 10949–10954. doi: 10.1073/pnas.0712334105

Thomas, S. C., Payne, D., Tamadonfar, K. O., Seymour, C. O., Jio, J.-Y., Murugapiran, S. K., et al. (2021). Genomics, exometabolomics, and metabolic probing reveal conserved proteolytic metabolism of *Thermoflexus hugenholtzii* and three candidate species from China and Japan. *Front. Microbiol.* 12:632731. doi: 10.3389/fmicb.2021.632731

Valentine, D. L. (2007). Adaptations to energy stress dictate the ecology and evolution of the Archaea. *Nat. Rev. Microbiol.* 5, 316–323. doi: 10.1038/nrmicro1619

Waite, D. W., Vanwonterghem, I., Rinke, C., Parks, D. H., Zhang, Y., Takai, K., et al. (2017). Comparative genomic analysis of the class Epsilonproteobacteria and proposed reclassification to Epsilonbacteraeota (phyl. nov.). *Front. Microbiol.* 8:682. doi: 10.3389/fmicb.2017.00682

Wörmer, L., Hoshino, T., Bowles, M. W., Viehweger, B., Adhikari, R. R., Xiao, N., et al. (2019). Microbial dormancy in the marine subsurface: global endospore abundance and response to burial. *Sci. Adv.* 5:eaav1024. doi: 10.1126/sciadv.aav1024

Zafeiropoulos, H., Viet, H. Q., Vasileiadou, K., Potirakis, A., Arvanitidis, C., Topalis, P., et al. (2020). PEMA: a flexible pipeline for environmental DNA metabarcoding analysis of the 16S/18S ribosomal RNA, ITS, and COI marker genes. *Gigascience* 9, 1–12.

Zhou, Z., Pan, J., Wang, F., Gu, J.-D., and Li, M. (2018). Bathyarchaeota: globally distributed metabolic generalists in anoxic environments. *FEMS Microbiol. Rev.* 42, 639–655. doi: 10.1093/femsre/fuy023

frontiers | Frontiers in Microbiology

TYPE Original Research
PUBLISHED 24 July 2023
DOI 10.3389/fmicb.2023.1203216

OPEN ACCESS

EDITED BY
Melina Kerou,
University of Vienna, Austria

REVIEWED BY
Byron J. Adams,
Brigham Young University, United States
Jesse Jorna,
Brigham Young University,
United States in collaboration with reviewer BA
Paraskevi Polymenakou,
Hellenic Centre for Marine Research (HCMR), Greece
Lyle Whyte,
McGill University, Canada

*CORRESPONDENCE
Don A. Cowan
✉ don.cowan@up.ac.za

RECEIVED 10 April 2023
ACCEPTED 23 June 2023
PUBLISHED 24 July 2023

CITATION
Mashamaite L, Lebre PH, Varliero G, Maphosa S, Ortiz M, Hogg ID and Cowan DA (2023) Microbial diversity in Antarctic Dry Valley soils across an altitudinal gradient.
Front. Microbiol. 14:1203216.
doi: 10.3389/fmicb.2023.1203216

Microbial diversity in Antarctic Dry Valley soils across an altitudinal gradient

Lefentse Mashamaite[1], Pedro H. Lebre[1], Gilda Varliero[1,2], Silindile Maphosa[1], Max Ortiz[1,3], Ian D. Hogg[1,4,5] and Don A. Cowan[1]*

[1]Department of Biochemistry, Genetics and Microbiology, Centre for Microbial Ecology and Genomics, University of Pretoria, Pretoria, South Africa, [2]Rhizosphere Processes Group, Swiss Federal Research Institute WSL, Birmensdorf, Switzerland, [3]Clemson University Genomics & Bioinformatics Facility, Clemson University, Clemson, SC, United States, [4]School of Science, University of Waikato, Hamilton, New Zealand, [5]Canadian High Arctic Research Station, Polar Knowledge Canada, Cambridge Bay, NU, Canada

Introduction: The Antarctic McMurdo Dry Valleys are geologically diverse, encompassing a wide variety of soil habitats. These environments are largely dominated by microorganisms, which drive the ecosystem services of the region. While altitude is a well-established driver of eukaryotic biodiversity in these Antarctic ice-free areas (and many non-Antarctic environments), little is known of the relationship between altitude and microbial community structure and functionality in continental Antarctica.

Methods: We analysed prokaryotic and lower eukaryotic diversity from soil samples across a 684 m altitudinal transect in the lower Taylor Valley, Antarctica and performed a phylogenic characterization of soil microbial communities using short-read sequencing of the 16S rRNA and ITS marker gene amplicons.

Results and Discussion: Phylogenetic analysis showed clear altitudinal trends in soil microbial composition and structure. Cyanobacteria were more prevalent in higher altitude samples, while the highly stress resistant Chloroflexota and Deinococcota were more prevalent in lower altitude samples. We also detected a shift from Basidiomycota to Chytridiomycota with increasing altitude. Several genera associated with trace gas chemotrophy, including *Rubrobacter* and *Ornithinicoccus*, were widely distributed across the entire transect, suggesting that trace-gas chemotrophy may be an important trophic strategy for microbial survival in oligotrophic environments. The ratio of trace-gas chemotrophs to photoautotrophs was significantly higher in lower altitude samples. Co-occurrence network analysis of prokaryotic communities showed some significant differences in connectivity within the communities from different altitudinal zones, with cyanobacterial and trace-gas chemotrophy-associated taxa being identified as potential keystone taxa for soil communities at higher altitudes. By contrast, the prokaryotic network at low altitudes was dominated by heterotrophic keystone taxa, thus suggesting a clear trophic distinction between soil prokaryotic communities at different altitudes. Based on these results, we conclude that altitude is an important driver of microbial ecology in Antarctic ice-free soil habitats.

KEYWORDS

Antarctic microbiology, McMurdo Dry Valleys, edaphic habitats, microbial diversity, altitudinal gradients

1. Introduction

The Antarctic McMurdo Dry Valleys, encompassing an area of some 4,800 km^2 and representing approximately 95% of the ice-free non-maritime land of the continent, have been the primary target for studies of Antarctic terrestrial soil microbiology for the past half-century (Freckman and Virginia, 1998; Virginia and Wall, 1999; Babalola et al., 2009; Cary et al., 2010; Lee et al., 2012; Schwartz et al., 2014). The Dry Valleys are geologically and edaphically diverse (Bockheim, 2002; Bockheim and McLeod, 2008), and comprise a wide variety of soil habitats such as exposed mineral soils and gravels (Cowan et al., 2002, 2010), desert pavements (Delpupo et al., 2017), transiently wetted sediments (Niederberger et al., 2015), crypto- (Goordial et al., 2017; Rego et al., 2019), endo- (Walker and pace, 2007) and chasmo-lithic niches (Pointing et al., 2009) and various "plant"-associated habitats such as moss beds, cyanobacterial mats, and crustose lichens (Pannewitz et al., 2003; Green et al., 2012; Power et al., 2020).

All terrestrial Antarctic habitats are subject to a variety of 'extreme' abiotic factors, including extreme cold, long periods with little or no light, extreme desiccation, extreme oligotrophy and physical disturbance (Vincent, 2004; Adriaenssens et al., 2017). It is widely assumed that exposure to these conditions over very long time periods will have shaped uniquely structured and adapted soil microbial communities.

Early studies, using culture-dependent methods, identified a range of cosmopolitan genera, many from the Firmicutes and Actinobacteria phyla (Friedmann and Thistle, 1993), although subsequent culturing studies have identified numerous polar-specific species (Cowan and Tow, 2004; Aislabie et al., 2006; Bottos et al., 2014; Lambrechts et al., 2019). With the advent of molecular phylogenetic methods, it was rapidly appreciated that Dry Valley soils and other terrestrial niches harboured a wide diversity of prokaryotic phylotypes (Cary et al., 2010; Lee et al., 2012; Koo et al., 2018) many of which remain uncultured.

In the absence of higher plants, trophic structures in continental Antarctic soils are largely driven by cyanobacterial photoautotrophy (Kirby et al., 2011; Makhalanyane et al., 2015; Van Goethem and Cowan, 2019), particularly in cryptic endolithic (Rego et al., 2019; Mezzasoma et al., 2022) and hypolithic (Makhalanyane et al., 2013; De los Ríos et al., 2014; Wei et al., 2016) niches. Chlorophytes, particularly microalgae, are present, although their contribution to carbon input to soil microbial communities is unknown. The recent discovery that the microbial oxidation of atmospheric trace gases, specifically H_2 and CO, can provide sufficient energy to support soil microbial communities (Ji et al., 2017) offers a new trophic paradigm. The capacity for this autotrophic metabolism is much more physically and phylogenetically widespread than originally thought (Ji et al., 2017), and Dry Valley soils have been shown to actively assimilate atmospheric hydrogen (Ortiz et al., 2021).

Landscape-scale phylogenetic studies have clearly shown that microbial communities in Dry Valley soils are far from homogeneous (Lee et al., 2012; Stomeo et al., 2012; Bottos et al., 2020), and that the drivers of microbial community composition are complex (Lee et al., 2012). A variety of abiotic factors, including altitude, temperature and soil nutrient status (Aislabie et al., 2006; Cowan et al., 2010; Stomeo et al., 2012; Adriaenssens et al., 2017; Bottos et al., 2020) have been implicated in microbial community assembly. While yet poorly understood, it is likely that biotic factors (particularly inter-species interactions) are also significant drivers of community structure (Hogg et al., 2006; Lee et al., 2012), and soil viruses and bacteriophages (Zablocki et al., 2014; Adriaenssens et al., 2017) may be important factors in microbial community dynamics.

Water availability in edaphic niches, a complex function of precipitation regimes, temperature and atmospheric humidity, is thought to be a key determinant of both microbial diversity and microbial functionality (Goordial et al., 2016). Altitude plays an important role in soil water availability and is implicated in microbial community composition (Lee et al., 2012; Coleine et al., 2019). Higher atmospheric relative humidities and more frequent cloud cover at high altitudes increase surface water availability, and together are probably responsible for the altitudinal distribution of crustose lichens such as *Buellia* species (Cowan et al., 2011). However, the lower mean temperatures at higher altitudes directly impact the availability of liquid water. A series of studies in the 1,677 m a.s.l. University Valley (McKay, 2009; Goordial et al., 2017) have shown that, where mean temperatures are consistently too low to melt shallow ground ice (Marinova et al., 2022), the limited availability of liquid water is a major constraint on microbial diversity (Goordial et al., 2016) and functionality (Goordial et al., 2017).

To address the effects of altitude on microbial community structure, here we assessed microbial diversity from a series of samples taken across a 684 m altitudinal gradient in the lower Taylor Valley, McMurdo Dry Valleys, Antarctica. In this study, we hypothesize that the soil microbial diversity and functional potential will significantly shift across the altitudinal transect, due to shifts in abiotic variables such as soil chemistry, temperature and water availability.

2. Materials and methods

2.1. Sample collection

Surface (0–5 cm depth) mineral soil samples were recovered from GPS-located sites at 50 m altitudinal intervals along a *ca.* 5.2 km transect (from 0 m a.s.l. to 684 m a.s.l.) in the New Harbour area (Lower Taylor Valley, McMurdo Dry Valleys, East Antarctica) in January 2018 (Figure 1 and Supplementary Table S1). At each location, four *ca.* 200 g soil samples from sites spaced horizontally 10 m apart were recovered into sterile Whirlpaks®, where each sample was a composite of four ca. 50 g sub-samples recovered from the corners of a 1 m^2 quadrat. All samples were retained at <0°C, transported on ice to Scott Base, Ross Island for storage at −20°C, and subsequently transported on dry ice via Christchurch, NZ to the University of Pretoria, Pretoria, South Africa where they were stored at −80°C prior to processing.

2.2. Soil analysis

For the soil chemistry analyses, four composite samples from each site were pooled together to generate one representative sample per site. The resulting 10 samples were analysed for geochemistry (Supplementary Table S2), including: soil pH, soil organic matter (% SOM), nitrate-nitrogen (NO_3-N), ammonia-nitrogen (NH_4-N) and total carbon (% C). Soil texture was also measured for % sand, % clay

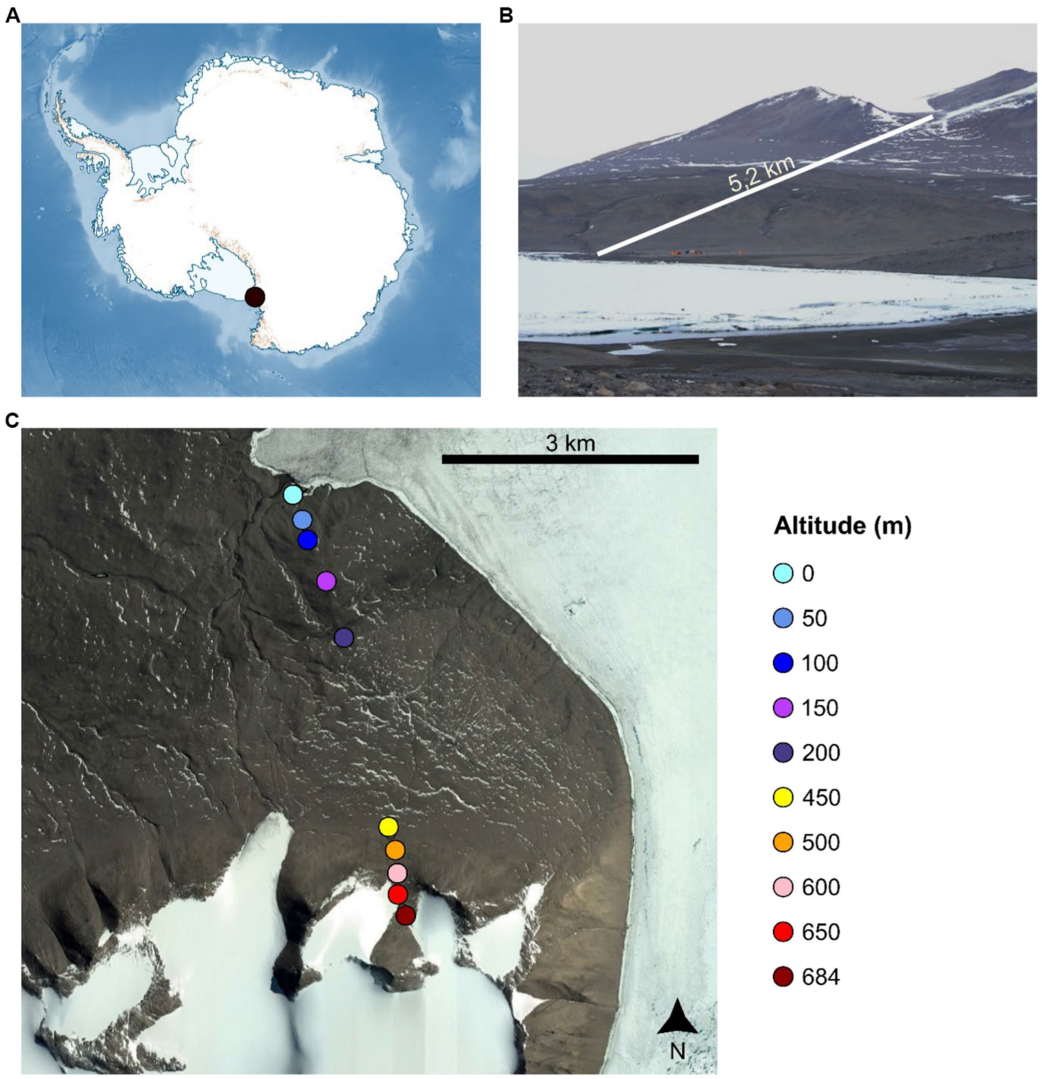

FIGURE 1
Sample location in the Antarctic continent **(A)**, and along the sampling transect in the New Harbour area (Lower Taylor Valley, McMurdo Dry Valleys, East Antarctica) **(B,C)**.

and % silt. Elemental analysis included K, Na, Ca, Mg, Fe, Mn, Cu, Zn, B, P and Al. All analyses were performed by NviroTek Laboratories (Hartbeespoort, South Africa).

2.3. DNA extraction and sequencing

DNA from the 40 samples collected from the 10 sites along the altitude gradient was extracted using DNeasy PowerSoil kits (QIAGEN, United States). DNA extraction followed the manufacturer's instructions excepting for these modifications: 1.5 g of soil was weighed and added to the glass bead tubes for each sample; soil samples were homogenised with the PowerLyzer 24 Bench Top Bead-Based Homogenizer (QIAGEN, United States) at 4000 rpm for 1 min following the addition of solution C1. DNA quality and quantity were assessed using a NanoDrop 2000 spectrophotometer (ThermoFisher, United States) and 1% agarose gel electrophoresis. Samples were sent to Admera Biosciences (United States) for amplification and sequencing of the V3–V4 regions of the 16S rRNA gene with standard Illumina 16S primers 341F (CCTACGGGNGGCWGCAG) and 805R (GACTACHVGGGTATCTAATCC) (Herlemann et al., 2011). Similarly, for Fungi, the ITS1 and ITS4 regions were amplified using the following ITS primers; ITS1F (CTTGGTCATTTAGAGGAAGTAA) and ITS4 (TCCTCCGCTTATTGATATGC) (White et al., 1990; Gardes and Bruns, 1993). Sequencing was performed using an Illumina MiSeq instrument with 300 bp paired-end reads. Raw sequences were deposited in the European Nucleotide Archive under the accession PRJEB55870.

2.4. Bioinformatics and statistical analysis

Illumina adapters were removed from all 16S rRNA gene and ITS reads using trimmomatic v 0.39 (Bolger et al., 2014). Raw reads were processed in the R environment (version 4.2.2) (R Core Team, 2022) using the R library dada2 v 1.22 (Callahan et al., 2016). For the 16S

rRNA gene dataset, forward and reverse reads were first quality filtered, true sequence variants were then identified in each sample, forward and reverse reads were merged into amplicon sequence variants (ASVs), and chimeric ASVs were removed. For ITS amplicons, only forward reads were used due to poor sequence quality of the reverse reads and the lack of overlap between forward and reverse reads. The ITS forward reads were treated using the same pipeline as for the 16S rRNA genes except the merging step which was not performed. Subsequently, sequences were taxonomically classified using the SILVA ribosomal RNA gene database v 138 (Quast et al., 2012) and UNITE reference database v 9.0 (Nilsson et al., 2019) for the 16S rRNA gene and ITS datasets, respectively. The number of reads in each sample is reported in Supplementary Table S3.

The ASV and taxonomy tables obtained from the dada2 pipeline were imported and analysed using phyloseq (McMurdie and Holmes, 2013). For the 16S rRNA gene dataset, only ASVs assigned to Bacteria and Archaea were retained, with the removal of ASVs assigned to mitochondria or chloroplasts. For the ITS dataset, only ASVs assigned to Fungi were retained. Only samples represented by at least 5,000 reads were retained. The dataset was then normalised using the R library SRS (Beule and Karlovsky, 2020) using the number of reads present in the smallest sample as cut-off (8,784 for 16S rRNA genes and 6,513 for the ITS dataset) (Supplementary Figure S1).

Alpha diversity was calculated using the R package vegan (Oksanen et al., 2022). Beta diversity was analysed using Bray–Curtis dissimilarity matrices obtained from the Hellinger transformed 16S rRNA gene and ITS datasets. This analysis was done by Principal Coordinates Analysis (PCoA), using ape package (Paradis and Schliep, 2019), and by performing a Permutational Multivariate Analyses of Variance (PERMANOVA) using vegan package (Oksanen et al., 2022). Plots were created using ggplot2 (Wickham et al., 2016).

Correlations between relative abundance for each phylum and altitude were calculated using the function cor.test() and then adjusting the *p* value using the False Discovery Rate (FDR) method (Benjamini and Hochberg, 1995).

The distribution of climatic and soil chemistry variables across different sites was calculated on log-standardized data using the "prcomp" function of the Vegan package, which performs a principal component analysis of the data (PCA) (Venables and Ripley, 2002). The resulting distance matrix between samples was plotted in a PCA graph, with the projected direction and magnitude of the distribution for each variable plotted in a separate loading plot. To compare samples with respect to differences in geochemical parameters, samples collected from sites between 0 and 200 m altitude are defined as "low altitude," and those collected from sites between 450 and 684 m are defined as "high altitude" (Supplementary Table S1). The significance of the differences in geochemical variables between these two groups was calculated using PERMANOVA, with 999 permutations. Significant differences in geochemical variables between the two altitudinal groups was calculated using the Wilcoxon Rank Sum test (Wilcoxon, 1945) in the stats (version 3.6.2) package (Ripley, 2001). Significant correlations between the soil geochemical parameters and the microbial Bray-Curtis distribution across samples were estimated using the envfit() function of the Vegan package. In order for the number of samples to correspond between the microbial abundance data and soil chemistry data, ASV counts were averaged for each site. The soil chemistry variables were also tested for collinearity prior to running envfit by using the vif() function from the car (version 3.0.11) package (Fox and Weisberg, 2019), with vif values above 10 being removed.

Significant differences in relative abundances of taxa at genus-level between low and high altitude groups was inferred using ANCOMBC 1.2.2 (Lin and Peddada, 2020). ASVs were clustered into genera and absolute counts were transformed to relative abundances using the tax_glom() and transform_sample_couts() functions of the Phyloseq package, respectively. ANCOMBC ran with 1,000 max iterations, a zero_cut of 0.90, and an alpha score of 0.05. The "FDR" method was chosen for the value of p adjustments. The results were subsequently plotted as heatmaps using the pheatmap package (Kolde, 2019). As the relative abundance of different ASVs can differ by orders of magnitude, each ASV abundance was scaled individually to aid in visualising changes in ASV abundance between clusters.

Co-occurrence network analysis of prokaryotic taxa in samples belonging to the two altitudinal groups was performed using the SPIEC-EASI package (Kurtz et al., 2015), which allows for the differentiation of direct and indirect associations between taxa, and therefore minimizes the detection of spurious correlations. To further decrease network complexity and minimize spurious connections, ASVs were clustered at genus level and only taxa that were present in five or more samples within each group were considered for the analysis. The resulting networks were loaded into Gephi (v 0.92) (Bastian et al., 2009), which was used to calculate the topological features of the networks. "Hubs" were defined at the top five taxa with the highest number of connections (degrees) and highest influence on the network (betweenness centrality). To infer the importance of trace gas chemotrophs (TGCs) and phototrophs to the interactions with the soil microbial communities of the sample sites, these were manually assigned to ASVs based on their genus level taxonomy. To identify potential TGCs within our dataset, a list of genera that have been shown to have the capability to perform hydrogen oxidation was compiled from previous studies (Supplementary Table S5) (Ortiz et al., 2021; Ray et al., 2022). All ASVs belonging to the classes *Cyanobacteriia* and *Chloroflexia* were considered phototrophic. Nodes in the co-occurrence networks were coloured according to this manual annotation of the taxa regarding their trophic status. The ratio of TGCs/Phototrophs was calculated using the summed relative abundances (per sample) of taxa that were classified in the two trophic groups. The significance of the difference in trace-gas scavengers (TGC)/Phototrophs ratio between low and high altitude samples was calculated using the Wilcoxon Rank-Sum test.

3. Results

3.1. Alpha and beta diversity

Bacterial richness ranged from 240 and 1,654 in all samples (Figure 2A), whereas Shannon indices ranged from 5.1 and 7.1 (Figure 2C). Richness ($F = 0.417$, $p = 0.916$) and Shannon index ($F = 0.343$, $p = 0.953$) did not significantly differ across different altitudes for the bacterial dataset. Richness ranged from 71 to 603, and 1.1 and 5.2 for the fungal dataset (Figures 2B,D). For fungal richness, higher diversity was observed for samples at 150, 200 and 450 meters where the average richness was 430, 344, and 387, respectively. Fungal richness significantly differed for the fungal dataset ($F = 2.373$, $p = 0.39$) but not for the Shannon index ($F = 1.013$, $p = 0.453$).

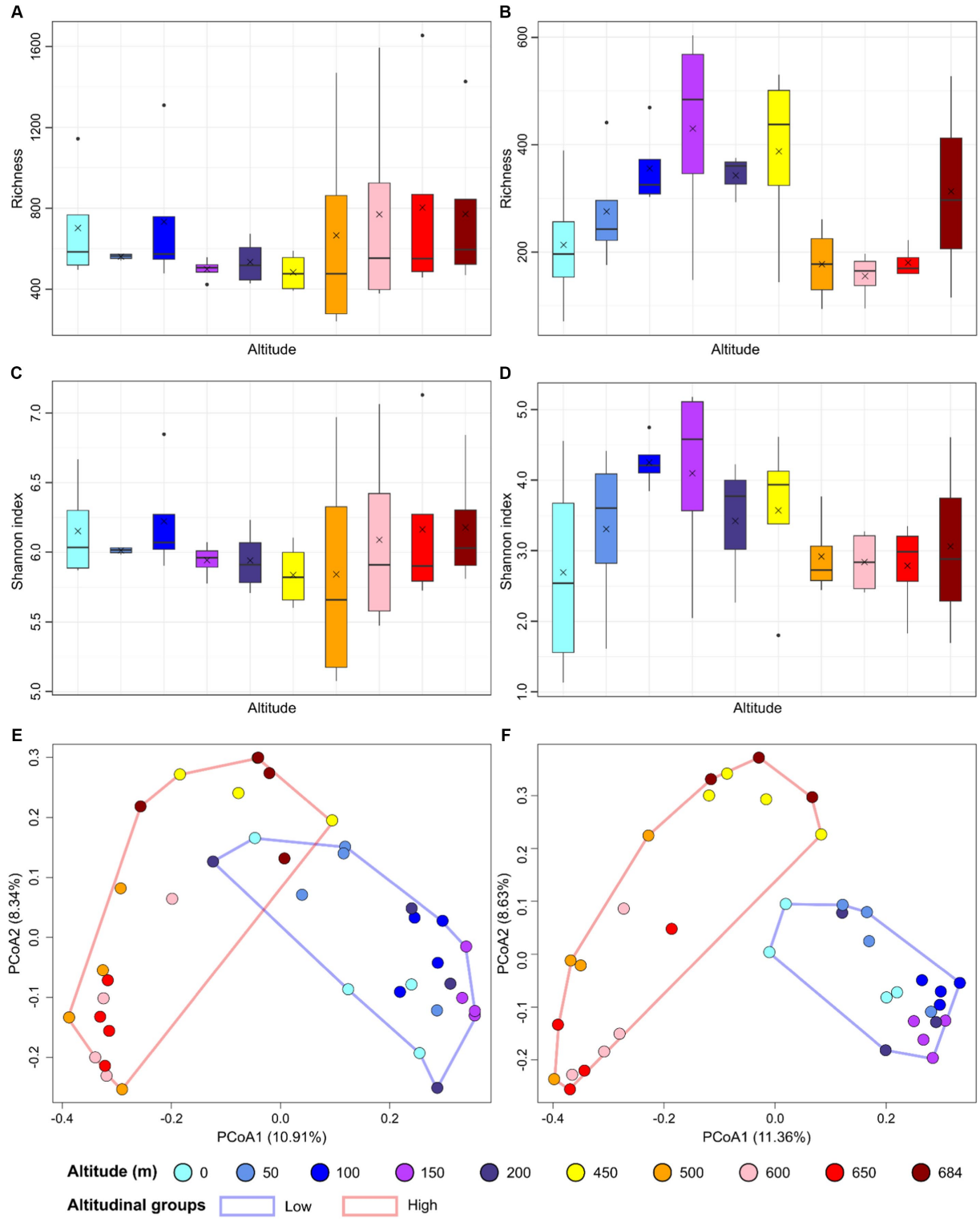

FIGURE 2
Alpha and beta diversity are represented as barplots reporting richness for bacterial **(A)** and fungal dataset **(B)**, and Shannon index for bacterial **(C)** and fungal dataset **(D)**, and principal coordinate analysis (PCoA) performed on the Hellinger-transformed ASV dataset for bacteria **(E)** and fungi **(F)**. In the boxplots, the median values are indicated with an horizontal line and the mean values with a cross for each altitude group.

The differences in community structure between samples was investigated using the Bray-Curtis distance index and Principal coordinate analysis (PCoA). Samples from the lower parts of the transect (0–200 m) formed a cluster differentiating from samples collected at higher altitudes (450–650 m) for both the prokaryotic and fungal datasets (Figures 2E,F). PERMANOVA showed an R^2 of 0.1238

($p = 0.0009$) for the bacterial dataset, and an R^2 of 0.1112 ($p = 0.0009$) for the fungal dataset.

3.2. Microbial community composition across the altitudinal transect

A total of 26 bacterial phyla was identified across the sample set, whereas no archaeal phyla were identified. The dominant community (i.e., phyla present with a relative abundance higher than 1% in at least 10% of samples) was composed of 12 phyla. Actinobacteria was the most dominant bacterial phylum across all the samples in the transect (13.9%–59.8%) representing 42.1% of the entire bacterial dataset, followed by Chloroflexota (12.0%), Pseudomonadota (previously Proteobacteria) (9.2%), Bacteroidota (7.2%), Acidobacteriota (6.8%), Plactomycetota (4.9%), Cyanobacteria (4.25%), Gemmatimonadota (4.1%), Deinococcota (3.8%), Verrucomicrobiota (3.0%), Patescibacteria (0.9%), and Abditibacteriota (0.5%) (Figure 3A). Five dominant phyla (Acidobacteriota, Cyanobacteria, Patescibacteria, Pseudomonadota and Verrucomicrobiota) had significant ($p < 0.05$) higher abundance in high altitude samples, whereas four dominant phyla (Actinobacteria, Chloroflexi, Deinococcota, and Gemmatimonadota) showed higher abundance in low altitude samples (Table 1). Bdellovibrionota, Elusimicrobiota, Myxococcota, Nitrospirota and SAR324 were not classified as dominant phyla but showed significant correlations between their relative abundance and altitude (Table 1). Organisms belonging to WPS-2 were present in only six samples of the dataset, with abundances ranging between 0.0% and 0.2%.

A total of nine fungal phyla were identified in the dataset. The fungal community was dominated by ASVs unclassified at the phylum-level (38.9%) (Figure 3B). The unclassified component was significantly higher in low altitude samples ($r = -0755$, $p = 0.0085$) (Table 1). The known phyla were dominated by Ascomycota, which was present in all samples across the transect (1.3%–96.4%) and represented 29.8% of the total fungal community. This was followed by Chytridiomycota which was also present in all dataset samples (0.2%–93.7%) and showed a positive significant correlation ($p < 0.05$) with altitude, being more abundant in high altitude samples (Table 1). Mortierellomycota was present with a relative abundance ranging between 0 and 20.9% of the fungal

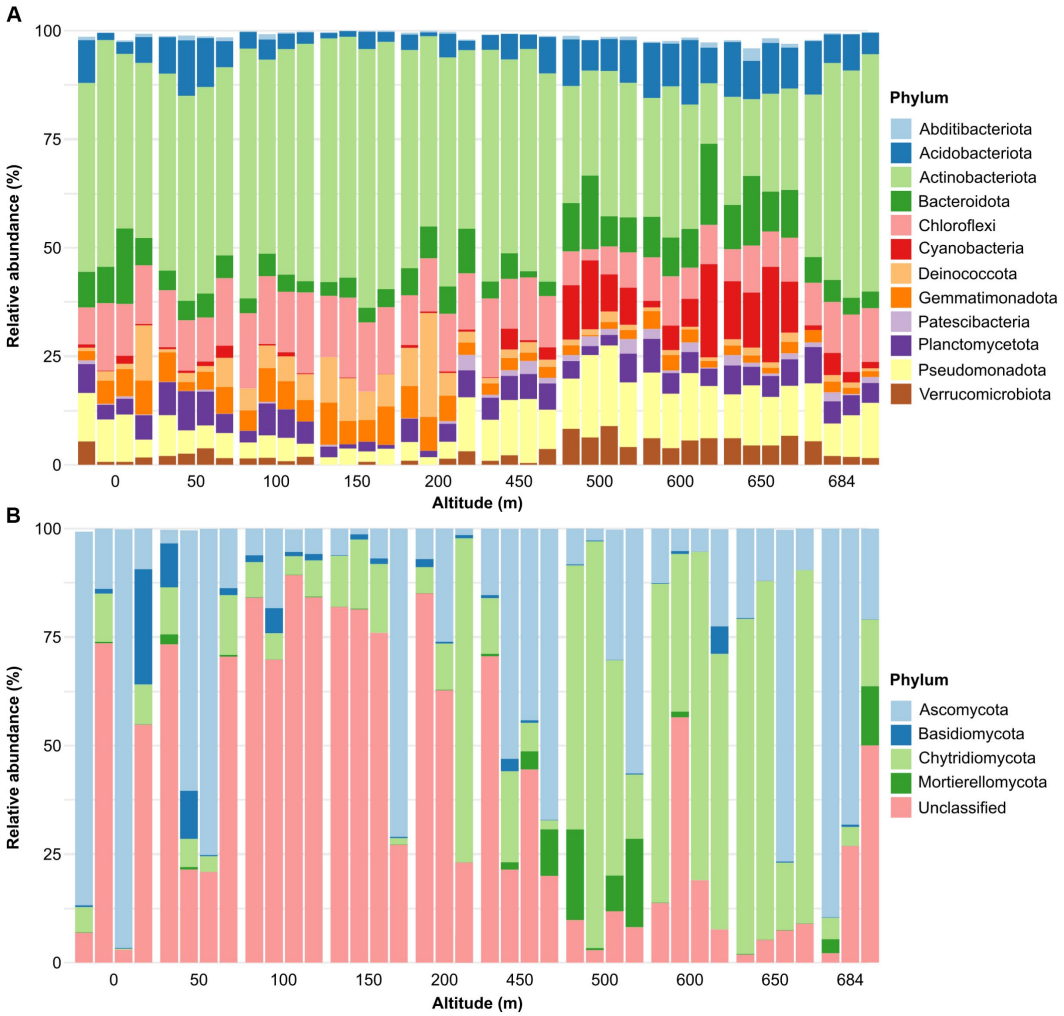

FIGURE 3
Phylum relative abundance of the bacterial **(A)** and fungal dataset **(B)**. Only dominant phyla were reported. We define dominant phyla as those present with a relative abundance higher than 1% in at least 10% of samples (i.e., four samples).

10.3389/fmicb.2023.1203216

TABLE 1 Spearman's correlations between altitude values (m) and bacterial (A) and fungal phyla (B).

Phylum	*r*	Adjusted *p*
A		
Abditibacteriota	−0.0015	0.9945
Acidobacteriota	0.4091	0.0215*
Actinobacteriota	−0.4019	0.0228*
Armatimonadota	0.3124	0.0838
Bacteroidota	0.2360	0.2026
Bdellovibrionota	0.3658	0.0421*
Chloroflexota	−0.5079	0.0032**
Crenarchaeota	0.2775	0.1319
Cyanobacteria	0.6320	0.0002**
Deinococcota	−0.4483	0.0112*
Dependentiae	0.1394	0.4591
Desulfobacterota	−0.0868	0.6685
Elusimicrobiota	0.3529	0.0492*
Firmicutes	−0.3428	0.0546
Fusobacteriota	0.1394	0.4591
Gemmatimonadota	−0.6221	0.0002**
Halobacterota	−0.1951	0.3073
Myxococcota	0.4207	0.0186*
Nitrospirota	0.6092	0.0003**
Patescibacteria	0.5681	0.0009**
Planctomycetota	0.0011	0.9945
Pseudomonadota	0.5557	0.0011**
SAR324 clade (Marine group B)	0.5098	0.0032**
Sumerlaeota	−0.1419	0.4591
Verrucomicrobiota	0.4992	0.0035**
WPS-2	−0.0146	0.9945
Unclassified	0.2527	0.1736
B		
Ascomycota	0.0751	0.9344
Basidiomycota	−0.5801	0.0013**
Blastocladiomycota	−0.1958	0.4773
Chytridiomycota	0.5141	0.0048**
Glomeromycota	−0.2807	0.2196
Monoblepharomycota	0.0301	0.9488
Mortierellomycota	0.1505	0.6120
Rozellomycota	−0.0108	0.9488
Zoopagomycota	−0.0407	0.9488
Unclassified	−0.4755	0.0085**

p values were adjusted using the False Discovery Rate (FDR) approach. *Adjusted $p < 0.05$. **Adjusted $p < 0.01$.

population and represented 2.4% of the total community. Basidiomycota represented 2.1% of the fungal community and showed significant ($p < 0.05$) higher abundances in low altitude samples (Table 1).

The microbial composition data suggested a clear differentiation in soil microbial communities between low and high altitude samples. To further explore these differences, ANCOMBC was performed to compare the two altitudinal groups of samples in order to identify taxa at the genus level that were over-represented in either of the groups. This analysis identified a total of 126 (74 with known phylogeny to genus level) bacterial and 11 (5 known taxa) fungal taxa that were differentially represented between low and high altitudinal samples. In both cases, there was a higher number of over-represented taxa in soils from high altitude samples (Figure 4). As suggested by the correlations between phyla abundance and altitude, soils in high altitudes were enriched in photosynthetic genera, including common cyanobacterial residents in the Antarctic continent such as *Tychonema* (Salmaso et al., 2016) and *Phormidium* (Lumian et al., 2021). By comparison, low altitude soils were enriched in *Truepera*, which is a multi-stress tolerant bacterial genus (Albuquerque et al., 2005), as well as the genera *Rubrobacter* and *Ornithinicoccus*, both of which have been recently associated with the capability to scavenge trace-gases from the atmosphere in cold deserts (Ortiz et al., 2021; Ray et al., 2022) (Figure 4A). In the case of soil fungal populations, the low altitude were dominated by fungi ASVs of unknown taxonomy (Figure 4B). While not as strong, a similar, statistically significant, trend was observed for bacteria, with a higher percentage of unknown genera in soils from low altitudes (Supplementary Figure S2). Samples from high altitude sites were enriched in the lichen-associated genus *Abrothallus* (Suija, 2006), as well as saprotrophic and pathogenic fungi, including several taxa from the phylum *Chytridiomycota* (Kaczmarek and Boguś, 2021), and the nematode pathogen *Pochonia* (Ghahremani et al., 2019).

3.3. Soil geochemical drivers of microbial community distribution across the transect

As with the results from the microbial data, we observed a differentiation in the soil physico-chemical characteristics between the low and high altitudinal sample sites (Supplementary Figure S3): i.e., sample sites showed clear differentiation according to their geochemical composition, forming two significantly distinct clusters ($R2 = 0.46$, $p < 0.01$) for low and high altitude samples (Supplementary Figures S3A,B). The principal differences between these two groups were ammonia (NH_4-N) and iron (Fe), which were enriched in soils at high altitude, and salts (K, Mg, Ca, Na), pH and phosphorus (P), which were higher in low altitude soils (Supplementary Figures S3A). In particular, potassium (K) and sodium (Na), which are considered indicators of proximity to coastal/marine areas, were found to be significantly enriched in soils at low altitudes (Supplementary Figures S3C,D).

Taking into consideration the similarities between the microbial patterns and soil geochemical properties across the altitudinal transect, we investigated the potential soil geochemical drivers of community distribution using correlation analyses. The results show that in addition to altitude, bacterial soil community compositions across the transect were significantly correlated to NH_4-N and phosphorus concentrations in the soil (Figure 5A). By contrast, fungal soil communities at high altitudes were positively correlated with iron and copper contents (Figure 5B). However, when using constrained analyses (db-RDA) to identify explanatory geochemical variables of soil microbial distribution, a non-significant model suggested that the geochemical data in this

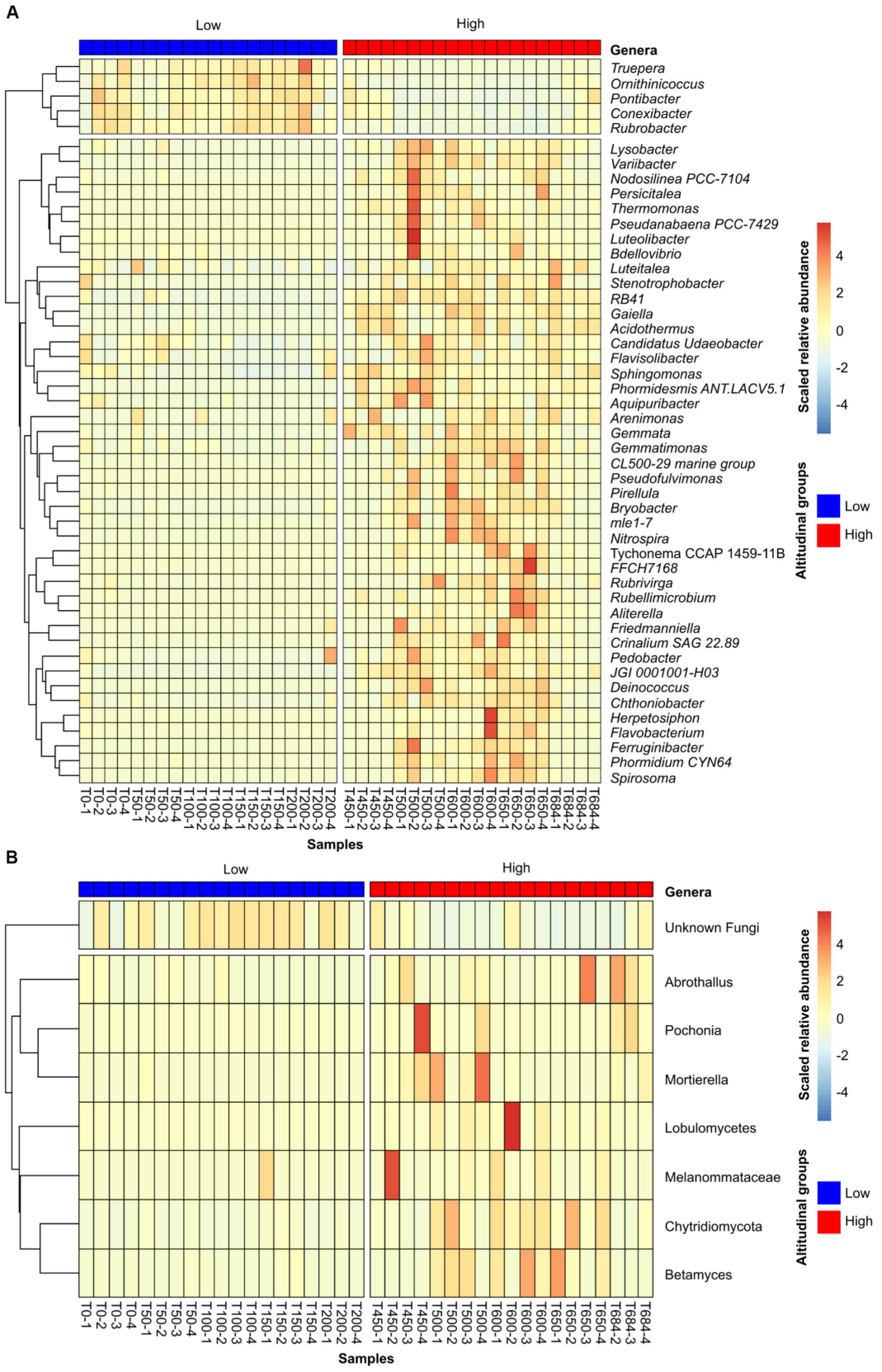

FIGURE 4
Heat maps showing the relative abundance of differentially abundant genera for the bacterial **(A)** and fungal dataset **(B)**. Samples were clustered into high/low groups according to their altitude, as established in the methods section. The heat maps only represent genera that were significantly (p-value < 0.05) over-represented in one of the groups, and present in at least half of the samples in the group in which they were over-represented (threshold of 10 samples for bacteria and 9 for fungi). Relative abundance values were scaled by row to emphasize the differential abundance across samples. Rows, representing taxa, were clustered according to their abundance across samples, and this clustering was visualized as dendrograms in the left-hand side of the heat maps.

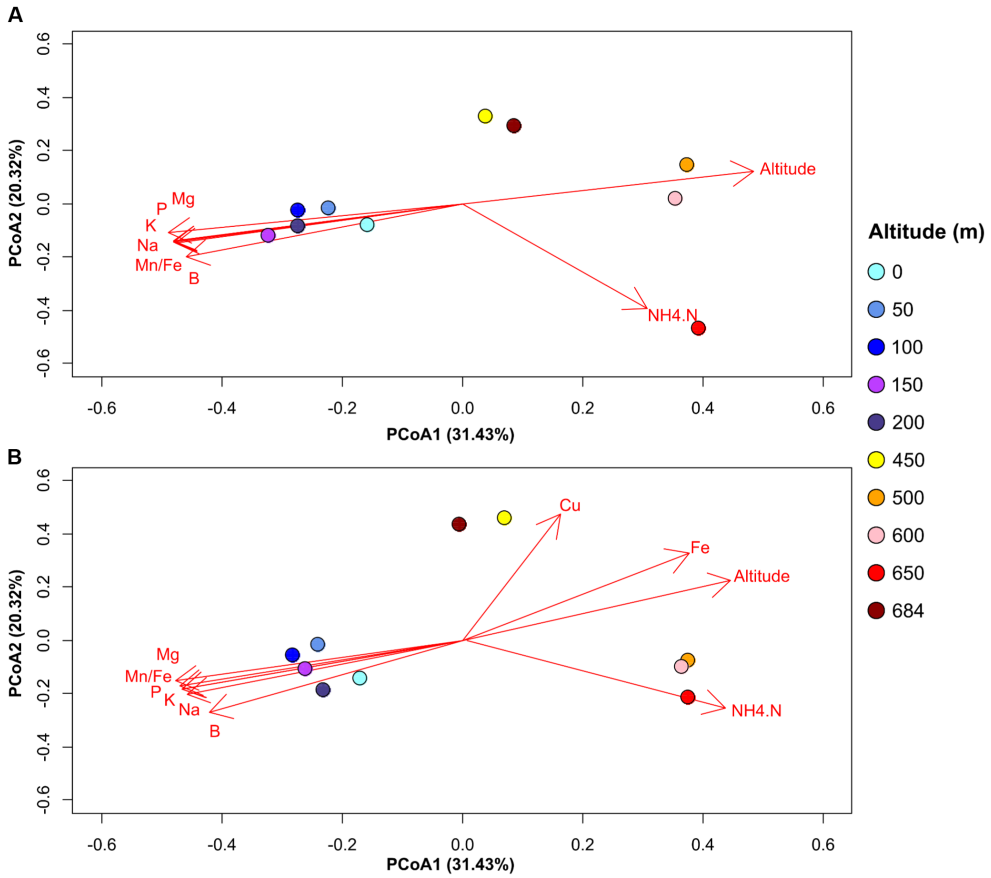

FIGURE 5
PCoA plot showing significant correlations between microbial community distribution and soil geochemical variables for bacterial **(A)** and fungal **(B)** datasets. The direction of the arrows represent the increasing trends in the values for the respective geochemical variables. Geochemical variables are represented using the following nomenclature: B—Boron (mg/kg); Cu—Copper (mg/Kg); Fe—Iron (mg/Kg); K—Potassium (mg/Kg); Mg—Magnesium (mg/Kg); Mn.Fe—ratio Manganese/Iron; Na—Sodium (mg/Kg); NH4.N—Ammonia (mg/Kg); P—Phosphorus (mg/Kg).

study lacked the statistical power to calculate reliable explanatory variables. Nonetheless, the results of the correlation analyses suggest that soil chemistry, particularly NH_4-N and salt contents, might play a role in driving microbial community structure across the altitudinal transect.

3.4. Potential trophic relationships within microbial communities at different altitudes

Co-occurrence network analysis was used to infer possible trophic relationships between taxa within soil communities in the two different elevation groups. This analysis resulted in very distinct networks across the altitudinal transect (Figure 6). Soil microbial communities from high elevation samples generated a highly connected network of 233 taxa from most of the dominant phyla in these soils, and with an average degree of 4.7 connections and a low modularity score (Modularity = 0.512) (Figure 6A). By contrast, microbial communities in low altitude samples generated a sparsely connected network with 79 taxa and an average degree of two connections, but with a higher modularity score of 0.726 (Figure 6B). We also observed large differences between the potential microbial "hubs" of the two networks, which for this study were defined as taxa with a highest number of connections (degrees) and highest influence on the network (betweenness centrality). Taking into account these two metrics, the top five hubs in the high elevation network were dominated by three Chloroflexota genera, two of which belonging to the class Chloroflexia and were therefore potentially photosynthetic (Supplementary Table S4). The top five hubs in the low altitude network consisted of mostly Actinobacteriota and Verrucomicrobiota, none of which have any predicted autotrophic capabilities based on their taxonomy (Supplementary Table S4). To further assess the possible role of trace gas chemoautotrophs and photoautotrophs in the trophic relationships of the soil communities at different altitudes, taxa in the networks were assigned as phototrophs or TGC based on a list of taxa identified in the published literature as having the genetic markers for these processes (Supplementary Table S5). Cyanobacteria and Chloroflexota phototrophs outnumbered TGCs by 20 to 11 taxa in the high elevation network, and also had an higher average degree of 5.5 (compared to 3.8 for TGCs) (Figure 6C). In the low elevation network TGC taxa outnumbered phototrophs eight to four, although phototrophs still exhibited a higher average degree (3.25 vs. 2.25) (Figure 6D). This dichotomy between phototrophs and trace gas chemotrophs across the altitudinal transect was confirmed by measuring the ratio between the relative abundances of TGCs to phototrophs in the soils (Supplementary Figure S4). TGC taxa were found to be more abundant than phototrophs across the whole dataset. However, the ratio

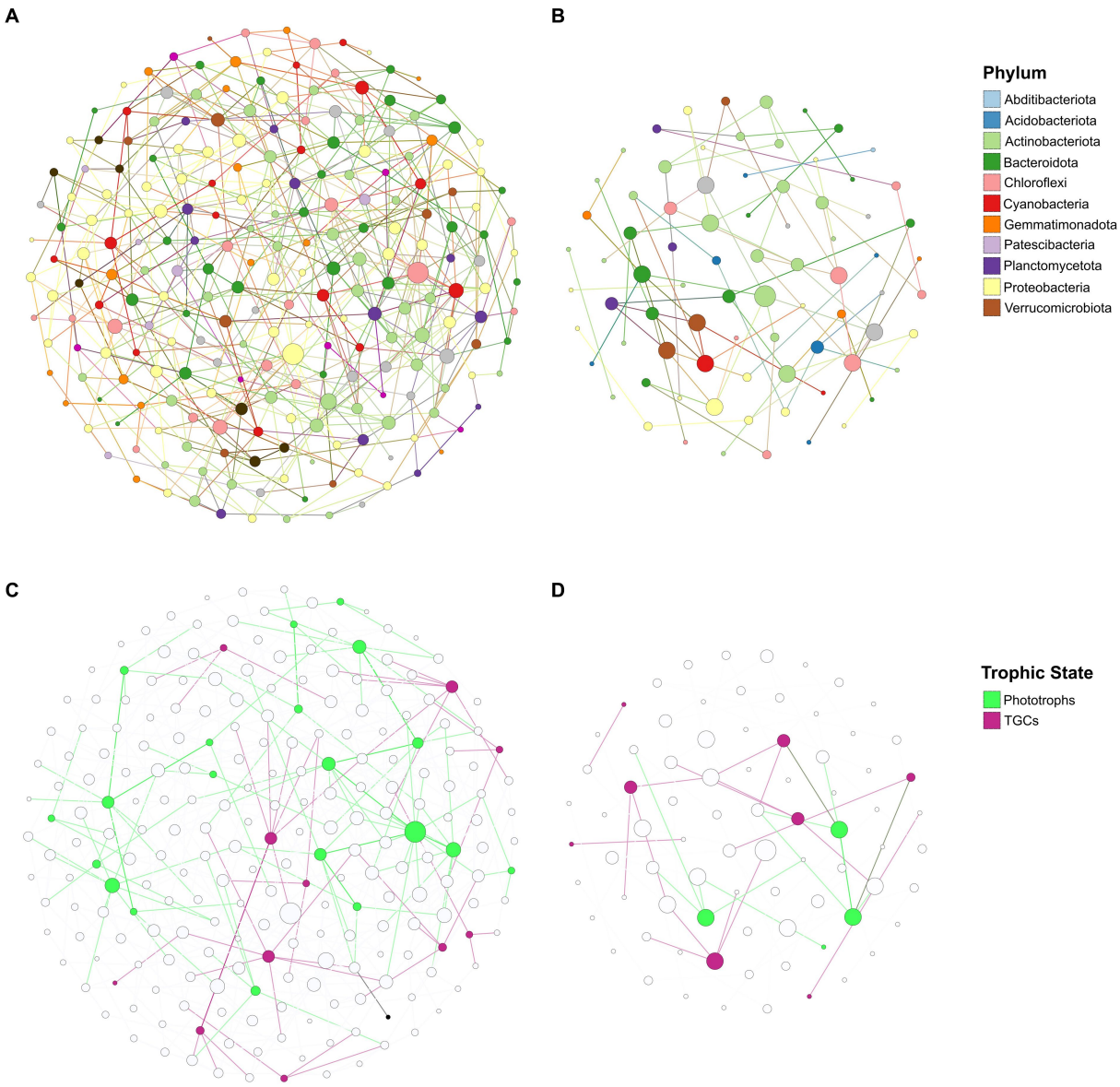

FIGURE 6
Co-occurrence networks of prokaryotic genera in high **(A)** and low **(B)** altitudinal sample groups based on their CLR-transformed abundances across samples. Node size was scaled according to degree (i.e., number of connections to other nodes) and colored according to Phylum. Edges (i.e., connections between nodes) were colored according to the source node. Nodes corresponding to phototrophs and trace-gas chemotrophs (TGC) were subsequently overlaid on the high **(C)** and low **(D)** altitudinal networks, with edges colored according to the trophic state (either TGC or phototroph) of the source node.

of TGCs/Phototrophs was significantly higher in lower elevation soils ($p < 0.05$), which was in accordance with the compositional data (Figure 3), in which the percentage of Cyanobacteria was strongly correlated with elevation.

4. Discussion

Water, nutrient and mineral availability for microbial communities is likely to change with global warming due to shifts in climatic conditions and slow but constant melting of Antarctic ice shelves and glaciers (Gooseff et al., 2011; Rignot et al., 2013; Buelow et al., 2016). Analysing microbial community composition along altitudinal transects and coastal-inland transects, which are characterised by soil water and nutrient availability gradients (Bockheim, 2002; Fountain et al., 2010), is therefore essential to understand how microbial communities will change as a result of global warming. In our dataset, soils close to the coast showed higher concentrations of ions common in seawater (Na, Mg, and K; Supplementary Table S2 and Supplementary Figure S3), suggesting a clear input from marine sources (Millero and Huang, 2013). This trend was also observed in other coastal areas of the McMurdo Valleys (Williamson et al., 2007). Higher concentrations of P and B were also found in low altitude samples (Supplementary Table S2 and Supplementary Figure S3), which could be indicative of increased biomass closer to the coast, perhaps as biomass deposition from marine sources (Cary et al., 2010). While no moisture or temperature data was collected in this study, it is expected that water availability will increase with increasing

elevation due to cloud and condensation processes (Cowan et al., 2011; Berrones Guapulema et al., 2022).

The clear differences in soil geochemistry between low and high elevation samples were also reflected in the community composition of these two groups of samples. Despite the lack of statistical robustness due to sample size (for the geochemistry analyses), our results suggest a possible correlation between the geochemistry of the transect soils and differences in community composition across the transect. For instance, the high salinity of lower altitude soils (closer to the coast) could have selected for genera such as *Rubrobacter*, *Pontibacter* and *Ornithinicoccus*, all of which are known to include extremely halotolerant species (Joshi et al., 2012; Zhang et al., 2016; Kouřilová et al., 2021). Conversely, the higher NH_4-N concentrations (together with the likely increase in water availability) in higher altitude sites could be correlated to the enrichment of Cyanobacteria, which are known to be driven by both water and ammonia availability (Boussiba and Gibson, 1991; Herrero et al., 2001), as well as putative nitrifiers of the genus *Nitrospira* (Daims et al., 2015). While the same geochemistry variables were significantly correlated with the soil fungal distribution across the altitudinal transect, the fungal taxa that were differentially represented across the two elevation groups suggest that other factors, such as life-style and predation might also be important drivers across the altitudinal transect. In particular, the over-representation of *Chytridiomycota* taxa in the high altitude samples could be related to the over-representation of *Cyanobacteria*, as *Chytridiomycota* is the only reported fungal taxon to be able to parasitize cyanobacterial phytoplankton (Rasconi et al., 2012). Chytridiomycota have also been reported as being widely abundant in Antarctic lake systems (Ilicic et al., 2022) and are positively correlated with meltwater from glaciers (Ilicic et al., 2022). Their enrichment in the soils at high altitude, which are in close proximity to a glacial tongue (Figure 1), might therefore suggest that these soils have received a recent input from glacial meltwater. In addition, the over-representation of the lichenicolous *Ascomycota* genus *Abrothallus* in high altitude samples is consistent with the prevalence at higher altitudes of crustose lichens such as *Buellia frigida* (Sancho et al., 2019).

However, it is important to re-iterate that due to the lack of temperature and moisture data, as well as the limited number of data points, the correlations observed between soil microbial diversity and soil geochemistry as well as altitude can only be interpreted as suggestive, rather than conclusive evidence that microbial communities in this Taylor Valley transect are driven by altitude and soil chemistry. In this study, we also could not account for other processes that could play a role in the microbial diversity differences between sites: for instance the deposition of atmospheric bioaerosols (Barberán et al., 2014), legacy effects from historic ice sheet movements and water incursions (Jackson et al., 2022), as well as snow cover and snow melt cycles (Sorensen et al., 2020). Additionally, the putative role of water in the enrichment of photosynthetic taxa at higher altitudes must be treated with care, as previous water amendment studies (Van Horn et al., 2014; Buelow et al., 2016) present a very distinct shift in soil microbial diversity in response to water when compared to those shown in this study. We strongly suggest that future studies in this region of the Taylor Valley to account for soil water moisture and temperature in order to provide conclusive evidence of the role of water availability to soil microbial diversity.

The increased complexity of trophic relationships within the soil communities of high altitude soils was suggested by the co-occurrence network analysis, which predicted a more connected community in high elevation soils. The higher average degree in the high altitude network not only indicated that the members in the network were more connected than in low altitude soils, but also suggests that soil communities at high elevations are more robust; i.e. removal of one member in the community could have a smaller impact on the overall relationships between the remaining members. The higher number of connections between different phyla in the high altitude network also suggests that these communities exhibit a broader range of trophic strategies, compared to microbial communities closer to the coast. Nevertheless, putative phototrophic genera were found to be major "hubs" of the high altitude network. The "central" role of the phototrophic genera further highlights the potential importance of phototrophic microbial taxa in soil microbial communities in Antarctic soils, particularly at higher altitudes where water from cloud condensation and snowfall might reduce the xeric stress typical of Dry Valley soil habitats (Doran et al., 2002).

Trace-gas chemotrophs (TGCs) were found to be ubiquitous across the transect, which is consistent with recent studies showing their widespread distribution across many phyla and polar ecosystems (Ortiz et al., 2021; Ray et al., 2022). Despite their prevalence, these taxa were predicted to have a lower impact on the trophic relationships of the soil communities in both elevation groups compared to phototrophs, as suggested by the lower average degree of these taxa in both networks. Interestingly, TGC and phototrophic taxa were not directly connected to each other (with the exception of one connection in the low altitude network), which suggests that these two trophic strategies might not occur simultaneously. It is possible that physicochemical factors might alter the balance between co-occurring phototrophy and gas scavenging processes, but recent studies have suggested that trace-gas chemoautotrophy only becomes a dominant survival strategy in ecosystems where photosynthesis is severely constrained (Ji et al., 2017; Leung et al., 2020; Bay et al., 2021). It is important to note that due to the lack of resolution in the taxonomic assignments (taxonomy could only be assigned accurately to genus level), the trophic TGC/phototroph predictions in this study do not take into account the possibility that some phototrophs, such as specific Chloriflexota clades, might be able to perform both trophic strategies simultaneously (Islam et al., 2019), a process that has also been observed in hot desert soils after hydration (Jordaan et al., 2020). As a result, we acknowledge that our results may underestimate the relevance of trace gas chemoautotrophy to microbial communities in the altitudinal transect soils. It is also worth noting that a recent study by Dragone et al. (2022) documented an opposite trend with regards to Phototrophs/Trace-gas Chemotrophs density across different altitudes in the Shackleton Glacier region, with soils at higher altitudes exhibiting higher abundances of TGCs and lower phototrophic signals. However, these soils were characterized by lower water content and higher salt concentrations, which would correlate with the coastal sites in the present study. Thus, Dragone's study provides further evidence that water availability might be a crucial driver of the interaction between phototrophs and TGCs in Antarctic soil communities.

In conclusion, we suggest that soil microbial communities across the elevation transect of the lower Taylor Valley are selected, through a combination of soil geochemical parameters and inputs from nearby marine and glacier sources, into distinct communities at different elevation points that exhibit distinct food-web strategies. In addition

to the effects of geochemistry and elevation on soil microbial ecology, the differences in the sampling sites of this study might also reflect a long-term temporal effect in relation to inland retreat of the glacier from the coast after successive melting events (Bradley et al., 2014; Fernández-Martínez et al., 2017; Nash et al., 2018), particularly as the last major glacial retreat in the McMurdo Dry Valleys would have followed the most recent glacial maximum (*ca.* 20 ka ago: Peltier and Fairbanks, 2006). As indicated above, future studies should involve a more comprehensive sampling strategy and expand the methodology to more comprehensively measure the possible factors (including water moisture and temperature) that might drive soil microbial diversity and functional potential in Antarctic Dry Valley soils.

Data availability statement

The datasets presented in this study can be found in online repositories. The names of the repository/repositories and accession number(s) can be found at: https://www.ebi.ac.uk/ena, PRJEB55870.

Author contributions

DC conceptualized the study, collected the samples, supervised the analysis of the results, and contributed to writing and editing of the manuscript. IDH helped with the study conceptualization and sample logistics, as well as contributed to the final editing of the manuscript. LM was responsible for the sample and data processing, and conducted the bulk of the analyses. MO supervised the sample and data processing, and contributed to the editing of the final manuscript. PHL, GV, and SM were involved in the second round of data curation and analyses, and contributed equally to the writing of the manuscript. All authors contributed to the article and approved the submitted version.

Acknowledgments

The authors gratefully acknowledge financial support and a PhD bursary (to LM) from the National Research Foundation (SANAP program; grant number 110730), the award of postdoctoral bursaries from the University of Pretoria (PHL, MO, SM, and GV), and logistics and funding support for the field work from Antarctica New Zealand and the New Zealand Ministry of Business Innovation and Employment (MBIE), respectively.

Conflict of interest

The authors declare that the research was conducted in the absence of any commercial or financial relationships that could be construed as a potential conflict of interest.

The reviewer BA declared a past co-authorship with the author IDH to the handling editor at the time of review.

Publisher's note

Supplementary material

The Supplementary material for this article can be found online at: https://www.frontiersin.org/articles/10.3389/fmicb.2023.1203216/full#supplementary-material

References

Adriaenssens, E. M., Kramer, R., Van Goethem, M. W., Makhalanyane, T. P., Hogg, I., and Cowan, D. A. (2017). Environmental drivers of viral community composition in Antarctic soils identified by viromics. *Microbiome* 5, 83–14. doi: 10.1186/s40168-017-0301-7

Aislabie, J. M., Chhour, K.-L., Saul, D. J., Miyauchi, S., Ayton, J., Paetzold, R. F., et al. (2006). Dominant bacteria in soils of marble point and Wright valley, Victoria land, Antarctica. *Soil Biol. Biochem.* 38, 3041–3056. doi: 10.1016/j.soilbio.2006.02.018

Albuquerque, L., Simões, C., Nobre, M. F., Pino, N. M., Battista, J. R., Silva, M. T., et al. (2005). *Truepera radiovictrix* gen. Nov., sp. nov., a new radiation resistant species and the proposal of Trueperaceae fam. Nov. *FEMS Microbiol. Lett.* 247, 161–169. doi: 10.1016/j.femsle.2005.05.002

Babalola, O. O., Kirby, B. M., Le Roes-Hill, M., Cook, A. E., Cary, S. C., Burton, S. G., et al. (2009). Phylogenetic analysis of actinobacterial populations associated with Antarctic Dry Valley mineral soils. *Environ. Microbiol.* 11, 566–576. doi: 10.1111/j.1462-2920.2008.01809.x

Barberán, A., Henley, J., Fierer, N., and Casamayor, E. O. (2014). Structure, inter-annual recurrence, and global-scale connectivity of airborne microbial communities. *Sci. Total Environ.* 487, 187–195. doi: 10.1016/j.scitotenv.2014.04.030

Bastian, M., Heymann, S., and Jacomy, M. (2009). Gephi: An open source software for exploring and manipulating networks. Proceedings of the International AAAI Conference on Web and Social Media, Vol. 3, 361–362.

Bay, S. K., Waite, D. W., Dong, X., Gillor, O., Chown, S. L., Hugenholtz, P., et al. (2021). Chemosynthetic and photosynthetic bacteria contribute differentially to primary production across a steep desert aridity gradient. *ISME J.* 15, 3339–3356. doi: 10.1038/s41396-021-01001-0

Benjamini, Y., and Hochberg, Y. (1995). Controlling the false discovery rate: a practical and powerful approach to multiple testing. *J. R. Stat. Soc., B: Stat. Methodol.* 57, 289–300.

Berrones Guapulema, G. M., Wilcox, B. P., Celleri Alvear, R. E., Ochoa Sanchez, A. E., and Crespo Sanchez, P. J. (2022). Importance of fog and cloud water contributions to soil moisture in the Andean Paramo. *Hydrology* 9:54. doi: 10.3390/hydrology9040054

Beule, L., and Karlovsky, P. (2020). Improved normalization of species count data in ecology by scaling with ranked subsampling (SRS): application to microbial communities. *PeerJ* 8:e9593. doi: 10.7717/peerj.9593

Bockheim, J. (2002). Landform and soil development in the McMurdo Dry Valleys, Antarctica: a regional synthesis. *Arct. Antarct. Alp. Res.* 34, 308–317. doi: 10.1080/15230430.2002.12003499

Bockheim, J., and McLeod, M. (2008). Soil distribution in the McMurdo Dry Valleys, Antarctica. *Geoderma* 144, 43–49. doi: 10.1016/j.geoderma.2007.10.015

Bolger, A. M., Lohse, M., and Usadel, B. (2014). Trimmomatic: a flexible trimmer for Illumina sequence data. *Bioinformatics* 30, 2114–2120. doi: 10.1093/bioinformatics/btu170

Bottos, E. M., Laughlin, D. C., Herbold, C. W., Lee, C. K., McDonald, I. R., and Cary, S. C. (2020). Abiotic factors influence patterns of bacterial diversity and community composition in the dry valleys of Antarctica. *FEMS Microbiol. Ecol.* 96:fiaa042. doi: 10.1093/femsec/fiaa042

Bottos, E. M., Woo, A. C., Zawar-Reza, P., Pointing, S. B., and Cary, S. C. (2014). Airborne bacterial populations above desert soils of the McMurdo Dry Valleys, Antarctica. *Microb. Ecol.* 67, 120–128. doi: 10.1007/s00248-013-0296-y

Boussiba, S., and Gibson, J. (1991). Ammonia translocation in cyanobacteria. *FEMS Microbiol. Rev.* 88, 1–14. doi: 10.1016/0168-6445(91)90002-Y

Bradley, J. A., Singarayer, J. S., and Anesio, A. M. (2014). Microbial community dynamics in the forefield of glaciers. *Proc. R. Soc. B Biol. Sci.* 281:20140882. doi: 10.1098/rspb.2014.0882

Buelow, H. N., Winter, A. S., Van Horn, D. J., Barrett, J. E., Gooseff, M. N., Schwartz, E., et al. (2016). Microbial community responses to increased water and organic matter in the arid soils of the McMurdo Dry Valleys, Antarctica. *Front. Microbiol.* 7:1040. doi: 10.3389/fmicb.2016.01040

Callahan, B. J., McMurdie, P., Rosen, M., Han, A., Johnson, A., and Holmes, S. P. (2016). DADA2: high-resolution sample inference from Illumina amplicon data. *Nat. Methods* 13, 581–583. doi: 10.1038/nmeth.3869

Cary, S. C., McDonald, I. R., Barrett, J. E., and Cowan, D. A. (2010). On the rocks: the microbiology of Antarctic Dry Valley soils. *Nat. Rev. Microbiol.* 8, 129–138. doi: 10.1038/nrmicro2281

Coleine, C., Stajich, J. E., Pombubpa, N., Zucconi, L., Onofri, S., Canini, F., et al. (2019). Altitude and fungal diversity influence the structure of Antarctic cryptoendolithic bacteria communities. *Environ. Microbiol. Rep.* 11, 718–726. doi: 10.1111/1758-2229.12788

Cowan, D. A., Khan, N., Pointing, S. B., and Cary, S. C. (2010). Diverse hypolithic refuge communities in the McMurdo Dry Valleys. *Antarct. Sci.* 22, 714–720. doi: 10.1017/S0954102010000507

Cowan, D. A., Pointing, S. B., Stevens, M. I., Craig Cary, S., Stomeo, F., and Tuffin, I. M. (2011). Distribution and abiotic influences on hypolithic microbial communities in an Antarctic Dry Valley. *Polar Biol.* 34, 307–311. doi: 10.1007/s00300-010-0872-2

Cowan, D. A., Russell, N. J., Mamais, A., and Sheppard, D. M. (2002). Antarctic Dry Valley mineral soils contain unexpectedly high levels of microbial biomass. *Extremophiles* 6, 431–436. doi: 10.1007/s00792-002-0276-5

Cowan, D. A., and Tow, L. A. (2004). Endangered Antarctic environments. *Annu. Rev. Microbiol.* 58, 649–690. doi: 10.1146/annurev.micro.57.030502.090811

Daims, H., Lebedeva, E. V., Pjevac, P., Han, P., Herbold, C., Albertsen, M., et al. (2015). Complete nitrification by Nitrospira bacteria. *Nature* 528, 504–509. doi: 10.1038/nature16461

De los Ríos, A., Cary, C., and Cowan, D. (2014). The spatial structures of hypolithic communities in the dry valleys of East Antarctica. *Polar Biol.* 37, 1823–1833. doi: 10.1007/s00300-014-1564-0

Delpupo, C., Schaefer, C. E. G. R., Roque, M. B., de Faria, A. L. L., da Rosa, K. K., Thomazini, A., et al. (2017). Soil and landform interplay in the dry valley of Edson Hills, Ellsworth Mountains, continental Antarctica. *Geomorphology* 295, 134–146. doi: 10.1016/j.geomorph.2017.07.002

Doran, P. T., McKay, C. P., Clow, G. D., Dana, G. L., Fountain, A. G., Nylen, T., et al. (2002). Valley floor climate observations from the McMurdo Dry Valleys, Antarctica, 1986–2000. *J. Geophys. Res. Atmos*. 107, ACL–13. doi: 10.1029/2001JD002045

Dragone, N. B., Henley, J. B., Holland-Moritz, H., Diaz, M., Hogg, I. D., Lyons, W. B., et al. (2022). Elevational constraints on the composition and genomic attributes of microbial communities in Antarctic soils. *mSystems* 7:e0133021. doi: 10.1128/msystems.01330-21

Fernández-Martínez, M. A., Pérez-Ortega, S., Pointing, S. B., Allan Green, T., Pintado, A., Rozzi, R., et al. (2017). Microbial succession dynamics along glacier forefield chronosequences in Tierra del Fuego (Chile). *Polar Biol.* 40, 1939–1957. doi: 10.1007/s00300-017-2110-7

Fountain, A. G., Nylen, T. H., Monaghan, A., Basagic, H. J., and Bromwich, D. (2010). Snow in the McMurdo Dry Valleys, Antarctica. *Int. J. Climatol.* 30, 633–642. doi: 10.1002/joc.1933

Fox, J., and Weisberg, S. (2019). *An R companion to applied regression*. *Third* Edn Thousand Oaks, CA, Sage.

Freckman, D. W., and Virginia, R. A. (1998). "Soil biodiversity and community structure in the McMurdo Dry Valleys, Antarctica" in *Ecosystem dynamics in a polar desert: the McMurdo Dry Valleys, Antarctica*, ed. J. C. Priscu. American Geophysical Union. vol. 72, 323–335.

Friedmann, E. I., and Thistle, A. B. (1993). *Antarctic microbiology*. eds. E Imre Friedmann and B. Anne. New York: Wiley-Liss.

Gardes, M., and Bruns, T. D. (1993). ITS primers with enhanced specificity for basidiomycetes-application to the identification of mycorrhizae and rusts. *Mol. Ecol.* 2, 113–118. doi: 10.1111/j.1365-294x.1993.tb00005.x

Ghahremani, Z., Escudero, N., Saus, E., Gabaldón, T., and Sorribas, F. J. (2019). Pochonia chlamydosporia induces plant-dependent systemic resistance to Meloidogyne incognita. *Front. Plant Sci.* 10:945. doi: 10.3389/fpls.2019.00945

Goordial, J., Davila, A., Greer, C. W., Cannam, R., DiRuggiero, J., McKay, C. P., et al. (2017). Comparative activity and functional ecology of permafrost soils and lithic niches in a hyper-arid polar desert. *Environ. Microbiol.* 19, 443–458. doi: 10.1111/1462-2920.13353

Goordial, J., Davila, A., Lacelle, D., Pollard, W., Marinova, M. M., Greer, C. W., et al. (2016). Nearing the cold-arid limits of microbial life in permafrost of an upper dry valley, Antarctica. *ISME J.* 10, 1613–1624. doi: 10.1038/ismej.2015.239

Gooseff, M. N., McKnight, D. M., Doran, P., Fountain, A. G., and Lyons, W. B. (2011). Hydrological connectivity of the landscape of the McMurdo Dry Valleys, Antarctica. *Geogr. Compass* 5, 666–681. doi: 10.1111/j.1749-8198.2011.00445.x

Green, T. G. A., Brabyn, L., Beard, C., and Sancho, L. G. (2012). "Extremely low lichen growth rates in Taylor Valley, dry valleys, continental Antarctica. *Polar Biol.* 35, 535–541. doi: 10.1007/s00300-011-1098-7

Herlemann, D. P., Labrenz, M., Jürgens, K., Bertilsson, S., Waniek, J. J., and Andersson, A. F. (2011). Transitions in bacterial communities along the 2000 km salinity gradient of the Baltic Sea. *ISME J.* 5, 1571–1579. doi: 10.1038/ismej.2011.41

Herrero, A., Muro-Pastor, A. M., and Flores, E. (2001). Nitrogen control in cyanobacteria. *J. Bacteriol.* 183, 411–425. doi: 10.1128/JB.183.2.411-425.2001

Hogg, I. D., Cary, S. C., Convey, P., Newsham, K. K., O'Donnell, A. G., Adams, B. J., et al. (2006). Biotic interactions in Antarctic terrestrial ecosystems: are they a factor? *Soil Biol. Biochem.* 38, 3035–3040. doi: 10.1016/j.soilbio.2006.04.026

Ilicic, D., Woodhouse, J., Karsten, U., Zimmermann, J., Wichard, T., Quartino, M. L., et al. (2022). Antarctic glacial meltwater impacts the diversity of fungal parasites associated with benthic diatoms in shallow coastal zones. *Front. Microbiol.* 13:805694. doi: 10.3389/fmicb.2022.805694

Islam, Z. F., Cordero, P. R., Feng, J., Chen, Y.-J., Bay, S. K., Jirapanjawat, T., et al. (2019). Two Chloroflexi classes independently evolved the ability to persist on atmospheric hydrogen and carbon monoxide. *ISME J.* 13, 1801–1813. doi: 10.1038/s41396-019-0393-0

Jackson, A. C., Jorna, J., Chaston, J. M., and Adams, B. J. (2022). Glacial legacies: microbial communities of Antarctic Refugia. *Biology (Basel)* 11:1440. doi: 10.3390/biology11101440

Ji, M., Greening, C., Vanwonterghem, I., Carere, C. R., Bay, S. K., Steen, J. A., et al. (2017). Atmospheric trace gases support primary production in Antarctic desert surface soil. *Nature* 552, 400–403. doi: 10.1038/nature25014

Jordaan, K., Lappan, R., Dong, X., Aitkenhead, I. J., Bay, S. K., Chiri, E., et al. (2020). Hydrogen-oxidizing bacteria are abundant in desert soils and strongly stimulated by hydration. *Msystems* 5, e01131–e01120. doi: 10.1128/mSystems.01131-20

Joshi, M., Sharma, A., Pandya, R., Patel, R., Saiyed, Z., Saxena, A., et al. (2012). Draft genome sequence of Pontibacter sp. nov. BAB1700, a halotolerant, industrially important bacterium. *Am. Soc. Microbiol.* 194, 6329–6330. doi: 10.1128/JB.01550-12

Kaczmarek, A., and Boguś, M. I. (2021). Fungi of entomopathogenic potential in Chytridiomycota and Blastocladiomycota, and in fungal allies of the Oomycota and microsporidia. *IMA Fungus* 12, 29–13. doi: 10.1186/s43008-021-00074-y

Kirby, B. M., Easton, S., Marla Tuffin, I., and Cowan, D. A. (2011). "Bacterial diversity in polar habitats" in *Polar microbiology: life in a deep freeze*. eds. R. V. Miller and L. G. Whyte. Wiley Online Library. 1–31.

Kolde, R. (2019). Pheatmap: pretty Heatmaps. R package version 1.0. 12.

Koo, H., Hakim, J. A., Morrow, C. D., Crowley, M. R., Andersen, D. T., and Bej, A. K. (2018). Metagenomic analysis of microbial community compositions and cold-responsive stress genes in selected Antarctic lacustrine and soil ecosystems. *Life* 8:29. doi: 10.3390/life8030029

Kouřilová, X., Schwarzerová, J., Pernicová, I., Sedlář, K., Mrázová, K., Krzyžánek, V., et al. (2021). The first insight into polyhydroxyalkanoates accumulation in multi-extremophilic Rubrobacter xylanophilus and Rubrobacter spartanus. *Microorganisms* 9:909. doi: 10.3390/microorganisms9050909

Kurtz, Z. D., Müller, C. L., Miraldi, E. R., Littman, D. R., Blaser, M. J., and Bonneau, R. A. (2015). Sparse and compositionally robust inference of microbial ecological networks. *PLoS Comput. Biol.* 11:e1004226. doi: 10.1371/journal.pcbi.1004226

Lambrechts, S., Willems, A., and Tahon, G. (2019). Uncovering the uncultivated majority in Antarctic soils: toward a synergistic approach. *Front. Microbiol.* 10. doi: 10.3389/fmicb.2019.00242

Lee, C. K., Barbier, B. A., Bottos, E. M., McDonald, I. R., and Cary, S. C. (2012). The inter-valley soil comparative survey: the ecology of dry valley edaphic microbial communities. *ISME J.* 6, 1046–1057. doi: 10.1038/ismej.2011.170

Leung, P. M., Bay, S. K., Meier, D. V., Chiri, E., Cowan, D. A., Gillor, O., et al. (2020). Energetic basis of microbial growth and persistence in desert ecosystems. *Msystems* 5, e00495–e00419. doi: 10.1128/mSystems.00495-19

Lin, A., and Peddada, S. (2020). Das. 2020. Analysis of microbial compositions: a review of normalization and differential abundance analysis. *NPJ Biofilms Microbiomes*, 6:60. doi: 10.1038/s41522-020-00160-w

Lumian, J. E., Jungblut, A. D., Dillion, M. L., Hawes, I., Doran, P. T., Mackey, T. J., et al. (2021). Metabolic capacity of the Antarctic cyanobacterium that sustains oxygenic photosynthesis in the presence of hydrogen sulfide. *Genes* 12. doi: 10.3390/genes12030426

Makhalanyane, T. P., Valverde, A., Birkeland, N.-K., Cary, S. C., Marla Tuffin, I., and Cowan, D. A. (2013). Evidence for successional development in Antarctic hypolithic bacterial communities. *ISME J.* 7, 2080–2090. doi: 10.1038/ismej.2013.94

Makhalanyane, T. P., Valverde, A., Velázquez, D., Gunnigle, E., Van Goethem, M. W., Quesada, A., et al. (2015). Ecology and biogeochemistry of cyanobacteria in soils, permafrost, aquatic and cryptic polar habitats. *Biodivers. Conserv.* 24, 819–840. doi: 10.1007/s10531-015-0902-z

Marinova, M. M., McKay, C. P., Heldmann, J. L., Goordial, J., Lacelle, D., Pollard, W. H., et al. (2022). Climate and energy balance of the ground in University Valley, Antarctica. *Antarct. Sci.* 34, 144–171. doi: 10.1017/S0954102022000025

McKay, C. P. (2009). Snow recurrence sets the depth of dry permafrost at high elevations in the McMurdo Dry Valleys of Antarctica. *Antarct. Sci.* 21, 89–94. doi: 10.1017/S0954102008001508

McMurdie, P. J., and Holmes, S. (2013). Phyloseq: an R package for reproducible interactive analysis and graphics of microbiome census data. *PLoS One* 8:e61217. doi: 10.1371/journal.pone.0061217

Mezzasoma, A., Coleine, C., Sannino, C., and Selbmann, L. (2022). Endolithic bacterial diversity in lichen-dominated communities is shaped by sun exposure in McMurdo Dry Valleys, Antarctica. *Microbial Ecol.* 83, 328–339. doi: 10.1007/s00248-021-01769-w

Millero, F. J., and Huang, F. (2013). Molal volumes and compressibilities of salts in seawater. *Geochim. Cosmochim. Acta* 104, 19–28. doi: 10.1016/j.gca.2012.11.023

Nash, M. V., Anesio, A. M., Barker, G., Tranter, M., Varliero, G., Eloe-Fadrosh, E. A., et al. (2018). Metagenomic insights into diazotrophic communities across Arctic glacier forefields. *FEMS Microbiol. Ecol.* 94:fiy114. doi: 10.1093/femsec/fiy114

Niederberger, T. D., Sohm, J. A., Gunderson, T. E., Parker, A. E., Tirindelli, J., Capone, D. G., et al. (2015). Microbial community composition of transiently wetted Antarctic Dry Valley soils. *Front. Microbiol.* 6:9. doi: 10.3389/fmicb.2015.00009

Nilsson, R. H., Larsson, K. H., Taylor, A. F. S., Bengtsson-Palme, J., Jeppesen, T. S., Schigel, D., et al. (2019). The UNITE database for molecular identification of fungi: handling dark taxa and parallel taxonomic classifications. *Nucleic Acids Res.* 47, D259–d264. doi: 10.1093/nar/gky1022

Oksanen, J., Simpson, G., Blanchet, F., Kindt, R., Legendre, P., Minchin, P., et al. (2022). Vegan: community ecology package–R package version 2.6-4.

Ortiz, M., Leung, P. M., Shelley, G., Jirapanjawat, T., Nauer, P. A., Van Goethem, M. W., et al. (2021). Multiple energy sources and metabolic strategies sustain microbial diversity in Antarctic desert soils. *Proc. Natl. Acad. Sci.* 118:e2025322118. doi: 10.1073/pnas.2025322118

Pannewitz, S., Green, T., Scheidegger, C., Schlensog, M., and Schroeter, B. (2003). Activity pattern of the moss *Hennediella heimii* (Hedw.) Zand. In the dry valleys, southern Victoria land, Antarctica during the mid-austral summer. *Polar Biol.* 26, 545–551. doi: 10.1007/s00300-003-0518-8

Paradis, E., and Schliep, K. (2019). Ape 5.0: an environment for modern phylogenetics and evolutionary analyses in R. *Bioinformatics* 35, 526–528. doi: 10.1093/bioinformatics/bty633

Peltier, W., and Fairbanks, R. G. (2006). Global glacial ice volume and last glacial maximum duration from an extended Barbados Sea level record. *Quat. Sci. Rev.* 25, 3322–3337. doi: 10.1016/j.quascirev.2006.04.010

Pointing, S. B., Chan, Y., Lacap, D. C., Lau, M. C., Jurgens, J. A., and Farrell, R. L. (2009). Highly specialized microbial diversity in hyper-arid polar desert. *Proc. Natl. Acad. Sci.* 106, 19964–19969. doi: 10.1073/pnas.0908274106

Power, S. N., Salvatore, M. R., Sokol, E. R., Stanish, L. F., and Barrett, J. (2020). Estimating microbial mat biomass in the McMurdo Dry Valleys, Antarctica using satellite imagery and ground surveys. *Polar Biol.* 43, 1753–1767. doi: 10.1007/s00300-020-02742-y

Quast, C., Pruesse, E., Yilmaz, P., Gerken, J., Schweer, T., Yarza, P., et al. (2012). The SILVA ribosomal RNA gene database project: improved data processing and web-based tools. *Nucleic Acids Res.* 41, D590–D596. doi: 10.1093/nar/gks1219

R Core Team. (2022). *R: A Language and Environment for Statistical Computing. R Foundation for Statistical Computing*, Austria: Vienna. Available at: https://www.R-project.org/

Rasconi, S., Niquil, N., and Sime-Ngando, T. (2012). Phytoplankton chytridiomycosis: community structure and infectivity of fungal parasites in aquatic ecosystems. *Environ. Microbiol.* 14, 2151–2170. doi: 10.1111/j.1462-2920.2011.02690.x

Ray, A. E., Zaugg, J., Benaud, N., Chelliah, D. S., Bay, S., Wong, H. L., et al. (2022). Atmospheric chemosynthesis is phylogenetically and geographically widespread and contributes significantly to carbon fixation throughout cold deserts. *ISME J.* 16, 2547–2560. doi: 10.1038/s41396-022-01298-5

Rego, A., Raio, F., Martins, T. P., Ribeiro, H., Sousa, A. G., Séneca, J., et al. (2019). Actinobacteria and cyanobacteria diversity in terrestrial Antarctic microenvironments evaluated by culture-dependent and independent methods. *Front. Microbiol.* 10:1018. doi: 10.3389/fmicb.2019.01018

Rignot, E., Jacobs, S., Mouginot, J., and Scheuchl, B. (2013). Ice-shelf melting around Antarctica. *Science* 341, 266–270. doi: 10.1126/science.1235798

Ripley, B. D. (2001). The R project in statistical computing. MSOR connections. *MSOR Connections* 1, 23–25. doi: 10.11120/msor.2001.01010023

Salmaso, N., Cerasino, L., Boscaini, A., and Capelli, C. (2016). Planktic Tychonema (Cyanobacteria) in the large lakes south of the Alps: phylogenetic assessment and toxigenic potential. *FEMS Microbiol. Ecol.* 92:fiw155. doi: 10.1093/femsec/fiw155

Sancho, L. G., Pintado, A., and Green, T. G. A. (2019). Antarctic studies show lichens to be excellent biomonitors of climate change. *Diversity* 11:42. doi: 10.3390/d11030042

Schwartz, E., Van Horn, D. J., Buelow, H. N., Okie, J. G., Gooseff, M. N., Barrett, J. E., et al. (2014). Characterization of growing bacterial populations in McMurdo Dry Valley soils through stable isotope probing with 18O-water. *FEMS Microbiol. Ecol.* 89, 415–425. doi: 10.1111/1574-6941.12349

Sorensen, P. O., Beller, H. R., Bill, M., Bouskill, N. J., Hubbard, S. S., Karaoz, U., et al. (2020). The snowmelt niche differentiates three microbial life strategies that influence soil nitrogen availability during and after winter. *Front. Microbiol.* 11:871. doi: 10.3389/fmicb.2020.00871

Stomeo, F., Makhalanyane, T. P., Valverde, A., Pointing, S. B., Stevens, M. I., Cary, C. S., et al. (2012). Abiotic factors influence microbial diversity in permanently cold soil horizons of a maritime-associated Antarctic Dry Valley. *FEMS Microbiol. Ecol.* 82, 326–340. doi: 10.1111/j.1574-6941.2012.01360.x

Suija, A. (2006). Variation of morphological characters in the lichenicolous ascomycete genus Abrothallus. *Ann. Bot. Fenn.* 43, 193–204. Available at: http://www.jstor.org/stable/23727208.

Van Goethem, M. W., and Cowan, D. A. (2019). "Role of cyanobacteria in the ecology of polar environments" in *The ecological role of micro-organisms in the Antarctic environment*, ed. S. Castro-Sowinski, Springer Polar Sciences. 3–23.

Van Horn, D. J., Okie, J. G., Buelow, H. N., Gooseff, M. N., Barrett, J. E., and Takacs-Vesbach, C. D. (2014). Soil microbial responses to increased moisture and organic resources along a salinity gradient in a polar desert. *Appl. Environ. Microbiol.* 80, 3034–3043. doi: 10.1128/AEM.03414-13

Venables, W., and Ripley, B. D. (2002). *Statistics and computing: modern applied statistics with S*. Springer-Verlag, New York Inc, New York. 978–970.

Vincent, W. F. (2004). *Microbial ecosystems of Antarctica*. Cambridge: Cambridge University Press.

Virginia, R. A., and Wall, D. H. (1999). How soils structure communities in the Antarctic Dry Valleys. *Bioscience* 49, 973–983. doi: 10.2307/1313731

Walker, J. J., and Pace, N. R. (2007). Endolithic microbial ecosystems. *Annu. Rev. Microbiol.* 61, 331–347. doi: 10.1146/annurev.micro.61.080706.093302

Wei, S. T., Lacap-Bugler, D. C., Lau, M. C., Caruso, T., Rao, S., De Los Rios, A., et al. (2016). Taxonomic and functional diversity of soil and hypolithic microbial communities in Miers Valley, McMurdo Dry Valleys, Antarctica. *Front. Microb.* 7:1642. doi: 10.3389/fmicb.2016.01642

White, T. J., Bruns, T., Lee, S., and Taylor, J. (1990). Amplification and direct sequencing of fungal ribosomal RNA genes for phylogenetics. In: M. A. Innis, D. H. Gelfand, J. J. Sninsky and T. J. White, Eds., *PCR protocols: a guide to methods and applications*, Academic Press, New York 315–322.

Wickham, H., Chang, W., and Wickham, M. H. (2016). Package 'ggplot2'. Create elegant data visualisations using the grammar of graphics. *Version* 2, 1–189. Available at: https://ggplot2.tidyverse.org

Wilcoxon, F. (1945). Individual comparisons by ranking methods. *Biom. Bull.* 1, 80–83. doi: 10.2307/3001968

Williamson, B., Kreutz, K. J., Mayewski, P. A., Bertler, N., Sneed, S., Handley, M., et al. (2007). A coastal transect of McMurdo Dry Valleys (Antarctica) snow and firn: marine and terrestrial influences on glaciochemistry. *J. Glaciol.* 53, 681–693. doi: 10.3189/002214307784409225

Zablocki, O., van Zyl, L., Adriaenssens, E. M., Rubagotti, E., Tuffin, M., Cary, S. C., et al. (2014). High-level diversity of tailed phages, eukaryote-associated viruses, and virophage-like elements in the metaviromes of antarctic soils. *Appl. Environ. Microbiol.* 80, 6888–6897. doi: 10.1128/AEM.01525-14

Zhang, Y.-G., Wang, H.-F., Yang, L.-L., Guo, J.-W., Xiao, M., Huang, M.-J., et al. (2016). Ornithinicoccus halotolerans sp. nov., and emended description of the genus Ornithinicoccus. *Int. J. Syst. Evol. Microbiol.* 66, 1894–1899. doi: 10.1099/ijsem.0.000964

frontiers | Frontiers in Microbiology

TYPE Original Research
PUBLISHED 24 August 2023
DOI 10.3389/fmicb.2023.1240798

OPEN ACCESS

EDITED BY
Melina Kerou,
University of Vienna, Austria

REVIEWED BY
John R. Battista,
Louisiana State University, United States
Patricia De Francisco,
Spanish National Research Council (CSIC), Spain
Min-Kyu Kim,
Korea Atomic Energy Research Institute (KAERI), Republic of Korea

*CORRESPONDENCE
Célia V. Romão
✉ cmromao@itqb.unl.pt

RECEIVED 15 June 2023
ACCEPTED 09 August 2023
PUBLISHED 24 August 2023

CITATION
Gouveia AG, Salgueiro BA, Ranmar DO, Antunes WDT, Kirchweger P, Golani O, Wolf SG, Elbaum M, Matias PM and Romão CV (2023) Unraveling the multifaceted resilience of arsenic resistant bacterium *Deinococcus indicus*. *Front. Microbiol.* 14:1240798. doi: 10.3389/fmicb.2023.1240798

Unraveling the multifaceted resilience of arsenic resistant bacterium *Deinococcus indicus*

André G. Gouveia[1], Bruno A. Salgueiro[1], Dean O. Ranmar[2], Wilson D. T. Antunes[3], Peter Kirchweger[4], Ofra Golani[2], Sharon G. Wolf[5], Michael Elbaum[4], Pedro M. Matias[1,6] and Célia V. Romão[1]*

[1]Instituto de Tecnologia Química e Biológica António Xavier (ITQB NOVA), Universidade Nova de Lisboa, Oeiras, Portugal, [2]Department of Life Sciences Core Facilities, Weizmann Institute of Science, Rehovot, Israel, [3]Instituto Universitário Militar, Centro de Investigação da Academia Militar (CINAMIL), Unidade Militar Laboratorial de Defesa Biológica e Química (UMLDBQ), Lisbon, Portugal, [4]Department of Chemical and Biological Physics, Weizmann Institute of Science, Rehovot, Israel, [5]Department of Chemical Research Support, Weizmann Institute of Science, Rehovot, Israel, [6]Instituto de Biologia Experimental e Tecnológica (iBET), Oeiras, Portugal

Arsenic (As) is a toxic heavy metal widely found in the environment that severely undermines the integrity of water resources. Bioremediation of toxic compounds is an appellative sustainable technology with a balanced cost-effective setup. To pave the way for the potential use of *Deinococcus indicus,* an arsenic resistant bacterium, as a platform for arsenic bioremediation, an extensive characterization of its resistance to cellular insults is paramount. A comparative analysis of *D. indicus* cells grown in two rich nutrient media conditions (M53 and TGY) revealed distinct resistance patterns when cells are subjected to stress via UV-C and methyl viologen (MV). Cells grown in M53 demonstrated higher resistance to both UV-C and MV. Moreover, cells grow to higher density upon exposure to 25 mM As(V) in M53 in comparison with TGY. This analysis is pivotal for the culture of microbial species in batch culture bioreactors for bioremediation purposes. We also demonstrate for the first time the presence of polyphosphate granules in *D. indicus* which are also found in a few *Deinococcus* species. To extend our analysis, we also characterized *Di*ArsC2 (arsenate reductase) involved in arsenic detoxification and structurally determined different states, revealing the structural evidence for a catalytic cysteine triple redox system. These results contribute for our understanding into the *D. indicus* resistance mechanism against stress conditions.

KEYWORDS

metals, UV-C, oxidative stress, PolyP granules, arsenate reductase, arsenate

Introduction

Arsenic presents high toxicity and has been classified as carcinogenic, mutagenic and teratogenic element (Machado et al., 1999; National Research Council, 2001; Wang et al., 2017). Due to the electronic configuration of its valence orbitals, it presents a unique chemical nature that allows several changes in oxidation states and bonding configurations, forming a wide diversity of inorganic and organic species (O'Day, 2006). In nature, four oxidation states are found, namely −3 (arsine), 0 (arsenic), +3 (arsenite) and +5 (arsenate); the latter two are of the

utmost interest due to their high toxicity and predominance in aquatic environments (Bissen et al., 2003; James et al., 2017). Arsenite, As(III), is mainly present in groundwater under reducing conditions while arsenate, As(V) is present in oxidizing conditions (Bissen et al., 2003; James et al., 2017). As a metalloid, arsenic is a pnictogen found in group 15 of the periodic table and presents high physicochemical similarities with phosphorus (Dani, 2011; Fekry et al., 2011; Tawfik and Viola, 2011; Varadwaj et al., 2022). The uptake of arsenate by cells follows through the phosphorus pathways mainly by phosphate transporters (Rosenberg et al., 1977; Jiang et al., 2014; Garbinski et al., 2019). Arsenate (AsO_4^{-3}) and phosphate (PO_4^{-3}) share similar chemical speciation, thus as a chemical analog of phosphorus, arsenate is able to act as substrate for several enzymes, leading to harmful cellular effects (Strawn, 2018). To cope with arsenic, most living organisms have evolved mechanisms to circumvent its toxicity. Most bacterial species bear an arsenic resistance (*ars*) operon that encompasses at least three main core genes: (1) an arsenic responsive repressor (*arsR*), (2) As(III) efflux permease (*arsB*) and (3) arsenate reductase (*arsC*) (Páez-Espino et al., 2009; Wang et al., 2016; Yang and Rosen, 2016). *Deinococcus indicus* Wt/1aT was isolated from an arsenic contaminated aquifer in West Bengal, India and it is the first known species of the *Deinococcus* genus able to withstand high concentrations of both arsenate and arsenite (Suresh et al., 2004). *D. indicus* contains the typical *arsRBC* operon that encodes two regulatory proteins (ArsR1 and ArsR2), two arsenate reductases (ArsC2 and ArsC3) and an arsenite efflux pump protein (ArsB). Besides this *ars* operon, it also encodes an additional arsenate reductase, ArsC1 (Suresh et al., 2004; Tawfik and Viola, 2011; Ranganathan et al., 2023).

The *Deinococcus* genus is widespread in the environment, colonizing extreme habitats such as deserts, hot springs and polar regions (Hirsch et al., 2004; De Groot et al., 2005; Makk et al., 2016; Jin et al., 2019). Members of this genus present high resistance to radiation and desiccation (Jin et al., 2019). Nevertheless, with the exception of *Deinococcus radiodurans*, the model organism for radiation resistance, and *Deinococcus geothermalis,* a biofilm forming organism that heavily affects the paper industry, most *Deinococcus* sp. have been poorly characterized to date (Kolari et al., 2001, 2003; Peltola et al., 2008; Slade and Radman, 2011; Gerber et al., 2015; Lim et al., 2019). *D. radiodurans* and *D. geothermalis* have shown high efficiency in the detoxification of toxic materials (Brim et al., 2000, 2003; Misra et al., 2012; Choi et al., 2017; Manobala et al., 2019). Nonetheless, before exploring the bioremediation capabilities of an organism, the characterization of its resistance to cellular insults is imperative. Moreover, the analysis of culture conditions is vital for the application of microbial species in batch bioreactors for toxic waste removal (Tekere, 2019). So far, *D. indicus* ability to survive under UV-B radiation was evaluated and no information is available regarding oxidative stress resistance (Suresh et al., 2004).

Here, *D. indicus* resistance to UV-C, oxidative stress and arsenate was investigated in two rich nutritional media (M53 and TGY). Interestingly, a media-dependent response was observed for UV-C and methyl viologen (MV) damage, with *D. indicus* presenting higher resistance in M53. Upon exposure to As(V), *D. indicus* was able to grow in the presence of 25 mM of As(V) and to tolerate 50 mM of As(V) while *D. radiodurans* had its growth compromised in the presence of 50 fold lower concentration. Polyphosphate granules have been shown to be involved in heavy metal detoxification in different microorganisms, and indeed elemental analysis by cryogenic scanning transmission electron microscopy with energy dispersive X-ray spectroscopy (STEM-EDX) revealed the presence of prominent polyphosphate granules in *D. indicus*. To extend our understanding of arsenic resistance in *D. indicus*, the crystal structure of *Di*ArsC2 arsenate reductase was determined in two states: native and bound to arsenic.

Materials and methods

Deinococcus cell growth

Deinococcus radiodurans R1 and *D. indicus* Wt/1aT (MTCC 4913) were grown either in: M53 medium, 1.0% (w/v) casein yeast peptone (Sigma-Aldrich), 0.5% (w/v) yeast extract (VWR Chemicals), 0.5% (w/v) glucose (Carl Roth) and 0.5% (w/v) NaCl (Merck); or Tryptone Glucose Yeast extract (TGY) medium, 1.0% (w/v) tryptone (VWR Chemicals), 0.5% (w/v) yeast extract (VWR Chemicals) and 0.1% (w/v) glucose (Carl Roth). For all assays, cells were grown at 30°C and 150 rpm agitation; for solid cultures, 1.5% (w/v) agar-agar (Carl Roth) was added. For each assay, two sequential subcultures were grown for 14–16 h prior to the final culture. Final cultures were diluted to an early-exponential phase either (Optical density at 600 nm (OD_{600}) of 0.2) for arsenate exposure growth curves and STEM-EDX or (OD_{600} = 0.5) for oxidative stress, in-plate arsenate stress and UV assays.

Oxidative and arsenate stress response

Oxidative and arsenate stress assays were performed by adapting the disk diffusion method (Bauer et al., 1966; Hudzicki, 2012). Briefly, 400 µl of cells grown in either M53 or TGY (at an OD_{600} = 2) were evenly spread on the surface of an agar plate (120.5 × 120.5 mm) using a cotton swab and allowed to dry for 15 min before the application of the disks (6 mm, PRAT DUMAS). Afterwards, oxidative stress inducer compounds or arsenic (20 µl) were applied on top of the disk in increasing concentrations. Plates were incubated for 3 days and halos were measured using Fiji/ImageJ (Schindelin et al., 2012). Oxidative stress compounds: (1) Methyl viologen dichloride, MV ($C_{12}H_{14}Cl_2N_2 \cdot xH_2O$, Sigma-Aldrich); (2) Hydrogen peroxide 30% (w/w), H_2O_2 (Sigma-Aldrich). Arsenic stress compound: sodium arsenate dibasic heptahydrate 98%, As(V), ($HAsNa_2O_4 \cdot 7H_2O$, Sigma Aldrich).

UV-C radiation survival curves

Ultraviolet (UV) irradiations were performed at UV-C (254 nm) with a fluence of 3 mW/cm^2 throughout the assay. Fluence was assessed using a MS-100 optical radiometer with a MS 125 UVC sensor (Ultra-Violet Products, Upland, CA). *D. indicus* cells grown in either M53 and TGY (at an OD_{600} = 2) were serially diluted and plated in duplicate for each dose. Plates were air dried for 15 min and placed under the UV lamp to be exposed from 300 to 1800 J/m^2 (in increments of 300 J/m^2 which corresponds to an exposure of 10 s). Afterwards, plates were incubated for 3 days and the colony forming

units (CFU) were assessed. The average CFU mL^{-1} of non-irradiated sample aliquots represented 100% survival. The surviving fraction at a given dose is the average CFU mL^{-1} from each irradiated sample (N) divided by the average CFU mL^{-1} of the non-irradiated sample (N_0). Survival curves were obtained by plotting the logarithm of N/N_0 versus the dose. To determine the survival curve parameters, the multi-hit model was applied (equation 1), S(D) = Survival fraction (where 1 is 100%); D = Dose (J/m^2); K = inactivation constant and n = extrapolation number (obtained by the intercept of the extrapolated semi-log straight-line), (Severin et al., 1983; Kowalski et al., 2000; Kowalski, 2009). For statistical intercomparison of the different D_{10} values extrapolated from the survival curves of M53 and TGY a Student's t-test was used and $P \leq 0.05$ were considered statistically significant (De La Vega et al., 2005).

$$S(D) = 1 - \left(1 - e^{-kD}\right)^n \quad (1)$$

Arsenic resistance growth curves

Arsenic resistance was assessed by adding As(V) to broth cultures (OD_{600} = 0.3) for both M53 and TGY. *D. indicus* cells were incubated with 10, 25 and 50 mM while *D. radiodurans* was incubated with 0.05, 0.5, 1, 5, 10, and 20 mM of As(V). Growth curves were obtained by plotting the measured OD_{600} versus time.

SEM of *Deinococcus indicus*

Deinococcus indicus cells were grown in M53 or TGY in 24 well plates for 3 days at 30°C. Grown cells were washed with Phosphate Buffer Saline (PBS) and applied over a lamella. Samples were fixed using a mixture of 2.5% glutaraldehyde and 1% formaldehyde in 0.1 M sodium cacodylate buffer for 1 h at room temperature. Afterwards, samples were washed 3 times with 0.1 M of sodium cacodylate buffer and dehydrated by sequential washing with increasing concentration of ethanol solutions (50, 70, 90, and 100%). Ethanol was removed and tert-butyl alcohol was added. Samples were incubated at 4°C for 30 min followed by 1 h in a vacuum desiccator and kept at room temperature until the scanning electron microscopy (SEM) analyses were performed. Samples were incubated for 10 min with 2% solution of osmium tetroxide and gold sputtered with 8 nm gold in an electron sputter (Cressington 108). Imaging was performed using a Hitachi TM3030Plus scanning electron microscope, at 1.5 kV.

STEM imaging and EDX of *Deinococcus indicus*

Deinococcus indicus cells were grown in M53 broth media (OD_{600} of 0.3) and washed twice with M53 at 4000 rpm, 4°C. Afterwards, cells were diluted to an appropriated concentration and 4 µL deposited onto a glow-discharged Quantifoil copper grid. The grids were blotted, and plunged into liquid ethane with an automated plunger (EM-GP, Leica Microsystems). STEM imaging was performed under cryogenic conditions with a field-emission Talos F200X (S)TEM microscope (Thermo Fisher Scientific) at 200 kV accelerating voltage (extraction voltage 3,850 V, gun lens 4, spot size 9), with a condenser aperture of 70 µm in microprobe mode with a semi convergence angle of 2.1 mrad. Energy-dispersive X-ray spectroscopy (EDX) was performed using an energy dispersive spectrometer encompassing a Super-X G2 detector that features 4 silicon drift detector (SDDs) for substantially enhanced sensitivity, which is critical for trace element detection, with 8 µs dwell time per pixel, and dispersion of 5 eV per channel. Acquired images and EDX data were processed using Velox™ (Thermo Fisher Scientific) software followed by analysis in ImageJ (Schindelin et al., 2012).

Co-localized *Deinococcus indicus*-granule size metrics

To identify *D. indicus* cells and the granules residing within them, grids were imaged using a Talos Arctica 200 kV FEG STEM (Thermo Fisher Scientific) applying the same settings described above with a few variations: spot size 4, camera length 160 mm and 6.66 nm pixel size with 1 µs dwell time per pixel. To quantify the size and distribution of granules within the bacteria, we used tiling and stitching images taken using TFS Tomography software to cover large field of view with multiple bacteria. Stitching was done using Fiji Grid/Collection stitching plugin (Preibisch et al., 2009). Segmentation of the individual bacteria and individual granules residing within them was performed and the number of granules and their average and total size within each bacterium was measured. To segment the bacteria and granules, we used a workflow combining Ilastik (Berg et al., 2019), pixel classifier followed by further processing using dedicated Fiji macro (Schindelin et al., 2012). We used multiple fields of view from different conditions for training two-stage machine-learning classifier in Ilastik "autocontext" approach to classify pixels into four categories: bacteria, granules, background and unclassified. The trained classifier was applied to the stitched images in Fiji (Schindelin et al., 2012). Bacteria were segmented based on connected component analysis of a filled mask of all pixels classified as bacteria, followed by size ($1.6 < \text{size}\ [\mu m^2] < 6$) and shape filtering (circularity >0.2). Granules were then segmented based on connected component analysis of a mask of all pixels classified as granules within segmented bacteria and further filtered by size ($0.012 < \text{size}\ [\mu m^2] < 0.12$) and shape (circularity >0.3). Manual correction was applied to correct the segmentation of some missed or falsely detected bacteria. The size and number of all valid bacteria and granules were extracted and analyzed.

Sequence alignment and phylogenetic tree

Multiple sequence alignments were performed using ClustalW (Thompson et al., 1994). Aligned sequences were used as input and the phylogenetic tree was generated using maximum likelihood (ML) in IQ-TREE2 (version 2.2.2.6) (Minh et al., 2020), software with the mod LG + G4 substitution model. The model was selected by running the first tree using the model finder option (Kalyaanamoorthy et al., 2017). The final tree was generated by performing bootstrap analysis of 1,000 data sets and was treated and displayed using the Interactive Tree Of Life (iTOL) (version 6) web service (Letunic and Bork, 2021).

Protein expression and purification

*Di*ArsC2 gene was cloned into a pET28a(+) plasmid that contains an His-tag followed by a TEV cleavage site (GenScript Inc.). The overexpression of *Di*ArsC2 was obtained in *Escherichia coli* BL21 (Gold) cells transformed with the plasmid pET28a(+)-*Di*ArsC2 and grown in Luria-Bertani (LB) medium at 37°C, 180 rpm. Cells at an OD_{600} of 0.7 were induced with 500 µM of isopropyl *β*-D-thiogalactopyranoside (NZYTech) and grown overnight at 20°C. Afterward, the cells were harvested and resuspended in lysis buffer [20 mM HEPES pH 7, 10% glycerol, 300 mM NaCl, 10 mM $MgCl_2$, 1 µg/ml DNase I and 0.1 mg/ml Lysozyme (Sigma-Aldrich)]. Cells were disrupted by 5 cycles of freeze and thaw, and the soluble fraction containing overexpressed *Di*ArsC2 was obtained by centrifugation at 25,931 x *g*, 20 min at 4°C. The supernatant was loaded onto a His Trap excel column (Cytiva) using as binding buffer 20 mM HEPES pH 7, 250 mM NaCl, 10% (v/v) glycerol, and 10 mM imidazole, and the elution buffer was 20 mM HEPES pH 7, 250 mM NaCl, 10% (v/v) glycerol and 1 M imidazole. *Di*ArsC2 eluted at 300 mM of imidazole and was further loaded onto a desalting column (Hiprep^{tm} 26/10 Desalting, Cytiva) using 20 mM HEPES pH 7, 250 mM NaCl, 10% glycerol (v/v). Afterward, the *Di*ArsC2 His-tag was cleaved by adding Tobacco Etch Virus (TEV) protease (Sigma) at 12°C with gentle shaking for 14 h. *Di*ArsC2 was loaded onto His Trap excel (Cytiva) using the same buffers as described above. The final purification step was done by size exclusion chromatography (Superdex 75 10/300 GL, Cytiva), with the buffer 20 mM HEPES pH 7 and 250 mM NaCl. The protein was pure as judged by sodium dodecyl sulphate polyacrylamide gel electrophoresis analysis and concentrated to 21 mg/mL prior to being used for crystallization trials.

Crystallization and X-ray diffraction data collection

Crystallization screens for *Di*ArsC2 were setup at the nL scale in a Crystallization Robot Mosquito LCP (SPT Labtech) with triple sitting drop 96-well plate (TTP Labtech) and using commercial screens Structure 1 and 2 (Molecular Dimensions). Needle- and plate-like crystals appeared in several conditions, three of which were selected for further optimization: #37 (0.2 M Sodium acetate trihydrate, 0.1 M Tris pH 8.5 and 30% (w/v) PEG 4000); #46 (0.05 M Potassium phosphate monobasic and 20% (w/v) PEG 8000); and #47 (15% (w/v) PEG1500). These were optimized by vapor diffusion using 2 µl hanging drops equilibrated against 500 µl reservoir solution in XRL 24-well crystallization plates (Molecular Dimensions), at 20 and 4°C with varying ratios of protein and crystallization solution in each drop. For the final optimized crystallization condition, a ratio of 1:1 (protein to crystallization solution) with 0.2 M Sodium acetate trihydrate, 0.1 M Tris pH 8.5 and 20% (w/v) PEG 4000 for *Di*ArsC2 native (henceforth referred to as *Di*ArsC2) at 4°C. In the case of *Di*ArsC2 bound to arsenic (*Di*ArsC2-As), a ratio of 1:0.8 (protein to crystallization solution) was used using 0.2 M Sodium acetate trihydrate, 0.1 M Tris pH 8.5 and 30% (w/v) PEG 4000, plus 0.2 µl of 0.1 M As(V) at 20°C. *Di*ArsC2 crystals appeared after 7 days while *Di*ArsC2-As crystals appeared after 3 days. Crystals were dipped in a cryoprotecting solution that consisted of the crystallization buffer supplemented with 10% (v/v) PEG 400 and flash-cooled in liquid nitrogen.

Structure determination, refinement, and quality assessment

*Di*ArsC2 crystals were initially screened in-house using Cu Kα radiation with 1.5418 Å wavelength in a Bruker AXS Proteum Pt135 CCD detector system coupled to an Incoatec Microfocus X-ray Source with Montel mirrors. Bruker Proteum software package were used to process and scale the images. The structure was solved by Molecular Replacement using MORDA (Vagin and Lebedev, 2015) and using as phasing model the structure of arsenate reductase from *Bacillus subtilis* (PDB code: 1JL3) (Bennett et al., 2001). In addition *Di*ArsC2-As crystal was also tested in-house and the structure was solved by PHASER (McCoy et al., 2007) in the PHENIX suite (Adams et al., 2010; Liebschner et al., 2019) using the *Di*ArsC2 as phasing model.

Diffraction data to higher resolution were collected at the XALOC beamline BL13 of the ALBA Synchrotron (Barcelona, Spain) (Juanhuix et al., 2014). The images were processed with autoPROC (Vonrhein et al., 2011), which makes use of XDS (Kabsch, 2010) and the CCP4 suite (Potterton et al., 2003) for integration and conversion of integrated intensities to structure factors. Each dataset was integrated with XDS, followed by POINTLESS (Evans, 2011) for space-group determination, scaling and merging with AIMLESS and application of an anisotropic resolution cut-off at $CC^{1/2} < 0.3$ with STARANISO (Tickle et al., 2018). The crystals belonged to the monoclinic space group $P2_1$ and contained two molecules per asymmetric unit, as estimated by the Mathews coefficient probability (Matthews, 1968; Kantardjieff and Rupp, 2003). The data processing statistics are given in Supplementary Table S1. Higher resolution crystallographic structures for both *Di*ArsC2 and *Di*ArsC2-As were determined by molecular replacement using PHASER-MR (McCoy et al., 2007) via the CCP4 Graphics User Interface (Potterton et al., 2003) or PHENIX Suite (Adams et al., 2010; Liebschner et al., 2019), and using the *Di*ArsC2-As structure obtained from the in-house data as the phasing model. For *Di*ArsC2, an initial refinement was done with REFMAC (Murshudov et al., 1997) and continued with PHENIX.REFINE (Terwilliger et al., 2007; Adams et al., 2010; Afonine et al., 2012) while for *Di*ArsC2-As refinements were done using PHENIX.REFINE. Throughout the refinement, the model was periodically checked and corrected with COOT against σ_A-weighted $2|F_o|-|F_c|$ and $|F_o|-|F_c|$ electron-density maps. Solvent molecules were added manually by inspection of electron-density maps in COOT (Emsley and Cowtan, 2004). TLS (translation-libration-screw) reciprocal space refinement was carried out for both structures. Hydrogen atoms were included in calculated positions with the PHENIX.READYSET tool and isotropic displacement parameters (ADPs) were refined for all non-hydrogen atoms. The final structures were validated using MOLPROBITY (Chen et al., 2010). Refinement statistics are given in Supplementary Table S2. Structure factors and associated structure coordinates of *Di*ArsC2 and *Di*ArsC2-As were deposited in the Protein Data bank (Berman et al., 2003) with accession code 8P6M and 8P5N, respectively (Supplementary Table S2).

A simple ensemble refinement protocol in PHENIX was run for both final structures *Di*ArsC2 and *Di*ArsC2-As considering one

domain per independent molecule in the asymmetric unit, of the crystal structure, and using 80% of the non-hydrogen atoms to include in the TLS fitting of the atomic displacement parameters (ADPs) from a previous refinement with isotropic ADPs (Burnley et al., 2012). The secondary structure was determined running PROCHECK within CCP4 Graphics User Interface (Laskowski et al., 1993; Potterton et al., 2003). Figures of the structures were prepared using PyMOL (Delano, 2022).

Results

Deinococcus indicus response to oxidative stress and UV-C

Deinococcus species are known for their extreme tolerance to radiation and oxidative stress (Lim et al., 2019). To evaluate *D. indicus* tolerance, we subjected the cells grown in M53 and TGY to hydrogen peroxide (H_2O_2) and methyl viologen (MV). MV is known to catalyze the formation of superoxide anion ($O^{2\bullet-}$), (Halliwell and Gutteridge, 1999; Halliwell, 2006). *D. indicus* cells presented higher resistance to H_2O_2 than to MV in both media (Figure 1). Upon exposure to MV, cells grown in M53 showed higher resistance than the ones grown in TGY. In fact, at 20 mM of MV, cells in M53 were neither inhibited nor had their cell growth compromised. However, the same was not observed when directly applying H_2O_2, in which case the cells responded in the same way independently of the culture medium (Figure 1B). *D. indicus* cells were also exposed to UV-C irradiation. It is known that when UV radiation is applied to microbial populations a slight delay is often observed before the onset of an exponential decay (Cerf, 1977; Munakata et al., 1991; Pruitt and Kamau, 1993; Kowalski et al., 2000; Kowalski, 2009). This effect is usually named as a shoulder curve due to its shape and for this reason the multi-hit model was applied to determine curve parameters and extrapolate the D_{10} (i.e., the dose required to yield 10% survival) for the cells grown in both culture media (Severin et al., 1983; Kowalski et al., 2000; Kowalski, 2009). Interestingly, in M53 cells exhibited significant higher resistance to UV-C in contrast to the ones grown in TGY (Figure 2). This was verified by calculating the D_{10} values ($P \leq 0.05$): in M53 a dose of 809 ± 66 J/m^2 (30s exposure) is required to eliminate 90% of cells, while in TGY 619 ± 82 J/m^2 (20s exposure) was sufficient to achieve the same result.

Arsenate tolerance assays

Deinococcus indicus Wt/1aT was originally isolated from an aquifer in West Bengal, India, and it was reported to survive 10 mM of As(V) in nutrient broth medium (Suresh et al., 2004). To evaluate its ability to cope with higher concentrations of As(V), *D. indicus* and *D. radiodurans* (non-arsenic resistant specie) were exposed to As(V) in their early exponential growth phase ($OD_{600} = 0.3$). *D. indicus* was able to grow in the presence of 25 mM As(V) in both media cultures. However, an extended lag phase was observed and at 50 mM As(V),

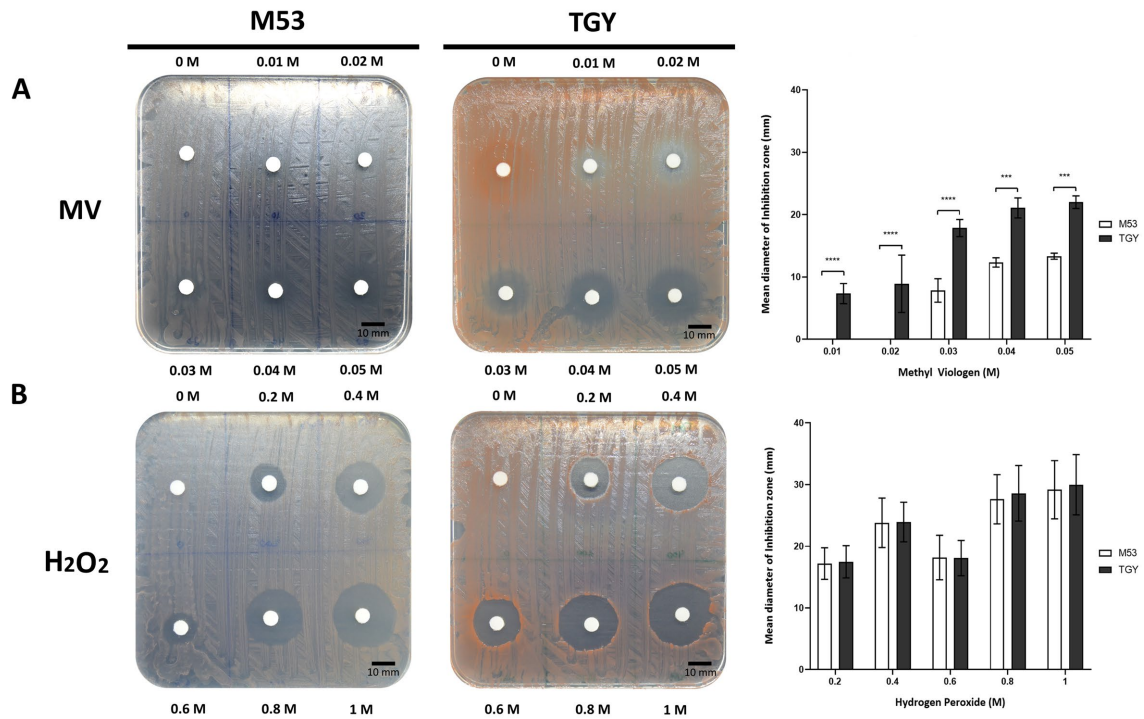

FIGURE 1
Survival of *D. indicus* at mid-exponential phase (OD_{600} = 2.0) to different oxidative stress conditions. **(A)** Cells exposed to methyl viologen (MV). **(B)** Cells exposed to hydrogen peroxide (H_2O_2). **(A,B)** Representative images of adapted Kirby-Bauer assays to cells grown in M53 and TGY exposed to increasing concentrations (left and middle panels). Inhibition halos correspond to the mean diameter of the inhibition zone (mm), (right panel). The error bars represent the standard deviations from three replicates of four independent experiments (n = 4). p-values were obtained by Two-Way ANOVA. $p \leq 0.001$ and $p \leq 0.0001$ are represented as: *** and ****, respectively.

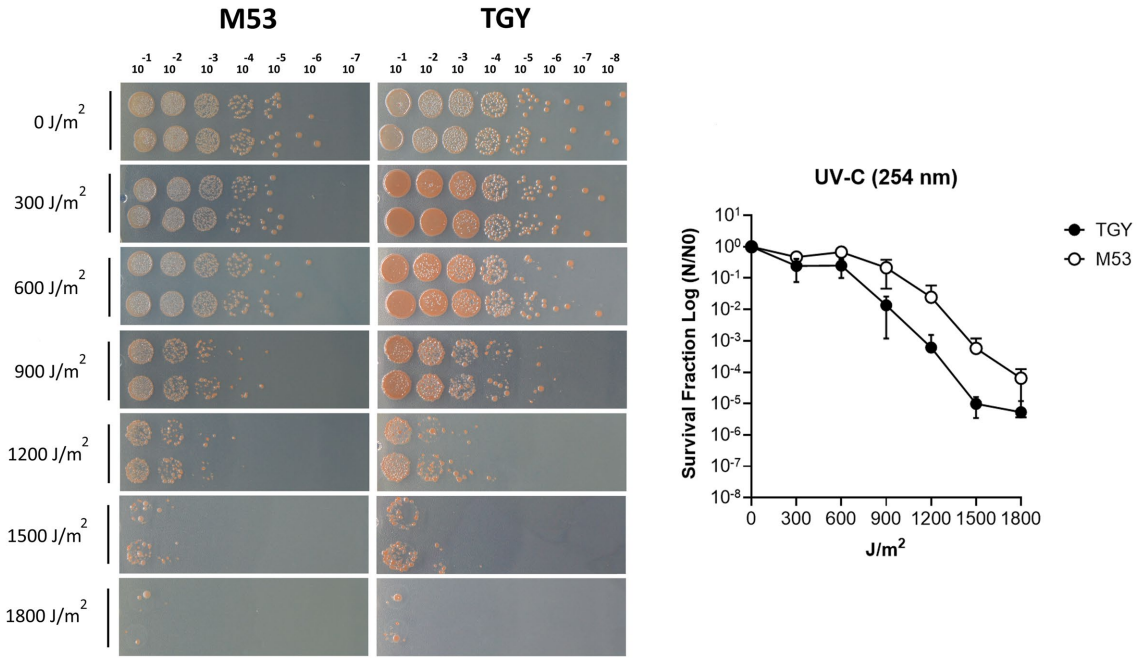

FIGURE 2
UV-C irradiation survival of *D. indicus* in M53 and TGY. **(A)** Representative image of *D. indicus* CFUs exposed to increasing doses of UV-C (254 nm) radiation in M53 and TGY. **(B)** Survival curves of *D. indicus*. The survival fraction was calculated by dividing the CFUs of UV-C irradiated cells (N) by the CFUs of non-irradiated cells (N_0). Filled circles correspond to cells grown in TGY while open circles correspond to cells grown in M53. The error bars represent the standard deviation of four independent experiments (n = 4).

cells were unable to grow (Figure 3A). Nevertheless, cells harvested and applied to fresh media were able to recover their growth in normal conditions (Supplementary Figure S1). Regarding *D. radiodurans*, different As(V) concentrations were tested, namely 0.05, 0.5, 1, 5, 10, and 20 mM, our results show that in the presence of 5, 10, or 20 mM, the cells are not able to recover the growth after 24H (Figure 3B). Cells were only able to display normal growth in 50 µM As(V), a 500-fold lower concentration than applied to *D. indicus*. When exposed to 1 mM, an evident decrease in growth was observed (Figure 3B). This observation was more evident in cells grown in TGY than for those grown in M53.

To further assess their resistance to As(V) in a solid matrix, *D. indicus* and *D. radiodurans* were exposed to increasing concentrations of arsenate ranging from 200 mM to 1 M (Figure 4). Interestingly, in the solid matrix *D. indicus* was not fully inhibited by 1 M of As(V) in either culture medium. Nevertheless, partial inhibition halos (reduction of cellular density) were observed in cells grown in M53 upon submission to 600 mM to 1 M of As(V). In contrast, *D. radiodurans* is inhibited by 200 mM of arsenate (Figure 4).

SEM of *Deinococcus indicus*

Previously, it was demonstrated that *D. indicus* presents growth media-induced morphotypes displaying a reversible behavior from single cells to multi-cell chain morphology (Chauhan et al., 2019b). To explore this capacity and understand if differences in morphotypes account for the behavior disparities observed against cell insults, *D. indicus* grown in M53 and TGY media were observed through Scanning Electron Microscopy (SEM). SEM data revealed small differences on the size of the cells, where *D. indicus* grown in TGY presented slightly lower cell lengths. However, no differences in cell chain clustering were observed (Figure 5). Nevertheless, the addition of 500 µM $MnCl_2$ seems to affect cells grown in TGY, where cell septation is compromised and cell length is vastly increased (Supplementary Figure S2).

Cryo-STEM EDX of *Deinococcus indicus*

Polyphosphate-like granules (pPLGs) are known to be involved in the sequestration of cation ions as well as in heavy-metal detoxification (Peverly et al., 1978; Urech et al., 1978; Scott and Palmer, 1990; Keasling, 1997; Kulakovskaya, 2018). *D. radiodurans, Deinococcus murrayi* and *Deinococcus proteolyticus* present pPLGs in their native compositions, but no information is available for *D. indicus* (Thornley et al., 1965; Sleytr et al., 1976; Ferreira et al., 1997; Eltsov and Dubochet, 2005; Copeland et al., 2012). Wolf et al. (2015) was carried out to image *D. indicus* in native conditions at the early-exponential phase in M53 medium. Through the ImageJ macro previously trained using ilastik "autocontext" approach, we were able to rapidly quantify and segment *D. indicus* cells and their granules using Cryo-STEM stitched images (Figure 6A). We observed a wide heterogeneity of electron dense granules distribution ranging from 0 to 8 granules per cell (Figure 6B). Overall, from the 435 cells analyzed 31.8% of the cells had no granules, followed by 17.2% of the cells containing 1 or 2 granules. Only 1.4 and 0.5% of the cells contained 7 and 8 granules, respectively (Figure 6B). The average granule area (n = 803) was 0.040 ± 0.019 µm^2 with the smallest granules measuring 0.012 µm^2 while the biggest granule measuring 0.107 µm^2 (Figure 6C). EDX

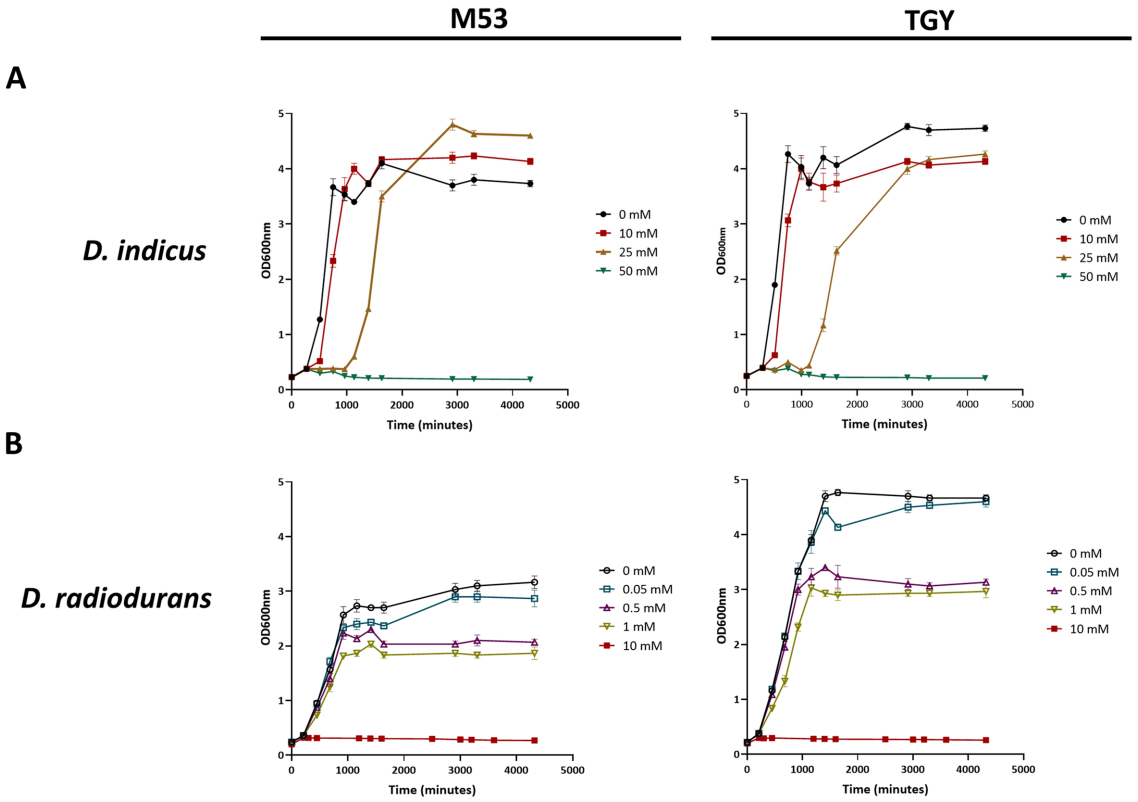

FIGURE 3
Growth curves in TGY and M53 media cultures of *Deinococcus* cells exposed to increasing concentrations of As(V) at an early exponential phase (OD_{600} = 0.3). **(A)** *D. indicus*, filled circles correspond to 0 mM of As(V), filled squares correspond to 10 mM of As(V), filled right side up triangles correspond to 25 mM of As(V) and filled upside down triangles correspond to 50 mM of As(V). **(B)** *D. radiodurans*, open circles correspond to 0 mM of As(V), open squares correspond to 0.05 mM of As(V), open right side up triangles correspond to 0.5 mM of As(V), open upside down triangles correspond to 1 mM of As(V) and filled squares correspond to 10 mM of As(V).

spectral analysis detected the enrichment in phosphorus of the intracellular granules, confirming that these structures are indeed polyphosphate-like granules (pPLGs) (Figure 7). The main counter ion found was magnesium (Supplementary Table S3).

*Di*ArsC2 (arsenate reductase) phylogenetic analysis

In order to explore the difference between the two species, *D. radiodurans* and *D. indicus*, to the arsenate resistance we analyzed the arsenate reductases that belong to the *ars* operon, which are able to convert As(V) into As(III) (Mukhopadhyay and Rosen, 2002). It is predicted that *D. indicus* possesses three genes that encode cytosolic arsenate reductases, *Di*ArsC1, *Di*ArsC2, and *Di*ArsC3 while *D. radiodurans* possesses two arsenate reductases, *Dr*ArsC1 and *Dr*ArsC2 (Figure 8). There are three families of cytosolic arsenate reductases: one belongs to the *E. coli* R773 plasmid and comprises glutaredoxin (Grx)-coupled enzymes, while another class belongs to the *Staphylococcus aureus* Plasmid pI258 comprising the thioredoxin (Trx)-coupled enzymes (Ji et al., 1994; Oden et al., 1994; Shi et al., 1999; Messens et al., 2002a; Messens and Silver, 2006) and the final class belongs to eukaryotic organisms, encompassing the ACR2p from *Saccharomyces cerevisiae* (Mukhopadhyay and Rosen, 1998; Mukhopadhyay et al., 2000). A sequence analysis of the different protein sequence, shows that the three arsenate reductases from *D. indicus, Di*ArsC1, *Di*ArsC2 and *Di*ArsC3 belong to three branches (Figure 8). Interestingly, *Di*ArsC1 and *Dr*ArsC1 branch closely to the *E. coli* ArsC from the Grx-linked prokaryotic family (Figure 8; Gladysheva et al., 1994; Rosen, 1999). *Di*ArsC3 and *Dr*ArsC2 branch closely to *Thermus thermophilus* ArsC that belongs to the Trx-linked prokaryotic ArsC reductases family. *Di*ArsC2 branch closely to *Desulfovibrio alaskensis* G20 ArsC3 (Nunes et al., 2014), which are in the main branch with *S. aureus* pI258 ArsC (Ji et al., 1994; Rosen, 1999; Figure 8). Since *Di*ArsC2 did not cluster together with any of *D. radiodurans* ArsCs, we decided to further unveil the structural mechanism for arsenate detoxification.

*Di*ArsC2 and *Di*ArsC2-As structural insights

The crystal structures of *Di*ArsC2 and *Di*ArsC2-As were determined and refined at resolutions of 1.65 and 1.50 Å, respectively. The space group of both crystal structures is $P2_1$, presenting two molecules in the asymmetric unit. *Di*ArsC2 and *Di*ArsC2-As structures were refined to final R_{factor}/R_{free} values of 0.224/0.254 and 0.152/0.172, respectively (Supplementary Table S2). The superposition of both chains based on the secondary structure matching algorithm yields a root-mean-square deviation (r.m.s.d.) of 0.6 Å between the superimposed C^{α} carbon atoms and 127 aligned amino acid residues.

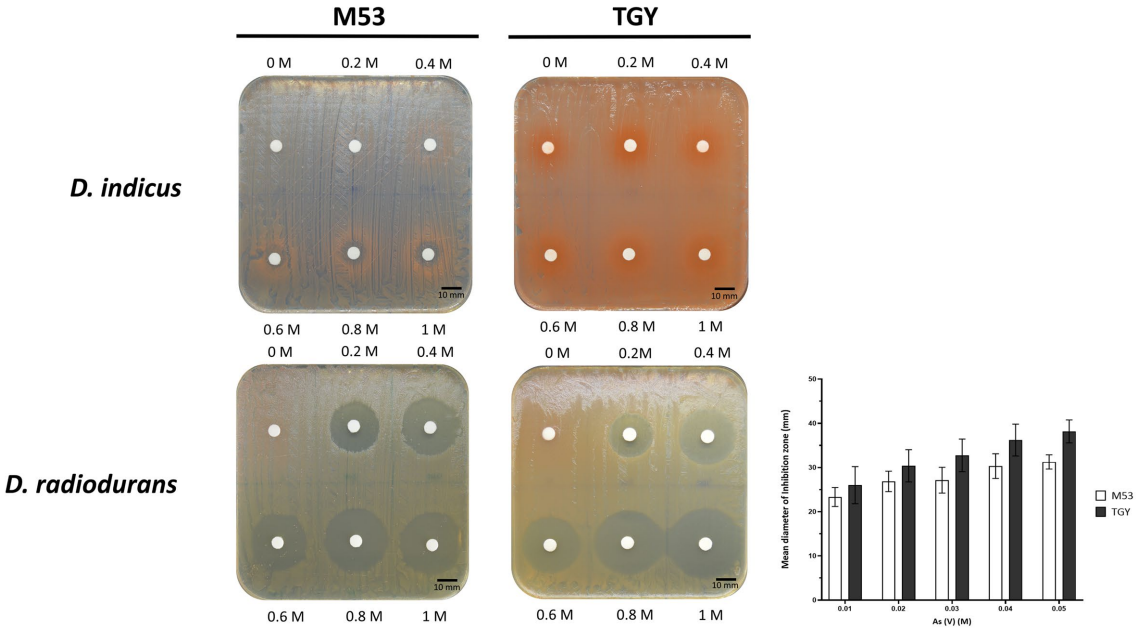

FIGURE 4
Survival of *D. indicus* and *D. radiodurans* in solid matrix (M53 and TGY culture media) in response to As(V). Cells at mid-exponential phase (OD_{600} = 2.0) were exposed to increasing concentrations of As(V) using an adapted Kirby-Bauer assay (Bauer et al., 1966; Hudzicki, 2012). Inhibition halos correspond to the mean diameter of inhibition zone (mm). The error bars represent the standard deviations from three replicates of four independent experiments (n = 4).

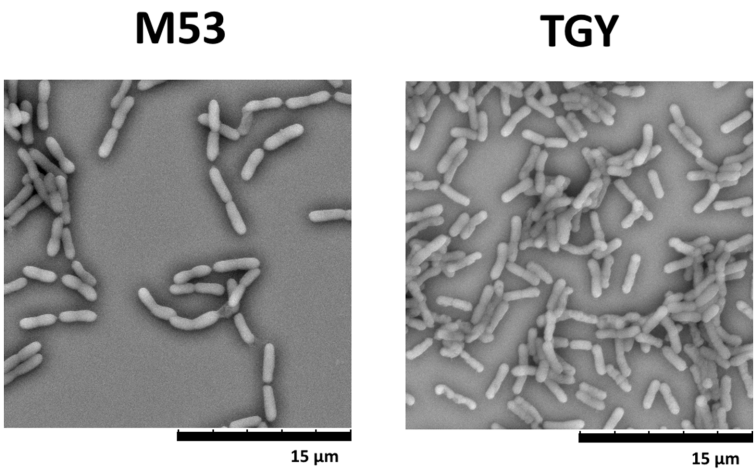

FIGURE 5
Scanning electron microscopy (SEM) images of *D. indicus* cells grown in M53 and TGY.

The largest deviations are in a loop region between residues 88–100 that presents high flexibility and for *Di*ArsC2 it lacks electron density for this region (Figures 9A,B). In fact, in *Di*ArsC2 it was not possible to build the protein chain between the residues 89–96 for Chain A and 89–93 for Chain B (Figure 9B). Thus, the structural analysis for both structures were performed with Chain B. Ensemble refinements (Burnley et al., 2012) were performed for *Di*ArsC2 and *Di*ArsC2-As (leading to R_{factor}/R_{free} values of 0.221/0.255 and 0.160/0.177 respectively) where the most flexible regions were residues 31–36 and the loop 86–97 that contains the two conserved cysteines (Cys87 and Cys94) involved in As(V) reduction (Figures 9C, 10). The loop that contains the conserved catalytic Cys15 does not show a high degree of structural flexibility between the two structures here presented.

*Di*ArsC2 structures are composed of an α/β domain and four parallel β-strands which are flanked by three helices and two small helices (Figures 10, 11). These crystal structures are similar to the arsenate reductases from *B. subtilis* (Bennett et al., 2001), (PDB 1JL3) and *S. aureus*, (PDB 1LJL) (Messens et al., 2002b). The crystal structures of *Di*ArsC2 and *Di*ArsC2-As presented an r.m.s.d. value of 1.3 Å with 127 aligned amino acid residues with the arsenate reductases from *B. subtilis* (Bennett et al., 2001) (PDB 1JL3). The arsenate reductase from *S. aureus*, (PDB 1LJL) presents an r.m.s.d.

10.3389/fmicb.2023.1240798

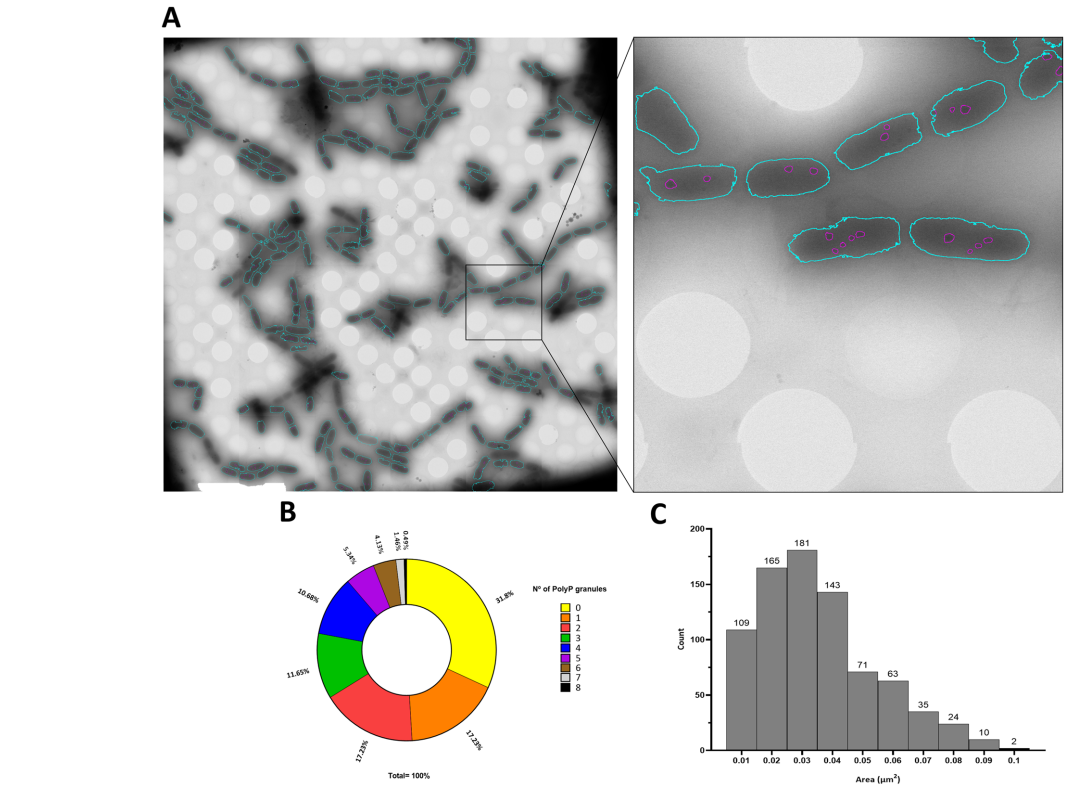

FIGURE 6
PolyP granules analysis by Cryo-STEM. **(A)** *D. indicus* STEM stitched image segmented trough the trained classifier, detected bacteria are colored in blue and granules within the bacteria are colored in purple. **(B)** Percentage of cells containing PolyP granules. **(C)** Area (µm²) of *D. indicus* PolyP granules.

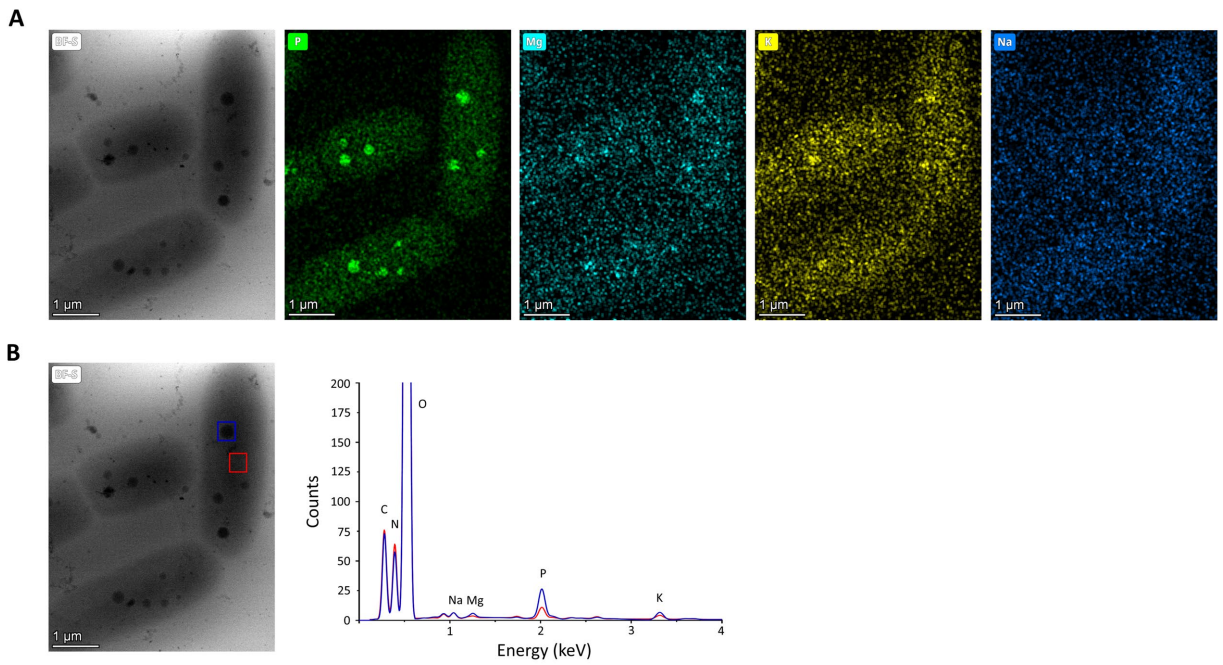

FIGURE 7
EDX analysis of *D. indicus* cells grown in M53. **(A)** Cryo-STEM images of control condition for which EDX spectra were measured, and elemental mapping for phosphorus (green), magnesium (cyan), potassium (yellow), and sodium (dark blue). **(B)** Blue square highlights a polyphosphate granule and red square a cytosol region, used to obtain the superimposed EDX spectra the polyphosphate granule (blue line) and the cytosol (red line).

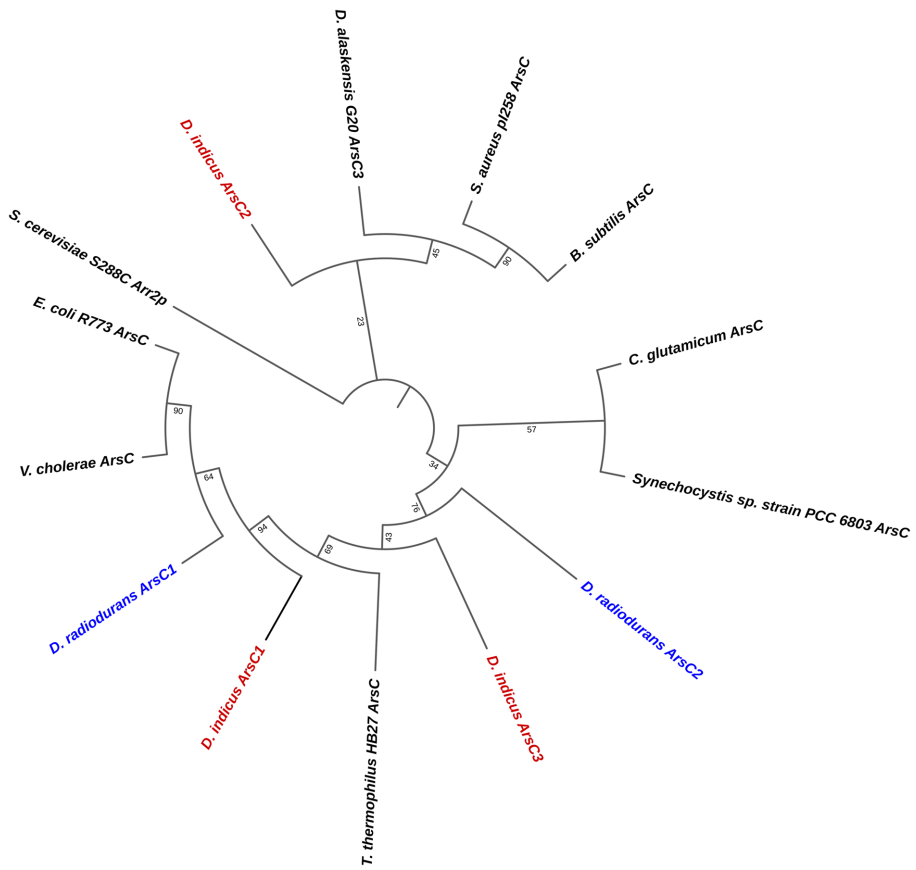

FIGURE 8
Phylogenetic tree of the three families of cytosolic arsenate reductases. Accession numbers for the amino acid sequences are: *B. subtilis* (P45947), *Corynebacterium glutamicum* (Q8NQC6), *D. indicus* ArsC1 (GHG23001.1), *D. indicus* ArsC2 (WP_088246862.1), *D. indicus* ArsC3 (WP_191300003.1), *D. radiodurans* ArsC1 (UDK99340.1), *D. radiodurans* ArsC2 (ANC72982.1), *Desulfovibrio alaskensis G20* (WP_011368603.1), *E. coli* R773 (P08692.1), *Saccharomyces cerevisiae* S288C Arr2P (DAA11614.1) *S. aureus* pI258 (P0A006), *Synechocystis* sp. PCC 6803 (P74313),*Thermus thermophilus* HB27 (AAS81844.1) and *Vibrio cholerae* (Q9KQ39). The three *D. indicus* ArsC and two *D. radiodurans* ArsC are shown in red and blue, respectively.

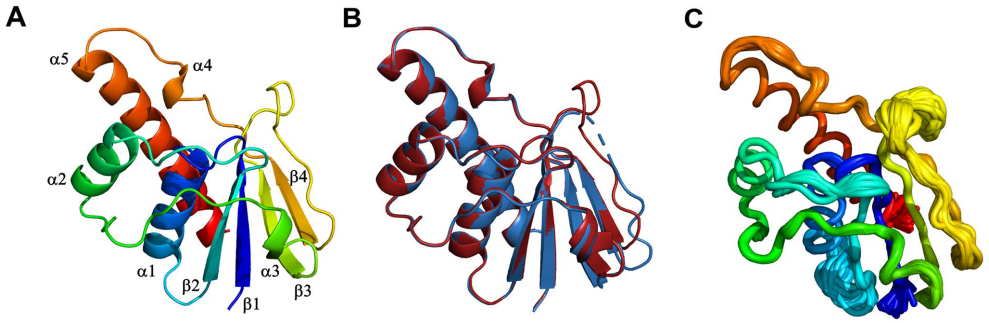

FIGURE 9
X-ray crystal structure of *D. indicus* arsenate reductase ArsC2. **(A)** Cartoon representation of the *Di*ArsC2-As, rainbow colored from blue (N-terminal) to red (C-terminal). **(B)** Superposition of the *Di*ArsC2-As (red) with the *Di*ArsC2 (blue) monomers. **(C)** C^{α} tube representation of the *Di*ArsC2-As monomer from the Ensemble refinement calculations.

value of 1.0 Å and 119 aligned amino acid residues with *Di*ArsC2 and an r.m.s.d. value of 1.2 Å and 121 aligned amino acid residues with *Di*ArsC2-As.

The reduction mechanism of arsenate involves three cysteines, Cys15, Cys87, and Cys94. In the case of the *Di*ArsC2-As structure, a disulfide bridge between Cys87 and Cys94 is formed. Although the protein was co-crystallized in the presence of arsenate (AsO_4^{3-}), the density observed close to the catalytic Cys15 suggests the presence of $AsHO_3^{2-}$. This molecule is located in a positively charged pocket and establishes a network of hydrogen bonds with the main-chain nitrogen atoms of residues G_{17}NTARS$_{22}$, Thr16 and Ser22 hydroxyl and Arg21$^{N\varepsilon}$ groups, as well as water molecules (Figures 11A,B). Cysteine 15 is part

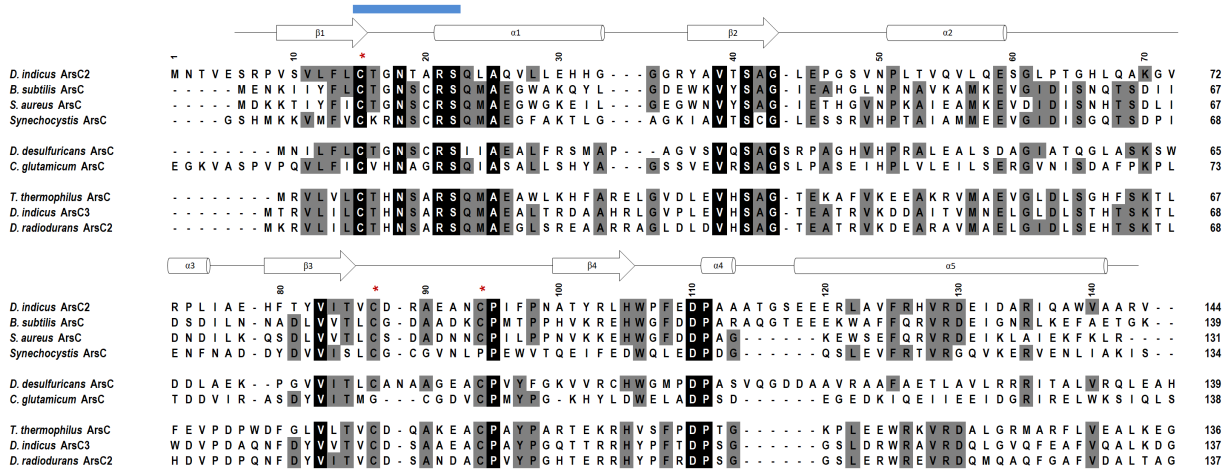

FIGURE 10
Amino acid sequence alignment of the *D. indicus* arsenate reductase ArsC2 with the Trx-linked family ArsC. The percentage identity of the ArsC of Trx-linked family with *D. indicus* ArsC2 (WP_088246862.1) is showed below. *B. subtilis* (34%, P45947); *S. aureus* pI258 (29%, P0A006); *Synechocystis* sp. PCC 6803 (27%, P74313); *D. desulfuricans* IC1 (26%, QCC86315.1); *C. glutamicum* (19%, Q8NQC6); *T. thermophilus* HB27 (28%, AAS81844.1); *D. indicus* ArsC3 (30%, WP_191300003.1); *D. radiodurans* ArsC2 (31%, ANC72982.1). *Di*ArsC2 secondary structure is shown above the alignment, and is indicated as α-helices and β-chains based on the output from PROCHECK (Laskowski et al., 1993). The three cysteine residues are marked with a red *. Amino acid residues that are part of the phosphate-binding loop are marked with a blue line. Strictly conserved amino acids represented as black boxes, whereas gray boxes represent the mostly conserved residues among the selected sequences.

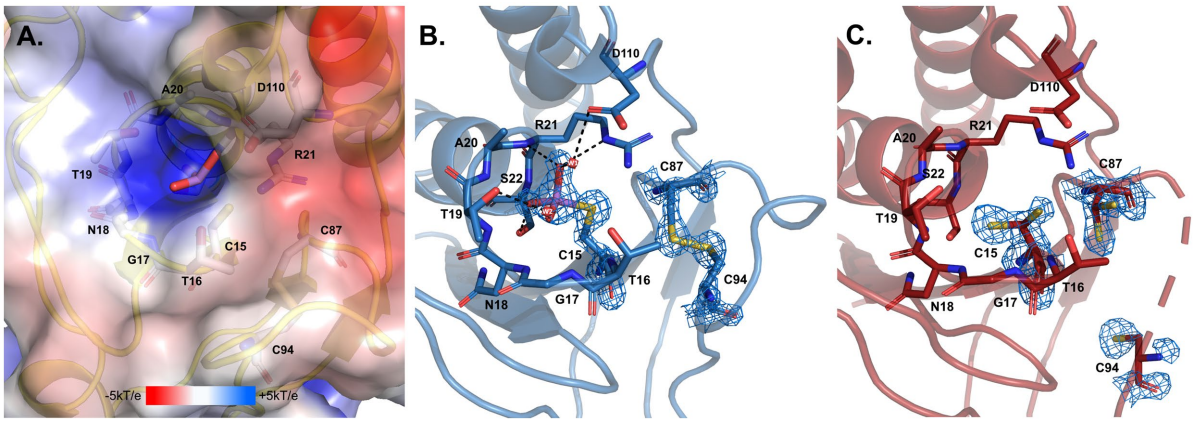

FIGURE 11
Arsenate catalytic site of *D. indicus* ArsC2. **(A)** Electrostatic potential mapped on the molecular surface of the pocket where arsenate enters, calculated by APBS (Baker et al., 2001; Dolinsky et al., 2004) integrated in the PYMOL (Delano, 2022). **(B)** *Di*ArsC2–As and **(C)** *Di*ArsC2 catalytic centers. In all the panels structures are shown in cartoon representation, with selected amino acid residues and arsenate drawn as sticks. In **(B,C)**, the final σ_A-weighted $2|F_o|-|F_c|$ electron density map is represented at the 2 σ and 1 σ contour levels, respectively around the cysteine residues and the arsenate ligand. In **(A–C)** carbons are colored in gray, blue and red, respectively; nitrogen in dark blue, oxygen in red, sulfur in yellow, and arsenic in purple. Two water molecules W1 and W2 are represented as small red spheres. Black dashes represent the hydrogen bond interaction with neighboring atoms to the arsenate and the water molecules.

of a well-known phosphate-binding loop (motif, CX_5R) of LMW PTPases which is conserved in the Trx-linked ArsC family (Figure 10; Bennett et al., 2001). In the native structure, there is no species present in this pocket, and all the residues in the phosphate binding loop $G_{17}NTARS_{22}$, are in a similar position as in the Arsenate-bound structure. Although no electron density was observed for the region 89–93 (Chain B), weak density for Cys94 was obtained (Figure 11C). Cys15 and Cys87 are involved in the reduction of As(V) to As(III), and in *Di*ArsC2 structure both residues were refined with a double side-chain conformation, suggesting the presence of a mixed state (Figure 11C).

Discussion

Deinococcus genus is ubiquitously present in nature and is able to tolerate high levels of radiation insults (Jin et al., 2019). *D. indicus* is a Gram-negative and arsenic resistant bacterium that presents a rod-shaped morphology in contrast to most *Deinococcus* sp. including *D. radiodurans* that present a coccus morphology (Suresh et al., 2004). It is known that arsenic induces oxidative stress in both eukaryotic and prokaryotic organisms (Huang et al., 2010; Ciprandi et al., 2012; Belfiore et al., 2013; Andres and Bertin, 2016; Shah and Damare, 2018; Castro-Severyn et al., 2019; Hu et al., 2020; De Francisco et al., 2021).

Here, we report an extensive characterization of *D. indicus* resistance to oxidative stress, UV-C and arsenate. Oxidative stress analysis revealed that different culture conditions promote dissimilar responses to oxidative stress agents, and *D. indicus* presents a higher resistance to MV when grown in M53 than in TGY, while the same resistance pattern is observed in both media when exposing the cells to H_2O_2. Interestingly, *D. indicus* cells are more resistant to H_2O_2 than to MV. In bacteria, an increase in the expression of superoxide dismutase (SOD) and catalases has been observed upon exposure to arsenic (Weiss et al., 2009; Ciprandi et al., 2012; Belfiore et al., 2013; Andres and Bertin, 2016; Shah and Damare, 2018). It is predicted that *D. indicus* has two superoxide dismutases (SOD), a MnSOD (accession number: GHG29236.1) a Cu/Zn SOD (accession number GHG15276.1) and one catalase (accession number: GHG14730.1). Moreover, both the superoxide anion and H_2O_2 can damage proteins containing iron sulfur clusters with the release of Fe^{2+} that can react with hydrogen peroxide, leading to the formation of hydroxyl radicals by the Fenton reaction (Koppenol, 1993; Valentine et al., 1998; Kehrer, 2000; Kohen and Nyska, 2002). *D. indicus* also possesses one DNA-binding protein under starved conditions, Dps (accession number: GHG25447.1). *D. radiodurans* Dps proteins are known to sequester iron and manganese (Ishikawa et al., 2003; Santos et al., 2015). *D. indicus* Dps presents high identity (75.5%) with *Dr*Dps1 which is known to utilize hydrogen peroxide for the oxidation of Fe^{2+} to Fe^{3+}(Santos et al., 2015). In addition, it has been previously reported that *D. radiodurans* protein extracts present a higher ROS scavenging ability than in *E. coli*, namely 30 fold-higher for H_2O_2 and 6 fold higher for $O_2^{\cdot-}$ (Tian et al., 2004).

So far, there is no information regarding UV-C resistance of *D. indicus*. In fact, *D. indicus* was screened for UV-B when first isolated by Suresh and co-workers, presenting 2–4% survival at 50000 J/m^2 in nutrient broth media (Suresh et al., 2004). Here, we showed that UV-C resistance in *D. indicus* is media-dependent: cells grown in M53 require a dose of 809 ± 66 J/m^2 to eliminate 90% of cells, while cells grown in TGY required a lower dose of 619 ± 82 J/m^2.

Moreover, *D. indicus* cells grown in M53 were also more resistant than the ones in TGY when subjected to MV. Interestingly, it has been previously reported that *D. radiodurans* response to UV-C exposure is also media-dependent (Chen et al., 2023). We can postulate that this media dependent response to MV and UV-C could indicate similar resistance mechanisms are in place and they act in a media dependent way, however the molecular mechanisms involved need to be further investigated.

Previously, it was demonstrated that *D. indicus* Wt/1aT can survive to 10 mM of arsenate As(V) (Suresh et al., 2004). To further extend arsenic resistance characterization, herein we showed that *D. indicus* is able to reach control conditions in the presence of 25 mM of As(V). Interestingly, in M53 medium and in the presence of 10 mM and 25 mM of arsenate, cells presented higher OD_{600} compared to control conditions, while the same behavior was not observed in TGY. This could be due to higher resistance to oxidative stress conditions, or perhaps other transcripts are modulated when cells are grown in M53. Moreover, an extended lag phase in the presence of 25 mM of arsenate before resuming normal growth was observed in both media although it was more pronounce when the cells were grown in TGY. This is a fairly common effect, for instance, methyl-mercury acetate causes an extended lag-phase on *Rhodopseudomonas capsulata* before resumption of normal growth (Nielsen and Sojka, 1979; Brochiero et al., 1984; Jaiganesh et al., 2012; Aljerf and AlMasri, 2018). In *E. coli*, cadmium quantum dots caused a longer lag-phase until normal proliferation was restored (Jaiganesh et al., 2012). Moreover, *D. indicus* growth was suppressed by the presence of 50 mM of As(V). However, upon As(V) removal, *D. indicus* was able to restore normal growth conditions. In this case, an extended lag-phase similar to post-antibiotic effect (PAE) noted on antibiotic applications was also observed (Zhanel et al., 1991; Li et al., 2016; Srimani et al., 2017). PAE is characterized as the time period after total removal of antibiotic during which no growth is observed. Our data for arsenic resistance is consistent with that for *D. indicus* strain DR1 isolated from the wetlands of Dadri, Uttar Pradesh, India (Chauhan et al., 2017, 2019a). Regarding *D. radiodurans,* no lag phase was observed upon exposure to 0.5 and 1 mM of As(V), even though cell growth was compromised. No differences were observed between media cultures in *D. radiodurans* and the same pattern was verified by exposing the cells to As(V) in a solid matrix. In contrast, *D. indicus* is able to survive up to 1 M of As(V) in solid matrix.

Since *D. indicus* presents higher resistance to MV, UV-C and a faster response and growth in M53 when submitted to As(V), a STEM-EDX analysis was performed. Here we reported for the first time the presence of polyphosphate-like granules (pPLGs) in *D. indicus*. Moreover, more than 30% of the cells contained no granules while a few cells contained up to 8 granules. This high heterogeneity reveals high plasticity in PolyP granules of *D. indicus* cells, and could indicate that cells adopt specific roles in the community, specializing in PolyP storage to gain an advantage upon environmental changes. pPLGs are also known to be involved in heavy-metal detoxification (Pan-Hou et al., 2001, 2002; Alvarez and Jerez, 2004; Ruiz et al., 2011; Orell et al., 2012; Jasso-Chávez et al., 2019; Sanz-Luque et al., 2020). In *Anabaena cylindrica* a higher accumulation of aluminum was observed on cells exhibiting pPLGs that were grown in a phosphate-rich medium (Annette et al., 1985). It is known that polyphosphate kinases (PPKs) are involved in the formation of inorganic polyphosphate (polyP) and pPLGs (Kornberg, 1999). In *E. coli,* higher resistance to Hg^{2+} was observed after the introduction of *ppk* into the *merA*-deleted *mer* operon (Pan-Hou et al., 2001, 2002). Moreover, it was proposed that polyP was involved in conversion of Hg^{2+} to a less toxic molecule via chelation mechanisms (Pan-Hou et al., 2001, 2002). Nevertheless, further analysis of *D. indicus* ability to utilize polyP for arsenic detoxification is required, especially since *D. radiodurans* also presents pPLGs and is sensitive to arsenic. It would be vital to understand if *D. indicus* pPLGs aid on the detoxification of arsenic either being directly involved or indirectly.

In order to complement our studies and to further understand the resistance to arsenate by *D. indicus* the arsenate reductase *DiArsC2* was chosen since it did not cluster with any of *ArsC* from *D. radiodurans*. Thus, we undertook the structural studies of *Di*ArsC2 and we were able to crystallize two different forms of the enzyme: native (*Di*ArsC2) and bound to arsenite (*Di*ArsC2-As). The crystal structures present high similarities with the *B. subtillis* ArsC that belongs to the Trx-linked family (Bennett et al., 2001). Based on the conservation of the 3 cysteines (Cys15, Cys87, and Cys94) (Figure 10) and structural analysis (Figures 9, 11), we infer the As(V) mechanism of reduction is identical to the one proposed for *B. subtillis,* i.e., a triple redox system (Bennett et al., 2001). The *Di*Arsc2-As structure represents the final stage, where Cys15 is bound to As(III), however the ligand cannot be released since Cys87 forms a disulfide bridge with Cys94 (Figure 11). Moreover, the arsenate is located in a positive-charged pocket which is accessible from the external environment. Since in our *Di*ArsC2 structure the disulfide bridge between

these two residues is not formed (at least in chain B, where density is observed) this could indicate that an As(V) reduction event already took place in the *Di*ArsC2-As structure, leading to the formation of the Cys87 – Cys94 disulfide bridge (Figure 11). The lack of mobility of the PTPase loop (where Cys15 is located) together with the high flexibility of the loop that contains Cys87 and Cys94 suggests that Cys87 is the residue responsible for the release of As(III) bound to the Cys15 (Figure 9). In fact this loop is readily accessible by the thioredoxin reductase system to reduce the Cys87 – Cys94 disulfide bridge and allow a new As(V) reduction cycle to occur (Messens et al., 1999; Bennett et al., 2001). It would be interesting to assess whether the presence of Cys87 in the *Di*ArsC2 structure is essential for the ligation of As(V). Moreover, the mutation of Cys87 could allow *Di*ArsC2 to be used has a tool for of As(V) removal by inhibiting the release of As(III).

Conclusion

Arsenic contamination severely damages ecosystems and compromises the integrity of water resources essential for human life. *D. indicus* is an arsenic resistant organism belonging to Deinococcaceae family that present high resistant to UV radiation. Here we performed a characterization of stress resistance of *D. indicus* and provide insights toward exploiting *D. indicus* as a tool for bioremediation. *D. indicus* exhibited a media-dependent response upon exposure to UV-C and MV, and demonstrated higher resistance in M53 compared to TGY. Moreover, cells grown in M53 upon exposure to 25 mM As(V) exhibited higher growth (OD_{600}). This may indicate that optimization of culture conditions could lead to a higher resistance to cellular insults including arsenic stress. Using STEM-EDX we were able to detect the presence of polyphosphate granules *in D. indicus*. Nevertheless, more studies are required to infer the potential utilization as a path for the detoxification process via arsenic bioaccumulation. Additionally, the *D. indicus ars* operon contains two arsenate reductases (*Di*ArsC2 and *Di*ArsC3). The *Di*ArsC2 structure revealed detailed insights into the molecular mechanism of the arsenate reduction, in which As(V) is converted to As(III) and remains bound to Cys15. These findings, contribute to the knowledge to apply *D. indicus* in bioremediation of arsenic either by following a cell-based approach or at the protein level using *Di*ArsC has a tool to remove As(V).

Data availability statement

The original contributions presented in the study are included in the article/Supplementary material, further inquiries can be directed to the corresponding author.

Author contributions

AG and CR: conceptualization and experimental design. AG, BS, WA, SW, ME, PM, and CR: methodology. CR, AG, SW, ME, and PK: STEM experiments. CR, AG, SW, OG, and DR: software, granules analysis, and data curation. WA and AG: SEM experiments. AG, BS, CR, and PM: protein purification and structure determination. AG and CR: UV-C, oxidative, and As(V) experiments. AG and CR analyzed the data and wrote the manuscript. CR: investigation, supervision, and project administration. AG, BS, DR, WA, PK, OG, SW, ME, PM, and CR: review and editing the manuscript. CR, SW, and ME: funding acquisition. All authors contributed to the article and approved the submitted version.

Funding

This study was financially supported by the Portuguese Fundação para a Ciência e Tecnologia (FCT), grants PTDC/BIA-BQM/31317/2017, Project MOSTMICRO-ITQB with references UIDB/04612/2020 and UIDP/04612/2020, and LS4FUTURE Associated Laboratory (LA/P/0087/2020). This project has received funding from the European Union's Horizon 2020 research and innovation program under grant agreement No. 857203. AG and BS are recipients of FCT grants SFRH/BD/06723/2020 and SFRH/BD/08066/2020, respectively. CR is recipient of FCT Institutional CEEC. Cryo-electron microscopy studies received partial support from the Weizmann Institute of Science (The Irving and Cherna Moskowitz Center for Nano and BioNano Imaging), and from the European Union (ERC-AdV grant, CryoSTEM, 101055413 to ME). This work benefited from access to the Weizmann Institute Electron Microscopy Unit, an Instruct-ERIC centre through the Access proposal PID: 19879.

Acknowledgments

We would like to acknowledge the ALBA Synchrotron Light Facility with the collaboration of ALBA staff for the data collection of *Di*ArsC2 structures performed at BL13-XALOC beamline. The image analysis was made available thanks to the de Picciotto Cancer Cell Observatory In Memory of Wolfgang and Ruth Lesser of the MICC Life Sciences Core Facilities Weizmann Institute of Science Israel. Teresa Silva and Cristina Timóteo from the Microbial Cell Production and Protein Purification and Characterization Research facilities at ITQB-NOVA are acknowledged for providing the competent cells of *Escherichia coli* strains and to purify TEV protease.

Conflict of interest

The authors declare that the research was conducted in the absence of any commercial or financial relationships that could be construed as a potential conflict of interest.

Publisher's note

Supplementary material

The Supplementary material for this article can be found online at: https://www.frontiersin.org/articles/10.3389/fmicb.2023.1240798/full#supplementary-material

References

Adams, P. D., Afonine, P. V., Bunkóczi, G., Chen, V. B., Davis, I. W., Echols, N., et al. (2010). PHENIX: A comprehensive Python-based system for macromolecular structure solution. *Acta Crystallogr. Sect. D Biol. Crystallogr.* 66, 213–221. doi: 10.1107/S0907444909052925

Afonine, P. V., Grosse-Kunstleve, R. W., Echols, N., Headd, J. J., Moriarty, N. W., Mustyakimov, M., et al. (2012). Towards automated crystallographic structure refinement with phenix.Refine. *Acta Crystallogr. Sect. D Biol. Crystallogr.* 68, 352–367. doi: 10.1107/S0907444912001308

Aljerf, L., and AlMasri, N. (2018). A gateway to metal resistance: bacterial response to heavy metal toxicity in the biological environment. *Ann. Adv. Chem.* 2, 032–044. doi: 10.29328/journal.aac.1001012

Alvarez, S., and Jerez, C. A. (2004). Copper ions stimulate polyphosphate degradation and phosphate efflux in *Acidithiobacillus ferrooxidans*. *Appl. Environ. Microbiol.* 70, 5177–5182. doi: 10.1128/AEM.70.9.5177

Andres, J., and Bertin, P. N. (2016). The microbial genomics of arsenic. *FEMS Microbiol. Rev.* 40, 299–322. doi: 10.1093/femsre/fuv050

Annette, P., Ljerka, K., Bergman, B., and Godfrie, M. R. (1985). Accumulation of aluminium by *Anabaena cylindrica* into polyphosphate granules and cell walls: an X-ray energy-dispersive microanalysis study. *J. Gen. Microbiol.* 131, 2545–2548.

Baker, N. A., Sept, D., Joseph, S., Holst, M. J., and McCammon, J. A. (2001). Electrostatics of nanosystems: application to microtubules and the ribosome. *Proc. Natl. Acad. Sci. U. S. A.* 98, 10037–10041. doi: 10.1073/pnas.181342398

Bauer, A. W., Kirby, W. M., Sherris, J. C., and Turck, M. (1966). Antibiotic susceptibility testing by a standardized single disk method. *Am. J. Clin. Pathol.* 45, 493–496. doi: 10.1308/rcsann.2013.95.7.532

Belfiore, C., Ordoñez, O. F., and Farías, M. E. (2013). Proteomic approach of adaptive response to arsenic stress in Exiguobacterium sp. S17, an extremophile strain isolated from a high-altitude Andean Lake stromatolite. *Extremophiles* 17, 421–431. doi: 10.1007/s00792-013-0523-y

Bennett, M. S., Guan, Z., Laurberg, M., and Su, X. D. (2001). *Bacillus subtilis* arsenate reductase is structurally and functionally similar to low molecular weight protein tyrosine phosphatases. *Proc. Natl. Acad. Sci. U. S. A.* 98, 13577–13582. doi: 10.1073/pnas.241397198

Berg, S., Kutra, D., Kroeger, T., Straehle, C. N., Kausler, B. X., Haubold, C., et al. (2019). Ilastik: interactive machine learning for (bio)image analysis. *Nat. Methods* 16, 1226–1232. doi: 10.1038/s41592-019-0582-9

Berman, H., Henrick, K., and Nakamura, H. (2003). Announcing the worldwide protein data Bank. *Nat. Struct. Biol.* 10:980. doi: 10.1038/nsb1203-980

Bissen, M., Frimmel, F. H., and Ag, C. (2003). Arsenic – a review. part i: occurrence, toxicity, speciation, mobility. *Acta Hydrochim. Hydrobiol.* 31, 9–18. doi: 10.1002/aheh.200390025

Brim, H., McFarlan, S. C., Fredrickson, J. K., Minton, K. W., Zhai, M., Wackett, L. P., et al. (2000). Engineering *Deinococcus radiodurans* for metal remediation in radioactive mixed waste environments. *Nat. Biotechnol.* 18, 85–90. doi: 10.1038/71986

Brim, H., Venkateswaran, A., Kostandarithes, H. M., Fredrickson, J. K., and Daly, M. J. (2003). Engineering *Deinococcus geothermalis* for bioremediation of high-temperature radioactive waste environments. *Appl. Environ. Microbiol.* 69, 4575–4582. doi: 10.1128/AEM.69.8.4575-4582.2003

Brochiero, E., Bonaly, J., and Mestre, J. C. (1984). Toxic action of hexavalent chromium on *Euglena gracilis* cells strain Z grown under heterotrophic conditions. *Arch. Environ. Contam. Toxicol.* 13, 603–608. doi: 10.1007/BF01056339

Burnley, B. T., Afonine, P. V., Adams, P. D., and Gros, P. (2012). Modelling dynamics in protein crystal structures by ensemble refinement. *elife* 1, e00311–e00329. doi: 10.7554/eLife.00311

Castro-Severyn, J., Pardo-Esté, C., Sulbaran, Y., Cabezas, C., Gariazzo, V., Briones, A., et al. (2019). Arsenic response of three Altiplanic Exiguobacterium strains with different tolerance levels against the metalloid species: a proteomics study. *Front. Microbiol.* 10:2161. doi: 10.3389/fmicb.2019.02161

Cerf, O. (1977). A review: tailing of survival curves of bacterial spores. *J. Appl. Bacteriol.* 42, 1–19. doi: 10.1111/j.1365-2672.1977.tb00665.x

Chauhan, D., Srivastava, P. A., Agnihotri, V., Yennamalli, R. M., and Priyadarshini, R. (2019a). Structure and function prediction of arsenate reductase from *Deinococcus indicus* DR1. *J. Mol. Model.* 25:15. doi: 10.1007/s00894-018-3885-3

Chauhan, D., Srivastava, P. A., Ritzl, B., Yennamalli, R. M., Cava, F., and Priyadarshini, R. (2019b). Amino acid-dependent alterations in cell wall and cell morphology of *deinococcus indicus* DR1. *Front. Microbiol.* 10:1449. doi: 10.3389/fmicb.2019.01449

Chauhan, D., Srivastava, A., Yennamalli, R. M., and Priyadarshini, R. (2017). Draft genome sequence of *Deinococcus indicus* DR1, a novel strain isolated from a freshwater wetland. *Genome Announc.* 5, e00754–e00717. doi: 10.1128/genomeA.00754-17

Chen, V. B., Arendall, W. B., Headd, J. J., Keedy, D. A., Immormino, R. M., Kapral, G. J., et al. (2010). MolProbity: all-atom structure validation for macromolecular crystallography. *Acta Crystallogr. Sect. D Biol. Crystallogr.* 66, 12–21. doi: 10.1107/S0907444909042073

Chen, Y., Zhang, Q., Wang, D., Shu, Y.-G., and Shi, H. (2023). Memory effect on the survival of *Deinococcus radiodurans* after exposure in near space. *Microbiol. Spectr.* 11:e0347422. doi: 10.1128/spectrum.03474-22

Choi, M. H., Jeong, S. W., Shim, H. E., Yun, S. J., Mushtaq, S., Choi, D. S., et al. (2017). Efficient bioremediation of radioactive iodine using biogenic gold nanomaterial-containing radiation-resistant bacterium, *Deinococcus radiodurans* R1. *Chem. Commun.* 53, 3937–3940. doi: 10.1039/c7cc00720e

Ciprandi, A., Baraúna, R. A., Santos, A. V., Gonçalves, E. C., Carepo, M. S. P., Schneider, M. P. C., et al. (2012). Proteomic response to arsenic stress in *chromobacterium violaceum*. *J. Integr. OMICS* 2, 69–73. doi: 10.5584/jiomics.v2i1.84

Copeland, A., Zeytun, A., Yassawong, M., Nolan, M., Lucas, S., Hammon, N., et al. (2012). Complete genome sequence of the orange-red pigmented, radioresistant *Deinococcus proteolyticus* type strain (MRPT). *Stand. Genomic Sci.* 6, 240–250. doi: 10.4056/sigs.2756060

Dani, S. U. (2011). The arsenic for phosphorus swap is accidental, rather than a facultative one, and the question whether arsenic is nonessential or toxic is quantitative, not a qualitative one. *Sci. Total Environ.* 409, 4889–4890. doi: 10.1016/j.scitotenv.2011.05.044

De Francisco, P., Martín-González, A., Rodriguez-Martín, D., and Díaz, S. (2021). Interactions with arsenic: mechanisms of toxicity and cellular resistance in eukaryotic microorganisms. *Int. J. Environ. Res. Public Health* 18:12226. doi: 10.3390/ijerph182212226

De Groot, A., Chapon, V., Servant, P., Christen, R., Fischer-Le Saux, M., Sommer, S., et al. (2005). *Deinococcus deserti* sp. nov., a gamma-radiation-tolerant bacterium isolated from the Sahara Desert. *Int. J. Syst. Evol. Microbiol.* 55, 2441–2446. doi: 10.1099/ijs.0.63717-0

De La Vega, U. P., Rettberg, P., Douki, T., Cadet, J., and Horneck, G. (2005). Sensitivity to polychromatic UV-radiation of strains of *Deinococcus radiodurans* differing in their DNA repair capacity. *Int. J. Radiat. Biol.* 81, 601–611. doi: 10.1080/09553000500309374

Delano, W. L. (2022). *He PyMOL molecular graphics system, Version 2.3*. Delano Scientific: San Carlos

Dolinsky, T. J., Nielsen, J. E., McCammon, J. A., and Baker, N. A. (2004). PDB2PQR: an automated pipeline for the setup of Poisson-Boltzmann electrostatics calculations. *Nucleic Acids Res.* 32, W665–W667. doi: 10.1093/nar/gkh381

Eltsov, M., and Dubochet, J. (2005). Fine structure of the *Deinococcus radiodurans* nucleoid revealed by cryoelectron microscopy of vitreous sections. *J. Bacteriol.* 187, 8047–8054. doi: 10.1128/JB.187.23.8047-8054.2005

Emsley, P., and Cowtan, K. (2004). Coot: model-building tools for molecular graphics. *Acta Crystallogr. Sect. D Biol. Crystallogr.* 60, 2126–2132. doi: 10.1107/S0907444904019158

Evans, P. R. (2011). An introduction to data reduction: space-group determination, scaling and intensity statistics. *Acta Crystallogr. Sect. D Biol. Crystallogr.* 67, 282–292. doi: 10.1107/S090744491003982X

Fekry, M. I., Tipton, P. A., and Gates, K. S. (2011). Kinetic consequences of replacing the internucleotide phosphorus atoms in DNA with arsenic. *ACS Chem. Biol.* 6, 127–130. doi: 10.1021/cb2000023

Ferreira, A. C., Nobre, M. F., Rainey, F. A., Silva, M. T., Wait, R., Burghardt, J., et al. (1997). *Deinococcus geothermalis* sp. nov. and *Deinococcus murrayi* sp. nov., two extremely radiation-resistant and slightly thermophilic species from hot springs. *Int. J. Syst. Bacteriol.* 47, 939–947. doi: 10.1099/00207713-47-4-939

Garbinski, L. D., Rosen, B. P., and Chen, J. (2019). Pathways of arsenic uptake and efflux. *Environ. Int.* 126, 585–597. doi: 10.1016/j.envint.2019.02.058.Pathways

Gerber, E., Bernard, R., Castang, S., Chabot, N., Coze, F., Dreux-Zigha, A., et al. (2015). Deinococcus as new chassis for industrial biotechnology: biology, physiology and tools. *J. Appl. Microbiol.* 119, 1–10. doi: 10.1111/jam.12808

Gladysheva, T. B., Oden, K. L., and Rosen, B. P. (1994). Properties of the arsenate reductase of plasmid R773. *Biochemistry* 33, 7288–7293. doi: 10.1021/bi00189a033

Halliwell, B. (2006). Redox biology is a fundamental theme of aerobic life. *Plant Physiol.* 141, 312–322. doi: 10.1104/pp.106.077073.312

Halliwell, B., and Gutteridge, J. M. (1999) in *Free radicals in biology and medicine*. eds. B. Halliwell and J. M. Gutteridge. *3rd* ed (Oxford: Oxford University Press)

Hirsch, P., Gallikowski, C. A., Siebert, J., Peissl, K., Kroppenstedt, R., Schumann, P., et al. (2004). *Deinococcus frigens* sp. nov., *Deinococcus saxicola* sp. nov., and *Deinococcus marmoris* sp. nov., low temperature and draught-tolerating, UV-resistant bacteria from continental Antarctica. *Syst. Appl. Microbiol.* 27, 636–645. doi: 10.1078/0723202042370008

Hu, Y., Li, J., Lou, B., Wu, R., Wang, G., Lu, C., et al. (2020). The role of reactive oxygen species in arsenic toxicity. *Biomol. Ther.* 10:240. doi: 10.3390/biom10020240

Huang, A., Teplitski, M., Rathinasabapathi, B., and Ma, L. (2010). Characterization of arsenic-resistant bacteria from the rhizosphere of arsenic hyperaccumulator *Pteris vittata*. *Can. J. Microbiol.* 56, 236–246. doi: 10.1139/W10-005

Hudzicki, J. (2012). Kirby-Bauer disk diffusion susceptibility test protocol author information. *Am. Soc. Microbiol.*, 1–13.

Ishikawa, T., Mizunoe, Y., Kawabata, S., Takade, A., Harada, M., Wai, S. N., et al. (2003). The iron-binding protein Dps confers hydrogen peroxide stress resistance to *Campylobacter jejuni*. *J. Bacteriol.* 185, 1010–1017. doi: 10.1128/JB.185.3.1010-1017.2003

Jaiganesh, T., Rani, D. V., and Girigoswami, A. (2012). Spectroscopically characterized cadmium sulfide quantum dots lengthening the lag phase of *Escherichia coli* growth. *Spectrochim. Acta - part A Mol. Biomol. Spectrosc.* 92, 29–32. doi: 10.1016/j.saa.2012.02.044

James, K. A., Meliker, J. R., and Nriagu, J. O. (2017). "Arsenic" in *International encyclopedia of public health*. ed. S. R. Quah (Academic Press), 170–175.

Jasso-Chávez, R., Lira-Silva, E., González-Sánchez, K., Larios-Serrato, V., Mendoza-Monzoy, D. L., Pérez-Villatoro, F., et al. (2019). Marine archaeon *methanosarcina acetivorans* enhances polyphosphate metabolism under persistent cadmium stress. *Front. Microbiol.* 10, 1–10. doi: 10.3389/fmicb.2019.02432

Ji, G., Garber, E. A. E., Armes, L. G., Chen, C. M., Fuchs, J. A., and Silver, S. (1994). Arsenate reductase of *Staphylococcus aureus* plasmid pI258. *Biochemistry* 33, 7294–7299. doi: 10.1021/bi00189a034

Jiang, W., Hou, Q., Yang, Z., Zhong, C., Zheng, G., Yang, Z., et al. (2014). Evaluation of potential effects of soil available phosphorus on soil arsenic availability and paddy rice inorganic arsenic content. *Environ. Pollut.* 188, 159–165. doi: 10.1016/j.envpol.2014.02.014

Jin, M., Xiao, A., Zhu, L., Zhang, Z., Huang, H., and Jiang, L. (2019). The diversity and commonalities of the radiation-resistance mechanisms of Deinococcus and its up-to-date applications. *AMB Express* 9:138. doi: 10.1186/s13568-019-0862-x

Juanhuix, J., Gil-Ortiz, F., Cuní, G., Colldelram, C., Nicolás, J., Lidón, J., et al. (2014). Developments in optics and performance at BL13-XALOC, the macromolecular crystallography beamline at the Alba synchrotron. *J. Synchrotron Radiat.* 21, 679–689. doi: 10.1107/S160057751400825X

Kabsch, W. (2010). XDS. *Acta Crystallogr. Sect. D Biol. Crystallogr* 66, 125–132. doi: 10.1107/S0907444909047337

Kalyaanamoorthy, S., Minh, B. Q., Wong, T. K. F., Von Haeseler, A., and Jermiin, L. S. (2017). ModelFinder: fast model selection for accurate phylogenetic estimates. *Nat. Methods* 14, 587–589. doi: 10.1038/nmeth.4285

Kantardjieff, K. A., and Rupp, B. (2003). Matthews coefficient probabilities: Improved estimates for unit cell contents of proteins, DNA, and protein–nucleic acid complex crystals. *Protein Sci.* 12, 1865–1871. doi: 10.1110/ps.0350503

Keasling, J. D. (1997). Regulation of intracellular toxic metals and other cations by hydrolysis of polyphosphate. *Ann. N. Y. Acad. Sci.* 829, 242–249. doi: 10.1111/j.1749-6632.1997.tb48579.x

Kehrer, J. P. (2000). The Haber-Weiss reaction and mechanisms of toxicity. *Toxicology* 149, 43–50. doi: 10.1016/S0300-483X(00)00231-6

Kohen, R., and Nyska, A. (2002). Oxidation of biological systems: oxidative stress phenomena, antioxidants, redox reactions, and methods for their Quanti?Cation. *Toxicolofic Pathol.* 30, 620–650. doi: 10.1080/0192623029016672

Kolari, M., Nuutinen, J., Rainey, F. A., and Salkinoja-Salonen, M. S. (2003). Colored moderately thermophilic bacteria in paper-machine biofilms. *J. Ind. Microbiol. Biotechnol.* 30, 225–238. doi: 10.1007/s10295-003-0047-z

Kolari, M., Nuutinen, J., and Salkinoja-Salonen, M. S. (2001). Mechanisms of biofilm formation in paper machine by *Bacillus* species: the role of *Deinococcus geothermalis*. *J. Ind. Microbiol. Biotechnol.* 27, 343–351. doi: 10.1038/sj.jim.7000201

Koppenol, W. H. (1993). The centennial of the Fenton reaction. *Free Radic. Biol. Med.* 15, 645–651. doi: 10.1016/0891-5849(93)90168-T

Kornberg, A. (1999). "Inorganic polyphosphate: A molecule of many functions" in *Progress in molecular and subcellular biology*. eds. H. C. Schroder and W. E. G. Muller (Berlin Heidelberg: Springer-Verlag), 1–5.

Kowalski, W. (2009). "Mathematical modeling of UV disinfection" in *Ultraviolet germicidal irradiation handbook: UVGI for air and surface disinfection* (Berlin: Springer Berlin, Heidelberg), 1–501.

Kowalski, W. J., Bahnfleth, W. P., Witham, D. L., Severin, B. F., and Whittam, T. S. (2000). Mathematical modeling of ultraviolet germicidal irradiation for air disinfection. *Quant. Microbiol.* 2, 249–270. doi: 10.1023/A:1013951313398

Kulakovskaya, T. (2018). Inorganic polyphosphates and heavy metal resistance in microorganisms. *World J. Microbiol. Biotechnol.* 34:139. doi: 10.1007/s11274-018-2523-7

Laskowski, R. A., MacArthur, M. W., Moss, D. S., and Thornton, J. M. (1993). PROCHECK: a program to check the stereochemical quality of protein structures. *J. Appl. Crystallogr.* 26, 283–291. doi: 10.1107/s0021889892009944

Letunic, I., and Bork, P. (2021). Interactive tree of life (iTOL) v5: an online tool for phylogenetic tree display and annotation. *Nucleic Acids Res.* 49, W293–W296. doi: 10.1093/nar/gkab301

Li, B., Qiu, Y., Shi, H., and Yin, H. (2016). The importance of lag time extension in determining bacterial resistance to antibiotics. *Analyst* 141, 3059–3067. doi: 10.1039/c5an02649k

Liebschner, D., Afonine, P. V., Baker, M. L., Bunkoczi, G., Chen, V. B., Croll, T. I., et al. (2019). Macromolecular structure determination using X-rays, neutrons and electrons: recent developments in Phenix. *Acta Crystallogr. Sect. D Struct. Biol.* 75, 861–877. doi: 10.1107/S2059798319011471

Lim, S., Jung, J. H., Blanchard, L., and De Groot, A. (2019). Conservation and diversity of radiation and oxidative stress resistance mechanisms in *Deinococcus* species. *FEMS Microbiol. Rev.* 43, 19–52. doi: 10.1093/femsre/fuy037

Machado, A. F., Hovland, D. N., Pilafas, S., and Collins, M. D. (1999). Teratogenic response to arsenite during neurulation: relative sensitivities of C57BL/6J and SWV/Fnn mice and impact of the splotch allele. *Toxicol. Sci.* 51, 98–107. doi: 10.1093/toxsci/51.1.98

Makk, J., Tóth, E. M., Anda, D., Pál, S., Schumann, P., Kovács, A. L., et al. (2016). Deinococcus budaensis sp. Nov., a mesophilic species isolated from a biofilm sample of a hydrothermal spring cave. *Int. J. Syst. Evol. Microbiol.* 66, 5345–5351. doi: 10.1099/ijsem.0.001519

Manobala, T., Shukla, S. K., Subba Rao, T., and Dharmendira Kumar, M. (2019). A new uranium bioremediation approach using radio-tolerant *Deinococcus radiodurans* biofilm. *J. Biosci.* 44, 1–9. doi: 10.1007/s12038-019-9942-y

Matthews, B. W. (1968). Solvent content of protein crystals. *J. Mol. Biol.* 33, 491–497. doi: 10.1016/0022-2836(68)90205-2

McCoy, A. J., Grosse-Kunstleve, R. W., Adams, P. D., Winn, M. D., Storoni, L. C., and Read, R. J. (2007). Phaser crystallographic software. *J. Appl. Crystallogr.* 40, 658–674. doi: 10.1107/S0021889807021206

Messens, J., Hayburn, G., Desmyter, A., Laus, G., and Wyns, L. (1999). The essential catalytic redox couple in arsenate reductase from *Staphylococcus aureus*. *Biochemistry* 38, 16857–16865. doi: 10.1021/bi9911841

Messens, J., Martins, J. C., Brosens, E., Van Belle, K., Jacobs, D. M., Willem, R., et al. (2002a). Kinetics and active site dynamics of *Staphylococcus aureus* arsenate reductase. *J. Biol. Inorg. Chem.* 7, 146–156. doi: 10.1007/s007750100282

Messens, J., Martins, J. C., Van Belle, K., Brosens, E., Desmyter, A., De Gieter, M., et al. (2002b). All intermediates of the arsenate reductase mechanism, including an intramolecular dynamic disulfide cascade. *Proc. Natl. Acad. Sci. U. S. A.* 99, 8506–8511. doi: 10.1073/pnas.132142799

Messens, J., and Silver, S. (2006). Arsenate reduction: thiol cascade chemistry with convergent evolution. *J. Mol. Biol.* 362, 1–17. doi: 10.1016/j.jmb.2006.07.002

Minh, B. Q., Schmidt, H. A., Chernomor, O., Schrempf, D., and Woodhams, M. D., von Haeseler, A. von von Haeseler, A., and Lanfear, R. (2020). IQ-TREE 2: new models and efficient methods for phylogenetic inference in the genomic era. *Mol. Biol. Evol.*, 37, 1530–1534, doi: 10.1093/molbev/msaa015

Misra, C. S., Appukuttan, D., Kantamreddi, V. S. S., Rao, A. S., and Apte, S. K. (2012). Recombinant *D. radiodurans* cells for bioremediation of heavy metals from acidic/neutral aqueous wastes. *Bioeng. Bugs* 3, 44–48. doi: 10.4161/bbug.3.1.18878

Mukhopadhyay, R., and Rosen, B. P. (1998). *Saccharomyces cerevisiae* ACR2 gene encodes an arsenate reductase. *FEMS Microbiol. Lett.* 168, 127–136. doi: 10.1016/S0378-1097(98)00430-3

Mukhopadhyay, R., and Rosen, B. P. (2002). Arsenate reductases in prokaryotes and eukaryotes. *Environ. Health Perspect.* 110, 745–748. doi: 10.1289/ehp.02110s5745

Mukhopadhyay, R., Shi, J., and Rosen, B. P. (2000). Purification and characterization of Acr2p, the *Saccharomyces cerevisiae* arsenate reductase. *J. Biol. Chem.* 275, 21149–21157. doi: 10.1074/jbc.M910401199

Munakata, N., Saito, M., and Hieda, K. (1991). Inactivation action spectra of *bacillus subtilis* spores in extended ultraviolet wavelengths (50–300nm) obtained with synchrotron radiation. *Photochem. Photobiol.* 54, 761–768. doi: 10.1111/j.1751-1097.1991.tb02087.x

Murshudov, G. N., Vagin, A. A., and Dodson, E. J. (1997). Refinement of macromolecular structures by the maximum-likelihood method. *Acta Crystallogr. Sect. D Biol. Crystallogr.* 53, 240–255. doi: 10.1107/S0907444996012255

National Research Council (2001). "National Research Council (US) Subcommittee to Update the 1999 Arsenic," in *Drinking Water Report. Arsenic in Drinking Water: 2001 Update*. Washington, DC: National Academies Press (US).

Nielsen, A. M., and Sojka, G. A. (1979). Photoheterotrophic utilization of acetate by the wild type and an acetate-adapted mutant of *Rhodopseudomonas capsulata*. *Arch. Microbiol.* 120, 39–42. doi: 10.1007/BF00413270

Nunes, C. I. P., Brás, J. L. A., Najmudin, S., Moura, J. J. G., Moura, I., and Carepo, M. S. P. (2014). ArsC3 from *Desulfovibrio alaskensis* G20, a cation and sulfate-independent highly efficient arsenate reductase. *J. Biol. Inorg. Chem.* 19, 1277–1285. doi: 10.1007/s00775-014-1184-8

O'Day, P. A. (2006). Chemistry and mineralogy of arsenic. *Elements* 2, 77–83. doi: 10.2113/gselements.2.2.77

Oden, K. L., Gladysheva, T. B., and Rosen, B. P. (1994). Arsenate reduction mediated by the plasmid-encoded ArsC protein is coupled to glutathione. *Mol. Microbiol.* 12, 301–306. doi: 10.1111/j.1365-2958.1994.tb01018.x

Orell, A., Navarro, C. A., Rivero, M., Aguilar, J. S., and Jerez, C. A. (2012). Inorganic polyphosphates in extremophiles and their possible functions. *Extremophiles* 16, 573–583. doi: 10.1007/s00792-012-0457-9

Páez-Espino, D., Tamames, J., De Lorenzo, V., and Cánovas, D. (2009). Microbial responses to environmental arsenic. *Biometals* 22, 117–130. doi: 10.1007/s10534-008-9195-y

Pan-Hou, H., Kiyono, M., Kawase, T., Omura, T., and Endo, G. (2001). Evaluation of ppk -specified polyphosphate as a mercury remedial tool. *Biol. Pharm. Bull.* 24, 1423–1426. doi: 10.1248/bpb.24.1423

Pan-Hou, H., Kiyono, M., Omura, H., Omura, T., and Endo, G. (2002). Polyphosphate produced in recombinant *Escherichia coli* confers mercury resistance. *FEMS Microbiol. Lett.* 207, 159–164. doi: 10.1111/j.1574-6968.2002.tb11045.x

Peltola, M., Kanto Öqvist, C., Ekman, J., Kosonen, M., Jokela, S., Kolari, M., et al. (2008). Quantitative contributions of bacteria and of *Deinococcus geothermalis* to deposits and slimes in paper industry. *J. Ind. Microbiol. Biotechnol.* 35, 1651–1657. doi: 10.1007/s10295-008-0409-7

Peverly, J. H., Adamec, J., and Parthasarathy, M. V. (1978). Association of Potassium and some Other Monovalent Cations with occurrence of polyphosphate bodies in *Chlorella pyrenoidosa*. *Plant Physiol.* 62, 120–126. doi: 10.1104/pp.62.1.120

Potterton, E., Briggs, P., Turkenburg, M., and Dodson, E. (2003). Biological crystallography A graphical user interface to the CCP4 program suite. *Acta Crystallogr. Sect. D Biol. Crystallogr.* 59, 1131–1137. doi: 10.1107/S0907444903008126

Preibisch, S., Saalfeld, S., and Tomancak, P. (2009). Globally optimal stitching of tiled 3D microscopic image acquisitions. *Bioinformatics* 25, 1463–1465. doi: 10.1093/bioinformatics/btp184

Pruitt, K. M., and Kamau, D. N. (1993). Mathematical models of bacterial growth, inhibition and death under combined stress conditions. *J. Ind. Microbiol.* 12, 221–231. doi: 10.1007/BF01584194

Ranganathan, S., Sethi, D., Kasivisweswaran, S., Ramya, L., Priyadarshini, R., and Yennamalli, R. M. (2023). Structural and functional mapping of ars gene cluster in *Deinococcus indicus* DR1. *Comput. Struct. Biotechnol. J.* 21, 519–534. doi: 10.1016/j.csbj.2022.12.015

Rosen, B. P. (1999). Families of arsenic transporters. *Trends Microbiol.* 7, 207–212. doi: 10.1016/S0966-842X(99)01494-8

Rosenberg, H., Gerdes, R. G., and Chegwidden, K. (1977). Two systems for the uptake of phosphate in *Escherichia coli*. *J. Bacteriol.* 131, 505–511. doi: 10.1128/jb.131.2.505-511.1977

Ruiz, O. N., Alvarez, D., Gonzalez-Ruiz, G., and Torres, C. (2011). Characterization of mercury bioremediation by transgenic bacteria expressing metallothionein and polyphosphate kinase. *BMC Biotechnol.* 11, 1–18. doi: 10.1186/1472-6750-11-82

Santos, S. P., Mitchell, E. P., Franquelim, H. G., Castanho, M. A. R. B., Abreu, I. A., and Romão, C. V. (2015). Dps from *Deinococcus radiodurans*: oligomeric forms of Dps1 with distinct cellular functions and Dps2 involved in metal storage. *FEBS J.* 282, 4307–4327. doi: 10.1111/febs.13420

Sanz-Luque, E., Bhaya, D., and Grossman, A. R. (2020). Polyphosphate: A multifunctional metabolite in Cyanobacteria and algae. *Front. Plant Sci.* 11, 1–21. doi: 10.3389/fpls.2020.00938

Schindelin, J., Arganda-Carreras, I., Frise, E., Kaynig, V., Longair, M., Pietzsch, T., et al. (2012). Fiji: an open-source platform for biological-image analysis. *Nat. Methods* 9, 676–682. doi: 10.1038/nmeth.2019

Scott, J. A., and Palmer, S. J. (1990). Sites of cadmiun uptake in bacteria used for biosorption. *Appl. Microbiol. Biotechnol.* 33, 221–225. doi: 10.1007/BF00176529

Severin, B. F., Suidan, M. T., and Engelbrecht, R. S. (1983). Kinetic modeling of U.V. disinfection of water. *Water Res.* 17, 1669–1678. doi: 10.1016/0043-1354(83)90027-1

Shah, S., and Damare, S. R. (2018). Differential protein expression in a marine-derived Staphylococcus sp. NIOSBK35 in response to arsenic(III). *Biotech* 8:287. doi: 10.1007/s13205-018-1307-y

Shi, J., Vlamis-Gardikas, A., Åslund, F., Holmgren, A., and Rosen, B. P. (1999). Reactivity of glutaredoxins 1, 2, and 3 from *Escherichia coli* shows that glutaredoxin 2 is the primary hydrogen donor to ArsC-catalyzed arsenate reduction. *J. Biol. Chem.* 274, 36039–36042. doi: 10.1074/jbc.274.51.36039

Slade, D., and Radman, M. (2011). Oxidative stress resistance in Deinococcus radiodurans. *Microbiol. Mol. Biol. Rev.* 75, 133–191. doi: 10.1128/MMBR.00015-10

Sleytr, U. B., Silva, M. T., Kocur, M., and Lewis, N. F. (1976). The fine structure of *Micrococcus radiophilus* and *Micrococcus radioproteolyticus*. *Arch. Microbiol.* 107, 313–320. doi: 10.1007/BF00425346

Srimani, J. K., Huang, S., Lopatkin, A. J., and You, L. (2017). Drug detoxification dynamics explain the postantibiotic effect. *Mol. Syst. Biol.* 13:948. doi: 10.15252/msb.20177723

Strawn, D. G. (2018). Review of interactions between phosphorus and arsenic in soils from four case studies. *Geochem. Trans.* 19, 10–13. doi: 10.1186/s12932-018-0055-6

Suresh, K., Reddy, G. S. N., Sengupta, S., and Shivaji, S. (2004). *Deinococcus indicus* sp. nov., an arsenic-resistant bacterium from an aquifer in West Bengal. *India. Int. J. Syst. Evol. Microbiol.* 54, 457–461. doi: 10.1099/ijs.0.02758-0

Tawfik, D. S., and Viola, R. E. (2011). Arsenate replacing phosphate: alternative life chemistries and ion promiscuity. *Biochemistry* 50, 1128–1134. doi: 10.1021/bi200002a

Tekere, M. (2019). Microbial bioremediation and different bioreactors designs applied. *Biotechnol. Bioeng.*, 1–19. doi: 10.5772/intechopen.83661

Terwilliger, T. C., Grosse-Kunstleve, R. W., Afonine, P. V., Moriarty, N. W., Zwart, P. H., Hung, L. W., et al. (2007). Iterative model building, structure refinement and density modification with the PHENIX AutoBuild wizard. *Acta Crystallogr. Sect. D Biol. Crystallogr.* 64, 61–69. doi: 10.1107/S090744490705024X

Thompson, D., Higgins, D. G., and Gibson, T. J. (1994). CLUSTAL W: improving the sensitivity of progressive multiple sequence alignment through sequence weighting, position-specific gap penalties and weight matrix choice. *Nucleic Acids Res.* 22, 4673–4680. doi: 10.1093/nar/22.22.4673

Thornley, M. J., Horne, R. W., and Glauert, A. M. (1965). The fine structure of micrococcus radiodurans. *Arch. Mikrobiol.* 51, 267–289. doi: 10.1007/BF00408143

Tian, B., Wu, Y., Sheng, D., Zheng, Z., Gao, G., and Hua, Y. (2004). Chemiluminescence assay for reactive oxygen species scavenging activities and inhibition on oxidative damage of DNA in *Deinococcus radiodurans*. *Luminescence* 19, 78–84. doi: 10.1002/bio.761

Tickle, I. J., Flensburg, C., Keller, P., Paciorek, W., Sharff, A., Vonrhein, C., et al. (2018). *Staraniso*. Glob. Phasing Ltd. Cambridge.

Urech, K., Dürr, M., Boller, T., Wiemken, A., and Schwencke, J. (1978). Localization of polyphosphate in vacuoles of *Saccharomyces cerevisiae*. *Arch. Microbiol.* 116, 275–278. doi: 10.1007/BF00417851

Vagin, A., and Lebedev, A. (2015). MoRDa, an automatic molecular replacement pipeline. *Found. Adv.* 71:S19. doi: 10.1107/S2053273315099672

Valentine, J. S., Wertz, D. L., Lyons, T. J., Liou, L. L., Goto, J. J., and Gralla, E. B. (1998). The dark side of dioxygen biochemistry. *Curr. Opin. Chem. Biol.* 2, 253–262. doi: 10.1016/S1367-5931(98)80067-7

Varadwaj, A., Varadwaj, P. R., Marques, H. M., and Yamashita, K. (2022). The Pnictogen bond: the covalently bound arsenic atom in molecular entities in crystals as a Pnictogen bond donor. *Molecules* 27, 23–29. doi: 10.3390/molecules27113421

Vonrhein, C., Flensburg, C., Keller, P., Sharff, A., Smart, O., Paciorek, W., et al. (2011). Data processing and analysis with the autoPROC toolbox. *Acta Crystallogr. Sect. D Biol. Crystallogr.* 67, 293–302. doi: 10.1107/S0907444911007773

Wang, L. K., Wang, M. H. S., Hung, Y. T., Shammas, N. K., and Chen, J. P. (2017). *Handbook of advanced industrial and hazardous wastes management*. Boca Raton: CRC Press.

Wang, L., Zhuang, X., Zhuang, G., and Jing, C. (2016). Arsenic resistance strategy in *Pantoea* sp. IMH: organization, function and evolution of ars genes. *Sci. Rep.* 6:39195. doi: 10.1038/srep39195

Weiss, S., Carapito, C., Cleiss, J., Koechler, S., Turlin, E., Coppee, J. Y., et al. (2009). Enhanced structural and functional genome elucidation of the arsenite-oxidizing strain *Herminiimonas arsenicoxydans* by proteomics data. *Biochimie* 91, 192–203. doi: 10.1016/j.biochi.2008.07.013

Wolf, S. G., Rez, P., and Elbaum, M. (2015). Phosphorus detection in vitrified bacteria by cryo-STEM annular dark-field analysis. *J. Mic.* 260, 227–233. doi: 10.1111/jmi.12289

Yang, H. C., and Rosen, B. P. (2016). New mechanisms of bacterial arsenic resistance. *Biom. J.* 39, 5–13. doi: 10.1016/j.bj.2015.08.003

Zhanel, G. G., Hoban, D. J., and Harding, G. K. M. (1991). The Postantibiotic effect: A review of in vitro and in vivo data. *DICP. Ann. Pharmacother.* 25, 153–163. doi: 10.1177/106002809102500210

frontiers | Frontiers in Microbiology

TYPE Original Research
PUBLISHED 12 September 2023
DOI 10.3389/fmicb.2023.1266785

OPEN ACCESS

EDITED BY
Melina Kerou,
University of Vienna, Austria

REVIEWED BY
Dario Piano,
University of Cagliari, Italy
Grzegorz Bartosz,
University of Rzeszow, Poland

*CORRESPONDENCE
Elin Moe
✉ elinmoe@itqb.unl.pt;
✉ elin.moe@uit.no

†PRESENT ADDRESS
Solenne Ithurbide,
Department of Microbiology, Infectious Diseases and Immunology, Faculty of Medicine, University of Montreal, Montreal, QC, Canada

RECEIVED 25 July 2023
ACCEPTED 29 August 2023
PUBLISHED 12 September 2023

CITATION
Rollo F, Martins GD, Gouveia AG, Ithurbide S, Servant P, Romão CV and Moe E (2023) Insights into the role of three Endonuclease III enzymes for oxidative stress resistance in the extremely radiation resistant bacterium *Deinococcus radiodurans*.
Front. Microbiol. 14:1266785.
doi: 10.3389/fmicb.2023.1266785

Insights into the role of three Endonuclease III enzymes for oxidative stress resistance in the extremely radiation resistant bacterium *Deinococcus radiodurans*

Filipe Rollo[1], Guilherme D. Martins[1], André G. Gouveia[1], Solenne Ithurbide[2†], Pascale Servant[2], Célia V. Romão[1] and Elin Moe[1,3*]

[1]Instituto de Tecnologia Química e Biológica António Xavier, Universidade NOVA de Lisboa, Oeiras, Portugal, [2]Université Paris-Saclay, CEA, CNRS, Institute for Integrative Biology of the Cell (I2BC), Gif sur Yvette, France, [3]Department of Chemistry, UiT - The Arctic University of Norway, Tromsø, Norway

The extremely radiation and desiccation resistant bacterium *Deinococcus radiodurans* possesses three genes encoding Endonuclease III-like enzymes (DrEndoIII1, DrEndoIII2, DrEndoIII3). *In vitro* enzymatic activity measurements revealed that DrEndoIII2 is the main Endonuclease III in this organism, while DrEndoIII1 and 3 possess unusual and, so far, no detectable EndoIII activity, respectively. In order to understand the role of these enzymes at a cellular level, DrEndoIII knockout mutants were constructed and subjected to various oxidative stress related conditions. The results showed that the mutants are as resistant to ionizing and UV-C radiation as well as H_2O_2 exposure as the wild type. However, upon exposure to oxidative stress induced by methyl viologen, the knockout strains were more resistant than the wild type. The difference in resistance may be attributed to the observed upregulation of the EndoIII homologs gene expression upon addition of methyl viologen. In conclusion, our data suggest that all three EndoIII homologs are crucial for cell survival in stress conditions, since the knockout of one of the genes tend to be compensated for by overexpression of the genes encoding the other two.

KEYWORDS

DNA repair, DNA glycosylase, radiation damage, base excision repair, oxidation damage

1. Introduction

Deinococcus species, especially *Deinococcus radiodurans* has been described as the most radiation resistant bacteria on earth. It can withstand up to 5 kGy of ionizing radiation (IR) with no loss of viability (Moseley and Mattingly, 1971; Battista, 1997). Exposure to such high doses of radiation generates hundreds of double strand breaks (DSBs), thousands of single strand breaks (SBDs) and greater than 1,000 sites of base damage, which *D. radiodurans* can repair within hours (Battista, 1997; White et al., 1999; Slade and Radman, 2011; Daly, 2012). The mechanism of this extreme resistance is not known but

generally believed to be due to a combination of factors such as its densely packed genome, high levels of pigments (e.g., deinoxanthin) in the membrane, a high level of intracellular Manganese, and an extremely efficient DNA repair mechanism.

The genome of *D. radiodurans* encodes several DNA glycosylases with homologs in all three domains of life involved in the Base Excision repair (BER) pathway (Makarova et al., 2001; Daly, 2012). Endonuclease III (EndoIII) is a bifunctional DNA glycosylase, belonging to the Helix-hairpin-Helix (HhH)-GDP superfamily of DNA glycosylases, which removes a broad range of oxidized DNA lesions like thymine glycol (Tg) and 5-hydroxycytosine (5OHC) in the BER pathway (Dizdaroglu, 2015; Sarre et al., 2019). The most common oxidized lesions are 5OHC and 5-hydroxyuracil (5OHU) which is generated by oxidation of cytosine and Tg which is generated through either oxidation of thymine or oxidation and deamination of 5-methylcytosine. Abasic sites (AP-sites) is caused by loss of a nucleobase, and dihydrothymine (DHT) and dihydrouracil (DHU) originate from IR damage of thymine and cytosine (Dizdaroglu, 1985; Breen and Murphy, 1995). The main substrate of EndoIII enzymes is Tg. This lesion is not mutagenic, but cytotoxic and has been shown to affect cell division by blocking DNA polymerases due to the perturbation induced in the DNA structure (Ide et al., 1985; Clark and Beardsley, 1986; Wallace, 2002; Dizdaroglu, 2015).

In chromosome I, *D. radiodurans* possesses three genes encoding for EndoIII-like glycosylases DR2438, DR0289 and DR0928 (*endoIII1*, *endoIII2* and *endoIII3,* respectively). The gene products of *endoIII1* and *endoIII3* (DrEndoIII1 and DrEndoIII3) were initially considered to be of archaeal origin, while *endoIII2* (DrEndoIII2) was found to be closest to yeast EndoIII (Makarova et al., 2001). Homologs of these three enzymes have been found in other *Deinococcus* species except in *D. peraridilitoris* which lacks the *endoIII3* (Lim et al., 2019; Sarre et al., 2019). Later, sequence alignments of the three EndoIII enzymes with homologs found in other bacterial, archaeal and eukaryotic species led to the hypothesis that these enzymes could be of bacterial origin and that DrEndoIII3 is specific to the *Deinococcaceae* genus (Sarre et al., 2015).

Structure determination of DrEndoIII1 and 3, and homology modelling of DrEndoIII2 revealed that they consist of two α-helical domains (A and B) divided by a positively charged DNA binding cleft, which contains the highly conserved HhH motif and the catalytic residues (aspartate and lysine). Domain A harbors a [4Fe-4S] cluster and a FeS cluster loop and domain B two DNA intercalating loops (DIL1 and DIL2) which are involved in the stabilization of DNA when the damaged base is flipped out of the DNA into the active site pocket. Even though all DrEndoIII homologs can bind undamaged and damaged DNA with various affinities, only DrEndoIII1 and DrEndoIII2 demonstrated activity towards the common EndoIII substrates (Sarre et al., 2015, 2019). DrEndoIII2 revealed catalytic properties that exceed those of *E. coli* EndoIII (EcEndoIII), while DrEndoIII1 acts mostly as a monofunctional DNA glycosylase with lower activity, being also able to process single stranded DNA (ssDNA) (Sarre et al., 2019). Mutational studies have been conducted to unravel the catalytic differences between these enzymes. Substitutions introduced in DIL1 and DIL2 of DrEndoIII1, revealed that these mutations led to a decreased activity due to a lower substrate affinity (Rollo et al., 2022). In the case of DrEndoIII3, none of the substitutions performed in the active site pocket led to an induction of EndoIII type activity (Rollo et al., 2022).

To unravel the role of these three enzymes in the repair of oxidative damages, transcriptome profiling and EndoIII knockout (KO) mutants have been generated and analyzed (Liu et al., 2003; Chen et al., 2007; Hua et al., 2012). However, several questions remain to be answered from these studies. Cells irradiated with a total dose of 15 kGy revealed a down regulation of *endoIII1* with no alterations of the expression of *endoIII2* and *endoIII3* (Liu et al., 2003). On the other hand, only *endoIII1* and *endoIII3* were observed to be damage activated, by gene up regulation, immediately after exposure to 2 kGy of IR (Chen et al., 2007). DrEndoIII KO mutants (Hua et al., 2012) showed no significant difference between the mutants and wild type (WT) when exposed to both IR and hydrogen peroxide (H_2O_2). This has also been observed in EndoIII KO mutant in *E. coli,* which was shown to be as resistant as the WT (Cunningham and Weiss, 1985). Moreover, in *D. radiodurans* each EndoIII KO mutant showed elevated levels of spontaneous mutation which were increased in the triple KO mutant leading to the hypothesis that the three EndoIII's are not only required to repair DNA damage but also have non-overlapping substrates (Hua et al., 2012).

To shed new light on the role of these enzymes at a cellular level in *D. radiodurans*, *endoIII1*, *endoIII2,* and *endoIII3* single KO mutants were constructed and analyzed after being subjected to various oxidative stress related conditions. Here we report the characterization of these strains in terms of their resistance to ionizing and UV-C radiation and exposure to H_2O_2 and methyl viologen (MV) (also known as the common herbicide Paraquat). In the latter case, the effect of stress on the expression level of the *endoIII* genes was also analyzed. Our data suggests that the KO mutants are as resistant as the WT to IR, UV-C and H_2O_2 exposure, however upon exposure to MV they were revealed to be more resistant than the WT which could be attributed to the observed upregulation of EndoIII homologs gene expression levels. Due to an increasing amount of *Deinococcus* sequenced genomes, we also performed a phylogenetic analysis in order to increase our insight regarding the origin of the genes.

2. Materials and methods

2.1. Phylogenetic analysis

A phylogenetic analysis was carried out based on the alignment of 100 EndoIII protein sequences from 17 genome sequenced *Deinococcus* species (*D. radiodurans, D. geothermalis, D. deserti, D. maricopensis, D. proteolyticus, D. gobiensis, D. peraridilitoris, D. swensis, D. soli, D. actinosclerus, D. puniceus, D. irradiatisoli, D. wulumuqiensis, D. ficus, D. grandis, D. psychrotolerans, D. radiophilus*) as well as representative EndoIII proteins from *Homo sapiens, Mus musculus, Xenopus tropicalis, Drosophila melanogaster, Danio rerio, Arabidopsis thaliana, Escherichia coli, Saccharomyces cerevisiae, Caenorhabditis elegans, Bacillus subtilis, Mycobacterium tuberculosis, Chroococcidiopsis thermalis, Thermococcus gammatolerans, Pyrobaculum aerophilum,* and *Archaeoglobus fulgidus*. Proteins aligned by ClustalW (Thompson et al., 1994) were used for development of a maximum likelihood phylogenetic tree with the WAG+G (Whelan and Goldman, 2001) model in MEGAX (Kumar et al., 2018). For calculation of the bootstrap values 1,000 replications were performed. The phylogenetic tree was visualized using iTOL (Letunic and Bork, 2021).

2.2. Bacterial strains, media, growth conditions and construction of *Deinococcus radiodurans* mutants

The *E. coli* strain DH5α was used to propagate plasmids in Luria Broth at 37°C with appropriate antibiotics used at the following concentrations: hygromycin 50 μg/mL, ampicillin 100 μg/mL. All *D. radiodurans* strains were derivatives of strain R1 ATCC 13939, and were grown at 30°C and shaking at 150 rpm in TGY medium [1% (w/v) of Tryptone (VWR), 0.5% (w/v) of Yeast Extract (VWR), 0.5% of Glucose (Carl Roth) 20% (w/v)]. The media were supplemented with the appropriate antibiotics used at the following concentrations: hygromycin 50 μg/mL, kanamycin 6 μg/mL, chloramphenicol 3.5 μg/mL. The GY16076 (Δ*dr2438Ωkan, alias* ΔEndoIII1), GY16078 (Δ*dr0289Ωcat, alias* ΔEndoIII2) and GY16080 (Δ*dr0982Ωhph, alias* ΔEndoIII3) mutant strains were constructed by replacement of the corresponding locus with the appropriate antibiotic resistance cassette using the tripartite ligation method (Mennecier et al., 2004). The transformation of *D. radiodurans* with PCR products was performed as previously described (Bonacossa de Almeida et al., 2002). p11086, p12625 and pPS6 plasmids (Meyer et al., 2018) were used as template to amplify kanamycin, hygromycin and chloramphenicol resistance genes, respectively.

2.3. DNA manipulations

Plasmid DNA was extracted from *E. coli* using the NucleoSpin® Plasmid miniprep kit (Macherey-Nagel). *D. radiodurans* chromosomal DNA was isolated as described previously (Norais et al., 2013). PCR reactions were carried out with Phusion DNA Polymerase (Thermo Scientific) to amplify fragments subsequently used for cloning, or with GoTaq Flexi DNA Polymerase (Promega) for diagnostic PCR. PCR products were purified using the PCR Clean-up kit (Macherey-Nagel). All the oligonucleotides used for the knockout mutant constructions are listed in Table 1.

TABLE 1 List of the primers used in the generation of knockout mutants.

Name	Sequence 5′-3′
EndoIII1 Up FP (SI78)	GCAGGAAGAACATGCCAAAG
EndoIII1 Up RP (SI79)	CTGATCTAGAAGCGAGAAACCGGTCAAAGG
EndoIII1 Kan FP (PS39BamHI)	GGAATCTAGAGCAAGCAGCAGATTACG
EndoIII1 Kan RP (PS178XbaI)	GGAAGGATCCGCATTCTGCTCCAGCATCTC
EndoIII1 Down FP (SI80XbaI)	ATTCGGATCCACACGTCGCCGAAGAGGGTC
EndoIII1 Down RP (SI81)	TCGAACGCCCGGTCAAACTC
EndoIII2 Up FP (SI78)	CGGCGGCGGGCAGTCCCAAG
EndoIII2 Up RP/ SI79BamHI	GCTAGGATCCCTAGGCCAGAAGGCTTAGTG
EndoIII2 CAM FP/ PS39BamHI	ACGGGATCCCTTTGGAACGGTGCTCGGTG
EndoIII2 CAM RP/ PS178XbaI	ATTTCTAGACGCGGCCGCACTTATTCA
EndoIII2 Down FP/ SI80XbaI	ATGCTCTAGAGGTGGAGCATGTCGAGGGTT
EndoIII2 Down RP (SI81)	GTCATCAGGGCGCTTTGCAC
EndoIII3 FP (SI90)	CCGTTGACCACGCCGATTTG
EndoIII3 Up RP (SI91Agel)	GACAACCGGTAGGGCACAGGGCAGCGTAAC
EndoIII3 Hph FP (SI97Agel)	TCAGACCGGTGCTTGATATCGAATTCGAGC
EndoIII3 Hph RP (EB87XbaI)	AATTCTAGAGATCCGTGTTTCAGTTAGCC
EndoIII3 down FP (SI92XbaI)	GTACTCTAGAAGCCGTCCGAGTTGGAGTGG
EndoIII3 down RP (SI93)	ACTCGTTTCCGGACACGTTC

The restriction sites used were underlined.

2.4. Sensitivity assays to γ-radiation

Cultured cells in the exponential growth phase were concentrated to an $A_{650nm} = 20$ in TGY2X and irradiated on ice with a ^{137}Cs irradiation system (Institut Curie, Orsay, France) at a dose rate of 41.8 Gy/min. Following irradiation, diluted samples were plated on TGY plates. Colonies were counted after 3–4 days incubation at 30°C.

2.5. Sensitivity assays to UV-C radiation

D. radiodurans strains grown in TGY to an optical density (OD_{600nm}) of 2.0 were sequentially diluted and plated on TGY medium. 5 μL drops were air dried and exposed to final doses between 900 J/m^2 and 1800 J/m2 of UV-C radiation (254 nm). A fluence rate of 3 mW/cm^2 was checked using a MS-100 optical radiometer equipped with an MS 125 UV-C sensor (Ultra-Violet Products, Upland, CA). Each independent assay consisted of two technical replicates within each biological replicate. After irradiation, the cells were incubated at 30°C for 3 days. Cell survival was assessed by measuring the colony-forming units (CFU) at any given dose (N) and dividing it by the control conditions (N_0), (which were not exposed to radiation). Cell survival curves were obtained by plotting the logarithm of (N/N_0) and dose (J/m^2).

2.6. Sensitivity assays to H_2O_2 and MV

The resistance of *D. radiodurans* to H_2O_2 and MV oxidative stress was assessed by adapting the Kirby Bauer method (Holder, 1989). Cells were grown to an OD_{600nm} of 2.0 and a total of 400 μL were swabbed evenly in a 120×120 mm plate (VWR) and air-dried for at

10.3389/fmicb.2023.1266785

least 15 min. Afterwards, 6 mm disks (Prat Dumas) were placed on top of the bacterial mat, and 20 µL of increasing concentrations of either H_2O_2 (0.2 to 1 M) or MV (WT, 2 to 10 mM while ΔEndoIII strains 10 to 50 mM) were applied. MilliQ H_2O was used for the control conditions and drops were air-dried. Plates were incubated at 30°C for 3 days and oxidative stress response was assessed by measuring the diameter of the inhibition zones using ImageJ (Schneider et al., 2012). Two independent assays with three replicates were performed.

2.7. Effects of MV-induced oxidative stress during cell growth

D. radiodurans strains were grown in TGY medium with the appropriate antibiotics, at 30°C, and 150 rpm. The effect of exposure to oxidative stress was tested by adding 0.1 mM MV to the culture flasks. This concentration was chosen based on initial growth experiments in liquid media with different concentrations of MV and is lower than in the sensitivity assays which were performed on solid media. The compound was added to the media when the cell cultures had obtained an optical density (OD_{600nm}) of 0.3. Growth curves of each strain in absence and presence of MV were generated from three independent growths, and evaluated by plotting OD_{600nm} against the incubation time, followed by an analysis of the gene expression at the mRNA level at different time points in the growth to analyse the expression profile of the different strains in both conditions.

2.8. RNA extraction cDNA synthesis and RT-PCR

Total RNA was extracted from cells which were harvested at different time points (0 h (before the addition of 0.1 mM MV ($OD_{600nm} = 0.3$)), 2 h (early exponential phase) and 5 h (mid exponential phase)) by using the RNAspin Mini RNA isolation kit (Cytiva, Buckinghamshire, UK) with some modifications. 5 mL of cultured *D. radiodurans* cells were harvested by centrifugation at 4°C, 11000 *g* for 5 min, and resuspended in 100 µL of Tris-EDTA (TE) buffer (10 mM Tris–HCl pH 8, 1 mM EDTA) containing 45 mg/mL lysozyme followed by 3 min of vigorous vortexing and incubation for 45 min at 37°C. After incubation, the total RNA extraction was performed according to the manufacturer's instruction. The RNA was quantified and tested for purity by calculating the A_{260}/A_{280} ratio using a spectrophotometer (Nanodrop) and gel quantification. Extracted RNA with a purity of 1.8–2.0 was used for cDNA synthesis. The cDNA synthesis was performed using 2 µg DNase treated RNA and the Transcriptor High Fidelity cDNA Synthesis Kit (Roche, Basel, Switzerland) according to the manufacturer's instructions.

For the RT-PCR, primers were designed for each gene of interest, *endoIII1*, *endoIII2* and *endoIII3,* and for two housekeeping genes (Glyceraldehyde 3-phosphate dehydrogenase (*GAPDH*) and DNA gyrase A (*gyrA*)) (Table 2) of *D. radiodurans* and checked for the absence of self-complementarity and gene selectivity. Gene expression levels were determined from a gel based semi-quantitative analysis and normalized against the housekeeping gene expression levels. RT-PCR products were loaded onto 1% TBE (100 mM Tris–HCl, 100 mM Boric acid, 2 mM EDTA) agarose gel and bands were visualized on a Fuji TLA-5100 scanner using a LPB filter (473 nm). Band quantification was performed using Fiji (Schindelin et al., 2012). The data presented for each gene is from three biological replicates and the gene expression levels were subjected to two-way ANOVA tests to detect significant ($p < 0.0332$) differences between expression levels.

TABLE 2 List of the primers used in the RT-PCR for gene expression levels analysis.

Name	Sequence 5′-3′
DrEndoIII1 RT-PCR FP	CGTATCTGTACGAGCTGCACATCA
DrEndoIII1 RT-PCR RP	TATCCTTTAGCCGGTTTCTCGCCT
DrEndoIII2 RT-PCR FP	ACAAAGTGGAAGCCGACCTGCAAA
DrEndoIII2 RT-PCR RP	TACTTTCGGACAGAAGCTCGCCAA
DrEndoIII3 RT-PCR FP	ACACTGAGCAGGATGGAGAATGGA
DrEndoIII3 RT-PCR RP	TGTTCGCTCAGAGGACGGGATTTA
DrGAPDH RT-PCR FP	AGGAAGTCAACAACGTCTTCCGTG
DrGAPDH RT-PCR RP	TACCACGAGAAGAACTTGACGAGG
DrgyrA RT-PCR FP	TCAGACCATCAGCGCGATGTACAA
DrgyrA RT-PCR RP	CTGGGTGTACTTGTAGAGCTGGTT

3. Results

3.1. Phylogenetic relationship of the DrEndoIII homologs

Due to an increasing amount of recently sequenced *Deinococcus* strains, we performed a phylogenetic analysis of these enzymes in order to understand their phylogenetic relationships. Our data unveiled four distinct clades of the EndoIII enzymes, EndoIII group 1, 2, 3 and 4, of which the DrEndoIII homologs (DrEndoIII1, 2 and 3) and their respective *Deinococcus* homologs, are observed in EndoIII groups 1, 2 and 3 (Figure 1). Group 4 contained mammalian, higher eukaryote and archea EndoIII homologs which were included as outgroups to the *Deinococcus* EndoIII enzymes.

Within the EndoIII group 1, 2 and 3, it is possible to observe that the EndoIII group 1 and 3 are more closely related to each other than to the EndoIII group 2. It also appears that DrEndoIII1, 2 and 3 are most closely related to their respective EndoIII homologs from *D. wulumuqiensis*. It can also be observed that both DrEndoIII1 and DrEndoIII2 are least related to the homologous EndoIII enzymes from *D. peraridilitoris*, which does not have a DrEndoIII3 homolog. Furthermore, DrEndoIII2 from the EndoIII group 2 is most closely related to bacteria, and actinobacteria such as *Bacillus subtilis*, *E.coli*, *Mycobacterium tuberculosis* and to the desiccation resistant extremophile cyanobacteria *Chroococcidiopsis thermalis*. Regarding DrEndoIII1 and DrEndoIII3, our data suggest that these enzymes are more related to archaea due to the clade formation of both groups with the hyperthermophilic archeum *Pyrobaculum aerophilum*. These phylogenetic relations are in agreement with what was described previously (Makarova et al., 2001).

10.3389/fmicb.2023.1266785

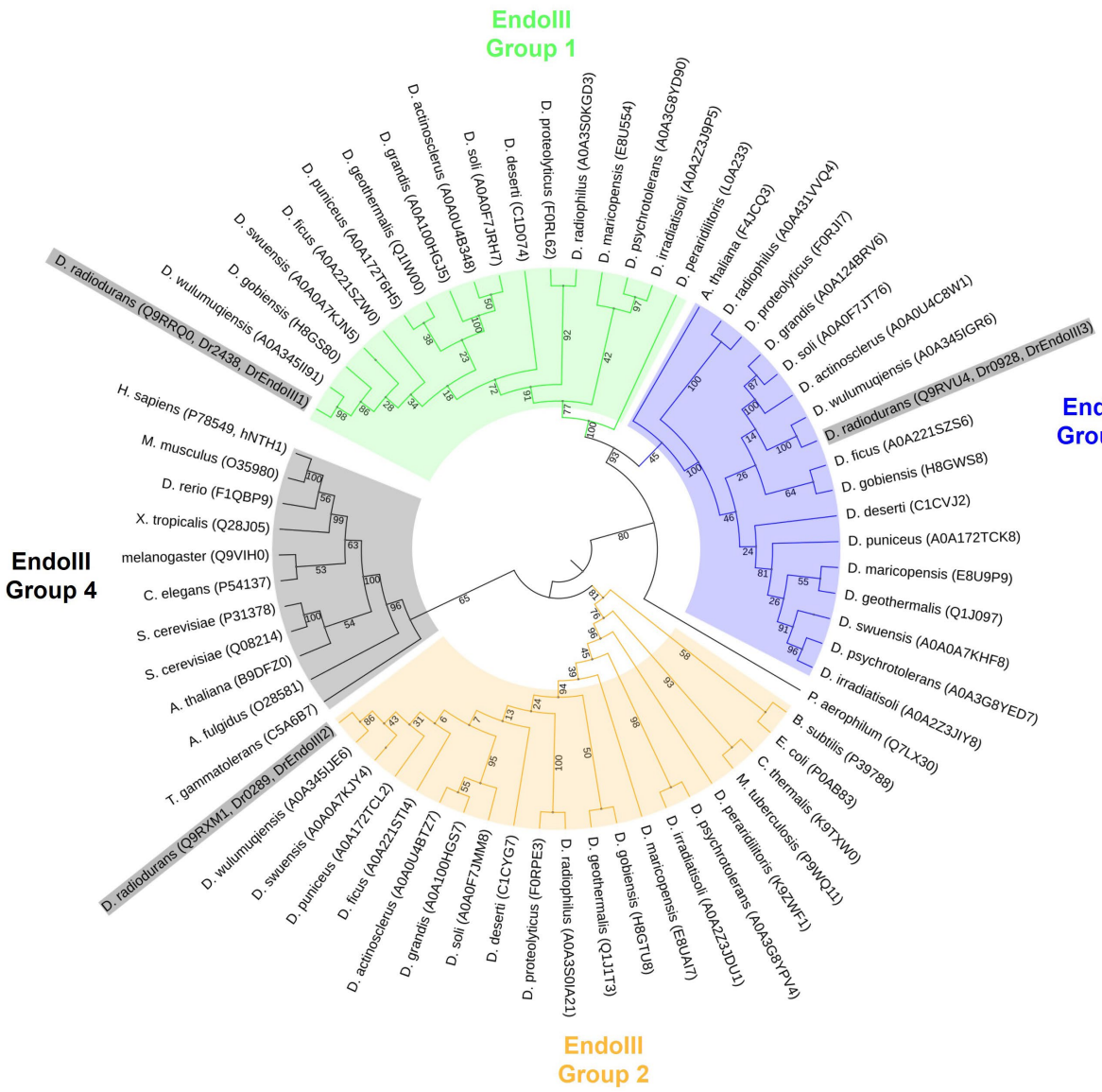

FIGURE 1
Maximum likelihood phylogenetic tree using model WAG+G in MegaX. Four groups of EndoIII family proteins were identified from 17 *Deinococcus* species (*D. radiodurans, D. geothermalis, D. deserti, D. maricopensis, D. proteolyticus, D. gobiensis, D. peraridilitoris, D. swensis, D. soli, D. actinosclerus, D. puniceus, D. irradiatisoli, D. wulumuqiensis, D. ficus, D. grandis, D. psychrotolerans, D. radiophilus*) and other organisms generally considered to be model organisms (*Homo sapiens, Mus musculus, Xenopus tropicalis, Drosophila melanogaster, Danio rerio, Arabidopsis thaliana, Escherichia coli, Saccharomyces cerevisiae, Caenorhabditis elegans, Bacillus subtilis, Mycobacterium tuberculosis, Chroococcidiopsis thermalis, Thermococcus gammatolerans, Pyrobaculum aerophilum* and *Archaeoglobus fulgidus*). Uniprot accession codes of each protein are included in parentheses following the species name. The node numbers are bootstrap values based on 1,000 replicates. DrEndoIII's are highlighted in grey in the figure.

Moreover, our data suggest that the enzymes within the EndoIII group 3 may not be specific for the *Deinococcus* genus as one of the *Arabidopsis thaliana* EndoIII enzymes (F4JCQ3) is included in this clade. However, a more in depth analysis has to be performed regarding this proposition as the bootstrap value of this relation is 45 in our study. The second *A. thaliana* EndoIII (B9DFZ0) can be found in the same clade as human EndoIII (hNTH1) along with the EndoIII homologs from *Sacharomyces cerevisae* in EndoIII group 4 (Figure 1). This clade, like the EndoIII group 1 and 3, revealed to be related to extremophilic archaea organisms such as *Archaeoglobus fulgidus* and *Thermococcus gammatolerans*.

3.2. DrEndoIII KO mutants are not sensitive to γ- or UV-C radiation

In order to determine the role of the DrEndoIII enzymes for radiation resistance of *D. radiodurans*, the KO strains ΔEndoIII1, ΔEndoIII2, and ΔEndoIII3 as well as the WT were exposed to increasing doses of both γ- and UV-C radiation followed by an analysis of their cell survival rates. The results of these experiments revealed no major differences in the sensitivity of the three mutants when exposed to γ-radiation, even up to a dose of 15 kGy (Figure 2A). Regarding the UV-C radiation, we observed that the sensitivities of

10.3389/fmicb.2023.1266785

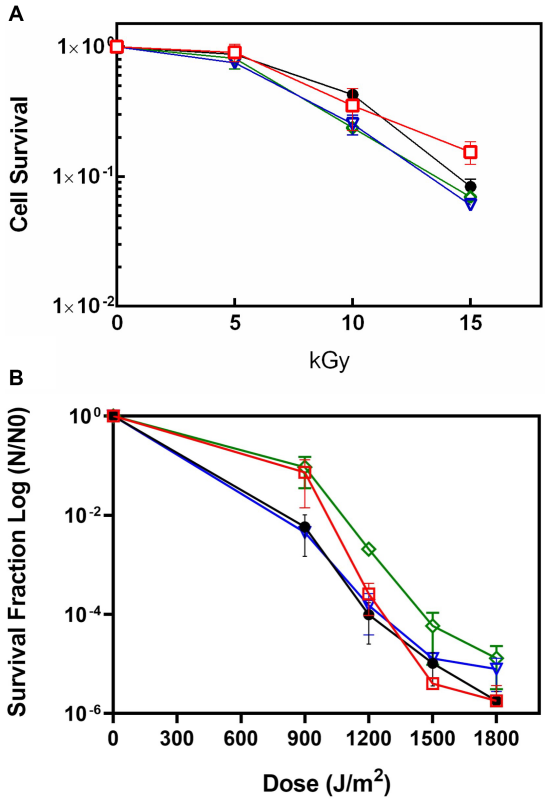

FIGURE 2
Survival rate of WT (●), ΔEndoIII1 (□), ΔEndoIII2 (▽) and ΔEndoIII3 (◇) strains upon exposure to ionizing irradiation **(A)** and UV-C irradiation **(B)**. Experimental data from one out of three replicates of all the knockout mutants are shown in Supplementary figure S1.

the KO strains are similar to the WT, except for at 900 J/m^2 where ΔEndoIII1 and ΔEndoIII3 are less sensitive than the WT and ΔEndoIII2 (Figure 2B and Supplementary Figure S1).

3.3. DrEndoIII KO mutants are not sensitive to H_2O_2 but more resistant to MV than the WT

The role of the three DrEndoIII homologs for oxidative stress resistance of *D. radiodurans* was analysed by growing the KO strains on solid media in presence of the oxidative stress agents H_2O_2 and MV. Regarding the H_2O_2 assay, the KO strains displayed the same resistance as the WT except at 200 mM where ΔEndoIII2 is more sensitive than the WT and at 600 mM where ΔEndoIII1 and ΔEndoIII3 are slightly more sensitive than the WT (Figure 3A). We suggest that this is caused by the WT being resistant to H_2O_2 at low concentrations, while it becomes more susceptible to stress at higher concentrations.

Regarding the MV assays, the ΔEndoIII strains presented a significant increase in resistance compared to the WT (Figure 3B). At a concentration of 10 mM MV, the diameter of inhibition for the WT was double the size of the mutants. At concentrations higher than 10 mM the inhibition zone of the WT extended the size of the plate, while it was still possible to measure the inhibition zone of the ΔEndoIII strains. It was thus not possible to compare the resistance between the WT and the mutants at these concentrations. Among the KO strains there were no significant differences in their sensitivity to MV at concentrations higher than 10 mM.

3.4. Effects of MV-induced oxidative stress during cell growth

Based on the observation that the KO strains were more resistant to MV than the WT we decided to perform detailed growth studies of them in presence of this stress agent. In these experiments the growth of *D. radiodurans* KO and WT strains in liquid TGY medium were monitored in absence and presence of MV (0.1 mM).

The results showed that the WT and the KO strains grow similarly under normal conditions for about 8 hours. After this point the growth starts diverting, which is reflected in different growth rates (calculated from the exponential phase - Supplementary Table S1) and with all the strains reaching different final optical densities (OD_{600nm}) ranging from 8 to 9.7 (Figure 4). The WT and ΔEndoIII3 were the strains which reached the lowest final OD_{600} (8.0 and 8.5, respectively), while ΔEndoIII1 and ΔEndoIII2 reached the highest cell densities (OD_{600} = 9.7) under these conditions (Figure 4; Supplementary Table S1). All strains reached the stationary phase at around 16–20 h after inoculation (Figure 4).

In the presence of MV the growth of all the strains was affected. The WT was most affected and only able to grow for one generation (OD_{600nm} ~ 0.6) before entering a lag phase as previously observed (Santos et al., 2019) (Figure 4B). Compared to the WT (Figure 4A) the three KO strains seem to be less sensitive to the stress induced by MV, being able to grow to final $OD_{600nm} \geq 4$ (Figure 4B). From all the KO strains, ΔEndoIII1 revealed to be most affected under oxidative stress with the highest difference in terms of final OD_{600nm} in stressed compared to unstressed condition (ΔOD_{600nm} = 5.3) and growth rate (8.13%) (Figure 4; Supplementary Table S1). Interestingly, the least sensitive strain was ΔEndoIII2, which demonstrated lowest differences in final OD_{600nm} in stress compared to no stress condition (ΔOD_{600nm} = 1.8). Simultaneously, it was the second most affected strain in terms of growth rate of all the KO strains (1.52%) (Figure 4; Supplementary Table S1). ΔEndoIII3, like ΔEndoIII1, was more affected to the stress agent than ΔEndoIII2 in terms of final OD_{600nm} differences (ΔOD_{600nm} = 4.44), however it revealed to be the least affected in terms of growth rates differences (0.83%) (Figure 4; Supplementary Table S1).

3.5. Expression profiling of *endoIII* genes under MV-induced stress

The observation that the ΔEndoIII2 KO strain reached a two times higher OD_{600} than the ΔEndoIII1 and ΔEndoIII3 strains under oxidative stress conditions, suggested that the lack of one gene encoding for a DrEndoIII enzyme might be compensated for by overexpression of the other two *endoIII* genes in this condition. In order to investigate this hypothesis an expression profiling analysis of the genes encoding for DrEndoIII1, DrEndoIII2 and DrEndoIII3 (*endoIII1*, *endoIII2* and *endoIII3*, respectively) was performed in *D. radiodurans* KO and WT strains in both normal and stressed conditions. Cells from each strain were collected at different time

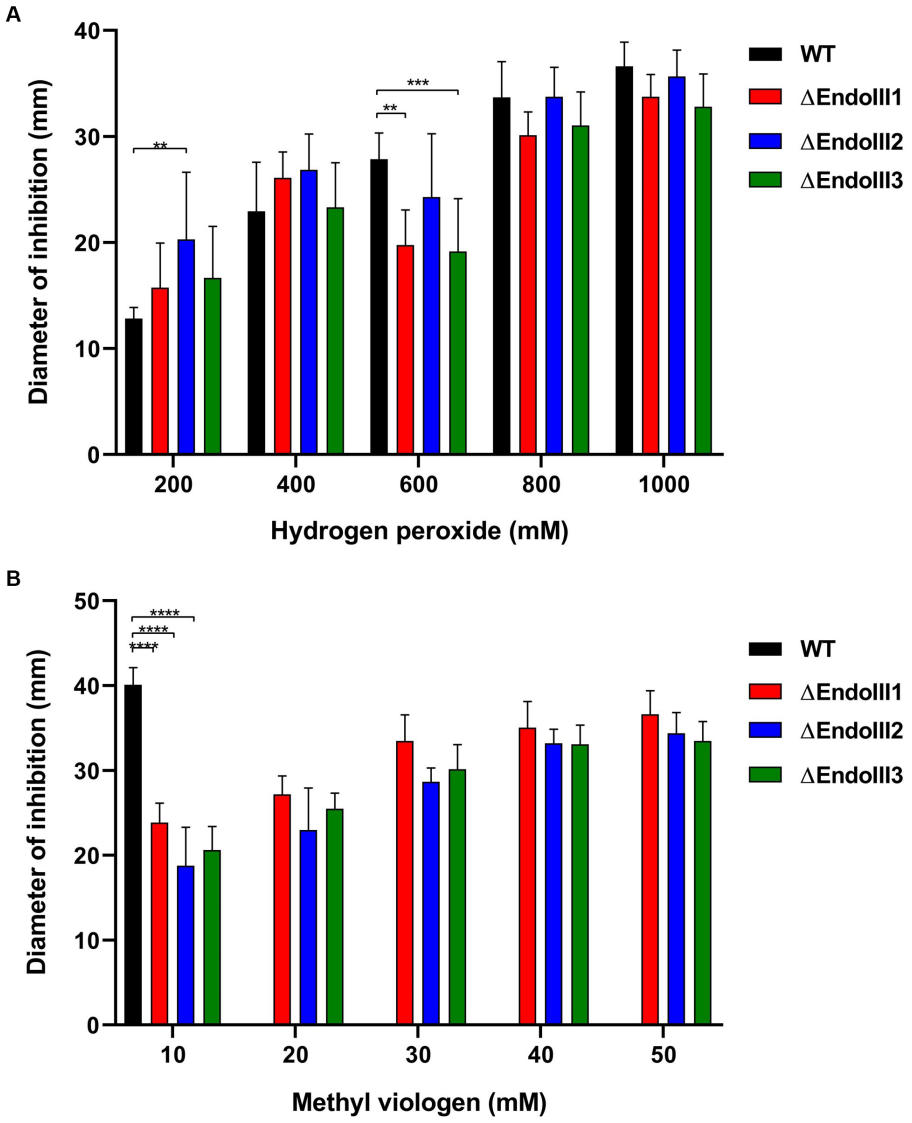

FIGURE 3
Sensitivity assays to H_2O_2 **(A)** and MV **(B)** of WT and ΔEndoIII1, ΔEndoIII2 and ΔEndoIII3. Data for the WT is not included in the graph for MV concentrations higher than 10 mM because the diameter of inhibition had reached the limit of the plate and was thus not possible to measure at this point. The statistic test of three replicates was done with a Two-Way ANOVA and the pvalues are represented following the GP style: 0.1234 (ns), 0.0332 (*), 0.0021 (**), 0.0002 (***), <0.0001 (****).

points (0, 2 and 5 h) under both conditions during cell growth and were used for total RNA extraction and cDNA synthesis followed by RT-PCR. The MV concentration in the stressed conditions was 0.1 mM. Two housekeeping genes (*GAPDH* and *gyrA*) were used for normalization of the gene expression levels.

Overall, one of the most noticeable results of this experiment is that the expression level of *endoIII3* is lower than of both *endoIII1* and *endoIII2* in the WT under normal conditions. We also observed that in the stressed condition the expression of *endoIII2* and *endoIII3* in the WT were significantly reduced (~50%) while the *endoIII1* expression was not significantly affected (Figures 5A–C; Supplementary Figure S2).

An analysis of the expression levels of *endoIII1* in the WT, ΔEndoIII2 and ΔEndoIII3 in normal and stressed conditions (Figure 5A), revealed that this gene is expressed at similar levels in all the strains in both conditions. Only in ΔEndoIII2 it is possible to observe a significant increase (16%) of the *endoIII1* expression level under stressed condition, compared to the WT (Figure 5A).

Furthermore, the expression levels of *endoIII2* in the WT and ΔEndoIII1 and ΔEndoIII3 (Figure 5B) in unstressed and stressed conditions are higher in the KO strains than in the WT in both conditions. Under normal conditions, we observed a significant increase (23%) in the *endoIII2* expression level in the ΔEndoIII1 strain compared to the WT, being overexpressed when compared with the housekeeping gene (> 100%). The increase in the expression level of *endoIII2* in ΔEndoIII3 was lower than in the WT (14%) in normal conditions. Furthermore, in stressed conditions a significant increase in the expression level of *endoIII2* to 42 and 45% was observed in both ΔEndoIII1 and ΔEndoIII3, respectively, when compared to the WT. Under the same condition a 32 and 13%

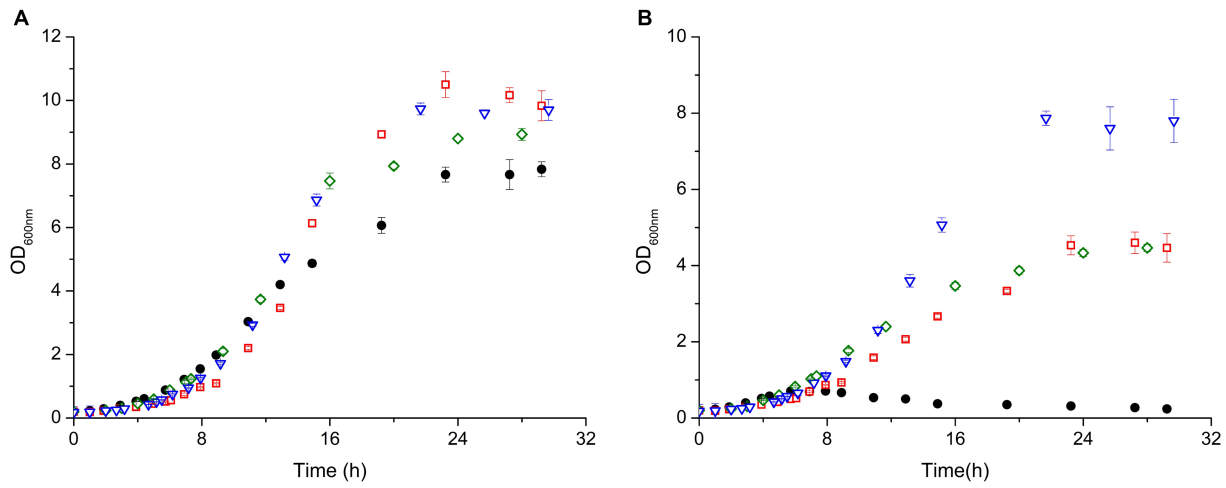

FIGURE 4
Growth curves of *D. radiodurans* (WT (●), ΔEndoIII1 (□), ΔEndoIII2 (▽) and ΔEndoIII3 (◇)) under control conditions **(A)** and in the presence of 0.1mM MV **(B)**. Growth rates from each strain were calculated in the exponential phase (Supplementary Table S1).

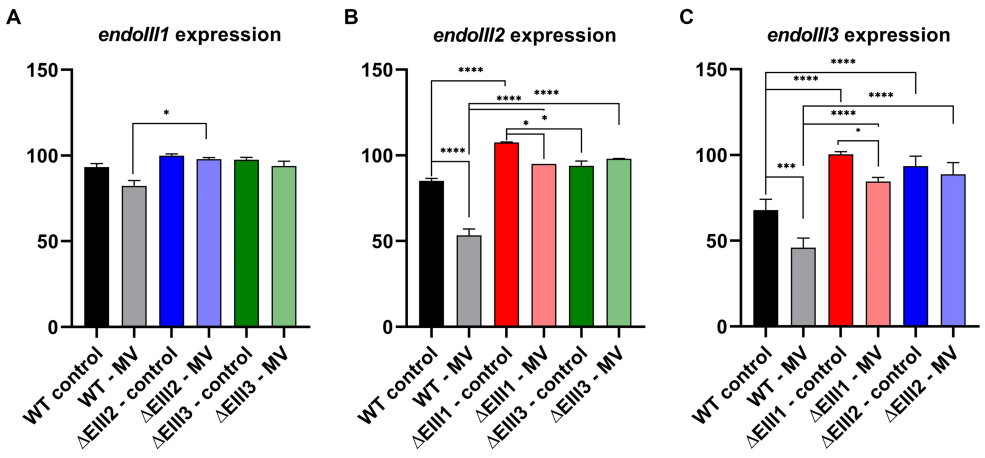

FIGURE 5
Gene expression analysis of *endoIII1* **(A)**, *endoIII2* **(B)** and *endoIII3* **(C)** in *D.radiodurans* strains (WT, ΔEndoIII1, ΔEndoIII2, ΔEndoIII3). Two growth conditions were analyzed (control and 0.1 mM MV). The data was normalized using housekeeping genes (*GAPDH* and *gyrA*) which correspond to 100% expression level. Two-Way ANOVA tests were performed to determine significant differences (*p* value under GP style: 0.1234 (ns), 0.0332 (*), 0.0021 (**), 0.0002 (***), <0.0001 (****)). Gene expression levels presented are for the last time point (5 h) since no significant differences were observed between the different time points (Supplementary Figure S3).

decrease in the level of *endoIII2* expression was observed in the WT and ΔEndoIII1, respectively, when compared to normal conditions (Figure 5B).

Finally, the expression levels of *endoIII3* were higher in ΔEndoIII1 and ΔEndoIII2 compared to the WT in both growth conditions (Figure 5C). In normal conditions an increase in expression of 33 and 26% of *endoIII3* was observed in ΔEndoIII1 and ΔEndoIII2 when compared with WT. We noticed also that the level of expression of *endoIII3* in the ΔEndoIII1 is similar to the housekeeping genes (~100%). The expression level of *endoIII3* is decreased in both the WT and ΔEndoIII1 by 22 and 16%, respectively, under stressed compared to normal conditions. Under stress conditions an increase in the *endoIII3* expression level is observed for both ΔEndoIII1 (39%) and ΔEndoIII2 (43%) compared to the WT (Figure 5C).

4. Discussion

Based on more available genome sequenced *Deinococcus* strains, we started this work by performing a phylogenetic analysis of the three Endonuclease III enzymes among these strains. Based on an analysis of 17 fully genome sequenced *Deinococcus* species, our data suggests that DrEndoIII1 and DrEndoIII3 are archaeal type enzymes as previously suggested (Makarova et al., 2001). We could also hypothesize that DrEndoIII3 may not be a specific variant for the *Deinococcus* species, however this requires further analysis and validation (Figure 1). Regarding DrEndoIII2 our data suggest that it is more closely related to bacteria than to yeast.

The survival of the ΔEndoIII strains upon exposure to IR revealed no significant differences when compared to the WT (Figure 2A). This

was surprising, especially in the case of ΔEndoIII2, since DrEndoIII2 is the apparent main EndoIII enzyme in *D. radiodurans* (Sarre et al., 2019). However, similar results from other IR experiments have been observed previously (Cunningham and Weiss, 1985; Hua et al., 2012), even in the case of multiple KO strains. In these cases, it was suggested that other repair pathways and enzymes from the BER pathway are able to repair the lesions that are introduced into the DNA under these conditions. It is likely that this is the case also for our experiment, knowing that IR causes both direct and indirect damage to DNA, leading to base modifications (e.g., 8-oxoG and Tg) and strand breaks which can be dealt with both in BER and homologous recombination (Cox and Battista, 2005; Slade and Radman, 2011; Krokan and Bjørås, 2013; Dizdaroglu, 2015; Timmins and Moe, 2016). We can also not exclude the possibility that the ROS scavenging system (e.g., catalases and SOD) and other irradiation protection mechanisms (e.g., high level of pigments in the membrane) is protecting *D. radiodurans* from severe damage in this case.

Exposure of our KO strains to UV-C radiation revealed no observable response and resistance differences to *D. radiodurans* WT (Figure 2B). The most abundant DNA lesions generated by UV-C radiation, are the mutagenic and cytotoxic cyclobutane pyrimidine dimers (CPDs) and pyrimidine–pyrimidone (6-4) photoproducts (6–4PPs) (Battista, 1997; Sinha and Häder, 2002; Slade and Radman, 2011; Timmins and Moe, 2016), which are repaired via the NER and the UV damage endonuclease (UVDE) pathways (Tanaka et al., 2005; Blasius et al., 2008; Slade and Radman, 2011; Timmins and Moe, 2016). UV radiation also generates other photoproducts and lesions normally associated with oxidative damages in DNA such as pyrimidine hydrate, Tg, dipurine adducts, ROS (mainly singlet oxygen ($^1O_2$), protein oxidation and 8-oxoG) (Demple and Linn, 1982; Zhang et al., 1997; Friedberg et al., 2006; Krisko and Radman, 2010; Chatterjee and Walker, 2017). Thus, we suggest that the UV-damages generated in this experiment might have been repaired in the NER and UVDE pathways and that the remaining oxidative damages might have been efficiently repaired by the BER DNA glycosylases (8-oxoG DNA glycosylase and the EndoIII's) even in the absence of one of the DrEndoIII enzymes.

In order to analyze the response of the *D. radiodurans* strains to oxidative stress, they were exposed to either H_2O_2 or MV (Figure 3). Both agents are responsible for damage of nucleobases, nucleotides (oxidized pyrimidines and purines (eg. Tg and 8 oxo-G)) (Demple and Linn, 1982; Petrovská and Dušinská, 1999; Slade and Radman, 2011), and proteins containing iron–sulfur and heme groups (Munteanu et al., 2015). Superoxide radicals can be converted to H_2O_2 and consequently to Hydroxyl radicals leading to major DNA modifications (Maynard et al., 2009; Dizdaroglu, 2015; Gonzalez-Hunt et al., 2018). Both H_2O_2 and superoxide radicals are generally detoxified by different scavengers systems such as superoxide dismutase, catalases and Mn complexes (Culotta and Daly, 2013). Here, exposure of the KO and WT strains to H_2O_2 demonstrated that they possessed similar sensitivity to this oxidation damaging agent (Figure 3A). This response have also been observed previously of other *D. radiodurans* and *E. coli* EndoIII KO mutants (Cunningham and Weiss, 1985; Hua et al., 2012).

Regarding the MV stress experiments, our data clearly revealed an effect on the growth demonstrating a reduction in both growth rate and final OD on all strains tested. As previously observed, the growth of the WT was severely affected, leading to a decrease of the growth before entering a lag phase (Santos et al., 2019) (Figure 4B). The three DrEndoIII KO strains proved to be more resistant being able to grow to a higher final optical density upon addition of the damaging agent than the WT (> 17x). Out of the three KO strains, ΔEndoIII1 was most severely affected by the addition of MV, reducing the final OD_{600} from 10 to almost 4 and a reduction in the growth rate from 0.2563 to 0.175 h^{-1} (Figure 4B; Supplementary Table S1). ΔEndoIII2 showed higher resistance levels than the other mutants (Figure 4B). This was not expected since DrEndoIII2 is considered the main EndoIII enzyme responsible for repair of oxidation damaged pyrimidines in DNA (Sarre et al., 2019). Although ΔEndoIII3 unveiled to be the strain with the lowest growth rate under normal conditions it was also the strain with the smallest difference in growth rates when comparing both growth conditions (Supplementary Table S1). This result suggests that DrEndoIII3, in general, is important for oxidative stress resistance in *D. radiodurans* despite its lack of classic EndoIII substrate specificity (Sarre et al., 2019).

A gene expression analysis was carried out to evaluate the importance of the three DrEndoIII homologs in oxidative stress resistance (MV) at the gene level (Figure 5). The results revealed that *endoIII1* is expressed at similar levels in all strains and conditions suggesting that it is important during cell growth (Figure 5A). These results do not correspond to findings in other transcriptome experiments where irradiation was used to induce oxidative stress. In one case it was shown that the expression levels of *endoIII1* were down regulated upon exposure to 15 kGy of IR compared to control conditions (Liu et al., 2003). In the other case it was shown that *endoIII1* was DNA-damage inducible immediately upon exposure to 2 kGy of IR (Chen et al., 2007). However, the stress induction in both cases is different and is thus not directly comparable to our experiment. Even so, it indicates that the level of expression may be different depending on the damage that is inflicted into the DNA. In our case, a generally high expression level of *endoIII1* was observed in both normal and stressed condition in WT as well as KO strains, indicating a generally high importance of this protein during cell growth.

Opposite to *endoIII1*, both *endoIII2* and *endoIII3* genes are upregulated in the KO strains under oxidative stress conditions compared to the WT (Figures 5B,C). We even observed that *endoIII2* is overexpressed surpassing the expression of the housekeeping genes when *endoIII1* is knocked out (ΔEndoIII1) under normal conditions and that *endoIII3* reaches the expression levels of the housekeeping genes. This is also in contrast to what has been reported previously. In these studies the level of expression of the *endoIII2* and *endoIII3* genes did not change (Liu et al., 2003), and the *endoIII2* gene was not significantly induced upon IR exposure (Chen et al., 2007). Again, the stress induction in those studies is not directly comparable to our study, and we can only assume that the level of damage induced by exposure of the cells to MV is not as dramatic as for IR. However, this brings support to our hypothesis about *endoIII1* being in general very important for *D. radiodurans* in both normal and stressed conditions, suggesting that this enzyme may play additional roles in the cells which goes beyond DNA repair. This corresponds well to our knowledge that DrEndoIII1 possesses specificity for oxidation damages in single stranded DNA in addition to its primary function as a DNA glycosylase in the presence of Tg in double stranded DNA substrates (Sarre et al., 2019). Multiple roles of DNA glycosylases have been observed previously, e.g., of human uracil DNA N-glycosylases

(UNG) which is involved in both BER and replication (Krokan et al., 2002). Due to its activity on single stranded DNA, it is thus not unlikely that DrEndoIII1 is involved in DNA replication repair, however, this will have to be explored in future experiments.

5. Conclusion

Here we have provided further insights into the role/importance of the three Endonuclease III enzymes in *D. radiodurans* when this bacterium is exposed to oxidative stress. Despite the lack of observed *in vitro* activity/function for DrEndoIII3 from previous studies, our data suggests that this gene product is extremely important for the bacteriums' oxidation damage resistance. This is noticeable in all the KO strains, with observed upregulation of *endoIII3* in both ΔEndoIII2 and ΔEndoIII1 KO strains. Also, in ΔEndoIII2 the overexpression of *endoIII3* coupled with *endoIII1* was revealed to be the best combination to cope with oxidative stress and is a good example of how the lack of one of the *endoIII* genes may be compensated for by overexpression of the other two. Moreover, the observation that the expression of *endoIII1* is important in all strains in both normal and stressed conditions, suggests that this enzyme may play multiple roles in *D. radiodurans*. The role of both DrEndoIII1 and DrEndoIII3 will therefore be further explored in future studies. Thus, we conclude that all three DrEndoIII enzymes are important in the resistance mechanisms of *D. radiodurans* towards oxidative stress, however, the contribution of the individual enzymes in this process is yet to be fully disclosed. One possible approach to reveal new information in this regard is to perform a comparative gene clustering analysis of each EndoIII group using available genome data of sequenced *Deinococcus* strains.

Data availability statement

The original contributions presented in the study are included in the article/Supplementary material, further inquiries can be directed to the corresponding author.

Author contributions

FR: Investigation, Methodology, Visualization, Writing – original draft, Formal analysis. GM: Investigation, Visualization, Writing – review & editing, Formal analysis. AG: Writing – review & editing, Methodology, Supervision, Formal analysis. SI: Investigation, Writing – review & editing. PS: Methodology, Writing – review & editing, Supervision, Visualization. CR: Supervision, Writing – review & editing, Conceptualization, Funding acquisition. EM: Conceptualization, Funding acquisition, Supervision, Writing – review & editing, Project administration.

Funding

The author(s) declare financial support was received for the research, authorship, and/or publication of this article. This work was supported by FCT—Fundação para a Ciência e a Tecnologia, I.P., through MOSTMICRO-ITQB R&D Unit (UIDB/04612/2020, UIDP/04612/2020) and LS4FUTURE Associated Laboratory (LA/P/0087/2020), Centre National de la Recherche Scientifique and the University Paris-Saclay, research projects PTDC/QUI/BIQ/100007/2008, PTDC/BBBBEP/0561/2014, PTDC/BIA-BFS/31026/2017, PTDC/BIA-BQM/31317/2017, post doc fellowship SFRH/BPD/97493/2013 (EM), PhD fellowships SFRH/BD/132966/2017 and COVID/BD/152598/2022 (FR) and SFRH/BD/06723/2020 (AGG). Funding is also acknowledged for the TIMB3 and IMpaCT project, European Union's Horizon 2020 research and innovation program, under grant agreement No 810856 and No 857203, respectively, and the Research Council of Norway, project number: 183626.

Conflict of interest

The authors declare that the research was conducted in the absence of any commercial or financial relationships that could be construed as a potential conflict of interest.

Publisher's note

Supplementary material

The Supplementary material for this article can be found online at: https://www.frontiersin.org/articles/10.3389/fmicb.2023.1266785/full#supplementary-material

References

Battista, J. R. (1997). AGAINST ALL ODDS: the survival strategies of *Deinococcus radiodurans*. *Annu. Rev. Microbiol.* 51, 203–224. doi: 10.1146/annurev.micro.51.1.203

Blasius, M., Sommer, S., and Hübscher, U. (2008). *Deinococcus radiodurans*: what belongs to the survival kit? *Crit. Rev. Biochem. Mol. Biol.* 43, 221–238. doi: 10.1080/10409230802122274

Bonacossa de Almeida, C., Coste, G., Sommer, S., and Bailone, A. (2002). Quantification of RecA protein in *Deinococcus radiodurans* reveals involvement of RecA, but not LexA, in its regulation. *Mol. Gen. Genomics.* 268, 28–41. doi: 10.1007/s00438-002-0718-x

Breen, A. P., and Murphy, J. A. (1995). Reactions of oxyl radicals with DNA. *Free Radic. Biol. Med.* 18, 1033–1077. doi: 10.1016/0891-5849(94)00209-3

Chatterjee, N., and Walker, G. C. (2017). Mechanisms of DNA damage, repair, and mutagenesis. *Environ. Mol. Mutagen.* 58, 235–263. doi: 10.1002/em.22087

Chen, H., Xu, Z., Tian, B., Chen, W., Hu, S., and Hua, Y. (2007). Transcriptional profile in response to ionizing radiation at low dose in *Deinococcus radiodurans*. *Prog. Nat. Sci.* 17, 529–536. doi: 10.1080/10020070708541032

Clark, J. M., and Beardsley, G. P. (1986). Thymlne glycol lesions terminate chain elongation by DNA polymerase I in vitro. *Nucleic Acids Res.* 14, 737–749. doi: 10.1093/nar/14.2.737

Cox, M. M., and Battista, J. R. (2005). *Deinococcus radiodurans* - the consummate survivor. *Nat. Rev. Microbiol.* 3, 882–892. doi: 10.1038/nrmicro1264

Culotta, V. C., and Daly, M. J. (2013). Manganese complexes: diverse metabolic routes to oxidative stress resistance in prokaryotes and yeast. *Antioxid. Redox Signal.* 19, 933–944. doi: 10.1089/ars.2012.5093

Cunningham, R. P., and Weiss, B. (1985). Endonuclease III (nth) mutants of *Escherichia coli*. *PNAS* 82, 474–478. doi: 10.1073/pnas.82.2.474

Daly, M. J. (2012). Death by protein damage in irradiated cells. *DNA Repair (Amst)* 11, 12–21. doi: 10.1016/j.dnarep.2011.10.024

Demple, B., and Linn, S. (1982). 5,6-saturated thymine lesions in DNA: production by ultraviolet light or hydrogen peroxide. *Nucleic Acids Res.* 10, 3781–3789. doi: 10.1093/nar/10.12.3781

Dizdaroglu, M. (1985). Application of capillary gas chromatography-mass spectrometry to chemical characterization of radiation-induced base damage of DNA: implications for assessing DNA repair processes. *Anal. Biochem.* 144, 593–603. doi: 10.1016/0003-2697(85)90158-7

Dizdaroglu, M. (2015). Oxidatively induced DNA damage and its repair in cancer. *Mutat. Res. Rev. Mutat. Res.* 763, 212–245. doi: 10.1016/j.mrrev.2014.11.002

Friedberg, E. C., Walker, G. C., Siede, W., Wood, R. D., Schultz, R. A., and Ellenberger, T.. *DNA repair and mutagenesis. 2nd*. Washington DC: ASM Press; (2006).

Gonzalez-Hunt, C. P., Wadhwa, M., and Sanders, L. H. (2018). DNA damage by oxidative stress: measurement strategies for two genomes. *Curr. Opin. Toxicol.* 7, 87–94. doi: 10.1016/j.cotox.2017.11.001

Holder, I. A. (1989). The wet disc antimicrobial solution assay. An in vitro method to test efficacy of antimicrobial solutions for topical use. *J. Burn Care Rehabil.* 10, 203–208.

Hua, X., Xu, X., Li, M., Wang, C., Tian, B., and Hua, Y. (2012). Three nth homologs are all required for efficient repair of spontaneous DNA damage in *Deinococcus radiodurans*. *Extremophiles* 16, 477–484. doi: 10.1007/s00792-012-0447-y

Ide, H., Kow, Y. W., and Wallace, S. S. (1985). Thymine glycols and urea residues in M13 DNA constitute replicative blocks in vitro. *Nucleic Acids Res.* 13, 8035–8052. doi: 10.1093/nar/13.22.8035

Krisko, A., and Radman, M. (2010). Protein damage and death by radiation in Escherichia coli and *Deinococcus radiodurans*. *Proc. Natl. Acad. Sci. U. S. A.* 107, 14373–14377. doi: 10.1073/pnas.1009312107

Krokan, H. E., and Bjørås, M. (2013). Base excision repair. *Cold Spring Harb. Perspect. Biol.* 5, 1–22. doi: 10.1101/cshperspect.a012583

Krokan, H. E., Drabløs, F., and Slupphaug, G. (2002). Uracil in DNA-occurrence, consequences and repair. *Oncogene* 21, 8935–8948. doi: 10.1038/sj.onc.1205996

Kumar, S., Stecher, G., Li, M., Knyaz, C., and Tamura, K. (2018). MEGA X: molecular evolutionary genetics analysis across computing platforms. *Mol. Biol. Evol.* 35, 1547–1549. doi: 10.1093/molbev/msy096

Letunic, I., and Bork, P. (2021). Interactive tree of life (iTOL) v5: an online tool for phylogenetic tree display and annotation. *Nucleic Acids Res.* 49, W293–W296. doi: 10.1093/nar/gkab301

Lim, S., Jung, J. H., Blanchard, L., and De Groot, A. (2019). Conservation and diversity of radiation and oxidative stress resistance mechanisms in Deinococcus species. *FEMS Microbiol. Rev.* 43, 19–52. doi: 10.1093/femsre/fuy037

Liu, Y., Zhou, J., Omelchenko, M. V., Beliaev, A. S., Venkateswaran, A., Stair, J., et al. (2003). Transcriptome dynamics of *Deinococcus radiodurans* recovering from ionizing radiation. *Proc. Natl. Acad. Sci. U. S. A.* 100, 4191–4196. doi: 10.1073/pnas.0630387100

Makarova, K. S., Aravind, L., Wolf, Y. I., Tatusov, R. L., Minton, K. W., Koonin, E. V., et al. (2001). Genome of the extremely radiation-resistant bacterium *Deinococcus radiodurans* viewed from the perspective of comparative genomics. *Microbiol. Mol. Biol. Rev.* 65, 44–79. doi: 10.1128/MMBR.65.1.44-79.2001

Maynard, S., Schurman, S. H., Harboe, C., de Souza-Pinto, N. C., and Bohr, V. A. (2009). Base excision repair of oxidative DNA damage and association with cancer and aging. *Carcinogenesis* 30, 2–10. doi: 10.1093/carcin/bgn250

Mennecier, S., Coste, G., Servant, P., Bailone, A., and Sommer, S. (2004). Mismatch repair ensures fidelity of replication and recombination in the radioresistant organism *Deinococcus radiodurans*. *Mol. Gen. Genomics.* 272, 460–469. doi: 10.1007/s00438-004-1077-6

Meyer, L., Coste, G., Sommer, S., Oberto, J., Confalonieri, F., Servant, P., et al. (2018). DdrI, a cAMP receptor protein family member, acts as a major regulator for adaptation of *Deinococcus radiodurans* to various stresses. *J. Bacteriol.* 200, e00129–e00118. doi: 10.1128/JB.00129-18

Moseley, B. E. B., and Mattingly, A. (1971). Repair of irradiated transforming deoxyribonucleic acid in wild type and a radiation-sensitive mutant of Micrococcus radiodurans. *J. Bacteriol.* 105, 976–983. doi: 10.1128/jb.105.3.976-983.1971

Munteanu, A. C., Uivarosi, V., and Andries, A. (2015). Recent progress in understanding the molecular mechanisms of radioresistance in Deinococcus bacteria. *Extremophiles* 19, 707–719. doi: 10.1007/s00792-015-0759-9

Norais, C., Servant, P., Bouthier-de-la-Tour, C., Coureux, P. D., Ithurbide, S., Vannier, F., et al. (2013). The *Deinococcus radiodurans* DR1245 protein, a DdrB partner homologous to YbjN proteins and reminiscent of type III secretion system chaperones. *PLoS One* 8:e56558. doi: 10.1371/journal.pone.0056558

Petrovská, H., and Dušinská, M. (1999). Oxidative DNA damage in human cells induced by Paraquat. *Altern. Lab. Anim* 27, 387–395. doi: 10.1177/026119299902700314

Rollo, F., Borges, P. T., Silveira, C. M., Rosa, M. T. G., Todorovic, S., and Moe, E. (2022). Disentangling unusual catalytic properties and the role of the [4Fe-4S] cluster of three endonuclease III from the extremophile *D. radiodurans*. *Molecules* 27:4270. doi: 10.3390/molecules27134270

Santos, S. P., Yang, Y., Rosa, M. T. G., Rodrigues, M. A. A., De La Tour, C. B., Sommer, S., et al. (2019). The interplay between Mn and Fe in *Deinococcus radiodurans* triggers cellular protection during paraquat-induced oxidative stress. *Sci. Rep.* 9:17217. doi: 10.1038/s41598-019-53140-2

Sarre, A., Ökvist, M., Klar, T., Hall, D. R., Smalås, A. O., McSweeney, S., et al. (2015). Structural and functional characterization of two unusual endonuclease III enzymes from *Deinococcus radiodurans*. *J. Struct. Biol.* 191, 87–99. doi: 10.1016/j.jsb.2015.05.009

Sarre, A., Stelter, M., Rollo, F., De Bonis, S., Seck, A., Hognon, C., et al. (2019). The three endonuclease III variants of *Deinococcus radiodurans* possess distinct and complementary DNA repair activities. *DNA Repair (Amst)* 78, 45–59. doi: 10.1016/j.dnarep.2019.03.014

Schindelin, J., Arganda-Carreras, I., Frise, E., Kaynig, V., Longair, M., Pietzsch, T., et al. (2012). Fiji: an open-source platform for biological-image analysis. *Nat. Methods* 9, 676–682. doi: 10.1038/nmeth.2019

Schneider, C. A., Rasband, W. S., and Eliceiri, K. W. (2012). NIH image to image J: 25 years of image analysis. *Nat. Methods* 9, 671–675. doi: 10.1038/nmeth.2089

Sinha, R. P., and Häder, D. P. (2002). UV-induced DNA damage and repair: a review. *Photochem. Photobiol. Sci.* 1, 225–236. doi: 10.1039/b201230h

Slade, D., and Radman, M. (2011). Oxidative stress resistance in *Deinococcus radiodurans*. *Microbiol. Mol. Biol. Rev.* 75, 133–191. doi: 10.1128/MMBR.00015-10

Tanaka, M., Narumi, I., Funayama, T., Kikuchi, M., Watanabe, H., Matsunaga, T., et al. (2005). Characterization of pathways dependent on the Uvs E, uvr A1, or uvrA2 gene product for UV resistance in *Deinococcus radiodurans*. *J. Bacteriol.* 187, 3693–3697. doi: 10.1128/JB.187.11.3693-3697.2005

Thompson, J. D., Higgins, D. G., and Gibson, T. J. (1994). CLUSTAL W: improving the sensitivity of progressive multiple sequence alignment through sequence weighting, position-specific gap penalties and weight matrix choice. *Nucleic Acids Res.* 22, 4673–4680. doi: 10.1093/nar/22.22.4673

Timmins, J., and Moe, E. (2016). A decade of biochemical and structural studies of the DNA repair machinery of *Deinococcus radiodurans*: major findings, functional and mechanistic insight and challenges. *Comput. Struct. Biotechnol. J.* 14, 168–176. doi: 10.1016/j.csbj.2016.04.001

Wallace, S. S. (2002). Biological consequences of free radical-damaged DNA bases. *Free Radic. Biol. Med.* 33, 1–14. doi: 10.1016/S0891-5849(02)00827-4

Whelan, S., and Goldman, N. (2001). A general empirical model of protein evolution derived from multiple protein families using a maximum-likelihood approach. *Mol. Biol. Evol.* 18, 691–699. doi: 10.1093/oxfordjournals.molbev.a003851

White, O., Eisen, J. A., Heidelberg, J. F., Hickey, E. K., Peterson, J. D., Dodson, R. J., et al. (1999). Genome sequence of the Radioresistant bacterium *Deinococcus radiodurans* R1. *Science* 286, 1571–1577. doi: 10.1126/science.286.5444.1571

Zhang, X., Rosenstein, B. S., Wang, Y., Lebwohl, M., and Wei, H. (1997). Identification of possible reactive oxygen species involved in ultraviolet radiation-induced oxidative DNA damage. *Free Radic. Biol. Med.* 23, 980–985. doi: 10.1016/S0891-5849(97)00126-3

frontiers | Frontiers in Microbiology

TYPE Original Research
PUBLISHED 12 October 2023
DOI 10.3389/fmicb.2023.1265216

OPEN ACCESS

EDITED BY
Melina Kerou,
University of Vienna, Austria

REVIEWED BY
Byung-Kwan Cho,
Korea Advanced Institute for Science and Technology, Republic of Korea
Sung Gyun Kang,
Korea Institute of Ocean Science and Technology (KIOST), Republic of Korea

*CORRESPONDENCE
Mirko Basen
✉ mirko.basen@uni-rostock.de

†These authors have contributed equally to this work

RECEIVED 22 July 2023
ACCEPTED 14 September 2023
PUBLISHED 12 October 2023

CITATION
Lehmann M, Prohaska C, Zeldes B, Poehlein A, Daniel R and Basen M (2023) Adaptive laboratory evolution of a thermophile toward a reduced growth temperature optimum. *Front. Microbiol.* 14:1265216. doi: 10.3389/fmicb.2023.1265216

Adaptive laboratory evolution of a thermophile toward a reduced growth temperature optimum

Maria Lehmann[1†], Christoph Prohaska[1†], Benjamin Zeldes[1], Anja Poehlein[2], Rolf Daniel[2] and Mirko Basen[1*]

[1]Department of Microbiology, Institute of Biological Sciences, University of Rostock, Rostock, Germany, [2]Genomic and Applied Microbiology and Göttingen Genomics Laboratory, Georg-August University, Göttingen, Germany

Thermophily is an ancient trait among microorganisms. The molecular principles to sustain high temperatures, however, are often described as *adaptations*, somewhat implying that they evolved from a non-thermophilic background and that thermophiles, i.e., organisms with growth temperature optima (T_{OPT}) above 45°C, evolved from mesophilic organisms (T_{OPT} 25–45°C). On the contrary, it has also been argued that LUCA, the last universal common ancestor of *Bacteria* and *Archaea*, may have been a thermophile, and mesophily is the derived trait. In this study, we took an experimental approach toward the evolution of a mesophile from a thermophile. We selected the acetogenic bacterium *T. kivui* (T_{OPT} 66°C) since acetogenesis is considered ancient physiology and cultivated it at suboptimal low temperatures. We found that the lowest possible growth temperature (T_{MIN}) under the chosen conditions was 39°C. The bacterium was subsequently subjected to adaptive laboratory evolution (ALE) by serial transfer at 45°C. Interestingly, after 67 transfers (approximately 180 generations), the adapted strain Adpt45_67 did not grow better at 45°C, but a shift in the T_{OPT} to 60°C was observed. Growth at 45°C was accompanied by a change in the morphology as shorter, thicker cells were observed that partially occurred in chains. While the proportion of short-chain fatty acids increased at 50°C vs. 66°C in both strains, Adpt45_67 also showed a significantly increased proportion of plasmalogens. The genome analysis revealed 67 SNPs compared to the type strain, among these mutations in transcriptional regulators and in the cAMP binding protein. Ultimately, the molecular basis of the adaptation of *T. kivui* to a lower T_{OPT} remains to be elucidated. The observed change in phenotype is the first experimental step toward the evolution of thermophiles growing at colder temperatures and toward a better understanding of the cold adaptation of thermophiles on early Earth.

KEYWORDS

adaptive laboratory evolution, origin of life, cold adaptation, acetogens, thermophiles, *Thermoanaerobacter kivui*

1. Introduction

Temperature is a key environmental factor that determines the biodiversity and species composition of habitats as it requires specific traits to allow organisms to thrive at distinct temperatures. The temperature range of habitats on Earth is huge, and living cells have been found from the polar environments and high-altitude regions (De Maayer et al., 2014) to terrestrial mud springs and submarine hot vents (Stetter, 2006).

The growth temperature profile of every species is characterized by the cardinal temperatures, the minimal (T_{MIN}), the maximal (T_{MAX}), and the optimal temperature (T_{OPT}) that allow growth (Wiegel, 1990). Organisms adapted to extremely cold or hot temperatures, or temperature extremophiles, are classified by their T_{OPT}. In contrast to mesophiles growing at more or less ambient temperatures (T_{OPT} 20–45°C), psychrophiles prefer a T_{OPT} lower than 15°C (De Maayer et al., 2014). Thermophiles thrive optimally at temperatures higher than 45°C, while organisms with a T_{OPT} >65–70°C are called extreme thermophiles, and hyperthermophiles possess a T_{OPT} of >80°C (Wiegel, 1990; Zeldes et al., 2015). The temperature range of individual thermophiles may be very broad (Wiegel, 1990). For example, the hyperthermophilic Archaeon *Pyrococcus furiosus* grows optimally at 100°C, with a T_{MAX} of 103°C and a T_{MIN} of 65°C (38 K; Fiala and Stetter, 1986), and the methanogen *Methanothermobacter thermautotrophicus* even has a span of 55 K (Wiegel, 1990).

The specific adaptations of thermophiles have been extensively studied and include the modification and protection of all types of cellular macromolecules. For example, DNA in (hyper)thermophiles is protected by (positively charged) polyamines and by histones in Archaea (Imanaka, 2011). Common features seen in proteins of thermophiles are increased van der Waals interactions, hydrogen bonds, ionic interactions to stabilize the secondary or tertiary structure of the protein, a more hydrophobic interior, and an increased packing density of the protein (Berezovsky and Shakhnovich, 2005; Imanaka, 2011). The folding of proteins in thermophiles is supported by the action of particular chaperones, and proteins and DNA are stabilized within the cell by compatible solutes (Imanaka, 2011). Mechanisms to stabilize the cytoplasmic membrane include ether-linked membrane lipids in archaea, while the degree of saturation and the amount of branched-chain and longer fatty acids increase with temperature in bacteria (Siliakus et al., 2017). Despite these and many other specific traits attributed to life at high temperatures, a comprehensive understanding of "thermophily" is still lacking (Canganella and Wiegel, 2014), particularly toward its evolution. On the one hand, the aforementioned molecular traits to thrive at high temperatures may be derived, having evolved from a mesophile background. On the other hand, these traits may be ancient, and mesophiles may have evolved from ancient thermophiles. For example, life may have emerged at moderately warm hydrothermal and alkaline vent fields such as Lost City (40–90°C; Kelley et al., 2005). This environment is cold enough to allow first (bio)molecular reactions but rich in trace elements and in H_2 and CO_2. These gaseous substrates may have supported the formation of biomass precursors coupled with energy conservation, as found in recent acetogenic bacteria and methanogenic archaea (Martin, 2020). Interestingly, to the best of our knowledge, the hypothesis that mesophiles are derived from thermophiles has never been tested in laboratory evolution experiments.

In this study, we aimed to evolve the bacterium *Thermoanaerobacter kivui* as acetogen with a T_{OPT} of 66°C is capable of growing in environments comparable to Lost City, and where the first life may have emerged, toward growth at lower temperatures. *T. kivui* has been described as an acetogen growing on a variety of substrates, including H_2+CO_2 but also on the sugars glucose, mannose, and fructose (Leigh et al., 1981). The physiology of *T. kivui* has recently been studied to a larger extent. For example, it has been shown to grow on the sugar alcohol mannitol (Moon et al., 2019), in bioelectrical systems on anodes (Deutzmann et al., 2022), and it has been subjected to ALE to grow on carbon monoxide (Weghoff and Müller, 2016). Genetic tools for genome modification (Basen et al., 2018) and plasmid-based protein production (Katsyv et al., 2021) were developed, allowing to study one of its energy-conserving hydrogenases (Katsyv and Müller, 2022), and the soluble hydrogen-dependent carbon dioxide reductase (Jain et al., 2020; Dietrich et al., 2022). This prompted us to pick *T. kivui* as a model thermophilic acetogen for ALE experiments. We grew five populations of *T. kivui* DSM2030 at 45°C (21 K below T_{OPT}) and used the fastest growing population as inoculum for the next five populations cultivated at 45°C (Figure 1). After 67 serial transfers, corresponding to ~180 generations, we studied the phenotype and the genotype of the evolved strain, Adpt45_67.

2. Materials and methods

2.1. Bacterial strains and cultivation

Thermoanaerobacter kivui strain LKT-1 (DSM2030), referred to as the type strain, and the adapted strain Adpt45_67 were cultivated under strict anoxic conditions at different temperatures between 40°C and 66°C in complex or defined media as described previously (Weghoff and Müller, 2016; Basen et al., 2018). Complex media contained $Na_2HPO_4 \times 2\ H_2O$, 50 mM; $NaH_2PO_4 \times 2\ H_2O$, 50 mM; K_2HPO_4, 1.2 mM; KH_2PO_4, 1.2 mM; NH_4Cl, 4.7 mM; $(NH_4)_2SO_4$, 1.7 mM; NaCl, 7.5 mM; $MgSO_4 \times 7\ H_2O$, 0.37 mM; $CaCl_2 \times 2\ H_2O$, 42 µM; $Fe(II)SO_4 \times 7\ H_2O$, 7.2 µM; $KHCO_3$, 54 mM; cysteine-HCl × H_2O, 3 mM; resazurin, 4.4 µM; 0.2% (w/v) yeast extract, 10 ml/l of trace element solution DSM141, and 10 ml/l of vitamin solution DSM141. Defined media were prepared similarly as complex media without the addition of yeast extract. The medium was flushed with N_2:CO_2 (80:20 [v:v], 1.1 x 10^5 Pa) before autoclaving. The pH of the medium was 7.5 after flushing. The agar medium was supplemented with 1.5% Bacto agar (BD Difco, BD Life Sciences, Heidelberg, Germany). All gases were purchased from Westfalen AG (Münster, Germany).

Growth experiments were carried out in 20 ml Hungate glass tubes with 5 ml of medium or in 100-ml or 200-ml serum bottles with 50 ml or 100 ml of medium, respectively. The glass tubes or serum bottles were sealed with butyl rubber stoppers under an atmosphere of N_2:CO_2 (80:20 [v:v], 1.1 x 10^5 Pa) unless denoted otherwise (Basen et al., 2018). Glucose was added as a carbon source from a sterile anoxic stock solution to a final concentration of 25 mM. If H_2 + CO_2 were used as substrates, tubes were only filled with medium to one-fourth of the volume, and the remaining headspace was replaced with H_2:CO_2 (80:20 [v:v], 2 x 10^5 Pa). For growth experiments of *T. kivui* at different temperatures, initial cultures were grown at 66°C to an OD_{600} of 1 and diluted 1/10 in fresh medium, followed by incubation at the desired temperature. Plating and cultivation of solid media were carried out according to Basen et al. (2018). The agar dilution series and the isolation of

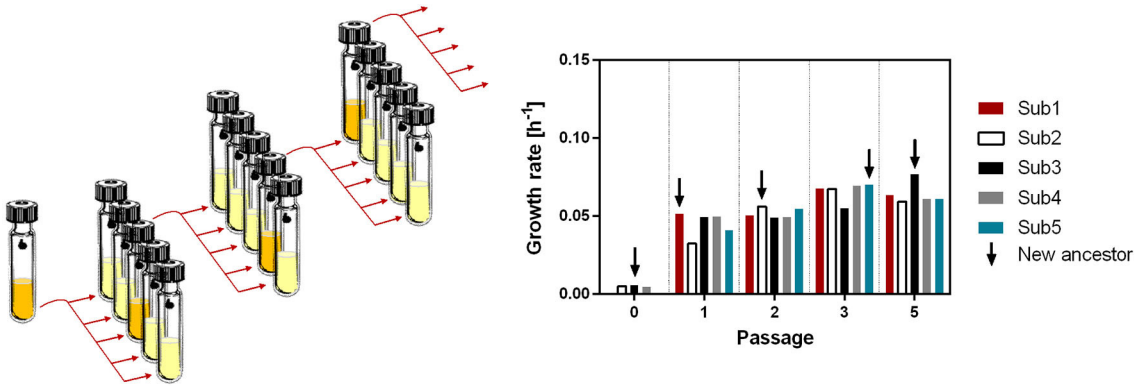

FIGURE 1
Serial passaging modified after Strauss et al. (2019). Five subpopulations of *T. kivui* were incubated for 24 h in a complex medium containing 25 mM glucose as a carbon source. The subpopulation with the highest increase in OD_{600} was used to generate five new subpopulations in a fresh medium.

single colonies from it were performed according to Widdel and Bak (1992).

2.2. Monitoring growth, cell morphology, and metabolites

Growth in the liquid medium was monitored by measuring the optical density at 600 nm (OD_{600}) with a spectrophotometer. Cell morphology was documented using a Nikon Eclipse Ni-U microscope equipped with a Nikon DSFi3 camera (Nikon, Tokyo, Japan). Glucose and organic acid concentrations were determined by HPLC as described previously (Zeldes et al., 2023).

2.3. Adaptative laboratory evolution

The ALE approach by serial passaging was performed as described by Wein and Dagan in Strauss et al. (2019). In brief, *T. kivui* DSM2030 was grown on agar plates at 66°C. Three colonies were randomly sampled as the ancestral clones. The serial passage experiment was initiated by inoculating the three clones in Hungate tubes containing 2 ml of complex medium and incubating at 45°C. Subsequently, the ancestral populations were sampled into five subpopulations of each replicate. The five subpopulations were grown at 45°C, and growth was monitored as described. The subpopulations of each replicate having the highest increase in OD_{600} after 24–28 h were selected as the ancestors for the next subpopulations.

2.4. Single-nucleotide polymorphism analysis

The genomes of adapted strains were analyzed for single-nucleotide polymorphisms as recently described (Zeldes et al., 2023).

2.5. Analysis of cellular fatty acids

T. kivui cultures were grown as described to an OD_{600} of approximately 1. Cultures were harvested for 5 min at 5,000 × *g* and 4°C. Cell pellets were suspended in 0.7% (w/v) aqueous $MgSO_4$ and centrifuged again. Cell pellets were freeze-dried, and ~40 mg of cell biomass (dry weight) was sent for fatty acid (FA) analysis at the Deutsche Sammlung von Mikroorganismen und Zellkulturen (DSMZ) in Braunschweig, Germany.

2.6. Statistical analysis

Datasets were analyzed by two-way ANOVA with Tukey's test using the software Graph Pad Prism Version 6.01 (GraphPad Software, Boston, USA).

3. Results

3.1. Growth of *T. kivui* at suboptimal temperatures

T. kivui was originally described to thrive at 50–72°C (Leigh et al., 1981). Compared to other *Thermoanaerobacter* species, this is a relatively narrow range (Onyenwoke and Wiegel, 2015), since, e.g., *T. pseudethanolicus* grows between 30°C and 80°C (Figure 2). The T_{OPT} of *T. kivui* (66°C) compares favorably with that of other *Thermoanaerobacter* species (55°C—75°C); however, its reported T_{MIN} of 50°C is among the highest, with many species able to grow at significantly lower temperatures between 30°C and 40°C. Wiegel also reported that they were able to cultivate *T. kivui* at 35°C (1990); however, growth parameters and culture conditions were not specified in the articles. These hints that the published T_{MIN} may be too high prompted us to test the growth of *T. kivui* at suboptimal temperatures. Toward that, we selected a complex medium with a reduced yeast extract content (Basen et al., 2018), and glucose as a substrate over H_2+CO_2, since the growth rates and final optical densities in a defined

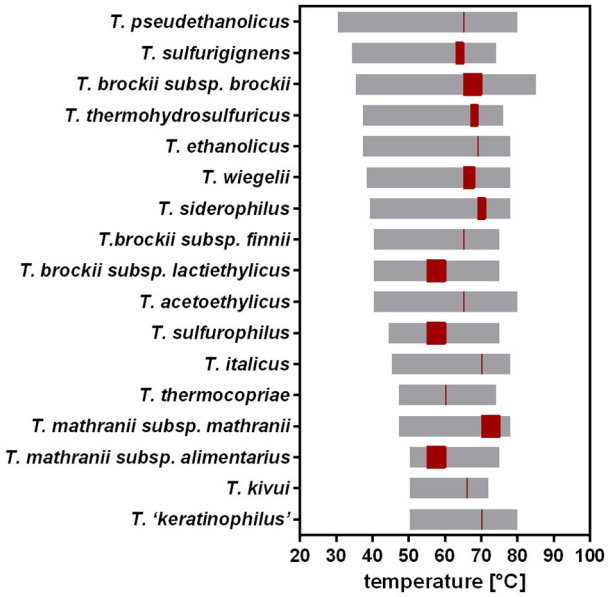

FIGURE 2
Previously reported temperature ranges and optimal growth temperatures for different *Thermoanaerobacter* species. Temperature range, gray; T_{OPT}, red. Data from Onyenwoke and Wiegel (2015).

medium and under autotrophic conditions are lower (Jain et al., 2020; Moon et al., 2020). Growth experiments within a temperature range of 40–66°C were performed (Figure 3A). Consistent with the literature, 66°C is the T_{OPT} for the type strain *T. kivui* DSM2030 (Leigh et al., 1981), at a specific growth rate of 0.45 h^{-1} (Figure 3 and Supplementary Table S1). Lower temperatures resulted in decreased growth rates, as expected. The growth of *T. kivui* was monitored at temperatures below 50°C, and slow growth (0.033 h^{-1}) was observed at 40°C. At temperatures below 39°C, *T. kivui* did not grow in our hands, in contrast to the report of Wiegel (1990); however, as described above, the author may have used different cultivation conditions. Corresponding to lower growth rates, the maximal OD_{600} as an indicator of the biomass yield was reached after longer incubation periods. For example, an OD_{600} >1 was reached after 7 h at 66°C and 60°C, after 12 h at 55°C, and after 23 h at 45°C. At a growth temperature of 40°C, an OD_{600} of 1 was not reached even after incubation for 108 h (Figure 3A).

3.2. Adaptive laboratory evolution of T. kivui to lower temperatures

We decided to use 45°C as the temperature for serial passaging of cultures for ALE, since it seems to provide a good balance of strong selective pressure (only a few degrees above the lowest temperature at which growth is observed) and fast enough growth to achieve a high number of generations through daily passaging. In ALE, organisms are observed under controlled laboratory conditions and specific growth conditions for extended periods of time, allowing the isolation of adapted phenotypes. Many different strategies for ALE have been developed and further improved (Dragosits and Mattanovich, 2013; Strauss et al., 2019), from simple long-term passaging experiments with *Escherichia coli* over several thousand generations (Cooper and Lenski, 2000), to ALE using increased mutation rate and targeted genetic engineering (Luan et al., 2013; Badran and Liu, 2015; Suzuki et al., 2015; Kang et al., 2019). In this study, a variant of the serial passaging strategy (Strauss et al., 2019) was selected, in which five populations were evolved in parallel to increase the number of genotypes tested (Figure 1). Targeted selection was performed continuously on the fastest growing population, defined by the highest increase in OD_{600} within a growth period of 24–28h. Within that time frame, *T. kivui* was still in the exponential growth phase, excluding a more complex adaptation to the stationary growth phase (Vasi and Lenski, 1999). After ~180 generations (passage 67—Supplementary Figure S3), the *T. kivui* population with the highest biomass increase (adapted strain Adpt45_67) was again selected, and a detailed study of the phenotype was performed.

3.3. The evolved strain *T. kivui* Adpt45_67 has a lower optimal growth temperature

We compared the growth of the type strain (DSM2030; acclimated, three transfers at 45°C) and the adapted strain Adpt45_67 (~180 generations at 45°C) during growth on the "adaptation" medium, complex medium plus 25 mM glucose, at temperatures between 40°C and 66°C (Figure 3B). We found that under these conditions, Adpt45_67 grows as fast as the type strain at 66°C (0.45 h^{-1} vs. 0.45 h^{-1}, Figure 3C, Supplementary Table S1). At 45°C, the temperature chosen for adaptation, Adpt45_67, unexpectedly does not grow faster than the type strain (0.08 h^{-1} vs. 0.104 h^{-1}). At 40°C, the lowest temperature tested, growth rates were reduced to below 10% of the rates at 66°C (0.017 h^{-1} and 0.033 h^{-1}), demonstrating the challenge of ALE at lower temperatures. Interestingly, the only significant changes were observed at 60°C and 55°C. At both temperatures, Adpt45_67 grew significantly faster than the type strain (0.523 h^{-1} vs. 0.391 h^{-1} at 60°C and 0.360 h^{-1} vs. 0.297 h^{-1} at 55°C), leading to a shift in the T_{OPT} from 66°C to 60°C (see also Supplementary Figure S1).

We then tested whether the effect is medium-dependent, since adaptations to medium types and compounds have been reported from the Lenski lab (Cooper and Lenski, 2000). We grew the type strain and Adpt45_67 at 66°C and 60°C in a defined medium, which is identical to the complex medium except for the omission of yeast extract (2 g l^{-1}). Since *T. kivui* is an acetogen, we initially confirmed that Adpt45_67 still grows on H_2+CO_2, forming acetate. Since all ALE experiments and growth rate comparisons (Figures 1, 3) were performed under heterotrophic growth conditions, we again used glucose as a substrate for the comparison of the growth phenotypes. We observed that Adpt45_67 has a significantly lower growth rate than the type strain (Figure 4) at either temperature without yeast extract. This phenotype in the non-adaptive environment was somewhat surprising, since in *E. coli* this has not been observed in short-term evolution experiments (~800 generations) (Kang et al., 2019), but fitness tradeoffs were rather observed in long-term

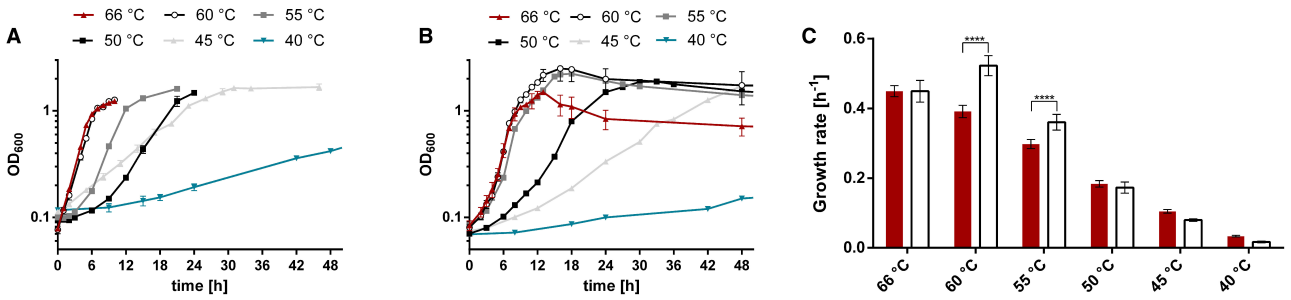

FIGURE 3
Growth of *T. kivui* strains **(A)** DSM2030 (type strain) and **(B)** Adpt45_67 at different temperatures, and **(C)** the corresponding growth rates. Cells were grown in 50 ml complex medium in 100 ml serum bottles with 25 mM glucose as a carbon source. Red triangles, 66°C; black open circles, 66°C; gray squares, 55°C; black squares, 50°C; gray triangles, 45°C; turquoise inverted triangles, 40°C. The error indicated shows the standard deviation from four biological replicates. Significant statistical differences (***$p < 0.0005$, two-way ANOVA with Tukey's test) between the type strain and the adapted strains at each temperature condition are shown.

ALE (Leiby and Marx, 2014). However, the observed decreased fitness in the non-adaptive condition (defined medium) described here may be the result of a single or few mutations rather than accumulated mutations, or of a single mutation that favors growth at low temperatures but not in the defined medium. Adpt45_67 still grew without yeast extract and maintained the ability to synthesize amino acids and putative other growth factors. Second, Adpt45_67 grew better at 60°C (0.176 h^{-1}) than at 66°C (0.134 h^{-1}), confirming the observed shift in T_{OPT} from 66°C to 60°C.

3.4. Changes in morphology, fatty acid composition, and in the genome of T. kivui Adpt45_67

The type strain of *T. kivui* DSM2030 is characterized by long slender rod-shaped cells during growth on glucose of a size of ~0.7 μm in width and up to 7.5 μm in length (Leigh et al., 1981), which we similarly observed after growth at 66°C for 20 h in the type strain (Figure 5A). Growth of the type strain and the Adpt45_67 at 45°C resulted in an increase in cell diameter and a shortening of cell length to 2–3 μm, as well as a striking number of long cell chains (Figures 5B, C). Interestingly, this morphology appeared to be reversible, since the incubation of Adpt45_67 at 66°C for 20 h resulted in a type strain such as morphology (Figure 5D).

These observations indicated, not unexpectedly, that the cells restructured their outer cell envelope in response to a temperature much below T_{OPT}. We next determined the fatty acid composition of the cytoplasmic membrane of *T. kivui* DSM2030 and Adpt45_67 at 66°C and 50°C (Figure 6 and Supplementary Figure S2). In the type strain, the major fatty acids with the largest fractions were i-$C_{15:0}$, *i*-$C_{17:0}$, and $C_{16:0}$, with branched fatty acids representing ~93% of total fatty acids. At the first glance, the membrane fatty acid composition of Adpt45_67 appears to be extremely similar; it also contains high amounts of the same fatty acids. A closer look revealed a much higher fraction of dimethyl acetals, indicative of plasmalogens (~37% vs. 17% in the type strain at 66°C, Figure 6B), including the plasmalogens *i*-$C_{16:0}$ P (at 66°C) and *a*-$C_{15:0}$ P (at 50°C) that were only detected in Adpt45_67. A surprising observation was the absence of unsaturated fatty acids in the fatty acid content of both strains, except for the type strain at 60°C, where a small amount of C(18:1) w7c was detected. In general, the fatty acid composition varies between bacterial species and can even be strain-specific, with nutrient availability and growth phase also showing an influence (Suutari and Laakso, 1992; Siliakus et al., 2017). Accordingly, bacteria have a number of options to adapt their fatty acid composition and thus membrane fluidity to environmental conditions. For the genus *Bacillus* and *Clostridia*, it is known that the major fatty acids are branched chained and that the regulation of fatty acid composition is mainly driven by the type of branching and chain length (Chan et al., 1971; Oshima and Miyagawa, 1974; Sikorski et al., 2008). When comparing thermophilic with mesophilic representatives, the utilization of iso-branched FAs in favor of anteiso-branched FAs was shown to decrease with decreasing temperature (Suutari and Laakso, 1992; Sikorski et al., 2008; Siliakus et al., 2017). This change in ratio was also observed between the type strain and Adpt45_67 as well as the reduction in chain length. Growth at a suboptimal temperature of 50°C resulted in a general shortening of fatty acids in the profiles of the strains studied, as expected, with an increase in C_{11} to C_{15} fatty acids and a decrease in C_{16} and C_{17} fatty acids. Notable among these were a sharp decrease in the plasmalogen *i*-$C_{17:0}$ P (from 11.4 to 3.5%) and a significant increase in *i*-$C_{15:0}$ (from 42.9 to 58.8%) in the type strain. Since their overall concentration decreased at 50°C in the type strain, plasmalogens likely do not represent a short-term response to growth at suboptimal temperatures in *T. kivui*. Plasmalogens are typical components of the cell membrane of strictly anaerobic bacteria (Goldfine, 2010; Jackson et al., 2021). They are characterized by the presence of a vinyl ether linkage at the sn-1 position and an ester linkage at the sn-2 position. Plasmalogens have a lower transition temperature than their diacyl counterparts, which is why they are considered to play a role in shaping the biophysical properties of cellular membranes (Goldfine, 2010; Koivuniemi, 2017; Vítová et al., 2021). Thus, the increased use of plasmalogens could be a way for *T. kivui* to fine-tune membrane fluidity at lower temperatures. In this

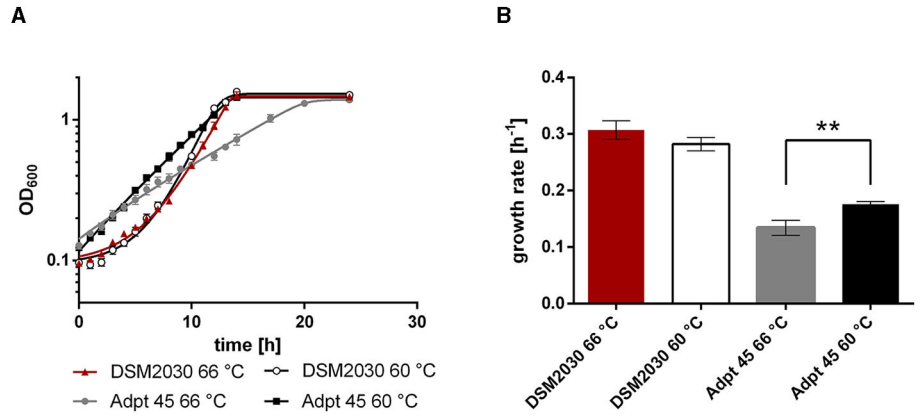

FIGURE 4
Growth of *T. kivui* strains **(A)** DSM2030 (type strain) and Adpt45_67 in the defined medium at 66°C and 60°C, and **(B)** the corresponding growth rates. Red, type strain at 66°C; white, Type strain at 60°C; gray, Adpt45_67 at 66°C; black, Adpt45_67 at 60°C. Cells were grown in 50 ml of medium in 100 ml serum bottles with 25 mM glucose as a carbon source. The error indicated shows the standard deviation from four biological replicates. Significant statistical differences (**$p < 0.005$, two-way ANOVA with Tukey's test) between the type strain and the adapted strains at each temperature condition are shown.

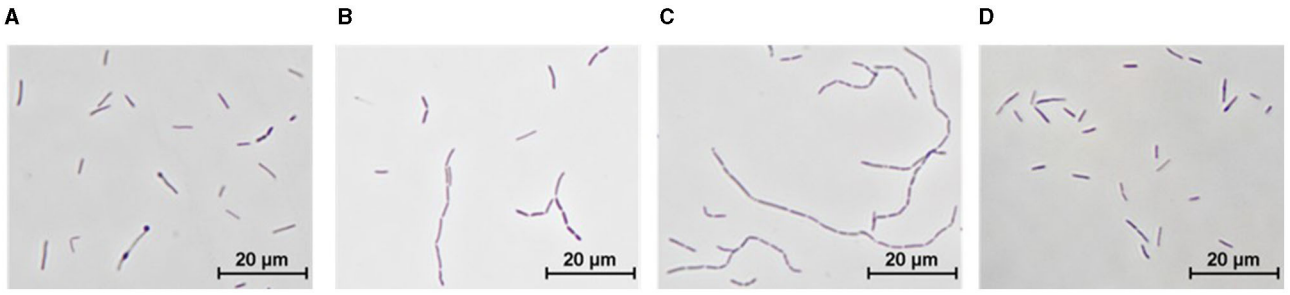

FIGURE 5
Morphology of *T. kivui* strains as observed by phase-contrast microscopy. *T. kivui* strains were grown in 50 ml of complex medium in 100 ml serum bottles with 25 mM glucose as a carbon source. **(A)** DSM2030 (type strain), 20 h at 66°C (T_{OPT}), **(B)** DSM2030 after five transfers at 45°C, 24 h at 45°C, **(C)** Adpt45_67, 24 h at 45°C, and **(D)** Adpt45_67, 24 h at 60°C (T_{OPT}).

study, Adpt45_67 shows a significantly higher concentration of plasmalogens than the type strain. It should be noted, however, that the plasmalogens are also subject to the aforementioned reduction in chain length with decreasing temperature.

In order to elucidate the genomic changes responsible for the phenotype observed, the genome of T. *kivui* Adpt45_67 was sequenced and compared to that of the type strain (Hess et al., 2014). Altogether, 67 single-nucleotide polymorphisms were observed across the 2.397 Mbp genome (Supplementary Table S2). Thirty-three of the SNPs were also in genomes of strains adapted to other environmental stresses in our laboratory (unpublished data). Among these was a mutation (P216L; CCA→ CTA) in *fabG,* a gene essential for fatty acid metabolism that encodes the 3-oxoacyl-[acyl-carrier-protein] reductase, which may have contributed to changes in fatty acid composition. Among the 34 remaining unique mutations, nine were found to be silent. Another 14 were attributed to genes with hypothetical or putative functions, leaving 11 unique, non-silent SNPs in genes or intergenic regions affecting gene expression with annotated functions (Table 1). Four of the SNPs were only found in part of the analyzed DNA, meaning that the majority of the population still contained the original base. This is likely as Adpt45_67 may be considered an adapted population, since it was not re-isolated from solid media, and therefore, the partial SNPs may be interpreted as transient toward a cold-adapted phenotype, and it will be studied whether they carry through in later generations of the ongoing ALE of *T. kivui* Adp45 at 45°C. Among those SNPs are two that affect the same transposase, TKV_c7000, indicating that this transposase may be involved in temperature response. Moreover, 5.7% of Adpt45_67 led to the mutation G28V in the alternative sigma factor H. This is of interest, since SigH has been described to be involved in several bacteria, including the Gram-positive *Corynebacterium glutamicum*, where it is involved in heat shock and oxygen stress responses (Kim et al., 2005), though the deletion of *sigH* in *Synechococcus* PCC 7002 does not affect growth at a suboptimal temperature (Inoue-Sakamoto et al., 2007). In *Staphylococcus aureus*, the gene is involved in competence for DNA uptake (Morikawa et al., 2012). Seven SNPs were found in 100% of the reads. Two of them are located in the intragenic regions and may affect the expression level of the genes encoding an ATPase and an alanine racemase, the latter of which is involved in cell wall

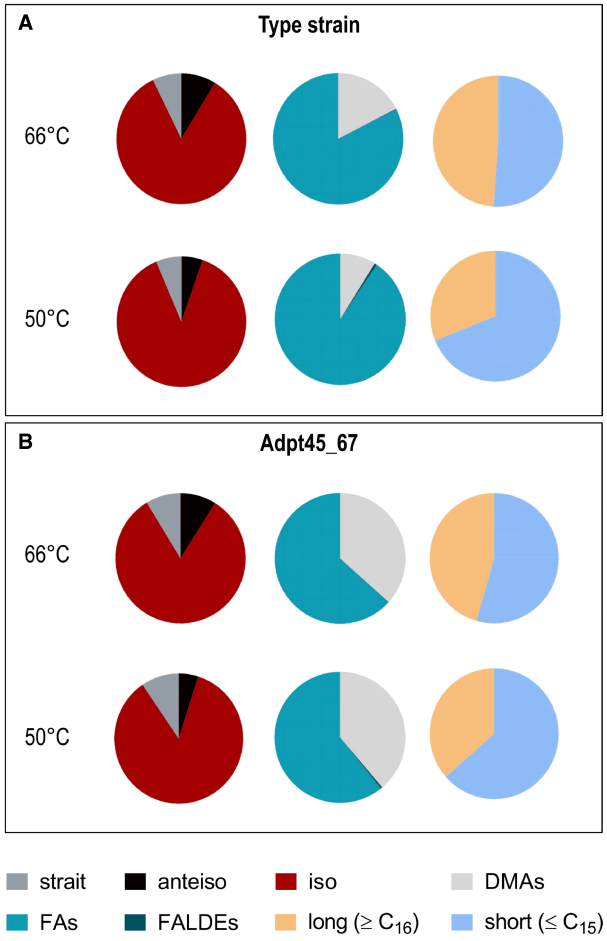

FIGURE 6
Effect of growth temperature on the total fatty acid composition of *T. kivui*. *T. kivui* strains DSM2030 **(A)** and Adpt45_67 **(B)** were grown in a complex medium with 25 mM glucose at optimal (66°C and 60°C) and suboptimal (50°C) temperatures to an OD_{600} of ~1. Left panels: red, iso-branched; gray, anteiso-unbranched; black, anteiso-branched. Middle panels: turquoise, fatty acids; light gray, plasmalogens; dark blue, fatty aldehydes. Right panels: yellow, long-chain $>C_{16}$; light blue, short-chain $<C_{16}$.

biogenesis. Two more are located in transcriptional regulators that have relatively low expression levels at 66°C (unpublished data), but may be of importance in cold adaptation. Since *T. kivui* easily takes up and integrates environmental DNA at 66°C (Basen et al., 2018; Zeldes et al., 2023), the SNP in Cas6-1, a CRISPR RNA maturation endonuclease (Jesser et al., 2019), may modulate the ability to acquire foreign DNA as a strategy for the adaptation of the environment. Another SNP was detected in the gene encoding the potassium ATPase *kdpC* N146K (AAT→ AAG). It is tempting to speculate that potassium has an influence on cold adaptation in *T. kivui* since, recently, the respective potassium uptake system has been shown to be involved in the cold adaptation of the mesophilic oligotrophic bacterium *Caulobacter crescentus* (de Araujo et al., 2021). Finally, an SNP R136T (AGG→ ACG) was found in the gene of the cAMP-binding protein, Crp (TKV_c24530). Crp is a global regulator (Ma et al., 2004) that, on the one hand, may be involved in temperature response, providing Adpt45_67 a fitness advantage at lower temperatures, and that is linked to sugar uptake via PTS systems, which, on the other hand, may explain the observed weaker growth of Adpt45_67 in a defined medium.

In conclusion, the genotype of *T. kivui* changed in response to prolonged incubation at 45°C in complex media at several loci that have been attributed to regulation or temperature adaptation in bacteria.

4. Discussion

There is an ongoing controversy about whether the first cells were (hyper)thermophilic or mesophilic. On the one hand, and from a human perspective, hot temperatures are extreme, and it seems straightforward to think that thermophiles must have evolved from mesophiles; on the other hand, ~4 billion years ago, when life arose, the Earth or at least parts of it such as the Hadean Ocean were still relatively warm (Lunine, 2006). One of the pro-arguments for a hot-start, however, is the existence of a reverse gyrase in both domains of life, Bacteria, and Archaea, which has been argued based on its phylogeny (Catchpole and Forterre, 2019), and beyond that, it might be acquired through horizontal gene transfer by either domain. It has also been suggested that the progenitor may have been a moderate thermophile that evolved at a submarine alkaline, moderately hot vent such as the Lost City hydrothermal vent field (Russell et al., 2010; Sousa et al., 2013). Moreover, the progenitor, or LUCA, the last universal ancestor of Archaea and Bacteria, was proposed to share features of recent acetogenic bacteria and methanogenic archaea (Martin and Sousa, 2016). Both acetogenesis and methanogenesis are dependent on energy conservation from the conversion of H_2+CO_2. Genes toward H_2+CO_2 utilization, the respective essential cofactor biosynthesis pathways and the terminal electron accepting pathway of acetogens and CO_2 fixation pathway in methanogens, the Wood–Ljungdahl pathway (WLP; Ljungdahl, 1986; Wood et al., 1986), were suggested to be present in the genome of LUCA (Weiss et al., 2016). Thus, acetogens are likely ancient (Basen and Müller, 2017; Martin, 2020). It may ultimately be unresolvable whether the progenitor was a thermophile or a mesophile. Undisputable, however, thermophiles are ancient, with many archaeal and bacterial phyla at the root of phylogenetic trees (Pace, 1997; Stetter, 2006), and it is likely that at least in some cases mesophilic microorganisms evolved from thermophilic ancestors, as reported for the ancient bacterial phylum *Thermotogales* (Zhaxybayeva et al., 2009) and for mesophilic *Methanococcus* species (Lecocq et al., 2021) based on phylogenetic analyses. It still remains intriguing how this evolution happened since it required a stepwise molecular adaptation based on modifications to the genome.

While the aforementioned studies are based on comparative and phylogenetic analyses of genomes, the ALE of a thermophile toward a lower T_{OPT} has never been tested experimentally, to the best of our knowledge. This triggered us to grow and transfer the acetogen *Thermoanaerobacter kivui* at 45°C, a temperature 5–10°C above its T_{MIN} and 21°C below its T_{OPT}. The choice fell on an acetogen since acetogenesis—as thermophily—is an ancient trait (Basen and Müller, 2017), as described above. After ~180 generations/67 transfers at 45°C, the *T. kivui* population (strain Adpt45_67) was surprisingly not better adapted to 45°C,

10.3389/fmicb.2023.1265216

TABLE 1 Non-silent or intergenic single-nucleotide polymorphisms (SNPs) unique to the genome of *T. kivui* Adpt45_67 (*i.e.*, not yet observed in other *T. kivui* adapted strains).

Position (Bp)	SNP	reads with SNPs (%)	Amino acid change	Gene number (→ plus strand, ← minus strand)	Annotation
268,757	C→T	100	A97V (GCG→GTG)	TKV_c02640 →	transcriptional regulator, TetR family
688,064	A→G	9.3	intergenic (+216/-54)	TKV_c07000 → / → TKV_c07010	transposase for insertion sequence element IS629/hypothetical protein
688,089	G→A	6.7	intergenic (+241/-29)	TKV_c07000 → / → TKV_c07010	transposase for insertion sequence element IS629/hypothetical protein
899,158	G→C	14.1	intergenic (-134/-42)	TKV_c09420 ← / → TKV_c09430	phosphatidylglycerophosphatase A-like protein/hypothetical protein
1,419,632	C→T	100	A116T (GCA→ACA)	TKV_c14800 ←	transcriptional regulator, TraR/DksA family
1,435,634	A→T	100	intergenic (-56/+41)	TKV_c14990 ← / ← TKV_c15000	alanine racemase domain-containing protein/membrane fusion protein
1,442,610	Δ1 bp	100	intergenic (-94/+15)	TKV_c15050 ← / ← *nadC*	ATPase associated with various cellular activities AAA_3/nicotinate-nucleotide pyrophosphorylase
1,758,229	A→C	100	N146K (AAT→AAG)	*kdpC* ←	potassium-transporting ATPase C chain
1,982,739	C→A	5.7	G28V (GGG→GTG)	*sigH* ←	RNA polymerase sigma-H factor SigH
2,348,017	G→T	100	A39E (GCG→GAG)	*cas6a* ←	CRISPR-associated endoribonuclease Cas6 1
2,372,359	C→G	100	R136T (AGG→ACG)	TKV_c24530 ←	cAMP-binding protein

In this study, only SNPs in genes with annotated function are listed (for a complete list of SNPs, see Supplementary Figure S2).

but to temperatures 5–10 K below the T_{OPT} (55–60°C). This is somewhat in line with an observation and hypothesis published over 30 years ago by Jürgen Wiegel. He reported on a temperature plateau below the T_{OPT} of certain anaerobic thermophiles, including *Thermoanaerobacter* species, allowing them to relatively quickly adapt to slightly lower temperatures. Moreover, their growth temperature (tolerance) range is large (35–78°C) compared to that of many mesophiles (Onyenwoke and Wiegel, 2015). Considering a scenario in which single *Thermoanaerobacter* sp. cells were suddenly exposed to a suboptimal temperature—in the ancient world or recently—their capability to cope at much lower temperatures may have prevented their rapid extinction in the environment, and that may equally hold true for other thermophiles with a broad temperature span (Wiegel, 1990). In that regard, it is worth noticing that there is increasing evidence for thermophiles in cold habitats far below their T_{MIN}, such as Arctic sediments, soils, seawater, and even ice (Milojevic et al., 2022). The perseverance of thermophiles in arctic habitats correlates well with their broad temperature range. These populations are likely transported from populations in warmer habitats such as deep sediments, subsurface petroleum reservoirs, or ocean ridges (Hubert et al., 2009), and they may resemble ancestral thermophiles in their development toward mesophile.

Considering the evolution of a mesophile to a thermophile, mesophiles possess a narrower temperature range, ~30–35°C (Wiegel, 1990). Particularly, they face the challenge that temperatures slightly exceeding the upper-temperature limit (T_{MAX}) may quickly lead to protein denaturation. Nonetheless, ALE experiments in mesophiles toward higher T_{OPT} have been carried out, with mixed results. A successful evolution of *E. coli* in a continuous system with gradually increasing temperatures (from 44°C to 49.7°C) was reported (Blaby et al., 2012). The resulting strain had a significantly increased T_{OPT} of 46°C, demonstrating that (moderate) thermophiles may have evolved from mesophilic ancestors. The adapted strain carried 31 single-nucleotide substitutions, among these putative critical mutations in the glycerol facilitator gene *glpF* and in the fatty acid desaturase/isomerase *fabA*. Interestingly, a mutation in the *kdpD* gene was recognized, a sensor kinase associated with the potassium ATPase gene *kdpC*, which we observed to carry a mutation. In another experiment, sequential transfer of a mutator strain *Zymomonas mobilis* and of *E. coli* with stepwise temperature increase for ~400 and 550 generations, respectively, resulted in an increased T_{MAX} of 2–3 K (to 41°C and to 47°C), with cells dying if the temperature was further increased (Kosaka et al., 2019). The number of mutations observed in the thermally adapted strains was surprisingly small (24 and 9, respectively), in the same range as observed in this study. While most studies of thermal adaptations aimed to increase T_{OPT} or T_{MAX}, often in the context of adaptation to climate change or toward a biotechnological application, recently, a community approach was carried out to evolve *Escherichia coli* (T_{OPT} 37°C) and *Saccharomyces cerevisiae* (T_{OPT} 30°C) to 20°C and 15°C, respectively, ~15 K below their T_{OPT} (Strauss et al., 2019). More than 20 groups from all over the world tried different approaches for a thermal adaptation of the two organisms to a suboptimal temperature. Most ALE approaches were successful; however, the two organisms behaved differently. In *E. coli*, the most common phenotype was a decrease in the lag phase, while in *S. cerevisiae*, the yield at the lower temperature increased. Improvement of growth rate was not observed or only

to a limited extent, similar to what we observed with *T. kivui* Adpt45_67; however, we did not observe a lag phase in *T. kivui* of >1 h when transferred to 45°C. Unfortunately, the authors do not report on whether T_{OPT} or T_{MIN} were affected.

Microorganisms persevering in an unfavorable environment, even if they grow at low rates, allow time for a population to "gather" mutations, some of which are selected for growth and adaptation to the unfavorable environment. Adpt45_67 obviously is not yet adapted for better growth at 45°C, but sustains at 39°C, and, compared to the wild type, showed a T_{OPT} shifted to 60°C. It is not clear yet, whether this adaptation halts on the plateau of 60–55°C (Wiegel, 1990), or whether more generations at 45°C will further shift the T_{OPT} and finally increase the growth rate at 45°C. In that case, the observed genotype here may be interpreted as transient. Only a few unique and non-silent mutations were identified (Table 1), with some of them potentially related to temperature adaptation or gene regulation. Targeted point mutations may identify which of these SNPs are essential to the adapted phenotype. Continuation of the ALE may identify further mutations and allow insights into their order of occurrence. We conclude that *Thermoanaerobacter* and many thermophiles are well prepared to survive or even thrive at ambient temperatures (Wiegel, 1990), which may have facilitated not only a slight transition of the T_{OPT} but a complete thermophile-to-mesophile transition over large evolutionary time scales.

The evolution of thermal adaptation has been linked to a generally different amino acid composition. From a pan-genome analysis, it is evident that the evolution of mesophilic *Methanococcus* sp. from thermophilic ancestors was directly linked to the replacement of lysine and an increase in the percentage of threonine, glutamine, serine, aspartate, and asparagine (Lecocq et al., 2021). The authors conclude that amino acid replacement via single mutations rather than horizontal gene transfer (HGT) events caused the adaptation to the lower temperature. This reflects, however, large evolutionary time scales, and cannot explain adaptations to slightly lower temperatures in a shorter time period as observed here. On a shorter time scale, it may be conceivable that thermophiles profit from HGT events in adaptation to lower temperatures. *T. kivui*, the organism used in this study, has recently been shown to efficiently take up and integrate foreign DNA from a laboratory environment into its genome, which allowed the strain to adapt to a certain medium type (Zeldes et al., 2023).

Further attempts to adapt thermophiles to lower temperatures in the laboratory are warranted to elucidate whether the observed shift toward a lower T_{OPT} can be reproduced or increased beyond the temperature plateau and whether growth also improves at the lower temperature end. A difficulty that we encountered was certainly the low growth rates at much lower temperatures, which decrease the number of generations (and thus the number of possible mutations) in ALE experiments. Nonetheless, experimental approaches toward a cold adaptation of thermophiles will be essential to ultimately prove considerations from genome comparisons. It will be of interest to see whether the ALE of thermophiles toward a lower T_{OPT} will lead to an increase in the GC content (Hu et al., 2022) or a change in the amino acid pattern (Sauer and Wang, 2019; Lecocq et al., 2021) in the long term. In the short term, these experiments may resolve the order of single evolutive events of particular importance, such as single gene (e.g., transcriptional regulators) inactivation by point mutations or HGT events (in case DNA of mesophiles is supplied), and enable the study of the respective phenotypic effects in single organisms, such as in the acetogen *T. kivui*.

Data availability statement

The datasets presented in this study can be found in online repositories. The names of the repository/repositories and accession number(s) can be found below: https://www.ncbi.nlm.nih.gov/sra/, SRR25301688.

Author contributions

ML: Data curation, Formal analysis, Investigation, Methodology, Validation, Visualization, Writing—original draft. CP: Validation, Writing—original draft, Data curation, Formal analysis, Investigation, Methodology, Visualization. BZ: Investigation, Validation, Data curation, Formal analysis, Methodology, Visualization, Writing—review and editing. AP: Resources, Software, Writing—review and editing, Data curation, Formal analysis, Investigation. RD: Writing—review and editing, Resources, Software. MB: Writing—original draft, Validation, Conceptualization, Funding acquisition, Project administration, Resources, Supervision.

Funding

The author(s) declare financial support was received for the research, authorship, and/or publication of this article. This study was funded by a grant from VolkswagenStiftung (Volkswagen Foundation, A123851) in the Experiment! program (exploratory phase). The authors acknowledge financial support from the Deutsche Forschungsgemeinschaft and Universität Rostock within the funding program Open Access Publishing.

Acknowledgments

This study was dedicated to Jürgen Wiegel, whose study inspired the authors to start working on thermophilic anaerobic bacteria and their evolution. The authors gratefully acknowledge Monika Timm, Ilona Boldt (both University of Rostock), and Melanie Heinemann (Georg-August University Göttingen) for technical support in the laboratory. Moreover, MB is grateful to Volker Müller for fruitful discussions. For the special feature on the 11th International Congress on Extremophiles in 2016, we wrote a review together, arguing about likely ancient acetogens thriving at high temperatures (Basen and Müller, 2017). This current report, for the Frontiers Research Topic on the 13th International Congress on Extremophiles, may be seen as a practical continuation of some of our thoughts in the abovementioned publication.

Conflict of interest

The authors declare that the research was conducted in the absence of any commercial or financial relationships that could be construed as a potential conflict of interest.

Publisher's note

All claims expressed in this article are solely those of the authors and do not necessarily represent those of their affiliated organizations, or those of the publisher, the editors and the reviewers. Any product that may be evaluated in this article, or claim that may be made by its manufacturer, is not guaranteed or endorsed by the publisher.

Supplementary material

The Supplementary Material for this article can be found online at: https://www.frontiersin.org/articles/10.3389/fmicb.2023.1265216/full#supplementary-material

References

Badran, A. H., and Liu, D. R. (2015). Development of potent *in vivo* mutagenesis plasmids with broad mutational spectra. *Nat. Commun.* 6, 8425. doi: 10.1038/ncomms9425

Basen, M., Geiger, I., Henke, L., and Müller, V. (2018). A genetic system for the thermophilic acetogenic bacterium *Thermoanaerobacter kivui*. *Appl. Environ. Microbiol.* 84, e02210–02217. doi: 10.1128/AEM.02210-17

Basen, M., and Müller, V. (2017). "Hot" acetogenesis. *Extremophiles* 21, 15–26. doi: 10.1007/s00792-016-0873-3

Berezovsky, I. N., and Shakhnovich, E. I. (2005). Physics and evolution of thermophilic adaptation. *Proc. Natl. Acad. Sci. USA* 102, 12742–12747. doi: 10.1073/pnas.0503890102

Blaby, I. K., Lyons, B. J., Wroclawska-Hughes, E., Phillips, G. C., Pyle, T. P., Chamberlin, S. G., et al. (2012). Experimental evolution of a facultative thermophile from a mesophilic ancestor. *Appl. Environ. Microbiol.* 78, 144–155. doi: 10.1128/AEM.05773-11

Canganella, F., and Wiegel, J. (2014). Anaerobic thermophiles. *Life* 4, 77. doi: 10.3390/life4010077

Catchpole, R. J., and Forterre, P. (2019). The evolution of reverse gyrase suggests a non-hyperthermophilic last universal common ancestor. *Mol. Biol. E*36, 2737–2747. doi: 10.1093/molbev/msz180

Chan, M., Himes, R. H., and Akagi, J. M. (1971). Fatty acid composition of thermophilic, mesophilic, and psychrophilic clostridia. *J. Bacteriol.* 106, 876–881. doi: 10.1128/jb.106.3.876-881.1971

Cooper, V. S., and Lenski, R. E. (2000). The population genetics of ecological specialization in evolving *Escherichia coli* populations. *Nature* 407, 736–739. doi: 10.1038/35037572

de Araujo, Martins, H. L., Vicente, B. P., Lorenzetti, A. M., and Koide, A. P. R. T., and Marques, M.V. (2021). Cold regulation of genes encoding ion transport systems in the oligotrophic bacterium *Caulobacter crescentus*. *Microbiol. Spectr.* 9, 21. doi: 10.1128/Spectrum.00710-21

De Maayer, Anderson, P., Cary, D. C., and Cowan, D .A. (2014). Some like it cold: understanding the survival strategies of psychrophiles. *EMBO Rep.* 15, 508–517. doi: 10.1002/embr.201338170

Deutzmann, J. S., Kracke, F., Gu, W. Y., and Spormann, A. M. (2022). Microbial electrosynthesis of acetate powered by Intermittent electricity. *Environ. Sci. Technol.* 56, 16073–16081. doi: 10.1021/acs.est.2c05085

Dietrich, H. M., Righetto, R. D., Kumar, A., Wietrzynski, W., Trischler, R., Schuller, S. K., et al. (2022). Membrane-anchored HDCR nanowires drive hydrogen-powered CO_2 fixation. *Nature* 607, 823–830. doi: 10.1038/s41586-022-04971-z

Dragosits, M., and Mattanovich, D. (2013). Adaptive laboratory evolution—Principles and applications for biotechnology. *Microb. Cell. Fact.* 12, 64. doi: 10.1186/1475-2859-12-64

Fiala, G., and Stetter, K. O. (1986). *Pyrococcus furiosus* sp.nov. represents a novel genus of marine heterotrophic archaebacteria growing optimally at 100°C. *Arch. Microbiol.* 145, 56–61. doi: 10.1007/BF00413027

Goldfine, H. (2010). The appearance, disappearance and reappearance of plasmalogens in evolution. *Prog. Lipid Res.* 49, 493–498. doi: 10.1016/j.plipres.2010.07.003

Hess, V., Poehlein, A., Weghoff, M. C., Daniel, R., and Müller, V. (2014). A genome-guided analysis of energy conservation in the thermophilic, cytochrome-free acetogenic bacterium *Thermoanaerobacter kivui*. *BMC Genom.* 15, 1139. doi: 10.1186/1471-2164-15-1139

Hu, E-. Z., Lan, X-. R., Liu, Z-. L., Gao, J., and Niu, D-. K. (2022). A positive correlation between GC content and growth temperature in prokaryotes. *BMC Genom.* 23, 110. doi: 10.1186/s12864-022-08353-7

Hubert, C., Loy, A., Nickel, M., Arnosti, C., Baranyi, C., Brüchert, V., et al. (2009). A constant flux of diverse thermophilic bacteria into the cold arctic seabed. *Science* 325, 1541–1544. doi: 10.1126/science.1174012

Imanaka, T. (2011). Molecular bases of thermophily in hyperthermophiles. *Proc. Jpn. Acad., Ser. B.* 87, 587–602. doi: 10.2183/pjab.87.587

Inoue-Sakamoto, K., Gruber, T. M., Christensen, S. K., Arima, H., Sakamoto, T., Bryant, D. A., et al. (2007). Group 3 sigma factors in the marine cyanobacterium *Synechococcus* sp. strain PCC 7002 are required for growth at low temperature. *J. Gen. Appl. Microbiol.* 53, 89–104. doi: 10.2323/jgam.53.89

Jackson, D. R., Cassilly, C. D., Plichta, D. R., Vlamakis, H., Liu, H., Melville, S. B., et al. (2021). Plasmalogen biosynthesis by anaerobic bacteria: identification of a two-gene operon responsible for plasmalogen production in *Clostridium perfringens*. *Acs. Chem. Biol.* 16, 6–13. doi: 10.1021/acschembio.0c00673

Jain, S., Dietrich, H. M., Müller, V., and Basen, M. (2020). Formate Is required for growth of the thermophilic acetogenic bacterium *Thermoanaerobacter kivui* lacking hydrogen-dependent carbon dioxide reductase (HDCR). *Front. Microbiol.* 11, 59. doi: 10.3389/fmicb.2020.00059

Jesser, R., Behler, J., Benda, C., Reimann, V., and Hess, W. R. (2019). Biochemical analysis of the Cas6-1 RNA endonuclease associated with the subtype I-D CRISPR-Cas system in *Synechocystis* sp. PCC 6803. *RNA Bio.* 16, 481–491. doi: 10.1080/15476286.2018.1447742

Kang, M., Kim, K., Choe, D., Cho, S., Kim, S. C., Palsson, B., et al. (2019). Inactivation of a mismatch-repair system diversifies genotypic landscape of *Escherichia coli* during adaptive laboratory evolution. *Front. Microbiol.* 10. doi: 10.3389/fmicb.2019.01845

Katsyv, A., and Müller, V. (2022). A purified energy-converting hydrogenase from *Thermoanaerobacter kivui* demonstrates coupled H^+ -translocation and reduction *in vitro*. *J. Biol. Chem.* 298. doi: 10.1016/j.jbc.2022.102216

Katsyv, A., Schoelmerich, M. C., Basen, M., and Müller, V. (2021). The pyruvate:ferredoxin oxidoreductase of the thermophilic acetogen, *Thermoanaerobacter kivui*. *FEBS Open Bio.* 11, 1332–1342. doi: 10.1002/2211-5463.13136

Kelley, D. S., Karson, J. A., Fruh-Green, G. L., Yoerger, D. R., Shank, T. M., Butterfield, D. A., et al. (2005). A serpentinite-hosted ecosystem: the lost city hydrothermal field. *Science* 307, 1428–1434. doi: 10.1126/science.1102556

Kim, T. H., Kim, H. J., Park, J. S., Kim, Y., Kim, P., Lee, H. S., et al. (2005). Functional analysis of *sigH* expression in *Corynebacterium glutamicum*. *Biochem. Biophys. Res. Commun.* 331, 1542–1547. doi: 10.1016/j.bbrc.2005.04.073

Koivuniemi, A. (2017). The biophysical properties of plasmalogens originating from their unique molecular architecture. *FEBS Lett.* 591, 2700–2713. doi: 10.1002/1873-3468.12754

Kosaka, T., Nakajima, Y., Ishii, A., Yamashita, M., Yoshida, S., Murata, M., et al. (2019). Capacity for survival in global warming: adaptation of mesophiles to the temperature upper limit. *PLoS ONE* 14, e0215614. doi: 10.1371/journal.pone.0215614

Lecocq, M., Groussin, M., Gouy, M., and Brochier-Armanet, C. (2021). The molecular determinants of thermoadaptation: *Methanococcales* as a case study. *Mol. Biol. Evol.* 38, 1761–1776. doi: 10.1093/molbev/msaa312

Leiby, N., and Marx, C. J. (2014). Metabolic erosion primarily through mutation accumulation, and not tradeoffs, drives limited evolution of substrate specificity in *Escherichia coli*. *PLoS Biol.* 12, e1001789. doi: 10.1371/journal.pbio.1001789

Leigh, J. A., Mayer, F., and Wolfe, R. S. (1981). *Acetogenium kivui*, a new thermophilic hydrogen-oxidizing, acetogenic bacterium. *Arch. Microbiol.* 129, 275–280. doi: 10.1007/BF00414697

Ljungdahl, L. G. (1986). The autotrophic pathway of acetate synthesis in acetogenic bacteria. *Annu. Rev. Microbiol.* 40, 415–450. doi: 10.1146/annurev.mi.40.100186.002215

Luan, G., Cai, Z., Li, Y., and Ma, Y. (2013). Genome replication engineering assisted continuous evolution (GREACE) to improve microbial tolerance for biofuels production. *Biotechnol. Biofuels* 6, 137. doi: 10.1186/1754-6834-6-137

Lunine, J. I. (2006). Physical conditions on the early Earth. *Philos. T R Soc. B* 361, 1721–1731. doi: 10.1098/rstb.2006.1900

Ma, H. W., Kumar, B., Ditges, U., Gunzer, F., Buer, J., Zeng, A. P., et al. (2004). An extended transcriptional regulatory network of *Escherichia coli* and analysis of its hierarchical structure and network motifs. *Nuc. Acids Res.* 32, 6643–6649. doi: 10.1093/nar/gkh1009

Martin, W. F. (2020). Older than genes: the acetyl CoA pathway and origins. *Front. Microbiol.* 11, 817. doi: 10.3389/fmicb.2020.00817

Martin, W. F., and Sousa, F. L. (2016). Early microbial evolution: the age of anaerobes. *Cold Spring Harbor Perspect. Biol.* 8, 18. doi: 10.1101/cshperspect.a018127

Milojevic, T., Cramm, M. A., Hubert, C. R. J., and Westall, F. (2022). Freezingandrdquo, thermophiles: from one temperature extreme to another. *Microorganisms* 10, 2417. doi: 10.3390/microorganisms10122417

Moon, J., Henke, L., Merz, N., and Basen, M. (2019). A thermostable mannitol-1-phosphate dehydrogenase is required in mannitol metabolism of the thermophilic acetogenic bacterium *Thermoanaerobacter kivui*. *Environ. Microbiol.* 21, 3728–3736. doi: 10.1111/1462-2920.14720

Moon, J., Jain, S., Müller, V., and Basen, M. (2020). Homoacetogenic conversion of mannitol by the thermophilic acetogenic bacterium *Thermoanaerobacter kivui* requires external CO_2. *Front. Microbiol.* 11, 571736. doi: 10.3389/fmicb.2020.571736

Morikawa, K., Takemura, A. J., Inose, Y., Tsai, M., Nguyen Thi, L. T., Ohta, T., et al. (2012). Expression of a cryptic secondary sigma factor gene unveils natural competence for DNA transformation in *Staphylococcus aureus*. *PLoS Pathog.* 8, e1003003. doi: 10.1371/journal.ppat.1003003

Onyenwoke, R. U., and Wiegel, J. (2015). "Thermoanaerobacter," in *Bergey's Manual of Systematics of Archaea and Bacteria,* eds M. E. Trujillo, S. Dedysh, P. DeVos, B. Hedlund, P. Kämpfer, F. A. Rainey et al. (Hoboken, NJ: Bergey's Manual Trust and John Wiley and Sons, Ltd), doi: 10.1002/9781118960608.gbm00751

Oshima, M., and Miyagawa, A. (1974). Comparative studies on the fatty acid composition of moderately and extremely thermophilic bacteria. *Lipids* 9, 476–480. doi: 10.1007/BF02534274

Pace, N. R. (1997). A molecular view of microbial diversity and the biosphere. *Science* 276, 734–740. doi: 10.1126/science.276.5313.734

Russell, M. J., Hall, A. J., and Martin, W. (2010). Serpentinization as a source of energy at the origin of life. *Geobiol.* 8, 355–371. doi: 10.1111/j.1472-4669.2010.00249.x

Sauer, D. B., and Wang, D-. N. (2019). Predicting the optimal growth temperatures of prokaryotes using only genome derived features. *Bioinformatics* 35, 3224–3231. doi: 10.1093/bioinformatics/btz059

Sikorski, J., Brambilla, E., Kroppenstedt, R. M., and Tindall, B. J. (2008). The temperature-adaptive fatty acid content in *Bacillus simplex* strains from 'Evolution Canyon', Israel. *Microbiol.-SGM* 154, 2416–2426. doi: 10.1099/mic.0.2007/016105-0

Siliakus, M. F., Van Der Oost, J., and Kengen, S. W. M. (2017). Adaptations of archaeal and bacterial membranes to variations in temperature, pH and pressure. *Extremophiles* 21, 651–670. doi: 10.1007/s00792-017-0939-x

Sousa, F. L., Thiergart, T., Landan, G., Nelson-Sathi, S. Pereira, I.a.C., Allen, J.F., Lane, N., et al. (2013). Early bioenergetic evolution. *Philos T R Soc. B* 36, 8. doi: 10.1098/rstb.2013.0088

Stetter, K. O. (2006). History of discovery of the first hyperthermophiles. *Extremophiles* 10, 357–362. doi: 10.1007/s00792-006-0012-7

Strauss, K. S., Schirman, D., Jona, G., Brooks, A.N., Kunjapur, A.M., Nguyen Ba, A.N., et al. (2019). Evolthon: a community endeavor to evolve lab evolution. *PLoS Biol.* 17, e3000182. doi: 10.1371/journal.pbio.3000182

Suutari, M., and Laakso, S. (1992). Changes in fatty acid branching and unsaturation of *Streptomyces griseus* and *Brevibacterium fermentans* as a response to growth temperature. *Appl. Environ. Microbiol.* 58, 2338–2340. doi: 10.1128/aem.58.7.2338-2340.1992

Suzuki, H., Kobayashi, J., Wada, K., Furukawa, M., and Doi, K. (2015). Thermoadaptation-directed enzyme evolution in an error-prone thermophile derived from *Geobacillus kaustophilus* HTA426. *Appl. Environ. Microbiol.* 81, 149–158. doi: 10.1128/AEM.02577-14

Vasi, F. K., and Lenski, R. E. (1999). Ecological strategies and fitness tradeoffs in *Escherichia coli* mutants adapted to prolonged starvation. *J. Gen.* 78, 43–49. doi: 10.1007/BF02994702

Vítová, M., Palyzová, A., and Rezanka, T. (2021). Plasmalogens—Ubiquitous molecules occurring widely, from anaerobic bacteria to humans. *Prog. Lipid Res.* 83, 101111. doi: 10.1016/j.plipres.2021.101111

Weghoff, M. C., and Müller, V. (2016). CO metabolism in the thermophilic acetogen *Thermoanaerobacter kivui*. *Appl. Environ. Microbiol.* 82, 2312–2319. doi: 10.1128/AEM.00122-16

Weiss, M. C., Sousa, F. L., Mrnjavac, N., Neukirchen, S., Roettger, M., Nelson-Sathi, S., et al. (2016). The physiology and habitat of the last universal common ancestor. *Nat. Microbiol.* 1, 16116. doi: 10.1038/nmicrobiol.2016.116

Widdel, F., and Bak, F. (1992). "Gram-negative mesophilic sulfate-reducing bacteria," in *The Prokaryotes,* eds. A.T. Balows, H.G. Dworkin, M. Harder, K. H. Schleifer (New York: Springer), 3352-3378. doi: 10.1007/978-1-4757-2191-1_21

Wiegel, J. (1990). Temperature spans for growth: hypothesis and discussion. *FEMS Microbiol. Lett.* 75, 155–169. doi: 10.1111/j.1574-6968.1990.tb04092.x

Wood, H. G., Ragsdale, S. W., and Pezacka, E. (1986). The acetyl-CoA pathway of autotrophic growth. *FEMS Microbiol. Lett.* 39, 345–362. doi: 10.1111/j.1574-6968.1986.tb01865.x

Zeldes, B., Poehlein, A., Jain, S., Baum, C., Daniel, R., Müller, V., et al. (2023). DNA uptake from a laboratory environment drives unexpected adaptation of a thermophile to a minor medium component. *ISME Commun.* 3, 2. doi: 10.1038/s43705-022-00211-7

Zeldes, B. M., Keller, M. W., Loder, A. J., Straub, C. T., Adams, M. W. W., Kelly, R. M., et al. (2015). Extremely thermophilic microorganisms as metabolic engineering platforms for production of fuels and industrial chemicals. *Front. Microbiol.* 6, 1209. doi: 10.3389/fmicb.2015.01209

Zhaxybayeva, O., Swithers, K. S., Lapierre, P., Fournier, G. P., Bickhart, D. M., Deboy, R. T., et al. (2009). On the chimeric nature, thermophilic origin, and phylogenetic placement of the *Thermotogales*. *Proceed. Nat. Acad. Sci.* 106, 5865–5870. doi: 10.1073/pnas.0901260106

frontiers | Frontiers in Microbiology

TYPE Original Research
PUBLISHED 16 November 2023
DOI 10.3389/fmicb.2023.1267570

OPEN ACCESS

EDITED BY
Eric Altermann,
Massey University, New Zealand

REVIEWED BY
Javier M. González,
CONICET Institute of Bionanotechnology of NOA (INBIONATEC), Argentina
Hirokazu Suzuki,
Tottori University, Japan

*CORRESPONDENCE
Simone A. De Rose
✉ S.A.De-Rose@exeter.ac.uk
Jennifer A. Littlechild
✉ J.A.Littlechild@exeter.ac.uk

RECEIVED 26 July 2023
ACCEPTED 28 September 2023
PUBLISHED 16 November 2023

CITATION
De Rose SA, Isupov MN, Worthy HL, Stracke C, Harmer NJ, Siebers B, Littlechild JA and The HotSolute consortium (2023) Structural characterization of a novel cyclic 2,3-diphosphoglycerate synthetase involved in extremolyte production in the archaeon *Methanothermus fervidus*. *Front. Microbiol.* 14:1267570. doi: 10.3389/fmicb.2023.1267570

Structural characterization of a novel cyclic 2,3-diphosphoglycerate synthetase involved in extremolyte production in the archaeon *Methanothermus fervidus*

Simone A. De Rose[1]*, Michail N. Isupov[1], Harley L. Worthy[2], Christina Stracke[3], Nicholas J. Harmer[4], Bettina Siebers[3] and Jennifer A. Littlechild[1]* and The HotSolute consortium

[1]Henry Wellcome Building for Biocatalysis, Biosciences, Faculty of Health and Life Sciences, University of Exeter, Exeter, United Kingdom, [2]Biosciences, Faculty of Health and Life Sciences, University of Exeter, Exeter, United Kingdom, [3]Department of Molecular Enzyme Technology and Biochemistry, Environmental Microbiology and Biotechnology, and Centre for Water and Environmental Research, University of Duisburg-Essen, Essen, Germany, [4]Living Systems Institute, Faculty of Health and Life Sciences, University of Exeter, Exeter, United Kingdom

The enzyme cyclic di-phosphoglycerate synthetase that is involved in the production of the osmolyte cyclic 2,3-diphosphoglycerate has been studied both biochemically and structurally. Cyclic 2,3-diphosphoglycerate is found exclusively in the hyperthermophilic archaeal methanogens, such as *Methanothermus fervidus*, *Methanopyrus kandleri*, and *Methanothermobacter thermoautotrophicus*. Its presence increases the thermostability of archaeal proteins and protects the DNA against oxidative damage caused by hydroxyl radicals. The cyclic 2,3-diphosphoglycerate synthetase enzyme has been crystallized and its structure solved to 1.7Å resolution by experimental phasing. It has also been crystallized in complex with its substrate 2,3 diphosphoglycerate and the co-factor ADP and this structure has been solved to 2.2Å resolution. The enzyme structure has two domains, the core domain shares some structural similarity with other NTP-dependent enzymes. A significant proportion of the structure, including a 127 amino acid N-terminal domain, has no structural similarity to other known enzyme structures. The structure of the complex shows a large conformational change that occurs in the enzyme during catalytic turnover. The reaction involves the transfer of the γ-phosphate group from ATP to the substrate 2,3 -diphosphoglycerate and the subsequent S_N2 attack to form a phosphoanhydride. This results in the production of the unusual extremolyte cyclic 2,3 -diphosphoglycerate which has important industrial applications.

KEYWORDS

extremolyte, cyclic 2,3-diphosphoglycerate, X-ray structure, thermophiles, synthetase

Introduction

Osmolytes are small organic molecules that accumulate within cells as a response to conditions of stress. These molecules increase the thermodynamic stability of cellular proteins and nucleic acids without compromising their native functional activities (Yancey et al., 1982). Osmolytes are tolerated within cells at concentrations, from millimolar to 1–2 molar, depending on the extracellular osmolarity (Brown, 1976).

Extremolytes are osmolytes from extremophilic organisms that are adapted to environmental extremes including high pressure, extremes of pH, high salinity, and high or low temperatures (Raddadi et al., 2015). Extremolytes have many biotechnological and industrial applications, including their use as additives for storage of high value macromolecules enzymes, drugs and antibodies (Barth et al., 2000; Cruz et al., 2006; Lentzen and Schwarz, 2006). They are also important as food and cosmetic product ingredients (Buenger and Driller, 2004; Graf et al., 2008; Marini et al., 2014).

In recent years there has been increased interest in the biotechnological application of extremolytes, most prominently ectoine and hydroxyectoine, due to their well established production and purification methods (Becker and Wittmann, 2020). Ectoines have excellent protein function preserving properties, which has led to their recognition as chemical chaperones. This has fostered the development of an industrial scale biotechnological production process for their exploitation in skin care and medicinal products (Czech et al., 2018).

Another extremolyte is cyclic 2,3-diphosphoglycerate (cDPG). cDPG has been exclusively found in the hyperthermophilic archaeal methanogens such as *Methanothermus fervidus, Methanopyrus kandleri* and *Methanothermobacter thermoautotrophicus*, at concentrations 0.3–1.1 M (Hensel and König, 1988; Ciulla et al., 1994; Matussek et al., 1998). cDPG is synthesized by a two-step enzymatic pathway from the glycolytic intermediate 2-phosphoglycerate (2PG). The process requires two enzymes, 2-phosphoglycerate kinase (2PGK) which forms 2,3-di-phosphoglycerate (2,3DPG) from 2PG, and cyclic di-phosphoglycerate synthetase (cDPGS) which cyclizes 2,3DPG to form the extremolyte cDPG (Lehmacher et al., 1990; Scheme 1).

In the native archaeal methanogenic species, cDPG biosynthesis is triggered by an increase in the growth temperature (Lehmacher et al., 1990). The accumulation of this extremolyte in the cells is correlated with the optimum growth temperature of the archaeal species. The concentration of cDPG increases from 70 mM in *M. thermoautotrophicum* (65°C), to 300 mM in *M. fervidus* (84°C), and 1 M in *M. kandleri* (98°C) (Shima et al., 1998). An additional role has been suggested for intracellular cDPG as a phosphate and energy storage compound (Sastry et al., 1992; Van Alebeek et al., 1994; Lentzen and Schwarz, 2006). Since the cDPGS reaction is exergonic at cellular concentrations, cDPG accumulation is favored thermodynamically until this reaction reaches equilibrium (Shima et al., 1998). cDPG appears to play a role in the thermoprotection of proteins, and increased thermostability has been demonstrated for several model enzymes in its presence. In addition, cDPG protects plasmid DNA against oxidative damage by hydroxyl radicals (Lentzen and Schwarz, 2006). It can also function as a superoxide scavenger, with efficiency reaching one third of that of the antioxidant ascorbic acid (Valentão et al., 2002). Both 2PGK and cDPGS are activated by potassium ions. High concentrations (0.3–0.5 M) of these ions have been reported to increase the activity of 2PGK and cDPGS by 2.4 and 1.4 fold, respectively, (Lehmacher et al., 1990; Van Alebeek et al., 1991, 1994). In physiological conditions, the activation is more modest and has been reported to be around 10% for both enzymes. Interestingly, NaCl at concentrations up to 1 M does not affect enzyme activities (Lehmacher et al., 1990).

In a recent study, we have established a process to produce cDPG using the thermophilic bacterium *Thermus thermophilus* as a whole-cell factory (De Rose et al., 2021). A protein BLAST (Altschul et al., 1990) search of the cDPGS and 2PGK sequences against the Protein Data Bank (PDB) revealed that there are no other known protein structures which share significant sequence similarity, making these enzymes of novelty and interest. Here, we report the high-resolution X-ray structures of cDPGS in its apoform and in complex with its substrate 2,3 DPG and its cofactor ADP. The overall structure is unique and only part of one domain has been shown to structurally align with the structures of other known unrelated enzyme activities. The details of the cDPGS structure described in this paper provides some important insight into its reaction mechanism.

Results

Expression and purification

The gene encoding the cDPGS was successfully cloned in the pLATE51 expression vector in frame with the N-terminal His6x-tag sequence and under the control of the lactose inducible promoter. The His-tagged cDPGS protein was successfully over-expressed in a soluble form in *Escherichia coli* BL21 (DE3). cDPGS was purified from the cell extracts by Ni^{2+}-NTA affinity chromatography with a recovery yield of 20 mg L^{-1}. This was followed by size exclusion chromatography (SEC), that showed that the purified cDPGS elutes in a dimeric form of ~100 kDa (Supplementary Figure S1). As previously reported (Lehmacher et al., 1990; Van Alebeek et al., 1991, 1994) the presence of at least 300 mM KCl is essential for the purification of cDPGS to maintain the enzyme correctly folded and in an active state. Protein purification using 500 mM NaCl instead of KCl lead to poor recovery.

The purified cDPGS was assayed for its thermal stability using differential scanning fluorimetry (DSF) Vivoli et al., 2014). However due to the high thermostability of the enzyme its melting only starts to appear at 95°C. Due to the instrument limitations it was not possible to obtain a precise apparent T_m value for this enzyme. This demonstrates that cDPGS is a highly thermostable enzyme with a melting temperature above 95°C (Supplementary Figure S2).

Activity assay

To confirm the expression of an active correctly folded protein suitable for crystallization studies, the activity of the cDPGS was measured by monitoring the ADP formation using a linked assay with pyruvate kinase (PK) and L-lactate dehydrogenase (LDH) (Scheme 2). The cDPGS was found to be active with a specific activity of 0.039 U/mg (Supplementary Figure S3). The direct production of cDPG was monitored by HPLC–MS to confirm the correct identification of the product (Figure 1 and Supplementary Figure S4).

10.3389/fmicb.2023.1267570

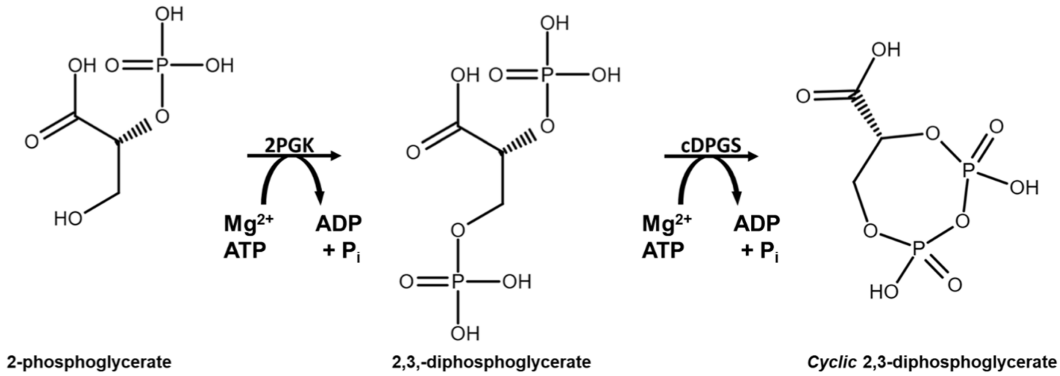

SCHEME 1
Reaction scheme for production of cyclic 2,3-diphosphoglycerate using the enzymes 2PGK and cDPGS derived from the archaeon *M. fervidus*.

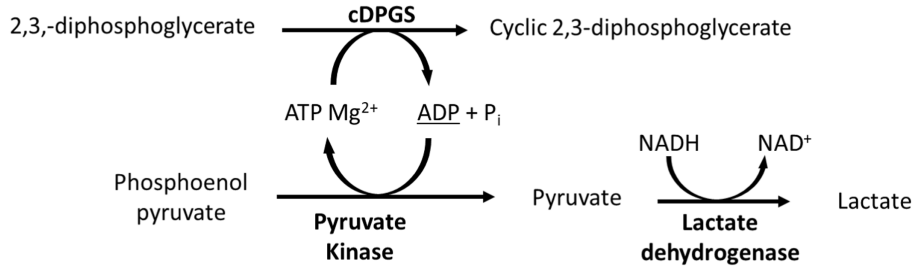

SCHEME 2
Schematic representation of the linked assay used to indirectly monitor the activity of cDPGS. The ADP production was determined spectrophotometrically by monitoring of the oxidation of NADH to NAD^+ at 340 nm.

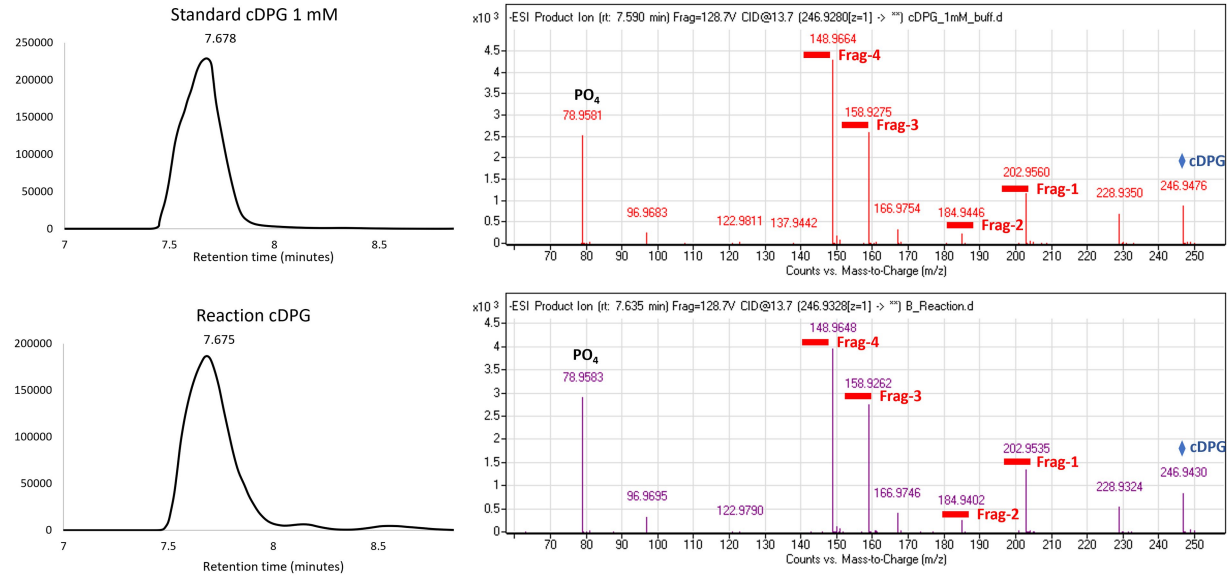

FIGURE 1
Extracted ion chromatogram and MS (Mass Spectrometry) fragmentation patterns for the control (top panel) and the cDPG reaction (bottom panel). The MS fragmentation confirms the identity of the molecule, with an accuracy of 27.2089 ppm and 20.7295 ppm, respectively, for the standard and reaction. The whole molecule mass (cDPG: 246.9 Da) is indicated by the blue diamond, while the four fragments' masses are underlined in red.

10.3389/fmicb.2023.1267570

Crystal structure and overall topology of apo-cDPGS

The cDPGS crystallized readily in many screening conditions and the structure of the apo-cDPGS was solved by the single wavelength anomalous dispersion (SAD) method using data collected from a selenomethionine protein crystal. The space group was determined to be *I*222 with a single protomer of cDPGS in the asymmetric unit. The structure was refined to 1.7 Å resolution and was found to contain the entire polypeptide chain. This has been refined to *R* and R_{free} values of 17.7 and 21.3%, respectively (Table 1).

The overall structure of the cDPGS showed only limited similarity to other known protein structures according to the DALI structural comparison server (Holm and Laakso, 2016; Holm, 2020). The results showed a few structural homologs with a DALI Z score of >7.0. The best scoring homologs were an *Aquifex aeolicus* tetraacyldisaccharide 4′-kinase (PDB entry 4EHX, Z score = 15.9), a *Klebsiella pneumoniae* urease accessory protein UreG (PDB entry 5XKT, Z score = 14.0) and the *Helicobacter pylori* hydrogenase/urease nickel incorporation protein H (PDB entry 4LPS, Z score = 13.2). Structural alignment with these proteins showed a core region that is conserved amongst other NTP-dependent enzymes (Figure 2). However, a portion of the structure, including a 127 amino acid N-terminal domain, shows no structural similarity to other known structures in the PDB. A protein BLAST (Altschul et al., 1997) search of the N-terminal domain sequence against the PDB did not produce any hits. The DALI server did not find any known protein domains with a fold close to that of the N-terminal domain of cDPGS.

The structure of cDPGS can be split into two domains. The smaller N-terminal domain contains a six-stranded β-sheet of mixed type with direction + + + + + − and connectivity -1x,-1x,3x,1x,1 (Richardson, 1981) flanked by 4 α-helices (α1–α4). The β-sheets of the two N-terminal domains in the cDPGS dimer form a large intersubunit 12 strand β-sheet on the molecular dyad. The C-terminal domain of cDPGS roughly aligns with the unusual P-loop kinase tetraacyldisaccharide 4′-kinase (LpxK) from *A. aeolicus* (Emptage et al., 2012). The cDPGS C-terminal domain and LpxK show the same Rossmann like α/β/α sandwich fold connected by two twisted, antiparallel β-strands. The larger C-terminal domain (residues 136–460) contains a twelve-stranded β-sheet (β7 – β18) surrounded by twelve α-helices. The strand direction is − − − − + + + + + + + − and connectivity is 2x,2,-1,-2x,-2x,-1x,-1x,-3,-1x,2x,1x (Supplementary Figure S5).

The cDPGS structure shows a tight dimer that buries a surface area of 2844.1 Å^2, accounting for 13.7% of the total solvent accessible area of the protomer (Figure 3A). The interface is stabilized by 36 hydrogen bonds and 24 salt bridges between the interacting subunits as estimated by PISA (Krissinel and Henrick, 2007). These include an intersubunit 12-strand β-sheet formed by the N-terminal domains. The dimer interface of cDPGS clearly shows a large positively charged patch at the interface of the C-terminal domain that interacts with the negatively charged N-terminal domain of the opposing molecule (Figure 3B). The high thermal stability of cDPGS appears to be due to both hydrophobic interactions and a high number of hydrogen bonds and ion pairs. Similar interactions have previously been observed in other thermostable proteins with temperature optima up to approximately 75°C (Sayer et al., 2012; Ferrandi et al., 2018).

TABLE 1 cDPGS data collection and refinement statistics.

cDPGS	Ligand free	ADP 2,3 DPG complex
Data collection statistics		
Beamline	IO3 Diamond	IO3 Diamond
Wavelength (Å)	0.9763	0.9763
Space group	I222	P1
Unit Cell Parameters a, b, c (Å)	74.5, 105.8, 157.0	71.1, 71.3, 103.3
a, β, g (°)	90.0, 90.0, 90.0	96.9, 103.4, 99.1
Resolution range (Å)[a]	42.71–1.64	69.62–2.23
Total reflections[a]	822,404	167,272
Unique reflections[a]	362,595 (15356)	92,153 (4558)
Completeness (%)[a]	100.0 (99.9)	97.7 (97.0)
Multiplicity[a]	5.0	1.8
R_{meas} (%)[a,b]	0.110	0.115
/[a]	8.0 (0.3)	6.3 (0.2)
$CC_{1/2}$[a,c]	0.99 (0.28)	0.98 (0.38)
Wilson B-factor[d] (Å^2)	37.8	70.3
Refinement statistics		
R_{work}	0.177	0.216
R_{free}	0.213	0.256
No. of protomers in a.u.	1	4
Number of atoms	4,232	14,537
Macromolecules	3,817	14,416
Ligands/Metal ions	119	77
Solvent	293	50
Number of protein residues	460	460
RMS bond lengths (Å)	0.010	0.005
RMS bond angles (°)	1.58	1.36
Ramachandran favored (%)[e]	98.03	97.81
Ramachandran outliers (%)[e]	0.0	0.0
Clashscore[e]	4.04	0.21
Average B-factor protein (Å^2)	37.942	74.855
Average B-factor ligands (Å^2)	47.274	96.300
Average B-factor solvent (Å^2)	45.201	51.956
RCBS PDB code	8ORK	8ORU

[a]Values for the highest resolution shell are given in parentheses.
[b]Rmeas = Σh [m/(m—1)]1/2 Σi|Ih,i— < Ih > |/Σh ΣiIh,i.
[c]CC1/2 is defined in Karplus and Diederichs (2012).
[d]Wilson B-factor was estimated by SFCHECK (Vaguine et al., 1999).
[e]The Ramachandran statistics and clashscore statistics were calculated using MOLPROBITY (Chen et al., 2010).

Multiple sequence alignments using the results from the structural comparison server revealed a number of highly conserved residues (Figure 4) that tend to cluster around the nucleotide and ligand binding sites, particularly a P-loop/ Walker A motif GxxGxGK[T/S] (Walker et al., 1982). This loop typically binds the phosphate groups of phosphorylated ribonucleotides and catalyzes phosphoryl transfer (Romero Romero et al., 2018).

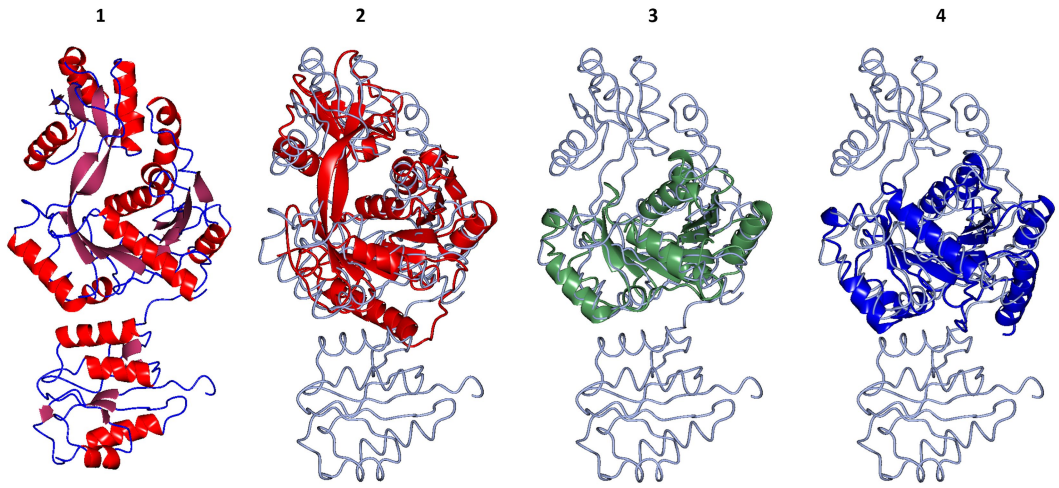

FIGURE 2
Structural superposition of the cDPGS monomer with its three closest structural homologs as reported by the DALI server (Holm and Laakso, 2016; Holm, 2020). From left to right: **(1)** cDPGS monomer colored by secondary structure elements, α-helices (red) β-sheets (pink), loops and turns (blue), in accordance with the topology diagram in Supplementary Figure S5, **(2)** *Aquifex aeolicus* tetraacyldisaccharide 4′-kinase (red), **(3)** *Klebsiella pneumoniae* urease accessory protein UreG (green), and **(4)** *Helicobacter pylori* hydrogenase/urease nickel incorporation protein H (blue). In panels 2, 3 and 4 cDPGS is depicted as a thin cyan tube. Figure prepared with CCP4mg (McNicholas et al., 2011).

Crystal structure of ADP/Mg^{2+} bound cDPGS

To elucidate the substrate binding residues of cDPGS, the structure of the 2,3 DPG, ADP/Mg^{2+} bound enzyme complex was solved by molecular replacement to a resolution of 2.2 Å resolution, resulting in R_{work} and R_{free} values of 21.5 and 25.6%, respectively (Table 1).

The 2,3 DPG binding site is located between the C-terminal domain of the one protomer and the N-terminal domain of the other protomer of the dimer (Figure 5A). The presence of the bound ligands is confirmed by the Fo-Fc difference map calculated with ADP Mg^{2+} and 2,3 DPG at zero occupancy. The ADP and Mg^{2+} are clearly resolved and reside in the pocket formed within the C-terminal domain (Figure 5B). The 2,3 DPG is clearly resolved in only three of the four protomers making up the asymmetric unit of the crystal. A phosphate molecule has been modeled in the active site of the 4th protomer. The Walker A/P-loop surrounds the pyrophosphate moiety of the ADP while coordinating with the Mg^{2+} atom. The adenosine moiety is bound in a pocket formed by α5, α14, β13, β14 and β15. The Walker B loop borders the 2,3 DPG binding site without directly interacting with it.

A superposition of the apo- and ADP/Mg^{2+} bound forms of cDPGS reveals a large movement of several α-helices that close around the nucleotide, which highlight the significant conformational changes that accompany ligand binding (Figure 6A). The helices α5, α8, α9 and α14 show a motion of up to 8.5, 7.0, 6.7, and 2.6 Å, respectively. The loops formed by residues 186–192, 396–400 and 420–427 make up the "hinge" regions. A closer look at the active site revealed that the closure is triggered by the binding of the substrate and ADP which brings the Walker A/P-loop close enough to contribute to the stabilization of 2,3 DPG. Residues K145 and R146 move closer to the substrate to form multiple hydrogen bonds with it (Figure 6B). The 2,3DPG is also stabilized by E45 from the opposing subunit (Figures 7A,B). The pyrophosphate moiety of ADP is held in place by an intricate network of hydrogen bonds with backbone amide nitrogen atoms, various side chains, and water molecules (Figure 7C). The magnesium atom is octahedrally coordinated by the side chain oxygens of D208, T150, the O3B oxygen of ADP, O9 oxygen of 2,3DPG and two water molecules. The domain movement causes the interaction of several residues with the ADP. Outside the P-loop, residues E305, P335, T353 and E404 appear to have a significant role in ATP binding since they form hydrogen bonds to the adenosine, ribose hydroxyl groups, or the α-phosphate of ADP.

Based on the apo structure and the ADP/Mg^{2+} complex structures, we propose a classical phosphoryl transfer mechanism for cDPGS as observed in other NTP dependent enzymes (Matte et al., 1998; Guixé and Merino, 2009; Gerlits et al., 2015). The conformational changes that accompany binding of ATP and 2,3 DPG bring the ATP into the proximity of 2,3 DPG in a sterically and energetically strained conformation, forming a 'near attack complex' (Bruice, 2002). Positively charged residues (K145, R146, K149, K406) and the magnesium ion will shield the negative charges on the phosphates, allowing the reactants to approach. The domain closure creates a hydrophobic environment allowing the phosphoryl transfer from the ATP γ-phosphate to the 2-phosphate of the 2,3 DPG through an S_N2 reaction, with the transition state stabilized by the magnesium ion, to form the intermediate. A second S_N2 reaction is initiated by attack of the 3-phosphate of the intermediate on the 2-pyrophosphate, releasing an inorganic phosphate. This step is facilitated by the magnesium ion, K145, and R146 providing positive charges to stabilize the transition state. Release of phosphate makes the reaction highly exergonic under standard conditions, providing the energy for the formation of the cDPG phosphoanhydride (Scheme 3).

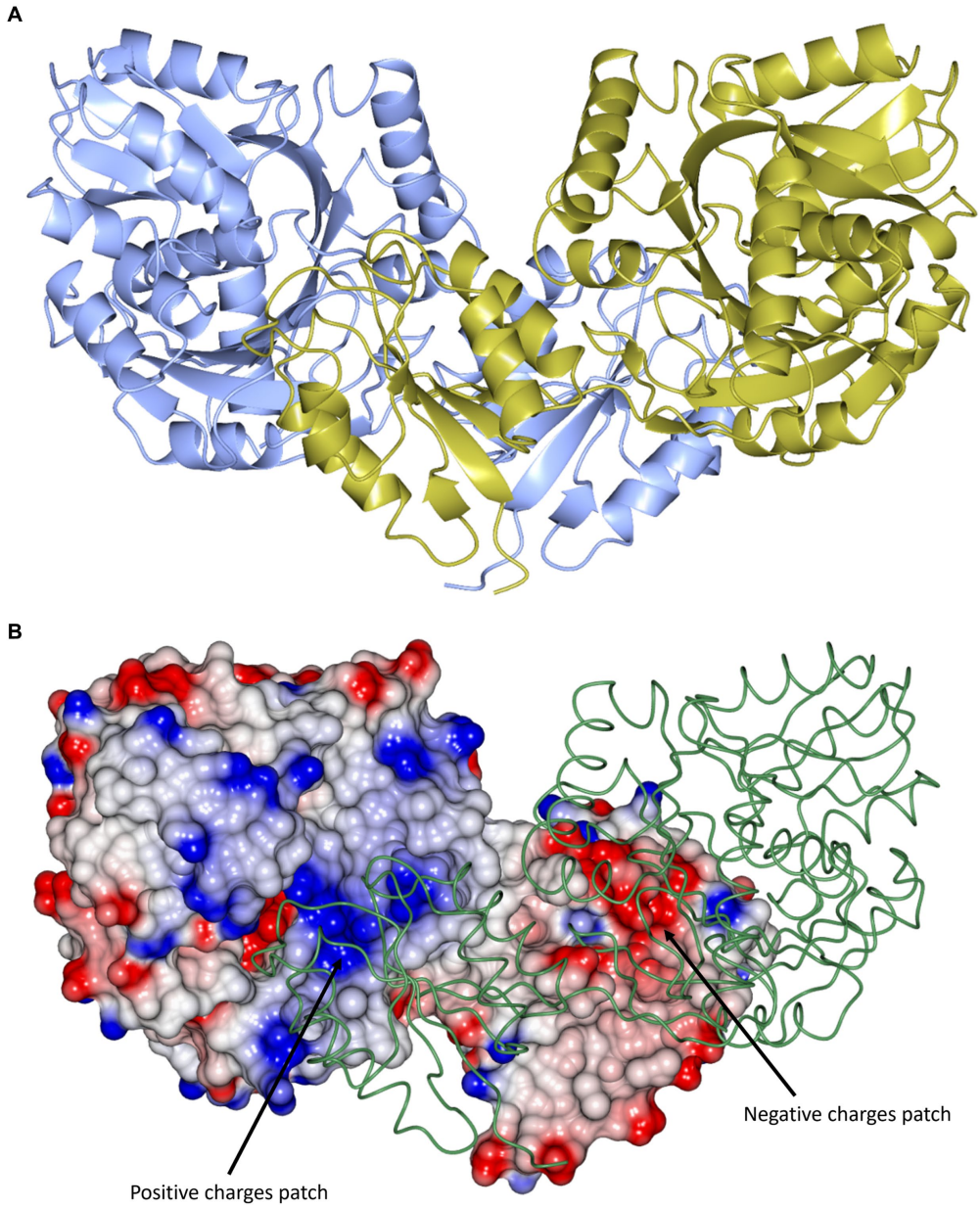

FIGURE 3
(A) A cartoon representation of the apo-cDPGS dimer viewed perpendicular to a molecular dyad with the two protomers in cyan and gold. **(B)** A cartoon diagram showing the hydrophobic interactions at the dimer interface of cDPGS. For clarity one protomers is shown in space filling mode with electrostatic surface potential and the other as a thin green tube. The areas of positive charge are shown in blue, with the areas of negative charge in red and the hydrophobic surfaces are represented in white, the two major charges patches involved in the dimer interaction are highlighted by black arrows. Figure prepared with CCP4mg (McNicholas et al., 2011).

Discussion

cDPGS has been long known for its role in the biosynthesis of cDPG. This extremolyte which is only found naturally in specific methanogenic archaea such as *M. fervidus* which was first isolated in 1981 by Karl Stetter (Stetter et al., 1981). This organism has attracted interest since it has the smallest genome known to date for a free-living archaeon, coding for only 1,311 proteins and 50 RNA genes (Martínez-Cano et al., 2015). *M. fervidus* only grows under strict anaerobic conditions and obtains its energy by the reduction of carbon dioxide with hydrogen to produce methane. It is known to use cDPG up to a 0.3 M intracellular concentration for protein stabilization at temperatures of 75°C and above. Since its discovery cDPG has been the subject of a limited number of research publications (Hensel and König, 1988; Lehmacher et al., 1990; Van Alebeek et al., 1991; Lehmacher and Hensel, 1994; Van Alebeek et al., 1994; Matussek et al., 1998) which have focused mainly on its identification, biochemical characterization and its production pathway.

This paper describes the cloning and over-expression in *E. coli* of cDPGS, involved in the cDPG production. This enzyme has been characterized both biochemically and structurally. The unique

10.3389/fmicb.2023.1267570

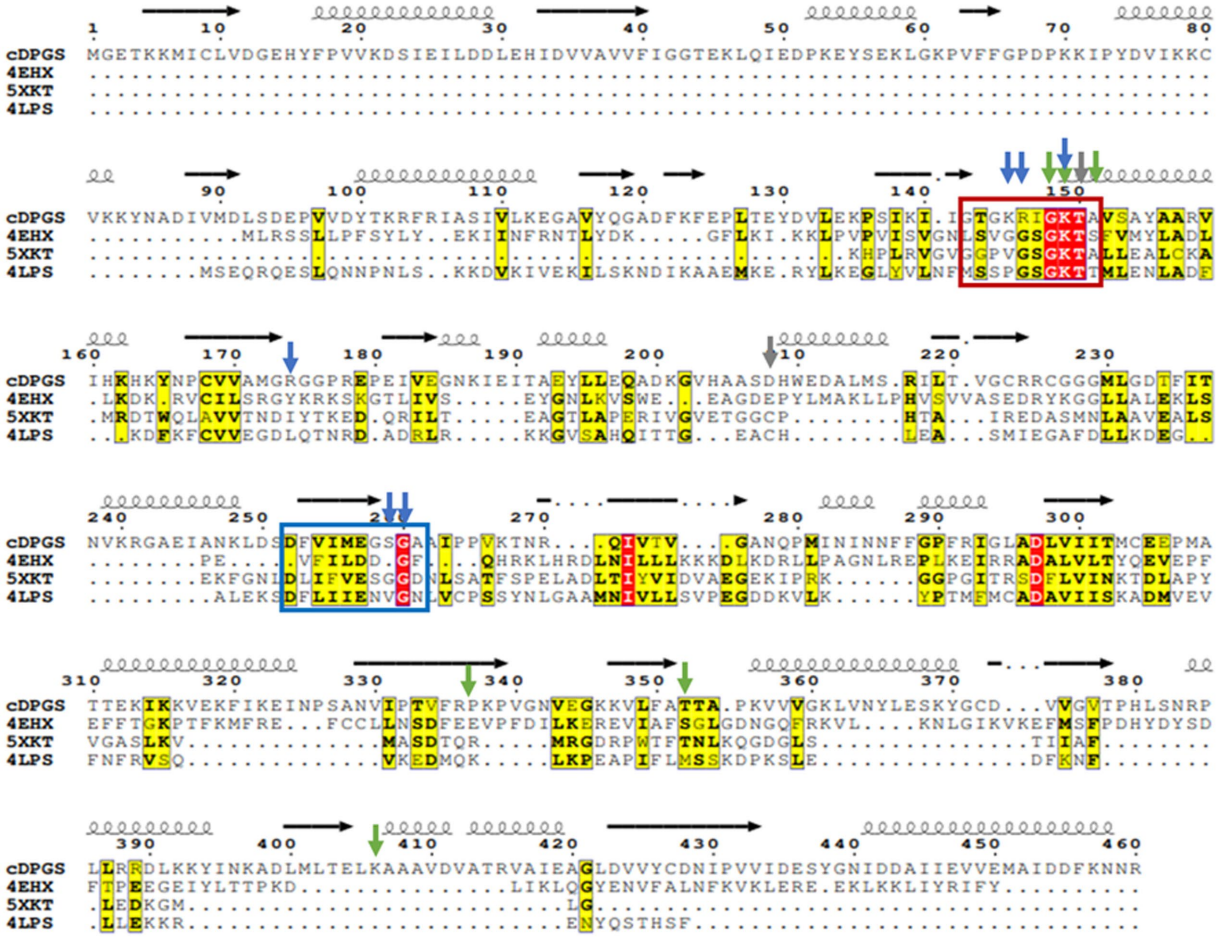

FIGURE 4
Multiple sequence alignment of cDPGS with its three closest structural homologs. Red and yellow residues have a high degree of conservation among the orthologues where "red" indicates absolute conservation, "yellow" indicates conservation between similar groups. The cDPGS secondary structure is depicted on top of the sequence as spring and arrows along with the location of the Walker A/P-loop and Walker B motifs in the red and blue boxes, respectively. The accession numbers of the cDPGS orthologues in order are as follows: 4EHX *Aquifex aeolicus* tetraacyldisaccharide 4′-kinase; 5XKT *Klebsiella pneumoniae* urease accessory protein UreG; 4LPS *Helicobacter pylori* hydrogenase/urease nickel incorporation protein H. Arrowheads indicate the residue directly interacting with the ADP (blue), magnesium (gray) and 2,3 DPG (green). The alignment was generated using ClustalO (Sievers et al., 2011), and visualized with Espirt3 (https://espript.ibcp.fr) (Robert and Gouet, 2014).

structure of cDPGS is made up of an N-terminal domain which is crucial for the stabilization of the active dimeric structure and the ligand interactions, and a C-terminal domain that contains a P-loop kinase fold as part of its structure. From a comparison with the closest structural homologs highlighted in the multiple sequence alignment shown in Figure 4 little can be observed apart from a few conserved regions that match with the P-loop kinases fold. The crystal structures of both the apo- and ADP/Mg^{2+}-bound forms of cDPGS have allowed us to understand its substrate specificity and mechanism, and to provide an insight into the features that determine its extreme thermostability. The functional dimeric form of cDPGS is seen to undergo a conformational change upon binding of ADP/Mg^{2+} and 2,3DPG during the cyclisation reaction. The super-imposition of the apo-cDPGS and its ADP/Mg^{2+} bound complex structures reveal a closure of the C-terminal domain around the ADP product in the active site of the enzyme.

We propose that cDPGS remains in the 'open' conformation until the substrate and ATP are bound in the correct orientation for turnover to occur, which then triggers domain closure providing a hydrophobic environment for the cyclisation reaction. The enzyme then is required to return to its 'open' conformation to release the product and ADP, as described for other ATP dependent enzymes (Davies et al., 1993; Auerbach et al., 1997; Bowler, 2013; Murillo-López et al., 2019; Recabarren et al., 2019).

More information could be derived from the crystal structure of the cDPGS in complex with cDPG, as well as the crystal structure of the ATP transition state that could be mimicked using a transition state analog such as AlF_3 where fluorine substitutes the ATP γ-phosphate (Baxter et al., 2006; Cliff et al., 2010). However, it has not been possible to date to crystallize these complexes.

This unusual 'primitive' cDPGS enzyme which is found only in methanogenic hyperthermophilic archaea has naturally evolved to form the unique protein structure described in this paper. This allows the production of cDPG, a natural extremolyte, to stabilize the proteins and DNA for growth and survival of the organism in extreme environments. The cDPG, due to its known protective roles

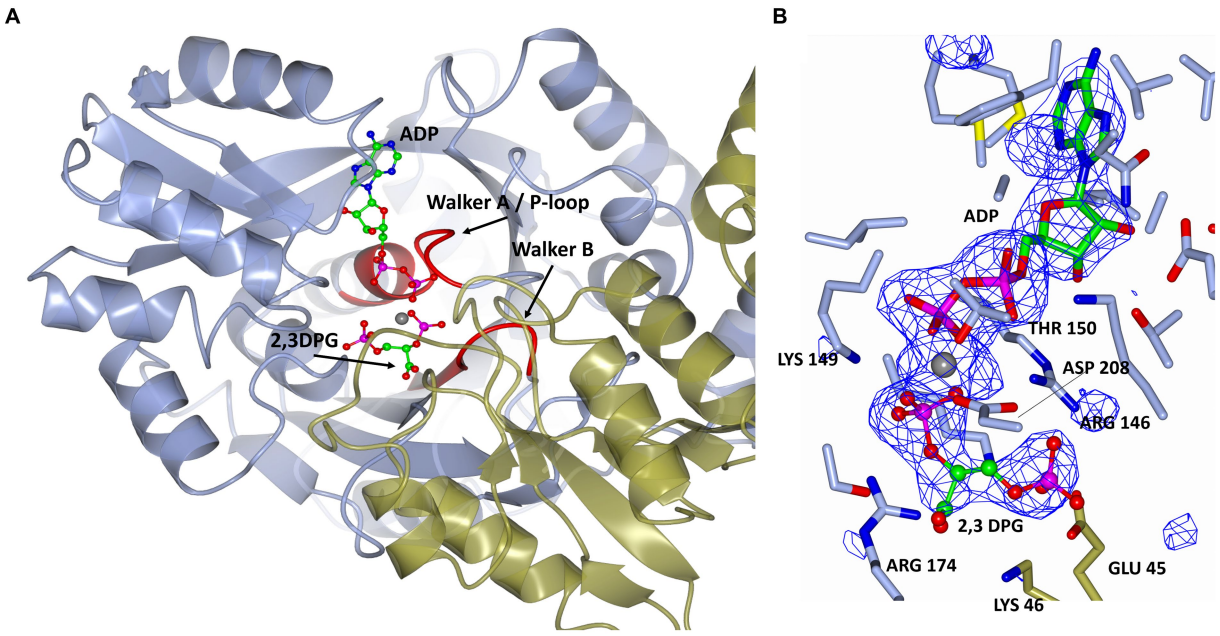

FIGURE 5
(A) A cartoon representation of the ADP and 2,3 DPG ligands bound to cDPGS. The two subunits are shown in cyan and green. ADP and 2,3 DPG are shown as a ball-and-stick model (carbon, green; oxygen, red; nitrogen, blue; phosphorus, pink). The Mg^{2+} atom is depicted as a gray sphere. The Walker A/ P-loop and Walker B loop are shown in red. **(B)** A view of 2,3 DPG and ADP bound in the active site of cDPGS showing neighboring protein residues. The magnesium atom is shown as a gray sphere; ADP and 2,3 DPG are shown as a ball-and-stick models (carbon, green; oxygen, red; nitrogen, blue; phosphorus, pink). Residues belonging to molecule A of the dimer are shown in ice blue while Glu45 and Lys46 from molecule B are shown in green. The Fo-Fc difference map calculated with ADP, Mg^{2+} and 2,3 DPG at zero occupancy is shown in blue contoured at 3.0σ. This clearly shows the presence of the ligand 2,3 DPG. Figure prepared with CCP4mg (McNicholas et al., 2011).

for proteins (Hensel and Jakob, 1993; Borges et al., 2002) and DNA (Lentzen and Schwarz, 2006) has industrial applications for a variety of high value cosmetic and healthcare products. The biosynthesis of cDPG has already been demonstrated in a cascade reaction using the two enzymes 2PGK and cDPG both *in vitro* or *in vivo* (De Rose et al., 2021). The optimisation of these methodologies will allow the scale-up of the production of this extremolyte for new biotechnological applications.

Materials and methods

Cloning, expression, and purification

The genes coding for *Mf*-cDPGS in its *E. coli* codon optimized version was kindly donated by the Siebers lab (Essen Germany) and sub-cloned into the pLATE51 vector (ThermoFisher) in frame with a N-terminal 6x His-Tag. pLATE51/cDPGS (Supplementary Figure S7) was introduced into *E. coli* DH5α (New England Biolabs, C2987H) using standard techniques. The plasmid was purified and sequenced to confirm the presence of the gene. The plasmid pLATE51/cDPGS (Addgene: 201561) was introduced into *E. coli* BL21 competent cells (Agilent Technologies, 230,132) according to the manufacturer's instructions.

The transformants obtained were grown in LB supplemented with 100 μg/mL ampicillin (LB_{amp100}) medium (50 mL) overnight and then inoculated in 0.5 L LB $_{amp100}$ at 37°C and 200 rpm. When the OD_{600} reached 0.5–0.6, gene expression was induced by the addition of 0.5 mM IPTG, and the culture was maintained at 25°C for 24 h. Cells were harvested by centrifugation (4,750 *g* for 30 min), and frozen at −20°C before proceeding with the protein purification.

A selenomethionine derivative (SeMet) of the enzyme was also produced in *E. coli* using the protocol described by Studier. Briefly the protein was expressed in PASM-5052 auto induction media, supplemented with 100 μg/mL ampicillin, 200 μg/mL each of 17 aa (no C, Y, M), 10 μg/mL methionine, 125 μg/mL selenomethionine and 100 nM vitamin B_{12} (Studier, 2005).

The frozen cell paste expressing cDPGS was thawed and re-suspended in 50 mM Tris–HCl pH 7.5, 300 mM KCl, and 20 mM imidazole. The cells were disrupted by sonication at 10 μm (Soniprep150; MSE) on ice for 4 min and the cell debris was removed by centrifugation at 24000 *g* at 4°C for 30 min. The clarified cell lysate was then heat-treated at 60°C for 30 min before being centrifuged at 24000 *g* at 4°C for 30 min to remove any denatured proteins. The protein was purified using a 1 mL HisTrap FF crude column (Cytiva) using a two-step gradient. Step one increased the imidazole concentration to 40 mM for 10 column volumes (CV), whilst step two increased the concentration to 300 mM imidazole for 20 CV. The eluate from the second step was applied to a calibrated Superdex 200 HiLoad 16/60 gel filtration column (Cytiva) and eluted with one column volume of 20 mM Tris–HCl pH 7.5, 300 mM KCl, at 1.0 mL min^{-1}.

Enzyme characterization

Indirect activity assay by coupled reaction

The enzymatic activity was determined using a coupled assay (Scheme 2). This couples the ADP formation from ATP to NADH

10.3389/fmicb.2023.1267570

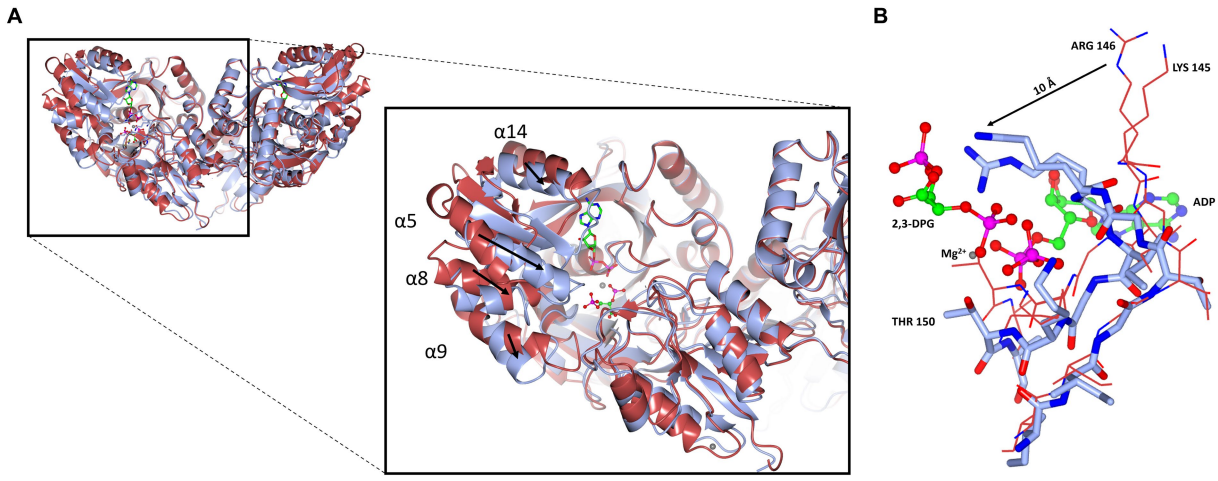

FIGURE 6
Cartoon representation of the domain closure induced by binding of ADP/Mg^{2+}. **(A)** A super-imposition of the apo-cDPGS (red) with the ADP and 2, 3DPG bound to cDPGS (cyan). Black arrows indicate the direction of movement induced by the conformational changes. **(B)** Close-up of the same super-imposition showing the local movements (black arrow) that follow ADP and 2,3DPG binding. Figure prepared with CCP4mg (McNicholas et al., 2011).

oxidation via pyruvate kinase (PK) (Merck, 10109045001) and L-lactate dehydrogenase (LDH) (Merck, 427217). The assay mixture (200 µL) contained 50 mM MES/KOH pH 6.5 with 2.5 mM $MgCl_2$, 400 mM KCl, 2.5 mM ATP, 0.5 mM NADH, 3.7 µg purified cDPGS, 8 U PK, 4 U LDH, and 2 mM phosphoenolpyruvate. The reactions were started by the addition of 2,3DPG and the oxidation of NADH was followed in an Infinite 200 pro spectrometer (Tecan) at 340 nm. All measurements were performed in triplicates at 37°C since higher temperatures could destabilize the coupling enzymes PK and LDH.

Differential scanning fluorimetry

Differential scanning fluorimetry DSF was used as a method to monitor protein unfolding with increasing temperature. In this method, proteins are incubated with a fluorescent dye which alters its fluorescence upon binding to the hydrophobic regions of the proteins. The protein dye mixture is then heated, and the fluorescence monitored as the heat rises. The unfolding of the protein and exposure of hydrophobic parts of the protein gives rise to a characteristic pattern of the fluorescence as a function of temperature (Vivoli et al., 2014). The DSF samples were prepared at the following concentrations in a final volume of 20 µL: 1 mg/mL protein, 10 mM HEPES pH 7.0, 150 mM NaCl, 8 × SYPRO Orange dye (Invitrogen). All samples were prepared in triplicate. The fluorescence was measured using a StepOne quantitative PCR machine (Applied Biosystems, Foster City, CA, USA) while heating the samples in a gradient from 25 to 99°C over 40 min. Measurements were taken every 0.37°C. The DSF curves obtained were used to calculate the midpoint temperature of the unfolding transition (T_m) using the differential of each DSF curve calculated using the Protein Thermal Shift software package (Applied Biosystems).

Direct activity assay by HPLC-MS

The direct activity of cDPGS was determined from the detection of cDPG formed from 2,3 DPG. 0.1 mg/mL of enzyme solution was incubated with 100 µL of a substrate mixture containing 25 mM Tris–HCl pH 8.0, 50 mM $MgCl_2$, 50 mM ATP, 250 mM 2,3-DPG and 300 mM KCl at 65°C for 60 min. The reaction was stopped with the addition of a 2:1 ratio of ice-cold acetonitrile. Samples were incubated for 10 min on ice and centrifuged at 13000 *g* for 10 min to precipitate all of the enzyme before the supernatant was collected and transferred into a HPLC vial. Samples were kept at 4°C and analyzed by HPLC–MS within 24 h. Reactions were performed in triplicate. The control reaction was performed in the same condition without the enzyme.

Analytical methods

LC-QTOF-MS polar metabolite profiling

cDPG profiling was performed using a Q-TOF 6520 mass spectrometer (Agilent Technologies) coupled to a 1,200 series Rapid Resolution HPLC system. 5 µL of sample extract was loaded onto an Agilent Infinity Lab Poroshell 120 HILIC-Z 2.7 µm, 2.1 × 250 mm analytical column. For detection using negative ion mode, mobile phase A comprised 100% water with 10 mM ammonium acetate and 5 µM medronic acid and mobile phase B was 90% acetonitrile with 10 mM ammonium acetate and 5 µM medronic acid. All solvents were LC-MS grade. The following gradient was used: 0 min – 95% B; 5 min – 65% B; 10 min – 50% B; 11 min – 95% B; 15 min – 95% B followed by 1 min post time. The flow rate was 0.25 mL min^{-1} and the column temperature was held at 25°C for the duration of the measurement. The source conditions for electrospray ionization were as follows: gas temperature was 325°C with a drying gas flow rate of 9 L min^{-1} and a nebulizer pressure of 35 psg. The voltages for the capillary, fragmentor, and skimmer were 3.5 kV, 115 V, and 70 V, respectively. Scanning was performed using the auto MS/MS function at 5 scans sec^{-1} for precursor ion

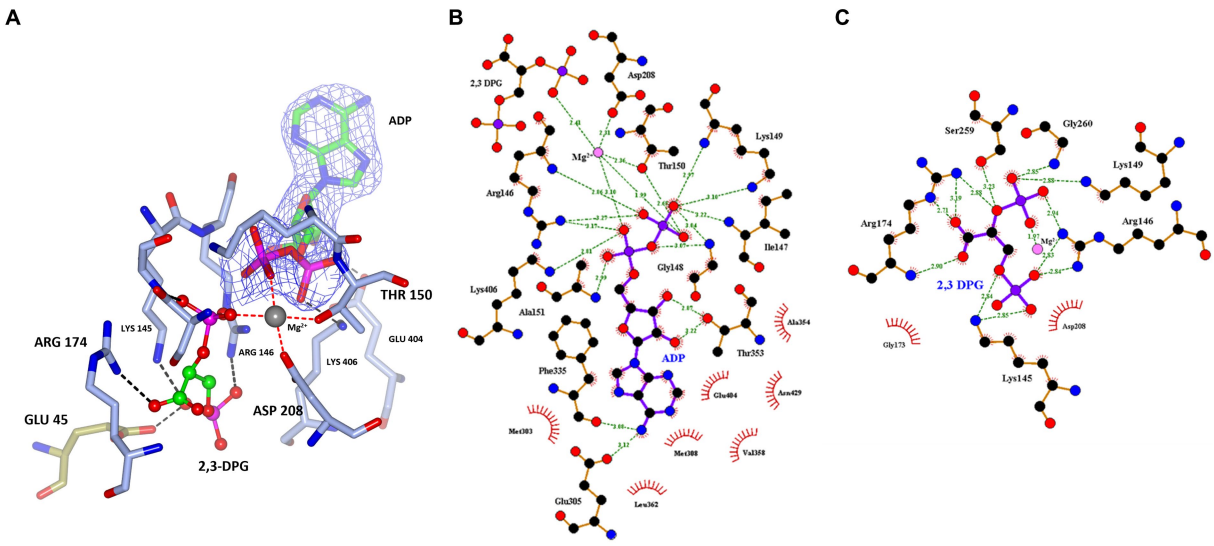

FIGURE 7
(A) A view of 2,3 DPG and ADP bound in the active site of cDPGS showing residues involved in the stabilization of the substrates. The magnesium atom is shown as a gray sphere; ADP and 2,3 DPG are shown as a ball-and-stick model (carbon, green; oxygen, red; nitrogen, blue; phosphorus, pink); the coordination bonds to the Mg^{2+} are shown as red dotted lines while hydrogen bonds are shown as black dotted lines. Residues belonging to molecule A of the dimer are shown in ice blue while GLU45 from molecule B is shown in green, the 2Fo-Fc electron density of the ADP molecule contoured at 1.5σ is shown in blue for better visual separation from the 2,3 DPG molecule and surrounding residues. Schematic overview of the **(B)** nucleotide/magnesium binding site and **(C)** 2,3 DPG pocket. Hydrogen bonds are indicated with green dashes and their distances indicated. Panel **(A)** prepared with CCP4mg (McNicholas et al., 2011), panels **(B,C)** generated using LigPlot+ (Wallace et al., 1995; Laskowski and Swindells, 2011).

surveying and 4 scans sec^{-1} for MS/MS, with a sloped collision energy of 3.5 V/100 Da with an offset of 5 V. MassHunter qualitative analysis (version B.07.00) was used to identify potentially interesting compounds with similar masses to the sugar phosphate of interest.

Crystallization and structure solution

A sample of cDPGS from the right side of Peak 2 _Supplementary Figure S1 corresponding to the dimeric form was concentrated to ~10 mg/mL using a 10 kDa membrane Vivaspin (Vivascience) and microbatch and sitting drop crystallization trials were set up using an Oryx8 crystallization robot (Douglas Instruments) using the Morpheus™ (Molecular Dimensions) protein crystallization screens. Microbatch trials were set in hydrophobic plates (VB-SILVER-2, Douglas Instruments), with a final drop volume of 0.5 µL. The droplet contained a 50:50 ratio of protein solution to screen and was covered with Al's oil (50,50 mix of silicon and paraffin oils) before being stored at 20°C. For sitting drop trials, hydrophilic plates were used (MRC96T-PS, SwissCL) with a drop volume of 1 µL the droplets contained 40:60 and 60:40 protein to screen ratio for each of the conditions.

cDPGS native crystals appeared within 1 week in most of the conditions of the Morpheus screen. The crystals were harvested straight from the crystallization droplet and plunged into liquid nitrogen. Preliminary data were collected to 7.0 Å resolution at 100 K on the Diamond beamline IO3. Further crystals grown with selenomethionine enriched protein diffracted to a higher resolution of 1.7 Å in space group *I*222 on the Diamond beamline IO3. The data were processed using DIALS (Waterman et al., 2016) within the Xia2 pipeline (Winter et al., 2013). These data were used for solution of the structure with single anomalous diffraction (SAD) method using CRANK-2 (Skubák and Pannu, 2013) in CCP4CLOUD (Krissinel et al., 2022).

The selenomethionine enriched crystals grew in condition F7 of the Morpheus screen consisting of 0.12 M Monosaccharides mix, 0.1 M Buffer System 2 pH 7.5 and 30% v/v Precipitant Mix 3. The substrate bound crystals grew (Supplementary Figure S6) in condition E12 of the Morpheus screen consisting of 0.12 M Ethylene glycols mix, 0.1 M Buffer System 3 pH 8.5 and 37.5% v/v of Precipitant Mix 4, with 10 mM 2,3 DPG, 20 mM $MgCl_2$ and 20 mM ADP.[1]

The substrate bound crystals diffracted to 2.2 Å in space group P1. Data were processed and scaled using XDS (Kabsch, 2010) and AIMLESS (Evans and Murshudov, 2013) in the Xia2 pipeline (Winter et al., 2013). The structure was solved by molecular replacement using MOLREP (Vagin and Teplyakov, 2010) using the native structure coordinates. All further data and model manipulations were carried out using the CCP4 suite of programs (Winn et al., 2011; Agirre et al., 2023). The resulting structure was subjected to refinement in REFMAC5 (Murshudov et al., 2011) and rebuilding in COOT (Emsley et al., 2010; Table 1). The PISA software (Krissinel and Henrick, 2007) was used for oligomeric state analysis of the cDPGS models.

1 https://calibrescientific.com/en/products/MDL-MD1-47

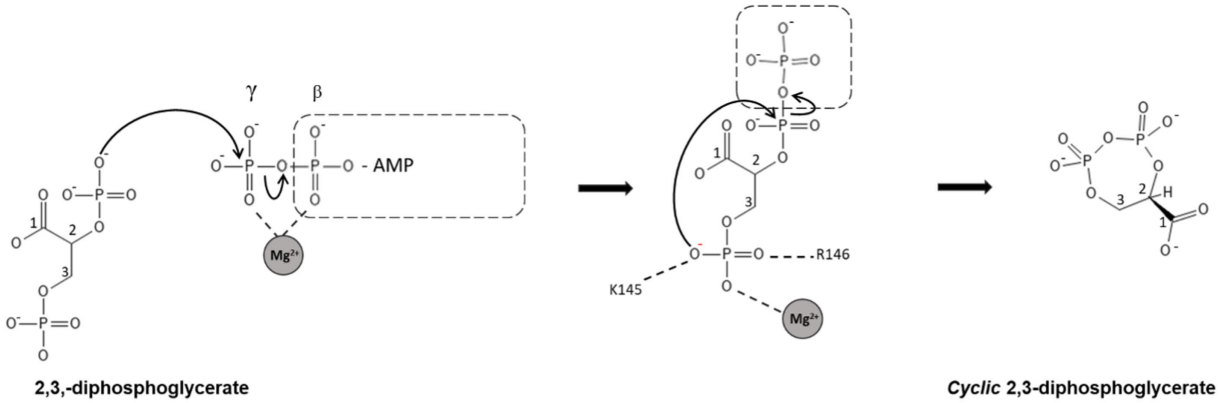

SCHEME 3
Schematic representation of the proposed mechanism for the synthesis of cDPG. In step 1, the cDPG 2-phosphate attacks the γ-phosphate of ATP, forming the 2-pyrophosphate intermediate. In the second step, the 3-phosphate attacks the pyrophosphate, releasing inorganic phosphate and forming cDPG. Both reactions are S_N2 reactions with simultaneous formation and breaking of the P-O bonds. The highly negatively charged transition states are stabilized by magnesium and positively charged amino acid side chains.

Data availability statement

The datasets presented in this study can be found in online repositories. The names of the repository/repositories and accession number(s) can be found at: https://www.rcsb.org/, PDB 80RK, PDB 80RU.

Author contributions

SR: Methodology, Writing – original draft, Writing – review & editing, Formal analysis, Investigation. MI: Investigation, Methodology, Writing – original draft, Writing – review & editing, Data curation, Software, Supervision, Validation. HW: Data curation, Investigation, Writing – review & editing. CS: Writing – review & editing, Methodology, Resources. NH: Investigation, Validation, Writing – review & editing. BS: Writing – review & editing, Methodology, Conceptualization, Project administration, Funding acquisition. JL: Writing – review & editing, Conceptualization, Funding acquisition, Methodology, Project administration, Resources, Supervision, Writing – original draft.

HotSolute

List of the HotSolute consortium participants: Bettina Siebers, bettina.siebers@uni-due.de; Christopher Bräsen, christopher.braesen@uni-due.de; Christina Stracke, christina.stracke@uni-due.de; Benjamin Meyer, benjamin.meyer@uni-due.de; Michail N. Isupov, misupov@exeter.ac.uk; Nicholas J. Harmer, N.J.Harmer@exeter.ac.uk; Simone Antonio De Rose, S.A.De-Rose@exeter.ac.uk; Jennifer Ann Littlechild, J.A.Littlechild@exeter.ac.uk; Elizaveta Bonch-Osmolovskaya, elizaveta.bo@gmail.com; Sergey Gavrilov, sngavrilov@gmail.com; Ilya Kublanov, kublanov.ilya@gmail.com; Daniela Monti, daniela.monti@scitec.cnr.it; Erica Ferrandi, erica.ferrandi@scitec.cnr.it; Eleonora Dore, eleonora.dore@scitec.cnr.it; Felix Müller, felix.mueller@evonik.com; and Jacky Snoep, jacky.snoep@mac.com.

Funding

The author(s) declare financial support was received for the research, authorship, and/or publication of this article. This project has received funding from the European Union's Horizon 2020 research and innovation programme under grant 722361. This work has been conducted as part of the HotSolute project under the ERA-CoBiotech and also financed by local countries' funding agencies. The project aimed to develop thermophilic bacterial (*Thermus thermophilus*) and archaeal (*Sulfolobus acidiocaldarius*) host systems and the development of new chassis for extremolyte production. The work conducted in this paper was funded in the UK by a BBSRC grant BB/R02166X/1 to JL, NH and MI. The University of Exeter is also thanked for their support. CS and BS acknowledge funding by an EVONIK Industries Ph.D. scholarship and the German Federal Ministry of Education and Research (BMBF) grant HotSolute, 031B0612A. The funder was not involved with this study design, collection, analysis, interpretation of data, the writing of this article, or the decision to submit it for publication.

Acknowledgments

The authors would also like to thank Deborah Salmon for her help and support in running the HPLC-MS experiments and for the data analysis. The authors would like to thank the Diamond Synchrotron Light Source for access to beamline I03, I04-1 and I04 (proposal Nos. mx22563) and beamline scientists for assistance.

Conflict of interest

The authors declare that the research was conducted in the absence of any commercial or financial relationships that could be construed as a potential conflict of interest.

The author(s) declared that they were an editorial board member of Frontiers, at the time of submission. This had no impact on the peer review process and the final decision.

Publisher's note

All claims expressed in this article are solely those of the authors and do not necessarily represent those of their affiliated organizations, or those of the publisher, the editors and the reviewers. Any product that may be evaluated in this article, or claim that may be made by its manufacturer, is not guaranteed or endorsed by the publisher.

Supplementary material

The Supplementary material for this article can be found online at: https://www.frontiersin.org/articles/10.3389/fmicb.2023.1267570/full#supplementary-material

References

Agirre, J., Atanasova, M., Bagdonas, H., Ballard, C. B., Baslé, A., Beilsten-Edmands, J., et al. (2023). The CCP4 suite: integrative software for macromolecular crystallography. *Acta Crystallogr. D Struct. Biol.* 79, 449–461. doi: 10.1107/S2059798323003595

Altschul, S. F., Gish, W., Miller, W., Myers, E. W., and Lipman, D. J. (1990). Basic local alignment search tool. *J. Mol. Biol.* 215, 403–410. doi: 10.1016/S0022-2836(05)80360-2

Altschul, S., Madden, T., Schaffer, A., Zhang, J., Zhang, Z., Miller, W., et al. (1997). Gapped BLAST and PSI- BLAST: a new generation of protein database search programs. *Nucleic Acids Res.* 25, 3389–3402. doi: 10.1093/nar/25.17.3389

Auerbach, G., Huber, R., Grättinger, M., Zaiss, K., Schurig, H., Jaenicke, R., et al. (1997). Closed structure of phosphoglycerate kinase from *Thermotoga maritima* reveals the catalytic mechanism and determinants of thermal stability. *Structure* 5, 1475–1483. doi: 10.1016/S0969-2126(97)00297-9

Barth, S., Huhn, M., Matthey, B., Klimka, A., Galinski, E. A., and Engert, A. (2000). Compatible-solute-supported periplasmic expression of functional recombinant proteins under stress conditions. *Appl. Environ. Microbiol.* 66, 1572–1579. doi: 10.1128/AEM.66.4.1572-1579.2000

Baxter, N. J., Olguin, L. F., Golicnik, M., Feng, G., Hounslow, A. M., Bermel, W., et al. (2006). A Trojan horse transition state analogue generated by MgF3- formation in an enzyme active site. *Proc. Natl. Acad. Sci. U. S. A.* 103, 14732–14737. doi: 10.1073/pnas.0604448103

Becker, J., and Wittmann, C. (2020). Microbial production of extremolytes — high-value active ingredients for nutrition, health care, and well-being. *Curr. Opin. Biotechnol.* 65, 118–128. doi: 10.1016/j.copbio.2020.02.010

Borges, N., Ramos, A., Raven, N. D. H., Sharp, R. J., and Santos, H. (2002). Comparative study of the thermostabilizing properties of mannosylglycerate and other compatible solutes on model enzymes. *Extremophiles* 6, 209–216. doi: 10.1007/s007920100236

Bowler, M. W. (2013). Conformational dynamics in phosphoglycerate kinase, an open and shut case? *FEBS Lett.* 587, 1878–1883. doi: 10.1016/j.febslet.2013.05.012

Brown, A. D. (1976). Microbial water stress. *Bacteriol. Rev.* 40, 803–846. doi: 10.1128/mmbr.40.4.803-846.1976

Bruice, T. C. (2002). A view at the millennium: the efficiency of enzymatic catalysis. *Acc. Chem. Res.* 35, 139–148. doi: 10.1021/ar0001665

Buenger, J., and Driller, H. (2004). Ectoin: an effective natural substance to prevent UVA-induced premature photoaging. *Skin Pharmacol. Physiol.* 17, 232–237. doi: 10.1159/000080216

Chen, V. B., Arendall, W. B., Headd, J. J., Keedy, D. A., Immormino, R. M., Kapral, G. J., et al. (2010). MolProbity: all-atom structure validation for macromolecular crystallography. *Acta Crystallogr. D Biol. Crystallogr.* 66, 12–21. doi: 10.1107/S0907444909042073

Ciulla, R. A., Burggraf, S., Stetter, K. O., and Roberts, M. F. (1994). Occurrence and role of Di-myo-Inositol-1,1'-phosphate in *Methanococcus igneus*. *Appl. Environ. Microbiol.* 60, 3660–3664. doi: 10.1128/aem.60.10.3660-3664.1994

Cliff, M. J., Bowler, M. W., Varga, A., Marston, J. P., Szabó, J., Hounslow, A. M., et al. (2010). Transition state analogue structures of human phosphoglycerate kinase establish the importance of charge balance in catalysis. *J. Am. Chem. Soc.* 132, 6507–6516. doi: 10.1021/ja100974t

Cruz, P. E., Silva, A. C., Roldao, A., Carmo, M., Carrondo, M. J. T., and Alves, P. M. (2006). Screening of novel excipients for improving the stability of retroviral and adenoviral vectors. *Biotechnol. Prog.* 22, 568–576. doi: 10.1021/bp050294y

Czech, L., Hermann, L., Stöveken, N., Richter, A. A., Höppner, A., Smits, S. H. J., et al. (2018). Role of the extremolytes ectoine and hydroxyectoine as stress protectants and nutrients: genetics, phylogenomics, biochemistry, and structural analysis. *Genes* 9, 1–58. doi: 10.3390/genes9040177

Davies, G. J., Gamblin, S. J., Littlechild, J. A., and Watson, H. C. (1993). The structure of a thermally stable 3-phosphoglycerate kinase and a comparison with its mesophilic equivalent. *Proteins* 15, 283–289. doi: 10.1002/PROT.340150306

De Rose, S. A., Finnigan, W., Harmer, N. J., Littlechild, J. A., The HotSolute consortiumBettina, S., et al. (2021). Production of the extremolyte cyclic 2,3-diphosphoglycerate using *Thermus thermophilus* as a whole-cell factory. *Front. Catal.* 1:803416. doi: 10.3389/fctls.2021.803416

Emptage, R. P., Daughtry, K. D., Pemble, C. W. IV, and Raetz, C. R. H. (2012). Crystal structure of LpxK, the 4′-kinase of lipid a biosynthesis and atypical P-loop kinase functioning at the membrane interface. *Proc. Natl. Acad. Sci. U. S. A.* 109, 12956–12961. doi: 10.1073/PNAS.1206072109/-/DCSUPPLEMENTAL

Emsley, P., Lohkamp, B., Scott, W. G., and Cowtan, K. (2010). Features and development of Coot. *Acta Crystallogr. D Biol. Crystallogr.* 66, 486–501. doi: 10.1107/S0907444910007493

Evans, P. R., and Murshudov, G. N. (2013). How good are my data and what is the resolution? *Acta Crystallogr. D Biol. Crystallogr.* 69, 1204–1214. doi: 10.1107/S0907444913000061

Ferrandi, E. E., Sayer, C., De Rose, S. A., Guazzelli, E., Marchesi, C., Saneei, V., et al. (2018). New thermophilic α/β class epoxide hydrolases found in metagenomes from hot environments. *Front. Bioeng. Biotechnol.* 6:144. doi: 10.3389/fbioe.2018.00144

Gerlits, O., Tian, J., Das, A., Langan, P., Heller, W. T., and Kovalevsky, A. (2015). Phosphoryl Transfer Reaction Snapshots in Crystals: Insights into the Mechanism of Protein Kinase A Catalytic Subunit. *J Biol Chem.* 290, 15538–15548. doi: 10.1074/jbc.M115.643213

Graf, R., Anzali, S., Buenger, J., Pfluecker, F., and Driller, H. (2008). The multifunctional role of ectoine as a natural cell protectant. *Clin. Dermatol.* 26, 326–333. doi: 10.1016/j.clindermatol.2008.01.002

Guixé, V., and Merino, F. (2009). The ADP-dependent sugar kinase family: Kinetic and evolutionary aspects. *IUBMB Life* 61, 753–761. doi: 10.1002/iub.217

Hensel, R., and Jakob, I. (1993). Stability of glyceraldehyde-3-phosphate dehydrogenases from hyperthermophilic archaea at high temperature. *Syst. Appl. Microbiol.* 16, 742–745. doi: 10.1016/S0723-2020(11)80348-6

Hensel, R., and König, H. (1988). Thermoadaptation of methanogenic bacteria by intracellular ion concentration. *FEMS Microbiol. Lett.* 49, 75–79. doi: 10.1111/j.1574-6968.1988.tb02685.x

Holm, L. (2020). "Using dali for protein structure comparison" in *Methods in molecular biology*. ed. Z. Gáspári (New York, NY: Humana), 29–42.

Holm, L., and Laakso, L. M. (2016). Dali server update. *Nucleic Acids Res.* 44, W351–W355. doi: 10.1093/nar/gkw357

Kabsch, W. (2010). XDS. *Acta Crystallogr. D Biol. Crystallogr.* 66, 125–132. doi: 10.1107/S0907444909047337

Karplus, P. A., and Diederichs, K. (2012). Linking crystallographic model and data quality. M&M, supporting info. *Science* 336, 1030–1033. doi: 10.1126/science.1218231

Krissinel, E., and Henrick, K. (2007). Inference of macromolecular assemblies from crystalline state. *J. Mol. Biol.* 372, 774–797. doi: 10.1016/j.jmb.2007.05.022

Krissinel, E., Lebedev, A. A., Uski, V., Ballard, C. B., Keegan, R. M., Kovalevskiy, O., et al. (2022). CCP4 cloud for structure determination and project management in macromolecular crystallography. *Acta Cryst. D* 78, 1079–1089. doi: 10.1107/S2059798322007987

Laskowski, R. A., and Swindells, M. B. (2011). LigPlot+: multiple ligand-protein interaction diagrams for drug discovery. *J. Chem. Inf. Model.* 51, 2778–2786. doi: 10.1021/ci200227u

Lehmacher, A., and Hensel, R. (1994). Cloning, sequencing and expression of the gene encoding 2-phosphoglycerate kinase from *Methanothermus fervidus*. *MGG Mol. Gen. Genet.* 242, 163–168. doi: 10.1007/BF00391009

Lehmacher, A., Vogt, A. B., and Hensel, R. (1990). Biosynthesis of cyclic 2,3-diphosphoglycerate. Isolation and characterization of 2-phosphoglycerate kinase and cyclic 2,3-diphosphoglycerate synthetase from *Methanothermus fervidus*. *FEBS Lett.* 272, 94–98. doi: 10.1016/0014-5793(90)80456-S

Lentzen, G., and Schwarz, T. (2006). Extremolytes: natural compounds from extremophiles for versatile applications. *Appl. Microbiol. Biotechnol.* 72, 623–634. doi: 10.1007/s00253-006-0553-9

Marini, A., Reinelt, K., Krutmann, J., and Bilstein, A. (2014). Ectoine-containing cream in the treatment of mild to moderate atopic dermatitis: a randomised, comparator-controlled, intra-individual double-blind, multi-center trial. *Skin Pharmacol. Physiol.* 27, 57–65. doi: 10.1159/000351381

Martínez-Cano, D. J., Reyes-Prieto, M., Martínez-Romero, E., Partida-Martínez, L. P., Latorre, A., Moya, A., et al. (2015). Evolution of small prokaryotic genomes. *Front. Microbiol.* 5:742. doi: 10.3389/fmicb.2014.00742

Matussek, K., Moritz, P., Brunner, N., Eckerskorn, C., and Hensel, R. (1998). Cloning, sequencing, and expression of the gene encoding cyclic 2, 3-diphosphoglycerate synthetase, the key enzyme of cyclic 2, 3-diphosphoglycerate metabolism in *Methanothermus fervidus*. *J. Bacteriol.* 180, 5997–6004. doi: 10.1128/JB.180.22.5997-6004.1998

Matte, A., Tari, L. W., and Delbaere, L. T. (1998). How do kinases transfer phosphoryl groups? *Structure* 6, 413–419. doi: 10.1016/s0969-2126(98)00043-4

McNicholas, S., Potterton, E., Wilson, K. S., and Noble, M. E. M. (2011). Presenting your structures: the CCP4mg molecular-graphics software. *Acta Crystallogr. D Biol. Crystallogr.* 67, 386–394. doi: 10.1107/S0907444911007281

Murillo-López, J., Zinovjev, K., Pereira, H., Caniuguir, A., Garratt, R., Babul, J., et al. (2019). Studying the phosphoryl transfer mechanism of the *E. coli* phosphofructokinase-2: from X-ray structure to quantum mechanics/molecular mechanics simulations. *Chem. Sci.* 10, 2882–2892. doi: 10.1039/C9SC00094A

Murshudov, G. N., Skubák, P., Lebedev, A. A., Pannu, N. S., Steiner, R. A., Nicholls, R. A., et al. (2011). REFMAC5 for the refinement of macromolecular crystal structures. *Acta Crystallogr. D Biol. Crystallogr.* 67, 355–367. doi: 10.1107/S0907444911001314

Raddadi, N., Cherif, A., Daffonchio, D., Neifar, M., and Fava, F. (2015). Biotechnological applications of extremophiles, extremozymes and extremolytes. *Appl. Microbiol. Biotechnol.* 99, 7907–7913. doi: 10.1007/s00253-015-6874-9

Recabarren, R., Osorio, E. H., Caballero, J., Tuñón, I., and Alzate-Morales, J. H. (2019). Mechanistic insights into the phosphoryl transfer reaction in cyclin-dependent kinase 2: a QM/MM study. *PLoS One* 14:e0215793. doi: 10.1371/journal.pone.0215793

Richardson, J. S. (1981). The anatomy and taxonomy of protein structure. *Adv. Protein Chem.* 34, 167–339. doi: 10.1016/S0065-3233(08)60520-3

Robert, X., and Gouet, P. (2014). Deciphering key features in protein structures with the new ENDscript server. *Nucleic Acids Res.* 42, W320–W324. doi: 10.1093/nar/gku316

Romero Romero, M. L., Yang, F., Lin, Y.-R., Toth-Petroczy, A., Berezovsky, I. N., Goncearenco, A., et al. (2018). Simple yet functional phosphate-loop proteins. *Proc. Natl. Acad. Sci.* 115, E11943–E11950. doi: 10.1073/pnas.1812400115

Sastry, M. V. K., Robertson, D. E., Moynihan, J. A., and Roberts, M. F. (1992). Enzymatic degradation of cyclic 2,3-diphosphoglycerate to 2,3-diphosphoglycerate in *Methanobacterium thermoautotrophicum*. *Biochemistry* 31, 2926–2935. doi: 10.1021/bi00126a012

Sayer, C., Bommer, M., Isupov, M., Ward, J., and Littlechild, J. (2012). Crystal structure and substrate specificity of the thermophilic serine:pyruvate aminotransferase from *Sulfolobus solfataricus*. *Acta Crystallogr. Sec. D Biol. Crystallogr.* 68, 763–772. doi: 10.1107/S0907444912011274

Shima, S., Hérault, D. A., Berkessel, A., and Thauer, R. K. (1998). Activation and thermostabilization effects of cyclic 2,3- diphosphoglycerate on enzymes from the hyperthermophilic *Methanopyrus kandleri*. *Arch. Microbiol.* 170, 469–472. doi: 10.1007/s002030050669

Sievers, F., Wilm, A., Dineen, D., Gibson, T. J., Karplus, K., Li, W., et al. (2011). Fast, scalable generation of high-quality protein multiple sequence alignments using clustal omega. *Mol. Syst. Biol.* 7:539. doi: 10.1038/msb.2011.75

Skubák, P., and Pannu, N. S. (2013). Automatic protein structure solution from weak X-ray data. *Nat. Commun.* 4:2777. doi: 10.1038/ncomms3777

Stetter, K. O., Thomm, M., Winter, J., Wildgruber, G., Huber, H., Zillig, W., et al. (1981). *Methanothermus fervidus*, sp. nov., a novel extremely thermophilic methanogen isolated from an Icelandic hot spring. *Zentralbl. Bakterial. Hyg. I Abt. Orig. C* 2, 166–178. doi: 10.1016/s0721-9571(81)80038-5

Studier, F. W. (2005). Protein production by auto-induction in high density shaking cultures. *Protein Expr Purif.* 41, 207–234. doi: 10.1016/j.pep.2005.01.016

Vagin, A., and Teplyakov, A. (2010). Molecular replacement with MOLREP. *Acta Crystallogr. D Biol. Crystallogr.* 66, 22–25. doi: 10.1107/S0907444909042589

Vaguine, A. A., Richelle, J., and Wodak, S. J. (1999). SFCHECK: a unified set of procedures for evaluating the quality of macromolecular structure-factor data and their agreement with the atomic model. *Acta Crystallogr. D Biol. Crystallogr.* 55, 191–205. doi: 10.1107/S0907444998006684

Valentão, P., Fernandes, E., Carvalho, F., Andrade, P. B., Seabra, R. M., and de Bastos, M. L. (2002). Antioxidant activity of *Hypericum androsaemum* infusion: scavenging activity against superoxide radical, hydroxyl radical and hypochlorous acid. *Biol. Pharm. Bull.* 25, 1320–1323. doi: 10.1248/bpb.25.1320

Van Alebeek, G.-J. W. M., Klaassen, C., Keltjens, J. T., van der Drift, C., and Vogels, G. D. (1991). ATP synthesis from 2,3-diphosphoglycerate by cell-free extract of *Methanobacterium thermoautotrophicum* (strain ΔH). *Arch. Microbiol.* 156, 491–496. doi: 10.1007/BF00245397

Van Alebeek, G.-J. W. M., Tafazzul, G., Kreuwels, M. J. J., Keltjens, J. T., and Vogels, G. D. (1994). Cyclic 2,3-diphosphoglycerate metabolism in *Methanobacterium thermoautotrophicum* (strain AH): characterization of the synthetase reaction. *Arch. Microbiol.* 162, 193–198. doi: 10.1007/BF00314474

Vivoli, M., Novak, H. R., Littlechild, J. A., and Harmer, N. J. (2014). Determination of protein-ligand interactions using differential scanning fluorimetry. *J. Vis. Exp.* 2014:51809. doi: 10.3791/51809

Wallace, A. C., Laskowski, R. A., and Thornton, J. M. (1995). LIGPLOT: a program to generate schematic diagrams of protein-ligand interactions. *Protein Eng.* 8, 127–134. doi: 10.1093/protein/8.2.127

Walker, J. E., Saraste, M., Runswick, M. J., and Gay, N. J. (1982). Distantly related sequences in the alpha- and beta-subunits of ATP synthase, myosin, kinases and other ATP-requiring enzymes and a common nucleotide binding fold. *EMBO J.* 1, 945–951. doi: 10.1002/j.1460-2075.1982.tb01276.x

Waterman, D. G., Winter, G., Gildea, R. J., Parkhurst, J. M., Brewster, A. S., Sauter, N. K., et al. (2016). Diffraction-geometry refinement in the DIALS framework. *Acta Crystallogr. Sec. D Struct. Biol.* 72, 558–575. doi: 10.1107/S2059798316002187

Winn, M. D., Ballard, C. C., Cowtan, K. D., Dodson, E. J., Emsley, P., Evans, P. R., et al. (2011). Overview of the CCP4 suite and current developments. *Acta Crystallogr. D Biol. Crystallogr.* 67, 235–242. doi: 10.1107/S0907444910045749

Winter, G., Lobley, C. M. C., and Prince, S. M. (2013). Decision making in xia2. *Acta Crystallogr. D Biol. Crystallogr.* 69, 1260–1273. doi: 10.1107/S0907444913015308

Yancey, P., Clark, M., Hand, S., Bowlus, R., and Somero, G. (1982). Living with water stress: evolution of osmolyte systems. *Science* 217, 1214–1222. doi: 10.1126/science.7112124

frontiers | Frontiers in Microbiology

TYPE Original Research
PUBLISHED 01 December 2023
DOI 10.3389/fmicb.2023.1267771

OPEN ACCESS

EDITED BY
Melina Kerou,
University of Vienna, Austria

REVIEWED BY
Maher Gtari,
Carthage University, Tunisia
Wasu Pathom-Aree,
Chiang Mai University, Thailand
Barny Whitman,
University of Georgia, United States

*CORRESPONDENCE
Yu-Qin Zhang
✉ yzhang@imb.pumc.edu.cn

†These authors share first authorship

RECEIVED 27 July 2023
ACCEPTED 03 November 2023
PUBLISHED 01 December 2023

CITATION
Jiang Z-M, Mou T, Sun Y, Su J, Yu L-Y and Zhang Y-Q (2023) Environmental distribution and genomic characteristics of *Solirubrobacter,* with proposal of two novel species.
Front. Microbiol. 14:1267771.
doi: 10.3389/fmicb.2023.1267771

Environmental distribution and genomic characteristics of *Solirubrobacter,* with proposal of two novel species

Zhu-Ming Jiang[1,2†], Tong Mou[1,2†], Ye Sun[1], Jing Su[1], Li-Yan Yu[1] and Yu-Qin Zhang[1,2*]

[1]Institute of Medicinal Biotechnology, Chinese Academy of Medical Sciences and Peking Union Medical College, Beijing, China, [2]State Key Laboratory of Dao-di Herb, Beijing, China

Solirubrobacter spp. were abundant in soil samples collected from deserts and other areas with high UV radiation. In addition, a novel *Solirubrobacter* species, with strain CPCC 204708^T as the type, was isolated and identified from sandy soil sample collected from the Badain Jaran Desert of the Inner Mongolia autonomous region. Strain CPCC 204708^T was Gram-stain positive, rod-shaped, non-motile, non-spore-forming, and grew optimally at 28–30°C, pH 7.0–8.0, and in the absence of NaCl. Analysis of the 16S rRNA gene sequence of strain CPCC 204708^T showed its identity within the genus *Solirubrobacter*, with highest nucleotide similarities (97.4–98.2%) to other named *Solirubrobacter* species. Phylogenetic and genomic analyses indicated that the strain was most closely related to *Solirubrobacter phytolaccae* KCTC 29190^T, while represented a distinct species, as confirmed from physiological properties and comparison. The name *Solirubrobacter deserti* sp. nov. was consequently proposed, with CPCC 204708^T (= DSM 105495^T = NBRC 112942^T) as the type strain. Genomic analyses of the *Solirubrobacter* spp. also suggested that *Solirubrobacter* sp. URHD0082 represents a novel species, for which the name *Candidatus* "Solirubrobacter pratensis" sp. nov. was proposed. Genomic analysis of CPCC 204708^T revealed the presence of genes related to its adaptation to the harsh environments of deserts and may also harbor genes functional in plant-microbe interactions. Pan-genomic analysis of available *Solirubrobacter* spp. confirmed the presence of many of the above genes as core components of *Solirubrobacter* genomes and suggests they may possess beneficial potential for their associate plant and may be important resources for bioactive compounds.

KEYWORDS

***Solirubrobacter*, pangenome, UV resistance, microbial resources, distribution**

1 Introduction

The genus *Solirubrobacter*, belonging to the family *Solirubrobacteraceae*, the order *Solirubrobacterales*, the phylum *Actinomycetota*, was first identified by Singleton et al. (2003) with *Solirubrobacter pauli* as the type species. Two other species, *Solirubrobacter soli* and *Solirubrobacter ginsenosidimutans*, were subsequently reported to be identified from soil samples in ginseng fields in 2007 (Kim et al., 2007). And in 2014, two additional species

(*S. phytolaccae* and *S. taibaiensis)* were identified after isolation from the roots and stems of *Phytolacca acinosa* Roxb., respectively (Wei et al., 2014; Zhang L. et al., 2014). These five currently known species generally inhabit soil and plant-based ecosystems.[1]

The boom in cultivation-independent techniques and multi-omics technologies enable improved studies on the diversity of yet-uncultivated microorganisms, also termed Microbial Dark Matter (MDM) (Jiao et al., 2020). It was found that the genus *Solirubrobacter* abundantly inhabits an Indian desert, just below members of the genera *Gaiella* and *Streptomyces* (Sivakala et al., 2018). In five different types of natural soil ecosystems in Northwest China, *Solirubrobacter* was a dominant genus (Zhang et al., 2019). It was also noted that members of the *Actinomycetales* and *Solirubrobacterales* are more abundant in soils with lower organic carbon available in varied agricultural landscapes (Shange et al., 2012).

Besides *Solirubrobacter* show potential for applications such as plant growth promotion and discovery of unique bioactive compounds and activities (Franke-Whittle et al., 2015). *S. ginsenosidimutans* DSM 22325^T, for instance, displayed ginsenoside conversion activity, transforming ginsenoside Rb1 into ginsenoside F2, a phytochemical with numerous pharmacological properties (Kim et al., 2021; Zhou et al., 2021).

Desert ecosystems worldwide are abundant and diverse sources of microbiota. Harsh conditions such as extreme ultraviolet radiation, carbon and nitrogen scarcity, limited energy, hyper-aridity, and extreme temperatures, characterize these ecosystems. However, these stressful ecosystems host remarkably diverse microbial communities. Therefore, deserts can be viewed as microbial resource hotspots (Bull et al., 2016; Leung et al., 2020). One primary stress factor in deserts is high ultraviolet radiation (UVR), which all desert inhabitants, including plants, have to mitigate. Interestingly, *S. pauli* JCM 13025^T, was reported to be a radiation-resistant strain, which has drawn considerable research attention (Singleton et al., 2003).

So far, the genus *Solirubrobacter* has been detected in soils (Sánchez-Marañón et al., 2017), biocrust (Miralles et al., 2020), rhizosphere habitats of various crops (Aguiar et al., 2020; Feng et al., 2021; Lee et al., 2021) and medicinal plants (Dong et al., 2018). It is also proposed that *Solirubrobacter* spp. may be pioneering organisms that enable microbiome develop in plant rhizospheres, thereby playing important roles in maintaining host plant health in ecologically stressful environments (Sivakala et al., 2018; Zhang et al., 2019). Its potential as plant-promoting, UV-resistant microorganisms is regarded as beneficial for desert ecosystem health, especially in the context of changing climate patterns.

In the current study, we investigated the ecological distribution of *Solirubrobacter* across different environmental samples, including desert soils. The research also resulted in isolation of *Solirubrobacter* strains leading to the discovery of a new species. Furthermore, we also conducted a global pan-genomic analysis of the genus *Solirubrobacter* to evaluate the functional and biological resource potential.

1 https://lpsn.dsmz.de/genus/solirubrobacter

2 Materials and methods

2.1 Sample collection

Twelve rhizosphere soil samples from herbs (IMB15101S–IMB15112S) were collected from high-altitude barren hills in Xinjiang. And another twelve rhizosphere soil samples from Yunnan Ethno-Medicinal plants (IMB21101S–IMB21112S) were collected from Ailao mountain in Yunnan. While desert soil samples (IMB19101D–IMB19112D, IMB15201D–IMB15212D, IMB16101D–IMB16112D) were collected from the Gurbantunggut Desert, the Tengger Desert and the Badain Jaran Desert, respectively. Cow feces samples (IMB20301F–IMB20312F) were collected from Fangshan in Beijing, while crow feces samples (IMB20101F–IMB20112F) were collected from Nanhaizi Wetland Park, Beijing. Soil samples were collected from the area surrounding Plateau Lakes (IMB20201S–IMB20212S) in the Guizhou province and sediment soil samples (IMB22101S–IMB22112S) were collected from fresh water reservoirs in the Sichuan province. Finally, water samples (IMB19301W–IMB19312W) were collected from Erhai Lake and phycosphere samples (IMB14101E–IMB14112E) were collected from the phycosphere of agar cultures maintained in our laboratory. Detailed information for samples is provided in **Supplementary Table 1**. Soil and sand samples were collected into sterile envelopes. Water samples were filtered through 3.0 μm pore-size filters to exclude most cyanobacterial colonies and other small particles, followed by filtering water to concentrate biomass on 0.22 μm pore-size filters. Samples were returned to the laboratory within 3 days of collection, with microbial isolation and DNA extraction carrying out immediately.

2.2 DNA extraction and 16S rRNA gene amplicon sequencing

Samples from the same biotopes were pooled into a single composite sample and subjected to DNA extraction for community compositional analyses. Total genomic DNA from each soil composite sample was extracted with a PowerSoil DNA isolation kit (MoBio, USA). The DNA from each composite water sample was extracted with a PowerWater DNA isolation kit (MoBio, USA) according to the manufacturer's protocols. Total DNA was then used as template for PCR amplification of the V3 to V4 hypervariable regions of 16S rRNA genes using the universal bacterial primers 5′-ACTCCTACGGGAGGCAGCAG-3′ (338F) and 5′-GGACTACHVGGGTWTCTAAT-3′ (806R). PCR amplifications were performed using high fidelity TransStart Fastpfu DNA Polymerase (Transgen, China) in 20 μL reaction mixtures containing 4 μL of 5 × FastPfu Buffer, 2 μL of 2.5 mmol/L dNTPs, 0.8 μL of each primer (5 μmol/L), 0.4 μL of FastPfu Polymerase (final concentration was 1 unit), and 10 ng of template DNA. PCR conditions comprised 5 min of an initial denaturation at 94°C followed by 35 cycles of denaturation at 94°C for 30 s, 45 s of primer annealing at 55°C, 40 s of elongation at 72°C, and then a final 10 min elongation step at 72°C.

Purified PCR amplicons were pooled in equimolar amounts and paired-end sequenced on the Illumina MiSeq PE300 platform (Illumina, San Diego, USA) using standard protocols at Majorbio Bio-Pharm Technology Co., Ltd. (Shanghai, China). Raw FASTQ files were de-multiplexed using an in-house perl script and then quality-filtered and merged using the following criteria: (i) 300 bp reads were truncated at any site with an average quality score of < 20 over a 50 bp sliding window, and truncated reads < 50 bp were discarded, in addition to reads containing ambiguous characters; (ii) only overlapping sequences > 10 bp were merged. The maximum mismatch ratio of the overlapping region was set to 0.2 and reads that could not be assembled were discarded. (iii) Samples were distinguished based on barcoded primers, sequence direction was adjusted, and exact barcode matching was specified, in addition to setting 2 nucleotide mismatches as the maximum for primer matching. The quality-filtered sequences were clustered into operational taxonomic units (OTUs) at the 97% nucleotide sequence similarity level. The taxonomic classification of each OTU representative sequence was analyzed using the RDP Classifier (version 2.2), with comparison against the Silva 16S rRNA gene database (version 138) using a classification confidence threshold of 0.7. We carried out the high throughput sequencing analysis using Majorbio online analysis platform.[2] The alpha diversity traits of each composite sample estimated by the Chao1 estimator, and the Shannon diversity index, in addition to the coverage estimated by Good's coverage. Rarefaction analyses was used to show whether the amount of sequencing data in these composite samples is reasonable. Relative abundance referred to the proportion of reads of a particular taxon (OTU) in all reads of a composite sample.

2.3 Isolation of microorganisms

The dilution plating method was used to isolate strains from each sample using previously described procedures (Deng et al., 2022). Strain CPCC 204708^T was obtained from soils of the Badain Jaran Desert (39°21′ N, 102°19′ E, 1,550 m), using media containing (L^{-1}): 2.0 g sodium malonate, 0.1 g NH_4NO_3, 0.1 g KCl, 0.05 g $MgSO_4{\cdot}7H_2O$, 0.05 g $FeSO_4{\cdot}7H_2O$, 0.38 g marine trace salt mixture, 15 g agar, and pH adjustment to 7.0–7.2. Aztreonam and potassium dichromate were added to the isolation medium to final concentrations of 25 and 50 mg L^{-1}, respectively, to prevent fungal and Gram-negative bacterial growth. Distinct colonies were chosen for subsequent streaking on R2A agar (Difco) to identify isolated and uniform colonies. Pure cultures were cultivated and maintained on R2A medium at 4°C and stored in aqueous glycerol suspensions (20%, v/v) at −80°C.

The reference strains *S. phytolaccae* KCTC 29190^T and *S. taibaiensis* KCTC 29222^T were obtained from the Korean Collection for Type Cultures (KCTC), while *S. pauli* JCM 13025^T was obtained from the RIKEN BioResource Research Center (JCM). *S. ginsenosidimutans* DSM 21036^T and *S. soli* DSM 22325^T were obtained from the DSMZ. The reference strains were included in subsequent assays in parallel with newly identified strains.

2 https://cloud.majorbio.com/page/project/overview.html

2.4 Identification of *Solirubrobacter* strains

The whole genome of *Solirubrobacter* sp. URHD0082, which was isolated from Mediterranean grassland soil, was retrieved from the NCBI database (accession: AUEK00000000[3]), and was included in the pan-genomic analysis of the genus *Solirubrobacter*. The 16S rRNA gene sequence extracted from the genome was used to identify *Solirubrobacter* sp. URHD0082 based on sequence comparisons and phylogenetic analyses. In addition, genomic comparisons were used to identify the taxon to which strain URHD0082 belonged.

The genomic DNA of new isolates was extracted and their 16S rRNA genes were PCR amplified, as previously described (Li et al., 2007). The sequences were then compared against those in GenBank using the BLAST program and the EzBioCloud[4] platform (Yoon et al., 2017) to determine approximate phylogenetic affiliations. Multiple sequence alignments of isolate and closely related 16S rRNA genes were conducted using the molecular evolutionary genetics analysis (MEGA) software package (version 7.0) (Kumar et al., 2016). Phylogenetic trees were inferred using Neighbor-Joining (Saitou and Nei, 1987), Maximum Parsimony (Kluge and Farris, 1969), and Maximum-Likelihood (Felsenstein, 1981) methods. Phylogenetic reconstruction topologies were evaluated with the bootstrap resampling method (Felsenstein, 1985) and 1,000 replicates. A phylogenetic tree was also conducted based on the concatenation of 120 ubiquitous single-copy maker genes (bac120 maker set) (Parks et al., 2018) by a pipeline called EasyCGTree (Xue et al., 2021). Average nucleotide identity (ANI) and digital DNA-DNA hybridization (dDDH) values among the strains CPCC 204708^T, URHD0082 and other validly described *Solirubrobacter* species were calculated using the ezbiocloud platform (Yoon et al., 2017) and the Genome-to-Genome Distance Calculator (GGDC, version 3.0)[5] (Auch et al., 2010), respectively.

2.5 Growth conditions, morphological characteristics, and physiological tests

Physiological characteristics of strain CPCC 204708^T were examined by observing growth at 28°C for 1–4 weeks on peptone yeast glucose (PYG; 3% trypticase soy broth, 0.3% yeast extract, 1.5% agar; pH 7.0–7.2), tryptone soy agar (TSA, Difco), ISP 2, yeast extract sucrose (YM, Difco), Luria-Bertani, R2A (Difco), ISP 4, and nutrient (Shirling and Gottlieb, 1966) media formulations. Growth temperature ranges were evaluated by incubation on R2A agar medium at 0, 4, 10, 20, 25, 28, 30, 32, 37, and 40°C for 14 d (Sun et al., 2017). The growth pH range was measured using a previously described buffer system (Xu et al., 2005), R2A as the basal medium, and evaluation over a pH range of 4.0–11.0 (at intervals of 1 pH unit). Salt (sodium chloride) tolerance was evaluated on R2A agar medium supplemented with NaCl concentrations of 0, 1, 2, 3, 4, 5, 6, 7, 8, 9, 10, and 15% (w/v). UV radiation tolerance

3 https://www.ncbi.nlm.nih.gov/nuccore/AUEK00000000.1
4 https://www.ezbiocloud.net/
5 http://ggdc.dsmz.de/ggdc.php

was evaluated using a UV-C radiation wavelength of 254 nm, following previously described procedures (Zhang et al., 2007). Growth after 10 days was determined to be either positive or negative for UV resistance compared to unirradiated controls. The strain *Deinococcus radiodurans* ATCC 13939^T was also used as a positive control. The strain *Escherichia coli* ATCC 25922 was used as a negative control.

Gram stains were conducted as previously described (Magee et al., 1975). Colony appearance and pigment production were evaluated after incubation at 28°C on R2A medium. Cellular morphological features were observed with 5–7-day-old cultures using light microscopy (Zeiss Axio Scope. A1 Vario) and transmission electron microscopy (JEOL JEM-1010). Cell motility was evaluated with inverted microscopic observations of cells suspended in a 0.85% NaCl solution. Oxidase activity was evaluated using an analytical profile index (API) oxidase reagent (bioMeriéux) according to the manufacturer's instructions, while catalase activity was determined by the presence of bubble production after application of 3% (v/v) H_2O_2. Metabolic characteristics were determined using Biolog GEN III (MicroPlate), API 50CH, and API ZYM (bioMerieux) test kits according to the manufacturer's instructions. The abilities of the strain to hydrolyze gelatin, cellulose, and starch, in addition to producing H_2S and indole were evaluated, as previously described (Gonzalez et al., 1978). The type strain *S. phytolaccae* KCTC 29190^T was included in the physiological and biochemical tests for comparison.

The ability of the strains to produce indole-3-acetic acid (IAA) was evaluated with colorimetric methods (Bric et al., 1991). Briefly, log-phase cells were inoculated into 1% tryptone aqueous solutions containing 3 mmol/L L-tryptophan and then cultured at 28°C for 4 days. Absorbance at 530 nm was then plotted against IAA standard solution concentration solutions (0, 0.625, 1.0, 1.25, 2.0, 2.5, 4.0, and 5.0 mg/L), followed by linear regression to obtain a standard curve for IAA (**Supplementary Figure 1**). IAA quantification was based on a linear regression equation ($y = 0.02x-0.001$) for the colorimetric IAA content assay that exhibited a good fit ($R^2 = 0.9994$), enabling quantification.

2.6 Chemotaxonomic assays

Chemotaxonomic and molecular systematic studies of strain CPCC 204708^T were conducted with cells after cultivation in TSB medium at 28°C for 7 days in shake flasks on a rotary shaker (150 r/min) until cells reached the logarithmic growth phase. Amino acids and peptides in whole cell hydrolysates were analyzed by two-dimensional ascending thin-layer chromatography (TLC) on cellulose plates using solvent systems described by Schleifer and Kandler (1973). Sugar profiles were evaluated with TLC, as previously described (Komagata and Suzuki, 1988). Polar lipids were extracted, as previously described and identified by two-dimensional TLC (Minnikin et al., 1984). Menaquinones were extracted as previously described (Collins et al., 1977) and analyzed by HPLC (Groth et al., 1997). Cellular fatty acids analysis was performed using the Microbial Identification System (Sherlock Version 6.0; MIDI database: ACTIN1) (Kroppenstedt, 1985; Sasser, 1990).

2.7 Whole genome sequencing and comparative genomics

2.7.1 Genome sequencing and assembly

Whole-genome sequencing of the new isolate CPCC 204708^T and the reference strains *S. phytolaccae* KCTC 29190^T, *S. taibaiensis* KCTC 29222^T, *S. ginsenosidimutans* DSM 21036^T were conducted on the Illumina HiSeq 4000 platform (Illumina, San Diego, CA, USA) at the Beijing Genomics Institute (Beijing, China) in this study. Genomic DNA was randomly sheared to construct three read libraries of length 300 bp using a Bioruptor ultrasonicator (Diagenode, Denville, NJ, USA) and physico-chemical methods. Paired-end fragment libraries were then sequenced using manufacturer protocols. Low quality reads (those with consecutive bases covered by fewer than five reads) were discarded and the remaining reads were assembled with the SOAPdenovo v1.05 software program (Xie Y. et al., 2014). The assembled genomes of strains *S. pauli* JCM 13025^T and *S. soli* DSM 22325^T were downloaded from NCBI database. The quality (index: completeness and contamination) of the draft genomes of the genus *Solirubrobacter* were accurately assessed by the CheckM pipeline (Parks et al., 2015).

2.7.2 Genome prediction, annotation and analysis of functional genes and biosynthetic gene clusters

The assembled genomes of strains CPCC 204708^T, *S. phytolaccae* KCTC 29190^T, *S. pauli* JCM 13025^T, *S. taibaiensis* KCTC 29222^T, *S. ginsenosidimutans* DSM 21036^T, *S. soli* DSM 22325^T, and URHD0082 were subjected to gene prediction using Hidden Markov models in the glimmer3 software program[6] (Delcher et al., 2007), followed by functional annotation through comparison against the Kyoto Encyclopedia of Genes and Genomes (KEGG) database[7] (Moriya et al., 2007). Functional genes related to stress response were identified in these genomes by comparison to the Uniprot[8] (UniProt Consortium, 2023) and Interpro[9] databases (Paysan-Lafosse et al., 2023). Further, biosynthetic gene clusters (BGCs) were detected and characterized using the antibiotics and secondary metabolite analysis shell platform (antiSMASH; version 6.0)[10] (Blin et al., 2021).

2.7.3 Pan-genome analysis of the genus *Solirubrobacter*

The bacterial pan-genome analysis (BPGA) pipeline (version 1.3) was used to analyze *Solirubrobacter* genomic diversity and characteristics. Protein sequences used for pan-genomic analysis were annotated with the Rapid Annotation using Subsystem Technology (RAST) server (version 2.0).[11] BPGA was conducted with default settings, as previously described (Chaudhari et al., 2016). Proteins encoded by the seven genomes were used to

6 http://www.cbcb.umd.edu/software/glimmer/
7 https://www.kegg.jp/
8 https://www.uniprot.org/
9 https://www.ebi.ac.uk/interpro/
10 https://antismash.secondarymetabolites.org/
11 https://rast.nmpdr.org/

generate orthologous gene/protein clusters (homologous families) using the USEARCH clustering tool and then to construct phylogenetic trees using concatenations of core genes to generate a pan-matrix in BPGA. Each homolog family was assigned a homologous gene family conservation value (HGFCV) based on its frequency in the three genomes. Different conservation values (CVs) reflect the distribution frequency of the gene homologs among the 7 strains, wherein higher CVs indicate a more widely conserved gene in the 7 *Solirubrobacter* strains. Gene families with HGFCVs of 7 were considered components of the core genome, while those with values of 2–6 or 1 were considered accessory or unique genes, respectively. Core, accessory, unique, and exclusively absent genes were retrieved from the genomes using the USEARCH clustering tool. BPGA was then used for evolutionary analysis based on concatenated core gene alignments and the binary pan-matrix. The gene matrix was calculated using shared gene value presence or absence within the orthologous gene clusters. The core genome phylogenetic tree was constructed in BPGA by first extracting the protein sequences (excluding paralogs) from 20 random orthologous gene clusters. MUSCLE was then used to generate multiple sequence alignments for each gene cluster. The alignments were concatenated and a Neighbor-Joining phylogenetic tree was constructed from the concatenated matrix.

3 Results, analysis, and discussion

3.1 The distribution of *Solirubrobacter*

Solirubrobacter spp. were detected in ecosystems based on high-throughput sequencing of 16S rRNA genes recovered from various environments. The alpha diversity of these composite samples from the different ecosystems exhibited different Chao1 and Shannon index values, suggesting significant difference in the richness or diversity of bacteria among these biotopes. Rarefaction analyses using the Shannon index as a diversity metric indicated that our sequencing efforts covered nearly all of the diversity that would be expected to be found in these composite samples. The highest abundances of *Solirubrobacter* spp. were observed in rhizosphere soils attached to medicinal plants in high-altitude areas of Xinjiang and Yunnan. They were also frequently observed in desert sandy soil samples. Low *Solirubrobacter* richness was observed in other ecosystems, including in crow feces and aquatic habitats (**Figure 1**). Further, *Solirubrobacter* spp. were not detected at all in the phycosphere of laboratory culture-systems, nor from cow feces collected from a Beijing farm. These results suggest that *Solirubrobacter* spp. may be adapted to life within extreme ecosystems like the high altitude barren hills of Xinjiang and Yunnan that exhibit strong solar radiation, in addition to arid deserts.

3.2 Identification of novel *Solirubrobacter* strains

Strain CPCC 204708^T was isolated from a desert sandy soil sample (IMB16109D) collected from the Badain Jaran Desert (39°56′12″ N, 102°05′39″ E; 1,157 mH) from within the Inner Mongolia autonomous region. An almost complete 16S rRNA gene sequence (1,500 bp) of strain CPCC 204708^T was obtained, and comparison against available sequences in GenBank revealed highest 16S rRNA gene sequence similarity to that of *Solirubrobacter phytolaccae* KCTC 29190^T (98.3% nucleotide identity). The 16S rRNA gene sequence (1,427 bp) from the genome of *Solirubrobacter* sp. URHD0082 (AUEK00000000) was also extracted and compared against the Genbank database, revealing highest 16S rRNA gene sequence to that of *S. ginsenosidimutans* DSM 21036^T (97.4% nucleotide similarity).

The draft genome sequences of strains CPCC 204708^T, *S. phytolaccae* KCTC 29190^T, *S. taibaiensis* KCTC 29222^T and *S. ginsenosidimutans* DSM 21036^T, were deposited in NCBI under the accessions JAPCID000000000, JAPDDP000000000, JAPDDQ000000000, and JAPDOD000000000, respectively (**Table 1**). The whole genome shotgun project accession number for strain URHD0082 is AUEK00000000. The GenBank accession numbers for the 16S rRNA gene sequences of strains CPCC 204708^T and URHD0082 are MH509728 and OQ674416, respectively.

Phylogenetic analysis of 16S rRNA gene sequences revealed that strains CPCC 204708^T and URHD0082 formed a distinct group with the five *Solirubrobacter* species, regardless of phylogenetic reconstruction method (**Supplementary Figure 2**), as confirmed by the pan-matrix constructed from BPGA (**Supplementary Figure 3**). Thus, strains CPCC 204708^T and URHD0082 were both phylogenetically affiliated to *Solirubrobacter*. In the core gene tree based on 120 ubiquitous single-copy maker genes (bac120 maker set) from whole genome sequences, strains CPCC 204708^T and URHD0082 occupied distinct species positions in the genus *Solirubrobacter* (**Figure 2**), which was supported by the phylogenetic tree based on the 16S rRNA gene sequences (**Supplementary Figure 2**). The ANI values between strain CPCC 204708^T, URHD0082, and the other validly described *Solirubrobacter* species were in the range of 77.3–84.4%, all being far lower than the threshold used for bacterial species delineation (ANI < 95%) (Kim et al., 2014). Further, the corresponding dDDH values ranged from 20.5 to 27.6% (**Supplementary Table 2**), which were also far below the threshold value (70%) used to identify bacterial strains of the same species (Auch et al., 2010). Based on these analyses, we proposed that the two strains identified here represent novel *Solirubrobacter* species, for which the epithets *Solirubrobacter deserti* sp. nov. and *Candidatus* "Solirubrobacter pratensis" sp. nov. are suggested, with strains CPCC 204708^T and URHD0082^T as the types, respectively.

3.3 Morphological and physiological characteristics

Strain CPCC 204708^T grew well on R2A, TSA and YM media, with moderate growth on ISP4 and PYG media, while no growth was observed on ISP 2, Luria-Bertani, and nutrient media. Strain CPCC 204708^T growth was observed at 20–37°C, pH 5.0–8.0, and in presence of 0–10% (w/v) NaCl. Optimum growth occurred at 28–30°C, pH 7.0–8.0, and without NaCl addition. Strain CPCC 204708^T colonies on R2A medium were circular, convex, and smooth, with pale pink color and approximately 1.9 mm in

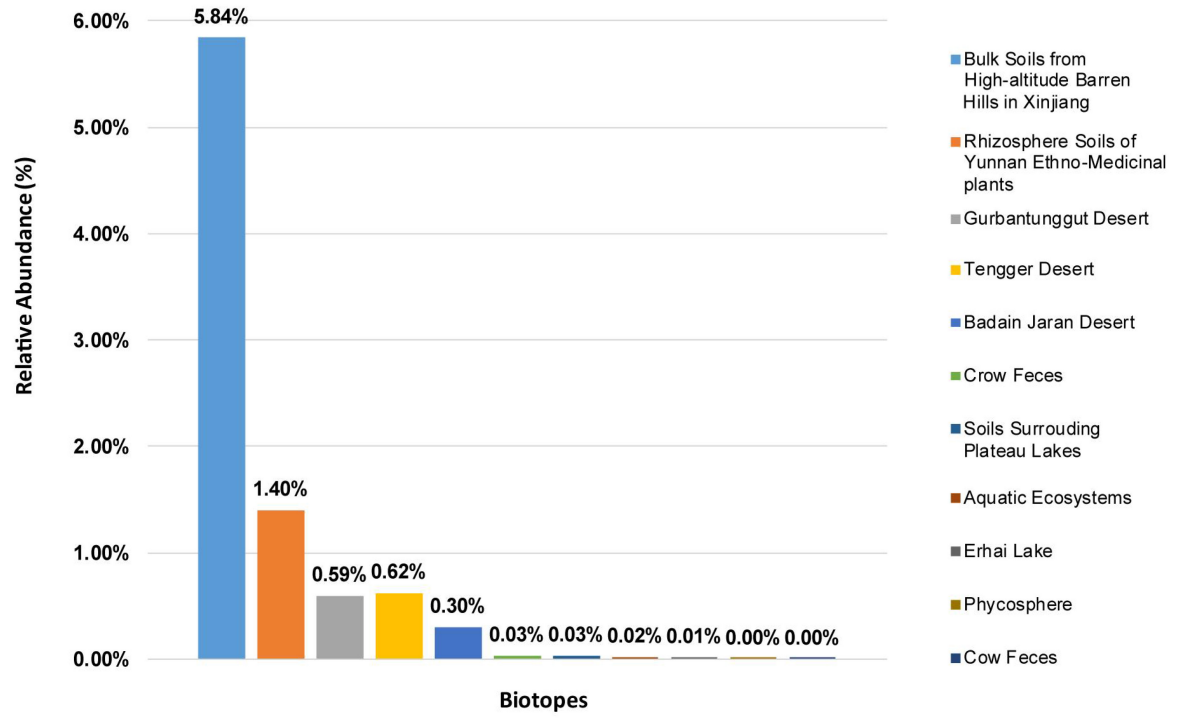

FIGURE 1
The relative abundances of *Solirubrobacter* among communities from eleven different biotopes, based on 16S rRNA gene analyses. The relative abundances are shown for composite samples from various environments, as indicated by the legend on the right.

diameter. Diffusible pigments were not produced in the media. When grown on R2A medium, cells were aerobic, Gram-stain positive, non-motile, non-spore-forming, and rod-shaped, with sizes of 0.6–0.8 × 1.2–1.9 μm (**Supplementary Figure 4**). The cells were positive for catalase activity, but negative for oxidase activity. Detailed physiological and biochemical characteristics of strain CPCC 204708^T are shown in **Table 2** and in the species description.

Ultraviolet radiation tolerance experiments showed that strains CPCC 204708^T, *S. phytolaccae* KCTC 29190^T and *S. pauli* JCM 13025^T could all survive when exposed to the dose of ultraviolet radiation (102 J/cm^2), with survival rates following the order of *S. pauli* JCM 13025^T, CPCC 204708^T and *S. phytolaccae* KCTC 29190^T. JCM 13025^T and CPCC 204708^T colony colors were both pink when grown on R2A media. Some radiation-resistant bacteria isolated from irradiated soils contain multiple pigments and are also more resistant to radiation than non-pigmented bacteria (An et al., 2011; Pulschen et al., 2015). For instance, the UV and cold tolerance of a purple violet pigment (PVP)-producing Antarctic bacterium *Janthinobacterium* sp. Ant5-2 was reported previously. Compared with the wild type *Janthinobacterium* sp. Ant5-2 PVP(+), the survival rate of mutant strain [PVP(-)] after ultraviolet irradiation (UV-B and UV-C) was significantly reduced (Mojib et al., 2013). Saxena et al. (2002) found that survival of Bt-m (an UV-resistant mutant of *Bacillus thuringiensis* subsp. *kurstaki*, producing a dark brown pigment, identified as melanin) spores and their insecticidal activity to irradiation at 254 nm and 366 nm were higher than those of the parent. Reis-Mansur et al. (2019) found that the increased survival of DNA repair-proficient *E. coli* grown overnight with added carotenoids (pigment extract) produced by *Microbacterium* sp. LEMMJ01 (isolated from Antarctic soil) revealed that part of the resistance of *Microbacterium* sp. LEMMJ01 against UV-B radiation seems to be connected with photoprotection by its pigments (carotenoids). Consequently, the pigment of strains JCM 13025^T and CPCC 204708^T may contribute greatly to their higher survival under UV radiation.

Indole-3-acetic acid is an important phytohormone that benefits plant growth and development. Many bacteria produce IAA, which when provided in an optimal concentration range, can stimulate plant root hair formation and increase the numbers and lengths of lateral roots and taproots (Davies, 1995). A positive correlation between the genus *Solirubrobacter* and plant growth was also observed (Franke-Whittle et al., 2015). Subsequently, the genus *Solirubrobacter* was detected as a dominant group in soils (Sánchez-Marañón et al., 2017), rhizosphere habitats of various crops and medicinal plants (Aguiar et al., 2020; Barajas et al., 2020; Feng et al., 2021; Lee et al., 2021), and was recognized as a kind of plant probiotic (Li et al., 2022). Several multifunctional rhizosphere soil microorganisms including *Bacillus*, *Solirubrobacter*, and *Lysobacter* with higher abundance in commercial organic fertilizer plus bioorganic fertilizer (CBF) were shown to promote plant growth (Franke-Whittle et al., 2015) by producing hormones such as IAA (indole-3-acetic acid), gibberellin, and cytokinin (Fabra et al., 2010; Mhatre et al., 2018). Our phenotypic experiments demonstrated that six strains of the genus *Solirubrobacter* could produce IAA. IAA was detected in the fermentation broths of strains CPCC 204708^T, *S. phytolaccae* KCTC 29190^T, *S. taibaiensis* KCTC 29222^T, *S. pauli* JCM 13025^T, *S. ginsenosidimutans* DSM 21036^T, and *S. soli* DSM 22325^T at

TABLE 1 Characteristics and distribution of core, accessory, unique, and exclusively absent genes of seven genomes included in the pan-genome of the genus *Solirubrobacter*.

Strain	Accession number	GenBank assembly accession	Total genes	Size (Mbp)	Isolation environment	Completeness (%)	Contamination (%)	No. of core genes	No. of accessory genes	No. of unique genes	No. of exclusively absent genes
Solirubrobacter deserti sp. nov. CPCC 204708^T	JAPCID000000000	GCA_027587175.1	6,863	6.9	Sand from the Badain Jaran Desert, China	98.7	0.4	2,474	2,919	1,100	80
Solirubrobacter ginsenosidimutans DSM 21036^T	JAPDOD000000000	GCA_027587205.1	8,947	9.4	Ginseng field soil from Baekdu Mountain, China.	99.6	4.4	2,474	3,767	2,099	56
Solirubrobacter pauli JCM 13025^T	RBIL00000000	GCA_003633755.1	6,707	7.1	Burrow of the epigeic earthworm *Lumbricus rubellus* in an agricultural soil, USA	98.7	0.9	2,474	3,087	843	39
Solirubrobacter phytolaccae KCTC 29190^T	JAPDDP000000000	GCA_027587195.1	7,265	7.5	The surface-sterilized roots of *Phytolacca acinosa* Roxb. collected from Taibai Mountain in Shaanxi Province, north-west China.	98.7	3.5	2,474	3,302	1,032	25
Solirubrobacter soli DSM 22325^T	AUIK00000000	GCA_000423665.1	8,699	9.3	Soil of a ginseng field in South Korea	98.7	1.7	2,474	3,749	1,914	53
Solirubrobacter taibaiensis KCTC 29222^T	JAPDDQ000000000	GCA_027587225.1	8,554	8.3	Surface-sterilized stem of *Phytolacca acinosa* Roxb. collected from Taibai Mountain in Shaanxi Province, north-west China.	98.7	7.8	2,474	3,447	1,351	27
"*Candidatus* Solirubrobacter pratensis" sp. nov. URHD0082	AUEK00000000	GCA_000425945.1	6,557	6.6	Mediterranean Grassland Soil	99.1	1.2	2,474	1,487	2,436	637

10.3389/fmicb.2023.1267771

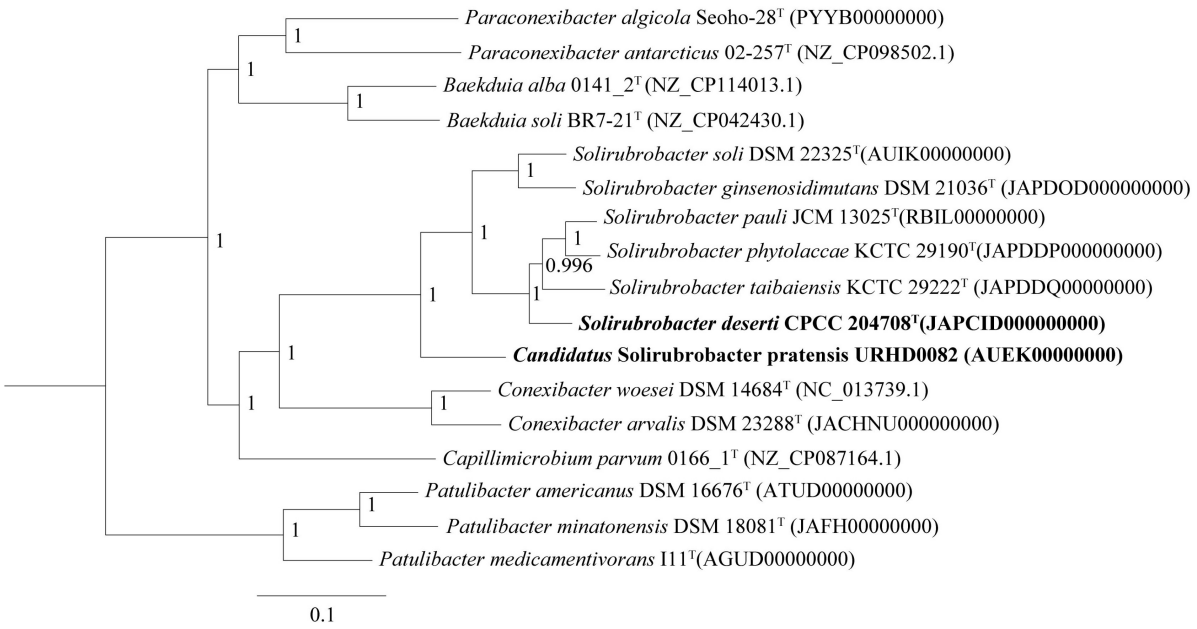

FIGURE 2
Core gene tree based on 120 ubiquitous single-copy maker genes (bac120 maker set) from whole genome sequences showing the relationship of strain CPCC 204708^T and URHD0082 with other species in the genus *Solirubrobacter* and other related species in the order *Solirubrobacterales*. Bootstrap values (those above 50%) are shown as percentages of 1,000 replicates. *Micrococcus luteus* ATCC 4698^T (GenBank accession no. QVMY00000000) was used as an outgroup (not shown). Bar, 0.1 nt substitution per nt.

concentrations of 0.77 ± 0.000, 1.12 ± 0.001, 0.80 ± 0.002, 3.50 ± 0.001, 2.22 ± 0.001, and 0.55 ± 0.002 mg/L, respectively (**Supplementary Figure 1**). Production of phytohormones (such as IAA) of plant endophytes (Crozier et al., 1988) stimulate growth and/or ameliorate the plant under harsh stressful conditions (Cohen et al., 2009; Piccoli et al., 2011). Given that all reported strains of the genus *Solirubrobacter* so far have been isolated from soils or the ecosystems that were vegetated or associated with crops, especially medicinal plants, we infer that the production of small amounts of IAA could represent an important mechanism of plant-microbe interaction for this genus (Duca et al., 2014). In addition, at the genomic level, we found that the IAA-production pathway was encoded by the seven *Solirubrobacter* strains. Specifically, the genes for aldehyde dehydrogenases (EC 1.2.1.3; *aldH*) and amidases (EC 3.5.1.4; *amiE*) were both present within the core genome of *Solirubrobacter* strains. Combining phenotypic and genotypic characteristics, the complete IAA production pathway (**Figure 3**) within the broader tryptophan metabolism pathways (**Supplementary Figure 5**) were identified for the strains based on annotation against the KEGG database.

3.4 Chemotaxonomic characteristics

Strain CPCC 204708^T showed chemotaxonomic features consistent with the genus *Solirubrobacter*. In the whole cell hydrolysates of strain CPCC 204708^T, *meso*-diaminopimelic acid was detected as the signature amino acid, and galactose, xylose, rhamnose, and ribose were the components of the sugar profile. Diphosphatidylglycerol (DPG), phosphatidylglycerol (PG), phosphatidylinositol (PI), phosphatidylinositol mannosides (PIM), an unidentified aminophospholipid (APL), and an unidentified phospholipid (PL) were the primary components of the polar lipid profile (**Supplementary Figure 6**). The predominant menaquinone of cells was MK-7(H_4), which is consistent with other species of the genus *Solirubrobacter* (Kim et al., 2007; An et al., 2011; Wei et al., 2014; Zhang L. et al., 2014). The major cellular fatty acids (>10%) were iso-$C_{16:0}$, $C_{18:1}\omega9c$, and iso-$C_{16:0}$ 2-OH, and the detailed composition is provided in the species description and in **Supplementary Table 3**. It was obvious that strain CPCC 204708^T shared the major fatty acids of iso-$C_{16:0}$ and $C_{18:1}\omega9c$ with other validly described *Solirubrobacter* species, while the detailed fatty acids profiles could differentiate them from each other (**Table 2**; **Supplementary Table 3**). Overall, the chemotaxonomic analyses supported the classification of strain CPCC 204708^T as a new member of the genus *Solirubrobacter*, consistent with the 16S rRNA gene sequence and phylogenetic analyses.

3.5 Genomic properties

The genomic DNA G + C content of strain CPCC 204708^T was 71.9% based on its draft genome sequence. Further detailed genomic characteristics for the seven strains were summarized in **Table 1** and **Supplementary Appendix 1**.

Putative genes encoding catalase (*katG*) and superoxide dismutase (*sodA*) were identified in all genomes that likely help mitigate oxidative stress. In addition, the UvrABC repair system (Truglio et al., 2006) and other DNA recombination and repair-related genes were identified. As well, genes were identified that were associated with polyamine transport, osmoprotectant capacity, carotenoid biosynthesis, IAA

TABLE 2 Differentiating characteristics between strain CPCC 204708^T and the type strains of other *Solirubrobacter* species.

Characteristic	1	2	3	4	5	6
Colony color	Pink	White	Pink	White	Pale yellow	White
Temperature range (°C)	20–37	15–33	15–42	7–33	25–37	15–37
pH range	5.0–8.0	6.0–9.0	6.0–7.5	6.0–10.0	6.0–7.0	6.0–10.0
NaCl Tolerance (%, w/v)	0–10	0–7[a]	0–10[a]	0–7[a]	0–3[a]	0–7[a]
Liquefaction of gelatin	–	+	–	+	–	+
Oxidase activity	–	–	–	+	+	+
Hydrolysis of starch	–	–	+	+	–	–
Acid production from						
N-acetylglucosamine	+	–	–	–	–	+
D-arabinose	–	+	+	–	+	+
D-glucose	–	–	+	–	–	+
D-maltose	–	–	+	–	–	+
Potassium gluconate	+	–	+	–	–	–
Enzyme activities						
Lipase (C 14)	+	+	+	+	–	–
β-galactosidase	–	+	–	–	+	+
N-acetyl-β-glucosaminidase	–	+	–	+	+	+
α-mannosidase	–	+	+	–	–	+
Concentration of IAA produced (mg/L)	0.77 ± 0.000	1.12 ± 0.000	3.50 ± 0.001	0.80 ± 0.002	2.22 ± 0.001	0.55 ± 0.002
Tolerance to UV-C radiation (102 J/cm^2)	+	+	+ +	–	–	–
Major fatty acids	iso-$C_{16:0}$, $C_{18:1}\omega9c$, iso-$C_{16:0}$ 2OH	iso-$C_{16:0}$, $C_{18:1}\omega9c$, iso-$C_{17:1}\omega8c$	iso-$C_{16:0}$, $C_{18:1}\omega9c$	iso-$C_{16:0}$, $C_{18:1}\omega9c$, $C_{17:1}\omega8c$, $C_{18:3}\omega6c$ (6, 9, 12)	iso-$C_{16:0}$, $C_{18:1}\omega9c$, $C_{18:3}\omega6c$ (6, 9, 12), iso-$C_{16:0}$ 3OH	iso-$C_{16:0}$, $C_{18:1}\omega9c$
G + C content (%)	71.9	71.6	72.1	71.6	70.6	71.5

1, CPCC 204708^T (data from this study); 2, *S. phytolaccae* KCTC 29190^T (data from this study); 3, *S. pauli* JCM 13025^T (Singleton et al., 2003); 4, *S. taibaiensis* KCTC 29222^T (Zhang L. et al., 2014); 5, *S. ginsenosidimutans* DSM 21036^T (An et al., 2011); 6, *S. soli* DSM 22325^T. + , positive (the number of " + " represents the degree of positivity); –, negative; w, weakly positive; [a]data from this study.

production, iron-siderophore transport system, carbon monoxide dehydrogenase, carbon storage regulation, nitrogen assimilation, and phosphate-transport and solubilization (Figure 4).

Besides lack of precipitation in such harsh ecosystems, heterotrophic microorganisms have to challenge extreme starvation for carbon and other energy substrates. Diverseand viable microbial communities are present in the sandy soils of most deserts. To explore the potential of the desert-derived strains of this study to assimilate carbon and other energy substrates, genes associated with these capacities were annotated and identified. Carbon monoxide dehydrogenase encoding genes (*coxL*, *coxM*, *coxS*, *cutL*, *cutM*, and *cutS*) and a carbon storage regulation coding gene (*csrA*) were retrieved from the genomes (Figure 4). In addition, several genes related to acquisition and assimilation of phosphorus were identified, including *phnB*, *phoA*, *phoB*, *phoD*, *phoH*, *phoP*, *phoU*, *ppk*, *pstA*, *pstB*, *pstC*, and *pstS* (Figure 4). Consistently, phenotypic experiments indicated that strain CPCC 204708^T encoded acid phosphatase and alkaline phosphatase. Nitrogen assimilation genes were also identified in the genomes of the seven strains (Figure 4). Specifically, genes encoding glutamine synthetase (*glnA*), the nitrogen regulatory protein P-II 1 (*glnB*), a probable glutamine ABC transporter permease protein (*glnM* and *glnP*), and the probable sodium/glutamine symporter GlnT (*glnT*) were identified. Glutamine synthetase encoded by *glnA* is a key multitasking protein involved in ammonium assimilation and in the regulation of genes involved in nitrogen metabolism (Schumacher et al., 2015). GlnA may bethat *glnA* is involved in ammonia assimilation under ammonia-starvation conditions, while P-II indirectly controls the transcription of *glnA*. The proteins encoded by *glnM* and *glnP* form components of the ABC transporter complex GlnHMPQ involved in glutamine transport (Yoshida et al., 2003). Moreover, plants have evolved sophisticated mechanisms to mitigate stress from fluctuating nitrate levels and can recruit microorganisms to improve nitrogen uptake (Chai et al., 2022). The bacteria associated with nitrogen transformation, such as *Solirubrobacter* spp., etc., were highly abundant; these bacteria may possess the ability to increase nitrogen availability in the crude oil-contaminated soil (Gao et al., 2022). Nitrogen

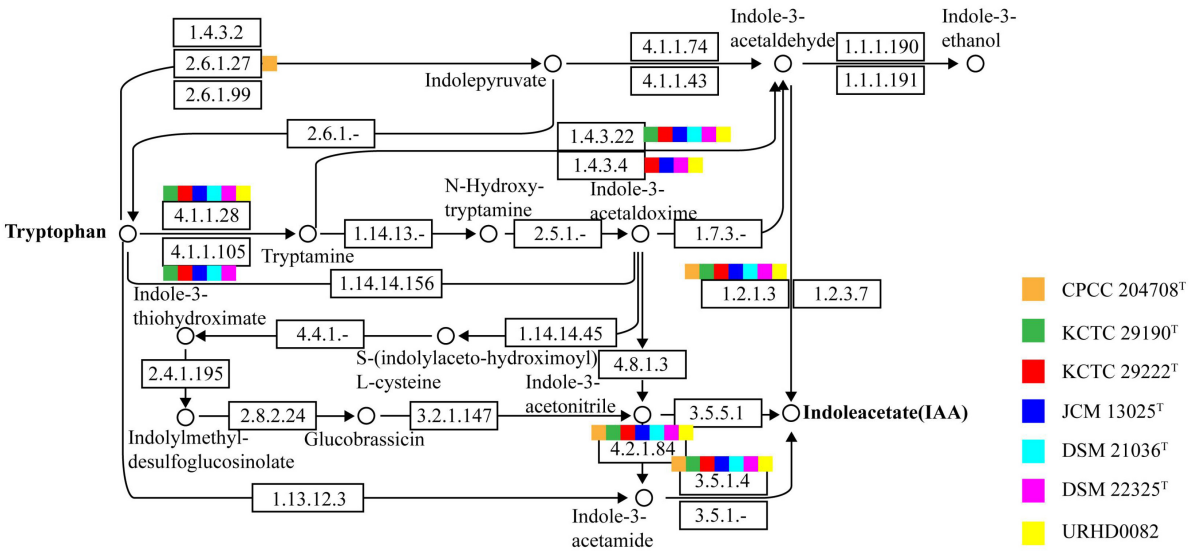

FIGURE 3
The indole-3-acetic acid (IAA) production pathway of *Solirubrobacter* species. Squares in orange, green, red, blue, light blue, pink, and yellow correspond to strains CPCC 204708^T, KCTC 29190^T, KCTC 29222^T, JCM 13025^T, DSM 21036^T, DSM 22325^T, and URHD0082, respectively.

fixation related gene *nifJ* was only retrieved from the genome of the strain *S. ginsenosidimutans* DSM 21036^T. Thus, these *Solirubrobacter* strains may potentially promote nitrogen absorption by their symbiotics in the desert environments, thereby potentially improving their growth in these niches. Consequently, these genomic observations highlight the potential important contributions of the proteins toward adaptation to carbon, nitrogen, and energy starvation in *Solirubrobacter*.

ATP-binding cassette (ABC) transporters are one of the largest known protein families, and are ubiquitous among bacteria. The transporters couple ATP hydrolysis to active transport of diverse substrates including ions, sugars, lipids, sterols, peptides, proteins, and drugs. To explore the transport potential of the seven strains, we analyzed the related genome sequences with KEGG database and blasted with TCDB[12] (**Supplementary Appendix 2**), and genes encoding ABC transporters were identified (**Supplementary Figure 7**). Annotation against the KEGG database revealed the presence of spermidine/putrescine transport related genes (*potA*, *potB*, *potC*, and *potD*) in the seven *Solirubrobacter* genomes (**Figure 4**). Higher polyamine levels in plants can minimize harmful effects resultant from biotic and abiotic stresses (salt, drought, UV, temperature, heavy metals, etc.) (Takahashi and Kakehi, 2010; Hussain et al., 2011; Shi and Chan, 2014). Inoculation with beneficial rhizobacterium *Pseudomonas putida* GAP-P45 led to increased levels of the expression of most polyamine biosynthetic genes and cellular polyamine levels in *Arabidopsis thaliana*, resulting in resistance to water-stressed conditions (Sen et al., 2018). Rhizobacteria also could modulate the redox state of salinity-affected plants by enhancing polyamines and antioxidants, which leads to increased photosynthetic efficiency (Radhakrishnan and Baek, 2017). Given that all reported strains of the genus *Solirubrobacter* so far were isolated from soils or the ecosystems that were vegetated or associated with crops, especially medicinal plants, and that polyamine transport-related genes were retrieved from the genomes of all seven strains of the genus, we concluded that *Solirubrobacter* spp. might have the potential or relate to the growth promotion of plants through the transport of polyamines. Other complete transport-related genes were identified in the seven genomes of the genus *Solirubrobacter*, including those related to transport of osmoprotectants, raffinose/stachyose/melibiose (*msmE*, *msmF*, *msmG* and *msmK*), nucleosides (*bmpA*, *nupB*, *nupC*, and *nupA*), D-xylose (*xylF*, *xylH*, and *xylG*), erythritol (*eryG*, *eryF*, and *eryE*), phosphate, branched-chain amino acids (*livK*, *livH*, *livG*, *livM*, and *livF*), D-methionine (*metQ*, *metI*, and *metN*), iron-siderophores, and lipo-oligosaccharides (*nodJ* and *nodI*).

Salt tolerance assays revealed that strains CPCC 204708^T, *S. phytolaccae* KCTC 29190^T, *S. taibaiensis* KCTC 29222^T, *S. pauli* JCM 13025^T, *S. ginsenosidimutans* DSM 21036^T, and *S. soli* DSM 22325^T grew in the presence of 0–10, 0–7, 0–7, 0–10, 0–3, and 0–7% NaCl (w/v), respectively. Thus, most *Solirubrobacter* species were able to tolerate certain levels of osmotic pressure. Genomic analysis revealed the presence of several genes related to osmoprotectant capacity, including genes encoding the choline transport system permease protein OpuBB (*opuBB*), choline ABC transporter substrate-binding lipoprotein OpuBC (*opuBC*), glycine betaine/carnitine/choline transport system permease protein OpuCB (*opuCB*), glycine betaine/carnitine/choline-binding protein OpuCC (*opuCC*), osmoprotectant import ATP-binding protein OsmV (*osmV*), osmoprotectant-binding protein OsmX (*osmX*), trehalose-6-phosphate synthase (*otsA*), trehalose-phosphate phosphatase (*otsB*), malto-oligosyltrehalose trehalohydrolase (*treZ*), trehalose synthase/amylase TreS (*treS*), maltooligosyl trehalose synthase (*treY*), HTH-type transcriptional regulator BetI (*betI*), oxygen-dependent choline dehydrogenase (*betA*), betaine aldehyde dehydrogenase (*betB*), and glycine betaine/proline betaine transport system ATP-binding protein ProV (*proV*) (**Figure 4**). Notably, many of these proteins are

12 https://tcdb.org/

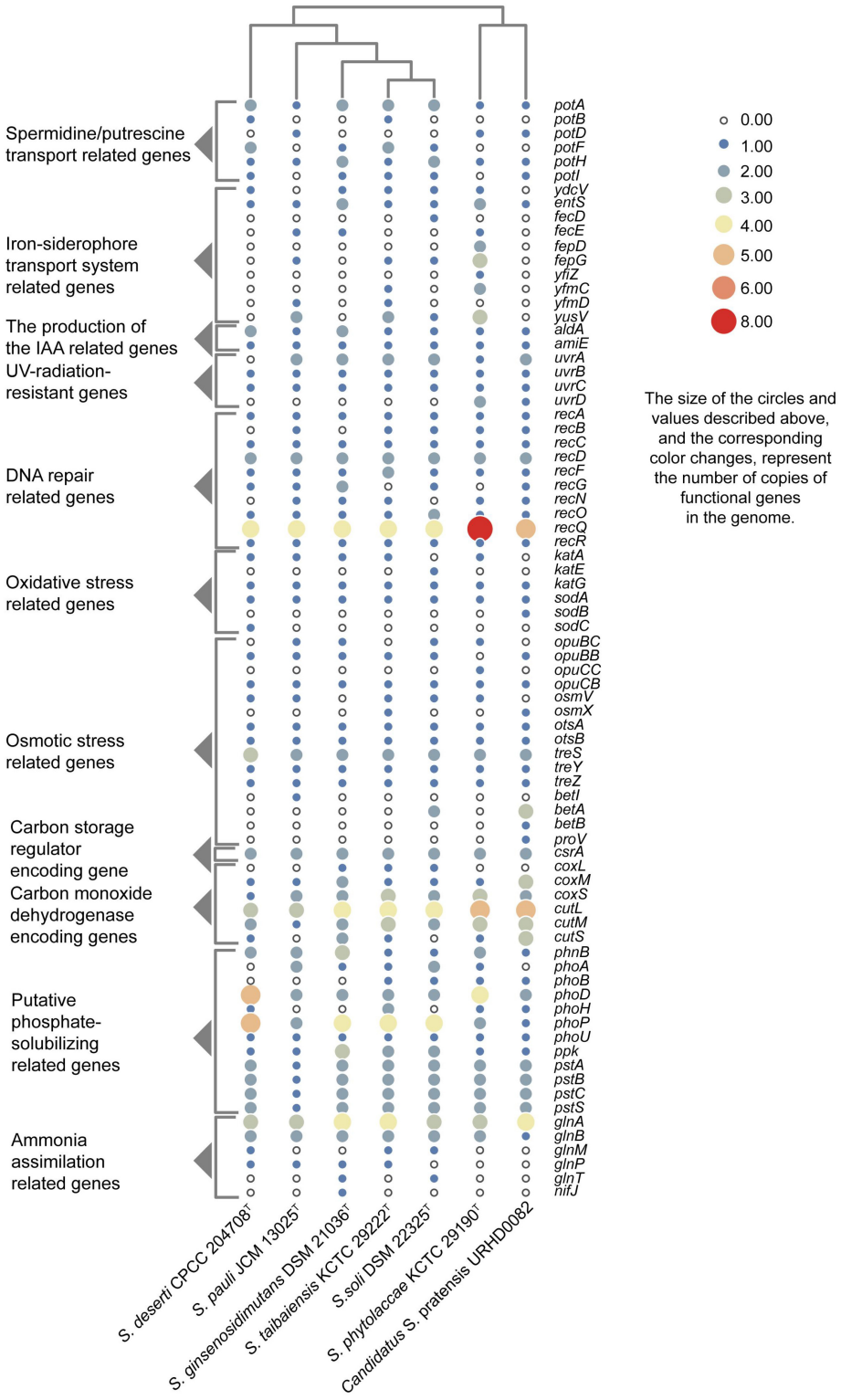

FIGURE 4
Heatmap showing the copy numbers of functional genes predicted in the genomes of seven *Solirubrobacter* species. Functional genes were identified based on comparison to the KEGG database.

involved in trehalose uptake and associated biosynthesis pathways. Trehalose is a major compatible solute involved in osmotic stress responses of cells, cellular adaptation, and survival under heat and desiccation stress (Reina-Bueno et al., 2012). Lee et al. (2021) found that in high-salinity rhizosphere soil habitats planted with tomato, the abundance of some actinobacteria (such as *Solirubrobacter*) increased and the community structure tended to be stable, indicating that strains of these groups could tolerate high osmotic

pressure and potentially help plants tolerate high salt environment through complex plant-microbial interaction.

3.6 Pan-genomic analysis of the genus *Solirubrobacter*

A total of 50,768 protein-coding genes (**Table 1**) were identified among the seven *Solirubrobacter* genomes that comprised 19,800 homologous families based on cluster analysis. Homologous gene family conservation values (HGFCVs) were evaluated among the homolog clusters (**Supplementary Figure 8A**). A total of 2,474 core genes were shared by the seven strains (HGFCV = 7), accounting for ~12.5% of the total homologous gene families, while accessory genes (HGFCVs = 2–6) accounted for ~33.1% of the gene families (6,551 genes) in the genus *Solirubrobacter*. In addition, unique genes (HGFCV = 1) comprised ~54.4% of the total (10,775 genes).

The functional relationship between pan-genome size (f_{pan}) and the number of genomes (n) was obtained by evaluating the following equation:

$$f_{pan}(n) = 7155.93 \times n^{0.522211}$$

In addition, the functional relationship between the number of core genes (f_{core}) and the number of genomes (n) was obtained by evaluating the following equation:

$$f_{core}(n) = 6920.36 \times e^{-0.211409n}$$

Please refer to the reference (Chaudhari et al., 2016) for detailed derivation. With increasing numbers of sequenced genomes, the pan-genome size increased, rather than plateauing (**Supplementary Figure 8B**), suggesting that pan-genome size may continue to enlarge if the number of genomes of this genus continue to increase. Thus, the pan-genome of *Solirubrobacter* may be of an open type. Open pan-genomes are associated with species of the genus inhabiting multiple environments and having multiple ways of exchanging genetic material (Medini et al., 2005). Therefore, it is reasonable to infer that many unknown species of the genus *Solirubrobacter* inhabited in other biotopes have yet to be discovered.

Of the 19,800 genes (clusters), BPGA mapped 6,216 (31.4%) to KEGG database pathways, including for 2,087 core genes (33.6%), 2,017 accessory genes (32.4%), and 2,112 unique genes (34.0%). KEGG pathway results related to eukaryotes (e.g., Human Diseases and Organismal Systems) were removed in order to construct a metabolic reconstruction of the *Solirubrobacter* pan-genome. Many core genes (1,997) were involved in carbohydrate metabolism (17.0%), other carbon metabolism pathways (biosynthesis of amino acids, 5.8%; carbon metabolism, 4.9%; 2-oxocarboxylic acid metabolism, 1.6%; fatty acid metabolism, 1.3%; and degradation of aromatic compounds, 0.4%) (14.0% total), amino acid metabolism (13.7%), energy metabolism (7.6%), metabolism of cofactors and vitamins (5.8%), nucleotide metabolism (4.9%), lipid metabolism (4.4%), replication and repair (4.3%), signal transduction (4.1%), xenobiotic biodegradation and metabolism (4.0%), translation (3.8%), membrane transport (2.8%), metabolism of other amino acids (2.7%), metabolism of terpenoids and polyketides (2.5%), biosynthesis of other secondary metabolites (1.9%), cell motility (1.9%), folding, sorting, and degradation (1.8%) and glycan biosynthesis and metabolism (1.3%). Accessory and unique genes were enriched in pathways related to carbohydrate metabolism, amino acid metabolism, and the metabolism of other substrates.

Among the accessory genes (1,886), most encoded proteins related to the pathways of carbohydrate metabolism (15.0%), amino acid metabolism (14.3%), other specific carbon metabolism pathways (carbon metabolism, 3.8%; biosynthesis of amino acids, 2.6%; fatty acid metabolism, 1.7%; degradation of aromatic compounds, 0.9% and 2-oxocarboxylic acid metabolism, 0.6%) (9.8%), signal transduction (8.8%), membrane transport (7.4%), xenobiotic biodegradation and metabolism (7.3%), lipid metabolism (6.3%), energy metabolism (6.0%), metabolism of cofactors and vitamins (5.6%), metabolism of other amino acids (3.2%), nucleotide metabolism (2.9%), biosynthesis of other secondary metabolites (2.6%), metabolism of terpenoids and polyketides (2.3%), cell motility (2.2%), translation (1.3%), transport and catabolism (1.1%), and glycan biosynthesis and metabolism (1.0%).

Among the 1,876 unique genes, their encoded proteins were related to pathways associated with carbohydrate metabolism (17.0%), amino acid metabolism (11.8%), other specific carbon compound metabolism (carbon metabolism, 4.3%; biosynthesis of amino acids, 2.8%; fatty acid metabolism, 2.3%; 2-oxocarboxylic acid metabolism, 0.7% and degradation of aromatic compounds, 0.6%) (10.7%), signal transduction (8.8%), membrane transport (7.1%), lipid metabolism (6.4%), energy metabolism (5.6%), xenobiotic biodegradation and metabolism (5.6%), metabolism of cofactors and vitamins (4.5%), biosynthesis of other secondary metabolites (2.9%), nucleotide metabolism (2.6%), metabolism of terpenoids and polyketides (2.6%), metabolism of other amino acids (2.1%), folding, sorting, and degradation (1.9%), glycan biosynthesis and metabolism (1.8%), transport and catabolism (1.5%), signaling molecules and interactions (1.4%), cellular community (1.3%), cellular motility (1.2%), translation (1.2%) and replication and repair (1.1%) (**Figure 5**).

The pan-genome of the genus *Solirubrobacter* is characterized by a high proportion of carbohydrate metabolism, amino acid metabolism, and energy metabolism, these genomic features suggest that these strains have the potential to assimilate more sources of carbon and nitrogen to cope with extreme starvation of carbon and other energy substrates. These genomic-level characteristics also suggest that members of the genus *Solirubrobacter* might play an important role in soil organic matter assimilation and biogeochemical cycling.

Compared with the core genomes of the species *Modestobacter deserti* (Jiang et al., 2021) and the genus *Geminicoccus* (Jiang et al., 2022) by BPGA in our previous studies, we found that spermidine/putrescine transport related genes (*potA*, *potB*, *potC* and *potD*) were retrieved only in the core genome of seven strains of the genus *Solirubrobacter*, with no spermidine/putrescine transport related genes in the genomes of *Modestobacter deserti* and the genus *Geminicoccus*. While spermidine/putrescine transport related genes were present in the genomes of *Conexibacter* spp., a group of actinobacteria mostly isolated from the vegetated biotopes, a small number of *Conexibacter* spp. isolated from desert and aquatic habitats had only *potA* genes, or were missing any *pot* genes (data unpublished). Integrating the information from all validly described strains of the genus *Solirubrobacter* derived from the

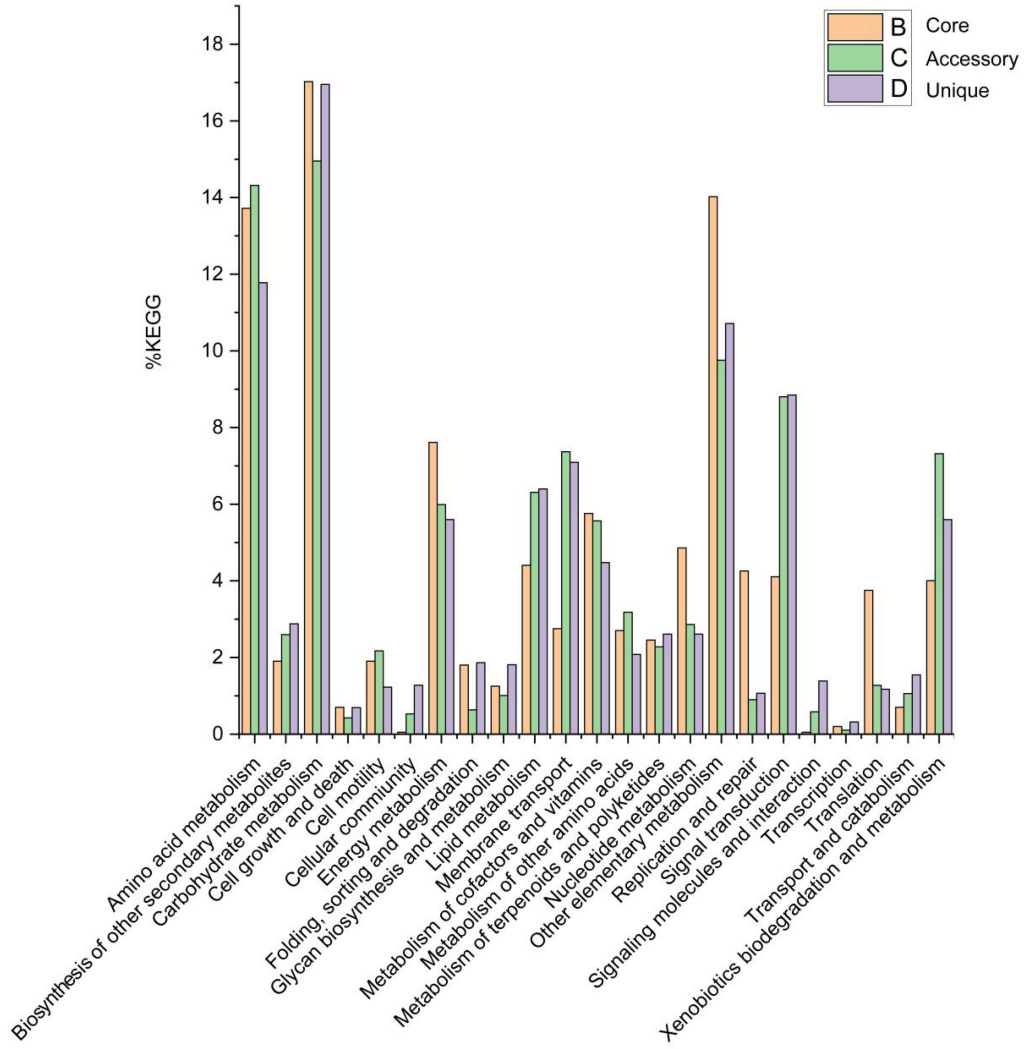

FIGURE 5
Abundances of metabolic pathways associated with core, accessory, and unique genes within the *Solirubrobacter* pan-genomic analyses. Metabolic pathways were identified from the KEGG database.

vegetated biotopes or the ecosystems associated with crops, we supposed that spermidine/putrescine transporter encoding genes might correlate to vegetation (Leontidou et al., 2020). Leontidou et al. (2020) experimentally verified that most selected Plant Growth Promoting Rhizobacteria (PGPR) harbored the genes responsible for polyamine biosynthesis. Accordingly, we supposed that the polyamine related pathway probably act as an additional PGPR-related mechanism involved in plant growth promotion, which need to be further explored. Polyamine (e.g., spermidine) is essential for eukaryotic cell viability and is correlated with lateral root development, pathogen resistance and alleviation of oxidative, osmotic and acidic stresses (Xie S. S. et al., 2014).

Genomes are subject to damage by chemical and physical agents in environments (e.g., UV and ionizing radiation, fungal or bacterial toxins, and chemical mutagens) and by free radicals endogenously generated during cellular metabolism (Tuteja et al., 2001). A variety of different DNA repair pathways help mitigate DNA damage and enable cells to withstand the high solar radiation encountered in desert habitats. UV radiation analysis revealed that strain CPCC 204708^T, *S. phytolaccae* KCTC 29190^T, and *S. pauli* JCM 13025^T survived exposure to 254 nm ultraviolet radiation. Within the core genome of the seven strains analyzed here, genes were identified associated with the UvrABC repair system (Truglio et al., 2006; **Supplementary Figure 9**) (*uvrA*, *uvrB*, *uvrC*, and *uvrD*) and other DNA recombination and repair pathways (*recA*, *recB*, *recC*, *recD*, *recF*, *recG*, *recO*, and *recR*) (Taylor and Smith, 1999; **Supplementary Figure 10**). The DNA repair pathways related genes *uvr* and *rec* were also retrieved in the core-genomes of the genus *Geminicoccus*, the genus *Herbiconiux*, the genus *Conexibacter* and the species *Modestobacter deserti*.

β-Glucosidase activity was also observed for strain DSM 21036^T and this activity was demonstrated as responsible for the gradual conversion of ginsenoside Rb_1 to the compound F_2 (An et al., 2011). β-glucosidase activity was also observed for strain CPCC 204708^T and the five other *Solirubrobacter* strains. Consistently, beta-glucosidase encoding genes (*bgl*) were identified in the core genome of the *Solirubrobacter* strains. The *bgl* gene (encoding β-glucosidase) was retrieved in the core-genomes of

the genus *Geminicoccus*, the genus *Herbiconiux*, and the species *Modestobacter deserti*, but not in the core-genome of the genus *Conexibacter*.

3.7 Secondary metabolite biosynthesis gene cluster analysis

The secondary metabolism of actinobacteria, especially actinobacteria from extreme habitats, is a rich source of novel bioactive compounds with potential medicinal value. In order to identify new drug candidates, microbiologists are increasingly combining multi-omics techniques to predict the potential for secondary metabolite synthesis by sequencing the genomes of various microorganisms. Here, we identified the secondary metabolite biosynthetic gene clusters (BGCs) of genus *Solirubrobacter* by antiSMASH.

The annotation of secondary metabolite biosynthesis gene clusters in the seven *Solirubrobacter* genomes revealed the presence within each genome of eight to thirteen secondary metabolite gene clusters, which exhibited low similarities to previously described secondary metabolite biosynthetic gene clusters. Specifically, the gene clusters exhibited 5–40% nucleotide similarities to known secondary metabolite biosynthetic gene clusters including those for accramycin A, microansamycin, calcium-dependent lipopeptide, lomofungin, tiancimycin, schizokinen, lankacidin C, linfuranone B/C, kitasetaline, fulvuthiacene A/B, macrotermycins. In addition, other unidentified secondary metabolite clusters were identified that were attributable to those encoding NAPS-independent-siderophores, lassopeptides, LAP thiopeptides, terpenes, NAPAAs, redox-cofactors, RiPP-like compounds, RRE-containing compounds, ranthipeptides, indole, and lanthipeptide-class-iv types (**Supplementary Table 4**). The analysis with antiSMASH also revealed the presence of a microansamycin gene cluster in strain CPCC 204708^T. Pentaketide ansamycins have rarely been reported and include compounds like the antioxidant Q-1047, lipoxygenase inhibitor tetrapetalones (Komoda et al., 2004), radical scavenger ansaetherones (Komoda et al., 2008), cebulactams (Pimentel-Elardo et al., 2009), and the macrodilactam juanlimycins (Zhang J. et al., 2014). The novel pentaketide ansamycin, Microansamycin D, was recently identified and its antioxidant activity was confirmed (Wang et al., 2018). Accramycin A is a new naphthacene-type aromatic natural product and was identified in the antiSMASH analysis of strain CPCC 204708^T. Accramycin A was first discovered from the metabolites of *Streptomyces* sp. MA37 (Maglangit et al., 2019). The antibacterial activities of accramycin A were also preliminarily evaluated against Group B *Streptococcus*, revealing a minimum inhibitory concentration (MIC) of 27 μg/mL, providing the first evidence of naphthacene-type aromatic polyketide bioactivity. The Lomofungin gene cluster was also identified in the antiSMASH analysis of strain *S. phytolaccae* KCTC 29190^T. This antibiotic exhibits antibacterial activity against fungi, yeast, and bacteria (Klo et al., 1973). Further, macrotermycins A and C have exhibited antimicrobial activity against human pathogenic *Staphylococcus aureus* in addition to selective antifungal activity against a fungal parasite from termite fungal gardens (Beemelmanns et al., 2017).

The pangenomes of the genera *Geminicoccus*, *Herbiconiux* and *Conexibacter*, as well as the species *Modestobacter deserti* were used as the control genomes of the genus *Solirubrobacter*. Upon comparison, it was discovered that secondary metabolism cluster profiles in the pangenome of the genus indeed showed specific. The secondary metabolite gene clusters responsible for accramycin A, microansamycin, calcium-dependent lipopeptide, lomofungin, tiancimycin, schizokinen, lankacidin C, linfuranone B/C, kitasetaline, fulvuthiacene A/B, and macrotermycins, were only retrieved from the genomes of genus *Solirubrobacter*, but not from those of the genus *Herbiconiux*, *Geminicoccus*, *Conexibacter* (data unpublished), and the species *Modestobacter deserti*.

4 Conclusion

In this study, the distribution of the genus *Solirubrobacter* was evaluated across numerous environments, revealing their enrichment in soils of areas with high UV radiation (e.g., desert soils). In addition, the novel strain *Solirubrobacter deserti* sp. nov. CPCC 204708^T was isolated, identified, and characterized, in addition to subsequent characterization of the genetic basis of *Solirubrobacter* adaptations to harsh environments and their potential mediation of plant-microbe interactions. Further, strain URHD0082 was identified as *Candidatus* "Solirubrobacter pratensis" based on genome information. Genome-scale analysis of strain CPCC 204708^T revealed the molecular basis for their adaptations to desert environments via mitigation of stress from UV radiation, carbon starvation, desiccation, and osmotic stress. In the absence of macrophytic phototrophs, such as in desert soils, such microorganism could potentially serve as significant contributors to both primary productivity and biogeochemical activities, thereby assuming the role of pioneering organisms. Global analysis of *Solirubrobacter* genomes and their environmental distributions suggest they are abundant in ecosystems associated with plants, where they may promote plant health.

5 Description of *Solirubrobacter deserti* sp. nov. and *Candidatus* "*Solirubrobacter pratensis*" sp. nov.

Solirubrobacter deserti (de.ser'ti. L. gen. n. *deserti* of a desert).

Cells are aerobic, Gram-stain positive, non-motile, non-spore-forming, and rod-shaped, with sizes of 0.6–0.8 × 1.2–1.9 μm. Diffusible pigments are not produced on any media. Colonies on R2A medium are circular, convex, smooth, and entire, with pale pink coloration and diameters of approximately 1.9 mm. Growth occurs at 20–37°C (optimum: 28–30°C) and at pH 5.0–8.0 (optimum: 7.0–8.0), and up to 10% (w/v) NaCl. Cells are catalase-positive and oxidase-negative, but negative for H_2S and indole production. Cells cannot hydrolyze cellulose, starch, Tween 40, and gelatin. API ZYM strip analysis indicated that cells are positive for enzymatic activities including acid phosphatase, alkaline phosphatase, cystine arylamidase, esterase (C4), esterase lipase (C8), N-acetyl-β-glucosaminidase, β-glucosidase, leucine

arylamidase, lipase (C 14), trypsin, and valine arylamidase. Acetoacetic acid, D-cellobiose, dextrin, D-fructose, D-galactose, D-galacturonic acid, D-galacturonic acid, D-gluconic acid, D-glucose-6-PO_4, D-glucuronic acid, D-maltose, D-mannitol, D-mannose, D-melibiose, D-saccharic acid, D-trehalose, D-turanose, gelatin, glucuronamide, glycerol, L-aspartic acid, L-fucose, L-histidine, L-rhamnose, mucic acid, N-Acetyl-D-glucosamine, pectin, quinic acid, sucrose, α-D-glucose, and α-keto-glutaric acid can be used as sole carbon sources. Alanine, glycine, glutamate, asparagine, and meso-diaminopimelic acid were identified in the whole cell hydrolysates. The whole cell sugar profiles contained galactose, xylose, rhamnose and ribose. Polar lipids comprise diphosphatidylglycerol, phosphatidylglycerol, an unidentified aminophospholipid, and an unidentified phospholipid. The predominant menaquinone is MK-7(H_4). The cellular fatty acids profile contains iso-$C_{16:0}$, $C_{18:1}\omega9c$, and iso-$C_{16:0}$ 2-OH as the major (>10%) components, with moderate (3–9%) amounts of iso-$C_{16:1}$ H, $C_{17:1}$ $\omega8c$ and 10-methyl $C_{17:0}$. The G + C content of the genomic DNA is 71.9%. The type strain CPCC 204708^T (= DSM 105495 ^{T} = NBRC 112942^T) was isolated from sandy soil collected from the Badain Jaran Desert in the Inner Mongolia autonomous region.

Candidatus "Solirubrobacter pratensis" (pra.ten'sis. L. fem. adj. *pratensis* growing in a meadow, referring to the isolation of the strain from grassland).

URHD0082 is temporarily proposed as the type genome for the species. The strain URHD0082 was isolated from the Mediterranean grassland soil. The accession number of the genome of the isolate URHD0082 is available in the DDBJ/ENA/Genbank database under accession AUEK00000000 and the Genbank accession number for the 16S rRNA gene sequence (extracted from the genome) is OQ674416. The genome of URHD0082 has the following characteristics: a draft genome of 6,640,086 bp, assembled from 28 qualified scaffolds, with total 6,557 genes, including 6,470 protein-coding genes and 87 RNA genes (consisting of 3 rRNA genes, 76 tRNA genes and 8 other RNA genes). The G + C content in the genomic DNA of URHD0082 is 72.2%.

Data availability statement

The datasets presented in this study can be found in online repositories. The names of the repository/repositories and accession number(s) can be found in the article/**Supplementary material**.

Ethics statement

The manuscript presents research on animals that do not require ethical approval for their study.

Author contributions

Z-MJ: Conceptualization, Data curation, Formal analysis, Investigation, Validation, Visualization, Writing—original draft, Writing—review and editing. TM: Data curation, Investigation, Validation, Writing—original draft. YS: Formal analysis, Investigation, Validation, Writing—review and editing. JS: Resources, Validation, Investigation, Writing—review and editing. L-YY: Resources, Validation, Writing—review and editing. Y-QZ: Conceptualization, Data curation, Funding acquisition, Investigation, Methodology, Project administration, Supervision, Validation, Writing—original draft, Writing—review and editing.

Funding

The author(s) declare financial support was received for the research, authorship, and/or publication of this article. This research was supported by the CAMS Innovation Fund for Medical Sciences (CIFMS, 2021-I2M-1-055), the National Natural Science Foundation of China (32170021; 31670010), the Beijing Natural Science Foundation (5212018), Key Project at central government level-the ability establishment of sustainable use for valuable Chinese Medicine Resources (2060302), and the National Infrastructure of Microbial Resources (NIMR-2022-3).

Acknowledgments

We sincerely thank Institute of Microbiology, Chinese Academy of Sciences, for the kind assistance in the cells morphology observation using transmission electron microscopy.

Conflict of interest

The authors declare that the research was conducted in the absence of any commercial or financial relationships that could be construed as a potential conflict of interest.

The author(s) declared that they were an editorial board member of Frontiers, at the time of submission. This had no impact on the peer review process and the final decision.

Publisher's note

Supplementary material

The Supplementary Material for this article can be found online at: https://www.frontiersin.org/articles/10.3389/fmicb.2023.1267771/full#supplementary-material

References

Aguiar, L. M., Souza, M. F., de Laia, M. L., de Oliveira Melo, J., da Costa, M. R., Gonçalves, J. F., et al. (2020). Metagenomic analysis reveals mechanisms of atrazine biodegradation promoted by tree species. *Environ. Pollut.* 267:115636. doi: 10.1016/j.envpol.2020.115636

An, D. S., Wang, L., Kim, M. S., Bae, H. M., Lee, S. T., and Im, W. T. (2011). *Solirubrobacter ginsenosidimutans* sp. nov., isolated from soil of a ginseng field. *Int. J. Syst. Evol. Microbiol.* 61, 2606–2609. doi: 10.1099/ijs.0.028431-0

Auch, A. F., von Jan, M., Klenk, H. P., and Göker, M. (2010). Digital DNA-DNA hybridization for microbial species delineation by means of genome-to-genome sequence comparison. *Stand. Genomic Sci.* 2, 117–134. doi: 10.4056/sigs.531120

Barajas, H. R., Martínez-Sánchez, S., Romero, M. F., Álvarez, C. H., Servín-González, L., Peimbert, M., et al. (2020). Testing the two-step model of plant root microbiome acquisition under multiple plant species and soil sources. *Front. Microbiol.* 11:542742. doi: 10.3389/fmicb.2020.542742

Beemelmanns, C., Ramadhar, T. R., Kim, K. H., Klassen, J. L., Cao, S., Wyche, T. P., et al. (2017). Macrotermycins A-D, glycosylated macrolactams from a termite-associated Amycolatopsis sp. M39. *Org. Lett.* 19, 1000–1003. doi: 10.1021/acs.orglett.6b03831

Blin, K., Shaw, S., Kloosterman, A. M., Charlop-Powers, Z., van Wezel, G. P., Medema, M. H., et al. (2021). Antismash 6.0: Improving cluster detection and comparison capabilities. *Nucleic Acids Res.* 49, W29–W35. doi: 10.1093/nar/gkab335

Bric, J. M., Bostock, R. M., and Silverstone, S. E. (1991). Rapid in situ assay for indoleacetic Acid production by bacteria immobilized on a nitrocellulose membrane. *Appl. Environ. Microbiol.* 57, 535–538. doi: 10.1128/aem.57.2.535-538.1991

Bull, A. T., Asenjo, J. A., Goodfellow, M., and Gomez-Silva, B. (2016). The atacama desert: Technical resources and the growing importance of novel microbial diversity. *Annu. Rev. Microbiol.* 70, 215–234. doi: 10.1146/annurev-micro-102215-095236

Chai, X., Wang, X., Pi, Y., Wu, T., Zhang, X., Xu, X., et al. (2022). Nitrate transporter MdNRT2.4 interacts with Rhizosphere bacteria to enhance nitrate uptake in apple rootstocks. *J. Exp. Bot.* 73, 6490–6504. doi: 10.1093/jxb/erac301

Chaudhari, N. M., Gupta, V. K., and Dutta, C. (2016). BPGA- an ultra-fast pan-genome analysis pipeline. *Sci. Rep.* 6:24373. doi: 10.1038/srep24373

Cohen, A. C., Travaglia, C. N., Bottini, R., and Piccoli, P. N. (2009). Participation of abscisic acid and gibberellins produced by endophytic *Azospirillum* in the alleviation of drought effects in maize. *Bot. Bot.* 87, 455–462. doi: 10.1139/B09-023

Collins, M. D., Pirouz, T., Goodfellow, M., and Minnikin, D. E. (1977). Distribution of menaquinones in actinomycetes and corynebacteria. *J. Gen. Microbiol.* 100, 221–230. doi: 10.1099/00221287-100-2-221

Crozier, A., Arruda, P., Jasmim, J. M., Monteiro, A. M., and Sandberg, G. (1988). Analysis of Indole-3-acetic acid and related indoles in culture medium from *Azospirillum lipoferum* and *Azospirillum brasilense*. *Appl. Environ. Microbiol.* 54, 2833–2837. doi: 10.1128/aem.54.11.2833-2837.1988

Davies, P. J. (1995). *Plant Hormones: Physiology, Biochemistry and Molecular Biology*. Boston, MA: Kluwer Academic.

Delcher, A. L., Bratke, K. A., Powers, E. C., and Salzberg, S. L. (2007). Identifying bacterial genes and endosymbiont DNA with Glimmer. *Bioinformatics* 23, 673–679. doi: 10.1093/bioinformatics/btm009

Deng, Y., Han, X. F., Jiang, Z. M., Yu, L. Y., Li, Y., and Zhang, Y. Q. (2022). Characterization of three *Stenotrophomonas* strains isolated from different ecosystems and proposal of *Stenotrophomonas mori* sp. nov. and *Stenotrophomonas* lacuserhaii sp. nov. *Front. Microbiol.* 13:1056762. doi: 10.3389/fmicb.2022.1056762

Dong, L., Cheng, R., Xiao, L., Wei, F., Wei, G., Xu, J., et al. (2018). Diversity and composition of bacterial endophytes among plant parts of Panax notoginseng. *Chin. Med.* 13:41. doi: 10.1186/s13020-018-0198-5

Duca, D., Lorv, J., Patten, C. L., Rose, D., and Glick, B. R. (2014). Indole-3-acetic acid in plant-microbe interactions. *Antonie Van Leeuwenhoek* 106, 85–125. doi: 10.1007/s10482-013-0095-y

Fabra, A., Castro, S., Taurian, T., Angelini, J., Ibañez, F., Dardanelli, M., et al. (2010). Interaction among *Arachis hypogaea* L. (peanut) and beneficial soil microorganisms: How much is it known? *Crit. Rev. Microbiol.* 36, 179–194. doi: 10.3109/10408410903584863

Felsenstein, J. (1981). Evolutionary trees from DNA sequences: A maximum likelihood approach. *J. Mol. Evol.* 17, 368–376. doi: 10.1007/BF01734359

Felsenstein, J. (1985). Confidence limits on phylogenies: An approach using the bootstrap. *Evolution* 39, 783–791. doi: 10.1111/j.1558-5646.1985.tb00420.x

Feng, W. M., Liu, P., Yan, H., Zhang, S., Shang, E. X., Yu, G., et al. (2021). Impact of bacillus on phthalides accumulation in *Angelica sinensis* (Oliv.) by stoichiometry and microbial diversity analysis. *Front. Microbiol.* 11:611143. doi: 10.3389/fmicb.2020.611143

Franke-Whittle, I. H., Manici, L. M., Insam, H., and Stres, B. (2015). Rhizosphere bacteria and fungi associated with plant growth in soils of three replanted apple orchards. *Plant Soil* 395, 317–333. doi: 10.1007/s11104-015-2562-x

Gao, Y., Yuan, L., Du, J., Wang, H., Yang, X., Duan, L., et al. (2022). Bacterial community profile of the crude oil-contaminated saline soil in the Yellow River Delta Natural Reserve, China. *Chemosphere* 289:133207. doi: 10.1016/j.chemosphere.2021.133207

Gonzalez, C., Gutierrez, C., and Ramirez, C. (1978). Halobacterium vallismortis sp. nov. An amylolytic and carbohydrate-metabolizing, extremely halophilic bacterium. *Can. J. Microbiol.* 24, 710–715. doi: 10.1139/m78-119

Groth, I., Schumann, P., Rainey, F. A., Martin, K., Schuetze, B., and Augsten, K. (1997). Demetria terragena gen. nov., sp. nov., a new genus of actinomycetes isolated from compost soil. *Int. J. Syst. Bacteriol.* 47, 1129–1133. doi: 10.1099/00207713-47-4-1129

Hussain, S. S., Ali, M., Ahmad, M., and Siddique, K. H. M. (2011). Polyamines: Natural and en-gineered abiotic and biotic stress tolerance in plants. *Biotechnol. Adv.* 29, 300–311. doi: 10.1016/j.biotechadv.2011.01.003

Jiang, Z. M., Deng, Y., Han, X. F., Su, J., Wang, H., Yu, L. Y., et al. (2022). *Geminicoccus flavidas* sp. nov. and *Geminicoccus harenae* sp. nov., two IAA-producing novel rare bacterial species inhabiting desert biological soil crusts. *Front. Microbiol.* 13:1034816. doi: 10.3389/fmicb.2022.1034816

Jiang, Z. M., Zhang, B. H., Sun, H. M., Zhang, T., Yu, L. Y., and Zhang, Y. Q. (2021). Properties of Modestobacter deserti sp. nov., a Kind of novel phosphate-solubilizing actinobacteria inhabited in the desert biological soil crusts. *Front. Microbiol.* 12:742798. doi: 10.3389/fmicb.2021.742798

Jiao, J. Y., Liu, L., Hua, Z. S., Fang, B. Z., Zhou, E. M., Salam, N., et al. (2020). Microbial dark matter coming to light: Challenges and opportunities. *Natl. Sci. Rev.* 8:nwaa280. doi: 10.1093/nsr/nwaa280

Kim, M., Oh, H. S., Park, S. C., and Chun, J. (2014). Towards a taxonomic coherence between average nucleotide identity and 16S rRNA gene sequence similarity for species demarcation of prokaryotes. *Int. J. Syst. Evol. Microbiol.* 64, 346–351. doi: 10.1099/ijs.0.059774-0

Kim, M. K., Na, J. R., Lee, T. H., Im, W. T., Soung, N. K., and Yang, D. C. (2007). Solirubrobacter soli sp. nov., isolated from soil of a ginseng field. *Int. J. Syst. Evol. Microbiol.* 57, 1453–1455. doi: 10.1099/ijs.0.64715-0

Kim, T. J., Kim, H. J., Kang, M., Cho, J. H., Kim, Y. G., Lee, S. M., et al. (2021). Ginsenoside F2 induces cellular toxicity to glioblastoma through the impairment of mitochondrial function. *Phytomedicine* 83:153483. doi: 10.1016/j.phymed.2021.153483

Klo, S. C., Cano, F. R., and Lampen, J. O. (1973). Lomofungin, an inhibitor of ribonucleic acid synthesis in yeast protoplasts: Its effect on enzyme formation. *Antimicrob Agents Chemother.* 3, 716–722. doi: 10.1128/aac.3.6.716

Kluge, A. G., and Farris, J. S. (1969). Quantitative phyletics and the evolution of anurans. *Syst. Biol.* 18, 1–32. doi: 10.1093/sysbio/18.1.1

Komagata, K., and Suzuki, K. I. (1988). 4 lipid and cell-wall analysis in bacterial systematics. *Methods Microbiol.* 19, 161–207. doi: 10.1016/S0580-9517(08)70410-0

Komoda, T., Akasaka, K., and Hirota, A. (2008). Ansaetherone, a new radical scavenger from Streptomyces sp. *Biosci. Biotechnol. Biochem.* 72, 2392–2397. doi: 10.1271/bbb.80282

Komoda, T., Yoshida, K., Abe, N., Sugiyama, Y., Imachi, M., Hirota, H., et al. (2004). Tetrapetalone A, a novel lipoxygenase inhibitor from Streptomyces sp. *Biosci. Biotechnol. Biochem.* 68, 104–111. doi: 10.1271/bbb.68.104

Kroppenstedt, R. M. (1985). Fatty acid and menaquinone analysis of actinomycetes and related organisms in society for applied bacteriology technical series: Chemical methods in bacterial systematics. *Soc. Appl. Bacteriol. Tech. Ser.* 20, 173–199.

Kumar, S., Stecher, G., and Tamura, K. (2016). MEGA7: Molecular evolutionary genetics analysis version 7.0 for bigger datasets. *Mol. Biol. Evol.* 33, 1870–1874. doi: 10.1093/molbev/msw054

Lee, S. A., Kim, H. S., Sang, M. K., Song, J., and Weon, H. Y. (2021). Effect of Bacillus mesonae H20-5 treatment on rhizospheric bacterial community of tomato plants under salinity stress. *Plant Pathol. J.* 37, 662–672. doi: 10.5423/PPJ.FT.10.2021.0156

Leontidou, K., Genitsaris, S., Papadopoulou, A., Kamou, N., Bosmali, I., Matsi, T., et al. (2020). Plant growth promoting rhizobacteria isolated from halophytes and drought-tolerant plants: Genomic characterisation and exploration of phyto-beneficial traits. *Sci. Rep.* 10:14857. doi: 10.1038/s41598-020-71652-0

Leung, P. M., Bay, S. K., Meier, D. V., Chiri, E., Cowan, D. A., Gillor, O., et al. (2020). Energetic basis of microbial growth and persistence in desert ecosystems. *mSystems* 5:e00495-19. doi: 10.1128/mSystems.00495-19

Li, W. J., Xu, P., Schumann, P., Zhang, Y. Q., Pukall, R., Xu, L. H., et al. (2007). Georgenia ruanii sp. nov., a novel actinobacterium isolated from forest soil in Yunnan (China), and emended description of the genus Georgenia. *Int. J. Syst. Evol. Microbiol.* 57, 1424–1428. doi: 10.1099/ijs.0.64749-0

Li, X., Chu, C., Ding, S., Wei, H., Wu, S., and Xie, B. (2022). Insight into how fertilization strategies increase quality of grape (Kyoho) and shift microbial

community. *Environ. Sci. Pollut. Res. Int.* 29, 27182–27194. doi: 10.1007/s11356-021-17759-x

Magee, C. M., Rodeheaver, G., Edgerton, M. T., and Edlich, R. F. (1975). A more reliable gram staining technic for diagnosis of surgical infections. *Am. J. Surg.* 130, 341–346. doi: 10.1016/0002-9610(75)90398-0

Maglangit, F., Fang, Q., Leman, V., Soldatou, S., Ebel, R., Kyeremeh, K., et al. (2019). Accramycin A, a new aromatic polyketide, from the soil bacterium, Streptomyces sp. MA37. *Molecules* 24:3384. doi: 10.3390/molecules24183384

Medini, D., Donati, C., Tettelin, H., Masignani, V., and Rappuoli, R. (2005). The microbial pan-genome. *Curr. Opin. Genet. Dev.* 15, 589–594. doi: 10.1016/j.gde.2005.09.006

Mhatre, P. H., Karthik, C., Kadirvelu, K., Divya, K. L., Venkatasalam, E. P., Srinivasan, S., et al. (2018). Plant growth promoting rhizobacteria (PGPR): A potential alternative tool for nematodes bio-control. *Biocatal. Agric. Biotechnol.* 17, 119–128. doi: 10.1016/j.bcab.2018.11.009

Minnikin, D. E., O'Donnell, A. G., Goodfellow, M., Alderson, G., Athalye, M., Schaal, A., et al. (1984). An integrated procedure for the extraction of bacterial isoprenoid quinones and polar lipids. *J. Microbiol. Methods* 2, 233–241. doi: 10.1016/0167-7012(84)90018-6

Miralles, I., Lázaro, R., Sánchez-Marañón, M., Soriano, M., and Ortega, R. (2020). Biocrust cover and successional stages influence soil bacterial composition and diversity in semiarid ecosystems. *Sci. Total Environ.* 709:134654. doi: 10.1016/j.scitotenv.2019.134654v

Mojib, N., Farhoomand, A., Andersen, D. T., and Bej, A. K. (2013). UV and cold tolerance of a pigment-producing Antarctic *Janthinobacterium* sp. Ant5-2. *Extremophiles* 17, 367–378. doi: 10.1007/s00792-013-0525-9

Moriya, Y., Itoh, M., Okuda, S., Yoshizawa, A. C., and Kanehisa, M. (2007). KAAS: An automatic genome annotation and pathway reconstruction server. *Nucleic Acids Res.* 35, W182–W185. doi: 10.1093/nar/gkm321

Parks, D. H., Chuvochina, M., Waite, D. W., Rinke, C., Skarshewski, A., Chaumeil, P. A., et al. (2018). A standardized bacterial taxonomy based on genome phylogeny substantially revises the tree of life. *Nat. Biotechnol.* 36, 996–1004. doi: 10.1038/nbt.4229

Parks, D. H., Imelfort, M., Skennerton, C. T., Hugenholtz, P., and Tyson, G. W. (2015). CheckM: Assessing the quality of microbial genomes recovered from isolates, single cells, and metagenomes. *Genome Res.* 25, 1043–1055. doi: 10.1101/gr.186072.114

Paysan-Lafosse, T., Blum, M., Chuguransky, S., Grego, T., Pinto, B. L., Salazar, G. A., et al. (2023). InterPro in 2022. *Nucleic Acids Res.* 51, D418–D427. doi: 10.1093/nar/gkac993

Piccoli, P., Travaglia, C., Cohen, A., Sosa, L., Cornejo, P., Masuelli, R., et al. (2011). An endophytic bacterium isolated from roots of the halophyte Prosopis strombulifera produces ABA, IAA, gibberellins A 1 and A 3 and jasmonic acid in chemically-defined culture medium. *Plant Growth Regul.* 64, 207–210. doi: 10.1007/s10725-010-9536-z

Pimentel-Elardo, S. M., Gulder, T., Hentschel, U., and Bringmann, G. J. C. (2009). Cebulactams A1 and A2, new macrolactams isolated from Saccharopolyspora cebuensis, the first obligate marine strain of the genus Saccharopolyspora. *Cheminform* 49, 6889–6892. doi: 10.1016/j.tetlet.2008.09.094

Pulschen, A. A., Rodrigues, F., Duarte, R. T., Araujo, G. G., Santiago, I. F., Paulino-Lima, I. G., et al. (2015). UV-resistant yeasts isolated from a high-altitude volcanic area on the Atacama Desert as eukaryotic models for astrobiology. *Microbiologyopen* 4, 574–588. doi: 10.1002/mbo3.262

Radhakrishnan, R., and Baek, K. H. (2017). Physiological and biochemical perspectives of non-salt tolerant plants during bacterial interaction against soil salinity. *Plant Physiol. Biochem.* 116, 116–126. doi: 10.1016/j.plaphy.2017.05.009

Reina-Bueno, M., Argandona, M., Nieto, J. J., Hidalgo-Garcia, A., Iglesias-Guerra, F., Delgado, M. J., et al. (2012). Role of trehalose in heat and desiccation tolerance in the soil bacterium Rhizobium etli. *BMC Microbiol.* 12:207. doi: 10.1186/1471-2180-12-207

Reis-Mansur, M. C. P. P., Cardoso-Rurr, J. S., Silva, J. V. M. A., de Souza, G. R., Cardoso, V. D. S., Mansoldo, F. R. P., et al. (2019). Carotenoids from UV-resistant Antarctic *Microbacterium* sp, LEMMJ01. *Sci. Rep.* 9:9554. doi: 10.1038/s41598-019-45840-6

Saitou, N., and Nei, M. (1987). The Neighbor-Joining method: A new method for reconstructing phylogenetic trees. *Mol. Biol. Evol.* 4, 406–425. doi: 10.1093/oxfordjournals.molbev.a040454

Sánchez-Marañón, M., Miralles, I., Aguirre-Garrido, J. F., Anguita-Maeso, M., Millán, V., Ortega, R., et al. (2017). Changes in the soil bacterial community along a pedogenic gradient. *Sci. Rep.* 7:14593. doi: 10.1038/s41598-017-15133-x

Sasser, M. (1990). Identification of bacteria by gas chromatography of cellular fatty acids. *Usfcc Newsl.* 20, 1–6.

Saxena, D., Ben-Dov, E., Manasherob, R., Barak, Z., Boussiba, S., and Zaritsky, A. (2002). A UV tolerant mutant of *Bacillus thuringiensis* subsp. *kurstaki* producing melanin. *Curr. Microbiol.* 44, 25–30. doi: 10.1007/s00284-001-0069-6

Schleifer, K. H., and Kandler, O. (1973). Peptidoglycan types of bacterial cell walls and their taxonomic implications. *Bacteriol. Rev.* 37:258. doi: 10.1128/br.37.2.258-258.1973

Schumacher, M. A., Chinnam, N. B., Cuthbert, B., Tonthat, N. K., and Whitfill, T. (2015). Structures of regulatory machinery reveal novel molecular mechanisms controlling *B. subtilis* nitrogen homeostasis. *Genes Dev.* 29, 451–464. doi: 10.1101/gad.254714.114

Sen, S., Ghosh, D., and Mohapatra, S. (2018). Modulation of polyamine biosynthesis in *Arabidopsis thaliana* by a drought mitigating *Pseudomonas* putida strain. *Plant Physiol. Biochem.* 129, 180–188. doi: 10.1016/j.plaphy.2018.05.034

Shange, R. S., Ankumah, R. O., Ibekwe, A. M., Zabawa, R., and Dowd, S. E. (2012). Distinct soil bacterial communities revealed under a diversely managed agroecosystem. *PLoS One* 7:e40338. doi: 10.1371/journal.pone.0040338

Shi, H., and Chan, Z. (2014). Improvement of plant abiotic stress tolerance through modulation of the polyamine pathway. *J. Integr. Plant. Biol.* 56, 114–121. doi: 10.1111/jipb.12128

Shirling, E. B., and Gottlieb, D. (1966). Methods for characterization of Streptomyces species. *Int. J. Syst. Bacteriol.* 16, 313–340. doi: 10.1099/00207713-16-3-313

Singleton, D. R., Furlong, M. A., Peacock, A. D., White, D. C., Coleman, D. C., and Whitman, W. B. (2003). Solirubrobacter pauli gen. nov., sp. nov., a mesophilic bacterium within the Rubrobacteridae related to common soil clones. *Int. J. Syst. Evol. Microbiol.* 53, 485–490. doi: 10.1099/ijs.0.02438-0

Sivakala, K. K., Jose, P. A., Anandham, R., Thinesh, T., Jebakumar, S. R. D., Samaddar, S., et al. (2018). Spatial physiochemical and metagenomic analysis of desert environment. *J. Microbiol. Biotechnol.* 28, 1517–1526. doi: 10.4014/jmb.1804.04005

Sun, Y., Chen, H. H., Sun, H. M., Ai, M. J., Su, J., Yu, L. Y., et al. (2017). Naumannella huperziae sp. nov., an endophytic actinobacterium isolated from Huperzia serrata (Thunb.). *Int. J. Syst. Evol. Microbiol.* 67, 1867–1872. doi: 10.1099/ijsem.0.001882

Takahashi, T., and Kakehi, J. (2010). Polyamines: Ubiquitous polycations with unique roles in growth and stress responses. *Ann. Bot.* 105, 1–6. doi: 10.1093/aob/mcp259

Taylor, A. F., and Smith, G. R. (1999). Regulation of homologous recombination: Chi inactivates RecBCD enzyme by disassembly of the three subunits. *Genes Dev.* 13, 890–900. doi: 10.1101/gad.13.7.890

Truglio, J. J., Croteau, D. L., Van Houten, B., and Kisker, C. (2006). Prokaryotic nucleotide excision repair: The UvrABC system. *Chem. Rev.* 106, 233–252. doi: 10.1021/cr040471u

Tuteja, N., Singh, M. B., Misra, M. K., Bhalla, P. L., and Tuteja, R. (2001). Molecular mechanisms of DNA damage and repair: Progress in plants. *Crit. Rev. Biochem. Mol. Biol.* 36, 337–397. doi: 10.1080/20014091074219

UniProt Consortium (2023). UniProt: The universal protein knowledgebase in 2023. *Nucleic Acids Res.* 251, D523–D531. doi: 10.1093/nar/gkac1052

Wang, J., Li, W., Wang, H., and Lu, C. (2018). Pentaketide ansamycin microansamycins A-I from Micromonospora sp. Reveal Diverse Post-PKS modifications. *Org. Lett.* 20, 1058–1061. doi: 10.1021/acs.orglett.7b04018

Wei, L., Ouyang, S., Wang, Y., Shen, X., and Zhang, L. (2014). Solirubrobacter phytolaccae sp. nov., an endophytic bacterium isolated from roots of Phytolacca acinosa Roxb. *Int. J. Syst. Evol. Microbiol.* 64, 858–862. doi: 10.1099/ijs.0.057554-0

Xie, S. S., Wu, H. J., Zang, H. Y., Wu, L. M., Zhu, Q. Q., and Gao, X. W. (2014). Plant growth promotion by spermidine-producing *Bacillus subtilis* OKB105. *Mol. Plant Microbe Interact.* 27, 655–663. doi: 10.1094/MPMI-01-14-0010-R

Xie, Y., Wu, G., Tang, J., Luo, R., Patterson, J., Liu, S., et al. (2014). SOAPdenovo-Trans: De novo transcriptome assembly with short RNA-Seq reads. *Bioinformatics* 30, 1660–1666. doi: 10.1093/bioinformatics/btu077

Xu, P., Li, W. J., Tang, S. K., Zhang, Y. Q., Chen, G. Z., Chen, H. H., et al. (2005). Naxibacter alkalitolerans gen. nov., sp. nov., a novel member of the family 'Oxalobacteraceae' isolated from China. *Int. J. Syst. Evol. Microbiol.* 55, 1149–1153. doi: 10.1099/ijs.0.63407-0

Xue, H. P., Zhang, D. F., Xu, L., Wang, X. N., Zhang, A. H., Huang, J. K., et al. (2021). *Actirhodobacter atriluteus* gen. nov., sp. nov., isolated from the surface water of the Yellow Sea. *Antonie Van Leeuwenhoek* 114, 1059–1068. doi: 10.1007/s10482-021-01576-w

Yoon, S. H., Ha, S. M., Kwon, S., Lim, J., Kim, Y., Seo, H., et al. (2017). Introducing EzBioCloud: A taxonomically united database of 16S rRNA gene sequences and whole-genome assemblies. *Int. J. Syst. Evol. Microbiol.* 67, 1613–1617. doi: 10.1099/ijsem.0.001755

Yoshida, K., Yamaguchi, H., Kinehara, M., Ohki, Y. H., Nakaura, Y., and Fujita, Y. (2003). Identification of additional TnrA-regulated genes of *Bacillus subtilis* associated with a TnrA box. *Mol. Microbiol.* 49, 157–165. doi: 10.1046/j.1365-2958.2003.03567.x

Zhang, B. L., Wu, X. K., Tai, X. S., Sun, L. K., Wu, M. H., Zhang, W., et al. (2019). Variation in actinobacterial community composition and potential function in different soil ecosystems belonging to the arid heihe river basin of Northwest China. *Front. Microbiol.* 10:2209. doi: 10.3389/fmicb.2019.02209

Zhang, J., Qian, Z., Wu, X., Ding, Y., Li, J., Lu, C., et al. (2014). Juanlimycins A and B, ansamycin macrodilactams from Streptomyces sp. *Org. Lett.* 16, 2752–2755. doi: 10.1021/ol501072t

Zhang, L., Zhu, L., Si, M., Li, C., Zhao, L., Wei, Y., et al. (2014). Solirubrobacter taibaiensis sp. nov., isolated from a stem of Phytolacca acinosa Roxb. *Antonie Van Leeuwenhoek* 106, 279–285. doi: 10.1007/s10482-014-0194-4

Zhang, Y. Q., Sun, C. H., Li, W. J., Yu, L. Y., Zhou, J. Q., Zhang, Y. Q., et al. (2007). Deinococcus yunweiensis sp. nov., a gamma- and UV-radiation-resistant bacterium from China. *Int. J. Syst. Evol. Microbiol.* 57, 370–375. doi: 10.1099/ijs.0.64292-0

Zhou, J., Zhang, J., Li, J., Guan, Y., Shen, T., Li, F., et al. (2021). Ginsenoside F2 suppresses adipogenesis in 3T3-L1 cells and obesity in mice via the AMPK Pathway. *J. Agric. Food. Chem.* 69, 9299–9312. doi: 10.1021/acs.jafc.1c03420

Frontiers in Microbiology

Explores the habitable world and the potential of microbial life

The largest and most cited microbiology journal which advances our understanding of the role microbes play in addressing global challenges such as healthcare, food security, and climate change.

Discover the latest Research Topics

See more →

Frontiers

Avenue du Tribunal-Fédéral 34
1005 Lausanne, Switzerland
frontiersin.org

Contact us

+41 (0)21 510 17 00
frontiersin.org/about/contact